OCRWM	MODEL COVER SHEET	1. QA: QA Page 1 of 362

DOC.20030804.0004

2. Type of Mathematical Model

☒ Process Model ☐ Abstraction Model ☐ System Model

Describe Intended Use of Model

This Model Report documents the THC Seepage Model and the DST THC Model. The THC Seepage Model is a drift-scale process model for predicting the composition of gas and water that could enter waste-emplacement drifts and the effects of mineral alteration on flow in rocks surrounding drifts. The Drift Scale Test (DST) THC model is a drift-scale process model relying on the same conceptual model and much of the same input data (i.e., physical, hydrological, thermodynamic, and kinetic) as the THC Seepage Model. The DST THC Model is the primary method for validating the THC Seepage Model by comparing predicted water and gas compositions, as well as mineral alteration patterns, with observed data from the Drift Scale Test. These models provide the framework to evaluate THC coupled processes at the drift scale, predict flow and transport behavior for specified thermal-loading conditions, and predict the evolution of mineral alteration and fluid chemistry around potential waste emplacement drifts. The DST THC Model is used solely for the validation of the THC Seepage Model and it is not used for calibration to measured data.

3. Title

Drift-Scale Coupled Processes (DST and THC Seepage) Models

4. DI (including Rev. No. and Change No., if applicable):

MDL-NBS-HS-000001 REV 02

5. Total Attachments	6. Attachment Numbers - No. of Pages in Each
11	I-2, II-4, III-2, IV-4, V-2, VI-4, VII-4, VIII-4, IX-4, X-8, XI-2

	Printed Name	Signature	Date
7. Originator	N. Spycher	SIGNATURE ON FILE	7/29/03
8. CSO	M. Zhu	SIGNATURE ON FILE	07/29/03
9. Checker	R.A. Wagner	SIGNATURE ON FILE	29 Jul 03
10. QER	S. Harris	SIGNATURE ON FILE	7-30-03
11. Responsible Manager/Lead	J.S.Y. Wang/Y. Tsang	SIGNATURE ON FILE	7-30-03
12. Responsible Manager	P. Dixon	SIGNATURE ON FILE	7-30-03

13. Remarks

Block 7. E.L. Sonnenthal contributed to all Sections; P.F. Dobson contributed to Sections 7.2 and 7.3; J. Apps and S. Salah contributed to Section 4; T. Kneafsey contributed to Sections 7.2 and 7.3; C.B. Haukwa contributed to Section 6.6; and C. Valladao contributed to Section 9.

Block 9. P. Persoff is the additional checker for Sections 1-5. SIGNATURE ON FILE 7/29/03

Technical review on REV 02A-Draft1 per YMP-LBNL-QIP-6.1 performed by: Y. Tsang (Sections 1-3, and 8), P. Dobson (Section 4), T. Xu (Sections 5, 6, and 6.1-6.4), G. Zhang (Sections 6.5–6.8, 7, and 7.1), J. Apps (Sections 7.2 and 7.3), C. Guay (Attachments).
Second independent technical review on REV 02A-Draft3 performed by J. Apps on entire Model Report.

Technical Error Report (TER) log number addressed in this Model Report
TER-02-0077

OFFICE OF CIVILIAN RADIOACTIVE WASTE MANAGEMENT
MODEL REVISION RECORD

2. Model Title:
Drift-Scale Coupled Processes (DST and THC Seepage) Models

3. DI (including Rev. No. and Change No., if applicable):
MDL-NBS-HS-000001 REV 02

4. Revision/Change No.	5. Description of Revision/Change
REV00	Initial Issue
REV01	Incorporated additional data from DST for model validation. Incorporated sensitivity studies, including effect of backfill versus no backfill. Additional Models/Updates: REV01 DST THC Model; Tptpmn THC No-Backfill Model; Tptpmn THC Heterogeneous Model; Tptpll THC Model; Plug-Flow Reactor Model Validation
REV01/ICN 01	Incorporated minor editorial changes to text and references. Incorporated additional figure (Figure 32b). Incorporated auditor's recommendations (Audit M&O-ARP-01-02). All changes are marked by a black vertical line on the margin of the affected page.
REV01/ICN02	-Removed incorrect reference DTN: MO0008THRMODYN.000 [153742], inserted correct reference DTN: MO0009THRMODYN.001 [152576] (this impacted sections 4, 8.3 and attachments V and VI). -Made editorial correction in section 5.A.7. -Added assumption 20 to section 5.A, to identify DTN: LA0008SC12213N.001 [153386] as data that augments DTN: MO0009THRMODYN.001 [152576]. -Revised three assumptions to indicate no further confirmation is required as the assumptions were adequately justified (C-1, C-4, and C-6). Revision of assumptions resulted in the removal of TBVs 5028, 5029, and 5030 in the Document Input Reference System (DIRS). -Updated section 8.3 to remove URNs where appropriate. -Changes to data status made in DIRS. -The following sections were revised in REV 01 ICN 02: Section 1 (p. 23), 2 (p. 27), 3 (p. 30), 4 (pp. 33, 37-38, 42), 5 (pp. 50, 53, 55), 6 (p. 107), 7 (p. 225), 8 (pp. 228-229, 235-240), Att. V (p. V-3), and VI (p. VI-3)
REV 02	Entire model documentation was revised. Side bars are not used because the changes were too extensive to use Step 5.9d)1) per AP-SIII.10Q/Rev.1/ICN 2.

CONTENTS

ACRONYMS 21

CHEMICAL ABBREVIATIONS 27

1. PURPOSE 29
   1.1 Background 29
   1.2 Overview of Models 30
   1.3 Model Limitations 31

2. QUALITY ASSURANCE 33

3. USE OF SOFTWARE 35

4. INPUTS 37
   4.1 DATA AND PARAMETERS 37
      4.1.1 Hydrological and Thermal Properties 37
      4.1.2 Mineralogical Data 37
      4.1.3 Water and Gas Chemistry 39
      4.1.4 Thermodynamic Data 41
      4.1.5 Kinetic Data 42
      4.1.6 Transport Parameters 45
      4.1.7 Design Information 45
   4.2 CRITERIA 49
   4.3 CODES AND STANDARDS 53

5. ASSUMPTIONS 55

6. MODEL DISCUSSION 57
   6.1 Relevant Features, Events, and Processes 60
   6.2 Conceptual Model 64
      6.2.1 Conceptualization of Coupled THC Processes 64
         6.2.1.1 TH Processes 65
         6.2.1.2 THC Processes 66
         6.2.1.3 Effects of Infiltration and Climate Changes on THC Processes 68
         6.2.1.4 Hydrological Property Changes in Fractures and Matrix 68
         6.2.1.5 Dual-Permeability Model for THC Processes 68
      6.2.2 Conceptualization of the Chemical System 69
         6.2.2.1 Initial Pore-Water and Pore-Gas Chemistry 70
         6.2.2.2 Geochemical Systems 77
      6.2.3 Conceptualization of the Model Domain 78
   6.3 Alternative COnceptual ModeLs 79
   6.4 Mathematical Model 80
      6.4.1 General Numerical Model for Coupled THC Processes 80
      6.4.2 Kinetic Rate Laws 83

CONTENTS (continued)

6.4.3 Fracture and Matrix Mineral Reactive Surface Areas 84
6.4.3.1 Fracture Mineral Reactive Surface Areas 84
6.4.3.2 Matrix Mineral Reactive Surface Areas 86
6.4.4 Effects of Mineral Precipitation/Dissolution on Hydrological Properties.....87
6.4.4.1 Porosity Changes 87
6.4.4.2 Fracture Permeability Changes 87
6.4.4.3 Matrix Permeability Changes 88
6.4.4.4 Effects of Permeability and Porosity Changes on Capillary Pressures 89
6.4.5 Mineral Precipitation in Dry Gridblocks 89
6.4.6 Principal Model Approximations and Approaches.....90
6.4.6.1. General Approximations in the Modeling of THC Processes 90
6.4.6.2 Approximations Specific to the THC Seepage Model.....94
6.4.7 Summary of Hydrological and Thermal Properties 95
6.4.8 Sources of Additional Model Inputs Used in Sensitivity Analyses.....95
6.4.8.1 Sensitivity to Historical (REV01) Model Inputs 95
6.4.8.2 Thermodynamic Data Sensitivity (REV02).....96
6.5 TPTPMN THC Model REV01 102
6.5.1 Numerical Mesh.....103
6.5.2 Boundary Conditions 107
6.5.3 Input Data and Modeling Procedure 108
6.5.4 Model Runs.....109
6.5.5 Simulation Results 110
6.5.5.1 Thermal-Hydrological Simulation Results 110
6.5.5.2 THC Simulation Results 116
6.6 TPTPMN THC Heterogeneous Model REV01 131
6.6.1 Model Set-Up.....132
6.6.1.1 Heterogeneous Fracture-Permeability Realizations.....132
6.6.1.2 Model Runs.....133
6.6.2 Simulation Results 134
6.6.2.1 Hydrological Effects of Fracture Permeability Heterogeneity 134
6.6.2.2 Thermal-Hydrological Effects of Fracture Permeability Heterogeneity.....135
6.6.2.3 THC Effects of Fracture Permeability Heterogeneity 136
6.7 TPTPLL THC Model REV01.....147
6.7.1 Numerical Mesh (Tptpll) 147
6.7.2 Boundary Conditions 150
6.7.3 Input Data and Modeling Procedure 150
6.7.4 Model Runs.....152
6.7.5 Simulation Results 152
6.7.5.1 Thermohydrology Simulation Results (Tptpll versus Tptpmn).....152
6.7.5.2 THC Simulation Results (Tptpll REV01).....159

CONTENTS (continued)

6.8 TPTPLL THC Model REV02 175
6.8.1 Numerical Mesh (Tptpll) 176
6.8.2 Boundary Conditions 176
6.8.3 Input Data and Modeling Procedure 178
6.8.4 Model Runs 179
6.8.5 Simulation Results (Tptpll THC Model REV02) 180
6.8.5.1 Simulations of Ambient Conditions (Thermodynamic Data Sensitivity) 180
6.8.5.2 TH Results (No Chemical Reactions) 185
6.8.5.3 Water Chemistry Trends 192
6.8.5.4 Mineral Alteration and Porosity/Permeability Changes (Tptpll REV02) 229
6.9 Model Uncertainty 239
6.9.1 Potential Sources of Uncertainty 239
6.9.2 Evaluation of Model Result Uncertainty 240

7. VALIDATION 247
7.1 THE DRIFT SCALE TEST THC MODEL 248
7.1.1 Modeling Approach 249
7.1.2 Drift Scale Test 2-D Numerical Grid 250
7.1.3 Heater Power 250
7.1.4 Hydrological and Geochemical Input Data 255
7.1.5 Initial and Boundary Conditions: Hydrological and Thermal 255
7.1.6 Initial and Boundary Conditions: Geochemical 256
7.1.7 Model Validation Methods, Criteria, and Limitations 256
7.1.7.1 Validation Method 1—Corroboration with Experimental Data 257
7.1.7.2 Validation Method 3—Corroboration with Refereed Journals or Literature 258
7.1.8 THC Simulations 260
7.1.8.1 REV01 Simulations 260
7.1.8.2 REV02 Updates and Simulations 260
7.1.9 Simulation Results: Thermal and Hydrological Evolution 261
7.1.10 Gas-Phase CO_2 Evolution: Measured Compositions and Simulation Results 266
7.1.10.1 Gas Sampling and CO_2 Measurements 266
7.1.10.2 Modeled Spatial Distribution of CO_2 267
7.1.10.3 Modeled and Measured CO_2 Concentrations Over Time 270
7.1.11 Aqueous Species Evolution 276
7.1.11.1 Chemistry of Waters Sampled during the Drift Scale Test 276
7.1.11.2 Evolution in the pH of Waters from the DST 283
7.1.11.3 Evolution of Anion and Cation Concentrations 289
7.1.12 Mineralogical Changes 312
7.1.13 Porosity and Permeability Changes 317

CONTENTS (continued)

7.1.14 Isotopic Compositions of Gases and Water: Model Corroboration Using ^{14}C in CO_2 319
7.2 Simulation of Plug-Flow Reactor Experiment....323
7.2.1 Validation Criteria 328
7.2.2 Results of Simulations and Comparison to Measured Data....328
7.3 Simulation of Fracture Sealing Experiment....330
7.3.1 Validation Criteria 335
7.3.2 Results of Simulations and Comparison to Measured Data....335

8. CONCLUSIONS....337
8.1 Modeled Coupled Processes and Uncertainty 337
8.2 THC Seepage Model Results....340
8.3 DST THC Model Results (Validation) 342
8.4 Uncertainties and Restrictions for Downstream Use 343

9. INPUTS AND REFERENCES....345
9.1 Documents Cited....345
9.2 Codes, Standards, Regulations, and Procedures 355
9.3 Source Data, Listed by Data Tracking Number....356
9.4 Output Data, Listed by Data Tracking Number....360

ATTACHMENT I – MINERAL INITIAL VOLUME FRACTIONS: Tptpmn THC Model REV01, Tptpmn THC Heterogeneous Model REV01 and DST THC Model REV01 ....I-1
ATTACHMENT II – MINERAL INITIAL VOLUME FRACTIONS: Tptpll THC Models (REV01 and REV02) and DST THC Model REV02 .... II-1
ATTACHMENT III – MINERAL REACTIVE SURFACE AREAS: Tptpmn THC Model REV01, Tptpmn THC Heterogeneous Model REV01 and DST THC Model REV01 .... III-1
ATTACHMENT IV – MINERAL REACTIVE SURFACE AREAS: Tptpll THC Models (REV01 and REV02) and DST THC Model REV02 ....IV-1
ATTACHMENT V – THERMODYNAMIC DATABASE: REV01 THC Models.... V-1
ATTACHMENT VI – THERMODYNAMIC DATABASE: REV02 THC Models VI-1
ATTACHMENT VII – WASTE PACKAGE AVERAGE HEAT TRANSFER: REV01 THC Seepage Models VII-1
ATTACHMENT VIII – WASTE PACKAGE AVERAGE HEAT TRANSFER: Tptpll THC Model REV02 .... VIII-1
ATTACHMENT IX – EFFECTIVE THERMAL CONDUCTIVITY FOR IN-DRIFT OPEN SPACES: Tptpmn and Tptpll THC Models IX-1
ATTACHMENT X – LIST OF MODEL INPUT AND OUTPUT FILES X-1
ATTACHMENT XI – REV02 Parameters for Fracture Permeability Modification....XI-1

LIST OF FIGURES

4.1-1. Sketch Corresponding to In-Drift Design Information for Drift-Scale Models for TSPA-SR 48
6.2-1. Schematic Diagram of THC Processes around a Heated Drift 66
6.2-2. Schematic Diagram of Fracture-Matrix Interface, Showing the Relation Between TH Processes and Geochemical Processes 67
6.2-3. Conceptual Model (Schematic) for Reaction-Transport Processes in Dual-Permeability Media 69
6.2-4. Piper Plot of Water Compositions (meq/L) from Repository Units 74
6.5-1. Tptpmn THC Model Mesh with Hydrogeologic Units Shown in the Vicinity of the Drift: Topopah Spring Tuff Upper Lithophysal (tsw33-circles), Middle Nonlithophysal (tsw34-dots), and Lower Lithophysal (tsw35-diamonds) Units 104
6.5-2. Discretization of the Repository Drift—Tptpmn THC Model 106
6.5-3. TH Simulation (Tptpmn Model): Time Profiles of Modeled Temperatures and Liquid Saturations in Fractures and Matrix at Three Drift-Wall Locations and in the Waste Package 112
6.5-4. TH Simulation (Tptpmn Model): Contour Plot of Modeled Temperatures (°C) and Liquid Saturations in the Matrix at 600 Years (Near Maximum Dryout—Mean Infiltration) 113
6.5-5. TH Simulation (Tptpmn Model): Contour Plot of Modeled Temperatures (°C) and Liquid Saturations in Fractures at 600 Years (near Maximum Dryout—Mean Infiltration) 114
6.5-6. TH Simulation (Tptpmn Model): Time Profiles of Modeled Air Mass Fractions in the Gas Phase in Fractures and Matrix at Three Drift-Wall Locations 115
6.5-7. TH Simulation (Tptpmn Model: Time Profiles of Modeled Water Flux at the Drift Crown (positive downward) 116
6.5-8. THC Simulation (Tptpmn Model): Time Profiles of Modeled CO_2 Concentrations in the Gas Phase in Fractures at Three Drift-Wall Locations under Heating (Heat) and Non-Heating (Ambient) Conditions for the Extended (E) and Base-Case (B) Geochemical Systems 119
6.5-9. THC Simulation (Tptpmn Model): Time Profiles of the Modeled pH of Fracture Water at Three Drift-Wall Locations under Heating (Heat) and Non-Heating (Ambient) Conditions for the Extended (E) and Base-Case (B) Geochemical Systems 120
6.5-10. THC Simulation (Tptpmn Model): Time Profiles of Modeled Total Aqueous Carbonate Concentrations (as HCO_3^-) in Fracture Water at Three Drift-Wall Locations under Heating (Heat) and Non-Heating (Ambient) Conditions for Extended (E) and Base-Case (B) Geochemical Systems 121
6.5-11. THC Simulation (Tptpmn Model): Time Profiles of Modeled Total Aqueous Calcium Concentrations in Fracture Water at Three Drift-Wall Locations under Heating (Heat) and Non-Heating (Ambient) Conditions for Extended (E) and Base-Case (B) Geochemical Systems 122

LIST OF FIGURES (Continued)

6.5-12. THC Simulation (Tptpmn Model): Time Profiles of Modeled Total Aqueous Sodium Concentrations in Fracture Water at Three Drift-Wall Locations under Heating (Heat) and Non-Heating (Ambient) Conditions for Extended (E) and Base-Case (B) Geochemical Systems 123

6.5-13. THC Simulation (Tptpmn Model): Time Profiles of Modeled Total Aqueous Silica Concentrations in Fracture Water at Three Drift-Wall Locations under Heating (Heat) and Non-Heating (Ambient) Conditions for Extended (E) and Base-Case (B) Geochemical Systems 124

6.5-14. THC Simulation (Tptpmn Model): Time Profiles of Modeled Total Aqueous Chloride Concentrations in Fracture Water at Three Drift-Wall Locations under Heating (Heat) and Non-Heating (Ambient) Conditions for Extended (E) and Base-Case (B) Geochemical Systems 125

6.5-15. THC Simulation (Tptpmn Model): Time Profiles of Modeled Total Fluoride Concentrations in Fracture Water at Three Drift-Wall Locations under Heating (Heat) and Non-Heating (Ambient) Conditions for Extended (E) and Base-Case (B) Geochemical Systems 126

6.5-16. THC Simulation (Tptpmn Model): Contour Plot of Modeled Fracture Porosity Change at 10,000 Years for (a) Base-Case and (b) Extended Geochemical Systems 128

6.5-17. TH and THC Simulations (Tptpmn Model): Comparison of Modeled Liquid Saturations in Fractures at Three Drift-Wall Locations under Heating (Heat) and Non-Heating (Ambient) Conditions for the Extended (E) and Base-Case (B) Geochemical Systems, and for the TH Simulation 129

6.5-18. TH and THC Simulations (Tptpmn Model): Comparison of Modeled Liquid Flux at the Drift Crown in Fractures under Heating (Heat) and Non-Heating (Ambient) Conditions for the Extended (E) and Base-Case (B) Geochemical Systems, and for the TH Simulation 130

6.6-1. Fracture-Permeability Realizations #1 (a), #2 (b), and #3 (c) 133

6.6-2. Steady-State Fracture Liquid Saturations (Infiltration Rate = 6 mm/yr) for Permeability Realizations #1 (a), #2 (b), and #3 (c) 135

6.6-3. Fracture Liquid Saturations at 600 Years from Thermal-hydrological Simulations (Infiltration Rate = 6 mm/yr) for Permeability Realizations #1 (a), #2 (b), and #3 (c) (with temperature contours shown in °C) 136

6.6-4. Fracture Permeability Ratio after 20,000 Years for Realization #1: (a) Extended and (b) Base-Case Geochemical Systems 138

6.6-5. Fracture Liquid Saturation for Realization #1: THC Simulation (Extended Case) after 20,000 Years 139

6.6-6. Amorphous Silica Changes (Volume %) in Fractures after 20,000 Years for Realization #1: (a) Extended and (b) Base-Case Geochemical Systems 141

6.6-7. Calcite Changes (Volume %) in Fractures after 20,000 Years for Realization #1: (a) Extended and (b) Base-Case Geochemical Systems 142

LIST OF FIGURES (Continued)

6.6-8. Illite Changes (Volume %) in Fractures after 20,000 Years for Realization #1: (a) Extended Geochemical System—Permeability Realization #1 and (b) Extended Geochemical System—Initially Homogeneous Tptpmn 143

6.6-9. Fracture Water pH after 600 Years (white area is dry): (a) Extended Geochemical System—Permeability Realization #1; (b) Extended Geochemical System—Initially Homogeneous Tptpmn; (c) Base-Case Geochemical System—Permeability Realization #1 144

6.6-10. Fracture Water pH after 1,400 Years (white area surrounding drift is dry): (a) Extended Geochemical System—Permeability Realization #1; (b) Extended Geochemical System—Initially Homogeneous Tptpmn; (c) Base-Case Geochemical System—Permeability Realization #1 144

6.6-11. Chloride (Cl) Concentrations in Fracture Water after 600 Years: (a) Extended Geochemical System—Permeability Realization #1 and (b) Extended Geochemical System—Initially Homogeneous Tptpmn 145

6.6-12. Fluoride (F^-) Concentrations in Fracture Water after 600 Years: (a) Extended Geochemical System—Permeability Realization #1 and (b) Extended Geochemical System—Initially Homogeneous Tptpmn 146

6.7-1. Tptpll THC Model Mesh with Hydrogeologic Units Shown in the Vicinity of the Drift: Topopah Spring Tuff Middle Nonlithophysal (tsw34—triangles), Lower Lithophysal (tsw35—dots), and Lower Nonlithophysal (tsw36—diamonds) Units 148

6.7-2. Discretization of the Repository Drift in the Tptpll THC Model 150

6.7-3. TH Simulation (Tptpll): Time Profiles of Modeled Temperatures in Fractures (Similar in Matrix) at Three Drift-Wall Locations and in the Waste Package 153

6.7-4. TH Simulation (Tptpll): Contour Plot of Modeled Temperatures (°C) and Liquid Saturations in the Matrix at 600 Years (Near Maximum Dryout-Mean Infiltration) 154

6.7-5. TH Simulation (Tptpll vs. Tptpmn): Time Profiles of Modeled Temperatures in Fractures at Three Drift-Wall Locations 155

6.7-6. TH Simulation (Tptpll vs. Tptpmn): Time Profiles of Modeled Liquid Saturations in Fractures at Three Drift-Wall Locations 156

6.7-7. TH Simulation (Tptpll vs. Tptpmn): Time Profiles of Modeled Liquid Saturations in Matrix at Three Drift-Wall Locations 157

6.7-8. TH Simulation (Tptpll vs. Tptpmn): Time Profiles of Modeled Air Mass Fractions in the Gas Phase in Fractures at Three Drift-Wall Locations 158

6.7-9. TH Simulation (Tptpll vs. Tptpmn): Time Profiles of Modeled Water Flux at the Drift Crown 159

6.7-10. THC Simulation (Tptpll): Time Profiles of Modeled CO_2 Concentrations in the Gas Phase in Fractures at Three Drift-wall Locations under Heating (Heat) and Non-Heating (Ambient) Conditions for the Extended (E) and Base-Case (B) Geochemical Systems 161

LIST OF FIGURES (Continued)

6.7-11. THC Simulation (Tptpll): Time Profiles of the Modeled pH of Fracture Water at Three Drift-Wall Locations under Heating (Heat) and Non-Heating (Ambient) Conditions for the Extended-Case (E) and Base-Case (B) Geochemical Systems.....162

6.7-12. THC Simulation (Tptpll): Time Profiles of Modeled Total Aqueous Carbonate Concentrations (as HCO_3^-) in Fracture Water at Three Drift-Wall Locations under Heating (Heat) and Non-Heating (Ambient) Conditions for the Extended (E) and Base-Case (B) Geochemical Systems.....163

6.7-13. THC Simulation (Tptpll): Time Profiles of Modeled Total Aqueous Calcium Concentrations in Fracture Water at Three Drift-Wall Locations under Heating (Heat) and Non-Heating (Ambient) Conditions for the Extended (E) and Base-Case (B) Geochemical Systems.....164

6.7-14. THC Simulation (Tptpll): Time Profiles of Modeled Total Aqueous Sodium Concentrations in Fracture Water at Three Drift-Wall Locations under Heating (Heat) and Non-Heating (Ambient) Conditions for the Extended (E) and Base-Case (B) Geochemical Systems.....165

6.7-15. THC Simulation (Tptpll): Time Profiles of Modeled Total Aqueous Silica Concentrations in Fracture Water at Three Drift-Wall Locations under Heating (Heat) and Non-Heating (Ambient) Conditions for the Extended (E) and Base-Case (B) Geochemical Systems.....166

6.7-16. THC Simulation (Tptpll): Time Profiles of Modeled Total Aqueous Chloride Concentrations in Fracture Water at Three Drift-Wall Locations under Heating (Heat) and Non-Heating (Ambient) Conditions for the Extended (E) and Base-Case (B) Geochemical Systems.....167

6.7-17. THC Simulation (Tptpll): Time Profiles of Modeled Total Fluoride Concentrations in Fracture Water at Three Drift-Wall Locations under Heating (Heat) and Non-Heating (Ambient) Conditions for the Extended (E) and Base-Case (B) Geochemical Systems.....168

6.7-18. THC Simulation (Tptpll): Contour Plot of Modeled Fracture Porosity Change at 10,000 Years for (a) Base-Case Geochemical System and (b) Extended-Case System.....170

6.7-19. THC Simulation (Tptpll): Contour Plot of Modeled Fracture Porosity Change at 20,000 Years for (a) Base-Case Geochemical System and (b) Extended-Case System.....170

6.7-20. THC Simulation (Tptpll): Contour Plot of Modeled Fracture Porosity Change at 100,000 Years for (a) Base-Case Geochemical System and (b) Extended-Case System.....171

6.7-21. THC Simulation (Tptpll): Contour Plot of Modeled Volume Fraction Change Due to Illite Precipitation in Fractures at 20,000 Years 171

6.7-22. THC Simulation (Tptpll): Contour Plot of Modeled Volume Fraction Change Due to Stellerite (Ca-Zeolite) Precipitation in Fractures at (a) 1,200 Years (Some Precipitation below the Drift) and (b) at 20,000 Years (Dissolution).....172

LIST OF FIGURES (Continued)

6.7-23. TH and THC Simulations (Tptpll): Comparison of Modeled Liquid Saturations in Fractures at Three Drift-Wall Locations under Heating (Heat) and Non-Heating (Ambient) Conditions for the Extended-Case (E) and Base-Case (B) Geochemical Systems 173

6.7-24. TH and THC Simulations (Tptpll): Comparison of Modeled Liquid Flux at the Drift Crown in Fractures under Heating (Heat) and Non-Heating (Ambient) Conditions for the Extended-Case (E) and Base-Case (B) Geochemical Systems, and without Chemical Reactions (TH) 174

6.8-1. Predicted Water Compositions without Thermal Loading (in the Tptpll Lithostratigraphic Unit at the Repository Location) Using the Thermodynamic Data Adopted for This Study (Data Set 1—Attachment VI) 182

6.8-2. Predicted Water Compositions without Thermal Loading (in the Tptpll Lithostratigraphic Unit at the Repository Location) Using Thermodynamic Data from Data Set 2 (Section 6.4.8.2) 183

6.8-3. Predicted Water Compositions without Thermal Loading (in the Tptpll Lithostratigraphic Unit at the Repository Location) Using Thermodynamic Data from Data Set 3 (Section 6.4.8.2) 184

6.8-4. TH Simulation (Tptpll, REV02): Time Profiles of Modeled Temperatures in Fractures (Similar in Matrix) at Three Drift-Wall Locations and in the Waste Package 186

6.8-5. TH Simulation (Tptpll, REV01 vs. REV02): Time Profiles of Modeled Temperatures in Fractures at Three Drift-Wall Locations 187

6.8-6. TH Simulation (Tptpll, REV02): Contour Plot of Modeled Temperatures (°C) and Liquid Saturations in the Matrix and Fractures at 600 Years (Near the Time of Maximum Dryout in Fractures) 188

6.8-7. TH Simulation (Tptpll, REV01 vs. REV02): Time Profiles of Modeled Liquid Saturations in Fractures at Three Drift-Wall Locations 189

6.8-8. TH Simulation (Tptpll, REV01 vs. REV02): Time Profiles of Modeled Liquid Saturations in Matrix at Three Drift-Wall Locations 190

6.8-9. TH Simulation (Tptpll, REV01 vs. REV02): Time Profiles of Modeled Air Mass Fractions in the Gas Phase in Fractures at Three Drift-Wall Locations 191

6.8-10. TH Simulation (Tptpll, REV01 vs. REV02): Time Profiles of Modeled Water Flux at the Drift Crown 192

6.8-11. THC Simulation (Tptpll, REV01 vs. REV02): Time Profiles of Modeled Temperatures at Three Drift-Wall Locations With and Without Water-Vapor-Pressure Lowering (eos4 and eos3, respectively) 195

6.8-12. THC Simulation (Tptpll, REV01 vs. REV02): Time Profiles of Modeled CO_2 Concentrations in the Gas Phase in Fractures at Three Drift-wall Locations under Heating (Heat) and Non-Heating (Ambient) Conditions, Including (eos4) and Excluding (eos3) Water-Vapor-Pressure Lowering 196

LIST OF FIGURES (Continued)

6.8-13. THC Simulation (Tptpll, REV01 vs. REV02): Time Profiles of the Modeled pH of Fracture Water at Three Drift-Wall Locations under Heating (Heat) and Non-Heating (Ambient) Conditions, Including (eos4) and Excluding (eos3) Water-Vapor-Pressure Lowering 197

6.8-14. THC Simulation (Tptpll, REV01 vs. REV02): Time Profiles of Modeled Total Aqueous Carbonate Concentrations (as HCO_3^-) in Fracture Water at Three Drift-Wall Locations, under Heating (Heat) and Non-Heating (Ambient) Conditions, Including (eos4) and Excluding (eos3) Water-Vapor-Pressure Lowering 198

6.8-15. THC Simulation (Tptpll, REV01 vs. REV02): Time Profiles of Modeled Total Aqueous Calcium Concentrations in Fracture Water at Three Drift-Wall Locations, under Heating (Heat) and Non-Heating (Ambient) Conditions, Including (eos4) and Excluding (eos3) Water-Vapor-Pressure Lowering 199

6.8-16. THC Simulation (Tptpll, REV01 vs. REV02): Time Profiles of Modeled Total Aqueous Sodium Concentrations in Fracture Water at Three Drift-Wall Locations, under Heating (Heat) and Non-Heating (Ambient) Conditions, Including (eos4) and Excluding (eos3) Water-Vapor-Pressure Lowering 200

6.8-17. THC Simulation (Tptpll, REV01 vs. REV02): Time Profiles of Modeled Total Aqueous Silica Concentrations in Fracture Water at Three Drift-Wall Locations, under Heating (Heat) and Non-Heating (Ambient) Conditions, Including (eos4) and Excluding (eos3) Water-Vapor-Pressure Lowering 201

6.8-18. THC Simulation (Tptpll, REV01 vs. REV02): Time Profiles of Modeled Total Aqueous Chloride Concentrations in Fracture Water at Three Drift-Wall Locations, under Heating (Heat) and Non-Heating (Ambient) Conditions, Including (eos4) and Excluding (eos3) Water-Vapor-Pressure Lowering 202

6.8-19. THC Simulation (Tptpll, REV01 vs. REV02): Time Profiles of Modeled Total Fluoride Concentrations in Fracture Water at Three Drift-Wall Locations, under Heating (Heat) and Non-Heating (Ambient) Conditions, Including (eos4) and Excluding (eos3) Water-Vapor-Pressure Lowering 203

6.8-20. THC Simulation (Tptpll, REV01 vs. REV02): Time Profiles of Modeled Total Nitrate Concentrations in Fracture Water at Three Drift-Wall Locations, under Heating (Heat) and Non-Heating (Ambient) Conditions, Including (eos4) and Excluding (eos3) Water-Vapor-Pressure Lowering 204

6.8-21. THC Simulation (Tptpll, REV01 vs. REV02): Time Profiles of Modeled Total Nitrate to Chloride Ratio at Three Drift-Wall Locations, under Heating (Heat) and Non-Heating (Ambient) Conditions, Including (eos4) and Excluding (eos3) Water-Vapor-Pressure Lowering 205

6.8-22. THC Simulations (Tptpll Model REV02): Location of Model Gridblocks for Data Shown on Figures 6.8-23–6.8-38, for Each Time When Model Output Is Produced 212

LIST OF FIGURES (Continued)

6.8-23. THC Simulations (Tptpll Model REV02): Time Profiles of Modeled Temperatures in Fracture Water, in Areas of Highest Liquid Saturation above the Drift Crown 213
6.8-24. THC Simulations (Tptpll Model REV02): Time Profiles of Modeled Liquid Saturations in Fracture Water, in Areas of Highest Liquid Saturation above the Drift Crown 214
6.8-25. THC Simulations (Tptpll Model REV02): Time Profiles of Modeled CO_2 Gas Concentrations in Fracture Water, in Areas of Highest Liquid Saturation above the Drift Crown 215
6.8-26. THC Simulations (Tptpll Model REV02): Time Profiles of Modeled pH in Fracture Water, in Areas of Highest Liquid Saturation above the Drift Crown 216
6.8-27. THC Simulations (Tptpll Model REV02): Time Profiles of Modeled Total Aqueous Carbonate Concentrations (as HCO_3) in Fracture Water, in Areas of Highest Liquid Saturation above the Drift Crown 217
6.8-28. THC Simulations (Tptpll Model REV02): Time Profiles of Modeled Total Aqueous Chloride Concentrations in Fracture Water, in Areas of Highest Liquid Saturation above the Drift Crown 218
6.8-29. THC Simulations (Tptpll Model REV02): Time Profiles of Modeled Total Aqueous Nitrate Concentrations in Fracture Water, in Areas of Highest Liquid Saturation above the Drift Crown 219
6.8-30. THC Simulations (Tptpll Model REV02): Time Profiles of Modeled Total Aqueous Calcium Concentrations in Fracture Water, in Areas of Highest Liquid Saturation above the Drift Crown 220
6.8-31. THC Simulations (Tptpll Model REV02): Time Profiles of Modeled Total Aqueous Calcium to Chloride Ratios in Fracture Water, in Areas of Highest Liquid Saturation above the Drift Crown 221
6.8-32. THC Simulations (Tptpll Model REV02): Time Profiles of Modeled Total Aqueous Sodium Concentrations in Fracture Water, in Areas of Highest Liquid Saturation above the Drift Crown 222
6.8-33. THC Simulations (Tptpll Model REV02): Time Profiles of Modeled Total Aqueous Sodium to Chloride Ratios in Fracture Water, in Areas of Highest Liquid Saturation above the Drift Crown 223
6.8-34. THC Simulations (Tptpll Model REV02): Time Profiles of Modeled Total Aqueous Calcium to Carbonate Ratios in Fracture Water, in Areas of Highest Liquid Saturation above the Drift Crown 224
6.8-35. THC Simulations (Tptpll Model REV02): Time Profiles of Modeled Total Aqueous Nitrate to Chloride Ratios in Fracture Water, in Areas of Highest Liquid Saturation above the Drift Crown 225
6.8-36. THC Simulations (Tptpll Model REV02): Time Profiles of Modeled Total Aqueous Magnesium Concentrations in Fracture Water, in Areas of Highest Liquid Saturation above the Drift Crown 226

LIST OF FIGURES (Continued)

6.8-37. THC Simulations (Tptpll Model REV02): Time Profiles of Modeled Total Aqueous Silica Concentrations in Fracture Water, in Areas of Highest Liquid Saturation above the Drift Crown 227
6.8-38. THC Simulations (Tptpll Model REV02): Time Profiles of Modeled Total Aqueous Fluoride Concentrations in Fracture Water, in Areas of Highest Liquid Saturation above the Drift Crown 228
6.8-39. TH Simulation (Tptpll): Contour Plot of Modeled Liquid Saturation and Temperature Contours (°C) in Fractures at 2,400 Years (No Chemical Reactions) 231
6.8-40. THC Simulation (Tptpll—Water W0): Contour Plot of Modeled (a) Liquid Saturation and Temperature Contours (°C) and (b) Permeability Change in Fractures at 2,400 Years 232
6.8-41. THC Simulation (Tptpll—Water W5): Contour Plot of Modeled (a) Liquid Saturation and Temperature Contours (°C) and (b) Permeability Change in Fractures at 2,400 Years 233
6.8-42. TH and THC Simulations (Tptpll): Comparison of Modeled Liquid Flux at the Drift Crown in Fractures at 2,400 Years 234
6.8-43. THC Simulations (Tptpll): Vertical Profile of Predicted Mineral Abundances above the Drift Crown 235
6.8-44. THC Simulations (Tptpll): Vertical Profile of Predicted Mineral Abundances above the Drift Crown 236
6.8-45. THC Simulations (Tptpll): Vertical Profile of Predicted Mineral Abundances above the Drift Crown 237
6.8-46. THC Simulations (Tptpll): Vertical Profile of Predicted Mineral Abundances above the Drift Crown 238
7.1-1a. Three-Dimensional Schematic Diagram of the DST Showing Perspective View of Numerical Mesh for DST THC Model Simulations (Mesh Extends In All Directions from Area Shown) 252
7.1-1b. Numerical Mesh for DST THC Model Simulations 253
7.1-1c. Enlarged View of the Numerical Grid Showing the Locations of Gridblocks Representing the Heated Drift, Wing Heaters, and Concrete Invert 253
7.1-2. Locations of Hydrology Boreholes, Sampling Intervals (numbered) and Temperature Sensors 259
7.1-3. Drift Center and Drift Crown Modeled Temperatures over the First Six Years of the DST 264
7.1-4. Comparison of Modeled and Measured Temperatures over Time for the Sensor Located at Hydrology Borehole Packer 60-4 264
7.1-5. Liquid Saturation (Colors) and Temperature (Contour Lines) in the DST (Base Case) at One Year (Matrix – a, Fracture – b) and at Four Years (Matrix – c, Fracture – d) 265

LIST OF FIGURES (Continued)

7.1-6. Measured Concentrations of CO_2 (Log Volume Fraction) in Gas Phase around the DST at 1 Year and at 15 Months 267
7.1-7. Modeled Gas Phase CO_2 Concentrations (Log ppmv) in Fractures during the Heating Phase of the DST at 1, 2, 3, and 4 years....268
7.1-8. Modeled Gas Phase CO_2 Concentrations (Log ppmv) in Fractures during the Cooling Phase of the DST at 5, 6, 7, and 8 years 269
7.1-9. Close-Up of DST Grid, Showing Nodes Used to Extract Model Data for Comparison to Concentrations Measured in Gas Samples....270
7.1-10. Comparison of Modeled CO_2 Concentrations (Base Case CC Kin and Extended Case CC Kin) in Fractures to Measured Concentrations in Boreholes: (a) Borehole Interval 74-3 at Node Above Interval; (b) Borehole Interval 75-3; (c) Borehole Interval 76-3; (d) Borehole Interval 78-3 at Node Near End of Interval 272
7.1-11. Comparison of REV02 Modeled CO_2 Concentrations (extended case) in Fractures to Measured (Corrected) Concentrations in Boreholes: (a) Borehole Interval 74-3 (Average of Bounding Gridblocks); (b) Borehole Interval 75-3; (c) Borehole Interval 76-3 274
7.1-12. Comparison of Measured and Corrected Concentrations for Borehole Interval 75-3 and the REV02 Model Simulation Results....275
7.1-13 Zones Where Water Was Collected from Hydrology Boreholes Superimposed (Thick Shading in Blue) on the Model Grid 281
7.1-14. Modeled Distribution of pH in Fractures at Various Times When Water Was Sampled from Hydrology Borehole Intervals (REV02 Simulation): (a) 6 Months, (b) 11 Months, and (c) 14 Months....284
7.1-15. Changes in pH in Water Samples Collected from Borehole Intervals (a) 60-3 and (b) 59-2 Compared to REV01 Modeled Fracture Water pH at Nearby Model Grid Nodes....286
7.1-16. Comparison of Measured pH in Water Samples Collected from Borehole Intervals (a) 60-3, (b) 59-2, and (c) 76-3 to REV02 Modeled Fracture Water pH at Representative Model GridBlocks....288
7.1-17. Modeled Distribution of Cl^- in Fractures and Matrix at One and Four Years during the Heating Phase of the DST (REV02 Simulation): (a) Fracture—1 year, (b) Matrix—1 Year, (c) Fracture—4 years, and (d) Matrix—4 years 290
7.1-18. Changes in Cl^- (mg/L) in Water Samples Collected from Borehole Intervals (a) 60-3 and (b) 59-2, Compared to REV01 Modeled Fracture Water Cl^- 291
7.1-19. SO_4^{2-} Concentrations (mg/L) in Water Samples Collected from Borehole Intervals (a) 60-3 and (b) 59-2, Compared to REV01 Modeled Fracture Water SO_4^{2-} 292
7.1-20. Cl^- Concentrations (mg/L) in Water Samples Collected from Borehole Intervals (a) 60-3, (b) 59-2, and (c) 76-3 Compared to REV02 Modeled Fracture Water Cl^- 293

LIST OF FIGURES (Continued)

7.1-21. SO_4^{2-} Concentrations (mg/L) in Water Samples Collected from Borehole Intervals (a) 60-3, (b) 59-2, and (c) 76-3 Compared to REV02 Modeled Fracture Water SO_4^{2-} 294
7.1-22. Na^+ Concentrations (mg/L) in Water Samples Collected from Borehole Intervals (a) 60-3 and (b) 59-2, Compared to REV01 Modeled Na^+ Concentrations in Fractures 295
7.1-23. Na^+ Concentrations (mg/L) in Water Samples Collected from Borehole Intervals (a) 60-3, (b) 59-2, and (c) 76-3 REV02 Modeled Na^+ Concentrations in Fractures 297
7.1-24. Ca^{2+} Concentrations (mg/L) in Water Samples Collected from Borehole Intervals (a) 60-3 and (b) 59-2 Compared to REV01 Modeled Ca^{2+} in Fracture Water 298
7.1-25. Ca^{2+} Concentrations (mg/L) in Water Samples Collected from Borehole Intervals (a) 60-3, (b) 59-2, and (c) 76-3 Compared to REV02 Modeled Ca^{2+} in Fracture Water 299
7.1-26. $SiO_{2(aq)}$ Concentrations (mg/L) in Water Samples Collected from Borehole Intervals (a) 60-3 and (b) 59-2 Compared to REV01 Modeled Fracture Water $SiO_{2(aq)}$ Concentrations 300
7.1-27. $SiO_{2(aq)}$ Concentrations (mg/L) in Water Samples Collected from Borehole Intervals (a) 60-3, (b) 59-2, and (c) 76-3 Compared to REV02 Modeled Fracture Water $SiO_{2(aq)}$ Concentrations 302
7.1-28. K^+ Concentrations (mg/L) in Water Samples Collected from Borehole Intervals (a) 60-3 and (b) 59-2 Compared to REV01 Modeled Fracture Water K^+ Concentrations 303
7.1-29. K^+ Concentrations (mg/L) in Water Samples Collected from Borehole Intervals (a) 60-3, (b) 59-2, and (c) 76-3 Compared to REV02 Modeled Fracture Water K^+ Concentrations 304
7.1-30. HCO_3^- Concentrations (mg/L) in Water Samples Collected from Borehole Intervals (a) 60-3 and (b) 59-2 Compared to REV01 Modeled Fracture Water HCO_3^- Concentrations 306
7.1-31. HCO_3^- Concentrations (mg/L) in Water Samples Collected from Borehole Intervals (a) 60-3, (b) 59-2, and (c) 76-3 Compared to REV02 Modeled Fracture Water HCO_3^- Concentrations 307
7.1-32. Mg^{2+} Concentrations (mg/L) in Water Samples Collected from Borehole Intervals (a) 60-3, (b) 59-2, and (c) 76-3 Compared to REV02 Modeled Fracture Water Mg^{2+} Concentrations 308
7.1-33. NO_3^- Concentrations (mg/L) in Water Samples Collected from Borehole Intervals (a) 60-3, (b) 59-2, and (c) 76-3 Compared to REV02 Modeled Fracture Water NO_3^- Concentrations 309

LIST OF FIGURES (Continued)

7.1-34. F^- Concentrations (mg/L) in Water Samples Collected from Borehole Intervals (a) 60-3, (b) 59-2, and (c) 76-3 Compared to REV02 Modeled Fracture Water F^- Concentrations....310
7.1-35. Modeled (REV01) Volume Percent Change in Calcite in Fractures after 3 Years of Heating....313
7.1-36. Modeled (REV01) Volume Percent Amorphous Silica in Fractures after 3 Years of Heating....314
7.1-37. Modeled Volume Percent Change in Calcite in Fractures as of November 2000 (35 Months of Heating)....315
7.1-38. Modeled Volume Percent Amorphous Silica in Fractures as of November 2000 (35 Months of Heating)....316
7.1-39. Modeled Volume Percent Gypsum in Fractures as of November 2000 (35 Months of Heating)....316
7.1-40. Change in Fracture Porosity after Four Years of Heating....318
7.1-41. Change in Matrix Porosity after Four Years of Heating....319
7.1-42. Measured Activities of ^{14}C (Expressed as a Fraction of Modern Carbon) in CO_2 from Gas Collected in Several Hydrology Boreholes over Most of the Heating Phase of the DST....321
7.1-43. Measured Activities of ^{14}C (Expressed as a Fraction of Modern Carbon) Compared to Measured CO_2 (Corrected for Water Vapor Removal) from Gas Collected in Some Hydrology Boreholes over Most of the Heating Phase of the DST....322
7.2-1. Schematic Diagram of the Tuff Plug-Flow and Fracture Sealing Experiments....323
7.2-2. SEM Image of Topopah Spring Tuff Grains Used for Plug-Flow Experiment....324
7.2-3. Comparison of Measured and Simulated Results of Tuff Dissolution Plug-Flow Experiment....327
7.3-1. Opened Fracture Faces at Conclusion of Fracture Sealing Experiment....332
7.3-2. Bridging Structures (Identified with Arrows) (a) Extending Outward from Flat Fracture Face; (b) Spanning Aperture in Cross-Cutting Natural Fracture....332
7.3-3. Porosity vs. Depth over Time for Simulated (a) Equilibrium and (b) Kinetic Control of Amorphous Silica in Fracture Sealing Experiment....334
7.3-4. Simulated Temperature Profile and Volume Fraction of Amorphous Silica vs. Depth at 5.01 Days....335
8-1. Key Findings of the THC Seepage Model....339

INTENTIONALLY LEFT BLANK

LIST OF TABLES

3-1. Qualified Software Used in This Report....36
4.1-1. Data Tracking Numbers for Sources of Direct Input Data for the Drift-Scale Coupled-Processes Models Used to Feed TSPA-LA Activities....38
4.1-2. Sources of Technical Information Used as Direct Input for Model Design Used to Feed TSPA-LA Activities....39
4.1-3. Input Pore-Water Compositions....40
4.1-4. REV02 Kinetic Data....43
4.1-5. Drift Design Parameters....46
4.2-1. Project Requirements and YMRP Acceptance Criteria Applicable to This Model Report....49
6-1. Summary of Changes from the REV01 to the REV02 THC Seepage Model....57
6-2. Scientific Notebooks....60
6.1-1. Features, Events, and Processes Relevant to this Model Report and Included into TSPA-LA....61
6.1-2. Features, Events, and Processes Relevant to this Model Report and Excluded from TSPA-LA....64
6.2-1. Input Pore-Water Compositions for the THC Seepage Model....73
6.2-2. Minerals, Aqueous, and Gaseous Species Used in the THC Seepage Model....78
6.4-1 Summary of Hydrological and Thermal Properties of Repository Units....98
6.4-2 Data Tracking Numbers for Sources of Model Inputs Used in REV01 and Sensitivity Analyses[1]....100
6.4-3. REV01 Kinetic Rate Law Data for Mineral-Water Dissolution and Precipitation....101
6.5-1. Vertical Mesh Dimensions and Geologic Contacts in the Tptpmn THC Model....105
6.5-2. Tptpmn THC Model REV01 Boundary Conditions....107
6.5-3. Tptpmn THC Model Infiltration Rates and Corresponding Rock-Property Sets....108
6.5-4. Tptpmn THC Model Runs (REV01)....110
6.6-1. Tptpmn THC Heterogeneous Model Runs....134
6.7-1. Vertical Mesh Dimensions and Geologic Contacts in the Tptpll THC Model....149
6.7-2. Tptpll THC Model REV01 Boundary Conditions....151
6.7-3. Tptpll THC Model REV01 Runs....152
6.8-1. Tptpll THC Model REV02 Boundary Conditions....177
6.8-2. Tptpll THC Model Infiltration Rates....177
6.8-3. Selected Input Waters (Section 6.2.2.1) for the Tptpll THC Model REV02....178
6.8-4. Tptpll THC Model REV02 Runs Using the Mean Infiltration Rock-Property Set for All Simulations....179

LIST OF TABLES (continued)

6.9-1. Summary of Uncertainties Affecting Chemical Processes in the THC Seepage Model 242
6.9-2. Standard Deviations[1] in Water and Gas Compositions Predicted Using Five Different Input Water Compositions (W0, W4, W5, W6, and W7) 246
7-1. Sources of Data Used for Model Validation or Corroboration....247
7.1-1. Input DTNs Used for Estimating Times/Dates of Power Reductions and Outages for REV02 Simulations....252
7.1-2. Step-Wise Averaged Power Data for REV02 Simulations....254
7.1-3. Measured Concentrations in Tptpmn Pore Water from Alcove 5 and Chemistry of Water Samples from Hydrology Boreholes 277
7.2-1. Initial Water Composition for Tuff Plug-Flow Simulations....325
7.2-2. Summary Table of Tuff Dissolution Simulations....326
7.2-3. Validation of Tuff Dissolution Simulations 329
7.3-1. Characteristics of Fracture Precipitate....333
7.3-2. Initial Water Composition for Fracture Sealing Simulations 334

ACRONYMS

1-D	one-dimensional
2-D	two-dimensional
3-D	three-dimensional
ACC	Accession Number
AP	Administrative Procedure (DOE)
BET	Brunauer-Emmett-Teller
BSC	Bechtel SAIC Company, LLC
CRWMS	Civilian Radioactive Waste Management System
DIRS	Document Input Reference System
DOE	Department of Energy
DST	Drift Scale Test
DTN	Data Tracking Number
ECRB	Enhanced Characterization of Repository Block
EOS	Equation of State
ESF	Exploratory Studies Facility
FEP	Features, Events and Processes
Kth_{max}	Maximum Thermal Conductivity
LA	License Application
LBNL	Lawrence Berkeley National Laboratory
M&O	Management and Operating Contractor
NRC	Nuclear Regulatory Commission
OCRWM	Office of Civilian Radioactive Waste Management
PA	Performance Assessment
Q	Qualified
QA	Quality Assurance
QIP	Quality Implementing Procedure
SCM	Software Configuration Management
SN	Scientific Notebook
SR	Site Recommendation
STN	Software Tracking Number

ACRONYMS (continued)

TDMS	Technical Data Management System
TH	Thermal-Hydrological
THC	Thermal-Hydrological-Chemical
TSPA	Total System Performance Assessment
TWP	Technical Work Plan
UZ	unsaturated zone
UZ Model	Unsaturated Zone Flow and Transport Model
XRD	X-ray Diffraction
YMP	Yucca Mountain Project
YMRP	*Yucca Mountain Review Plan, Final Report*
WP	Waste Package

Major Hydrogeologic Units

CFu	Crater Flat undifferentiated hydrogeologic unit
CHn	Calico Hills nonwelded hydrogeologic unit
PTn	Paintbrush Tuff nonwelded hydrogeologic unit
TCw	Tiva Canyon welded hydrogeologic unit

Geologic and Model Layer Abbreviations

Stratigraphic Unit[a]						Abbreviation[a]	UZ Model Layer[b]
Group	Formation	Member	Zone	Subzone			
	Alluvium and Colluvium					Qal, Qc	
Timber Mountain Group						Tm	
	Rainier Mesa Tuff					Tmr	
Paintbrush Group						Tp	
		Post-tuff unit “x” bedded tuff				Tpbt6	
		Tuff unit “x”				Tpki (informal)	
		Pre-tuff unit “x” bedded tuff				Tpbt5	
	Tiva Canyon Tuff					Tpc	
		Crystal-Rich Member				Tpcr	
			Vitric zone			Tpcrv	
				Nonwelded subzone		Tpcrv3	
				Moderately welded subzone		Tpcrv2	
				Densely welded subzone		Tpcrv1	
			Nonlithophysal subzone			Tpcrn	**tcw11**
				Subvitrophyre transition subzone		Tpcrn4	
				Pumice-poor subzone		Tpcrn3	
				Mixed pumice subzone		Tpcrn2	
				Crystal transition subzone		Tpcrn1	
			Lithophysal zone			Tpcrl	
				Crystal transition subzone		Tpcrl1	
		Crystal-Poor Member				Tpcp	
			Upper lithophysal zone			Tpcpul	
				Spherulite-rich subzone		Tpcpul1	
			Middle nonlithophysal zone			Tpcpmn	
				Upper subzone		Tpcpmn3	
				Lithophysal subzone		Tpcpmn2	**tcw12**
				Lower subzone		Tpcpmn1	
			Lower lithophysal zone			Tpcpll	
				Hackly-fractured subzone		Tpcpllh	
			Lower nonlithophysal zone			Tpcpln	

Geologic and Model Layer Abbreviations (continued)

Stratigraphic Unit[a]					Abbreviation[a]	UZ Model Layer[b]
Group	Formation	Member	Zone	Subzone		
				Hackly subzone	Tpcplnh	tcw12 (continued)
				Columnar subzone	Tpcplnc	
			Vitric zone		Tpcpv	tcw13
				Densely welded subzone	Tpcpv3	
				Moderately welded subzone	Tpcpv2	
				Nonwelded subzone	Tpcpv1	ptn21
		Pre-Tiva Canyon bedded tuff			Tpbt4	ptn22
	Yucca Mountain Tuff				Tpy	ptn23
		Pre-Yucca Mountain bedded tuff			Tpbt3	ptn24
	Pah Canyon Tuff				Tpp	ptn 25
		Pre-Pah Canyon bedded tuff			Tpbt2	ptn26
	Topopah Spring Tuff				Tpt	
		Crystal-Rich Member			Tptr	
			Vitric zone		Tptrv	
				Nonwelded subzone	Tptrv3	
				Moderately welded subzone	Tptrv2	
				Densely welded subzone	Tptrv1	tsw31
			Nonlithophysal zone		Tptrn	tsw32
				Dense subzone	Tptrn3	
				Vapor-phase corroded subzone	Tptrn2	
				Crystal transition subzone	Tptrn1	
			Lithophysal zone		Tptrl	tsw33
				Crystal transition subzone	Tptrl1	
		Crystal-Poor Member			Tptp	
			Lithic-rich zone		Tptpf or Tptrf	
			Upper lithophysal zone		Tptpul	
			Middle nonlithophysal zone		Tptpmn	tsw34
				Nonlithophysal subzone	Tptpmn3	
				Lithophysal bearing subzone	Tptpmn2	
				Nonlithophysal subzone	Tptpmn1	
			Lower lithophysal zone		Tptpll	tsw35
			Lower nonlithophysal zone		Tptpln	tsw36, tsw37

Geologic and Model Layer Abbreviations (continued)

Stratigraphic Unit[a]					Abbreviation[a]	UZ Model Layer[b]
Group	Formation	Member	Zone	Subzone		
			Vitric zone		Tptpv	**tsw38**
				Densely welded subzone	Tptpv3	
				Moderately welded subzone	Tptpv2	**tsw39**
				Nonwelded subzone	Tptpv1	**ch1**
		Pre-Topopah Spring bedded tuff			Tpbt1	
	Calico Hills Formation				Ta	**ch2**, **ch3**, **ch4**, **ch5**
		Bedded tuff			Tacbt	**ch6**
Crater Flat Group					Tc	**pp4**
	Prow Pass Tuff				Tcp	
			Prow Pass Tuff upper vitric nonwelded zone		Tcpuv	
			Prow Pass Tuff upper crystalline nonwelded zone		Tcpuc	**pp3**
			Prow Pass Tuff moderately-densely welded zone		Tcpmd	**pp2**
			Prow Pass Tuff lower crystalline nonwelded zone		Tcplc	
			Prow Pass Tuff lower vitric nonwelded zone		Tcplv	**pp1**
		Pre-Prow Pass Tuff bedded tuff			Tcpbt	
	Bullfrog Tuff				Tcb	
			Bullfrog Tuff upper vitric nonwelded zone		Tcbuv	
			Bullfrog Tuff upper crystalline nonwelded zone		Tcbuc	**bf3**
			Bullfrog Tuff welded zone		Tcbmd	
			Bullfrog Tuff lower crystalline nonwelded zone		Tcblc	
			Bullfrog Tuff lower vitric nonwelded zone		Tcblv	**bf2**
		Pre-Bullfrog Tuff bedded tuff			Tcbbt	
	Tram Tuff				Tct	
			Tram Tuff upper vitric nonwelded zone		Tctuv	

Geologic and Model Layer Abbreviations (continued)

Stratigraphic Unit[a]					Abbreviation[a]	UZ Model Layer[b]
Group	Formation	Member	Zone	Subzone		
			Tram Tuff upper crystalline nonwelded zone		Tctuc	tr3
			Tram Tuff moderately-densely welded zone		Tctmd	
			Tram Tuff lower crystalline nonwelded zone		Tctlc	
			Tram Tuff lower vitric nonwelded zone		Tctlv	tr2
		Pre-Tram Tuff bedded tuff			Tctbt	
		Lava and flow breccia (informal)			Tll	
		Bedded tuff			Tllbt	
	Lithic Ridge Tuff				Tr	
		Bedded tuff			Tlrbt	
		Lava and flow breccia (informal)			Tll2	
		Bedded tuff			Tllbt	
		Lava and flow breccia (informal)			Tll3	
		Bedded tuff			Tll3bt	
		Older tuffs (informal)			Tt	
			Unit a (informal)		Tta	
			Unit b (informal)		Ttb	
			Unit c (informal)		Ttc	
		Sedimentary rocks and calcified tuff (informal)			Tca	
		Tuff of Yucca Flat (informal)			Tyf	
Pre-Tertiary sedimentary rock						
	Lone Mountain Dolomite				Slm	
	Roberts Mountain Formation				Srm	

Sources: [a] BSC 2002 [159124], Table 4.
[b] BSC 2003 [160109], Table 11.

CHEMICAL ABBREVIATIONS

Elements

Al	Aluminum
C	Carbon
Ca	Calcium
Cl	Chlorine
F	Fluorine
Fe	Iron
H	Hydrogen
K	Potassium
Mg	Magnesium
N	Nitrogen
Na	Sodium
O	Oxygen
S	Sulfur
Si	Silicon

Chemical Compounds, Aqueous Species and Gases

AlO_2	Aluminum primary aqueous species (essentially same as $Al(OH)_4^-$); here used to describe total aqueous aluminum concentrations as AlO_2
CO_2	Carbon dioxide gas
H_2O	Water
HCO_3^-	Bicarbonate aqueous species; here used to describe total aqueous
$HFeO_2^0$	Iron primary aqueous species (essentially same as $Fe(OH)_3^0$; here used to describe total aqueous iron concentrations as $HFeO_2^0$
KSO_4	Potassium sulfate (solid; mineral name: arcanite)
$MgSO_4$	Magnesium sulfate (solid)

CHEMICAL ABBREVIATIONS (continued)

Na_2SO_4	Sodium sulfate (solid; mineral name: thenardite)
NaCl	Sodium chloride (solid; mineral name: halite)
$NaNO_3$	Sodium nitrate (solid)
NO_3^-	Nitrate aqueous species
O_2	Oxygen gas
P_{CO2}	Carbon dioxide partial pressure (in bar)
pH	Negative logarithm of the hydrogen ion activity
SiO_2	Silica
SO_4^{-2}	Sulfate aqueous species

Chemical Units

meq	milliequivalent (mol x 10^3 x ionic charge)
meq/L	milliequivalent per liter of solution
mg/L	milligram per liter of solution
mol	moles
mol/kg	moles per kilogram water (molality)
ppm	parts per million
ppmv	parts per million volume

1. PURPOSE

1.1 BACKGROUND

The purpose of this Model Report (REV02) is to document the unsaturated zone (UZ) models used to evaluate the potential effects of coupled thermal-hydrological-chemical (THC) processes on UZ flow and transport. This Model Report has been developed in accordance with the *Technical Work Plan for: Performance Assessment Unsaturated Zone* (Bechtel SAIC Company, LLC (BSC) 2002 [160819]). The technical work plan (TWP) describes planning information pertaining to the technical scope, content, and management of this Model Report in Section 1.12, Work Package AUZM08, *Coupled Effects on Flow and Seepage*. The plan for validation of the models documented in this Model Report is given in Attachment I, Model Validation Plans, Section I-3-4, of the TWP. Except for variations in acceptance criteria (Section 4.2), there were no deviations from this TWP. This report was developed in accordance with AP-SIII.10Q, *Models*.

This Model Report documents the THC Seepage Model and the Drift Scale Test (DST) THC Model. The THC Seepage Model is a drift-scale process model for predicting the composition of gas and water that could enter waste emplacement drifts and the effects of mineral alteration on flow in rocks surrounding drifts. The DST THC model is a drift-scale process model relying on the same conceptual model and much of the same input data (i.e., physical, hydrological, thermodynamic, and kinetic) as the THC Seepage Model. The DST THC Model is the primary method for validating the THC Seepage Model. The DST THC Model compares predicted water and gas compositions, as well as mineral alteration patterns, with observed data from the DST. These models provide the framework to evaluate THC coupled processes at the drift scale, predict flow and transport behavior for specified thermal-loading conditions, and predict the evolution of mineral alteration and fluid chemistry around potential waste emplacement drifts. The DST THC Model is used solely for the validation of the THC Seepage Model and is not used for calibration to measured data.

Data developed with the THC Seepage Model are to be abstracted for inclusion in the Model Report *Abstraction of Drift-Scale Coupled Processes* (upcoming revision of MDL-NBS-HS-000018 REV00 (CRWMS M&O 2000 [123916])). The abstracted results are used for Performance Assessment (PA). PA results support the License Application (LA).

The work scope for this Model Report is presented in the TWP cited above and summarized as follows: continue development of the repository drift-scale THC Seepage Model used in support of the Total System Performance Assessment (TSPA) in-drift geochemical model; study sensitivity of results to changes in input data and mineral assemblage; validate the models by comparison with field and experimental data; perform simulations to predict mineral dissolution and precipitation and their effects on fracture properties and chemistry of water (but not flow rates) that may seep into drifts; submit modeling results to the Technical Data Management System (TDMS) and document the models; and evaluate model uncertainty and the effect of uncertainty propagation to other models.

Major revisions in this document (REV02) compared to previous versions (REV00 and REV01) include the addition of new simulations that make use of improved treatment of various modeled

processes, together with updated rock properties and some new kinetic and thermodynamic input data. In addition, the uncertainties associated with predictions of the THC Seepage Model are further evaluated by considering five different input water compositions, some variations in infiltration rates, CO_2 effective diffusivity, and the effect of vapor-pressure lowering due to capillary pressure. Results of earlier THC work considering the emplacement of backfill over waste canisters has been removed from this revision, because the use of backfill is no longer being considered.

1.2 OVERVIEW OF MODELS

The DST THC Model, constructed for the DST, is used to investigate THC processes during the DST. The spatial scale and temperatures for the DST are similar to those for current designs of the repository. This similarity, combined with the relatively long time that it has been operating (four years of heating, ending in January 2002, and monitoring is continuing during cooling), makes the DST the best available experiment for validating drift-scale THC coupled process models (such as the THC Seepage Model). Measured data from the DST are used to evaluate and validate the conceptual and numerical models. Throughout the DST study, the conceptual model and its numerical formulation were improved and revised as necessary, so that results of the DST and laboratory experiments could be best reproduced. These revisions did not incorporate any adjustments to measured geochemical data.

The THC Seepage Model provides an analysis of the effects of THC processes on percolation water chemistry and gas-phase composition in the near-field host rock around the emplacement drifts. This analysis includes a complete description of the pertinent mineral-water processes in the host rock and their effect on the near-field environment. Several alternative conceptualizations of the THC Seepage Model (see below) are used to evaluate the effects of mineral dissolution and precipitation, the effects of CO_2 exsolution and transport in the region surrounding emplacement drifts, the potential for forming calcite, silica, or other mineral assemblage "precipitation caps," and the resulting changes to porosity, permeability, and percolation. Sensitivity studies are documented on the effect of varying rock properties, including fracture-permeability heterogeneity, reaction rates, repository emplacement-horizon lithology, geochemical systems, infiltration rates, and input water compositions. The effects of various model refinements and improvements implemented through successive revisions of this report are also documented. These include, for example, the effects of improved treatment of porosity-permeability coupling, improved treatment of mineral precipitation at the boiling front, and consideration of vapor-pressure lowering caused by capillary pressure.

The following designations have been assigned to the models and their alternative conceptualizations presented in this report:

- DST THC Model REV01: DST THC Model and simulations developed for the previous revision (REV01) of this Model Report (Section 7.1).

- DST THC Model REV02: DST THC Model and simulations developed for the current Model Report revision (Section 7.1). This model is an update of the DST THC model, using the same general setup except for updated rock properties and other various input data.

- Tptpmn THC Model REV01: THC Seepage Model considering a heat load in the Topopah Spring Tuff middle nonlithophysal lithostratigraphic unit (Tptpmn) (Section 6.5). This model was developed for REV01 of this Model Report.

- Tptpmn THC Heterogeneous Model REV01: THC Seepage Model considering a heat load in the Tptpmn with initial heterogeneous fracture permeability variations (Section 6.6). This model uses the same grid and THC parameters as in the Tptpmn THC Model. It was developed for the previous revision (REV01) of this Model Report.

- Tptpll THC Model REV01: THC Seepage Model considering a heat load in the Topopah Spring Tuff lower lithophysal lithostratigraphic unit (Tptpll) (Section 6.7). This model was developed for the previous revision (REV01) of this Model Report.

- Tptpll THC Model REV02: THC Seepage Model developed for this current Model Report revision (Section 6.8). This model is an update of the Tptpll THC Model REV01, using the same general setup except for updated rock properties and other various input data.

The first two models are collectively referred to as the DST THC Model, and the last four as alternative conceptualizations of the THC Seepage Model. These models are fully described in Sections 6 and 7.

It should be noted, here, that results handed to downstream users for LA work consist only of the Tptpll THC Model REV02 results. Other historical (REV01) results are presented here because they provide important complementary information to REV02 work with respect to the evaluation of model output uncertainty.

These REV01 results are treated as sensitivity analyses. As mentioned later in this report, the Tptpll THC Model REV02 was run using a range of input water compositions from various lithostratigraphic units (including Tptpmn, Tptpll, and Tptpul) and representative of natural variability. The spread in model results from the use of these different water compositions mostly encompasses the spread related to other factors such as drift location and infiltration rate, and other model conceptualizations discussed in Section 6.3. Therefore, the REV02 model results for the Tptpll unit (taking into account the variability introduced by the different input water compositions) should be applicable to other repository host rock units.

1.3 MODEL LIMITATIONS

A limitation of the THC Seepage Model, as in all predictive models, is the increased uncertainty associated with predictions required for times far beyond the duration of field tests. The model is also limited by its mathematical formulations and associated assumptions (Section 5) and approximations (Section 6.4.6). For example, neither the THC Seepage nor DST THC models were designed for accurate computation of mineral precipitation from very saline waters (ionic strength > 4 molal) resulting from evaporative concentration. Other model limitations affecting the uncertainty of model results are discussed in Section 6.9. Another limitation of the THC Seepage Model is that it is computationally intensive (run times up to ten days for one simulation). Hence, the number of simulations that have been performed for sensitivity study is

limited. Nevertheless, these limitations were for the most part overcome by evaluating the model sensitivity to key input parameters (Sections 6.5–6.8), and by comparing model results against data from the DST and laboratory experiments (Section 7). Also, the model conceptualization and mathematical formulation (Section 6.2–6.4) have been improved, through the successive revisions of this Model Report, such that a reasonably good agreement between calculated and measured data has been achieved.

The THC Seepage Model was developed with data for the Tptpmn and Tptpll lithostratigraphic units. Although many aspects of the model are applicable to other host rock units of the repository, differences in the mineralogy, geochemistry, and thermal-hydrological (TH) properties must be considered before the results can be directly applied elsewhere. These differences, however, are expected to be reflected in the range of pore-water compositions input into the model (Section 6.2.2.1), such that results of the THC Seepage Model as a whole (i.e., including the variability introduced by using various input water compositions) could be reasonably applied to other locations within the repository footprint. One limitation of the model is that it is a continuum model, with averaged properties or realizations of idealized permeability fields, and therefore is meant to represent overall changes in space and time. Thus, it must be applied with caution at any specific location.

The DST THC Model is a two dimensional (2-D) representation with homogeneous properties of a three-dimensional (3-D) experiment in heterogeneous fractured rock. Therefore, the model is meant to capture overall changes as a function of space and time, but cannot be expected to match data exactly at any one point in time.

By definition, models are idealizations of the real world. Input data summarized in Section 4 characterize the physical properties of the rock, but cannot include every detail of a natural system. In particular, the infiltration of water is laterally uniform over the model top boundary. As a result of such simplifications, the model results describe overall changes in space and time within the model domain, but must be applied with caution when predicting future conditions at any specific location.

The various alternative conceptualizations of the THC Seepage Model presented in this report consider a half-drift symmetrical and laterally homogenous model (thus resulting in the symmetric flow of heat away from one emplacement drift). Therefore, these conceptualizations cannot capture potential “edge effects” that could occur as the result of uneven heat flow around drifts at the boundaries of the repository. Edge effects have been evaluated with mountain-scale simulations in BSC (2001 [155950], Section 3.3.6) and will be further addressed in an upcoming revision (REV01) of MDL-NBS-HS-000007 (CRWMS M&O 2000 [144454]). Water and gas compositions predicted at the edge of the repository (BSC 2001 [155950], Section 3.3.6) are within the range of compositions simulated in this Model Report. For this reason, results presented here could be used to represent potential effects of THC processes on the composition of seepage at all waste package locations.

2. QUALITY ASSURANCE

Development of this Model Report and the supporting modeling activities have been determined to be subject to the Yucca Mountain Project's quality assurance (QA) program as indicated in *Technical Work Plan for: Performance Assessment Unsaturated Zone,* TWP-NBS-HS-000003 REV 02 (BSC 2002 [160819], Section 8.2, Work Package (WP) AUZM08). Approved QA procedures identified in the TWP (BSC 2002 [160819], Section 4) have been used to conduct and document the activities described in this Model Report. Electronic management of information was evaluated in accordance with Administrative Procedure (AP) SV.1Q, *Control of the Electronic Management of Information* and controlled under YMP-LBNL Quality Implementing Procedure—(QIP) SV.0, *Management of YMP-LBNL Electronic Data*, as planned in BSC (2002 [160819], Section 8.4).

This Model Report provides drift-scale THC processes of natural barriers that are important to the demonstration of compliance with the postclosure performance objective prescribed in 10 CFR 63.113 [156605]. Therefore it is classified as "Quality Level – 1" with regard to importance to waste isolation as defined in AP-2.22Q, *Classification Criteria and Maintenance of the Monitored Geologic Repository Q-List*. The report contributes to the analyses and modeling data used to support performance assessment (PA); the conclusions do not directly impact engineered features important to safety, as defined in AP-2.22Q.

INTENTIONALLY LEFT BLANK

3. USE OF SOFTWARE

The qualified software used in this study are listed in Table 3.1. These software have been baselined in accordance with AP-SI.1Q, *Software Management*, are appropriate for the intended use, have been used strictly within the range of validation, and were obtained from the Software Configuration Management (SCM).

TOUGHREACT V2.4 (LBNL 2001 [160880]), and V3.0 (LBNL 2002 [161256]) are the primary codes used for the DST THC and THC Seepage models. (Only use of TOUGHREACT V3.0 was planned in BSC 2002 [160819], Attachment II; both codes are qualified.) The code SOLVEQ/CHILLER V1.0 (LBNL 1999 [153217]) was utilized to prepare water-chemistry data for input to the models. SUPCRT92 V1.0 (LBNL 1999 [153218]) was used to generate thermodynamic data for use by SOLVEQ/CHILLER V1.0 (LBNL 1999 [153217]) and the various TOUGHREACT versions. The code TOUGH2 V1.4 (LBNL 2000 [146496]) was used to generate boundary conditions. The code AMESH V1.0 (LBNL 1999 [153216]) was used to generate grids for the models, and GSLIB V1.0SISIMV1.204 (LBNL 2000 [153100]) was used to create geostatistical permeability realizations. Other routines listed in Table 3.1 were used for various data pre- and post-processing tasks.

Results of historical simulations performed for Site Recommendation (SR), first presented in the previous revision (REV01) of this Model Report, are included in this report to supplement the results of more recent simulations carried out for this report revision (REV02). These earlier simulations, carried out only for SR, were for the most part run using an interim unqualified version of TOUGHREACT (Version 2.3, LBNL 2001 [153101]) because interim use of unqualified software was allowed for SR work. During the validation process, the source code for TOUGHREACT V2.3 changed to TOUGHREACT V2.4 (LBNL 2001 [160880]) which was subsequently validated and baselined. A comparison of unqualified TOUGHREACT V2.3 with qualified TOUGHREACT V2.4 was performed including an associated impact review, which concluded that the simulations with unqualified V2.3 were verified with the qualified V2.4 BSC (2001 [164414]).

This Model Report documents the DST THC and THC Seepage models as listed in Section 1. The input and output files for the model runs presented in this Model Report are listed in Attachment X.

Table 3-1. Qualified Software Used in This Report

Software Name and Version	Software Tracking Number (STN)	DIRS Reference Number
TOUGHREACT V3.0	10396-3.0-00	161256
TOUGHREACT V2.4	10396-2.4-00	160880[1]
TOUGHREACT V2.2	10154-2.2-00	153219 (retired)[1]
SOLVEQ/CHILLER V1.0	10057-1.0-00	153217
SUPCRT92 V1.0	10058-1.0-00	153218
TOUGH2 V1.4	10007-1.4-01	146496
AMESH V1.0	10045-1.0-00	153216
GSLIB V1.0SISIMV1.204	10397-1.0SISIMV1.204-00	153100
flipk V1.0	10320-1.0-00	152883
switch V1.0	10322-1.0-00	152899
regress V1.0	10321-1.0-00	152900
mk_incon V1.0	10350-1.0-00	152901
kreg V1.0	10318-1.0-00	152902
KREG V1.1	10318-1.1-00	161258
kswitch V1.0	10319-1.0-00	153087
KSWITCH V1.1	10319-1.1-00	161259
THERMOCHK V1.1	10895-1.1-00	161262
DBCONV V1.0	10893-1.0-00	161263
CUTCHEM V1.0	10898-1.0-0.0	161127
exclude.f V1.0	10316-1.0-00	153089
assign.f V1.0	10315-1.0-00	153090
merggrid2.f V1.0	10314-1.0-00	153091
mk_circ2 V1.0	10312-1.0-00	153092
mk_rect2 V1.0	10313-1.0-00	153093
2kgridv1a.for V1.0	10382-1.0-00	153067
mk_grav2.f V1.0	10379-1.0-00	153068
sav1d_dst2d.f V1.0	10381-1.0-00	153083
mrgdrift.f V1.0	10380-1.0-00	153082
avgperm.f V1.0	10378-1.0-00	153085

[1] Software used for historical simulations only – not used for REV02 simulations

4. INPUTS

4.1 DATA AND PARAMETERS

This section presents all input data used for the drift-scale coupled-processes models feeding TSPA-LA activities (simulations presented in Section 6.8). The qualified (Q) status of all direct inputs is shown in the Document Input Reference System (DIRS) database. Because this Model Report documents models of coupled phenomena, a wide variety of input data is required. Sources of direct input data are summarized in Table 4.1-1, and sources of design technical information are reported in Table 4.1-2. Input data and parameter uncertainties are further addressed in Sections 6 and 7. Model inputs related to sensitivity analyses and model validation are documented in Sections 6.4.8 and 7.

Results of historical simulations carried out for REV01 of this Model Report are presented in this report revision (Sections 6.5–6.7, 7.1.8, 7.2) to supplement results of more recent (REV02) work (Section 6.8 and 7.1). These REV01 simulations were included in this report because they provide valuable information for assessing the sensitivity of THC models to various input data and model improvements from REV01 to REV02. These historical simulations were not used to generate any results for TSPA-LA; their sources are presented in Section 6.4.8.

No unqualified data have been qualified in the report. The status of unqualified data used is indicated in the DIRS.

4.1.1 Hydrological and Thermal Properties

Source DTNs for hydrological and thermal properties are listed in Table 4.1-1. Specific values of hydrological and thermal properties for the repository hydrogeologic model units tsw33, tsw34, and tsw35 (Topopah Spring Tuff upper-lithophysal, middle-nonlithophysal, and lower-lithophysal units, respectively) are summarized later in Section 6 (Table 6.4-1).

Modeling analyses utilized data from the “mean calibrated” hydrological property sets for the present-day climate. The data sets include properties that were calibrated, such as fracture and matrix permeabilities and van Genuchten parameters, and properties such as porosity, heat capacity, and thermal conductivity obtained from field measurements. DTNs for infiltration rates and model-boundary temperatures are also included in Table 4.1-1. Specific hydrological and thermal properties for the in-drift components of the THC Seepage Model are given in Section 4.1.7.

4.1.2 Mineralogical Data

These input data consist of mineral volume fractions per total solid volume and their reactive surface areas. Reactive surface areas are used to characterize minerals either in the matrix of the rock (cm^2/g mineral), or those on the surface of fractures (m^2/m^3 of total medium, including pore space), respectively.

These data were taken from DTN: LB0101DSTTHCR1.002 [161277] and DTN: LB0101DSTTHCR1.004 [161279]. For convenience, these data are shown in Attachment II (volume fractions) and Attachment IV (reactive surface areas), respectively. The mineralogical data are for a stratigraphic column near the center of the repository.

Table 4.1-1. Data Tracking Numbers for Sources of Direct Input Data for the Drift-Scale Coupled-Processes Models Used to Feed TSPA-LA Activities

DTNs	Data/Parameter Description[1]
Hydrological and Thermal Rock Properties	
LB991091233129.006 [111480]	Fracture tortuosity
LB0205REVUZPRP.001 [159525]	Fracture parameters: permeability, porosity, van Genuchten m, residual saturation, satiated saturation, fracture frequency, fracture to matrix area
LB0208UZDSCPMI.002 [161243]	Fracture and matrix van Genuchten alpha, matrix permeability
LB0207REVUZPRP.002 [159672]	Matrix parameters: van Genuchten m, residual saturation, satiated saturation
LB0210THRMLPRP.001 [160799]	Matrix porosity and thermal properties: dry- and wet-rock grain conductivity, grain specific heat, and grain density
LL000114004242.090 [142884]	Infiltration rates—average infiltration rate (mean, lower bound, and upper bound for present day, monsoon, and glacial transition climates) from the TH drift-scale models.
Mineralogical Data	
LA9908JC831321.001 [113495]	Model input and output files for Mineralogic Model "MM3.0" Version 3.0.
LA0009SL831151.001 [153485]	Mineralogical characterization of the ESF SHT Block
LA9912SL831151.001 [146447] LA9912SL831151.002 [146449]	DST and SHT fracture mineralogy data
LB0101DSTTHCR1.002 [161277][2] LB0101DSTTHCR1.004 [161279][2]	Mineral volume fractions Mineral surface areas
Kinetic Data	
LB0307KNTDBRTM.001 [164433]	Rate constants and activation energies
Thermodynamic Data	
LB0307THMDBRTM.001 [164434]	Thermodynamic data for aqueous species and minerals: equilibrium constants, molecular weights, molar volumes, Debye-Hückel parameters, CO_2 molecular diameter
Analytical Water and Gas Chemistry Data	
MO0005PORWATER.000 [150930]	Analyses of pore waters from Alcove 5 core samples in the ESF (HD-PERM-2 and HD-PERM-3 samples)
GS020408312272.003 [160899]	Pore water analyses from Cross Drift and USW SD-9 borehole core samples (see Table 4.1-3)
Tptpmn and Tptpll THC Model Grid Data	
LB990501233129.004 [111475]	Stratigraphy (Z coordinates of hydrogeologic units) for: Borehole USW SD-9 (column i64) in UZ site-scale calibration model grid (Tptpmn THC models) Central location (column j34) (Tptpll THC Model)
LB990701233129.002 [125604]	Top and bottom boundary temperatures, pressure, liquid/gas saturations, and boundary elevations
LB990601233124.001 [105888]	Permeability Measurements in Tptpmn

NOTES: [1] Values of thermal and hydrological properties used in the THC models are summarized in Table 6.4-1
[2] Intermediate results from REV01. These can be used here or in future report revisions.

Table 4.1-2. Sources of Technical Information Used as Direct Input for Model Design Used to Feed TSPA-LA Activities

DTNs/Sources	Parameter Description
Repository Drift Design Data	
800-IED-EBS0-00402-000-00B (BSC 2003 [161727])	Drift spacing
800-IED-EBS0-00201-000-00A (BSC 2003 [164069])	Drift diameter
800-IED-WIS0-00201-000-00A (BSC 2002 [164053])	Waste package diameter
CRWMS M&O 2000 [151014]	Hydrological and thermal properties of drift design elements (Table 4.1-5)
SN0002T0872799.009 [153364]	Effective thermal conductivity
CRWMS M&O 2000 [149137] (Design Criterion, p. 23)	Lower-invert thermal conductivity
BSC 2002 [159906]	Upper-invert thermal conductivity
800-IED-EBS0-00403-000-00B (BSC 2003 [161731])	Heat load (1.45 kW/m) (see text)
ANL-EBS-MD-00030 REV01 ICN 01 (BSC 2002 [160975], Table 6-6) [1]	Heat removal by ventilation (86.3%)

NOTE: [1] This has been superseded by BSC (2002 [161760], Table 6-5) showing slightly smaller (84%) heat removal. The impact of this difference on rock temperature around the drift is much smaller than the range of temperature conditions evaluated.

4.1.3 Water and Gas Chemistry

Sources of water- and gas-chemistry data are provided in Table 4.1-1. The pore-water compositions used as inputs to the models are shown in Table 4.1-3.

The only nearly complete pore-water analyses available at the start of these investigations, for samples collected from a repository unit near the repository footprint, were obtained in 1998 from the Tptpmn geologic unit in Alcove 5 near the DST. At the time, three pore-water samples were ultracentrifuged from Alcove 5 core. These analyses were reported in DTN: MO0005PORWATER.000 [150930]. The average of two of these analyses with the closest compositions (HD-PERM-2 and HD-PERM-3, Table 4.1-3) was initially chosen as the input water composition for pre-REV02 work and referenced hereafter as the Alcove 5 or HD-PERM water (see Section 6.2.2.1).

More recently, as part of REV02 work, a series of pore-water samples were ultracentrifuged from core collected in the Enhanced Characterization of Repository Block (ECRB) Cross Drift and from core obtained from the drilling of borehole SD-9. These samples were analyzed and the data were reported under DTN: GS020408312272.003 [160899]. Four of these samples (ECRB-SYS-CS7.3-7.7/UC, ECRB-SYS-CS2000/16.5-21.1/UC, SD-9/990.4-991.7/UC, and ECRB-SYS-CS500/12.0-16.7/UC) and HD-PERM water were selected as input water compositions for REV02 of the THC Seepage Model (Table 4.1-3). The rationale for selecting these samples and the determination of concentrations for constituents that were not measured are discussed in Section 6.2.2.1.

Table 4.1-3. Input Pore-Water Compositions

Sample ID →		ESF-HD-PERM-2 (30.1'-30.5')[1] (ESF Alcove 5)	ESF-HD-PERM-3 (34.8'-35.1')[1] (ESF Alcove 5)	ECRB-SYS-CS1000/7.3-7.7/UC[2]	ECRB-SYS-CS2000/16.5-21.1/UC[2]	SD-9/990.4-991.7/UC[2]	ECRB-SYS-CS500/12.0-16.7/UC[2]
Lithostratigraphic Unit →		**Tptpmn**	**Tptpmn**	**Tptpul (base)**	**Tptpll**	**Tptpll**	**Tptpul**
	Units						
pH (measured)	pH	8.32	8.31	7.6	7.4	7.9	8.0
Na^+	mg/L	61	62	39	130	84	57
K^+	mg/L	7	9	7.6	10.6	7.9	10.3
Ca^{+2}	mg/L	106	97	94	82	56	120
Mg^{+2}	mg/L	16.6	17.4	18.1	5.3	0.9	19.3
SiO_2	mg/L	31 (as Si)	35 (as Si)	42	48	50	49
Cl^-	mg/L	110	123	21	26	23	54
SO_4^{-2}	mg/L	111	120	36	39	10	78
HCO_3^- (measured)	mg/L	-	-	333	382	313	286
NO_3^-	mg/L	3	10	2.6	4.2	17	6.1
F^-	mg/L	0.96	0.76	3.4	11	2.5	4.8

NOTES: (1) Pore water analyses from Alcove 5 (Tptpmn) reported with DTN: MO0005PORWATER.000 [150930]. The sample ID corresponds to the ESF borehole ID and is followed by the sampling depth in feet from collar.
(2) Pore water analyses from the ECRB cross-drift and borehole SD-9 reported in DTN: GS020408312272.003 [160899]. Note, for ECRB samples, the sample ID contains the cross-drift station in meters (e.g., CS1000) and the sampled interval in feet from collar (e.g., 7.3-7.7). The ID of the SD-9 sample contains the sampled depth interval in feet from the ground surface.

4.1.4 Thermodynamic Data

These data consist mostly of chemical equilibrium constants in logarithmic form, log(*K*), as function of temperature (not to be confused with thermal conductivity, often described also using the letter *K*), for reactions describing the dissociation of secondary aqueous species, minerals, and gases involved in the model (e.g., Section 6.4.1). Molecular weight and diameter, molar volume, and ion size data for the calculation of aqueous activity coefficients are also included in the thermodynamic data sets. Kinetic rate constants *k* (always in lower case), are provided in separate databases discussed in Sections 4.1.5 (also see Sections 6.4.2 and 6.4.8) and are also not to be confused with equilibrium constants *K*.

Thermodynamic data for REV02 simulations (reported in Section 6.8) were taken from DTN: LB0307THMDBRTM.001 [164434]. For convenience, this data set is shown in Attachment VI (zeolite phases used are those identified in Attachment VI with names "heul/10-r02," "stell/10-r02," "mord/10-r02," and "clpt/10-r02," except for alternative data sets as discussed in Section 6.4.8.2). Most of these data are originally from the Yucca Mountain Project (YMP) thermodynamic database data0.ymp.R2 (DTN: MO0302SPATHDYN.000 [161756]). Documentation on changes from the data0.ymp.R2. database is provided in DTN: LB0307THMDBDRTM.001 [164434]. Most important changes from data0.ymp.R2 include:

- Aluminum aqueous species data consistent with thermodynamic data used in earlier revisions of this report. These aluminum data were derived from Pokrovskii and Helgeson (1995 [101699]). In the weakly-acid-to-alkaline pH values covered in this study, and at temperatures below 150°C, the Pokrovskii and Helgeson (1995 [101699]) data yield essentially the same gibbsite solubility as the data currently in data0.ymp.R2 (DTN: MO0302SPATHDYN.000 [161756]), and essentially the same pK values for the protonation of the AlO_2^- (or $Al(OH)_4^-$) to $HAlO_2$ (or $Al(OH)_3$).

- Revised aqueous silica thermodynamic properties yielding solubility constants (log(K)) values very similar to those reported by Rimstidt (1997 [101709]) for quartz and Gunnarsson and Arnórsson (2000 [160465]) for amorphous silica. These data are also consistent with thermodynamic data used in earlier revisions of this report, and provide more accurate amorphous silica solubilities than the data0.ymp.R2 data.

- Solubility constants for albite and anorthite from Arnórsson and Stefánsson (1999 [153329], p. 173). These data are consistent with those used in earlier versions of this report and with the aqueous silica data used here.

- Solubility constants for K-feldspar adjusted to yield equilibration of the HD-PERM pore water (Table 6.2-1) with illite (below) and K-feldspar. This adjustment results in a Gibbs free energy value for this phase at 25°C within the range of literature data reported by Arnórsson and Stefánsson 1999 [153329] (their Table 1) and within 700 calories of the value reported by Robie et al. (1979 [107109]). Without this adjustment, calculated potassium concentrations in pore waters are too small.

- Revised clay (smectite and illite) data consistent with those used in earlier versions of this report. The revisions include log(K) values for illite derived from accurate solubility

measurements by Kulik and Aja (1997 [128132]), and log(K) values for smectites adjusted to yield equilibration as an ideal solid solution at 25°C with the HD-PERM pore water (Table 6.2-1). The latter adjustment required less than 0.5% change in the Gibbs free-energy values of these smectites, well within the uncertainty of these values. Without this revision, the calculated pH of pore waters through time, under ambient conditions (no thermal load), becomes unrealistically elevated (Section 6.8.5.1).

- Revised zeolite (stellerite, heulandite, mordenite, and clinoptilolite) data for consistency with new stellerite data reported by Fridriksson et al. (2001 [160460]). Without this revision, an unrealistic calcium depletion is predicted to occur in pore waters under ambient conditions (no thermal load), due to the precipitation of large amounts of calcium zeolites (Section 6.8.5.1)

Of these changes, the last two have the most significant effect on simulation results compared to results obtained using the project database data0.ymp.R2 (DTN: MO0302SPATHDYN.000 [161756]) (Section 6.8.5.1). The stellerite thermodynamic data in data0.ymp.R2 reflect a significantly higher stability for this mineral than the new data from Fridriksson et al. (2001 [160460]) suggest. The clay data in data0.ymp.R2 also reflect a greater stability than the revised data used here. More details on all changes from the data0.ymp.R2. database are provided in the documentation accompanying the data filed under DTN: LB0307THMBDRTM.001 [164434].

Ambient simulations (Section 6.8.5.1) were conducted using alternative data sets including the data0.ymp.R2 database. These ambient simulations were run to provide a justification for the use of data from DTN: LB0307THMDBRTM.001 [164434] (which include the changes described above). Sources of data for the alternative data sets are presented in Section 6.4.8.2.

4.1.5 Kinetic Data

Kinetic data refer to the reaction rate constants (k_o), activation energies (E_a), and related data required to describe the rates of dissolution and precipitation of minerals as a function of temperatures and fluid chemistry.

Reaction rate laws can take numerous forms, of which a restricted number are used for the model analyses. The form of these rate laws and their significance are described in Section 6.4.2. Listed kinetic parameters are defined and used in Equations 6.4-5 through 6.4-8.

REV02 simulations were conducted using the kinetic data from DTN: LB0307KNTDBRTM.001 [164433]. For convenience, these data are shown in Table 4.1-4. These data were used in the absence of other existing qualified kinetic data.

Table 4.1-4. REV02 Kinetic Data

MINERAL	$k_{+/-}$ (mol m^{-2} s^{-1})(1) at 298.15 K	E_a (kJ/mol)(2)	m(3)	n(3)	Comment (4)
α-Cristobalite SiO_2	3.45×10^{-13}	68.9	1	1	dissolution only
Quartz SiO_2	4.52×10^{-14}	90.1	1	1	dissolution only
Tridymite SiO_2	3.45×10^{-13}	68.9	1	1	dissolution only
Amorphous silica SiO_2	7.32×10^{-13}	60.9	1	1	dissolution
	1.0×10^{-10}	50	4.4	1	precipitation
Opal-proxy SiO_2	7.32×10^{-13}	60.9	1	1	dissolution only
Microcline = K-spar $KAlSi_3O_8$	1.78×10^{-13}	36	1	1	reversible
Albite-low $NaAlSi_3O_8$	7.08×10^{-13}	67.7	1	1	reversible
Anorthite $CaAl_2Si_2O_8$	3.16×10^{-12}	67.7	1	1	dissolution only
Illite $K_{0.5}(Mg_{0.22}Al_{1.78})(Si_{3.72}Al_{0.28})O_{10}(OH)_2$	2.0×10^{-14}	58.6	1	1	reversible
Smectite-Ca $Ca_{0.145}(Mg_{0.26}Al_{1.74})(Si_{3.97}Al_{0.03})O_{10}(OH)_2$	2.0×10^{-14}	58.6	1	1	reversible
Smectite-Mg $(Mg_{0.405}Al_{1.74})(Si_{3.97}Al_{0.03})O_{10}(OH)_2$	2.0×10^{-14}	58.6	1	1	reversible
Smectite-Na $Na_{0.29}(Mg_{0.26}Al_{1.74})(Si_{3.97}Al_{0.03})O_{10}(OH)_2$	2.0×10^{-14}	58.6	1	1	reversible
Sepiolite $Mg_2Si_3O_{7.5}OH{\cdot}3H_2O$	2.67×10^{-14}	58.6	1	1	reversible

Table 4.1-4. REV02 Kinetic Data (continued)

MINERAL	$k_{+/-}$ (mol m^{-2} s^{-1})(1) at 298.15 K	E_a (kJ/mol)(2)	m(3)	n(3)	Comment (4)
Kaolinite $Al_2Si_2O_5(OH)_4$	1.0×10^{-13}	7.1 (± 2.5)	1	1	reversible
Heulandite $Ca_{0.33}K_{0.04}Na_{0.1}(Al_{0.8}Si_{2.8}O_{7.2}) \cdot 2.6H_2O$	5.66×10^{-13}	58.0	1	1	dissolution
Clinoptilolite $Ca_{0.28}K_{0.08}Na_{0.04}(Al_{0.68}Si_{2.92}O_{7.2}) \cdot 2.6H_2O$	2.37×10^{-13}	58.0	1	1	reversible
Stellerite $Ca_{0.39}Na_{0.01}(Al_{0.79}Si_{2.81}O_{7.2}) \cdot 2.8H_2O$	5.66×10^{-13}	58.0	1	1	reversible
Mordenite $Ca_{0.15}Na_{0.21}K_{0.09}(Al_{0.6}Si_3O_{7.2}) \cdot 2.2H_2O$	5.66×10^{-13}	58.0	1	1	reversible
Calcite	1.60×10^{-6}	48.1	1	1	reversible
$CaCO_3$	equilibrium	NA	NA	NA	local equilibrium
Gypsum $CaSO_4 \cdot 2H_2O$	equilibrium	NA	NA	NA	local equilibrium
Fluorite CaF_2	1.22×10^{-7}	0.0	1	2	reversible
Hematite Fe_2O_3	equilibrium	NA	NA	NA	local equilibrium
Goethite FeOOH	equilibrium	NA	NA	NA	local equilibrium
Glass (vitrophyre)	7.72×10^{-15}	91.0	1	1	dissolution only

DTN: LB0307KNTDBRTM.001 [164433]

NOTES: (1) $k_{+/-}$: dissolution/precipitation rate constants at 298.15 K.

(2) E_a: Activation energy.

(3) Exponents m and n in Equations 6.4-5, 6.4-7, and 6.4-8.

(4) "dissolution only" means precipitation of this mineral is not allowed, "reversible" indicates the same precipitation and dissolution rate apply.

4.1.6 Transport Parameters

Transport parameters considered in the model are diffusion coefficients for aqueous and gaseous species and tortuosities of the fracture, matrix, and engineered system components.

Diffusion coefficients for all aqueous species are direct inputs to the model and entered as the tracer diffusion coefficient of the chloride anion (Cl) at infinite dilution. The aqueous diffusion coefficient of Cl at infinite dilution is 2.03×10^{-9} m^2/s at 25°C (Lasaga 1998 [117091], Table 4.1, p. 315), which in the model input was rounded to 2.0×10^{-9} m^2/s. The value of 2.03×10^{-9} m^2/s is corroborated by Lide (1993 [123032], p. 5-111). The rationale for using these data sources is that they are accepted throughout the scientific community as reliable references.

The CO_2 diffusion coefficient is approximated from ideal gas behavior as described in Section 6.4.6.1, using direct inputs for molecular diameter (d_m) and molecular weight (M) as follows (unless specified otherwise in Section 6):

$d_m = 2.5 \times 10^{-10}$ m (DTN: LB0307THMDBRTM.001 [164434])

M = .04401 kg/mol (DTN: MO0302SPATHDYN.000 [161756])

Tortuosities were set to 0.7 for fractures (DTN: LB991091233129.006 [111480]) based on models of *in situ* testing data, and further modified as described in Section 6.4.6.1. Matrix tortuosities are unknown and assumed in Section 5, with rationale given in that section.

4.1.7 Design Information

Design information are specified, in contrast to data resulting from measurements. Design information are not "data" and are presented in this section for convenience because they are required for model input. Sources of design information are summarized in Table 4.1-2.

Two time periods are considered in the THC Seepage Model:

- A 50-year preclosure period during which a large amount of the heat released by the waste packages is removed by ventilation (see below)
- A postclosure period immediately following the initial 50-year preclosure period and extending to 100,000 years (the total simulation time), during which a drip shield is placed above the waste packages and no heat is removed by ventilation.

Accordingly, some of the drift-specific model-input design information are not the same for the preclosure and postclosure time periods. The model drift geometry and thermophysical properties of design elements are shown in Table 4.1-5 and Figure 4.1-1. Sources of this technical information are shown in this table and also referenced in Table 4.1-2. This drift design information is the same as that used for Site Recommendation. However, an important difference from previous model revisions is that the drift is modeled here as open to both advective and diffusive fluxes of liquid and gas. As a result, hydrological properties had to be assigned to open in-drift areas. These properties are included in Table 4.1-5. The discretization of the drift is consistent with the dimensions shown in Figure 4.1-1, within the limits imposed by the resolution of the model mesh.

Table 4.1-5. Drift Design Parameters

Parameter	Model Input		Information Exchange Drawing (IED)[1]	
	Source	Value	Current Value	Source
Drift diameter	800-IED-EBS0-00201-000-00A (BSC 2003 [164069])	5.5 m	5.5 m	800-IED-EBS0-00201-000-00A (BSC 2003 [164069])
Waste package outer diameter	800-IED-WIS0-00201-000-00A (BSC 2002 [164053]) (44-BWR waste package)	1.67 m (rounded off from 1.674 m)	1.318 – 2.110 m (1.674 m for 44-BWR waste package)	800-IED-WIS0-00201-000-00A (BSC 2002 [164053])
Top of invert as measured from bottom of drift	800-IED-WIS0-00301-000-00A (BSC 2003 [164052])	0.8 m (rounded off from 0.806 m)	0.806 m	800-IED-WIS0-00301-000-00A (BSC 2003 [164052])
Location of waste package center above bottom of drift	CRWMS M&O (2000 [151014], Table 2)	1.945 m	1.637 – 2.088 m	800-IED-EBS0-00201-000-00A (BSC 2003 [164069]) (center line of waste package height above invert) and 800-IED-WIS0-00301-000-00A (BSC 2003 [164052]) (invert thickness)
Location of waste package center below the drift springline	CRWMS M&O (2000 [151014], Table 2)	0.805 m	0.662 – 1.113 m	800-IED-EBS0-00201-000-00A (BSC 2003 [164069]) (drift diameter; center line of waste package height above invert) and 800-IED-WIS0-00301-000-00A (BSC 2003 [164052]) (invert thickness)
Drip shield thickness	CRWMS M&O (2000 [151014], Table 2)	0.02 m	0.015 m	000-MW0-TED0-00102-000-00A (BSC 2003 [161519]
Air gap between waste package surface and the inside of drip shield	CRWMS M&O (2000 [151014], Table 2)	0.396 m	0.079 – 0.920 m	800-IED-EBS0-00201-000-00A (BSC 2003 [164069]) (center line of waste package height above invert), 800-IED-WIS0-00201-000-00A (BSC 2002 [164053]) (diameter of waste package), and 000-MW0-TED0-00102-000-00A (BSC 2002 [161519] (inside height of drip shield)
Inside radius of drip shield	CRWMS M&O (2000 [151014], Table 2)	1.231 m	1.350 m	000-MW0-TED0-00102-000-00A (BSC 2002 [161519]
Waste package thermal conductivity	CRWMS M&O (2000 [151014], Table 2)	14.42 W/m K	Not in an IED	Not Applicable
Waste package density	CRWMS M&O (2000 [151014], Table 2)	8189.2 kg/m^3	Not in an IED	Not Applicable

Table 4.1-5. Drift Design Parameters (continued)

Parameter	Model Input		Information Exchange Drawing (IED)[1]	
	Source	Value	Current Value	Source
Waste package specific heat	CRWMS M&O (2000 [151014], Table 2)	488.86 J/kg K	Not in an IED	Not Applicable
Invert intrinsic permeability	CRWMS M&O (2000 [151014], Table 2)	6.152×10^{-10} m^2	Not in an IED	Not Applicable
Invert porosity	CRWMS M&O (2000 [151014], Table 2)	0.545	Not in an IED	Not Applicable
Invert grain density	CRWMS M&O (2000 [151014], Table 2)	2530 kg/m^3	Not in an IED	Not Applicable
Invert specific heat	CRWMS M&O (2000 [151014], Table 2)	948 J/kg K	Not in an IED	Not Applicable
Invert thermal conductivity (upper invert)	BSC 2002 [159906], Table 6-48 (100°C data, average between ballast K = 0.1 and 0.2 W/m-K)	1.52 W/m K	Not in an IED	Not Applicable
Invert thermal conductivity (lower invert)	CRWMS M&O 2000 [149137], Design Criterion, p. 23	0.15 W/m K (average measurement on two samples)	Not in an IED	Not Applicable
Open areas (linear capillary pressure and relative permeability functions)	Model setup (Section 6.4.6)		Not in an IED	Not Applicable
Permeability		1×10^{-10} m^2		
Residual saturation (drift wall / all other areas)		0.01 / 0.0		
Porosity		1.0		
Capillary pressure		0.0 Pa		
Invert capillarity (linear capillary pressure function)	Set equal to 1/(Van Genuchten alpha), with alpha = 1.2×10^{-3} Pa^{-1} (rounded off from value in CRWMS M&O 2000 [151014], Table 2)	833 Pa	Not in an IED	Not Applicable
Invert residual saturation	Rounded off from value in CRWMS M&O (2000 [151014], Table 2)	0.1	Not in an IED	Not Applicable

Source: [1] IEDs were not always used because many IEDs were not completed before the start of this study. Differences between values used and those in IEDs are not expected to significantly affect model results for locations in rock around the drift because these results are primarily dependent on the applied heat load and not on the specifics of in-drift engineered features.

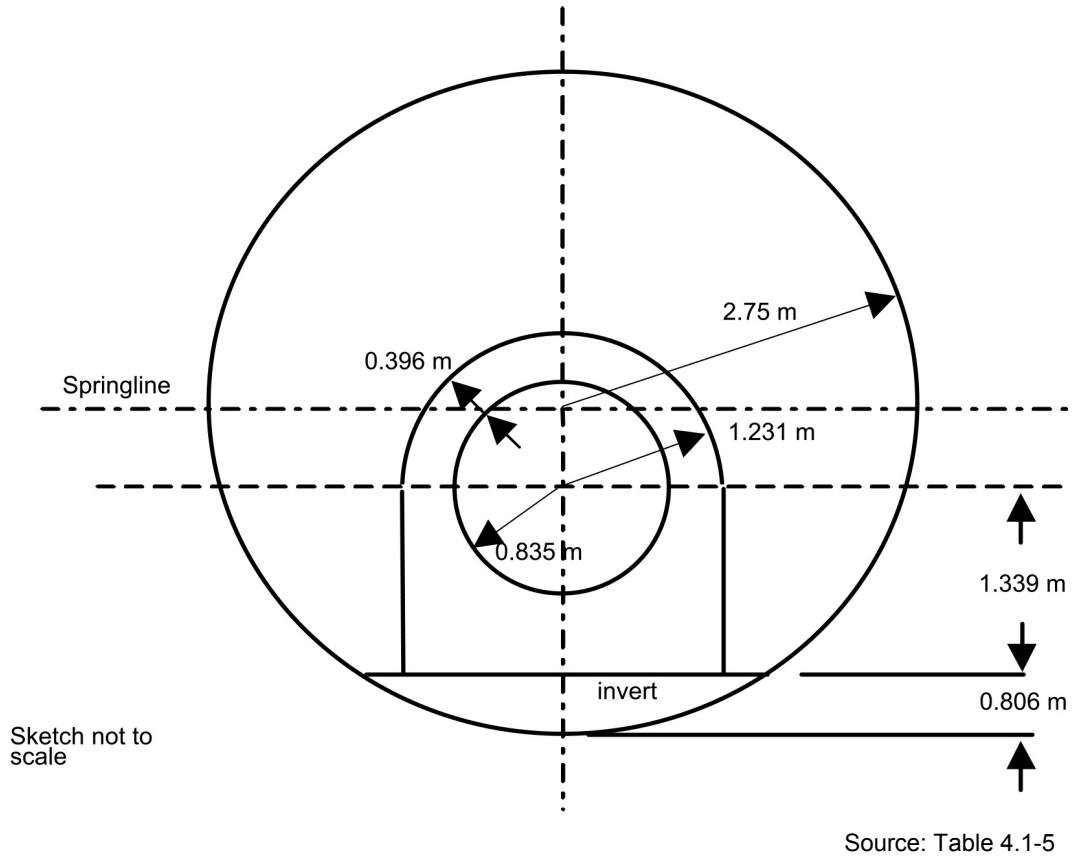

Figure 4.1-1. Sketch Showing Modeled In-Drift Dimensions

The drip shield was not explicitly modeled, but its thickness and thermal conductivity were considered in the width and thermal properties, respectively, of the open zone between the waste package and drip shield during the postclosure period.

The total (unventilated) heat load in REV02 simulations was obtained from BSC (2002 [159527]) (Attachment VIII). The initial heat transfer from the waste package is 1.45 $kW/m_{(drift)}$ which decays after 50 years to 0.593 kW/m and to 0.0684 W/m after 1,000 years. This is essentially the same heat load as shown in BSC 2003 [161731] which superseded BSC 2002 [159527], and also is very similar to the REV01 heat load. The heat removal rate during the 50-year preclosure period is 86.3% (BSC 2002 [160975], Table 6-6), which is significantly larger than the 70% used in REV01.

Heat transfer from the waste package to the drift wall is implemented in the model by using time-varying "effective" thermal conductivities (for open spaces within the drift) that were calculated to account for radiative and convective heat transport. These time-varying variables were input into the model as coefficients (values between 0 and 1) for each open zone within the drift. Each zone was also assigned a constant maximum thermal conductivity (Kth_{max}), which was then multiplied by the corresponding time-varying coefficients to obtain effective conductivities as a function of time (Attachment IX). The sources of this design information are listed in Table 4.1-2.

The effective thermal conductivities and corresponding open zones of the drift prior to closure are not the same as those following closure. Only one open space between the waste package and the drift wall is considered for the preclosure period. For postclosure, two zones are considered: (1) the open space between the waste package and the drip shield (Inner Zone, drip shield included) and (2) the open space between the drip shield and the drift wall (Outer Zone) (Figure 4.1-1). For preclosure, Kth_{max} = 10.568 W/m-K for the zone between the waste package and the drift wall. For postclosure, Kth_{max} = 2.298 W/m-K for the Inner Zone (between the waste package and the drip shield), and Kth_{max} = 14.407 W/m-K for the Outer Zone (between the drip shield and the drift wall). The sources of this design information are listed in Table 4.1-2. Accordingly, model runs were started with the preclosure thermal conductivities, then stopped after 50 years and restarted with the corresponding postclosure data.

The invert is divided into two zones with different thermal conductivities: 1.52 W/m-K for the upper half and 0.15 W/m-K for the lower half (Table 4.1-4).

The implementation of the drift design in the model is further documented in Spycher (2001 [160898], pp. 11–14; 116–129).

4.2 CRITERIA

Technical requirements to be satisfied by performance assessment (PA) are based on 10 CFR 63.114 [156605] (*Requirements for Performance Assessment*). These technical requirements are also identified in the Yucca Mountain *Project Requirements Document* (Canori and Leitner 2003 [161770], Section 3). The acceptance criteria that will be used by the Nuclear Regulatory Commission (NRC) to determine whether the technical requirements have been met are identified in the *Yucca Mountain Review Plan, Final Report* (YMRP; NRC 2003 [163274]). The pertinent requirements and acceptance criteria for this Model Report are summarized in Table 4.2-1. Note that different Acceptance Criteria were identified in the TWP (BSC 2002 [160819], Section 3) because the YMRP has been revised since completion of the TWP.

Table 4.2-1. Project Requirements and YMRP Acceptance Criteria Applicable to This Model Report

Requirement Number[a]	Requirement Title[a]	10 CFR 63 Link	YMRP Acceptance Criteria
PRD-002/T-015	Requirements for Performance Assessment	10 CFR 63.114(a-c) [156605]	Criteria 1 to 4 for *Quantity and Chemistry of Water Contacting Engineered Barriers and Waste Forms* [b]
PRD-002/T-016	Requirements for Multiple Barriers	10 CFR 63.115(c) [156605]	Criterion 3 for *Quantity and Chemistry of Water Contacting Engineered Barriers and Waste Forms* [c]

NOTES: [a] from Canori and Leitner (2003 [161770], Section 3)
[b] from NRC (2003 [163274], Section 2.2.1.3.3.3)
[c] from NRC (2003 [163274], Section 2.2.1.1.3)

The acceptance criteria identified in Section 2.2.1.3.3.3 of the YMRP (NRC 2003 [163274]) are given below, followed by a short description of their applicability to this Model Report:

- Acceptance Criterion 1, *System Description and Model Integration are Adequate*:

  The applicable subcriteria are:

  Subcriterion 1. This subcriterion requires that the total system performance assessment adequately incorporates important design features, physical phenomena, and couplings, and uses consistent and appropriate assumptions throughout the quantity and chemistry of water contacting waste packages and waste forms abstraction process. This subcriterion is addressed in Sections 6.2, 6.3, and 6.4.

  Subcriterion 2. This subcriterion requires that the abstraction of the quantity and chemistry of water contacting waste packages and waste forms uses assumptions, technical bases, data and models, that are appropriate and consistent with other related U.S. Department of Energy abstractions. Sections 5, 6, and 7 address this subcriterion regarding water chemistry.

  Subcriterion 4. This subcriterion requires that spatial and temporal abstractions appropriately address physical couplings (thermal-hydrologic-mechanical-chemical). Sections 6.8.5.3 and 6.8.5.4 address this subcriterion.

  Subcriterion 5. This subcriterion requires that sufficient technical bases and justification are provided for total system performance assessment assumptions and approximations for modeling coupled thermal-hydrologic-mechanical-chemical effects on seepage and flow, the waste package chemical environment, and the chemical environment for radionuclide release. This subcriterion also requires that the effects of distribution of flow on the amount of water contacting the waste packages and waste forms are consistently addressed, in all relevant abstractions. This report addresses coupled THC effects on water chemistry and flow in the UZ up to the drift wall (Section 6). It therefore addresses parts of this subcriterion.

  Subcriterion 8. This subcriterion requires that adequate technical bases are provided, including activities such as independent modeling, laboratory or field data, or sensitivity studies, for inclusion of any thermal-hydrologic-mechanical-chemical couplings and features, events, and processes (FEPs). FEPs are addressed in Section 6.1, technical bases in Sections 6.2–6.4, modeling and sensitivity studies in Sections 6.5–6.8, and modeling of field and laboratory experiments in Section 7.0, thus addressing this subcriterion.

  Subcriterion 9. This subcriterion requires that performance-affecting processes that have been observed in thermal-hydrologic tests and experiments are included into the performance assessment. Simulations presented in this report reproduce coupled THC effects observed in thermal test (Section 7.1) and laboratory experiments (Sections 7.2 and 7.3), and therefore address this subcriterion.

Subcriteria 3, 6, 7, 10, 11, and 12 are not applicable.

- Acceptance Criterion 2, *Data Are Sufficient for Model Justification*:

  The applicable subcriteria are:

  Subcriterion 1. This subcriterion requires that geological, hydrological and geochemical values used in the safety case are adequately justified, and that adequate descriptions of how data were used, interpreted, and appropriately synthesized into the parameters are provided. This subcriterion is addressed in Section 4.1, 6.2 (and in particular 6.2.2), 6.3, and 6.4.

  Subcriterion 2. This subcriterion requires that sufficient data were collected on the characteristics of the natural system and engineered materials to establish initial and boundary conditions for conceptual models of thermal-hydrologic-chemical coupled processes that affect seepage and flow and the waste package chemical environment. This report addresses parts of this subcriterion by considering variations in pore-water compositions (Section 6.2.2 and 6.8.5) and rock properties (Sections 6.5–6.8) representative of the natural system.

  Subcriterion 3. This subcriterion requires that thermo-hydrologic tests were designed and conducted with the explicit objectives of observing thermal-hydrologic processes for the temperature ranges expected for repository conditions and making measurements for mathematical models. This subcriteria also requires that data are sufficient to verify that thermal-hydrologic conceptual models address important thermal-hydrologic phenomena. Section 7.1, which presents details on results of the Drift Scale Test and simulations reproducing results of this test, addresses this subcriteria.

  Subcriteria 4 and 5 are not applicable.

- Acceptance Criterion 3, *Data Uncertainty Is Characterized and Propagated Through the Model Abstraction*

  Subcriterion 1. This subcriterion requires that models use parameter values, assumed ranges, probability distributions, and/or bounding assumptions that are technically defensible and reasonably account for uncertainties and variabilities. In this report, this subcriterion is addressed by using ranges if input data (e.g., pore-water composition, Section 6.2.2) and alternative conceptualizations of the modeled systems (Section 6.3) to model uncertainty is also discussed in Section 6.9.

  Subcriterion 2. This subcriterion requires that parameter values, assumed ranges, probability distributions, and bounding assumptions used in the calculations of quantity and chemistry of water contacting waste packages and waste forms are technically defensible and reasonable, based on data from the Yucca Mountain region (i.e., DST), and a combination of techniques that include laboratory experiments and field measurements and process-level modeling studies. This report addresses the parts of this subcriterion that relate to the uncertainty of the chemistry of water that could potentially

enter drifts, with inputs and results discussed in Sections 6.2.2, 6.8.5, 6.9, and validation including the results of the DST and laboratory experiments presented in Section 7.

Subcriterion 3. This subcriterion requires that input values used in the total system performance assessment calculations of quantity and chemistry of water contacting engineered barriers (e.g., drip shield and waste package) are consistent with the initial and boundary conditions and the assumptions of the conceptual models and design concepts for the Yucca Mountain site. This criterion also requires that correlations between input values are appropriately established in the U.S. Department of Energy total system performance assessment; that parameters used to define initial conditions, boundary conditions, and computational domain in sensitivity analyses involving coupled thermal-hydrologic-mechanical-chemical effects on seepage and flow, the waste package chemical environment, and the chemical environment for radionuclide release, are consistent with available data; and that reasonable or conservative ranges of parameters or function relations are established. This subcriterion is addressed with respect to the chemistry of water that could potentially enter drifts, with the conceptual models described in Sections 6.3–6.4 initial and boundary conditions discussed in Sections 6.5.2, 6.7.2 and 6.8.2, and ranges of input parameters presented in Sections 6.5.3, 6.6.1, 6.7.3 and 6.8.3.

Subcriterion 4. This subcriterion requires that adequate representation of uncertainties in the characteristics of the natural system and engineered materials is provided in parameter development for conceptual models, process-level models, and alternative conceptual models. This subcriterion also states that the U.S. Department of Energy may constrain these uncertainties using sensitivity analyses or conservative limits. This subcriterion is addressed by considering ranges of input parameters and alternative conceptualizations (e.g., Table 6-1 and Sections 6.2.2 and 6.3), as well as evaluations of the spread of model results (Section 6.9).

Subcriterion 5 is not applicable.

- Acceptance Criterion 4, *Model Uncertainty Is Characterized and Propagated Through the Model Abstraction*:

  Subcriterion 1. This subcriterion requires that alternative modeling approaches of features, events, and processes (FEPs), consistent with available data and current scientific understanding, are investigated. This subcriterion also requires that the results and limitations are appropriately considered in the abstraction. This subcriterion is addressed by reviewing FEPs (Section 6.1), by using alternative conceptual models (Section 6.3), and evaluating model limitation and uncertainty (Sections 1.3, 6.9 and 8.4).

  Subcriterion 2. This subcriterion requires that alternative modeling approaches are considered and the selected modeling approach is consistent with available data and current scientific understanding, and the results and limitations and uncertainties of the chosen model are provided. This subcriterion is addressed by considering various model conceptualizations (Section 6.3), evaluating spread in model results (Section 6.8.5), and reporting on limitations and uncertainties (Section 1.3, 6.9 and 8.4).

Subcriterion 3. This subcriterion requires that consideration of conceptual model uncertainty is consistent with available site characterization data, laboratory experiments, field measurements, natural analog information and process-level modeling studies; and that the treatment of conceptual model uncertainty does not result in an under-representation of the risk estimate. This subcriterion is addressed by using site-specific data (Section 4.1) as well as data from field and laboratory experiments (Section 7), and considering ranges of key input parameters (e.g. Section 6.2.2), alternative conceptualizations (Section 6.3), and spread in model results (Section 6.9).

Subcriterion 4. This subcriterion requires that adequate consideration is given to effects of thermal-hydrologic-mechanical-chemical coupled processes in the assessment of alternative conceptual models. These effects may include: (i) thermal-hydrologic effects on gas, water, and mineral chemistry; (ii) effects of microbial processes on the waste package chemical environment for radionuclide release; (iii) changes in water chemistry that may result from the release of corrosion products from the waste package and interactions between engineered materials and ground water; and (iv) changes in boundary conditions (e.g., drift shape and size) and hydrologic properties, relating to the response of the geomechanical system to thermal loading. This report addresses part (i) of this subcriterion through conceptual and mathematical models described in Sections 6.2 and 6.4, and model results presented in Sections 6.5.5, 6.6.2, 6.7.5, and 6.8.5.

Subcriterion 5 is not applicable.

The acceptance criterion identified in Section 2.2.1.1.3 of the YMRP (NRC 2003 [163274]) is given below, followed by a short description of its applicability to this Model Report

- Acceptance Criterion 3, *Technical Basis for Barrier Capability is Adequately Presented*:

  This model report documents the drift-scale coupled THC processes model that provides input to downstream users to predict the chemistry of water potentially contacting waste packages and waste forms. The technical bases for this model are consistent with the technical basis for the performance assessment, including consideration of the natural barrier created by host rocks, and the capillary pressure barrier at the drift wall (Sections 6.8.1, 6.8.5.2, and 6.8.5.4). The effect of a potential barrier created by mineral precipitation around the drift is also evaluated (Section 6.8.5.4).

4.3 CODES AND STANDARDS

No specific formally established standards have been identified as applying to this modeling activity.

INTENTIONALLY LEFT BLANK

5. ASSUMPTIONS

Development of methodology for the numerical modeling of heat and fluid flow in unsaturated fractured porous media, the calculation of mineral-water reactions, and the transport of aqueous and gaseous species are discussed in Section 6. Many simplifications and approximations underlie this methodology. Yet other simplifications and approximations are inherent in data that describe repository designs and associated parameters on which model simulations rely. In this section, only cases in which an assumption is made where there is an absence of data or information for the parameter or concept are described. These are listed below. Approximations and simplifications related to the development and implementation of the mathematical model applied for this study are presented as part of the model documentation in Section 6.4.6.

- The estimated matrix tortuosity of 0.2 is assumed to be applicable to the tuff matrix at Yucca Mountain (see Section 4.1.6). Because this value is within a range of values that differ by less than one order of magnitude, and is a factor applied along with the porosity to the diffusion coefficient, the effect on reaction-transport processes of a deviation in this number from the true value would be small. Therefore, no further justification or confirmation is necessary. A tortuosity of 0.7 is assumed for the invert. These values only slightly affect diffusive transport of CO_2 in the drift. The tortuosity of sand is about 0.7 (de Marsily 1986 [100439], p. 233), and because the invert is coarse granular material, its tortuosity would be expected to be between 0.7 and 1.0. Because reactions involving CO_2 are minimal in the drift, the diffusivity of CO_2 within in-drift components has a negligible effect on THC processes outside of the drift. Therefore, this assumption needs no further justification or confirmation.

INTENTIONALLY LEFT BLANK

6. MODEL DISCUSSION

This section presents the conceptual and mathematical models implemented for the development of the Drift Scale THC Seepage Model. Relevant features, events, and processes are also briefly discussed in Section 6.1. Details on the conceptualization and the mathematical treatment of the various coupled processes considered in the THC Seepage Model follow in Sections 6.2 through 6.4. The results of the THC Seepage Model are presented in Sections 6.5 through 6.8. In these sections, coupled THC processes are evaluated for 100,000 years under boundary conditions that are varied to represent the effects of potential climatic change, two repository host units, various input water compositions, and other alternative model conceptualizations. The validation of the THC Seepage Model is presented in Section 7. The model validation consists of simulating the water, gas, and mineral evolution in the Drift Scale Test using the DST THC Model (Section 7.1) and laboratory water-rock interaction experiments (Sections 7.2 and 7.3). The laboratory experiments are used to compare simulated and measured water compositions evolved during interaction with crushed tuff and mineral precipitation patterns in a fracture where boiling and reflux are taking place. These validation simulations rely on the same conceptualizations and mathematical formulations presented in this section.

The development of the THC Seepage Model is summarized in Table 6-1, which include changes between model revisions and a summary of the various conceptualizations and sensitivities considered.

Table 6-1. Summary of Changes from the REV01 to the REV02 THC Seepage Model

	Tptpmn THC Model REV01	**Tptpmn THC Heterogeneous Model REV01**	**Tptpll THC Model REV01**	**Tptpll THC Model REV02 (Current Model Report Revision)**
Chronological order of model development	1	2	3	4
Main use of model	Compare with the Tptpll Model (REV01) to evaluate the effect of host hydrogeologic unit and stratigraphic location	Compare with the Homogenous Tptpmn Model (REV01) to evaluate the effect of fracture permeability heterogeneity	Compare with the Tptpmn model (REV01) to evaluate the effect of host hydrogeologic unit and stratigraphic location	Evaluate the effect of model improvements comparisons with the Tptpmn Model (REV01) and provides sensitivities to various data and conceptualizations as shown
TOUGHREACT version	2.3	2.3	2.3	3
Model dimensions: Thermal loading Ambient conditions (baseline)	 2-D 2-D (with drift)	 2-D 2-D (with drift)	 2-D 2-D (with drift)	 2-D 1-D (no drift)
Stratigraphic column location	SD-9	SD-9	Center of repository	Center of repository
Host lithostratigraphic unit	Tptpmn	Tptpmn	Tptpll	Tptpll

Table 6-1. Summary of Changes between the REV01 and REV02 THC Seepage Model (Continued)

	Tptpmn THC Model REV01	Tptpmn THC Heterogeneous Model REV01	Tptpll THC Model REV01	Tptpll THC Model REV02 (Current Model Report Revision)
Heterogeneous permeability	No	Yes	No	No
Geochemical system (Table 6.2-2)	Base Extended	Base Extended	Base Extended	Extended
Input pore water composition (Table 6.2-1)	ESF Alcove 5	ESF Alcove 5	ESF Alcove 5	ESF Alcove 5 ECRB, 500 m (sensitivity) ECRB, 1000 m (sensitivity) ECRB, 2000 m (sensitivity) SD-9, 990 ft (sensitivity)
Infiltration rates (mm/yr)	Stepped up 6, 16, 25	Stepped up 6, 16, 25	Stepped up 6, 16, 25	Stepped up 6, 16, 25 Constant 6 (sensitivity) Constant 25 (sensitivity)
Heat Load (kW/m) (Attachments VII and VIII)	1.45	1.45	1.45	1.45
Ventilation Period (yr)	50	50	50	50
Ventilation efficiency (% heat removal)	70	70	70	86.3
Drift wall conceptualization	Closed to advective fluid flow	Closed to advective fluid flow	Closed to advective fluid flow	Open
Invert thickness	0.6	0.6	0.8	0.8
Vapor-pressure lowering due to capillary pressure	No	No	No	Yes No (sensitivity)
CO_2 diffusion coefficient change	None	None	None	Six-fold increase No change (sensitivity)
Improved treatment of mineral precipitation at boiling front	No	No	No	Yes
Chronological changes in Mineralogy (see Table 6.2-2 and Attachments I and II)	Initial data	No change	Added fluorite and opal as primary minerals in host rock	Added sepiolite and removed goethite as possible secondary minerals
Main chronological changes in thermal properties (see Table 6.4-1)	Initial data	No change	In Tptpll versus Tptpmn: 23 and 13 % decrease in effective K_{dry} and K_{wet}, respectively	For Tptpll, 6% increase in K_{dry} and 6% decrease in K_{wet} (effective values)
Main chronological changes in hydrological properties (see Table 6.4-1)	Initial data	In Tptpmn fractures: heterogeneous, 4-order-of- magnitude spread in fracture permeabilities in Tptpmn (3 different realizations)	In Tptpll versus Tptpmn fractures: six times higher permeability, 80% increase in porosity, and six times higher capillarity (1/alpha)	In Tptpll fractures: 62% decrease in permeability, 47% decrease in porosity and 20% decrease in capillarity (1/alpha)

NOTE: Sources of model input data and technical information shown here are discussed in Section 4.

Results of earlier investigations (REV01) are presented in Sections 6.5 (Tptpmn THC Model REV01), 6.6 (Tptpmn THC Heterogeneous Model REV01), and 6.7 (Tptpll THC Model REV01). Many model revisions have been implemented since the completion of this earlier work. These revisions include updated model input parameters, a change in the drift wall conceptualization (open versus closed), and a more accurate treatment of mineral precipitation at the boiling front (Section 6.4.5). Results of simulations including these revisions are presented in Section 6.8, together with model results for various input water compositions, infiltration rates, and two boiling/evaporation conceptual models, (including/excluding vapor-pressure lowering caused by capillary pressure). Simulations of ambient conditions using various sources of thermodynamic data are also presented in Section 6.8 as a means of justifying the thermodynamic data (Section 4) used in the model.

REV01 simulations are included in this Model Report revision because they provide an important assessment of the sensitivity of model results to the drift geologic host unit (Tptpmn versus Tptpll) and fracture permeability heterogeneity. However, the significant model revisions between REV01 and REV02 hamper pinpointing direct cause-effect relationships between a given specific change between REV01 and REV02 and its effect on simulation results. For these reasons, the REV01 results are best regarded as a qualitative assessment of model sensitivity to drift location and fracture permeability heterogeneity. For predictive evaluations, preference should be given to the most recent results, keeping in mind that the model uncertainty encompasses the results of both earlier and recent work. REV01 results indicate that the effect of drift location and fracture heterogeneity on predicted water chemistry and mineral alteration may not be as significant as the effect of uncertainties in input water composition, thermodynamic data, and infiltration rates. Therefore, evaluating the latter uncertainties is given priority in this Model Report revision.

The model development, data, and results are documented in the scientific notebooks (SNs) listed in Table 6-2 below. The intended use of output data from this Model Report is discussed in Section 1.1. Applicable acceptance criteria from the YMRP were discussed in Section 4.2, with pointers referring to sections addressing these criteria. The barrier capability of the host rocks, the capillary barrier at the drift wall, and potential barrier resulting from mineral precipitation around the drift are given consideration in this report (e.g., Sections 6.8.2, 6.8.5.2, and 6.8.5.4).

Table 6-2. Scientific Notebooks

LBNL Scientific Notebook ID	M&O Scientific Notebook ID	Relevant Pages	Citation
YMP-LBNL-YWT-ELS-1	SN-LBNL-SCI-109-V1	35–70, 87–91, 120–179	Wang 2003 [161665]
YMP-LBNL-DSM-ELS-1	SN-LBNL-SCI-142-V1	3–20, 27–52, 87–96, 104–115	Wang 2003 [161665]
YMP-LBNL-DSM-NS-1	SN-LBNL-SCI-141-V1	1–143	Spycher 2001 [160898]
YMP-LBNL-YWT-NS-1.2	SN-LBNL-SCI-112-V2	13–14, 21–40, 60–66	Wang 2003 [161665]
YMP-LBNL-DSM-ELS-PD-1	SN-LBNL-SCI-190-V1	7–60, 66–70, 86–144	Dobson 2001 [160252]
YMP-LBNL-GSB-1.6.4	SN-LBNL-SCI-085-V2	24–33	Haukwa 2001 [160900]
YMP-LBNL-DSM-NS-2	SN-LBNL-SCI-141-V2	94, 99-191	Wang 2003 [161665]
YMP-LBNL-DSM-ELS-PD-2	SN-LBNL-SCI-190-V2	7–35, 37–38, 43–81, 85, 95–124	Wang 2003 [161665]

6.1 RELEVANT FEATURES, EVENTS, AND PROCESSES

The results of this model abstraction are part of the basis for the treatment of Features, Events, and Processes (FEPs) as discussed in the *Total System Performance Assessment-License Application Methods and Approach* (BSC 2002 [160146], Section 3.2.2). FEPs that are included and excluded from TSPA-LA, and that are the subject matter of this report, are summarized in Tables 6.1-1 and 6.1-2, respectively. These were taken from the LA FEP List (MO0301SEPFEPS1.000 [161496]). The LA FEP List is a revision to the previous project FEP list (Freeze et al. 2001 [154365]) used to develop the list of included FEPs in the *Technical Work Plan for: Performance Assessment Unsaturated Zone* (BSC 2002 [160819], Table 2-6). The cross-reference for each FEP to the relevant section (or sections) in this Model Report is given in Tables 6.1-1 and 6.1-2.

Complete or partial treatment of FEPs is provided herein. The results of this and other model reports are used to fully document the technical basis for the include/exclude status of these FEPs for TSPA-LA. The UZ department's documentation for the included FEPs listed in Table 6.1-1 is compiled from this and other model reports and can be found in the model abstraction reports as described in Sections 2.1.2 and 2.4 of the TWP (BSC 2002 [160819]) and the FEPs report as described in Section 1.12.10 of the TWP (BSC 2002 [160819]). Excluded FEPs are to be documented in the FEPs report as described in Section 1.12.10 of the TWP (BSC 2002 [160819]).

Table 6.1-1. Features, Events, and Processes Relevant to this Model Report and Included into TSPA-LA

LA FEP Number	FEP Name	YMP Description	Sections Discussing FEPs-Related Items In this Model Report
1.1.02.02.0A	Pre-closure ventilation	The duration of pre-closure ventilation acts together with waste package spacing (as per design) to control the extent of the boiling front.	4.1.7
1.2.02.01.0A	Fractures	Groundwater flow in the Yucca Mountain region and transport of any released radionuclides may take place along fractures. The rate of flow and the extent of transport in fractures are influenced by characteristics such as orientation, aperture, asperity, fracture length, connectivity, and the nature of any linings or infills.	6.2.1 6.4.3
1.3.01.00.0A	Climate change, global	Climate change may affect the long-term performance of the repository. This includes the effects of long-term change in global climate (e.g., glacial/interglacial cycles) and shorter-term change in regional and local climate. Climate is typically characterized by temporal variations in precipitation and temperature.	6.2.1.3 6.5.2 6.7.2 6.8.2
1.4.01.01.0A	Climate modification increases recharge	Climate modification (natural or artificial) causes an increase in recharge in the Yucca Mountain region. Increased recharge might lead to increased flux through the repository, perched water, or water table rise.	6.2.1.3 6.5.2 6.7.2 6.8.2
2.1.08.01.0A	Water influx at the repository	An increase in the unsaturated water flux at the repository affects thermal, hydrological, chemical, and mechanical behavior of the system. Increases in flux could result from climate change, but the cause of the increase is not an essential part of the FEP.	6.5.2 (climate) 6.7.2 (climate) 6.8.2 (climate) 6.5.5.1 (reflux) 6.7.5.1 (reflux) 6.8.5.2 (reflux)
2.2.03.01.0A	Stratigraphy	Stratigraphic information is necessary information for the performance assessment. This information should include identification of the relevant rock units, soils and alluvium, and their thickness, lateral extents, and relationships to each other. Major discontinuities should be identified.	4.1.2 6.5.1 6.7.1 6.8.1
2.2.03.02.0A	Rock properties of host rock and other units	Physical properties such as porosity and permeability of the relevant rock units, soils, and alluvium are necessary for the performance assessment. Possible heterogeneities in these properties should be considered. Questions concerning events and processes that may cause these physical properties to change over time are considered in other FEPs	4.1.1 6.2.1 6.4.4 6.6.1.1
2.2.07.02.0A	Unsaturated groundwater flow in the geosphere	Groundwater flow occurs in unsaturated rocks in most locations above the water table at Yucca Mountain, including at the location of the repository. See other FEPs for discussions of specific issues related to unsaturated flow. See related FEPs 2.2.07.03.0A (capillary rise), 2.2.07.04.0A (focusing of unsaturated flow), 2.2.07.05.0A (effects of episodic infiltration), 2.2.07.07.0A (perched water), 2.2.07.08.0A (fracture flow), 2.2.07.09.0A (matrix imbibition), 2.2.07.10.0A (condensation zone forms), 2.2.07.11.0A (resaturation of dry-out zone), and 2.2.10.10.0A (two-phase flow / heat pipes).	6.2.1

Table 6.1-1. Features, Events, and Processes Relevant to this Model Report and Included into TSPA-LA (continued)

LA FEP Number	FEP Name	YMP Description	Sections Discussing FEPs-Related Items In this Model Report
2.2.07.04.0A	Focusing of unsaturated flow (fingers, weeps)	Unsaturated flow can differentiate into zones of greater and lower saturation (fingers) that may persist as preferential flow paths. Heterogeneities in rock properties, including fractures and faults, may contribute to focusing. Focused flow may become locally saturated.	6.2.1 6.6.2.2
2.2.07.08.0A	Fracture flow in the UZ	Fractures or other analogous channels act as conduits for fluids to move into the subsurface to interact with the repository and as conduits for fluids to leave the vicinity of the repository and be conducted to the SZ. Water may flow through only a portion of the fracture network, including flow through a restricted portion of a given fracture plane.	6.2.1 6.4.3
2.2.07.09.0A	Matrix imbibition in the UZ	Water flowing in fractures or other channels in the unsaturated zone is imbibed into the surrounding rock matrix. This may occur during steady flow, episodic flow, or into matrix pores that have been dried out during the thermal period.	6.2.1
2.2.07.10.0A	Condensation zone forms around drifts	Condensation of the two-phase flow generated by repository heat forms in the rock where the temperature drops below the local vaporization temperature. Waste package emplacement geometry and thermal loading will affect the scale at which condensation caps form (over waste packages, over panels, or over the entire repository), and to the extent to which “shedding” will occur as water flows from the region above one drift to the region above another drift or into the rock between drifts.	6.2.1 6.5.5.1 6.6.2.1 6.8.5.4
2.2.07.11.0A	Resaturation of geosphere dryout zone	Following the peak thermal period, water in the condensation cap (see FEP 2.2.07.10.0A) may flow downward into the drifts. Influx of cooler water from above, such as might occur from episodic flow, may accelerate return flow from the condensation cap by lowering temperatures below the condensation point. Percolating groundwater will also contribute to resaturation of the dry out zone. Vapor flow, as distinct from liquid flow by capillary processes, may also contribute.	6.2.1 6.5.5 6.6.2 6.7.5 6.8.5
2.2.07.20.0A	Flow diversion around repository drifts	Flow in unsaturated rock tends to be diverted by openings such as waste emplacement drifts due to the effects of capillary forces. The resulting diversion of flow could have an effect on seepage into the repository. Flow diversion around the drift openings could also lead to the development of a zone of lower flow rates and low saturation beneath the drift, known as the drift shadow (see FEP 2.2.07.21.0A).	6.2.1 6.5.5.1 6.6.2.1 6.8.5.4

Table 6.1-1. Features, Events, and Processes Relevant to this Model Report and Included into TSPA-LA (continued)

LA FEP Number	FEP Name	YMP Description	Sections Discussing FEPs-Related Items In this Model Report
2.2.08.01.0B	Chemical characteristics of groundwater in the UZ	Chemistry and other characteristics of groundwater in the unsaturated zone may affect groundwater flow and radionuclide transport of dissolved and colloidal species. Groundwater chemistry and other characteristics, including temperature, pH, Eh, ionic strength, and major ionic concentrations, may vary spatially throughout the system as a result of different rock mineralogy.	4.1.3 6.2.2. 6.5.5.2 6.6.2.3 6.7.5.2 6.8.5.3 (Radionuclide and colloidal transport are addressed)
2.2.08.04.0A	Redissolution of precipitates directs more corrosive fluids to containers	Redissolution of precipitates which have plugged pores as a result of evaporation of groundwater in the dry-out zone, produces a pulse of fluid reaching the waste packages when gravity-driven flow resumes, which is more corrosive than the original fluid in the rock. See FEP 2.2.07.11.0A for a discussion of return flow from the condensation cap.	6.4.5 6.8.5.3
2.2.08.12.0A	Chemistry of water flowing into the drift	Inflowing water chemistry may be used in analysis or modeling that requires initial water chemistry in the drift. Chemistry of water flowing into the drift is affected by initial water chemistry in the rock, mineral and gas composition in the rock, and thermal hydrological-chemical processes in the rock.	6.2.1.2 6.2.2 6.5.5.2 6.6.2.3 6.7.5.2 6.8.5.3
2.2.10.10.0A	Two-phase buoyant flow / heat pipes	Heat from waste generates two-phase buoyant flow. The vapor phase (water vapor) escapes from the mountain. A heat pipe consists of a system for transferring energy between a hot and a cold region (source and sink respectively) using the heat of vaporization and movement of the vapor as the transfer mechanism. Two-phase circulation continues until the heat source is too weak to provide the thermal gradients required to drive it. Alteration of the rock adjacent to the drift may include dissolution, which maintains the permeability necessary to support the circulation (as inferred for some geothermal systems).	6.2.1
2.2.10.12.0A	Geosphere dry-out due to waste heat	Repository heat evaporates water from the UZ rocks near the drifts as the temperature exceeds the vaporization temperature. This zone of reduced water content (reduced saturation) migrates outward during the heating phase (about the first 1000 years) and then migrates back to the containers as heat diffuses throughout the mountain and the radioactive sources decay.	6.2.1 6.5.5.1 6.6.2.2 6.7.5.1 6.8.5.2

Table 6.1-2. Features, Events, and Processes Relevant to this Model Report and Excluded from TSPA-LA

LA FEP Number	FEP Name	YMP Description	Sections Discussing FEPs-Related Items In this Model Report
2.2.08.03.0B	Geochemical interactions and evolution in the UZ	Groundwater chemistry and other characteristics, including temperature, pH, Eh, ionic strength, and major ionic concentrations, may change through time, as a result of the evolution of the disposal system or from mixing with other waters. Geochemical interactions may lead to dissolution and precipitation of minerals along the groundwater flow path, affecting groundwater flow, rock properties and sorption of contaminants. Effects on hydrological flow properties of the rock, radionuclide solubilities, sorption processes, and colloidal transport are relevant. Kinetics of chemical reactions should be considered in the context of the time scale of concern. See also FEPs 2.2.08.01.0B (groundwater chemistry) and 2.2.08.07.0B (solubility).	6.2.2. 6.5.5.2 6.6.2.3 6.7.5.2 6.8.5.3 (Sorption effects and colloidal transport are not addressed)
2.1.09.12.0A	Rind (chemically altered zone) forms in the near-field	Thermal-chemical processes involving precipitation, condensation, and re-dissolution alter the properties of the adjacent rock. These alterations may form a rind, or altered zone, in the rock, with hydrological, thermal, and mineralogical properties different from the initial conditions.	6.2.1 6.4.4 6.5.5.2 6.6.2.3.1 6.7.5.2 6.8.5.4

6.2 CONCEPTUAL MODEL

This section describes the conceptual model underlying the Drift-Scale THC Seepage Model. The THC Seepage Model conceptualization is presented below in several parts. The first part deals with the conceptualization of the coupled processes that need to be taken into account to model water-gas-rock interactions in a heated unsaturated and fractured rock environment. In the second part, the conceptualization of the chemical system is presented, and a rationale is laid out for selecting input water compositions, mineral phases, and chemical constituents included within the model. Finally, the conceptualization of the physical model domain being modeled is discussed.

6.2.1 Conceptualization of Coupled THC Processes

The THC conceptual model underlies the numerical simulations of THC processes in the DST THC Model and in the THC Seepage Model. The TH conceptual model must be able to describe processes involving liquid and vapor flow, heat transport, and thermal effects resulting from boiling and condensation. The THC Conceptual Model must treat the transport of aqueous and gaseous species, mineralogical characteristics and changes, and aqueous and gaseous chemistry. A conceptual model of reaction-transport processes in the fractured welded tuffs of the repository host rock must also account for different rates of transport in highly permeable fractures compared to the much less permeable rock matrix (see for example, Steefel and Lichtner 1998 [144878], pp. 186–187).

In addition to the unsaturated hydrological properties required to simulate THC processes in the UZ, the data necessary for the evaluation of THC processes include the initial and boundary water and gas chemistry, the initial mineralogy, mineral volume fractions, reactive surface areas, equilibrium thermodynamic data for minerals, aqueous and gaseous species, kinetic data for mineral-water reactions, and diffusion coefficients for aqueous and gaseous species. The following subsections describe the conceptual model for thermal-hydrological (TH), geochemical, and coupled THC processes in the fractured tuffs.

6.2.1.1 TH Processes

TH processes in the fractured welded tuffs at Yucca Mountain have been examined theoretically and experimentally since the early 1980s (Pruess et al. 1984 [144801]; Pruess et al. 1990 [100818]; Buscheck and Nitao 1993 [100617]; Pruess 1997 [144794]; Tsang and Birkholzer 1999 [137577]; Kneafsey and Pruess 1998 [145636]). A conceptual model showing the important TH processes occurring around a drift (as derived through these studies and through observations of the Single Heater Test and the DST) is shown in Figure 6.2-1. This diagram also indicates (in boxes) the important parameters and issues addressed in the THC Seepage Model simulations. To summarize the processes as depicted in the figure, heat conduction from the drift wall into the rock matrix results in vaporization and boiling, with vapor migration out of matrix blocks into fractures. The vapor moves away from the drift through the permeable fracture network by buoyancy, by the increased vapor pressure caused by heating and boiling, and through local convection. In cooler regions, the vapor condenses on fracture walls, where it drains through the fracture network either down toward the heat source from above or away from the drift into the zone underlying the heat source. Slow imbibition of water from fractures into the matrix gradually leads to increases in the liquid saturation in the rock matrix. Under conditions of continuous heat loading, a dryout zone may develop closest to the heat source separated from the condensation zone by a nearly isothermal zone maintained at about the boiling temperature. Where this nearly isothermal zone is characterized by a continuous process of boiling, vapor transport, condensation, and migration of water back to the heat source (either by capillary forces or gravity drainage), this zone may be termed a heat pipe (Pruess et al. 1990 [100818], p. 1235).

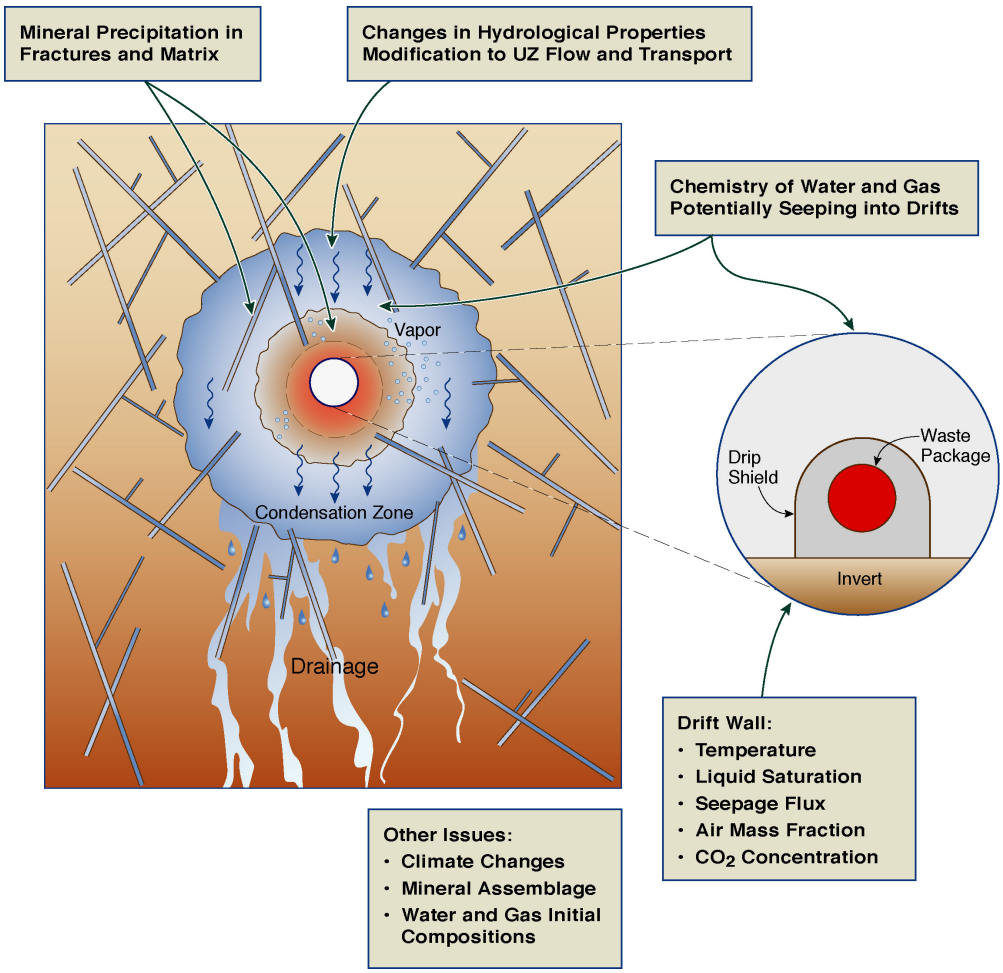

Figure 6.2-1. Schematic Diagram of THC Processes around a Heated Drift

6.2.1.2 THC Processes

The chemical evolution of waters, gases, and minerals is intimately coupled to the TH processes (boiling, condensation, and drainage) discussed in the previous section. The distribution of condensate in the fracture system determines where mineral dissolution and precipitation can occur in the fractures and where there can be direct interaction (via diffusion) between matrix pore waters and fracture waters. Figure 6.2-2 shows schematically the relationships between TH and geochemical processes in the zones of boiling, condensation, and drainage in the rock mass at the fracture-matrix interface outside of the drift and above the heat source.

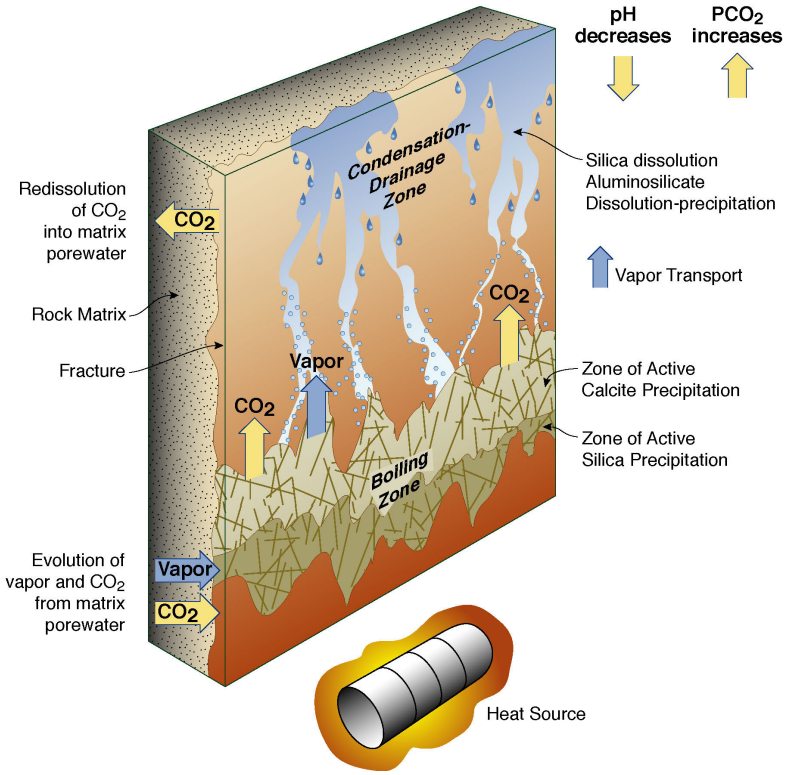

Figure 6.2-2. Schematic Diagram of Fracture-Matrix Interface, Showing the Relation Between TH Processes and Geochemical Processes

One important aspect of the system is the exsolution of CO_2 from the liquid phase as temperature increases. The exsolution of CO_2 in the boiling zone results in a local increase in pH, and a decrease in pH in the condensation zone into which the vapor enriched in CO_2 is transported and condensed. The extent to which the pH is shifted depends strongly on the rates of mineral-water reactions, which can buffer the change in pH. Because the diffusivities of gaseous species are several orders of magnitude greater than those of aqueous species, and because the advective transport of gases can be more rapid than that of liquids, the region where CO_2 degassing affects water and gas chemistry could be much larger than the region affected by the transport of aqueous species.

The effects of TH processes on water chemistry are varied and depend on the behavior of the dissolved species and their relation to mineral-water reactions. Conservative species (i.e., those that are unreactive and nonvolatile), such as chloride (Cl^-), become concentrated in waters undergoing vaporization or boiling, but are essentially absent from the vapor condensing in the fractures. Therefore, the concentration of conservative species in the draining condensate waters is determined by mixing with fracture pore waters and diffusive mixing with matrix pore waters. Concentrations of aqueous species, such as calcium (Ca^{+2}), are also affected by calcite dissolution or precipitation, as well as by reactions involving Ca-bearing zeolites, clays, and plagioclase feldspar.

Zonation in the distribution of mineral phases can occur as a result of differences in mineral solubility as a function of temperature. The inverse relation between temperature and calcite solubility (as opposed to the silica phases, which are more soluble at higher temperatures) can

cause zonation in the distribution of calcite and silica phases in both the condensation and boiling zones (Figure 6.2-2). Precipitation of amorphous silica or another silica phase is likely to be confined to a narrower zone where evaporative concentration from boiling exceeds its solubility. In contrast, calcite could precipitate in fractures over a broad zone of elevated temperature and where CO_2 has exsolved because of temperature increases or boiling. Alteration of feldspars to clays and zeolites is likely to be most rapid in the boiling zone because of their increased solubility (as well as having higher dissolution and precipitation rates) at higher temperatures (Lasaga 1998 [117091], p. 66). In drainage zones, mineral alteration could be zoned within the rock matrix adjacent to a fracture, in a similar manner to that observed as a function of distance along the transport path (Steefel and Lichtner 1998 [144878], p. 186).

6.2.1.3 Effects of Infiltration and Climate Changes on THC Processes

Early in the thermal period of the repository, much of the chemistry of the UZ around drifts will be constrained by the chemistry of ambient fracture and matrix pore water, which could change as a result of boiling, dilution with condensate water, or mineral-water-gas reactions. Once the peak thermal period has subsided, percolating water will mix with the condensate above the repository and eventually rewet the dryout zone. The composition of the percolating waters (before mixing) could be similar to that presently found above the repository as matrix pore water, or it could be more dilute, reflecting wetter climate conditions. Changes in the percolation flux also affect the extent of mineral deposition and dissolution, because of the changes in the flux of dissolved species to the region around drifts. For example, the greater the flux of calcium, the more calcite would precipitate, for a given initial calcium concentration in percolating water. Higher percolation fluxes could increase the dissolution rates of minerals that are undersaturated in the fluid, because it could increase the degree to which the mineral is undersaturated.

6.2.1.4 Hydrological Property Changes in Fractures and Matrix

Mineral precipitation and dissolution in fractures and matrix have the potential for modifying the porosity, permeability, and unsaturated hydrological properties of the system. Because the molar volumes of minerals created by hydrolysis reactions (i.e., anhydrous phases, such as feldspars, reacting with aqueous fluids to form hydrous minerals, such as zeolites or clays) are commonly larger than the molar volumes of the primary reactant minerals, dissolution-precipitation reactions commonly lead to porosity reductions. The extent of mineral-water reaction is controlled by the surface areas of the mineral phases in contact with the aqueous fluid, and heterogeneity in the distribution of minerals in the fractures. Therefore, changes in porosity and permeability caused by these processes may also be heterogeneously distributed. Other factors that could lead to heterogeneity in property changes are the distribution of liquid saturation in fractures, the proportion of fractures having actively flowing water, and the rates of evaporative concentration due to boiling, which could change the dominant mechanisms of crystal growth and nucleation.

6.2.1.5 Dual-Permeability Model for THC Processes

Transport rates by fluid flow in fractures greater than the rate of equilibration via diffusion necessarily leads to disequilibrium between waters in fractures and matrix. This disequilibrium can lead to differences in the prevailing mineral assemblage and to differences in reaction rates.

Because the system is unsaturated and undergoes boiling, the transport of gaseous species is an important consideration. The model must also capture the differences between the initial mineralogy in fractures and matrix and their evolution. These separate yet interacting processes in fractures and matrix were treated by adapting the dual-permeability model to include geochemical as well as hydrological and thermal processes. In the dual-permeability model, each gridblock is partitioned into matrix and fracture continua, each characterized by its own pressure, temperature, liquid saturation, water and gas chemistry, and mineralogy. Figure 6.2-3 illustrates the dual-permeability conceptual model used for THC processes in the Drift-Scale THC Seepage Model and the DST THC Model.

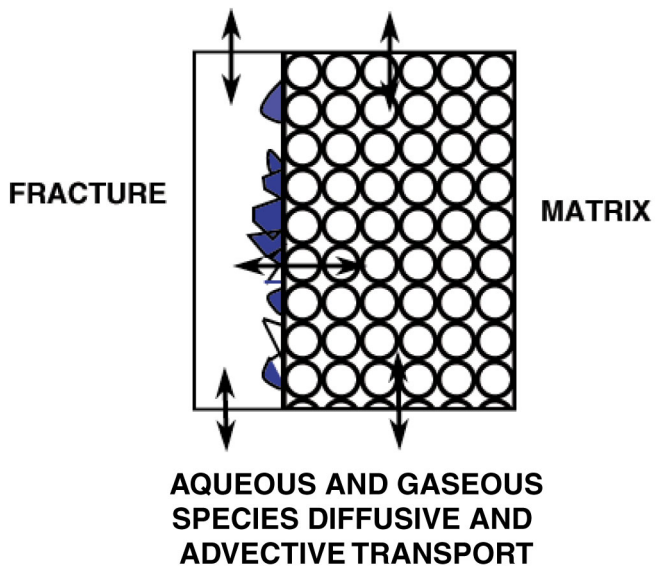

NOTE: Arrows refer to aqueous and gaseous species transport pathways. Angular objects in the fracture are minerals coating the fracture surface.

Figure 6.2-3. Conceptual Model (Schematic) for Reaction-Transport Processes in Dual-Permeability Media

As summarized in the preceding subsection, the conceptual model for THC processes incorporates a wide range of coupled physical and chemical processes. The following subsection describes the implementation of this conceptual framework into a numerical model.

6.2.2 Conceptualization of the Chemical System

The rationale used for defining the types and concentrations of chemical constituents (solid and gaseous) included in the THC Seepage Model is presented below. It includes the selection of initial pore-water and pore-gas compositions, the types and initial abundance of primary minerals, and the secondary minerals that may precipitate as the result of water-gas-rock interactions.

6.2.2.1 Initial Pore-Water and Pore-Gas Chemistry

The initial water composition input into the model could be chosen from either the pore-water chemistry in the UZ at or above the repository horizon, or from the perched water or saturated zone. The perched waters are generally much more dilute than UZ pore waters. Isotopic compositions ($^{36}Cl/Cl$, $^{18}O/^{16}O$, D/H, ^{14}C) and chloride concentrations suggest that the perched waters have a large proportion of late Pleistocene/early Holocene water (Levy et al. 1997 [126599], p. 906; Sonnenthal and Bodvarsson 1999 [117127], pp. 107–108). The saturated zone water is also more dilute than pore waters, and neither saturated nor perched water reflect calculated CO_2 partial pressures consistent with CO_2 concentrations in gas measured in the unsaturated zone in repository units. The saturated zone and perched-water compositions are therefore deemed poor candidates as initial input water compositions for the THC Seepage Model. Preference is given instead to actual pore waters from unsaturated regions within or above the repository units.

A conceptual model that explains the aqueous chemistry and background $^{36}Cl/Cl$ isotopic ratios in the ESF holds that percolating water must pass mostly through the Paintbrush nonwelded hydrogeologic unit (PTn) matrix (because of its high permeability and low fracture density) before reverting to predominantly fracture flow in the Topopah Spring welded hydrogeologic unit (TSw). As discussed in Levy et al. (1997 [126599], pp. 907–908), this seems to be true everywhere except near large structural discontinuities in the PTn (i.e., faults). Hence, percolating water in the TSw ultimately had come predominantly through the PTn matrix. Analyses of PTn pore waters (and some at the top of the TSw) and many chloride analyses of TSw pore waters are consistent with this interpretation (Sonnenthal and Bodvarsson 1999 [117127], pp. 140–141). The relatively higher concentrations of anions and cations in pore waters (compared to perched water) from the TSw, similar to PTn waters, are consistent with the premise that the waters had flowed through the PTn matrix.

The initial composition of water in fractures is taken to be the same as in the rock matrix throughout the model domain, using the same initial composition in all hydrogeologic units. The composition of water infiltrating the top of the model domain (in the Tiva Canyon welded hydrogeologic unit—TCw) is also set to be the same as the initial fracture and matrix pore-water composition, with the exception of minor changes related to a pH adjustment, reflecting a higher CO_2 partial pressure and a lower temperature at the top model boundary than deeper into the model domain (see below). Setting nearly identical compositions for infiltration at the top model boundary and initial fracture-matrix waters is a simplification of the natural system to avoid having to consider complex near-surface geochemical and transport processes such as evapotranspiration and biologically mediated reactions. It is also expected that the high matrix permeability and low fracture density in the PTn hydrogeologic unit (overlying the TSw) homogenize flow in this unit and thus homogenize the compositions of waters originating further up the stratigraphic column, further justifying this modeling approach.

At the initiation of this study, only a few nearly complete pore-water analyses from a repository unit were available. These were of water ultracentrifuged from core samples collected from the Tptpmn geologic unit in Alcove 5 near the DST. Three water samples were analyzed (HD-PERM-1, HD-PERM-2, and HD-PERM-3) from the same suite of core and yielded very similar compositions. Two of these analyses with nearly identical compositions were averaged for use as

an input water composition for pre-REV02 work (Table 6.2-1). Since then, a series of pore-water samples from repository host units have been analyzed. These samples were ultracentrifuged from core collected in the ECRB Cross Drift and in boreholes SD-9 and NRG-7/7A. The compositions of these waters are shown on a Piper diagram in Figure 6.2-4, together with the composition of HD-PERM samples, of perched water and pore water at similar depths (base of Tptpln) in borehole UZ-14, and of groundwater from well J-13. This figure also shows the hydrogeologic units from which the water samples were extracted. It is evident from Figure 6.2-4 that the span of potential initial water compositions to use in the THC Seepage Model is wide, with HD-PERM samples at one end (calcium-sulfate-chloride type) and groundwater from well J-13 at the other end (sodium-bicarbonate type). This figure also shows a tendency for samples from deeper hydrogeologic units to exhibit higher sodium (plus potassium) concentrations relative to calcium (plus magnesium) concentrations, and a higher proportion of aqueous carbonate (relative to chloride and sulfate) compared to shallower waters. The sodium increase relative to calcium with depth has been noted previously in pore-waters from hydrogeologic units above and below the repository units (Yang et al. 1996 [100194], p. 13). It is likely caused by the hydrolysis of volcanic glass and feldspars and, mostly below the repository units, exchange reactions with zeolites (e.g., BSC 2002 [160247]; Vaniman et al. 2001 [157427]). The precipitation of calcite in fractures under the ambient geothermal gradient would also exacerbate the decrease in calcium relative to sodium concentrations with depth. Trends in carbonate concentrations relative to chloride and sulfate concentrations are subject to large uncertainties as a result of the determination of total aqueous carbonate concentrations. An increase in aqueous carbonate concentration with depth could be attributed to the pH increase expected to accompany glass and feldspar hydrolysis reactions.

The differences in the proportions (not absolute values) of cations and anions in analyzed waters have an important bearing on the types of residual brines that could develop upon evaporation and boiling due to thermal loading (*In-Drift Precipitates/Salts Analysis*, see upcoming revision of BSC 2001 [156065]. Should these waters seep onto the surface of a hot waste package, knowledge of their end-brine composition is important to assess the likelihood and intensity of waste package corrosion (*Engineered Barrier System: Physical and Chemical Environment Model*, see upcoming revision of CRWMS M&O 2000 [151951]). Therefore, the span of selected input water compositions should take into account factors that influence the end-brine composition of these waters. One important factor is whether calcium (and magnesium) chloride brines could develop instead of sodium chloride brines. Calcium chloride brines can “survive” higher temperatures (i.e., exist at a lower relative humidity, more hygroscopic) than sodium chloride brines. Such brines are more likely to form if the total calcium concentration (in meq/L) exceeds the total aqueous carbonate concentration (in meq/L) in the initial water (calcite precipitation chemical divide; e.g., Drever 1997 [140067]). Waters with such compositions would have a tendency to plot in the upper half of the diamond-shaped area in Figure 6.2-4, although other waters may also plot in this area if their magnesium concentration were high relative to calcium. Other chemical divides after calcite precipitation (e.g., Drever 1997 [140067], p. 331; see also Rosenberg et al. 2001 [154862], p. 1238) could result in the development of brines that are less hygroscopic than calcium or magnesium chloride, even though the calcium content of the original waters (in equivalents) exceeds their total carbonate content. Less hygroscopic brines are more likely to develop if the nitrate and sulfate concentration in the original solution were elevated relative to chloride (*In-Drift*

Precipitates/Salts Analysis, see upcoming REV01 (BSC 2001 [156065])). No simple *a priori* criteria have been developed to determine with certainty the end-brine composition of a given water. However, factors such as composition plotting in the upper half of the diamond-shape area of Figure 6.2-4, together with low nitrate and sulfate concentrations relative to chloride, could be used to infer a higher likelihood of potentially deleterious brines developing.

The choice of input water composition must also consider the natural variability of pore-water compositions in the repository units. This natural variability is illustrated in Figure 6.2-4. The spatial coverage of these data is too small to associate a probability of occurrence for any of these pore-water compositions. From the considerations discussed above, one could expect deeper waters to exhibit lower calcium and higher total carbonate concentrations and therefore be less conducive to the formation of calcium chloride brines. However, other factors could affect the spatial distribution of pore-water compositions in the repository units. These factors include variations of infiltration rates in various parts of the repository footprint (Sonnenthal and Bodvarsson 1999 [117127], pp. 122–123) and possibly the presence or absence of ion-exchanging zeolites in areas above the repository. Furthermore, as noted above, the evolution of brine composition upon evaporation and boiling follows many other chemical divides besides the first calcite divide mentioned earlier.

Table 6.2-1. Input Pore-Water Compositions for the THC Seepage Model

Sample ID:		HD-PERM[1] (Alcove 5)		ECRB-SYS-CS1000/7.3-7.7/UC[2]		ECRB-SYS-CS2000/16.5-21.1/UC[2]		SD-9/990.4-991.7/UC[2]		ECRB-SYS-CS500/12.0-16.7/UC[2]	
Lithostratigraphic Unit:		Tptpmn		Tptpul (base)		Tptpll		Tptpll		Tptpul	
Simulation Water ID:		W0		W5		W4		W6		W7	
Water Input Type:		Fract/Matrix	Boundary	Fract/Matrix	Boundary	Fract/Matrix	Boundary	Fract/Matrix	Boundary	Fract/Matrix	Boundary
	Units										
Temperature	°C	25	17	25	17	25	17	25	17	25	17
pH (measured)	pH	8.31	-	7.6	-	7.4	-	7.9	-	8.0	-
pH (calc)[3]	pH	-	7.750	8.062	8.026	8.175	8.140	8.001	7.964	8.073	8.038
Na^+	mg/L	61.5	61.5	39	39	130	130	84	84	57	57
K^+	mg/L	8	8	7.6	7.6	10.6	10.6	7.9	7.9	10.3	10.3
Ca^{+2}	mg/L	101	101	94	94	82	82	56	56	120	120
Mg^{+2}	mg/L	17	17	18.1	18.1	5.3	5.3	0.9	0.9	19.3	19.3
SiO_2	mg/L	70.5	70.5	42.0	42.0	48	48	50	50	49	49
Cl^-	mg/L	117	117	21	21	26	26	23	23	54	54
SO_4^{-2}	mg/L	116	116	36	36	39	39	10	10	78	78
HCO_3^- (measured)	mg/L	-	-	333	-	382	382	313	-	286	-
HCO_3^- (calc)[4]	mg/L	200	216	395	400	515	515	335	338	412	417
NO_3^-	mg/L	6.5	6.5	2.6	2.6	4.2	4.2	17	17	6.1	6.1
F^-	mg/L	0.86	0.86	3.4	3.4	6.01[9] (11)	5.52	2.5	2.5	4.8	4.8
Al^{+3} (calc)[5]	molal	6.173E-10	9.775E-11	1.112E-09	3.415E-10	1.082E-09	3.305E-10	1.00E-09	3.08E-10	8.061E-10	2.477E-10
Fe^{+3} (calc)[6]	molal	1.155E-12	5.162E-13	1.138E-12	5.000E-13	1.143E-12	4.984E-13	1.14E-12	5.02E-13	1.138E-12	5.006E-13
$\log(PCO_2)$[7]	bar	-3.1	-2.5	-2.5	-2.5	-2.5	-2.5	-2.5	-2.5	-2.5	-2.5
CO_2 (approx)[8]	ppmv	900	3100	3100	3100	3100	3100	3100	3100	3100	3100

NOTES: Compositions shown are those used for initial fracture and matrix water (column labled "Fract/Matrix") and infiltration water at the model top boundary (column labeled "Boundary")

(1) Average of Tptpmn porewater analyses ESF-HD-PERM-2 (30.1'-30.5') and ESF HD-PERM-3 (34.8'-35.1'), DTN: MO0005PORWATER.000 [150930]

(2) Pore water analyses from the ECRB cross-drift and borehole SD-9 reported with DTN: GS020408312272.003 [160899]

(3) pH calculated by speciation at the temperature and $\log(P_{CO2})$ shown (using SOLVEQ/CHILLER V1.0 [153217]).

(4) Total aqueous carbonate as HCO_3^-, calculated from charge balance computed by speciation at the temperature and pH shown (at measured pH for HD-PERM sample; at calculated pH for other samples) (using SOLVEQ/CHILLER V1.0 [153217]). Note: these are slightly different values than values calculted fom charge balance reported in DTN: GS020408312272.003 [160899] because the latter do not include the effect of speciation .

(5) Calculated by equilibrating with illite at the temperature and calculated pH shown (using SOLVEQ/CHILLER V1.0 [153217]) (Section 6.2.2.1).

(6) Calculated by equilibrating with hematite at the temperature and calculated pH shown (using SOLVEQ/CHILLER V1.0 [153217]) (Section 6.2.2.1).

(7) Set at values shown except for HD-PERM sample at 25°C (calculated in this case) (Section 6.2.2.1).

(8) Approximate conversion assuming 1 bar total pressure.

(9) Value shown is calculated at equilibrium with fluorite at 25°C. Value in parentheses is measured value.

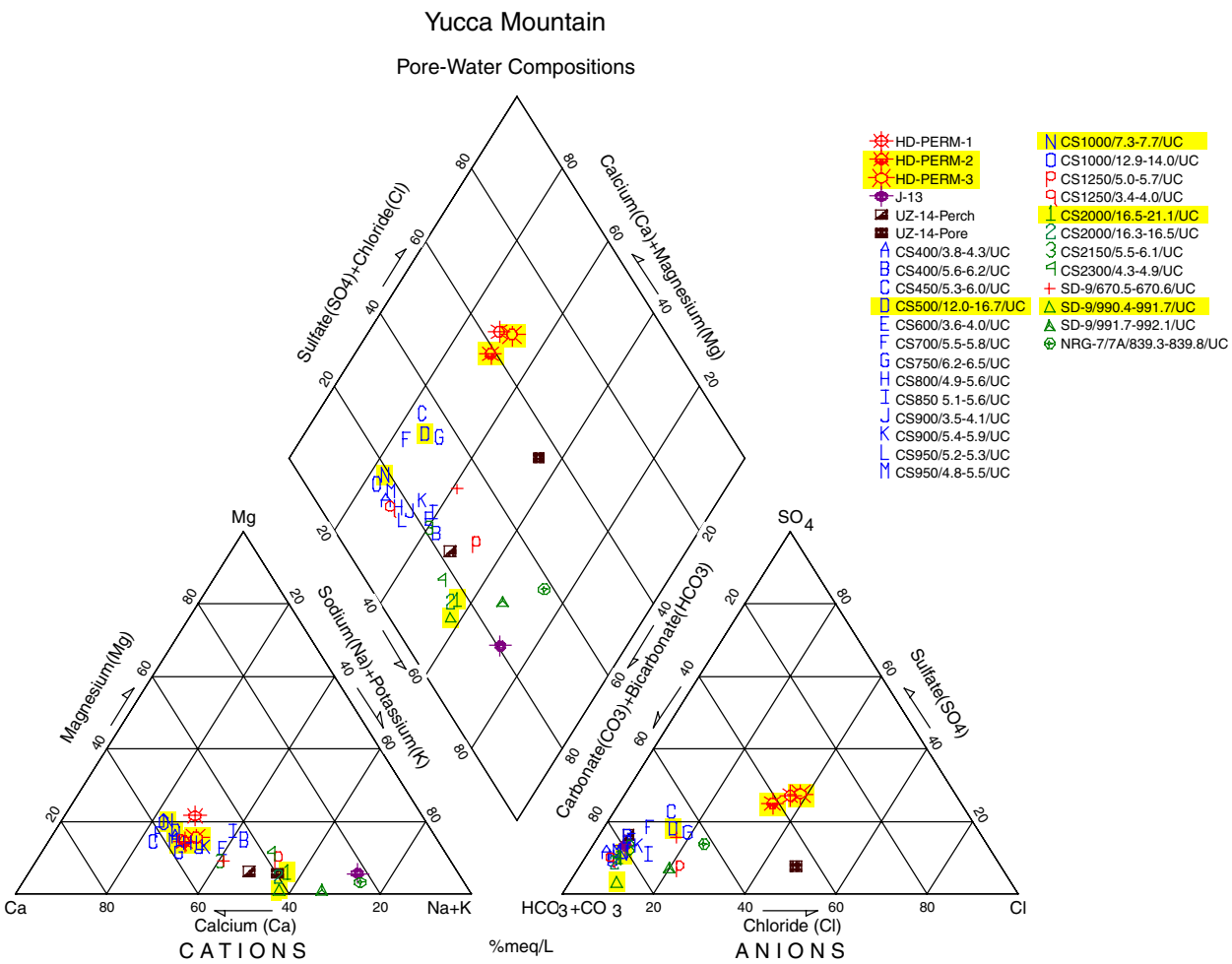

DTNs: GS020408312272.003 [160899], MO0005PORWATER.000 [150930]

NOTE: Samples labeled HD-PERM are pore waters from the Tptpmn unit in Alcove 5 of the ESF. Samples ID's starting with CS represent pore waters from the ECRB cross drift and are listed in order of increasing distance (m) into the drift (down stratigraphy), with labels reflecting lithostratigraphic units as follows: Tptpul (capitals A-O), Tptpmn (lower case p-q), and Tptpll (numbers 1-4). Additional borehole interval information after each CS sample labeling is sample interval distances from borehole collar given in feet. CS is abbreviation for Construction Station indicating distance along the ECRB cross drift in meters. Sample ID's starting with SD-9 and NRG-7 represent pore waters from boreholes with the same names and show the sampling interval in feet from ground surface. The first SD-9 sample at 670 ft is from the base of the Tptpul, and the others are from the Tptpll. The NRG7 sample is from the Tptpmn. Highlighted samples were chosen for this study (see text).

Figure 6.2-4. Piper Plot of Water Compositions (meq/L) from Repository Units

Given these considerations, initial water compositions were selected for REV02 simulations based on the following criteria:

(1) Capture the spread of pore-water compositions shown on Figure 6.2-4 and include, to the extent practicable, waters that may yield different end-brine compositions

(2) Include at least one pore water from the most important repository host unit (Tptpll)

(3) Use analyses that best balance charge if more than one sample meets the other criteria

On these bases, the following water compositions were selected, listed here with an arbitrary identification (W0, W5, etc.) assigned for this Model Report:

"W0": HD-PERM water, from the Tptpmn unit in Alcove 5. This is an average composition (from Samples HD-PERM-2 and HD-PERM-3) used for all REV01 work. The HD-PERM samples plot higher than other pore waters on the diamond-shaped area in Figure 6.2-4, bounding the range of compositions in the calcium-sulfate-chloride field.

"W5": Sample CS-1000/7.3-7.7/UC, from the base of the Tptpul lithostratigraphic unit in the ECRB Cross Drift. This sample was selected because it exhibits one of the highest (Ca+Mg)/(Na+K) ratio of the ECRB Cross Drift samples, and exhibits better charge balance than other samples with high (Ca+Mg)/(Na+K) ratios.

"W4": Sample CS-2000/16.5-21.1/UC, from the Tptpll lithostratigraphic unit in the ECRB Cross Drift. This sample exhibits the lowest (Ca+Mg)/(Na+K) ratio of the ECRB Cross Drift samples and exhibits better charge balance than other samples of similar composition. Also, this sample is from the main repository host unit. It also contains a higher fluoride concentration than the other samples.

Upon further evaluation and a request from "downstream" project personnel, two additional samples were considered:

"W6": Sample SD-9/990.4-991.7, from the Tptpll lithostratigraphic unit in borehole SD-9. This sample exhibits a low (Ca+Mg)/(Na+K) ratio nearly identical to that of W4, but exhibits a better charge balance than W4 and a higher nitrate concentration compared to most other samples. This water is very similar in composition to Water W4.

"W7": Sample CS500/12.0-16.7, from the Tptpul lithostratigraphic unit in ECRB Cross Drift. This sample plots between the HD-PERM waters and Water W5 on Figure 6.2-4, further capturing the variability of water compositions in the upper part of Figure 6.2-4.

The compositions of these waters are given in Table 6.2-1. This table also includes calculated concentrations used for input into the THC Seepage Model, and distinguishes between the compositions used for initial fracture and matrix waters and slightly adjusted compositions used for infiltration water at the top model boundary, as discussed further below.

It is shown in Figure 6.2-4 that the water compositions chosen for input into the THC Seepage Model capture fairly well the spread of currently available pore-water compositions in repository units. Water compositions W4, W5, and W6 plot in the lower half of the diamond-shaped area on Figure 6.2-4. The HD-PERM waters and W7 plot in the upper half of this area, and for this reason may be more likely to evolve toward a calcium chloride brine than the other waters upon evaporation.

The set of analyzed species for these samples do not include iron and aluminum. Because these components are needed to include aluminum silicates in simulations, their concentrations were

calculated assuming equilibrium with hematite and illite, respectively. Illite was chosen to set the initial aluminum concentration because waters from Yucca Mountain typically plot on, or near, the illite-K-feldspar equilibrium boundary (Wang 2003 [161665], SN-LBNL-SCI-141-V2, pp. 176 and 184). Hematite is the most abundant iron oxide mineral found in the tuffs at Yucca Mountain and is a reasonable candidate to use for setting the initial iron concentration in solution.

The total aqueous carbonate concentration (reported here as HCO_3^-) was not measured in HD-PERM samples and was calculated from charge balance, after full speciation calculations (using SOLVEQ/CHILLER V1.0 (LBNL 1999 [153217])). Doing so yielded a partial pressure of CO_2 (at equilibrium with the HD-PERM water) near 10^{-3} bar, consistent with CO_2 concentrations near 1,000 ppmv measured in repository units in the ESF (DTN: LB0208ISODSTHP.001 [161638]) and in borehole UZ-1 (Yang et al. 1966 [100194], p. 43).

Total aqueous carbonate concentrations were reported for the other samples. However, the analyses of these samples reflect a fairly significant charge imbalance (2 to 11%). Also, it is known that aqueous carbonate analyses can be easily impacted by interference with atmospheric carbon dioxide during sample preparation. For these reasons, the carbonate concentrations were recalculated from charge balance after full speciation calculations.

Other adjustments were made to some of the reported analytical data before input into the model as follows. The pH reported for the ECRB and SD-9 samples yield equilibrium carbon dioxide partial pressures significantly higher (up to 14,000 ppmv) than what is observed in the repository units (typically around 1,000 ppmv). For this reason, the pH of these waters was recalculated to yield lower CO_2 partial pressures values more in line with concentrations measured in repository units. Bringing the CO_2 partial pressure down to near 1,000 ppmv required raising the water pH to values of 8.5 and higher. Such pH values seemed too high in comparison to values of 7.79, 8.31, and 8.32 reported for the HD-PERM samples (DTN: MO0005PORWATER.000 [150930]). Therefore, an intermediate but still reasonable CO_2 partial pressure around 3,100 ppmv ($\log(P_{CO_2}) \sim -2.5$) was used, yielding pH values in the 8–8.2 range (Table 6.2-1). In this respect, these water compositions are likely to represent high-end CO_2 concentrations, whereas the HD-PERM samples represent a somewhat lower bound.

Another adjustment to input water concentrations involved fluoride in sample ECRB-SYS-CS2000/16.5-21.1/UC. The fluoride concentration in this sample (11 mg/L) reflects a significant supersaturation with respect to fluorite (CaF_2 solid) at 25°C. The precipitation of fluorite is typically quite rapid (Section 4.1.5) and, for this reason, the fluoride concentration of this sample was lowered to a concentration reflecting saturation with fluorite (near 6 mg/L for this water).

As mentioned earlier, infiltration water at the top model boundary was taken to have the same composition as the initial pore water, but with adjusted total aqueous carbonate, aluminum, and iron concentrations to reflect a lower temperature (17°C) and higher CO_2 partial pressure near the ground surface. Using this boundary water yielded chemically steadier ambient water compositions at the location of the modeled drift (Section 6.4.3).

The initial CO_2 partial pressure in fractures and matrix was calculated as the partial pressure of CO_2 in chemical equilibrium with the input water composition at 25°C, assuming ideal gas

behavior (i.e., partial pressure is equal to fugacity). The 25°C temperature is close to the initial temperature at the location of the drift. For the Tptpmn THC Seepage Model, the initial CO_2 partial pressure in the drift was set to be consistent with a CO_2 concentration of 400 parts per million by volume (ppmv) in the drift, which is within the range of measured ambient concentrations in the ESF (DTN: LB990630123142.003 [111476]). For the Tptpll Seepage Model, the initial CO_2 partial pressure in the drift was assumed to be at equilibrium with the initial composition of pore water around the drift. The CO_2 concentration at the top model boundary was set (approximately 3,100 ppmv) to reflect a value consistent with the range of higher concentrations measured in shallow geologic units in borehole UZ-1 (Table 8 in Yang et al. 1996 [100194]). These higher CO_2 concentrations are most likely the result of biological activity near the ground surface.

6.2.2.2 Geochemical Systems

Minerals and chemical-aqueous components considered in this study are shown in Table 6.2-2. Initial mineral types and abundances were derived from x-ray diffraction (XRD) measurements on cores reported in the Yucca Mountain Mineralogical Model: LA9908JC831321.001 [113495] and analyses of fracture surfaces (Carlos et al. 1993 [105210], p. 47; LA9912SL831151.001 [146447]; LA9912SL831151.002 [146449]). Amounts of minerals observed, but present in quantities below the detection limit (typically around a percent for XRD) were estimated. Potential secondary minerals (i.e., those allowed to precipitate but which may not necessarily form) were determined from field observation of thermal alteration (e.g., Vaniman et al. 2001 [157427], p. 3409) and corroborated by running multicomponent heterogeneous equilibrium simulations of water-rock interaction (Wang 2003 [161665], SN-LBNL-SCI-141-V2, pp. 94–95) using SOLVEQ/CHILLER V1.0 (LBNL 1999 [153217]). From these simulations, the stable mineral assemblage at each reaction step was calculated from a large list of possible minerals (after suppressing phases known not to form under ambient pressures and low temperatures). For example, amorphous silica is allowed to precipitate instead of the other silica polymorphs, such as opal, tridymite, α-cristobalite, and quartz, because it is observed in experiments (Section 7). Anorthite is not observed as a secondary phase, so calcium enters other minerals such as zeolites and calcite.

The basis for selection of aqueous species included in this study were: (1) use the major components of pore water, (2) use all components in major rock-forming minerals considered in the model, and (3) use additional components specifically requested by downstream users (nitrate, iron, and fluoride).

Two alternative conceptualizations of the modeled geochemical system were used. The systems were denoted as “base case” and “extended case,” and differ somewhat from one model variation to another (Table 6.2-2). The extended case includes the major solid phases (minerals and glass) encountered in geologic units at Yucca Mountain, together with a range of possible reaction product minerals, CO_2 gas, and the aqueous species necessary to include these solid phases and the pore-water composition within the THC model. The base case is a subset of the extended case excluding aluminum silicate minerals, which form or dissolve much less easily than minerals such as calcite or gypsum, and for which thermodynamic and kinetic data are not as well established as for the other minerals. As such, the base-case system conceptualizes a geochemical system in which aluminum silicate minerals are nonreactive. The base-case system

also does not include Fe- and Mg-bearing phases and aqueous species. The base-case system, in addition to the extended-case system, was only used in REV01 models. For REV02 work, only an extended-case geochemical system was considered.

Table 6.2-2. Minerals, Aqueous, and Gaseous Species Used in the THC Seepage Model

Aqueous Species		Minerals		
	Alternative Models		Alternative Models	Mineral Type[1]
H_2O	All	Calcite	All	P,S
H^+	All	Tridymite	All	P
Na^+	All	α–Cristobalite	All	P
K^+	a	Quartz	All	P
Ca^{+2}	All	Amorphous Silica	All	S
Mg^{+2}	a	Hematite	a	P,S
SiO_2	All	Fluorite	All	P,S
AlO_2^-	a	Gypsum	All	S
$HFeO_2^{-2}$	a	Goethite	d	S
HCO_3^-	All	Albite	a	P,S
Cl^-	All	K-Feldspar	a	P,S
SO_4^{-2}	All	Anorthite	a	P
F^-	All	Ca-Smectite	a	P,S
		Mg-Smectite	a	P,S
Gases		Na-Smectite	a	P,S
CO_2	All	Opal_proxy	b	P
H_2O	All	Illite	a	P,S
Air	All	Kaolinite	a	S
		Glass [2]	All	P
		Stellerite	a	P,S
		Heulandite	a	P,S
		Mordenite	a	P,S
		Clinoptilolite	a	P,S
		Sepiolite	c	S

NOTES: a Extended-case geochemical system only
b Only Tptpll REV01 and all REV02 models
c Only REV02 models
d Only REV01 extended-case models

[1] Primary (P) and secondary (S) minerals
[2] For base-case models, glass has the same thermodynamic properties as amorphous silica but is not allowed to precipitate.

6.2.3 Conceptualization of the Model Domain

The current repository design includes a planar series of parallel, equidistant, and horizontal waste emplacement drifts laid out over a large surface area. As such, encompassing all areas of the repository would require a large and detailed 3-D model. However, the scope of this Model Report covers THC processes at the drift scale. Therefore, the model was reduced and simplified to focus on areas surrounding a typical waste emplacement drift. Because the number of

gridblocks directly affects the simulation time, the model domain is reduced as much as possible without losing important information. The dip of repository host units is subhorizontal, and rock properties are laterally homogeneous between drifts. Under these conditions, a planar and parallel drift layout can be conceptualized, in two dimensions, as a series of symmetrical, identical half-drift X-Z models (X representing the horizontal distance in a direction perpendicular to the length of the drifts, and Z the vertical distance) with no-flux (heat, fluid, chemical) vertical boundaries between them. Note that this half-drift simplification based on symmetry is theoretically applicable only for homogeneous properties. It is, however, also a good approximation for the heterogeneous fracture permeability fields used in this report because of their weak spatial correlation.

Accordingly, the THC Seepage Model was reduced to a half-drift model with a width corresponding to the midpoint between drifts. The model is refined in the vicinity of the drift, and extends in a progressively coarser fashion to the TCw (near the ground surface) above the drift and to the water table below the drift. This symmetrical "chimney" model adequately represents coupled THC processes at the drift scale in areas that are not affected by repository-edge effects (i.e., effects resulting from the cooler temperature distribution at the repository edge). The evaluation of edge effects are not within the scope of this Model Report. Edge effects have been evaluated with mountain-scale THC simulations in BSC (2001 [155950], Section 3.3.6) and will be further addressed in upcoming revision of MDL-NBS-HS-000007, REV01. Water and gas compositions predicted at the edge of the repository (BSC 2001 [155950], Section 3.3.6) are within the range of compositions simulated in this Model Report. For this reason, results presented here could be used to represent potential effects of THC processes on the composition of seepage at all waste package locations.

6.3 ALTERNATIVE CONCEPTUAL MODELS

The THC Seepage Model includes various conceptualizations of drift location, drift representation, modeled stratigraphic column, geochemical systems, and boiling/evaporation mathematical models. These conceptualizations were implemented in various model variations and summarized as follows (see also Table 6-1):

- Tptpmn THC Model REV01 (Section 6.5). This model represents a stratigraphic column on the edge of the repository (borehole SD-9) and considers a drift in the Tptpmn lithostratigraphic unit. Two alternative geochemical systems are used with this model: a base-case system and an extended-case system (Section 6.2.2.2).

- Tptpmn THC Heterogeneous Model REV01 (Section 6.6). This model includes the same conceptualizations as the above model, except that it considers heterogeneous fracture permeability variations.

- Tptpll THC Model REV01 (Section 6.7). This model represents a stratigraphic column at the center of the repository with a drift in the Tptpll lithostratigraphic unit. Both base-case and extended-case geochemical systems (Section 6.2.2.2) are considered.

- Tptpll THC Model REV02 (Section 6.8). This model is an update of the REV01 Tptpll model. The following alternative conceptualizations are considered, compared to the

REV01 model: drift wall open to gas and liquid flow (versus closed in REV01), fixed versus stepwise increase in infiltration rate, and the effect of vapor-pressure lowering (resulting from capillary pressure) versus its absence.

Additional details on each of these alternative conceptualizations can be found in the sections noted above for each model variation. Alternative conceptualizations not treated here could yield differences in model results. Examples of such alternative models include the use of more than two porous media continua (to better represent lithophysae, and/or better capture gradients between fractures and matrix), heterogeneous fracture porosity (in addition to heterogeneous permeability), a wider range of infiltration rates, or other sets of potential secondary minerals, etc. These alternatives were not considered because they were expected to result in smaller differences in model results than the alternatives considered here. This is primarily because the range of input water compositions considered in the model (Section 6.2.2.1), by itself, already introduces a significant spread in model results (Section 6.8.5).

6.4 MATHEMATICAL MODEL

This section describes the mathematical formulations that underlie the THC Seepage Model (and the DST THC Model presented in Section 7). Reactive transport simulators other than TOUGHREACT and using various formulations exist. However, these simulators either have limitations that make them unsuitable for use in this study (e.g., dealing only with fully liquid-saturated conditions, or only with one continuum), or have drawbacks in terms of availability, technical support, and qualification status. TOUGHREACT (all versions) is the only software of its type that is qualified for Yucca Mountain work. Also, the authors of this report have contributed to the development of this software, and most particularly to its development for applications to the repository at Yucca Mountain. Therefore, it is natural that this software and its formulation were selected for this study.

For brevity, unless a formulation is used that is specific to a particular version of TOUGHREACT, hereafter the code version and reference are not cited.

6.4.1 General Numerical Model for Coupled THC Processes

Thermal and hydrological processes modeled using TOUGHREACT (all versions) are equivalent to those using TOUGH2 V1.6 (LBNL 2003 [161491]), and described in detail in BSC (2003 [161530], Section 6.2.1.1) and in the TOUGHREACT V3.0 User's Manual (BSC 2002 [164454]; LBNL 2002 [161256]).

The geochemical module incorporated in TOUGHREACT (V2.2 (LBNL 1999 [153219]); V2.3 (LBNL 2001 [153101]); V2.4 (LBNL 2001 [160880]); and V3.0 (LBNL 2002 [161256])) simultaneously solves a set of chemical mass-action, kinetic-rate expressions for mineral dissolution/precipitation, and mass-balance equations. This provides the extent of reaction and mass transfer between a set of given aqueous species, minerals, and gases at each gridblock of the flow model. Equations for heat, liquid and gas flow, aqueous and gaseous species transport, and chemical reactions are summarized in Xu and Pruess (2001 [156280], p. 30, Tables A and B (see also Xu and Pruess 1998 [117170]; Xu et al. 1998 [101751]; Xu et al. 2001 [161864])). Flow and reaction/transport equations are solved sequentially (e.g., Steefel and Lasaga 1994

[101480], p. 550). Equations for mineral-chemical equilibrium, kinetic rates, and permeability/porosity changes are given further below.

The setup of mass-action and mass-balance equations in TOUGHREACT V2.2 (LBNL 1999 [153219]), V2.3 (LBNL 2001 [153101]), and V3.0 (LBNL 2002 [161256]) is similar to the formulation implemented in Reed (1982 [117901], pp. 514–516). Additional provisions are made for mineral dissolution and precipitation under kinetic constraints and a volume-dependent formulation for gas equilibrium, as described below. The chemical system is described in terms of primary aqueous species (the independent variables). Minerals, gases, and secondary aqueous species are defined in terms of reactions involving only the primary species. It has been shown that if the diffusivities of all aqueous species are equal, only the transport of primary species (in terms of total dissolved concentrations) needs to be considered to solve the entire reactive flow/transport problem (Steefel and Lasaga 1994 [101480], p. 546).

The system of nonlinear equations describing chemical mass-balance, mass-action, and kinetic-rate expressions is solved by a Newton-Raphson iterative procedure. In TOUGHREACT V2.2 (LBNL 1999 [153219]), activity coefficients of aqueous species are computed by an extended Debye-Hückel equation (e.g., Drever 1997 [140067], p. 28, Equation 2-12). In TOUGHREACT V2.2 (LBNL 1999 [153219]), activity coefficients of neutral species are assumed equal to one, and the activity of water is computed using a method described in Garrels and Christ (1990 [144877], pp. 64–66), which essentially equates the water activity to its mole fraction. These methods are generally reliable for ionic strengths up to 2 molal. In TOUGHREACT V2.3 (LBNL 2001 [153101]), V2.4 (LBNL 2001 [160880]), and V3.0 (LBNL 2002 [161256]), activity coefficients of charged species and the activity of water are calculated with the method of Helgeson et al. (1981 [106024], Equations 298, 190, 106, and Tables 1, 3, 29, and 30) as further described in Wang 2003 ([161665], SN-LBNL-SCI-112-V2, pp. 21–27). Using this method, activities of water and activity coefficients of electrolytes typical of natural systems (NaCl, $CaCl_2$, Mg_2SO_4, Ca_2SO_4) were fairly well reproduced up to ionic strengths of 6 molal (Wang 2003 [161665], SN-LBNL-SCI-112-V2, pp. 28–30 and 32). In TOUGHREACT V2.3 (LBNL 2001 [153101]), V2.4 (LBNL 2001 [160880]), and V3.0 (LBNL 2002 [161256]), activity coefficients of selected neutral species are calculated using salting-out coefficients as described in Langmuir (1997 [100051], Equation 4.62 and Table 4.1-4).

Equilibration with mineral phases is computed by adding a mass-action equation, for each saturated mineral, into the system of nonlinear equations as follows:

$$\log(K_i) = \log(Q_i) \qquad \text{(Eq. 6.4-1)}$$

where K_i denotes the equilibrium constant and Q_i the product of the ion activities in the reaction that expresses mineral i in terms of the primary aqueous species. A term representing the amount of primary aqueous species consumed or produced by equilibration of minerals is added to the mass-balance equation for each primary species involved in mineral reactions, and this term is solved simultaneously with the concentrations of all primary species. Minerals thus dissolve if $\log(Q_i/K_i) < 0$ and precipitate if $\log(Q_i/K_i) > 0$. For some minerals (e.g., calcite in this report, see Section 6.4.3), a "supersaturation gap" can be specified, by which the mineral is not allowed to precipitate if $\log(Q_i/K_i)$ is greater than zero but less than a specified "gap" value (positive).

This gap can be set to decrease exponentially with temperature, as described in Wang 2003 ([161665], SN-LBNL-SCI-112-V2, p. 33).

Gas species, such as CO_2, are treated as ideal mixtures of gases in equilibrium with the aqueous solution. A mass-action equation is added to the system of simultaneous equations for each saturated gas present—except for H_2O vapor and air, which are handled separately through the flow module in TOUGHREACT. The gas mass-action equation takes the form:

$$\log(K_i) = \log(Q_i) - \log(P_i) \qquad \text{(Eq. 6.4-2)}$$

where P_i is the partial pressure of gaseous species i. P_i is first calculated from the advective-diffusive gas transport equation in TOUGHREACT. Then P_i is replaced with the ideal gas law,

$$P_i = \frac{n_i RT}{V_g} \qquad \text{(Eq. 6.4-3)}$$

where n_i denotes the number of moles of gas species i, R is the gas constant, T is the absolute temperature, and V_g is the gas total volume. By expressing V_g in terms of the gas saturation S_g, the porosity of the medium ϕ, and the volume of each gridblock in the flow model V_{block}, Equation 6.4-3 is rewritten as:

$$P_i = \frac{n_i RT}{V_{block} \phi S_g} \qquad \text{(Eq. 6.4-4)}$$

The gas saturation is computed in the flow module of TOUGHREACT (reflecting H_2O and air partial pressures computed in this module). The amount of trace gas species (n_i/V_{block}) is then obtained by substitution of Equation 6.4-4 into Equation 6.4-2 and solving together with the concentrations of all primary species.

The partial pressures of trace gas species are not fed back to the multiphase flow module of TOUGHREACT V2.2 (LBNL 1999 [153219]) and V2.3 (LBNL 2001 [153101]) for solving the water and gas flow equations. Therefore, this method should only be applied to gases (excluding H_2O and air) with partial pressures significantly lower than the total gas pressure. No absolute cutoff exists at which this approximation breaks down, and therefore it is validated by comparison to DST-measured CO_2 concentrations. For cases where the partial pressures of a trace gas become closer to the total pressure, chemical equilibrium with the aqueous phase is computed correctly, but the gas pressure will be underestimated in the mass-balance equation solved for gas flow. Because CO_2 concentrations encountered in the DST and model simulations are generally less than a few percent, and rarely over 10%, this model for the gas species is a reasonable approximation for this particular system (see Section 6.4.6).

6.4.2 Kinetic Rate Laws

Rates of mineral dissolution and precipitation close to equilibrium can be described via a relationship of the rate to the saturation index (*Q/K*), as follows (Steefel and Lasaga 1994 [101480], p. 540):

$$Rate(mol\ s^{-1}kg_{water}^{-1}) = \mathrm{sgn}\left[\log\left(Q/K\right)\right]kA\prod_i a_i^p\left|\left[\left(Q/K\right)^m - 1\right]\right|^n \qquad \text{(Eq. 6.4-5)}$$

where a_i is the activity of each inhibiting or catalyzing species, and p is an empirically determined exponent and the variable A is the reactive surface area expressed in units of $m^2_{mineral} / kg_{water}$. The rate constant k (in mol m^{-2} s^{-1}) is given as (Steefel and Lasaga 1994 [101480], p. 541):

$$k = k_0 \exp\left[\frac{-E_a}{R}\left(\frac{1}{T} - \frac{1}{298.15}\right)\right] \qquad \text{(Eq. 6.4-6)}$$

where the temperature dependence of reaction rate is related to the activation energy (E_a) in units of kJ/mol and T is the temperature in Kelvin units. Following Steefel and Lasaga (1994 [101480], p. 568), by neglecting the effect of pH or other aqueous species activities on reaction rates, we set p=0 for each species so that the product $\prod_i a_i^p = 1$ has been eliminated from Equation 6.4-5. The ratio of the species activity product (Q) and the equilibrium constant (K) describes the extent to which a mineral is in disequilibrium with a given solution composition. For *Q/K* equal to one, the mineral is at equilibrium, and thus the net rate of reaction becomes zero. For *Q/K* greater than one, the mineral is oversaturated and thus the rate becomes negative. The expression "*sgn [log(Q/K)]*" ensures that the correct sign is enforced when the exponents m and n are not equal to one. The variable A is the reactive surface area expressed in units of $m^2_{mineral} / kg_{water}$. In the case of ideal solutions, the saturation index of the solid solution is calculated as the sum of the saturation indices of the individual endmembers, and the reaction rate of the solid solution is calculated as described in Wang 2003 ([161665], SN-LBNL-SCI-112-V2, pp. 37–40).

Carroll et al. (1998 [124275], p. 1379) noted that the calculated rates of amorphous silica precipitation, based on Rimstidt and Barnes (1980 [101708], p. 1683), are about three orders of magnitude lower than those observed in geothermal systems. Carroll et al. (1998 [124275], p. 1379) presented experimental data on amorphous silica precipitation for more complex geothermal fluids at higher degrees of supersaturation, and also for a near-saturation simple fluid chemistry. Under far from equilibrium conditions, the rate law for amorphous silica precipitation has been expressed as (Carroll et al. 1998 [124275], p. 1382):

$$Rate(mol\ s^{-1}kg_{water}^{-1}) = kA\left(Q/K\right)^{m} \qquad \text{(Eq. 6.4-7)}$$

This rate does not tend to zero as *Q/K* goes to one, and therefore a modification was made to this law so that it tends to zero as *Q/K* approaches one (described in Wang 2003 ([161665], SN-LBNL-SCI-109-V1, p. 45), as follows:

$$Rate(mol\ s^{-1}kg_{water}^{-1}) = kA\left[\left(Q/K\right)^{m} - \frac{1}{\left(Q/K\right)^{2m}}\right] \qquad \text{(Eq. 6.4-8)}$$

Over a finite time step (Δt), the change in the concentration of each primary species j on account of mineral precipitation or dissolution under kinetic constraints is computed from the sum of the rates, r_i, of all j-containing minerals i as follows:

$$\Delta C_j = -\sum r_i \nu_{ij} \Delta t \qquad \text{(Eq. 6.4-9)}$$

where ν_{ij} is the stoichiometric coefficient of component j in mineral i. These concentration changes are incorporated into the mass-balance equation of each primary species involved in mineral reactions, using Equations 6.4-5 through 6.4-7, and solved simultaneously with the concentrations of all primary species.

6.4.3 Fracture and Matrix Mineral Reactive Surface Areas

6.4.3.1 Fracture Mineral Reactive Surface Areas

Reactive surface areas of minerals on fracture walls were calculated from the fracture-matrix interface area/volume ratio, the fracture porosity, and the derived mineral volume fractions. The fracture-matrix interface areas and fracture porosities for each unit were taken from appropriate calibrated properties sets (Table 4.1-1). These areas were based on the fracture densities, fracture porosities, and mean fracture diameter. The wall of the fracture is treated as a surface covered by mineral grains having the form of uniform hemispheres. The grain diameter and spatial density are not included in this calculation, so that the area is actually only marginally greater than the fracture geometric surface area. An alternative method to approximating the surface area in excess of the geometric area would be to include a roughness factor. The geometric surface area of the fracture wall can be approximated by:

$$A_r = \frac{\pi A_{f\text{-}m}}{2\phi_{f-m}} \qquad \text{(Eq. 6.4-10)}$$

where, A_r is the reactive surface area ($\mathrm{m}^2/\mathrm{m}^3_{\text{fracture medium}}$), $A_{f\text{-}m}$ is the fracture-matrix interface area/volume ratio ($\mathrm{m}^2_{\text{fracture}}/\mathrm{m}^3_{\text{fracture+matrix}}$ volume), and $\phi_{f\text{-}m}$ is the fracture porosity of the rock. $A_{f\text{-}m}$

is the surface area used as input to the model simulations as an approximation of the reactive surface area. This model for the fracture surface area considers that the areal coverage is approximately equivalent to the mineral volume fraction. A further modification, which was implemented in TOUGHREACT V2.3 (LBNL 2001 [153101]), relates the 3-D cross-sectional area to the 2-D surface area in the fracture, which yields a factor of 3/2, i.e., an increase of 50% in the reactive surface area. This relation was used for all DST THC Model REV01 sensitivity studies, Tptpmn, and Tptpll THC simulations, discussed in Sections 6.4–6.6.

The reactive surface area of each mineral (in units of $\mathrm{m}^2_{\mathrm{mineral}} / \mathrm{kg}_{\mathrm{water}}$) used in Equations 6.4-5 and 6.4-8 is then given by:

$$A_i\ (\mathrm{m}^2/\ \mathrm{kg}_{\mathrm{water}}) = \frac{A_r f_i}{\rho_w \phi_f} \qquad \text{(Eq. 6.4-11)}$$

where f_i is the volume fraction of the mineral in the mineral assemblage, ρ_w is the density of water (taken as a constant 1,000 kg/m^3), and ϕ_f is the porosity of the fracture medium, as opposed to the fracture porosity of the rock. This is the surface area/water mass ratio for a mineral in a liquid-saturated system. Calculated volume fractions of minerals are tabulated in Attachments I and II.

To provide the correct rock/water ratio in an unsaturated system, the form of this surface area can be written as:

$$A_i\ (\mathrm{m}^2/\ \mathrm{kg}_{\mathrm{water}}) = \frac{A_r f_i}{\rho_w \phi_f S_w} \qquad \text{(Eq. 6.4-12)}$$

where S_w is the water saturation. However, as S_w goes to zero, the reactive surface area would tend to infinity. Clearly, at a very low liquid saturation, the surface area of the rock contacted by water is likely much smaller than the total area.

Two methods have been implemented to address this phenomenon. The first method considers that the surface area contacted by water diminishes proportionately to the saturation. This yields the saturated surface area given by Equation 6.4-10. The second method employs the active-fracture-model concept (Liu et al. 1998 [105729], pp. 2636–2638) modified to consider water-rock reactions taking place below the residual saturation. The form of the active fracture parameter for reaction is then given by the following set of equations:

$$S_{ar} = (S_w - S_m)/(1 - S_m) \qquad \text{(Eq. 6.4-13)}$$

$$a_{fmr} = S_{ar}^{(1+\gamma)} \qquad \text{(Eq. 6.4-14)}$$

where S_m is the minimum liquid saturation for which water-rock reactions are considered and S_{ar} is the effective saturation available for reaction. The active fracture parameter, γ, is obtained from the calibrated hydrological property set (DTN: LB990861233129.001 [110226]). The factor that reduces the surface area contacted by the water phase is given by a_{fmr}. In all simulations S_m is set to the very small saturation of 1×10^{-4} or 1×10^{-5} to ensure that reactions take place until virtually no water is left (e.g., during dryout via ventilation or heating). Finally, the reactive surface area, using this modified form of the active fracture model, is given by:

$$A_i(\mathrm{m}^2/\mathrm{kg}_{\mathrm{water}}) = \frac{A_r a_{fmr}}{\rho_w \phi_f S_w} \qquad \text{(Eq. 6.4-15)}$$

The surface area calculated in this way is applicable only to reactions taking place in the fracture medium and is used directly in Equations 6.4-5 and 6.4-8. Note that this area is not comparable to the input surface areas that are listed in Attachments III and IV.

In the dual permeability method, the porosity of the fracture medium can be taken as 1.0; however, for modeling of mineral dissolution and precipitation, there would then be no rock to dissolve. Because the dissolution rates of many minerals are quite slow at temperatures below 100°C, only a small volume of rock adjoining the open space of the fracture needs to be considered as the starting rock fraction. In the DST THC REV01 and Tptpmn THC REV01 models, the porosity of the fracture medium was set to 0.99, thus making available 1% of the total fracture volume for reaction. In the Tptpll THC Model (REV01 and REV02) and other REV02 models, the fracture medium porosity was set to 0.5 (Section 6.4.6.1).

6.4.3.2 Matrix Mineral Reactive Surface Areas

Mineral surface areas in the rock matrix (Attachments III and IV) were taken from DTNs shown in Table 4.1-1. These values were estimated using the geometric area of a cubic array of truncated spheres that make up the framework of the rock. Clay minerals are considered as coatings of plate-like grains. The mineral surface areas of framework grains (truncated spheres) in contact with the open pore space are calculated using an initial grain diameter, followed by successive truncation of the grains in the vertical direction until the porosity of this system is close to the measured porosity of the rock. In the welded tuff, crystals are often tightly intergrown with little or no pore space within the aggregate. Thus, a check is made so that the resultant mean pore throat size and spacing yields a permeability (from a modified Hagen-Poiseuille relation (Ehrlich et al. 1991 [117799], p. 1582, Equation 11)) that is relatively close to the measured saturated permeability.

The grains forming the framework of this rock are considered to be the primary high-temperature phases of the tuff (i.e., quartz, cristobalite, tridymite, and feldspars). The abundance of secondary phases (i.e., those that formed as alteration products or low-temperature coatings on the primary assemblage), such as clay minerals, are used to reduce the free surface area of the framework grains. The surface areas of the secondary phases are approximated using a tabular morphology.

6.4.4 Effects of Mineral Precipitation/Dissolution on Hydrological Properties

6.4.4.1 Porosity Changes

Changes in porosity and permeability resulting from mineral dissolution and precipitation have the potential to modify percolation fluxes and seepage fluxes at the drift wall. In this analysis, porosity changes in matrix and fractures are directly tied to the volume changes that result from mineral precipitation and dissolution. The molar volumes of hydrous minerals, such as zeolites and clays, created by hydrolysis reactions with anhydrous phases, such as feldspars, are commonly larger than those of the primary reactant minerals. Therefore, constant molar dissolution-precipitation reactions can lead to porosity reductions. These changes are taken into account in this analysis. The porosity of the medium (fracture or matrix) is given by

$$\phi = 1 - \sum_{m=1}^{nm} fr_m - fr_u \qquad \text{(Eq. 6.4-16)}$$

where nm is the number of minerals, fr_m is the volume fraction of mineral m in the rock ($V_{mineral}/V_{medium}$, including porosity), and fr_u is the volume fraction of nonreactive rock. As the fr_m of each mineral changes, the porosity is recalculated at each time step. The porosity is not allowed to go below zero.

6.4.4.2 Fracture Permeability Changes

Fracture permeability changes can be approximated using the porosity change and considering plane parallel fractures of uniform aperture (cubic law—Steefel and Lasaga 1994 [101480], p. 556). If the fracture spacing and density remain constant, the updated permeability, k, is given by

$$k = k_i \left(\frac{\phi}{\phi_i} \right)^3 \qquad \text{(Eq. 6.4-17)}$$

where k_i and ϕ_i are the initial permeability and porosity, respectively. This law yields zero permeability only under the condition of zero fracture porosity.

In most experimental and natural systems, permeability reductions to values near zero occur at porosities significantly greater than zero. This generally is the result of mineral precipitation preferentially closing the narrower interconnecting apertures. The hydraulic aperture, as calculated from the fracture spacing and permeability (as determined through air-permeability measurements) using a cubic law relation, is a closer measure of the smaller apertures in the flow system. Using the hydraulic aperture, a much stronger relationship between permeability and porosity can be developed. This relationship can be approximated as follows:

The initial hydraulic aperture $b_{0,h}$ (m) is calculated using the following cubic law relation:

$$b_{0,h} = \left[12 k_0 s \right]^{1/3} \qquad \text{(Eq. 6.4-18)}$$

where k_0 is the initial fracture permeability (m^2) and s is the fracture spacing (m) for a single fracture set. The permeability (k') resulting from a change in the hydraulic aperture is given by

$$k' = \frac{\left(b_{0,h} + \Delta b\right)^3}{12s} \qquad \text{(Eq. 6.4-19)}$$

where Δb is the aperture change resulting from mineral precipitation/dissolution. The aperture change resulting from a calculated volume change can be approximated by assuming precipitation of a uniform layer over the entire geometric surface area of the fracture, assuming also that this area (as well as the fracture spacing) remains constant. In geologic systems, the actual distribution of mineral alteration is much more heterogeneous and depends on many factors that are active at scales much smaller than the resolution of the model. The combined effect of the initial heterogeneities and localized precipitation processes can only be treated through model sensitivity studies and experiments. The initial aperture available for precipitation (b_g, the geometric, rather than the hydraulic, aperture) can be calculated (Attachment XI) from the ratio of the initial fracture porosity ($\phi_{f,0}$) to the fracture surface area (A_f), as follows:

$$b_g = \phi_{f,0} / A_f \qquad \text{(Eq. 6.4-20)}$$

For a dual-permeability model, changes in the fracture porosity are calculated based on the porosity of the fracture medium, so that Δb can be approximated by

$$\Delta b = \frac{\left(\phi'_{fm} - \phi_{fm,0}\right)}{\phi_{fm,0}} b_g \qquad \text{(Eq. 6.4-21)}$$

Equations 6.4-18, 6.4-19, and 6.4-21 were implemented in TOUGHREACT V2.3 (LBNL 2001 [153101]) with input parameters of b_g and s. This relation was used for sensitivity studies on the Tptpmn THC Model simulations (heterogeneous and homogeneous permeability fields), DST THC REV01 and REV02 Model simulations, and Tptpll THC Model simulations.

6.4.4.3 Matrix Permeability Changes

Matrix permeability changes are calculated from changes in porosity using ratios of permeabilities calculated from the Carmen-Kozeny relation (Bear 1988 [101379], p. 166, Equation 5.10.18, symbolically replacing n by ϕ), and neglecting changes in grain size, tortuosity, and specific surface area as follows:

$$k = k_i \frac{(1-\phi_i)^2}{(1-\phi)^2} \left(\frac{\phi}{\phi_i}\right)^3 \qquad \text{(Eq. 6.4-22)}$$

6.4.4.4 Effects of Permeability and Porosity Changes on Capillary Pressures

Changing permeability and porosity also results in changes in the unsaturated flow properties of the rock. These effects are treated by modifying the calculated capillary pressure (*Pc*) using the Leverett scaling relation (Slider 1976 [128146], p. 280) to obtain a scaled *Pc´* as follows:

$$Pc' = Pc\sqrt{\frac{k_i\phi}{k\phi_i}} \qquad \text{(Eq. 6.4-23)}$$

Simulations performed with TOUGHREACT V3.0 (LBNL 2002 [161256]) have the maximum value of *Pc´* (in Eq. 6.4-23) limited by the cutoff prescribed in the input file. All simulations done using earlier TOUGHREACT versions have the cutoff apply to *Pc* (not *Pc´*) in Eq. 6.4-23 unless an extrapolation in the *Pc*-saturation curve was performed, in which case no cutoff was applied. Capillary pressure cutoff values used in various model revisions are discussed in Section 6.4.6.1 (approximation no. 15).

6.4.5 Mineral Precipitation in Dry Gridblocks

In certain cases of evaporation or boiling, a gridblock may experience an influx of water that evaporates completely during the solution of the flow equations. After the flow equations are solved, TOUGHREACT solves the transport equations followed by the speciation and reaction equations. The speciation and reaction equations require that the gridblock is "wet,"—that is, the liquid saturation is greater than zero (or a small value). Because of the lack of water in the gridblock, a method was developed for storing all residual aqueous species in a solid "salt" assemblage.

The amount of solute "stored" is simply the product of the concentration in the upstream gridblock and the flux of water into the gridblock that dries out. Also, any water that is initially present in the gridblock, and dries out, gives rise to some solute mass that is transformed into solid phases. For these cases, the mass of each primary solute species is saved and may be assigned to minerals in a prescribed order in the chemical input file. This approximation is performed so that solute mass loss is minimized and most of the solute mass can be accounted for in a solid mineral phase. Simulations performed with TOUGHREACT V2.4 (LBNL 2001 [160880]) and V3.0 (LBNL 2002 [161256]) have this option, whereas V2.2 (LBNL 1999 [153219]) and V2.3 (LBNL 2001 [153101]) do not.

In the simulations presented in this Model Report (REV02), for the specific cases when water flows into gridblocks that dry out in the flow calculation (by boiling or evaporation), the following solid phases are formed, stoichiometrically and in the following order: silica, calcite, gypsum, hematite, fluorite, $NaNO_3$, K_2SO_4, Na_2SO_4, $MgSO_4$, halite, and sylvite. The order is predetermined (i.e., nitrates are formed before chlorides) to ensure nitrate mass is not lost in cases where insufficient sodium remains to form $NaNO_3$ (in the absence of other nitrate salts that could have formed). The goal, here, is not to model evaporation accurately but to save as much mass of the dissolved constituents as possible for gridblocks that completely dry out.

Upon rewetting, the salt minerals (i.e., $NaNO_3$, K_2SO_4, Na_2SO_4, $MgSO_4$, halite, sylvite) are assumed to dissolve kinetically with a relatively fast rate constant (set here at 10^{-6} mol/m^2/s) and

a dissolution rate limited by their solubility (Section 6.4.2). The salt solubilities were taken from the data0.ymp.R2 database (DTN: MO0302SPATHDYN.000 [161756]), except that $NaNO_3$ (not in that database) was given the solubility of KNO_3 in that database. Therefore, this model captures the general behavior of salt dissolution as the boiling front recedes. However, the predicted major ion concentrations during the short time when these salts dissolve are approximate, because the identity of the salt phases is not based on a thermodynamic speciation/precipitation model, and their dissolution rates are only approximate.

6.4.6 Principal Model Approximations and Approaches

6.4.6.1. General Approximations in the Modeling of THC Processes

1. The rock is described by a dual-permeability model (Section 6.2.1.5), which considers separate but interacting fracture and matrix continua, each with specified permeabilities. In the dual-permeability model, the fracture continuum is considered as co-located but interacting with the matrix continuum, in terms of the flow of heat, water, and vapor through advection, diffusion, and conduction (for heat). The aqueous and gaseous species are transported via advection and molecular diffusion between the fractures and matrix. Each continuum has its own well-defined initial physical and chemical properties. The dual-permeability approach for modeling physical processes in fractured porous media is discussed in detail in Doughty (1999 [135997], pp. 76–77). This approach is validated by comparing geochemical data obtained from the DST to results of simulations of the DST (Section 7.1). It is also further validated in BSC (2003 [161530], Section 7).

2. The mass of minerals precipitated is small and its thermal properties are similar to those of the host rock. Therefore, the thermal properties are not modified to account for precipitated minerals.

3. The infiltrating water and the fracture water are set to the same chemical composition as the matrix pore-water samples that were collected (Table 6.2-1). The rationale for this modeling approach is given in Section 6.2.2.1.

4. Effects of changes in the partial pressure of CO_2 (resulting from heating, water reaction with calcite, and gas-phase transport) on the density of the gas phase are neglected. This is justified because, in this study, CO_2 generally accounts for less than 5% and always less than 10% of the gas phase volume (air, water, and CO_2). Although the molecular weight of CO_2 is greater than that of air (approximately 44 g/mol versus 29 g/mol), the density is only increased proportionally to the volume fraction of CO_2 and the ratio of the molecular weights. This would result in a density increase of about 5% for a gas with a CO_2 volume fraction of 10%. These conditions make the effect of evolved CO_2 on the physical properties of the gas phase negligibly small and justify the use of this approximation. The effect of CO_2 on the density of steam (molecular weight approximately 18 g/mol) would be somewhat greater, however increases in the steam fraction accompanying boiling would tend to dilute the CO_2 fraction.

5. The effects of changes in water chemistry on the water density and viscosity are neglected. This approximation is justified because aqueous-species concentrations are low in waters at most values of the liquid saturation (in the rock matrix or fractures). In cases where concentrations are significantly higher, the liquid saturation is generally much less than 1%. Therefore, the liquid is nearly immobile because of the very small relative permeability for the liquid phase under such conditions.

6. Diffusion coefficients of all aqueous species are set to the same value (the value for the chloride anion; see Section 4.1.6). This is justified because the tracer diffusion coefficients of aqueous species differ by at most about one order of magnitude, with many differing by less than a factor of 2 (Lasaga 1998 [117091], p. 315). The strong effects of water-rock interaction, boiling condensation, and rapid fracture drainage overwhelm effects of aqueous species diffusion.

   Diffusion coefficients for gases are calculated. In the gas phase, CO_2 is the only transported reactive species (other than H_2O vapor). For an ideal gas, the tracer diffusion coefficient of a gaseous species can be expressed as a function of temperature and pressure in the following form (Lasaga 1998 [117091], p. 322):

$$D = \frac{RT}{3\sqrt{2}\pi P N_A d_m^2}\sqrt{\frac{8RT}{\pi M}} \qquad \text{(Eq. 6.4-24)}$$

   where

   D = diffusion coefficient (m^2/s)
   R = gas constant (8.31451 m^2 kg s^{-2} mol^{-1} K^{-1})
   T = temperature in Kelvin units
   P = pressure (kg m^{-1} s^{-2})
   N_A = Avogadro's number (6.0221367×10^{23} mol^{-1})
   d_m = molecular diameter (m)
   M = molecular weight (kg/mol)

   The CO_2 diffusion coefficient is calculated using input values of d_m and M (Section 4.1.6).

7. Mineral precipitation or dissolution is modeled to occur uniformly over the smooth plane-parallel fracture walls (Section 6.4.4.2). However, mineral precipitation could be non-uniform, leading to a different relationship between changes in permeability and porosity. This approximation can be justified by the use of bulk permeabilities and porosities that initially account for the net effect of variability in fracture aperture at a macroscopic scale. Furthermore, effective (hydraulic) apertures are used instead of true apertures, the latter being much larger (Section 6.4.4.2). As a result, the permeability change is quite sensitive to porosity changes (in this study, a 10–14% drop in fracture porosity leads to zero permeability in fractures in the modeled repository units).

8. CO_2 gas is treated as an ideal gas (i.e., obeys the ideal gas law and its partial pressure equals its fugacity). This approximation is valid for the low ambient pressures (near atmospheric) considered in this study (Langmuir 1997 [100051], p. 15).

9. Except for smectites, the chemical and physical properties of minerals that form solid solutions are approximated by their individual endmember compositions and properties. Because smectite endmembers are (individually) near equilibrium with pore waters, some of the smectite endmembers could be calculated to precipitate while others dissolve. For this reason, an ideal solid-solution model is implemented for smectite (Na, Ca, and Mg endmembers), with each endmember's activity equaling its mole fraction. Treating the smectite as a solid solution, results in individual smectite endmembers either all dissolving or all precipitating, providing a better physical representation of dissolution/precipitation processes. Feldspar solid solutions are not considered because albite (Na-feldspar) and anorthite (Ca-feldspar) are generally strongly undersaturated in the simulations, and thus their dissolution rates are governed primarily by the kinetic-rate constant rather than the saturation index (Equation 6.4-5). In addition, nearly pure secondary K-feldspar compositions are observed in geothermal systems (Stefánsson and Arnórsson 2000 [153578], p. 2578). Therefore, the precipitation of secondary K-feldspar can be approximated fairly well with a pure endmember. These approximations are further validated by comparison of model results to measured water chemistry in the DST (Section 7.1) and in a plug-flow reactor experiment (Section 7.2).

10. The fracture continuum is modeled with grid blocks having an initial fraction of void space less than one (0.99 in the DST THC REV01 Model and Tptpmn THC REV01 Model, and 0.5 in the Tptpll THC REV01 and REV02 models). These values are chosen such that that the fracture medium always contains solids that can react with fluids in fractures. It is verified that there is always enough solid initially present in the fracture continuum to avoid the possibility that some of the primary rock forming minerals become exhausted (through dissolution). Note that the volume of each grid block assigned to the fracture continuum is then calculated in such a way that the true fracture porosity (i.e., the fraction of the bulk rock occupied by fracture void space) is always reproduced.

11. The thermal conductivities of fracture and matrix gridblocks are calculated assuming a linear interpolation between dry and wet conductivities as a function of liquid saturation. These are the thermal conductivities for the solid + fluid system. For fractures, thermal conductivities are multiplied by the fracture porosity to account for the correct fracture-to-fracture connection area in calculations of heat conduction (i.e., this is needed because full gridblock areas are input into the model). Fracture thermal conductivities are also multiplied by 0.1 (an arbitrary value less than 1) to account for the limited spatial continuity and connectivity between fracture gridblocks. The volume of the fracture continuum is, however, only a small fraction of the matrix continuum. Therefore heat conduction occurs primarily through the matrix continuum and, as a result, the model is not sensitive to the amount of heat conduction in fractures.

12. In REV01 simulations (Sections 6.5–6.7), vapor-pressure lowering due to capillary pressure (the Kelvin effect) is neglected. This effect is taken into account in simulations carried out for this current model revision (REV02) (Section 6.8 and 7.1). The impact of including or neglecting this effect is evaluated in Section 6.8.5.3.

13. Upon boiling or evaporation, the aqueous phase is treated as unreactive and is not concentrated further, once its ionic strength reaches an input upper limit of 4 or if the liquid saturation drops below an input lower limit of 10^{-4} to 10^{-5}. This ensures that the calculated ionic strength remains within the range of applicability of activity coefficient models (Section 6.4.1). Past these limits, different schemes are implemented in the various model revisions, as discussed below.

    In REV01 simulations (Sections 6.5–6.7), concentrations of aqueous species are saved (unchanged) during dryout and become available again for reaction at the time of rewetting, when the liquid saturation increases and the ionic strength decreases. This scheme has the effect that all salts that would precipitate from the point of the liquid saturation or ionic-strength limits (up to the point of complete dryout) would instantly redissolve upon rewetting.

    In REV02 simulations (Sections 6.8 and 7.1), solid phases are formed during dryout as described in Section 6.4.5. These solid phases are then available for dissolution upon rewetting (using a fast dissolution rate arbitrarily set at 10^{-6} mol s^{-1} kg_{H2O}^{-1}).

    At liquid saturations as small as 10^{-5}, the total amount of dissolved mass present in any given model gridblock is exceedingly small. Thus, ignoring chemical reaction for such small mass amounts (and over a limited time period) does not significantly affect the general computed trends of aqueous phase concentrations and precipitated mineral amounts over long periods of time and a wide range of liquid saturations.

14. Hydrogeologic rock properties in each hydrogeologic unit of the model are approximated as being laterally homogeneous, except in the Tptpmn Heterogeneous THC Model (Section 6.6). Results of the Tptpmn Heterogeneous THC Model (Section 6.6.2), including the natural heterogeneity in fracture permeability (4 orders of magnitude), do not show significantly different water chemistry in either space or time when compared to the homogeneous model (Section 6.5.5). Furthermore, good comparisons are obtained between modeled and measured water and gas chemistry for the DST (Section 7.1).

15. The capillary pressure in both fractures and matrix must reach some maximum, finite value upon complete dryout (zero liquid saturation). In REV01 simulations (Sections 6.5–6.7), for fractures and matrix in the Tptpmn, Tptpll, and Tptpln lithostratigraphic units (model units tsw34, tsw35, and tsw36, respectively), the limit is set by the calculated slope of the P_{cap} versus liquid saturation curve at a liquid saturation value equal to $S_r + \varepsilon$, with S_r being the residual saturation, and $\varepsilon = 0.01$ (Table 6.4-1). In these units, this results in maximum P_{cap} values of 10^{11}–10^{13} Pa in the matrix, and 10^{3}–10^{4} Pa in fractures. In other hydrogeologic units, in REV01 simulations, the limit is set to 10^{10} Pa by default. For the matrix, these values exceed the maximum tensile

strength of water (on the order of 10^8 Pa; e.g., Mercury and Tardy 2001 [161130]), and were therefore lowered in subsequent REV02 simulations.

In REV02 simulations (Sections 6.8 and 7.1), the default limit is set to 10^8 Pa. For fractures and matrix in the Tptpmn, Tptpll, and Tptpln lithostratigraphic units (model units tsw34, tsw35, and tsw36, respectively), the limit is set, as previously, by the calculated slope of the P_{cap} versus liquid saturation curve at a liquid saturation value equal to $S_r + \varepsilon$. For these units, ε values for the matrix yield maximum P_{cap} values of 10^8 Pa (Table 6.4-1); for fractures, ε is set to 0.01 as done for REV01 simulations (maximum P_{cap} values around 10^3–10^4 Pa).

The unrealistic maximum P_{cap} values used in REV01 previous do not have much effect on simulation results because vapor-pressure lowering (due to capillary pressure) is neglected in these simulations. Low values of maximum capillary pressures in fractures are justifiable, on the basis that the capillary suction in fractures is orders of magnitude less than in the rock matrix.

16. Open spaces in the drift are approximated as a porous medium with a large permeability (10^{-10} m^2) greater than in surrounding rocks, but not so large as to create numerical difficulties when computing flow. In addition, these open spaces are modeled with no capillarity, a unit porosity, and no residual saturation except directly against the drift wall (arbitrary small value of 0.01 to account for some water condensation, if any, against the drift wall). These approximations are made because the mathematical model is not formulated to handle fluid flow in non-porous media.

17. The fracture tortuosity value (0.7) (Section 4.1.6) is based on models of *in situ* testing data (DTN: LB991091233129.006 [111480]) and also corresponds to the highest tortuosity given by de Marsily (1986 [100439], p. 233), with the rationale that fracture tortuosity should be high compared to matrix tortuosity (i.e., less tortuous path in fractures than in the matrix). This fracture tortuosity was modified for fracture-fracture connections by multiplication of the tortuosity by the fracture porosity of the bulk rock. This operation yields a better approximation for the fracture-to-fracture interconnection area (only for calculation of diffusive fluxes; the entire gridblock connection area is used for calculating advective fluxes, because the bulk fracture permeability of the entire gridblock is entered into the model).

6.4.6.2 Approximations Specific to the THC Seepage Model

1. For the Tptpmn and Tptpll THC Model REV01 simulations (Sections 6.5–6.7), the drift wall is always closed to fluid fluxes except for gaseous CO_2 diffusive fluxes. The latter are limited because the drift, as modeled, is closed at each end. Therefore, the drift has a finite volume that is small compared to the near-field rock volume. If chemical reactions inside the drift do not take place to a large extent, the effect of exchange of components with the near-field environment would have little effect on near-field THC processes. There are further reasons for closing the drift to advective fluid fluxes. First, our objective is to calculate the water and gas compositions that reach the drift wall, and not THC processes in the drift itself (in-drift THC processes are considered in other model reports). Processes in the rock outside the drift are the most likely to govern compositions of aqueous liquids and gases entering the drift.

Second, for a homogeneous fracture system with constant vertical infiltration (from the top model boundary), the wall acts as a capillary barrier and water cannot seep into the drift even with an open drift and infiltration rates much larger than considered here. In this case, water fluxes into the drift could be conservatively approximated as the liquid fluxes very close to the drift wall.

For REV02 simulations, the drift wall is open to all fluid fluxes. No specific boundary conditions of pressure, relative humidity, or gas compositions are applied inside the drift (i.e., as if the repository were sealed off, and neglecting sources or sinks of CO_2 due to microbial activity or atmospheric CO_2). Computing fluid flow through open spaces of the drift using a model designed to calculate flow through porous media is by itself a very coarse approximation. Thus, modeling the drift wall as either open or closed to advective fluid flow are equally coarse approximations. However, the scope of this Model Report is to model THC processes in the near-field outside the drift and not in the drift itself. Comparisons between these alternatives are presented in Section 6.8. Note that for the open drift case (REV02), the invert is allowed to react with any water present in it (pore water or condensation).

2. The initial composition of water in fractures is taken to be the same as in the rock matrix throughout the model domain. Also, this initial water composition is set to be the same in all hydrogeologic units. Justifications for this modeling approach are provided in Section 6.2.2.1.

6.4.7 Summary of Hydrological and Thermal Properties

The hydrological and thermal properties of repository units used in simulations presented in the following sections of this report are summarized in Table 6.4-1. Sources of properties used for all modeled hydrogeological units and other input data are listed in Section 4.1 and 6.4.8.

6.4.8 Sources of Additional Model Inputs Used in Sensitivity Analyses

This section describes model inputs used for simulations considered as sensitivity analyses and which were not used for TSPA-LA. All direct input data and technical information used for simulations feeding TSPA-LA are summarized in Section 4.1. Data used for model validation are presented in Section 7. Sources of model input data used to evaluate model sensitivity, if different from data listed in Sections 4.1 and 7, are discussed below and summarized in Table 6.4-2.

6.4.8.1 Sensitivity to Historical (REV01) Model Inputs

Results of historical simulations carried out for REV01 of this report are presented in this report revision (REV02) in Sections 6.5, 6.6, and 6.7. These REV01 simulations provide useful information to assess the sensitivity of the THC Seepage Model to various input data and model improvements from REV01 to REV02. Sources of historical data for these simulations are shown in Table 6.4-2. For convenience, REV01 mineralogical data are listed in Attachments I and III, REV01 thermodynamic data in Attachment V, and REV01 kinetic data in Table 6.4-3.

6.4.8.2 Thermodynamic Data Sensitivity (REV02)

Simulations of "ambient" conditions (i.e., without thermal loading, under natural geothermal gradient, and without drift opening) were run using alternative thermodynamic data sets to evaluate the model sensitivity to these data (Section 6.8.5.1) and to justify the thermodynamic data (Set 1, below) selected for other REV02 simulations in this report. For these ambient simulations, the following three sets of data were used:

Set 1

This is the thermodynamic data set adopted for all REV02 simulations (DTN: LB0307THMDBRTM.001 [164434]) (Attachment VI) and discussed in Section 4.1.4.

Set 2

This thermodynamic data set contains all data from the YMP thermodynamic database data0.ymp.R2 (DTN: MO0302SPATHDYN.000 [161756]), except for necessary changes to data for a few minerals (not prevalent in the vicinity of the drift) as described below (see also Wang 2003 [161665], SN-LBNL-SCI-141-V2, pp. 158–160).

Heulandite in database data0.ymp.R2 contains significant amounts of barium and strontium. These chemical components are not considered in this study. For this reason, the data from database data0.ymp.R2 for heulandite could not be used. Instead, log(K) values used in Set 2 for heulandite were taken as the uncorrected log(K) values given in DTN: LB0307THMDBRTM.001 [164434] ("heuland/10" in Attachment VI). The source of these data and the calculation methods are the same as those used for the stellerite log(K) values in the data0.ymp.R2 database (DTN: MO0302SPATHDYN.000 [161756]).

Log(K) values for sepiolite are not given in database data0.ymp.R2 for temperatures above 100°C. For this reason, sepiolite log(K) values were taken from an earlier revision of this database (DTN: MO0204SPATHDYN.000 [158910]), containing sepiolite data consistent with the data in Set 1 above.

For clinoptilolite, log(K) values were taken for the mineral identified as clinoptilolite-Ca in database data0.ymp.R2, because this phase has a similar composition to the phase used in Set 1. However, this phase contains a very small amount of iron, which is not included in the clinoptilolite in Set 1. By using this phase, the already very small amount of iron in the aqueous phase was completely depleted, causing chemical convergence problems in simulations. For this reason, iron was removed from this phase. It was not deemed necessary to recompute log(K) values because the amount of iron in this phase is very small (approximately 0.1% stoichiometric proportion of Fe relative to Si).

No other changes were made to the data0.ymp.R2 database for Set 2. For calcium, magnesium, and sodium smectites, the phases identified as montmorillonite-Ca, montmorillonite-Mg, and montmorillonite-Na in the data0.ymp.R2 database were used. For potassium feldspar, the phase identified as maximum_microcline was used. Glass data from Set 1 were included in Set 2 because no glass data are included in the data0.ymp.R2 database. Note that if a mineral was specified with different unit cell stoichiometries in Set 1 and Set 2 (i.e. some clays and zeolites),

the kinetic rate of that mineral (Section 4.1.5) was corrected to account for the same stoichiometric Si release (or consumption) per unit time, for consistency between data sets.

Set 3

This set is identical to Set 2 (data0.ymp.R2 database), except that all zeolite thermodynamic data were taken from Set 1 (minerals identified as “mord/10-r02”, “heul/10-r02”, “stell/10-r02”, and “clpt/10-r02 in Attachment VI”).

Table 6.4-1 Summary of Hydrological and Thermal Properties of Repository Units

		REV01				REV02			
Model Layer > ***Lithostratigraphic Unit >***		***tsw33*** ***Tptpul***	***tsw34*** ***Tptpmn***	***tsw35*** ***Tptpll***		***tsw33*** ***Tptpul***	***tsw34*** ***Tptpmn***	***tsw35*** ***Tptpll***	
MATRIX DATA					**DTN:**				**DTN:**
permeability	k_m (m^2)	3.08E-17	4.07E-18	3.04E-17	LB990861233129.001	6.57E-18	1.77E-19	4.48E-18	LB0208UZDSCPMI.002
porosity	ϕ_m	0.154	0.110	0.131	LB990861233129.001	0.1425	0.1287	0.1486	LB0210THRMLPRP.001
van Genuchten α	α_m (1/Pa)	2.13E-5	3.86E-6	6.44E-6	LB990861233129.001	6.17E-6	8.45E-6	1.08E-5	LB0208UZDSCPMI.002
van Genuchten m (or λ)	m_m	0.298	0.291	0.236	LB990861233129.001	0.283	0.317	0.216	LB0207REVUZPRP.002
residual saturation	S_{lrm}	0.12	0.19	0.12	LB990861233129.001	0.12	0.19	0.12	LB0207REVUZPRP.002
satiated saturation	S_{lsm}	1.00	1.00	1.00	LB990861233129.001	1.00	1.00	1.00	LB0207REVUZPRP.002
epsilon (for max P_{cap})	ε	0.01	0.01	0.01	(Section 6.4.6.1)	0.138	0.091	0.216	Yield maximum P_{cap} = 10^8 Pa (Section 6.4.6.1)
rock grain density	ρ_g (kg/m^3)	2510	2530	2540	LB990861233129.001	2358	2466	2325	LB0210THRMLPRP.001
rock grain specific heat	Cp (J/kg-K)	882	948	900	LB990861233129.001	985	985	985	LB0210THRMLPRP.001
dry conductivity	λ_{dry} (W/m-K)	0.79	1.56	1.20	LB990861233129.001	1.164*	1.419*	1.278*	LB0210THRMLPRP.001
wet conductivity	λ_{wet} (W/m-K)	1.68	2.33	2.02	LB990861233129.001	1.675*	2.074*	1.890*	LB0210THRMLPRP.001
tortuosity	t	0.2	0.2	0.2	Assumed (Section 5) from range of Accepted Data (de Marsily 1986 [100439])	0.2	0.2	0.2	Assumed (Section 5) from range of Accepted Data (de Marsily 1986 [100439])
FRACTURE DATA[1]									
permeability	k_f (m^2)	8.79E-13	3.68E-13	2.38E-12	LB0011DSTFRAC1.001	7.80E-13	3.30E-13	9.10E-13	LB0205REVUZPRP.001
porosity (Tptpmn Model)	ϕ_f	8.5E-3	1.0E-2	1.5E-2	LB997141233129.001	-	-	-	-
porosity (Tptpll Model)	ϕ_f	6.6E-3	1.0E-2		LB990861233129.001	5.8E-3	8.5E-3	9.6E-3	LB0205REVUZPRP.001
	ϕ_f			1.8E-2	LB0011DSTFRAC1.001				
van Genuchten α	α_f (1/Pa)	1.46E-3	5.16E-4		LB990861233129.001	1.59E-3	1.04E-4	1.02E-4	LB0208UZDSCPMI.002
	α_f (1/Pa)			8.23E-5	LB0011DSTFRAC1.001				

Table 6.4-1 Summary of Hydrological and Thermal Properties of Repository Units (continued)

		REV01				REV02			
Model Layer > ***Lithostratigraphic Unit >***		***tsw33*** ***Tptpul***	***tsw34*** ***Tptpmn***	***tsw35*** ***Tptpll***		***tsw33*** ***Tptpul***	***tsw34*** ***Tptpmn***	***tsw35*** ***Tptpll***	
van Genuchten m (or λ)	m_f	0.608	0.608	0.611	LB990861233129.001	0.633	0.633	0.633	LB0205REVUZPRP.001
residual saturation	S_{lrf}	0.01	0.01	0.01	LB990861233129.001	0.01	0.01	0.01	LB0205REVUZPRP.001
satiated saturation	S_{lsf}	1.00	1.00	1.00	LB990861233129.001	1.00	1.00	1.00	LB0205REVUZPRP.001
active fracture parameter	gamma	0.41	0.41	0.41	LB990861233129.001	0.60	0.57	0.57	LB0208UZDSCPMI.002
frequency	f (1/m)	0.81	4.32	3.16	LB990861233129.001	0.81	4.32	3.16	LB0205REVUZPRP.001
fracture to matrix area	A (m^2/m^3)	4.44	13.54	9.68	LB990861233129.001	4.44	13.54	9.68	LB0205REVUZPRP.001
tortuosity	t	0.7	0.7	0.7	LB991091233129.006	0.7	0.7	0.7	LB991091233129.006
epsilon (for max P_{cap})	ε	0.01	0.01	0.01	Model Setup (Section 6.4.6.1)	0.01	0.01	0.01	Model Setup (Section 6.4.6.1)

NOTE: [1] Fracture thermal properties are derived using matrix properties as discussed in Section 6.4.6

* Bulk conductivities converted from grain conductivity values and lithophysal porosities listed in DTN shown, using $K_{bulk} = K_{grain}\ (1-\phi_{lith}) + \phi_{lith}\ K_{air}$, with K_{air} = 0.028 (W/m-K) (extrapolated at 50°C from Lide 1993 [123032], p. 6-172).

Table 6.4-2 Data Tracking Numbers for Sources of Model Inputs Used in REV01 and Sensitivity Analyses[1]

DTNs	THC Model	Data/Parameter Description
Hydrological and Thermal Rock Properties		
LB990861233129.001 [110226]	Tptpmn REV01 and DST REV01	Permeability (except tsw33, tsw34 and tsw35 fractures), matrix porosity, van Genuchten m, van Genuchten alpha (except tsw35 fractures), residual saturation, satiated saturation, active fracture parameter, fracture frequency, fracture to matrix area; matrix thermal properties: bulk dry and wet conductivity, grain specific heat, and grain density
LB997141233129.001 [104055]		Fracture porosity
LB0011DSTFRAC1.001 [153470]		Fracture parameters: permeability (tsw33, tsw34, and tsw35 only) and van Genuchten alpha (tsw35 only)
LB990861233129.001 [110226]	Tptpll REV01	Permeability (except tsw33, tsw34 and tsw35 fractures), porosity (except tsw35 fractures), van Genuchten m, van Genuchten alpha (except tsw35 fractures), residual saturation, satiated saturation, active fracture parameter, fracture frequency, fracture to matrix area; matrix thermal properties: bulk dry and wet conductivity, grain specific heat, and grain density
LB0011DSTFRAC1.001 [153470]		Fracture parameters: permeability (tsw33, tsw34, and tsw35 only), porosity (tsw35 only), and van Genuchten alpha (tsw35 only)
Mineralogical Data		
LB991200DSTTHC.003 [161276]	DST REV01 and Tptpmn REV01	Mineral volume fractions (Attachment I)
LB0101DSTTHCR1.003 [161278]	DST REV01 and Tptpmn REV01	Mineral surface areas (Attachment III)
Thermodynamic and Kinetic Data		
LB0101DSTTHCR1.006 [161280]	All REV01 models	Thermodynamic data for aqueous species and minerals: equilibrium constants, molecular weights, molar volumes, Debye-Hückel parameters, CO_2 molecular diameter (Attachment V)
MO0302SPATHDYN.000 [161756]	Tptpll REV02 (sensitivity only)	Equilibrium constants, molecular weights, molar volumes
BSC (2002 [158375], Table 4)	All REV01	Rate constants and activation energies (Table 6.4-3)
Repository Drift Design Data		
CRWMS M&O 2000 [151014]	Tptpmn REV01	Invert thickness (0.6 m)
LB0101DSTTHCR1.007 [161281]	All REV01 THC Seepage models	Heat load (Attachment VII)
CRWMS M&O 2000 [120903], Section 4.2	All REV01 THC Seepage models	Heat removal by ventilation (70%)

NOTE: [1] Not used for TSPA-LA

able 6.4-3. REV01 Kinetic Rate Law Data for Mineral-Water Dissolution and Precipitation

Mineral	k_0 (mol m^{-2} s^{-1})	E_a (kJ/mol)	m(1)	n(1)	Comment(2)
α-Cristobalite	3.1623×10^{-13}	69.08	1	1	dissolution
Quartz	1.2589×10^{-14}	87.5	1	1	dissolution only
Tridymite	3.1623×10^{-13}	69.08	1	1	dissolution only
Amor. Silica	7.9433×10^{-13}	62.8	1	1	dissolution
	1.0×10^{-10}	0.0	4.4	1	precipitation
Opal_proxy	7.9433×10^{-13}	62.8	1	1	no precip.
Calcite	1.6×10^{-6}	41.87	1	1	reversible
	equilibrium	NA	NA	NA	local equilibrium
Microcline	1.0×10^{-12}	57.78	1	1	reversible
Albite-Low	1.0×10^{-12}	67.83	1	1	reversible
Anorthite	1.0×10^{-12}	67.83	1	1	dissolution only
Smectite-Ca	1.0×10^{-14}	58.62	1	1	reversible
Smectite-Na	1.0×10^{-14}	58.62	1	1	reversible
Smectite-Mg	1.0×10^{-14}	58.62	1	1	reversible
Smectite-K	1.0×10^{-14}	58.62	1	1	reversible
Illite	1.0×10^{-14}	58.62	1	1	reversible
Kaolinite	1.0×10^{-13}	62.8	1	1	reversible
Sepiolite	1.0×10^{-14}	58.62	1	1	reversible
Stellerite	1.99×10^{-12}	62.8	1	1	reversible
Heulandite	1.99×10^{-12}	62.8	1	1	reversible
Mordenite	1.99×10^{-12}	62.8	1	1	reversible
Clinoptilolite	1.99×10^{-12}	62.8	1	1	reversible
Glass (vphyr)†	7.7233×10^{-15}	91	1	1	dissolution only
Gypsum	equilibrium	NA	NA	NA	local equilibrium
Hematite	7.9433×10^{-13}	62.8	1	1	dissolution only
Goethite	equilibrium	NA	NA	NA	NA
Fluorite	1.2224×10^{-7}	0	1	2	reversible

Source: Taken from Table 4 in MDL-NBS-HS-000001 REV01, ICN02 (BSC 2002 [158375]) (not used for TSPA-LA).

NOTES: k_o Rate Constant

E_a Activation Energy

NA Not Applicable

† "Vphyre" refers to the basal vitrophyre of the Topopah Spring welded hydrogeologic unit (TSw) unit. The composition of this glass was used for all glass-bearing units, including the nonwelded Paintbrush nonwelded hydrogeologic unit (PTn) glassy tuffs.

(1) Exponents *m* and *n* in Equation 6.4-8.

(2) "dissolution only" means precipitation of this mineral is not allowed. "reversible" indicates the same precipitation and dissolution rate apply.

6.5 Tptpmn THC MODEL REV01

The Tptpmn THC Model REV01 is an earlier variation of the THC Seepage Model completed as part of the previous version (REV01) of this Model Report. The conceptualizations and mathematical formulations developed for this model are presented in Sections 6.1 to 6.4. The Tptpmn THC Model is a two-dimensional numerical model along a laterally continuous, vertical geologic section with stratigraphy similar to that in borehole USW SD-9 (at Nevada State Plane coordinates E171234, N234074; DTN: LB990501233129.004 [111475]). The modeled drift is located in the Topopah Spring Tuff middle nonlithophysal geologic unit (Tptpmn unit, corresponding to model layer name tsw34, DTN: LB990501233129.004 [111475]). Only part of the repository is planned to be located in the Tptpmn, and therefore the model is not representative of the entire repository. However, most hydrogeologic data available for the repository horizon are from the Tptpmn unit, including data from the Single Heater Test, DST, and many other data collected in the ESF. Alternative models presented in Sections 6.7 and 6.8 consider a drift in the Topopah Spring Tuff lower lithophysal lithostratigraphic unit, or Tptpll, where most of the repository is planned to be located.

The key elements of the Tptpmn THC Model REV01 include:

- Initial heat load of (1.45 kW/m) (Attachment VII)
- 50-year preclosure period with 70% ventilation efficiency
- Drift in the Tptpmn unit
- Model stratigraphy from geology at borehole SD-9
- Consideration of a base-case and extended-case geochemical system (Section 6.2.2.2)
- Drift wall closed to fluid and gas advection (but open to diffusive fluxes)
- Omission of vapor-pressure lowering by capillary pressure
- Older set of rock thermal and hydrological properties (Table 6.4-1)
- Slightly older thermodynamic database (Attachment V), although not much different than newer data
- Utilization of an older TOUGHREACT version (V2.3 (LBNL 2001 [153101])), a version which does not consider precipitation of solids in dry gridblocks, but into which water influx occurs (Section 6.4.5), and thus underestimates mineral precipitation
- Most useful for comparison with the Tptpll THC Model REV01 results to evaluate effects of drift location (Tptpmn versus Tptpll, see Section 6.7) and model stratigraphy

6.5.1 Numerical Mesh

Simulations were performed on a vertical 2-D mesh, using a drift spacing of 81 m (center to center, 800-IED-EBS0-00402-000-00B (BSC 2003 [161727])) and a drift diameter of 5.5 m (800-IED-EBS0-00301-000-00A, BSC 2003 [162444]). With rock properties laterally homogeneous between drifts (Section 6.4.6.1), this setup can be viewed as a series of symmetrical, identical half-drift models with vertical no-flow boundaries between them. Accordingly, the numerical mesh was reduced to a half-drift model with a width of 40.5 m, corresponding to the midpoint between drifts (Figure 6.5-1). Geologic data from borehole USW SD-9, as implemented in UZ model grid UZ99_2_3D.mesh (DTN: LB990501233129.004 [111475]), were used as a basis to map geologic contacts into the 2-D mesh. The mesh coordinate system was set with reference to the center of the drift (Table 6.5-1). The gridblock size was kept sufficiently fine to provide enough resolution at key model locations (such as at the vicinity of drift and geologic contacts), but as coarse as possible to provide the computing efficiency needed for reasonable simulation times. The area extending approximately 50 m above the drift is more finely gridded than other areas to capture THC effects potentially affecting seepage into the drift. Outside the drift, the smallest grid spacing was specified at the drift wall (20 cm) and increased outward. Because of its minor relevance to this modeling effort, the geology below the tsw38 model layer was simplified compared to the original USW SD-9 data, thus allowing for coarser gridding in this area. The mesh has a total of 2,510 gridblocks, including those representing matrix, fracture, and in-drift design elements.

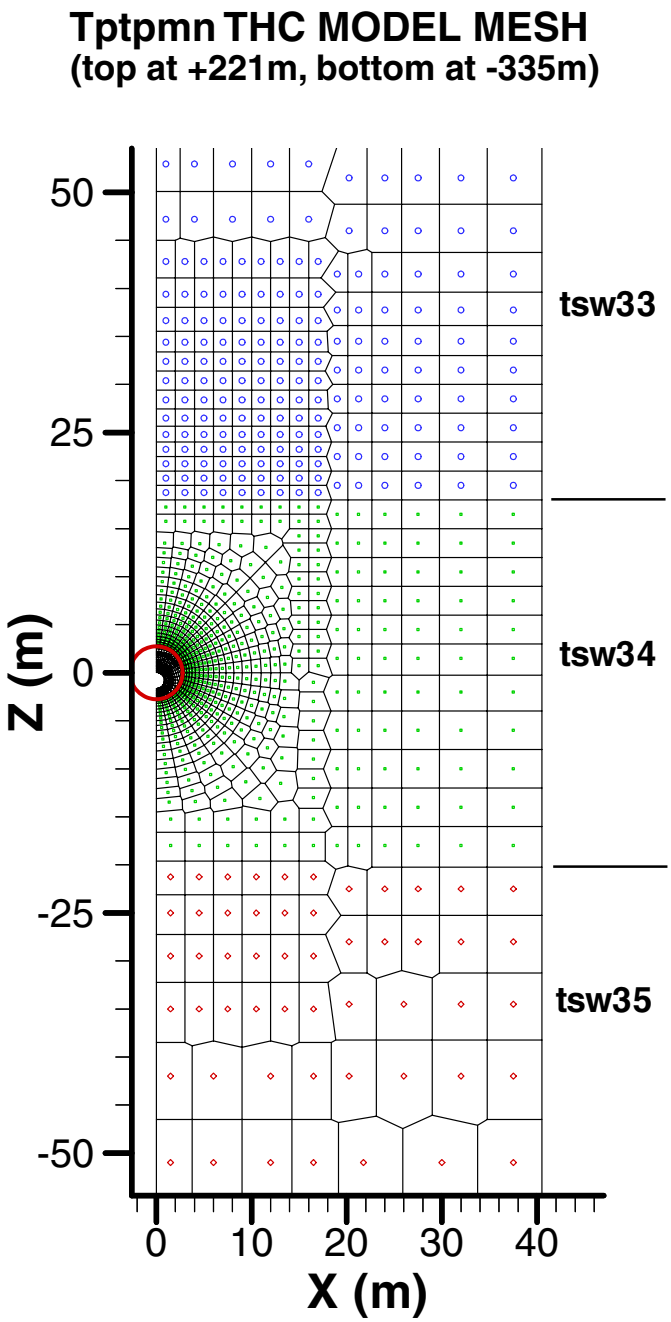

DTN: LB991200DSTTHC.002 [142162]

NOTE: Grid detail around (0, 0) is shown in Figure 6.5-2.

Figure 6.5-1. Tptpmn THC Model Mesh with Hydrogeologic Units Shown in the Vicinity of the Drift: Topopah Spring Tuff Upper Lithophysal (tsw33-circles), Middle Nonlithophysal (tsw34-dots), and Lower Lithophysal (tsw35-diamonds) Units

Table 6.5-1. Vertical Mesh Dimensions and Geologic Contacts in the Tptpmn THC Model

Model Layer	USW SD-9 Top of Layer Elevation (m)	Mesh Top of Layer Z Coordinate (m)
Top	1286.0	220.7
tcw13	1285.4	220.1
ptn21	1279.6	214.2
ptn22	1275.0	209.7
ptn23	1269.1	203.7
ptn24	1264.5	199.2
ptn25	1255.5	190.1
ptn26	1233.8	168.4
tsw31	1221.0	155.7
tsw32	1219.0	153.7
tsw33	1165.7	100.4
tsw34	1080.4	18.0*
Drift center	1065.3	0.0
tsw35	1045.1	-20.2
tsw36	942.6	-122.7
tsw37	906.9	-158.4
tsw38	889.1	-176.3
ch2z	868.4	-197.0
Bottom	730.0	-335.3

DTN: LB990501233129.004 [111475]

NOTE: * Contact raised, compared to USW SD-9 data, to provide for better lateral continuity between the fine mesh above the drift and coarser mesh laterally away from the drift (See Figure 6.5-1).

The drift was discretized to include the design elements and dimensions shown on Figure 4.1-1 (338 gridblocks total) (Figure 6.5-2). The drip shield is not explicitly modeled (Section 4.1.7). The gridblock size inside the drift was chosen small enough to provide a realistic drift model (compare Figure 6.5-2 to Figure 4.1-1). Two in-drift configurations are considered in this model:

- Preclosure configuration (during the first 50 years): waste package, upper invert, lower invert, and the open space between the waste package and the drift wall

- Postclosure configuration (after 50 years): waste package, upper invert, lower invert, drip shield, and two open zones: the inner zone, between the waste package and the drip shield; and the outer zone, between the drip shield and drift wall.

The discretization of the drift was kept the same for the two configurations. As such, the preclosure period was simulated by assigning identical open-space properties to gridblocks representing the inner zone and outer zone.

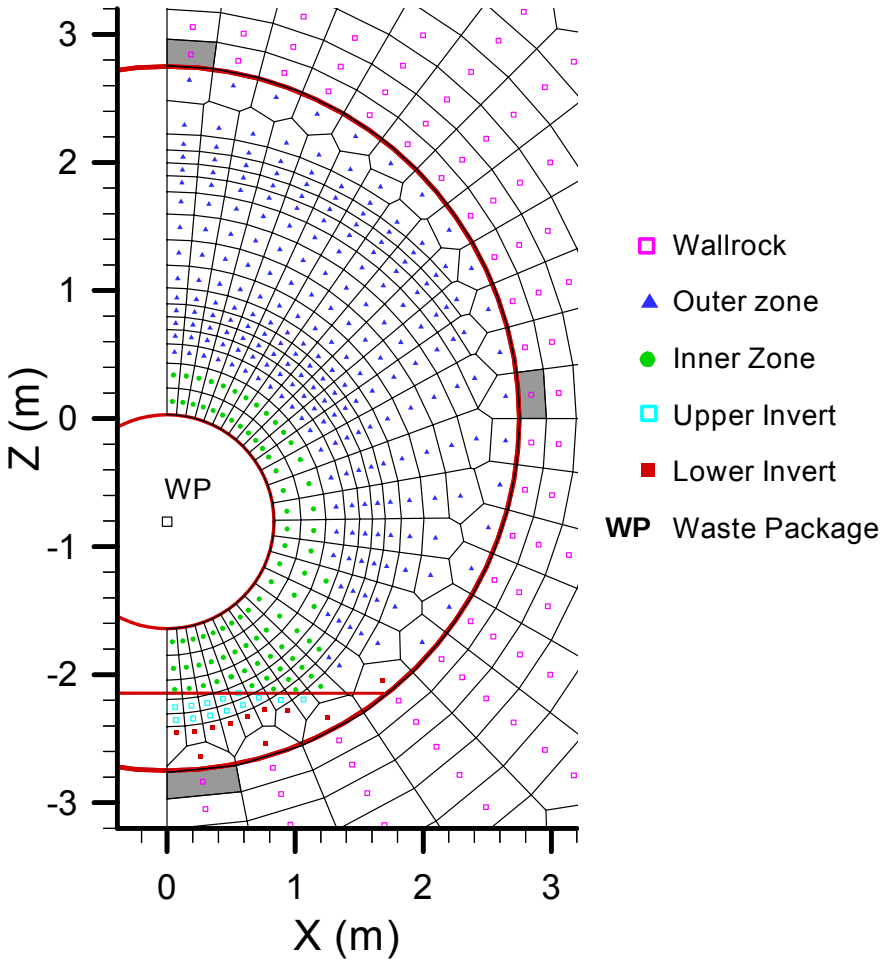

DTN: LB0011DSTTHCR1.001 [154759]

NOTE: Shaded gridblocks are those with top, side, base designations in other figures.

Figure 6.5-2. Discretization of the Repository Drift—Tptpmn THC Model

6.5.2 Boundary Conditions

The following boundary conditions were imposed on the Tptpmn THC Model (Table 6.5-2):

- Top boundary: stepwise changing infiltration rate (Table 6.5-3), temperature, pressure, and gas saturation (representing open atmosphere); constant CO_2 partial pressure and composition of infiltrating water
- Bottom boundary: constant temperature, pressure, and liquid saturation (representing the water table). Constant water composition and CO_2 partial pressure at equilibrium
- Side boundaries: no heat, fluid, and chemical fluxes
- Waste package: variable heat load with time, including effect of 70% heat removal by ventilation for first 50 years (preclosure).

One mean infiltration regime was modeled, simulating future climatic conditions including present day, monsoon, and glacial-transition periods (Table 6.5-3).

Table 6.5-2. Tptpmn THC Model REV01 Boundary Conditions

Boundary	Boundary Condition	Reference
Top	T = 17.68°C	Table 4.1-1
	S_g = 0.99	Table 4.1-1
	P = 86339 Pa	Table 4.1-1
	Time-varying infiltration rate (mean infiltration regime only)	Table 6.5-3
	Constant composition of infiltration and PCO_2	Table 6.2-1
Bottom	T = 31.68°C	Table 4.1-1
	S_L = 0.99999	Table 4.1-1
	P = 92000 Pa	Table 4.1-1
	Constant water composition and PCO_2	Table 6.2-1
Sides	No flux for water, gas, heat, and chemical species	Not Applicable
Drift Wall	No flux for water, gas and chemical species (except for CO_2 diffusive flux); conduction only for heat (zero permeability in drift gridblocks)	Not Applicable
Waste Package	Initial full heat load of 1.45 kW/m decreasing with time (due to radioactive decay), and reduced by 70% during the first 50 years (due to heat removal by ventilation)	Attachment VII and Table 6.4-2

NOTES: T = Temperature
S_g = Gas saturation
S_L = Liquid saturation
P = Pressure

Table 6.5-3. Tptpmn THC Model Infiltration Rates and Corresponding Rock-Property Sets

Case	Infiltration Rate (mm/yr)	Time Period (years)	Calibrated Properties Set	Reference
Mean Infiltration	6	0 to 600 (present day)	Present Day Mean	Table 4.1-1
	16	600 to 2000 (monsoon)		
	25	2000 to 100,000 (glacial transition)		

6.5.3 Input Data and Modeling Procedure

Simulations for the Tptpmn THC Model were run using TOUGHREACT V2.3 (LBNL 2001 [153101]), the thermodynamic data shown in Attachment V, and kinetic data in Table 6.4-3. Input water and gas compositions are shown in Table 6.2-1. Initial mineralogy and mineral surface areas are given in Attachments I and III, respectively. This model was run using the base-case and extended-case sets of chemical components and mineral assemblages described in Section 6.2.2.2. Rock hydraulic properties calibrated for a mean infiltration case were used (Table 6.4-1).

To provide initial thermal and hydrological conditions, a simulation was performed without reactive transport, heat load, or a drift (i.e., with rock at the location of the drift) until steady-state thermal and hydrological conditions were achieved. A steady state was considered to have been met under at least one of the following conditions:

1. Liquid saturations, temperatures, and pressures remained constant within the model over a time span of at least 100,000 years.

2. The total liquid and gas inflow at the top of the model matched the total liquid and gas outflow at the base of the model within 0.01 percent.

THC simulations were then run with the drift in place and heat transfer from the waste package, using the steady-state temperatures, pressures, and liquid saturations as initial conditions. Open spaces within the drift were set to zero liquid saturation and permeability.

“Ambient” reactive-transport simulations with the drift in place but without heating (i.e., no heat release from the waste package) were also performed for comparison of chemical trends to simulations under thermal loading. These simulations of ambient conditions were run using the same mean infiltration regime as the simulations of thermal loading (Table 6.5-3).

As discussed in Section 4.1.7, THC simulations were run for an initial period of 50 years, using the preclosure drift configuration and thermal properties. The simulations were then restarted using the postclosure drift configuration and properties from 50 years to a total simulation time of 100,000 years. At times corresponding to changes in infiltration rates (at 600 and 2,000 years, Table 6.5-3), the simulations were stopped and then restarted with the new infiltration rate (thus resulting in a stepwise change in infiltration).

Maximum time steps of 1, 2, 5, and 10 years were used for the time periods spanning 50–600, 600–2,000, 2,000–20,000, and 20,000-100,000 years, respectively. The runs were restarted for each of these time periods to accommodate for the change in maximum time step and/or infiltration rate.

In this model, calcite was set to remain locally at equilibrium because calcite reaction rates reported in the literature (Table 6.4-3) are quite rapid. Very similar results in simulations of the DST are obtained when using local equilibrium for calcite and assuming a kinetically controlled reaction rate (Section 7.1). Using equilibrium has the advantage of allowing simulations with larger time steps than would be required with a kinetically controlled fast calcite reaction rate.

Using pH and calcium concentrations measured in pore-water samples (Table 6.2-1), together with independently measured CO_2 partial pressures in ambient pore-gas samples (see data sources in Table 7-1), calcite is calculated to supersaturate in pore waters by approximately 1 log(Q/K) unit at 25°C. The reason for this supersaturation has not been determined and could be the result of various factors, including (but not limited to) analytical errors, kinetic inhibition caused by organic or other compounds in solution, or effects caused by high capillary pressure or pressures developed during the ultra-centrifuge water-extraction process. To reconcile measured pH, calcium, and CO_2 concentrations, calcite was allowed to remain supersaturated by approximately 1 log(Q/K) unit at 25°C. This "precipitation gap" was set to decrease exponentially with temperature and become negligible (one hundredth of the gap value at 25°C) at an arbitrarily selected temperature of 200°C. This approach (using a precipitation gap) can be viewed as a crude approximation of precipitation with a nucleation threshold. Note that dissolution still occurs only if log(Q/K) < 0.

A fairly stable (near steady-state) hydrochemical system was achieved using revised thermodynamic data (Attachment V) primarily for smectites and zeolites. More recent simulations of ambient conditions (no thermal pulse) using various sources of thermodynamic data are presented in Section 6.8 and provide an additional justification for using the thermodynamic data selected here. The stability of water and gas concentrations calculated for ambient conditions over long periods of time was also improved by implementing the calcite supersaturation gap as described above.

6.5.4 Model Runs

A total of five simulations were completed, as summarized in Table 6.5-4.

Table 6.5-4. Tptpmn THC Model Runs (REV01)

Infiltration-Property Set (Table 6.5-3)	Geochemical System (Section 6.2.2.2)	Simulation Type	Run ID (used in DTN: LB0011DSTTHCR1.002 [161282]; also see Attachment X)
Mean Infiltration	None	TH	th6_16_25_7
Mean Infiltration	Base Case	THC	thc6_16_25_9
	Base Case	THC - Ambient	thc6_16_25_9_amb
	Extended Case	THC	thc6_16_25_10
	Extended Case	THC - Ambient	thc6_16_25_10_amb

NOTES: TH: Thermal-hydrological
THC: Thermal-hydrological-chemical

6.5.5 Simulation Results

Simulation results are presented below in Figures 6.5-3 through 6.5-18, and focus on areas in the vicinity of the drift. THC effects in other geologic horizons, even though considered in the simulations, are not discussed in this Model Report because they are not directly relevant to the primary purpose of evaluating THC effects at the drift scale. Much of the data (temperatures, liquid saturations, water compositions, CO_2 concentrations, and liquid/gas fluxes) are examined as a function of time at three locations around the modeled drift. These are the crown, the side (approximately 20 cm above the springline) and the base (model gridblocks F257, F 92, and F272, respectively) at points located 10 cm to the outside of the drift wall (i.e., in the rock) (Figure 6.5-2). These data were tabulated and submitted to the technical database under DTN: LB0011DSTTHCR1.001 [154759] and are discussed below.

6.5.5.1 Thermal-Hydrological Simulation Results

For comparison to the THC simulations, a model run was performed considering only thermal and hydrological (TH) processes. This simulation was run using the mean infiltration case (Table 6.5-3) and serves as a baseline for interpreting the effects of water-gas-rock chemical interaction on the thermal and hydrological behavior of the system.

Calculated temperatures, liquid saturation, and air mass fractions around the drift are shown in Figures 6.5-3 through 6.5-6. Postclosure temperatures quickly climb above the boiling point (near 96°C at Yucca Mountain), with temperatures at the drift crown peaking to around 135°C between the times of 55 and 75 years. The highest modeled temperature in the waste package is attained during this time interval as well (the highest output value is near 155°C). Temperatures are lower at the base of the drift (approximately 10°C or less than at the crown) because of the insulating effect of the invert (Figure 6.5-3). The return to ambient temperatures after heating takes 50,000 to 100,000 years.

Around the drift, the matrix is predicted to rewet at times between 1,200 and 1,400 years (Figure 6.5-3). Rewetting of fractures occurs within the same time frame, except at the drift base where fractures do not rewet until approximately 2,000 years (Figure 6.5-3). A contour plot of temperatures and matrix saturations in the vicinity of the drift at a simulated time of 600 years

(near maximum dryout) shows the dryout zone (represented by zero matrix saturations) extending approximately 8 m above the drift, 10 m to the side of it, and 13 m below it (Figure 6.5-4). In fractures, liquid saturations (Figure 6.5-5) show strong diversion of water around the dryout zone. Air mass fractions in the gas phase at the drift wall (the complement of the steam mass fraction; Figure 6.5-6) drop to near-zero values during dryout (i.e., the gas phase is almost entirely water vapor) and is essentially identical in both matrix and fractures.

The calculated rate of vertical water influx in fractures at the drift crown (Figure 6.5-7) shows a small short-lived influx peak at the time of rewetting. However, the intensity of this peak may only reflect the time intervals at which data are output from the model. The general flux increase after 2,000 years reflects the increase in infiltration rate at that time (from 16 to 25 mm/y). For the ambient simulation, the flux increase at 600 years also reflects the infiltration rate increase at that time (from 6 to 16 mm/yr).

Note that TH results presented in this section do not exactly match results presented in BSC (2003 [161530], Section 6.2.2) for a similar TH model. This is because simulations presented in this section were run with an older set (REV01) of rock properties (see Table 6.4-1) than in BSC (2003 [161530], Section 6.2.2.

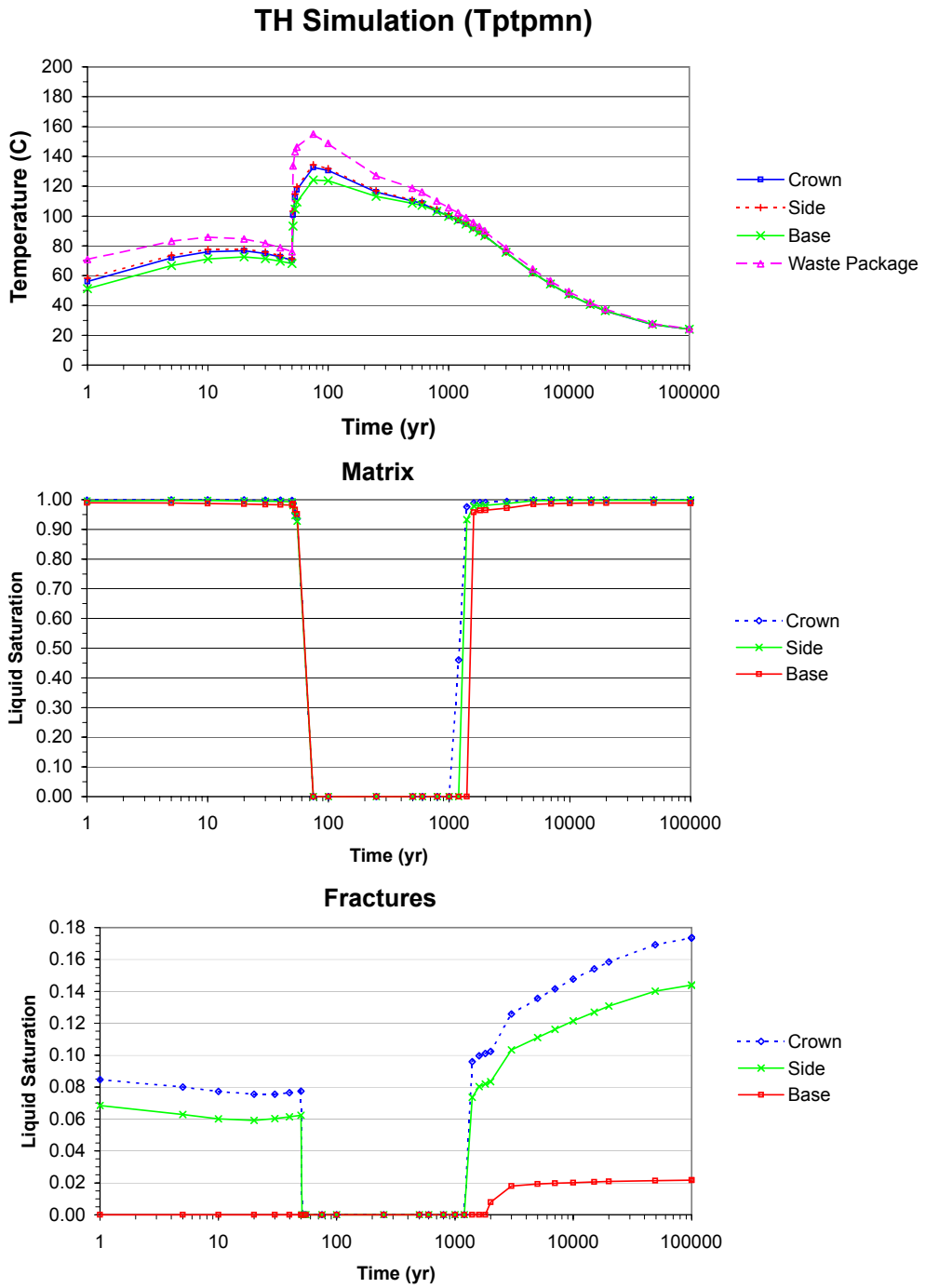

DTN: LB0011DSTTHCR1.001 [154759]

Figure 6.5-3. TH Simulation (Tptpmn Model): Time Profiles of Modeled Temperatures and Liquid Saturations in Fractures and Matrix at Three Drift-Wall Locations and in the Waste Package

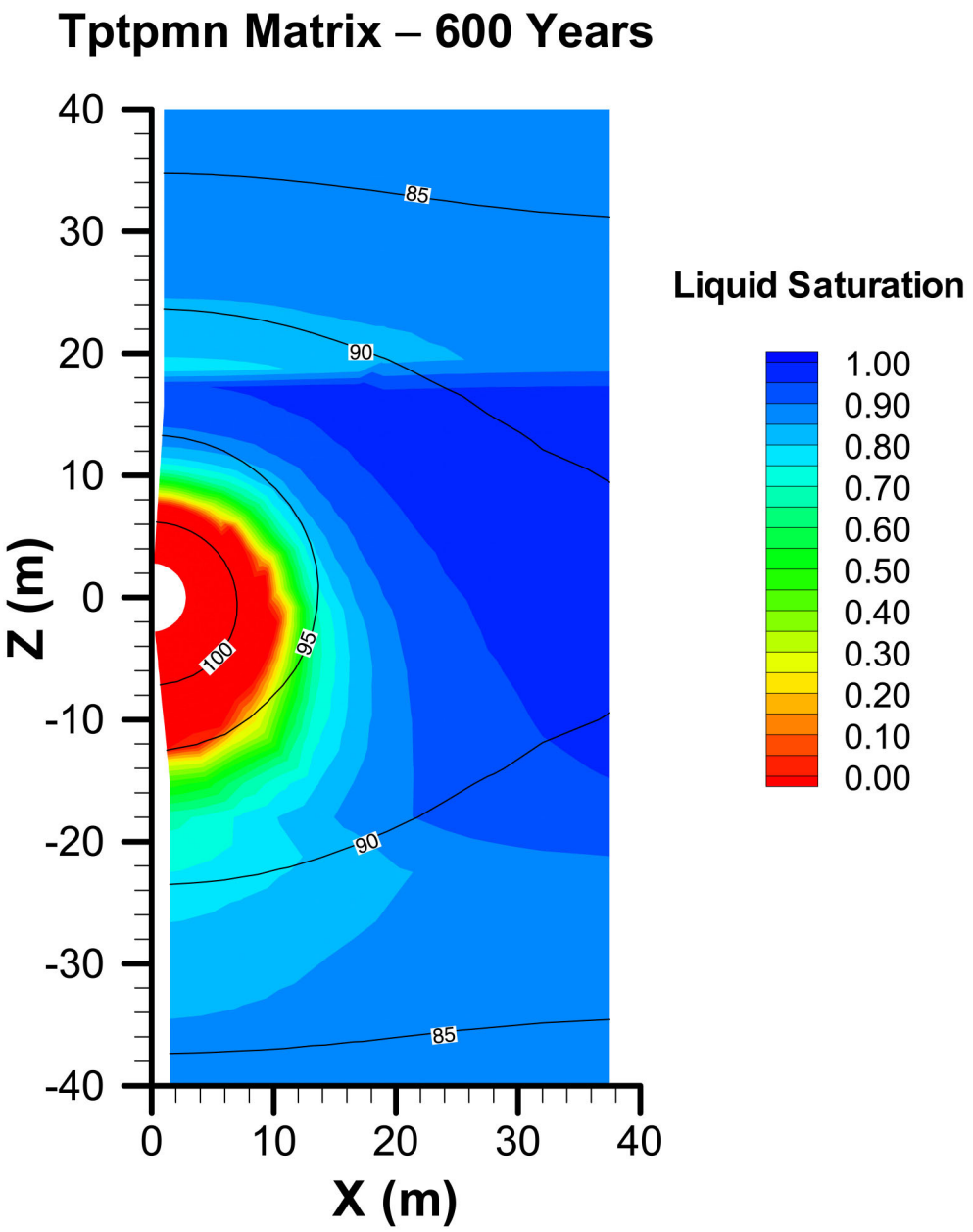

DTN: LB0011DSTTHCR1.002 [161282]

Figure 6.5-4. TH Simulation (Tptpmn Model): Contour Plot of Modeled Temperatures (°C) and Liquid Saturations in the Matrix at 600 Years (Near Maximum Dryout—Mean Infiltration)

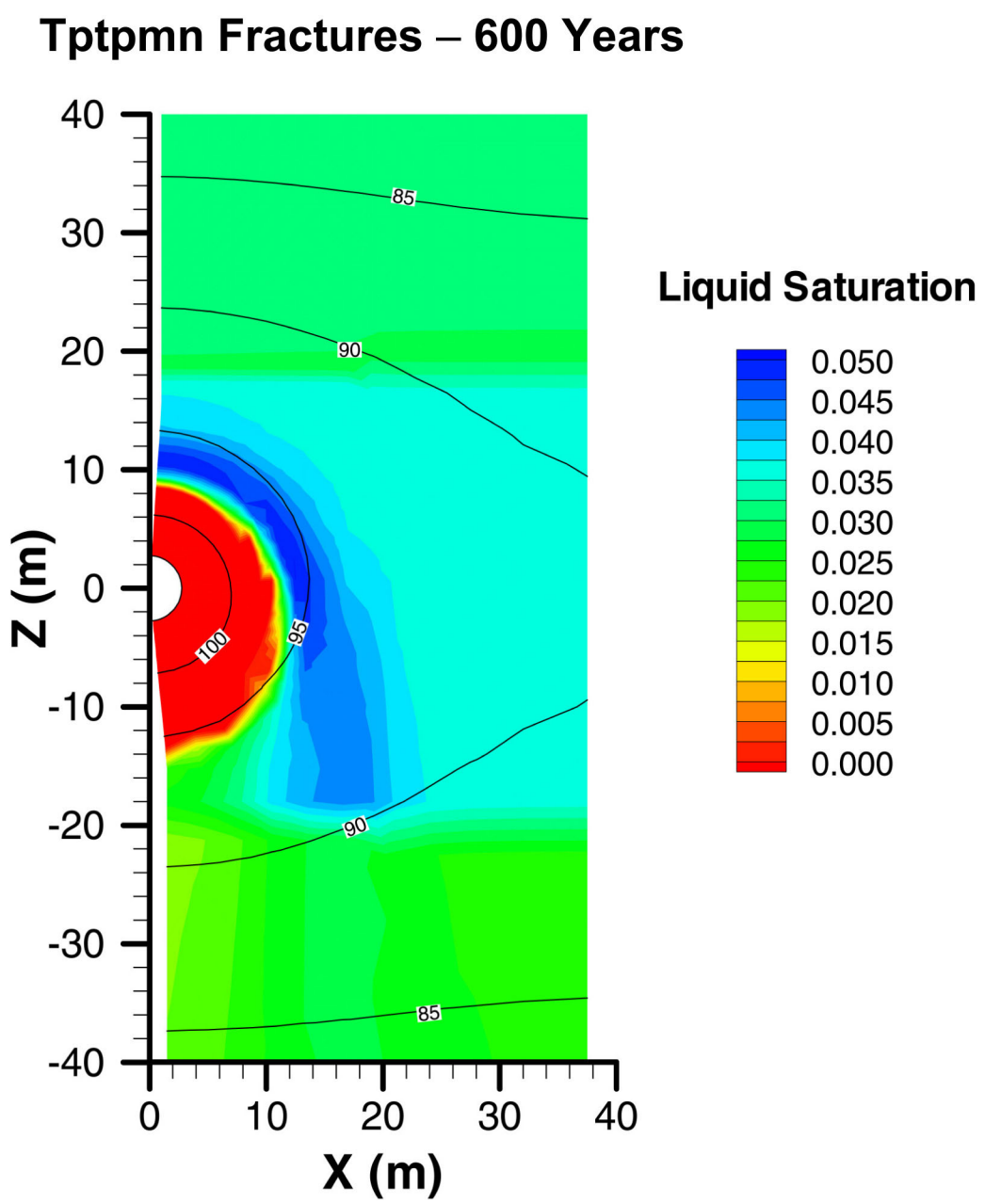

DTN: LB0011DSTTHCR1.002 [161282]

Figure 6.5-5. TH Simulation (Tptpmn Model): Contour Plot of Modeled Temperatures (°C) and Liquid Saturations in Fractures at 600 Years (near Maximum Dryout—Mean Infiltration)

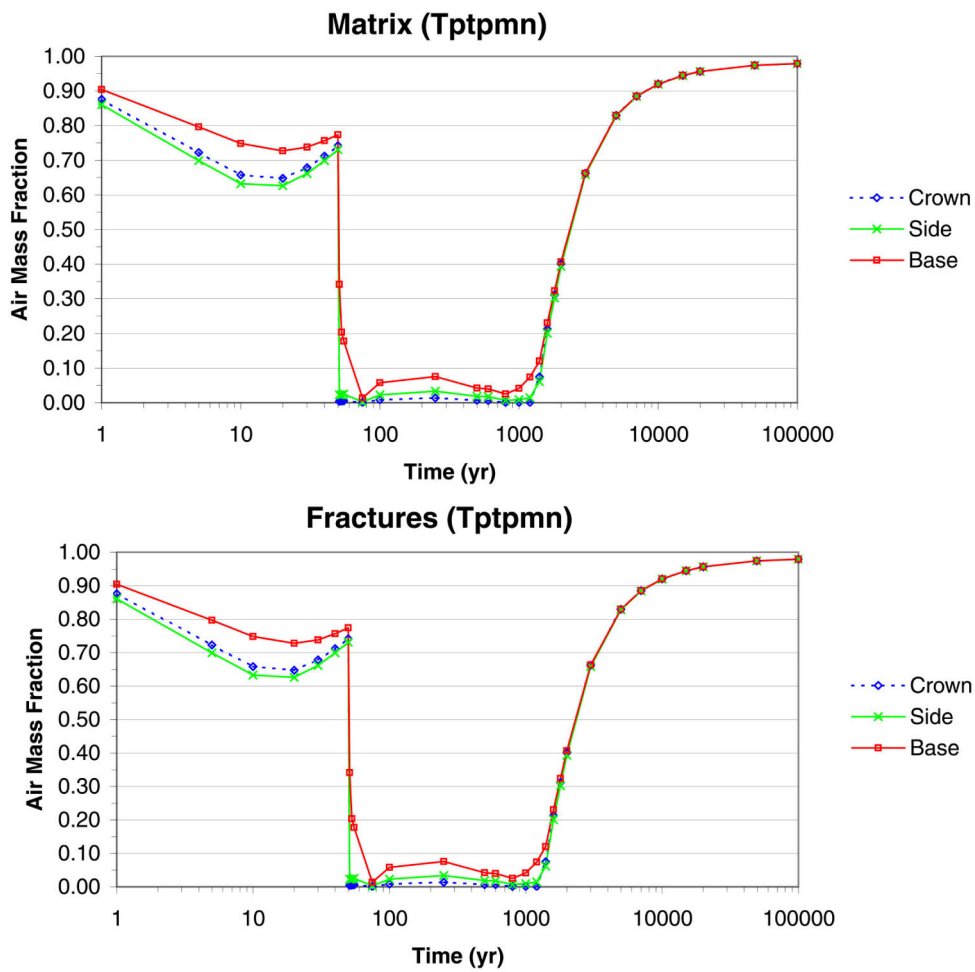

DTN: LB0011DSTTHCR1.001 [154759]

Figure 6.5-6. TH Simulation (Tptpmn Model): Time Profiles of Modeled Air Mass Fractions in the Gas Phase in Fractures and Matrix at Three Drift-Wall Locations

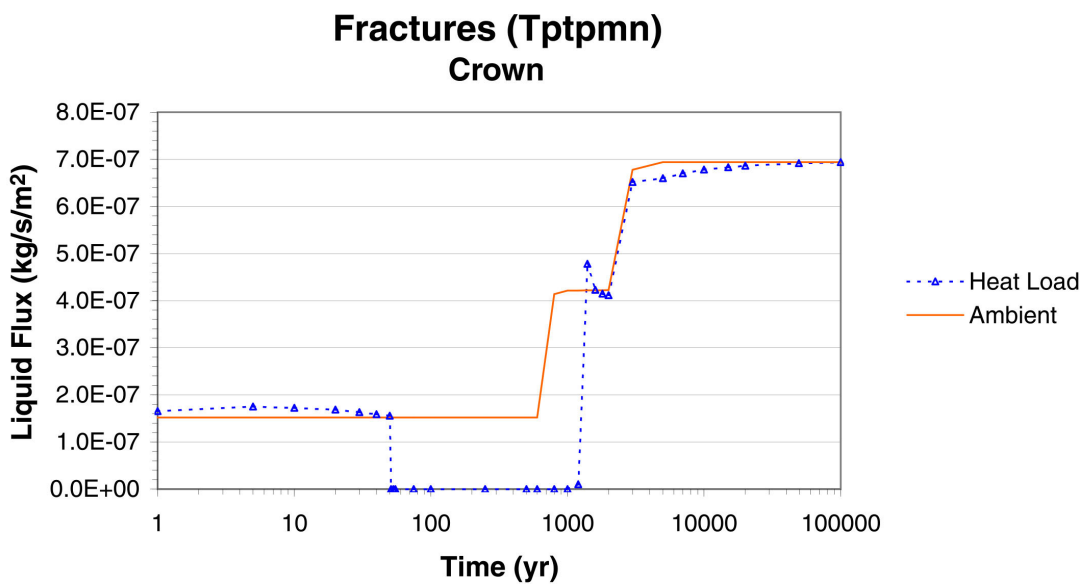

DTN: LB0011DSTTHCR1.001 [154759]

Figure 6.5-7. TH Simulation (Tptpmn Model: Time Profiles of Modeled Water Flux at the Drift Crown (positive downward)

6.5.5.2 THC Simulation Results

Time profiles of predicted CO_2 and various aqueous species concentrations in fractures are shown in Figures 6.5-8 to 6.5-15. These figures combine the results of ambient and heat-load calculations for both base-case (no aluminum silicates) and extended-case geochemical systems (Section 6.2.2.2).

The results of simulations under ambient conditions are presented to provide a baseline by which comparisons can be made with simulations of thermal loading. Obtaining an initial "steady-state" hydrochemical system yielding aqueous species concentrations consistent with measured concentrations in pore water is difficult. This is because the stability of the system depends on reaction rates and relative mineral thermodynamic stability, as well as infiltration rates and rock properties. The difficulty in reaching a chemical steady state increases with the number of reactive minerals included in the system, because each additional mineral adds its own uncertainty in reaction rate to the total model uncertainty. A reasonably "steady" ambient hydrochemical state was achieved here by reducing the stability of smectites and zeolites (Attachment V), and allowing some degree of calcite supersaturation (Section 6.5.3) in pore waters. In earlier simulations with unrevised thermodynamic data (DTN: LB991200DSTTHC.002 [142162]), smectites and zeolites were too stable and formed in unreasonable amounts. This yielded an unrealistic predicted pH increase, calcium depletion, and an increase in sodium in the pore waters under ambient conditions. Similar unrealistic trends predicted with new simulations using unrevised thermodynamic data for clays and zeolites are discussed in Section 6.8.5.1. These trends are governed by feldspar and glass hydrolysis reactions such as those discussed below.

The use of alternative geochemical systems is useful in assessing the sensitivity of the model to inclusion of aluminum silicate minerals. Extended-case simulations are quite sensitive to the

effective reaction rates of aluminum silicates, particularly clays and calcium zeolites. For example, the dissolution of albite (a sodium feldspar) to form sodium smectite (a clay) results in an increase in pH (decrease in H^+ activity), as follows:

$$2.33NaAlSi_3O_8 \text{ (albite)} + 2H^+ \Longrightarrow$$

$$Na_{0.33}Al_{2.33}Si_{3.67}O_{10}(OH)_2 \text{ (smectite)} + 3.32SiO_2 + 2Na^+ \qquad \text{(Eq. 6.5-1)}$$

The alteration of albite to stellerite (a calcium zeolite) can also drive pH to higher values if the calcium necessary to form stellerite originates from calcite dissolution, as in the following reaction:

$$2NaAlSi_3O_8 \text{ (albite)} + SiO_2 + CaCO_3 \text{ (calcite)} + H^+ + 7H_2O \Longrightarrow$$

$$CaAl_2Si_7O_{18} \bullet 7H_2O \text{ (stellerite)} + 2Na^+ + HCO_3^- \qquad \text{(Eq. 6.5-2)}$$

In addition, the consumption of calcium to form calcium zeolites or clays inhibits calcite precipitation as a means of controlling the increase of pH and total aqueous carbonate concentrations. As a result of such reactions, simulations with the extended geochemical system generally yield higher pH and total aqueous carbonate concentrations, and generally lower CO_2 partial pressures than with the base-case system. Also, because of these reactions, predicted calcium concentrations under ambient conditions tend to decrease with time, while the sodium concentrations increase—trends that are not observed with base-case simulations.

The predicted trend of CO_2 concentrations with time in fracture gas (Figure 6.5-8) generally shows a large decline during dryout, followed by a steep increase during the initial cooling and rewetting stage. The decrease during dryout is the direct result of displacement by steam upon boiling. The increase after dryout remains below 10,000 ppmv for both the base case and the extended case, and concentrations are predicted to return to ambient values after 20,000 to 50,000 years.

The predicted pH of fracture water around the drift (Figures 6.5-9) is higher in the extended case (approximate range 7.7 to 8.4) than in the base case (approximate range 7.4 to 7.8). Total aqueous carbonate concentrations (as HCO_3^-) (Figure 6.5-10) are similar in the base and extended cases, showing a typical decrease at the drift wall during the thermal pulse due to temperature-driven decarbonation. During preclosure, pH and carbonate concentrations drop quickly to values near pH 7.8 and 80 mg/L, respectively, as a result of calcite precipitation accompanying increasing temperature.

Calcium concentrations (Figure 6.5-11) are predicted to be generally lower in the extended case than the base case, resulting from increased calcite precipitation (caused by higher pH) and precipitation of calcium zeolites and clays as in reactions discussed earlier. Predicted ambient sodium concentrations (Figure 6.5-12) approximately double over the 100,000-year simulated time period, which could reflect somewhat higher feldspar and/or glass dissolution rates relative to the precipitation rate of clay minerals. Relatively elevated calcium and sodium concentrations during rewetting at the drift wall at the base of the drift are the result of remobilization of water containing dissolved salts previously concentrated by evaporation at the time of dryout. Note that in these REV01 simulations, the formation of residual salts upon complete dryout and their

redissolution upon rewetting is not modeled. The water, however, is concentrated up to a limit ionic strength of 4 upon drying, then is saved for reintroduction into the system at the time of rewetting—see Section 6.4.6.1.

Upon heating, aqueous silica concentrations (Figure 6.5-13) rise significantly above ambient values because of the dissolution of silica phases at higher temperatures. Simulations with the extended geochemical system yield higher aqueous silica concentrations because of the dissolution of aluminosilicate minerals. These minerals are not included in base-case simulations (mostly cristobalite dissolves in the base-case simulations). Upon boiling to dryness, aqueous silica concentrations may significantly exceed the solubility of amorphous silica (near 370 mg/L at 100°C) because the precipitation rate of this mineral, even though quite fast, does not keep up with boiling rates. During the initial cooling stage, primarily the 600- to 2,000-year time interval, aqueous silica around the drift precipitates as amorphous silica and, as will be discussed later, accounts for most of the reduction in porosity around the drift during this time. With the base-case geochemical system, ambient aqueous silica concentrations remain fairly constant and well below the solubility of amorphous silica (approximately 120 mg/L at 25°C), increasing slightly with increasing infiltration rates, thus reflecting a kinetic control on the dissolution of silica phases. With the extended case, modeled ambient aqueous silica concentrations increase to values at or near amorphous silica solubility (higher than measured pore water concentrations), which seems to indicate that the dissolution rate of feldspar and or glass may be somewhat overestimated relative to the precipitation rate of clays.

Chloride concentrations in fracture water computed for both the base case and the extended case (Figure 6.5-14) are essentially identical because of the conservative behavior of this aqueous species (i.e., it is not affected by pH or the reaction rates of other minerals in the simulation). The profiles also show, at the time of rewetting, the effect of remobilization of concentrated solutions that was mentioned earlier. After rewetting, chloride concentrations drop relatively quickly towards ambient values near 110 mg/L.

Upon rewetting, fluoride concentrations in fracture water (Figure 6.5-15) quickly drop towards ambient values of less than 1 mg/L. In this chemical system, at intermediate to high pH, fluoride concentrations are not affected significantly by pH. Therefore, there are not many differences between base-case and extended-case simulations. It should be remembered that no fluorite (CaF_2 mineral) is present as a primary mineral here. In the Tptpll simulations presented in Sections 6.7 and 6.8, fluorite is included as a mineral in the repository host rock, causing higher fluoride concentrations to be predicted during the cooling phase.

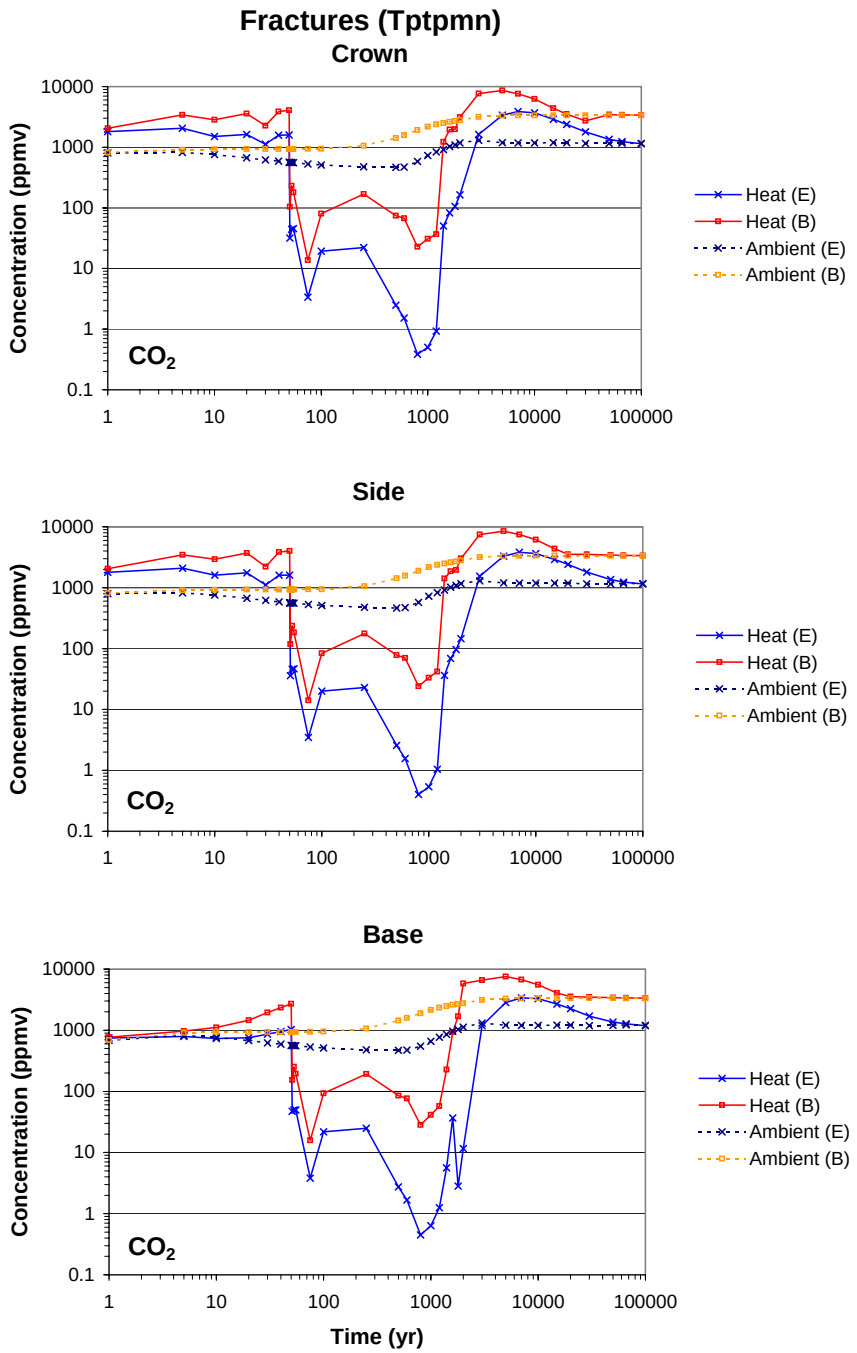

DTN: LB0011DSTTHCR1.001 [154759]

Figure 6.5-8. THC Simulation (Tptpmn Model): Time Profiles of Modeled CO_2 Concentrations in the Gas Phase in Fractures at Three Drift-Wall Locations under Heating (Heat) and Non-Heating (Ambient) Conditions for the Extended (E) and Base-Case (B) Geochemical Systems

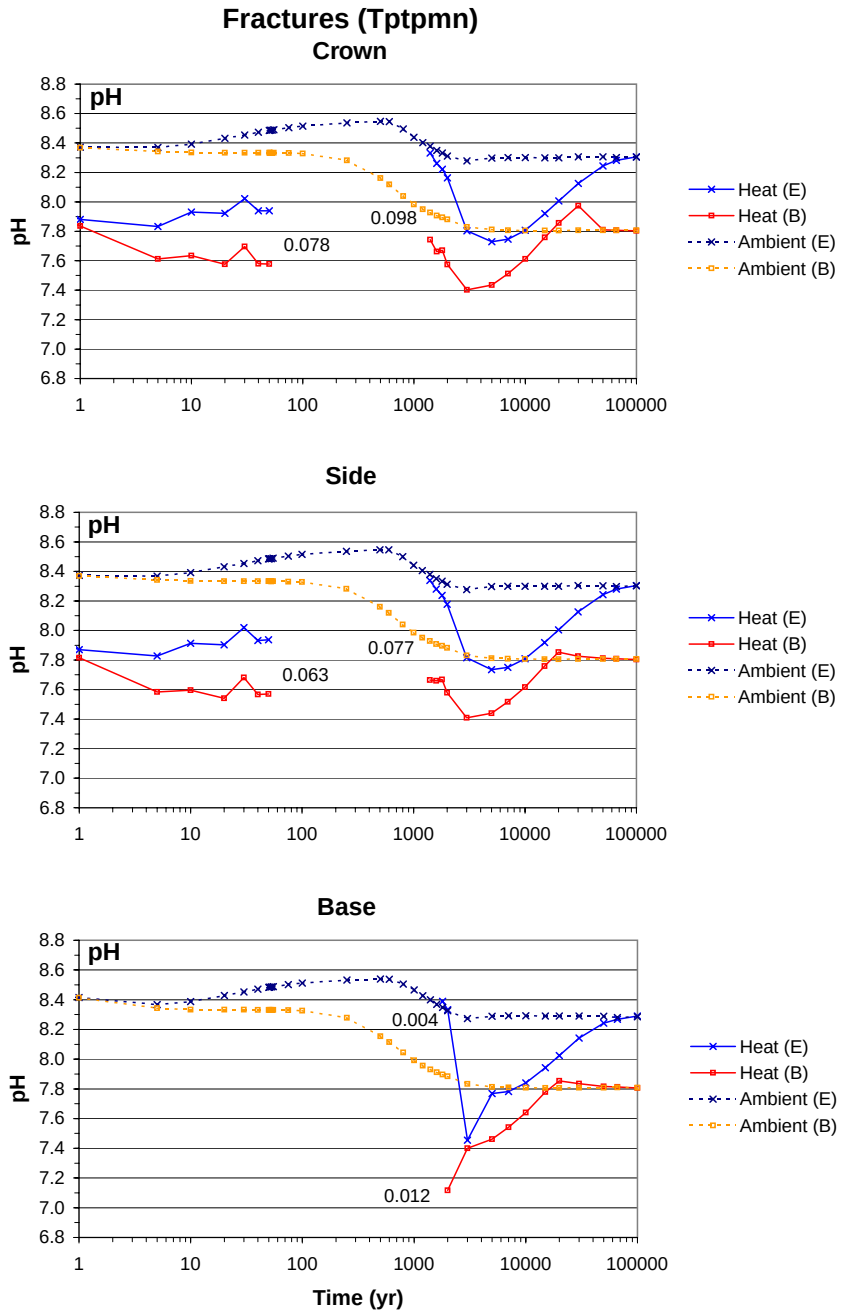

DTN: LB0011DSTTHCR1.001 [154759]

NOTE: The dryout period is left blank. Numbers by each curve indicate the last output liquid saturation before dryout and the first output liquid saturation during rewetting.

Figure 6.5-9. THC Simulation (Tptpmn Model): Time Profiles of the Modeled pH of Fracture Water at Three Drift-Wall Locations under Heating (Heat) and Non-Heating (Ambient) Conditions for the Extended (E) and Base-Case (B) Geochemical Systems

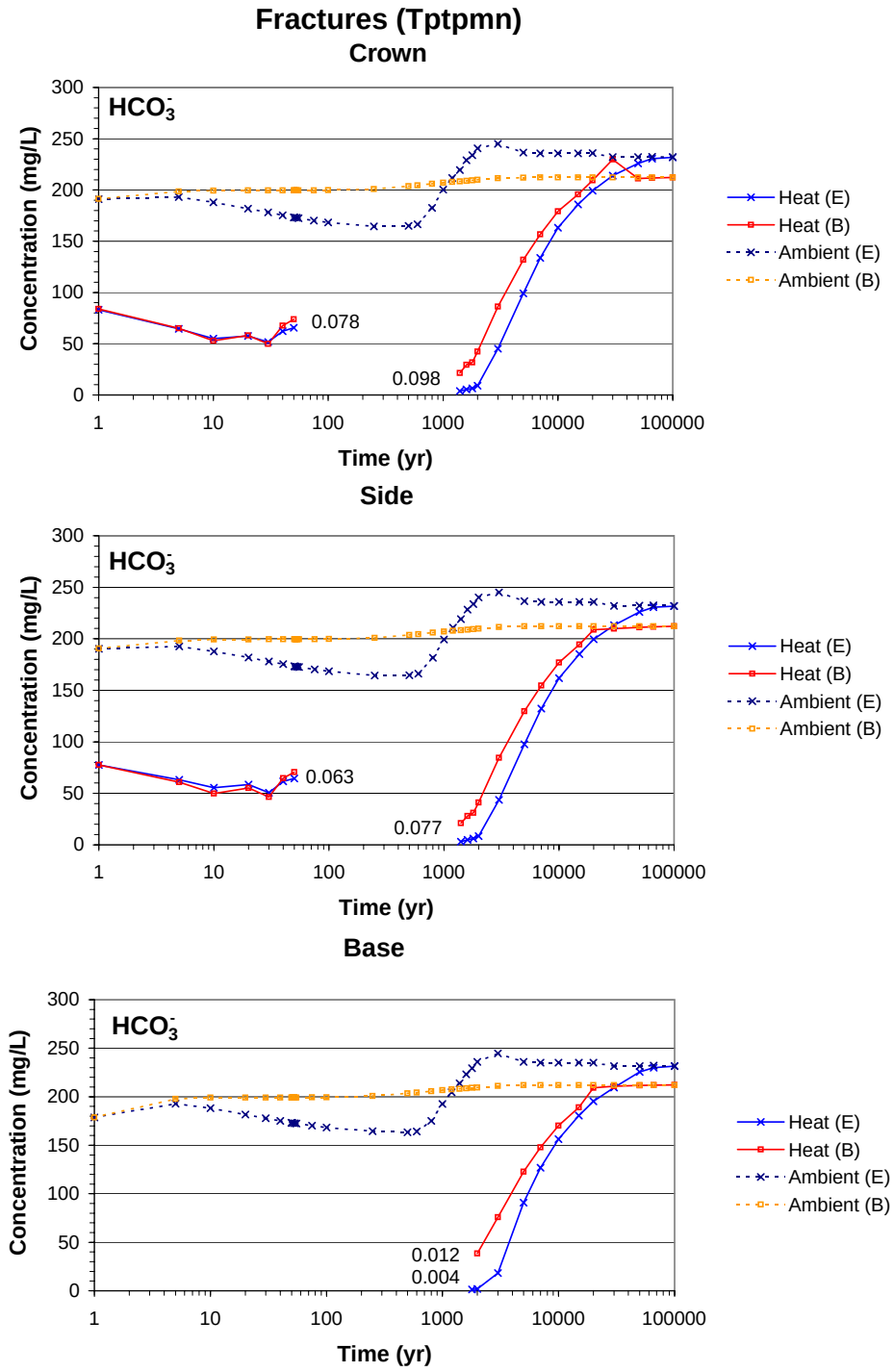

DTN: LB0011DSTTHCR1.001 [154759]

NOTE: The dryout period is left blank. Numbers by each curve indicate the last output liquid saturation before dryout and the first output liquid saturation during rewetting.

Figure 6.5-10. THC Simulation (Tptpmn Model): Time Profiles of Modeled Total Aqueous Carbonate Concentrations (as HCO_3^-) in Fracture Water at Three Drift-Wall Locations under Heating (Heat) and Non-Heating (Ambient) Conditions for Extended (E) and Base-Case (B) Geochemical Systems

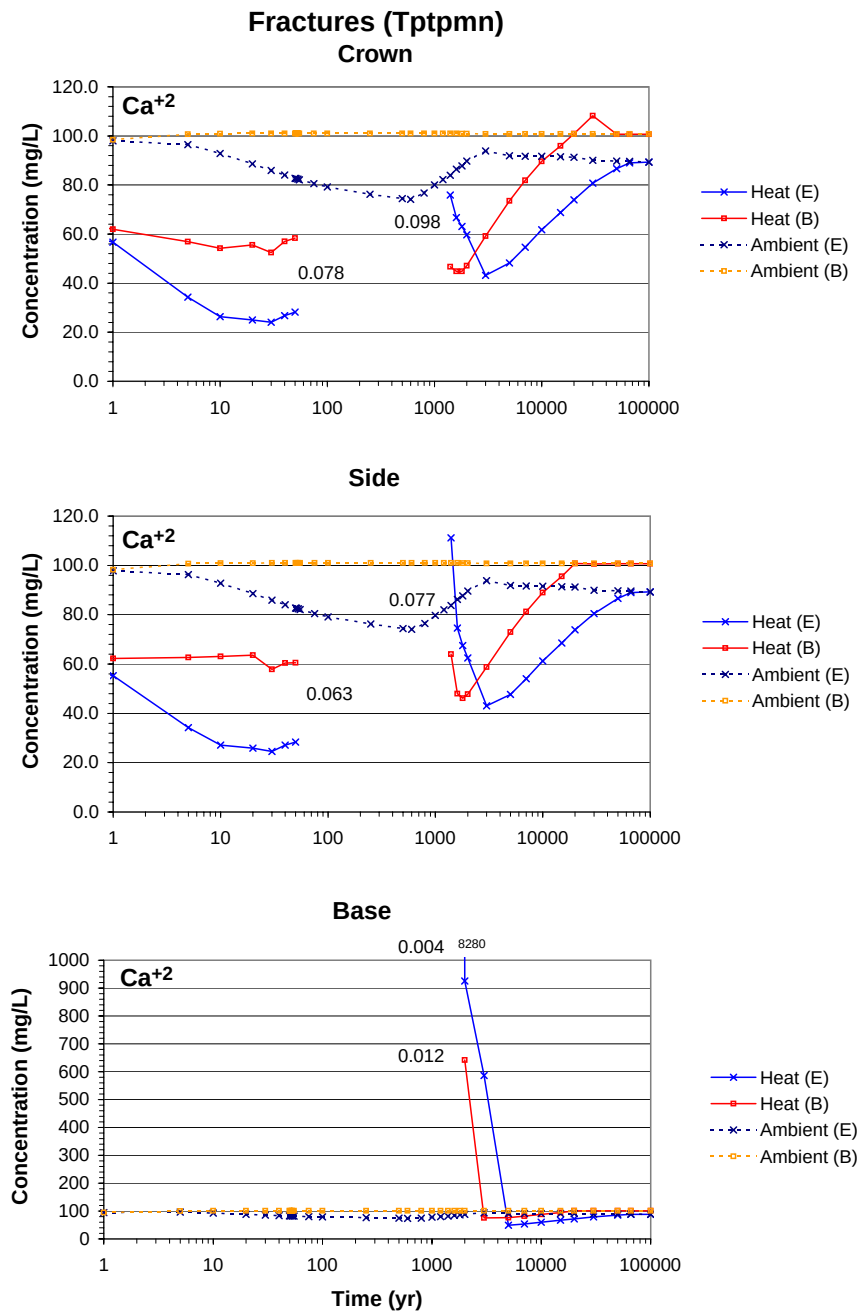

DTN: LB0011DSTTHCR1.001 [154759]

NOTE: The dryout period is left blank. Numbers by each curve indicate the last output liquid saturation before dryout and the first output liquid saturation during rewetting.

Figure 6.5-11. THC Simulation (Tptpmn Model): Time Profiles of Modeled Total Aqueous Calcium Concentrations in Fracture Water at Three Drift-Wall Locations under Heating (Heat) and Non-Heating (Ambient) Conditions for Extended (E) and Base-Case (B) Geochemical Systems

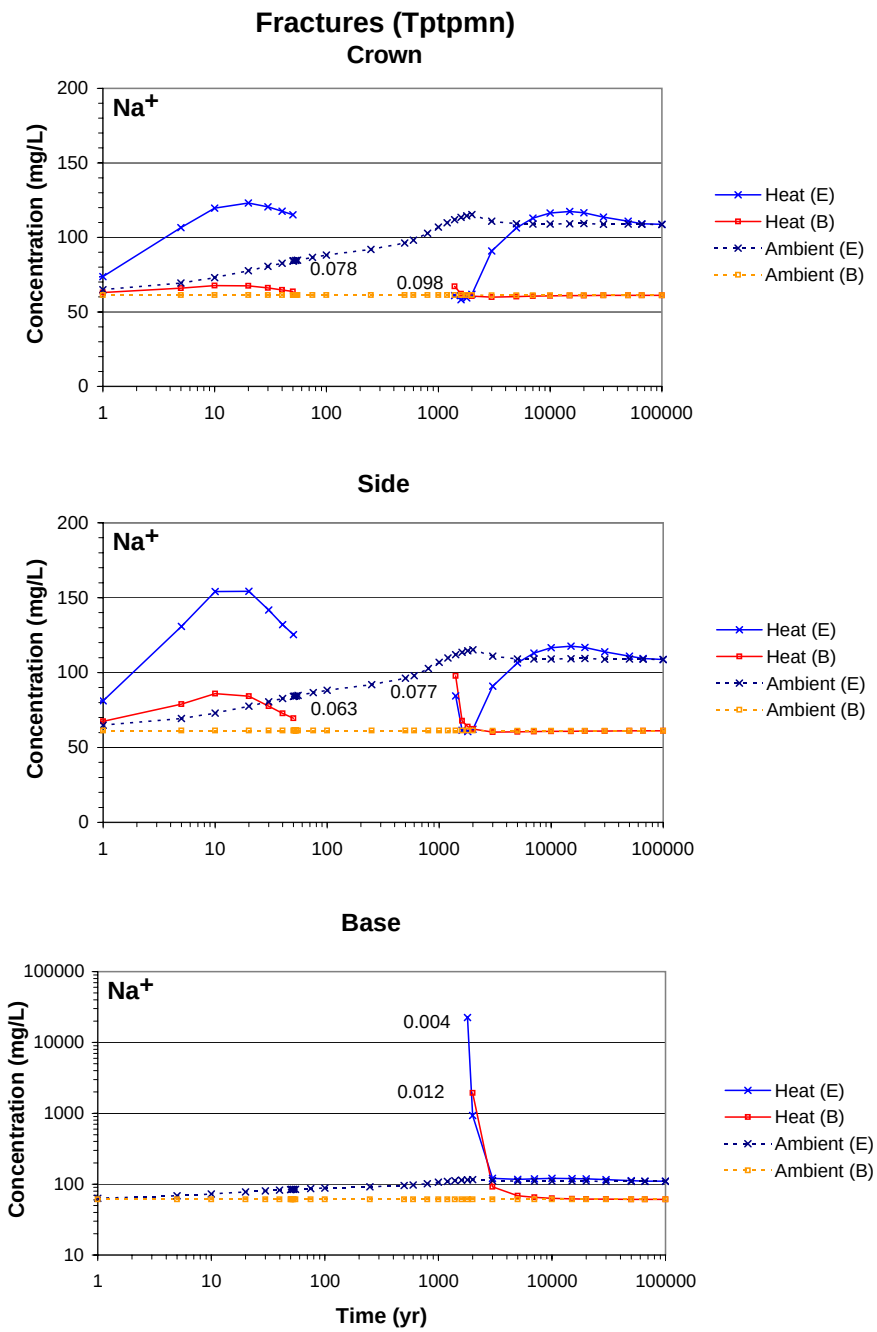

DTN: LB0011DSTTHCR1.001 [154759]

NOTE: The dryout period is left blank. Numbers by each curve indicate the last output liquid saturation before dryout and the first output liquid saturation during rewetting.

Figure 6.5-12. THC Simulation (Tptpmn Model): Time Profiles of Modeled Total Aqueous Sodium Concentrations in Fracture Water at Three Drift-Wall Locations under Heating (Heat) and Non-Heating (Ambient) Conditions for Extended (E) and Base-Case (B) Geochemical Systems

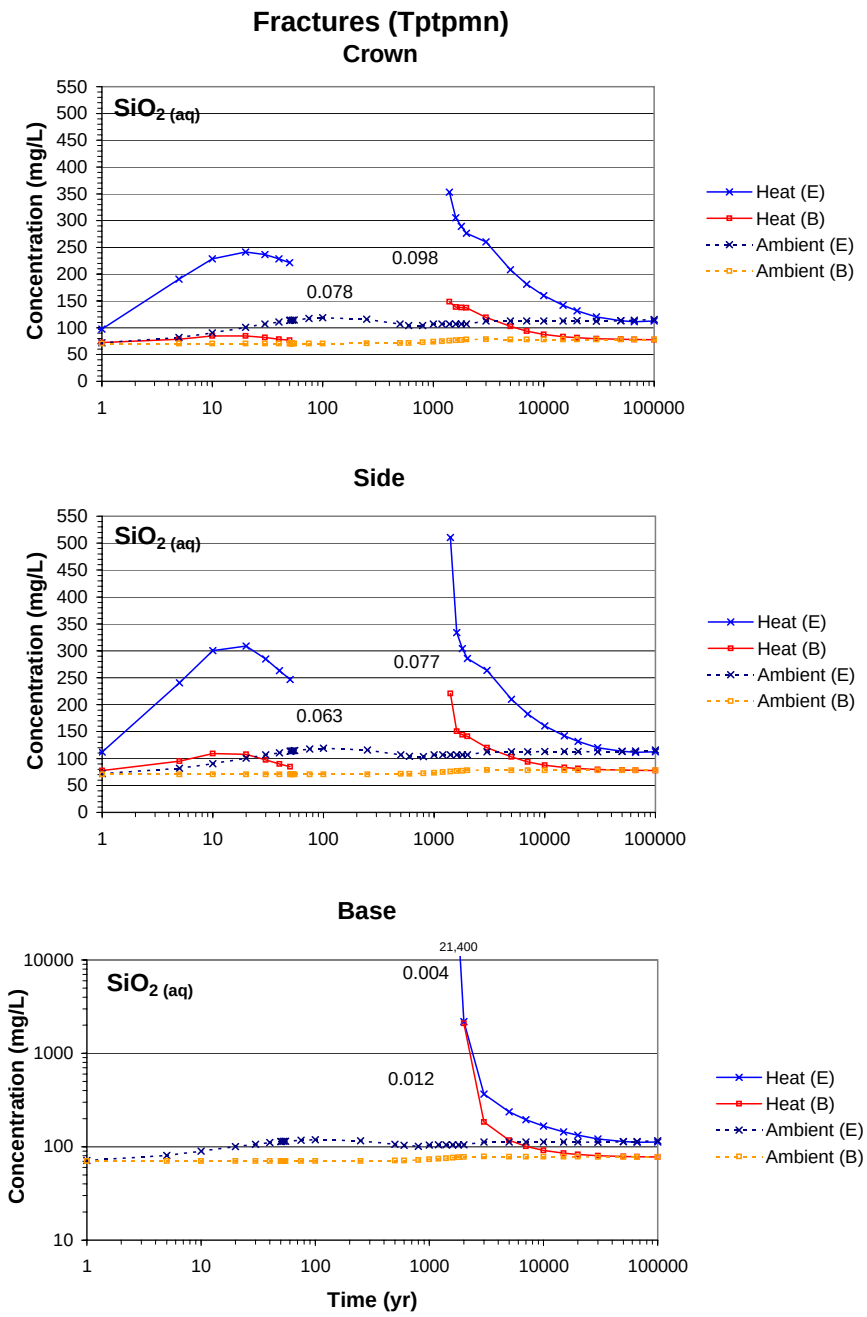

DTN: LB0011DSTTHCR1.001 [154759]

NOTE: The dryout period is left blank. Numbers by each curve indicate the last output liquid saturation before dryout and the first output liquid saturation during rewetting.

Figure 6.5-13. THC Simulation (Tptpmn Model): Time Profiles of Modeled Total Aqueous Silica Concentrations in Fracture Water at Three Drift-Wall Locations under Heating (Heat) and Non-Heating (Ambient) Conditions for Extended (E) and Base-Case (B) Geochemical Systems

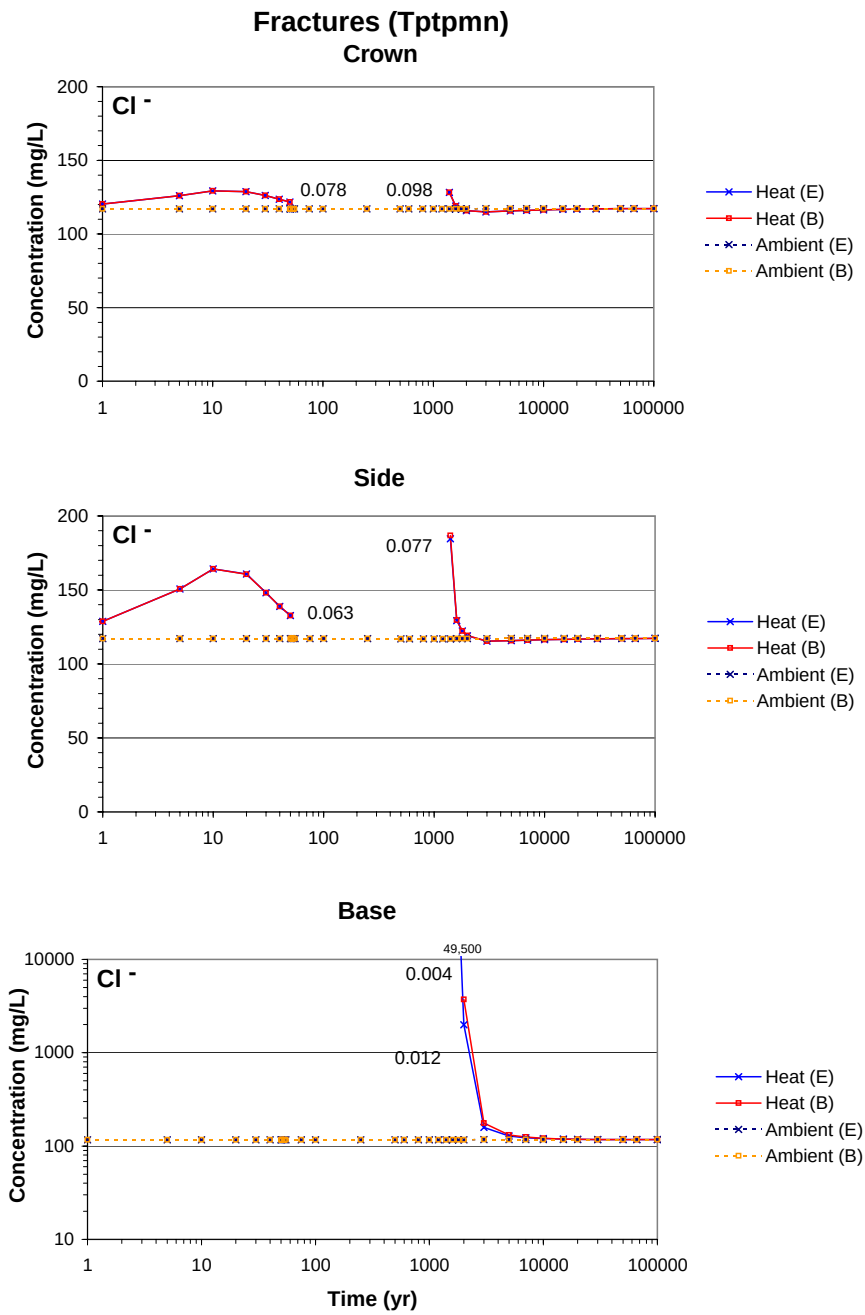

DTN: LB0011DSTTHCR1.001 [154759]

NOTE: The dryout period is left blank. Numbers by each curve indicate the last output liquid saturation before dryout and the first output liquid saturation during rewetting.

Figure 6.5-14. THC Simulation (Tptpmn Model): Time Profiles of Modeled Total Aqueous Chloride Concentrations in Fracture Water at Three Drift-Wall Locations under Heating (Heat) and Non-Heating (Ambient) Conditions for Extended (E) and Base-Case (B) Geochemical Systems

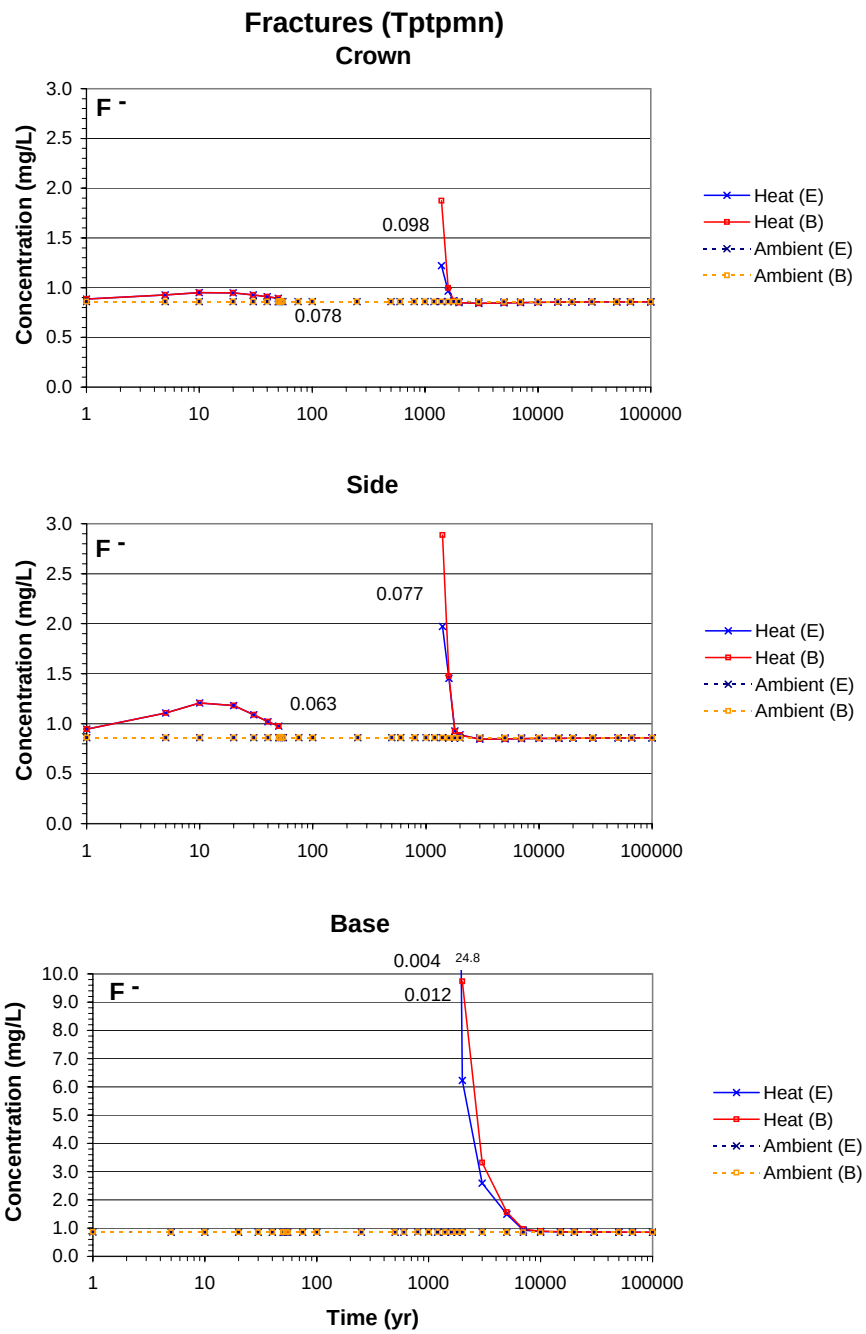

DTN: LB0011DSTTHCR1.001 [154759]

NOTE: The dryout period is left blank. Numbers by each curve indicate the last output liquid saturation before dryout and the first output liquid saturation during rewetting.

Figure 6.5-15. THC Simulation (Tptpmn Model): Time Profiles of Modeled Total Fluoride Concentrations in Fracture Water at Three Drift-Wall Locations under Heating (Heat) and Non-Heating (Ambient) Conditions for Extended (E) and Base-Case (B) Geochemical Systems

Modeled fracture porosities around the drift all decrease over time (negative). The maximum reductions occur approximately 8 to 9 m above the drift center, in a pattern approximately delineating the maximum extent of the dryout zone (Figure 6.5-16). At this location, the porosity decreases by approximately 1% after 20,000 years and 3% after 100,000 years. This reduction results primarily from the precipitation of amorphous silica and calcite. Amorphous silica precipitates mostly from 600 to 2,000 years, accounting for approximately a 0.5% porosity reduction. Amorphous silica precipitation is followed at later times by calcite precipitation as infiltration waters, replenished in aqueous carbonate and calcium, are heated as they percolate back towards the drift where temperatures remain above ambient values for several tens of thousands of years. Lesser amounts of gypsum (to a maximum near 0.3% volume at 600 years) and very small amounts of fluorite also precipitate in the same zone, but dissolve rapidly upon rewetting. The magnitude of porosity changes predicted for the base-case and extended-case systems is similar. The maximum porosity reduction is predicted with the extended case, but the overall extent of the decrease is slightly larger for the base case because of somewhat more widespread calcite precipitation than with the extended case. The predicted porosity change is smaller than modeled with the REV02 simulations (Section 6.8), because the code version (TOUGHREACT V2.3 (LBNL 2001 [153101])) used for REV01 does not account for mineral precipitation into dry gridblocks upon influx of water. Also, this older model considers a somewhat larger fracture porosity than more recent simulations (Table 6.4-1).

Note that in this model, zeolites in fractures around the drift (mostly stellerite) primarily dissolve. Small amounts of stellerite (less than 0.02% volume) precipitate in the rock matrix mostly below the drift during the initial cooling stage, but redissolve entirely after approximately 5,000 years. More recent simulations (Section 6.8) with somewhat revised stellerite thermodynamic properties predict more stellerite precipitation than in this simulation (although not much more). Clay minerals are predicted to precipitate around the drift, but only in minute quantities (less than 10^{-4}% by volume). Figures showing predicted patterns for some of these minerals around the drift are shown in Section 6.6, where the effect of heterogeneous permeability fields are investigated. Predicted mineral patterns of illite and stellerite are similar to those shown in Section 6.7.5.2 for the Tptpll THC Model REV01.

Slightly higher liquid saturations in fractures during the cooling phase are calculated when THC processes are considered (Figure 6.5-17). This is the direct result of increased capillarity caused by permeability reduction. However, the permeability reduction is not large enough to significantly affect modeled fluxes at the drift crown (Figure 6.5-18) or the general thermohydrology around the drift. This is in contrast with more recent simulations (Section 6.8) incorporating updated rock properties and a better treatment of mineral precipitation at the boiling front. These more recent simulations show a significant diversion of percolating water around the drift because of a zone of reduced permeability above the drift (Section 6.8.5.2). In the current case, the only visible effect of mineral precipitation is a slight flux increase (relative to ambient values) after 20,000 years predicted with the extended geochemical system (Figure 6.5-18). This effect is caused by minor flow focusing, stemming from an uneven precipitation of calcite artificially enhanced by numerical discretization effects. In this case, an average of a few gridblocks would give a closer approximation to the flux at the drift crown. Changes in permeability caused by THC effects around the drift are further investigated for alternative models in the next sections. It should also be noticed that steps in the curves displayed for ambient simulations in Figures 6.5-17 and 6.5-18 reflect a change in infiltration rates input into the model (Table 6.5-3).

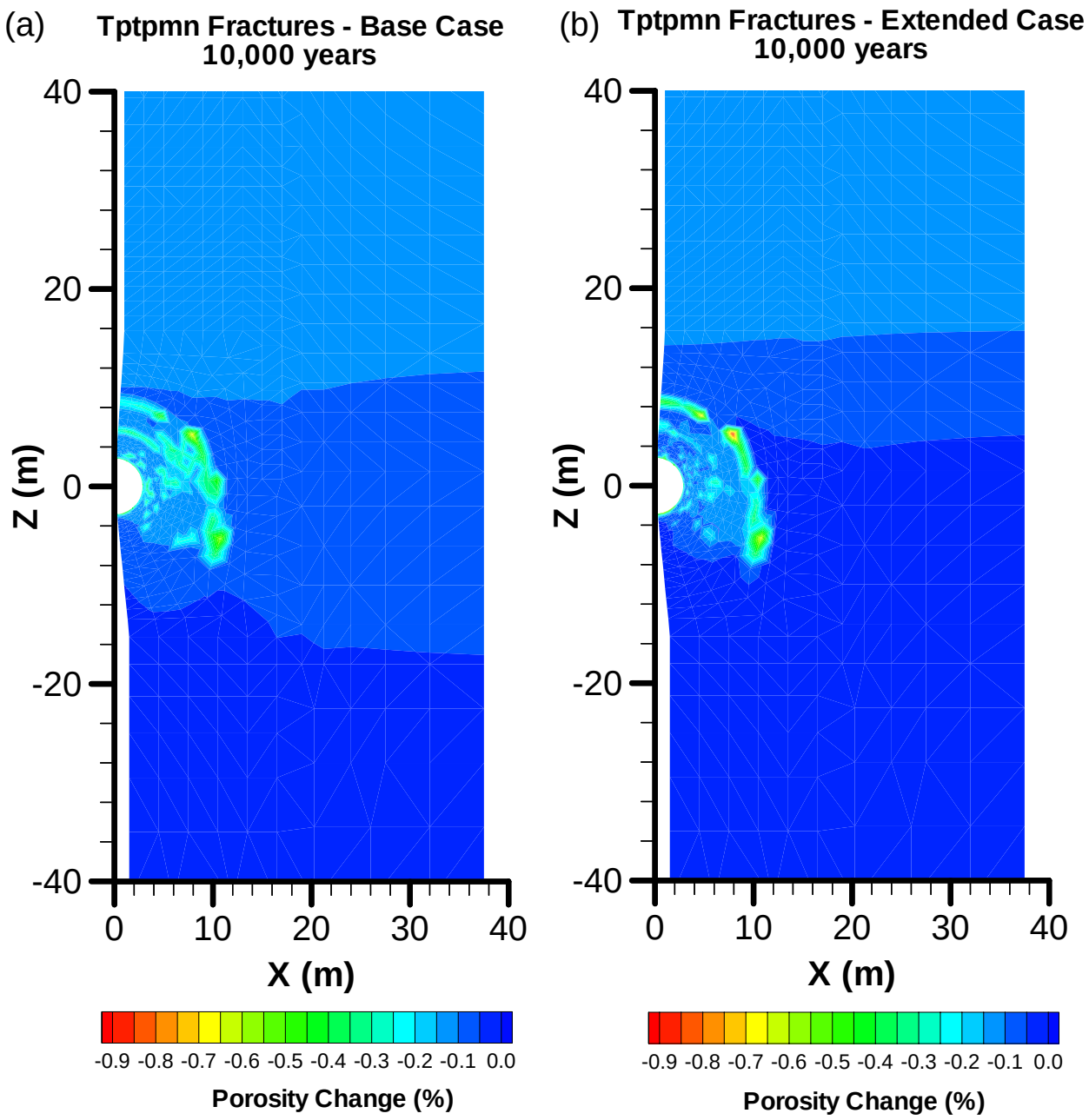

DTN: LB0011DSTTHCR1.002 [161282]

NOTE: Decrease in porosity is primarily due to the precipitation of calcite and amorphous silica.

Figure 6.5-16. THC Simulation (Tptpmn Model): Contour Plot of Modeled Fracture Porosity Change at 10,000 Years for (a) Base-Case and (b) Extended Geochemical Systems

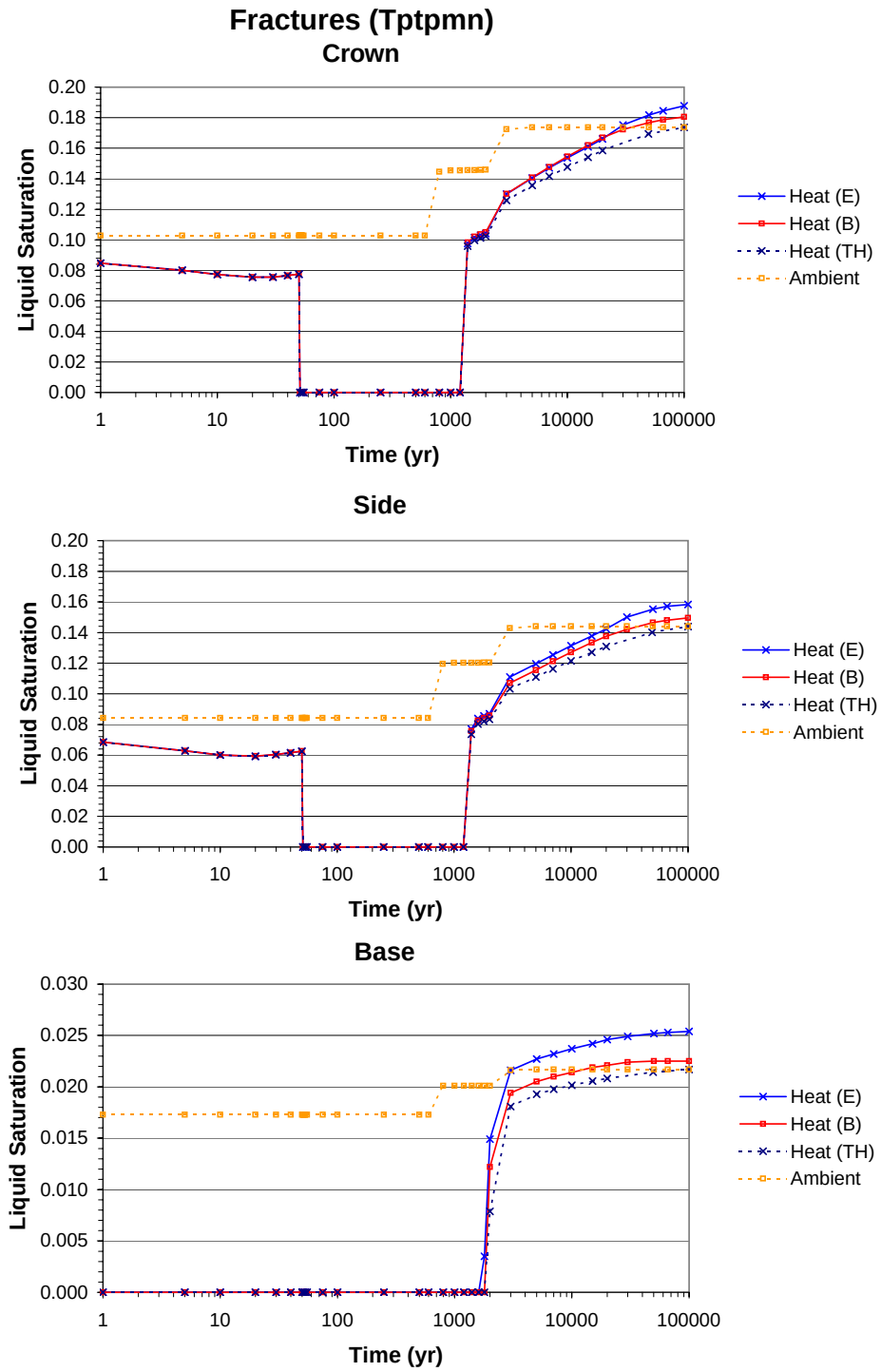

DTN: LB0011DSTTHCR1.001 [154759]

Figure 6.5-17. TH and THC Simulations (Tptpmn Model): Comparison of Modeled Liquid Saturations in Fractures at Three Drift-Wall Locations under Heating (Heat) and Non-Heating (Ambient) Conditions for the Extended (E) and Base-Case (B) Geochemical Systems, and for the TH Simulation

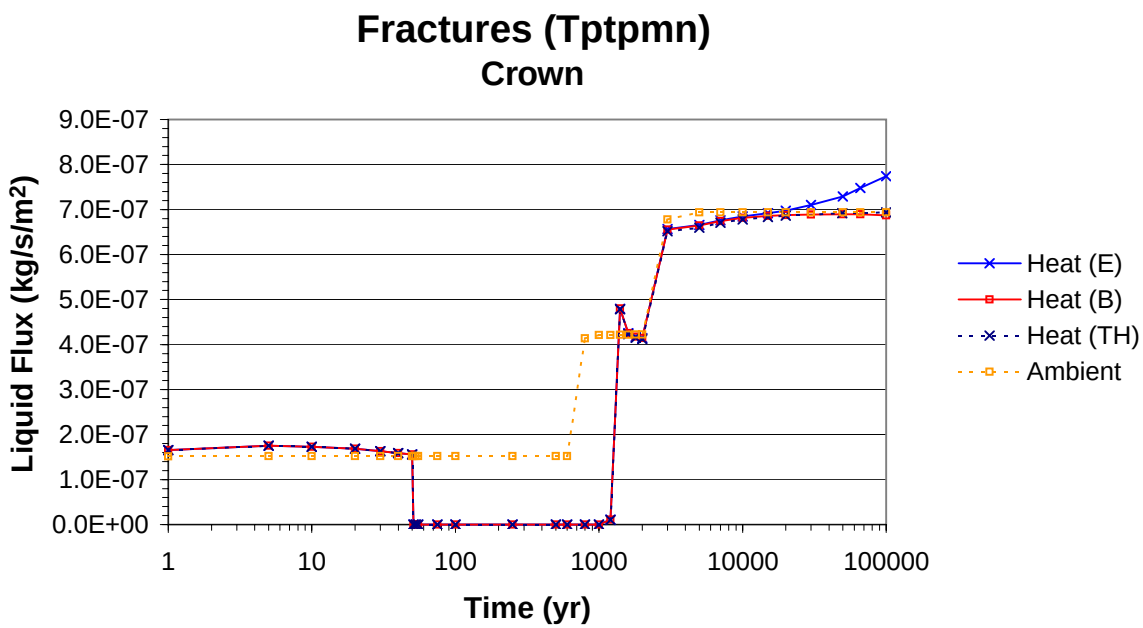

DTN: LB0011DSTTHCR1.001 [154759]

NOTE: The small flux increase above ambient values after 20,000 years is in part due to numerical discretization effects (see text).

Figure 6.5-18. TH and THC Simulations (Tptpmn Model): Comparison of Modeled Liquid Flux at the Drift Crown in Fractures under Heating (Heat) and Non-Heating (Ambient) Conditions for the Extended (E) and Base-Case (B) Geochemical Systems, and for the TH Simulation

6.6 Tptpmn THC HETEROGENEOUS MODEL REV01

Fracture permeabilities vary locally over several orders of magnitude in the Tptpmn unit (DTN: LB990601233124.001 [105888]). The initial spatial heterogeneity in fracture permeability and how it affects coupled THC processes in the Tptpmn has not been treated prior to this study. The purpose of this alternative conceptual model is to address the effects of fracture permeability heterogeneity at the drift scale on water and gas chemistry, hydrological properties, UZ flow, and the potential for enhanced or reduced percolation fluxes owing to THC processes. Several realizations were performed, because the location of higher and lower permeabilities will differ in relation to the drift crown and therefore the areas of maximum mineral precipitation will differ as a result of THC effects. Note that the effect of heterogeneity in matrix permeabilities on THC processes and flow is not investigated because matrix permeabilities are orders of magnitude lower than fracture permeabilities, such that the effect of matrix heterogeneity on flow is insignificant compared to the effect of fracture heterogeneity.

Key elements of this model are listed below. Except for initially heterogeneous fracture permeabilities in the repository host unit, the model setup and input data are the same as for the Tptpmn THC Model (Section 6.5).

- Heterogeneous fracture permeability
- Initial heat load of 1.45 kW/m (Attachment VII)
- 50-year preclosure period with 70% ventilation efficiency
- Drift in the Tptpmn unit
- Model stratigraphy from geology at borehole SD-9
- Consideration of a base-case and extended-case geochemical system (Section 6.2.2.2)
- Drift wall closed to fluid and gas advection (but open to diffusive fluxes)
- Omission of vapor pressure lowering by capillary pressure
- Earlier set of rock thermal and hydrological properties (Table 6.4-1)
- Earlier thermodynamic database (Attachment V), although not much different than newer data
- Utilization of TOUGHREACT V2.3 (LBNL 2001 [153101]), which does not consider precipitation of solids in gridblocks that are dry, but into which water influx and complete evaporation occurs (Section 6.4.5), thus underestimating mineral precipitation amounts
- Most useful for comparison with the Tptpmn THC Model REV01 results (Section 6.5) to evaluate differences in results caused by homogeneous versus heterogeneous conceptualizations of fracture permeability.

6.6.1 Model Set-Up

The numerical mesh, boundary conditions, and modeling procedure are the same as those described in Sections 6.5.1 to 6.5.3 for the Tptpmn THC Model. Additional model set-up information described in this section relates to the heterogeneous permeability realizations used in the simulations. The various simulations are summarized in Table 6.6-1.

6.6.1.1 Heterogeneous Fracture-Permeability Realizations

Three 2-D heterogeneous fracture permeability fields were generated using the GSLIB V1.0 module SISIM V1.204 (LBNL 2000 [153100]), based on a cumulative distribution function obtained through analysis of air-permeability testing (Haukwa 2001 [160900], pp. 24–28). The range in fracture permeability is four orders of magnitude (DTN: LB990601233124.001 [105888]), with the mean given by the drift-scale calibrated property set (DTN: LB990861233129.001 [110226]). Each realization is equally representative of the spatial variability because each realization reproduces the observed statistical properties of the permeability distribution (e.g., mean, standard deviation, etc.). These heterogeneous permeability fields were generated for a region 150 m above and below the drift center at a spatial resolution of 0.2 m, based on the scale of air-permeability measurements. Because the Tptpmn THC Model grid has gridblocks varying from about 0.2 m across near the drift wall to several meters across in areas away from the drift, the fine resolution field had to be mapped onto the numerical mesh using an appropriate averaging scheme. A circular area was defined around the nodal point within each gridblock corresponding to the average distance of the nodal point to the gridblock edges. Geometric means of the permeability multipliers within this area were calculated and used to modify the mean permeability assigned to the numerical mesh gridblocks. The net result of this averaging is that the permeabilities near the drift wall have the same or similar spatial variability, whereas areas away from the drift reflect a smoother averaged field appropriate to the resolution of the mesh in these areas. The averaging was performed using the software routine avgperm.f V1.0 (LBNL 2000 [153085]). Plots of the three realizations of averaged permeability fields used in the Tptpmn THC simulations are shown in Figures 6.6-1.

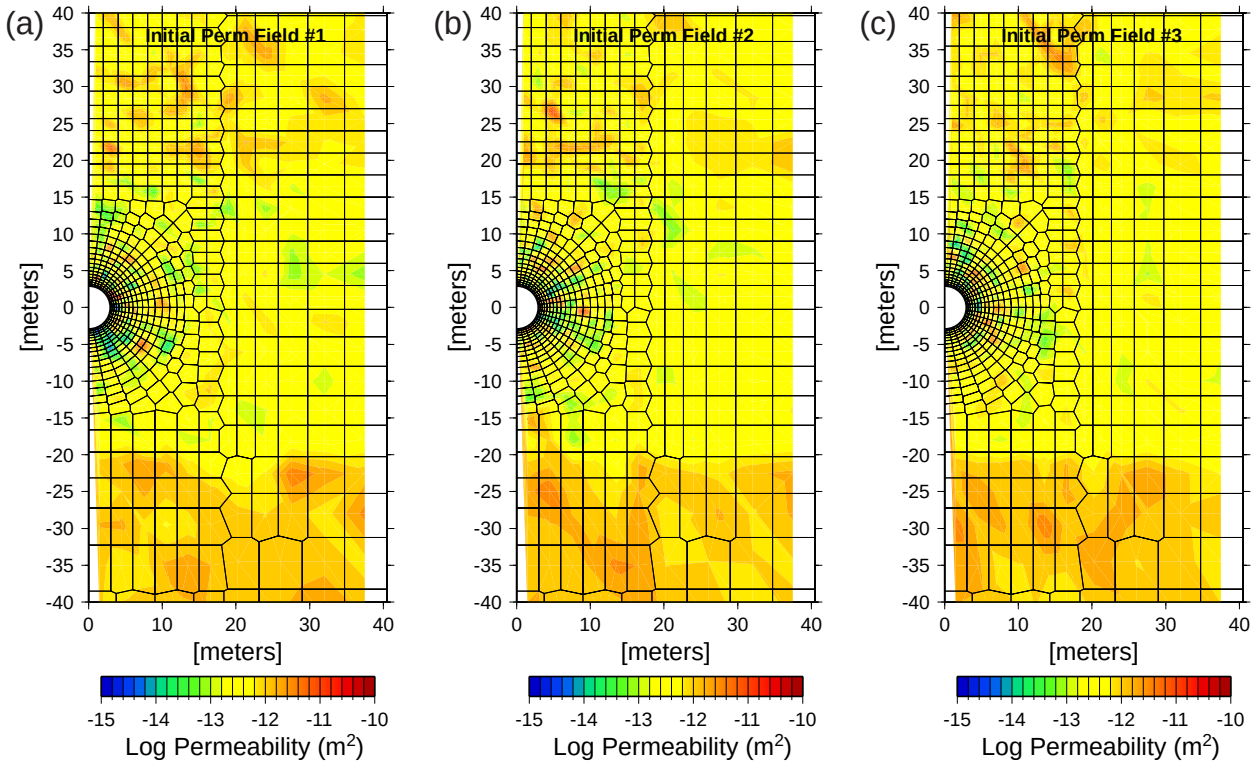

DTN: LB0011DSTTHCR1.002 [161282]

Figure 6.6-1. Fracture-Permeability Realizations #1 (a), #2 (b), and #3 (c)

6.6.1.2 Model Runs

THC simulations were performed using the same two sets of chemical components and mineral assemblages as those used for the Tptpmn THC Model simulations presented in Section 6.5 (extended case and base case, Section 6.2.2.2). All simulations were performed using the mean-infiltration-rate climate-change scenario (Table 6.5-3). TOUGHREACT V2.3 (LBNL 2001 [153101]) was used for all simulations.

Table 6.6-1. Tptpmn THC Heterogeneous Model Runs

Infiltration-Property Set (Table 6.5-3)	Permeability Realization	Geochemical System (Section 6.2.2.2)	Simulation Type	Run ID (used in DTN: LB0011DSTTHCR1.002 [161282]; also see Attachment X)
Mean Infiltration	#1	None	Steady-State	ds00ss_het1
		None	TH	ds00th_het1
		Extended Case	Ambient	ds00amb1_het1
		Base Case	Ambient	ds00amb2_het1
		Extended Case	THC	ds00thc1_het1
		Base Case	THC	ds00thc2_het1
Mean Infiltration	#2	None	Steady-State	ds00ss_het2
		None	TH	ds00th_het2
		Extended Case	THC	ds00thc1_het2
		Base Case	THC	ds00thc2_het2
Mean Infiltration	#3	None	Steady-State	ds00ss_het3
		None	TH	ds00th_het3
		Extended Case	THC	ds00thc1_het3
		Base Case	THC	ds00thc2_het3

6.6.2 Simulation Results

6.6.2.1 Hydrological Effects of Fracture Permeability Heterogeneity

The steady-state liquid saturations obtained for the three heterogeneous permeability fields with an infiltration rate of 6 mm/yr show a range of fracture saturations from approximately 2% to 90% (Figures 6.6-2a–c). This large range results from the roughly four-orders-of-magnitude variation in fracture permeability and its effect on capillary pressure through the Leverett scaling relation (Equation 6.4-23). For comparison, the steady-state fracture liquid saturation for the Tptpmn in the Tptpmn THC model simulations (homogeneous permeability) was about 4.7%. The greatest differences in fracture saturation are within about 3 m of the drift wall, where there was little or no averaging of the stochastically generated fine-scale permeabilities. Because some of the mesh volumes have high fracture liquid saturations, there exists an initial condition more conducive to seepage, although these regions also have much smaller absolute permeabilities. Further from the drift, differences in fracture saturation between gridblocks are much less, owing to the much smoother averaged permeabilities.

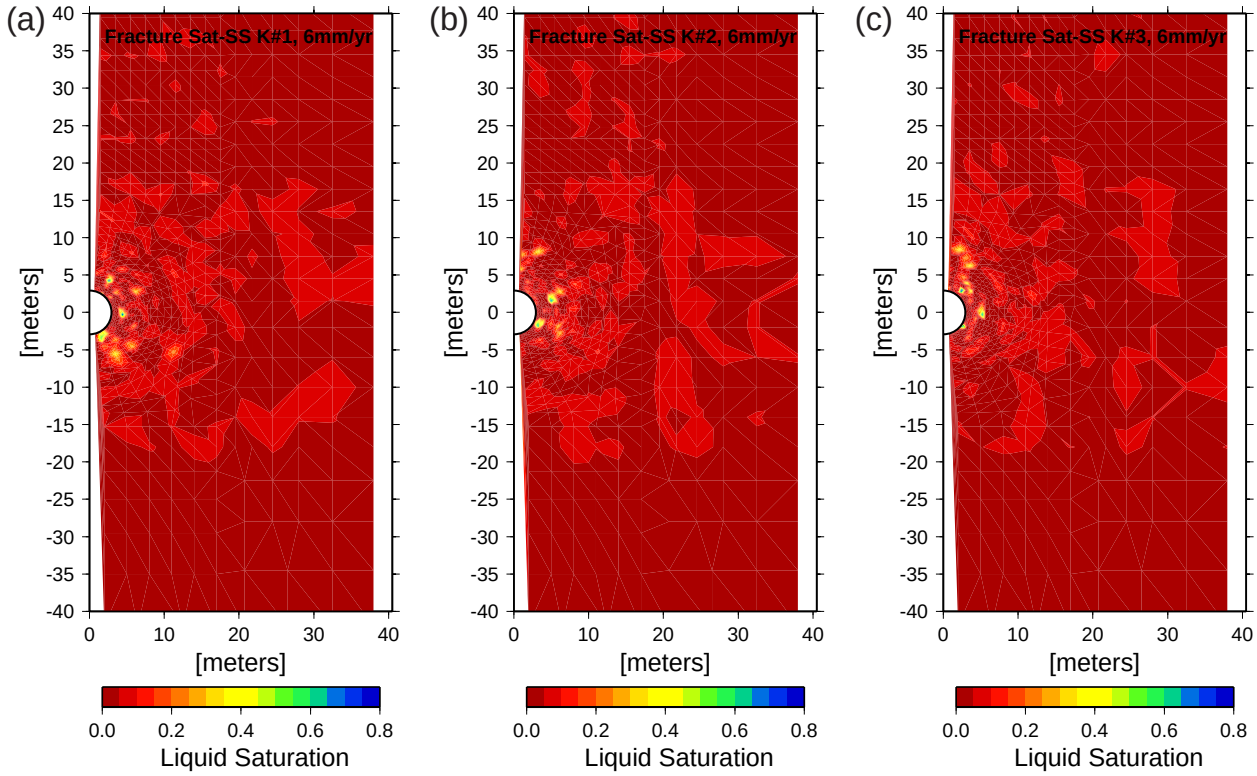

DTN: LB0011DSTTHCR1.002 [161282]

Figure 6.6-2. Steady-State Fracture Liquid Saturations (Infiltration Rate = 6 mm/yr) for Permeability Realizations #1 (a), #2 (b), and #3 (c)

6.6.2.2 Thermal-Hydrological Effects of Fracture Permeability Heterogeneity

The heterogeneity in fracture permeability can have varied effects on thermohydrology, including flow-focusing and irregularity in isotherms and liquid saturations. Thermal-hydrological simulations were performed for the three heterogeneous fracture permeability realizations under the mean infiltration climate-change scenario. Fracture liquid saturation at approximately the maximum extent of the dryout zone (600 years) for the three permeability realizations are shown in Figures 6.6-3a–c. This time is just prior to an increase in infiltration rate from 6 mm/yr to 16 mm/yr. Regions of higher fracture liquid saturation are evident within the zone that is predominantly dry, with a maximum penetration of no more than one meter. Strong local differences in fracture liquid saturations are much greater than the more dispersed overall effect of condensate shedding, although it is clear that the higher saturation areas are concentrated above and to the side of the drift, with the zone below the drift significantly drier.

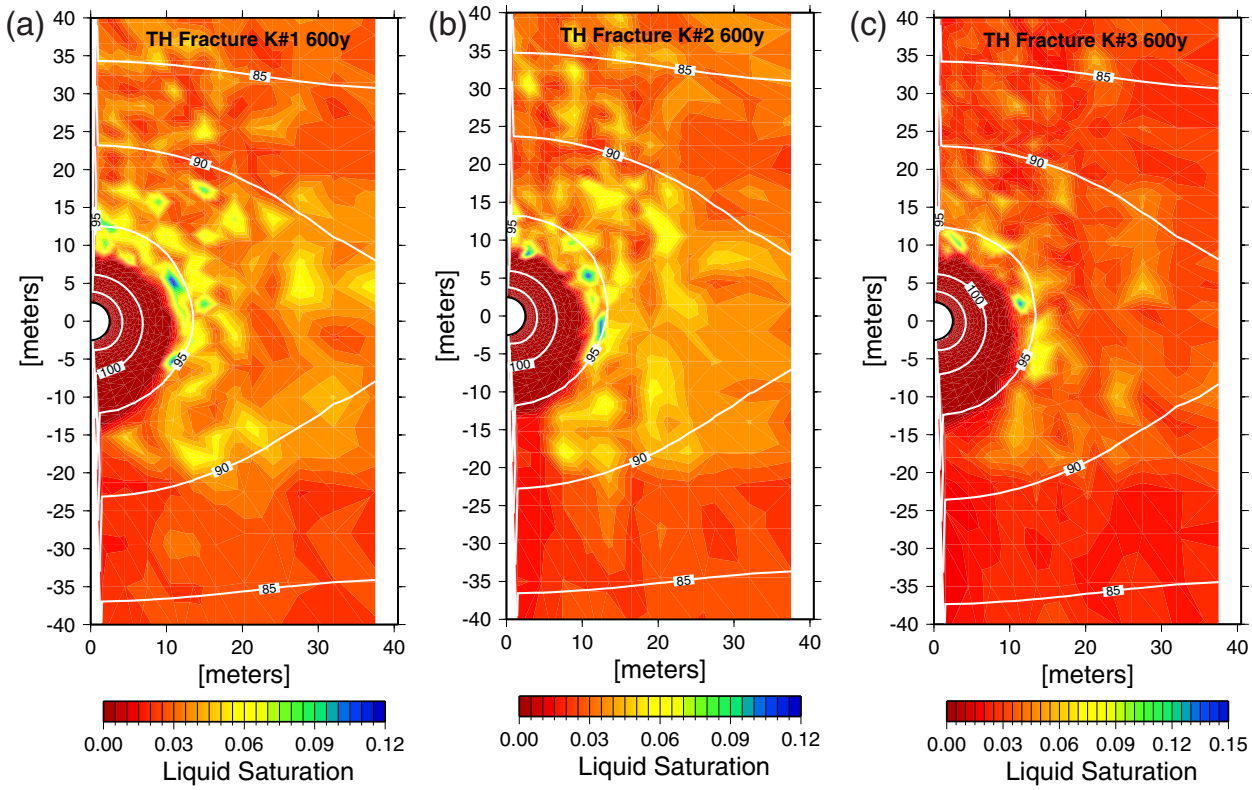

DTN: LB0011DSTTHCR1.002 [161282]

Figure 6.6-3. Fracture Liquid Saturations at 600 Years from Thermal-hydrological Simulations (Infiltration Rate = 6 mm/yr) for Permeability Realizations #1 (a), #2 (b), and #3 (c) (with temperature contours shown in °C)

Matrix liquid saturations were not affected significantly by the variations in fracture permeability, and their distribution is similar to those for the simulations employing a homogeneous Tptpmn unit.

6.6.2.3 THC Effects of Fracture Permeability Heterogeneity

The two most important questions regarding the effect of fracture permeability heterogeneity on THC processes are (1) the effect on flow owing to localized mineral precipitation or dissolution, and (2) the effect on the chemistry of the water that may seep into drifts.

As mentioned earlier, REV01 simulations did not include the more accurate treatment of mineral precipitation at the boiling front described in Section 6.4.5. Therefore, REV01 simulations likely underestimate porosity changes and effects on flow. More recent simulations for REV02 (Section 6.8) incorporate this more accurate treatment and show more effect on flow (Section 6.8.5.4). However, REV02 simulations do not consider heterogeneous fracture permeabilities. Results presented below show that fracture permeability heterogeneity does not have a significant effect on water chemistry in the vicinity of the drift. This conclusion is not likely to change if simulations including fracture permeability heterogeneity were repeated using the REV02 model improvements. This is because temperature is the main driving force for chemical reactions occurring during the thermal pulse and is not affected significantly by fracture

permeability heterogeneity (i.e. heterogeneities in fracture permeability do not affect the thermal response of rocks surrounding the drift).

The effect of REV02 model improvements on flow would be more significant, resulting in a greater overall diversion of water around the drift than shown here (compare results below with those in Section 6.8.5.4), but potentially also focusing flow on a local scale. However, using the REV02 model improvements, significant porosity and permeability change due to THC processes are predicted to occur only during the boiling period, at a significant distance from the drift wall (5–10m), and in a very thin zone (e.g. Figure 6.8-41). Local focusing of flow through such thin zone away from the drift wall is unlikely to affect seepage at the drift wall. Furthermore, another study considering flow through focusing factors of 5 and 10 (i.e. increased fluxes at the drift wall and at the boiling front by factors of 5 and 10 respectively) (BSC 2003 [161530], Section 6.2.3.2.3) shows that thermal seepage is predicted to occur only at late times after waste emplacement, when temperatures are below boiling, and thus when effects of THC processes are not significant. The flow focusing factors used in this study are "generic," representing increases in flux that could be caused by heterogeneities and/or any other effects including THC processes. Given the above considerations and the results of the BSC (2003 [161530]) study regarding flow focusing, results of THC simulations using heterogeneous fracture permeability and REV02 model improvements are not expected to predict a significantly higher potential for seepage into drifts than the results presented below and in Section 6.8.5.4.

6.6.2.3.1 THC Effects on Permeability and Liquid Flow in a Heterogeneous Medium

The conceptual model for fracture permeability changes employed in the THC simulations of the heterogeneous Tptpmn THC Model (and alternative models in Sections 6.5, and 6.7, and 6.8) is based on changes to the hydraulic aperture, resulting from mineral precipitation or dissolution, as described in Section 6.4.4.2, Equations 6.4-18 through 6.4-21. Therefore, in fractures, changes in permeability are much more sensitive to changes in porosity than in the matrix, where the cubic law formulation (Equation 6.4-17), which is dependent directly on porosity changes, is used to calculate permeability changes.

The changes in fracture permeability after 20,000 years are shown as the ratio of the permeability to its initial value in Figure 6.6-4 for the extended- and base-case geochemical systems (Realization #1). Results are shown for this time period because the permeability does not change much after this time (i.e., very little mineral precipitation/dissolution occurs after this time). Areas of highest initial liquid saturation, also having lower permeability and generally residing above the drift, tend to show the greatest reduction in fracture permeability, reaching a minimum of about 25% of the initial value. The effect of this localized permeability reduction tends to cause some additional flow focusing. However, the permeability changes are considerably less than the initial range in permeability. The corresponding maximum fracture porosity reductions are approximately 5% of the initial value. Porosity reductions for the extended geochemical system are slightly greater than those for the base-case system, owing to more mineral species precipitating and somewhat higher silica concentrations in the former.

This REV01 model neglects the effect of mineral precipitation upon influx of water into dry gridblocks. This effect would cause further porosity and permeability reduction. REV02 simulations for a drift in the Tptpll unit consider this effect, and predict a maximum fracture

porosity reduction around 8% (mainly above the drift), and a permeability decrease up to around two orders of magnitude (Section 6.8.5.4). The REV02 simulations, however, consider an initially homogeneous fracture permeability. Using initially heterogeneous permeabilities, the porosity and permeability could locally decrease further, although the four-order-of-magnitude natural range in fracture permeability would still most likely encompass the bulk of the range in permeability change.

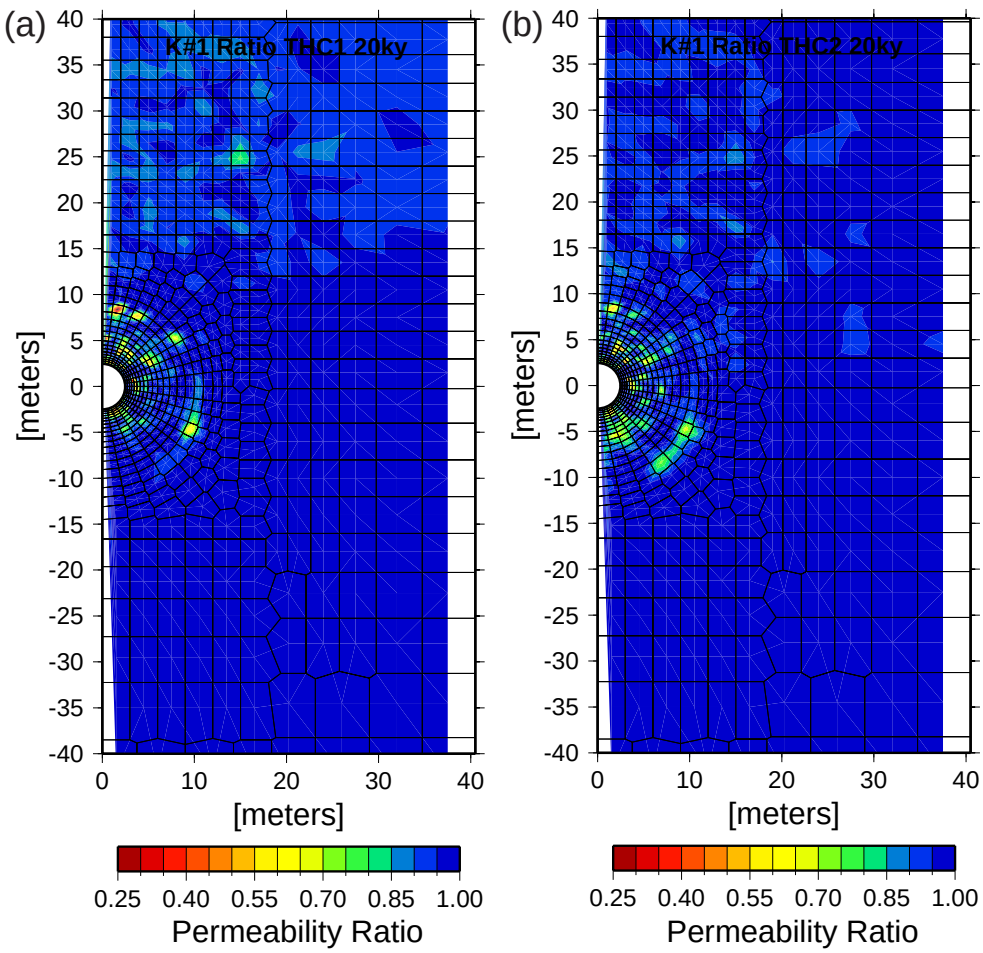

DTN: LB0011DSTTHCR1.002 [161282]

Figure 6.6-4. Fracture Permeability Ratio after 20,000 Years for Realization #1: (a) Extended and (b) Base-Case Geochemical Systems

The spatial variations in fracture liquid saturation as a result of permeability reduction from mineral precipitation are little different from the effect of the initial heterogeneity. The fracture saturations after 20,000 years show a similar distribution to the steady-state pattern, although somewhat higher overall because of a larger infiltration rate (at 600 years and 2,000 years) than those of the 6 mm/yr steady-state simulation (Figure 6.6-5). This similarity implies that liquid fluxes to the drift wall are not dramatically modified. Otherwise, significant changes in liquid saturation near the drift wall would be evident.

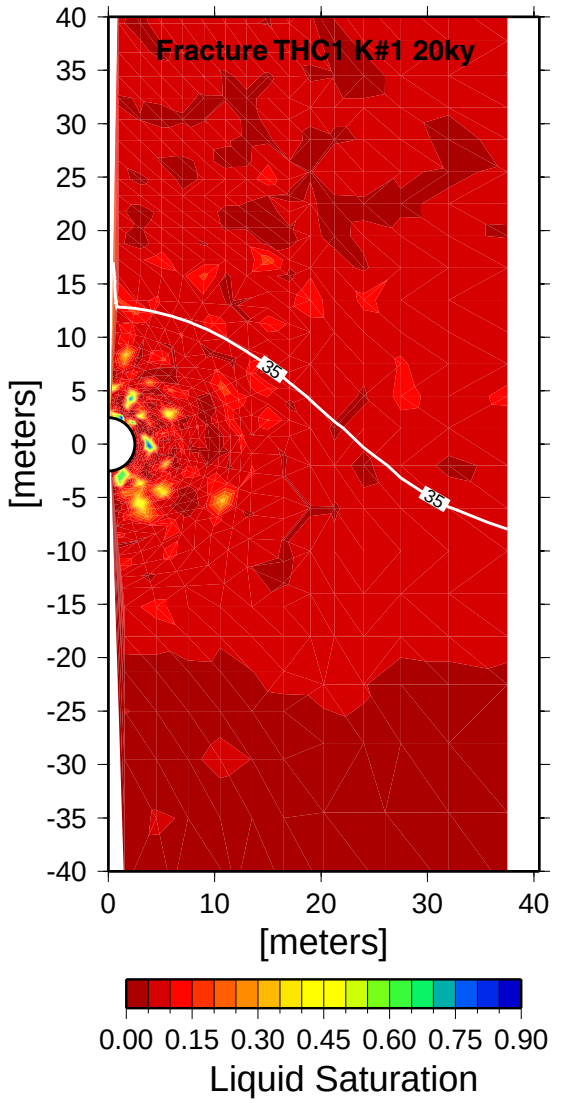

DTN: LB0011DSTTHCR1.002 [161282]

NOTE: Temperature contour is shown in °C.

Figure 6.6-5. Fracture Liquid Saturation for Realization #1: THC Simulation (Extended Case) after 20,000 Years

6.6.2.3.2 THC Effects on Geochemistry in a Heterogeneous Medium

Spatial differences in liquid saturation within fractures, resulting from variations in capillary suction, affect geochemical reactions in a number of ways. Reactive surface areas increase with increasing saturation via the modified active fracture model (Equation 6.4-15). Given roughly uniform concentrations, higher liquid saturation results in a greater amount of precipitate formed during complete evaporation. Higher liquid saturations also lead to an increase in the liquid relative permeability, which tends to reduce the effect of lower absolute permeability on flow and transport in these same fractures. Relatively small variations in aqueous species concentrations may lead to large variations in mineral amounts over time, owing to a cumulative effect.

Quantitatively, minerals such as amorphous silica and calcite are the most important for changing permeability and affecting flow (although clays and to a lesser extent zeolites have the potential for reducing permeability at smaller degrees of alteration, because of their higher surface area and/or lower density than the primary minerals). Amorphous silica is undersaturated in the ambient pore water at Yucca Mountain and thus precipitates only when the silica concentration in the water increases significantly, which usually occurs during evaporation or boiling. Up to the point of boiling, silica tends to increase in heated waters because of its increased solubility and the increased dissolution rate of such minerals as cristobalite, tridymite, quartz, and feldspars. As temperatures decline to below the boiling point and rewetting occurs, amorphous silica tends to redissolve slowly because percolating waters are undersaturated with respect to this mineral.

The distribution of amorphous silica after 20,000 years is shown for both geochemical cases in Figure 6.6-6. The precipitation patterns in the two cases are similar, with maximum amounts in the high saturation zones near the drift. The maximum amount of amorphous silica precipitated is about 2% (volume % of fracture) in the extended case and somewhat less in the base case. This overall behavior is consistent with the results of the DST validation studies (Section 7.1), which show the extended case giving higher silica concentrations in refluxing waters. Because the higher silica concentrations in the DST extended-case simulations are closer to the measured concentrations in waters sampled from boreholes, the extended case likely produces more justifiable amounts of precipitated silica in the Tptpmn THC model simulations. As for the homogeneous model (Section 6.5), the effect of mineral precipitation upon influx of water into dry gridblocks is neglected here, which likely results in an underpredicted porosity reduction. This effect is considered in more recent simulations (Section 6.8) predicting a maximum fracture porosity decrease around 8%. These more recent simulations, however, do not consider heterogeneous initial fracture permeabilities, and one would expect heterogeneous fracture permeability to result in an even larger decrease in porosity, at least at a local scale.

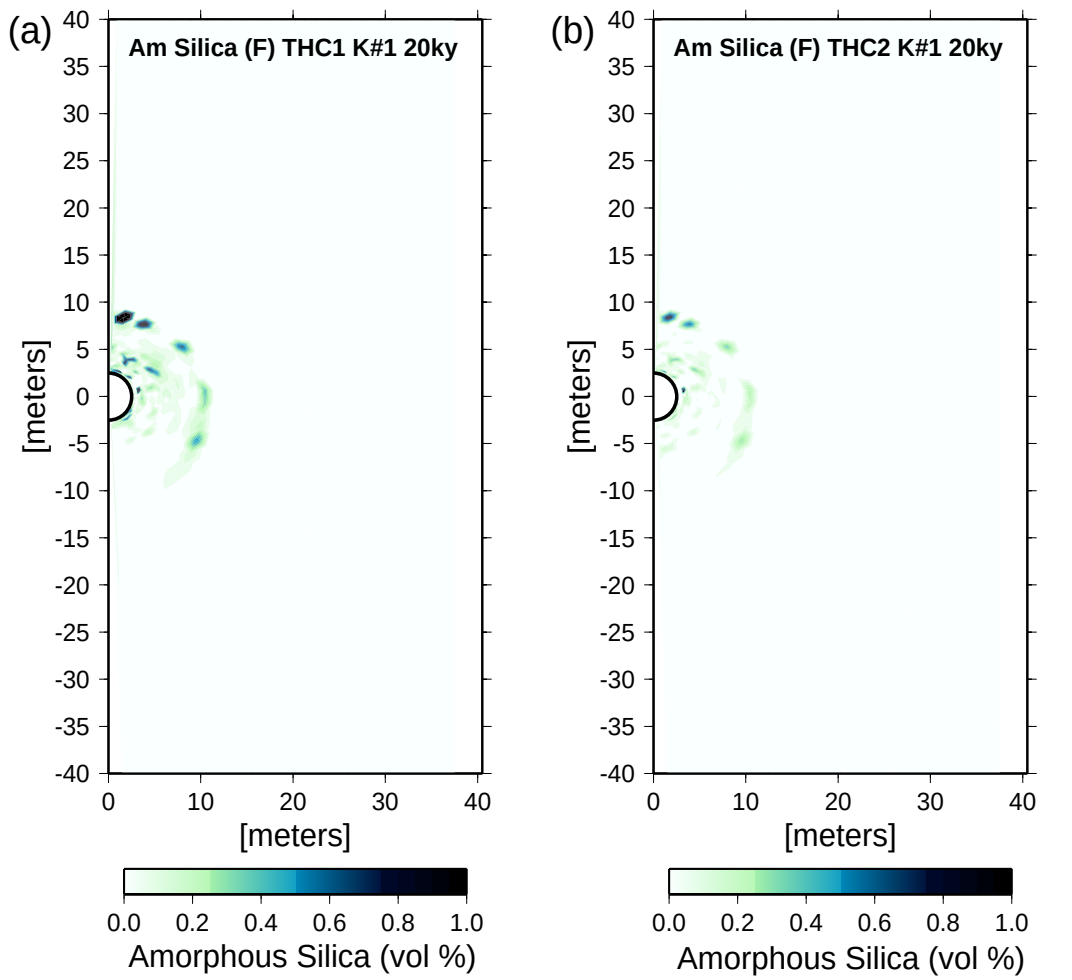

DTN: LB0011DSTTHCR1.002 [161282]

Figure 6.6-6. Amorphous Silica Changes (Volume %) in Fractures after 20,000 Years for Realization #1: (a) Extended and (b) Base-Case Geochemical Systems

Calcite is an important phase because it provides a strong buffer for preventing the formation of acidic waters and is the major source of calcium and carbonate in the fractures. The extended case considers calcite as an equilibrium mineral for Tptpmn THC simulations. Calcite becomes less soluble with increasing temperature and pH, and therefore shows a broader area of precipitation (Figure 6.6-7) than for amorphous silica (Figure 6.6-6). In the vicinity of the drift, calcite is more abundant in the base-case simulations, whereas in the extended case, more calcite is deposited in the Topopah Spring Upper lithophysal unit (Tptpul) above the drift, leading to less precipitation around the drift. Maximum calcite precipitation amounts to about 1.4% (volume % of fracture).

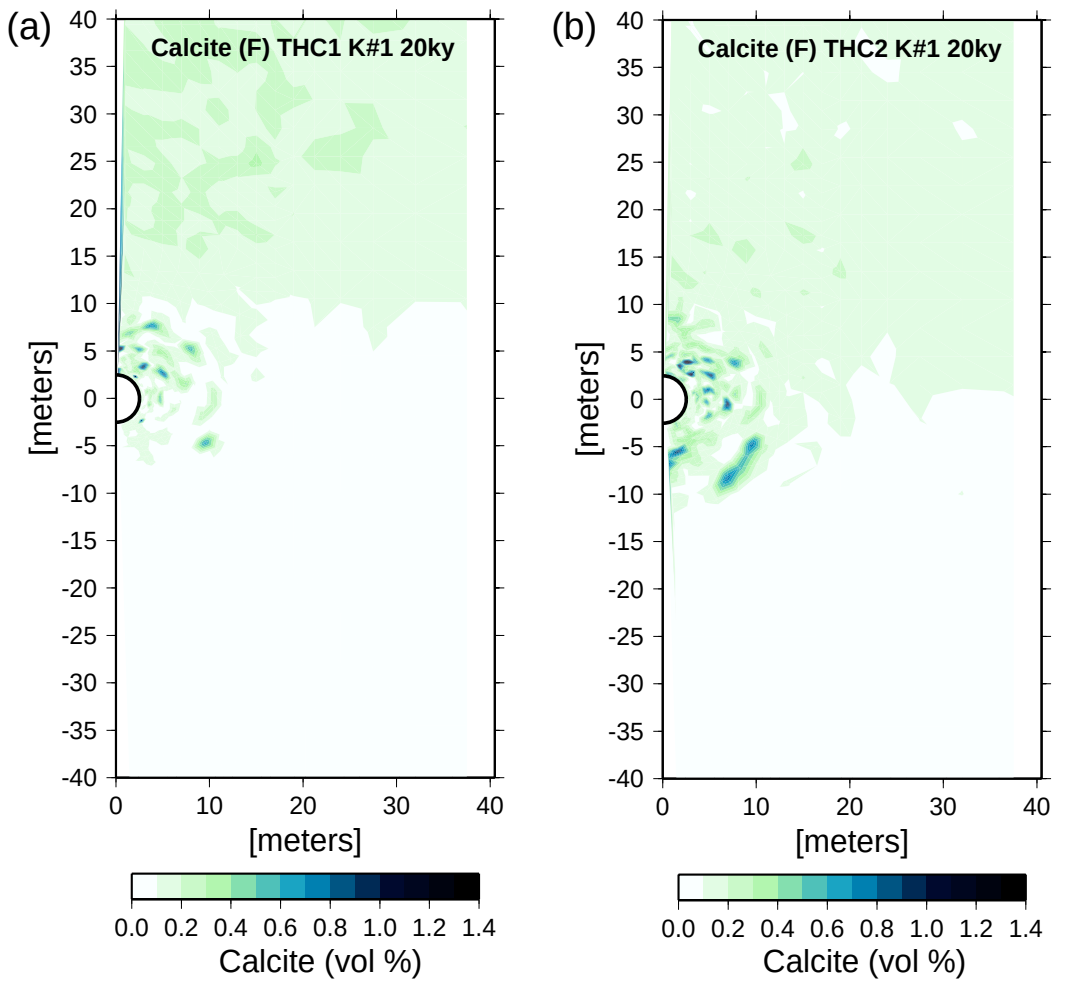

Figure 6.6-7. Calcite Changes (Volume %) in Fractures after 20,000 Years for Realization #1: (a) Extended and (b) Base-Case Geochemical Systems

Clays (e.g., illite, smectites) are important because of their greater potential for reducing permeability and as potential sorbers of radionuclides. Precipitated clay phases are very low in abundance, with a maximum volume percent (mostly illite) of less than 0.0001 after 20,000 years (Figure 6.6-8). In zones of low permeability and high fracture saturation, the largest quantities of illite form, with the homogeneous Tptpmn showing a much more uniform band of illite around the drift and at the contact of the Tptpul with the Tptpmn.

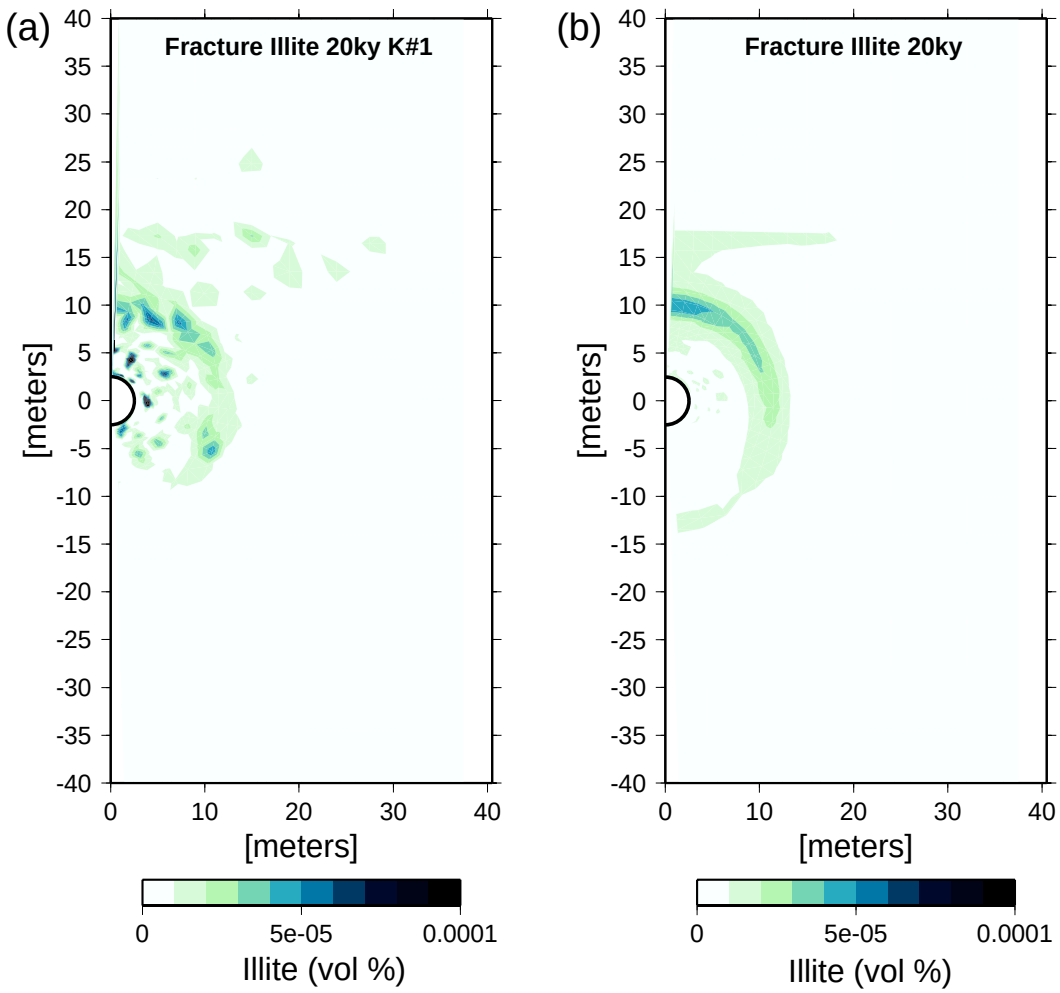

DTN: LB0011DSTTHCR1.002 [161282]

Figure 6.6-8. Illite Changes (Volume %) in Fractures after 20,000 Years for Realization #1: (a) Extended Geochemical System—Permeability Realization #1 and (b) Extended Geochemical System—Initially Homogeneous Tptpmn

The distribution of pH in fracture water near the time of maximum dryout (600 years) is shown in Figure 6.6-9, using the extended geochemical case for Permeability Realization #1. White areas are zones of dryout. For comparison to the model without locally heterogeneous permeability initial conditions, the pH for that simulation is shown in Figure 6.6-9b for the extended geochemical system. Small local variations appear in the pH of water in the fractures, caused by permeability heterogeneities, but otherwise the distribution is similar to the system without heterogeneities. A large plume of higher pH (maximum about pH 9) fracture water formed around the drift and is transported below the drift via percolation. At the approximate time of crown rewetting at 1,400 years (Figure 6.6-10), the pH of fracture water around the drift is in the range of 8 to 8.5 for the extended case, similar to the initial pore water and 0.5 to 1 unit higher than for the base case. The higher pH water near the drift at 600 years is well below the drift after 1,400 years. (Recall that the infiltration rate increased to 16 mm/yr from 6 mm/yr at 600 years.) The pH increase is caused by CO_2 degassing from the pore water upon heating and by the alteration of feldspars to clays (extended case), which consumes H^+.

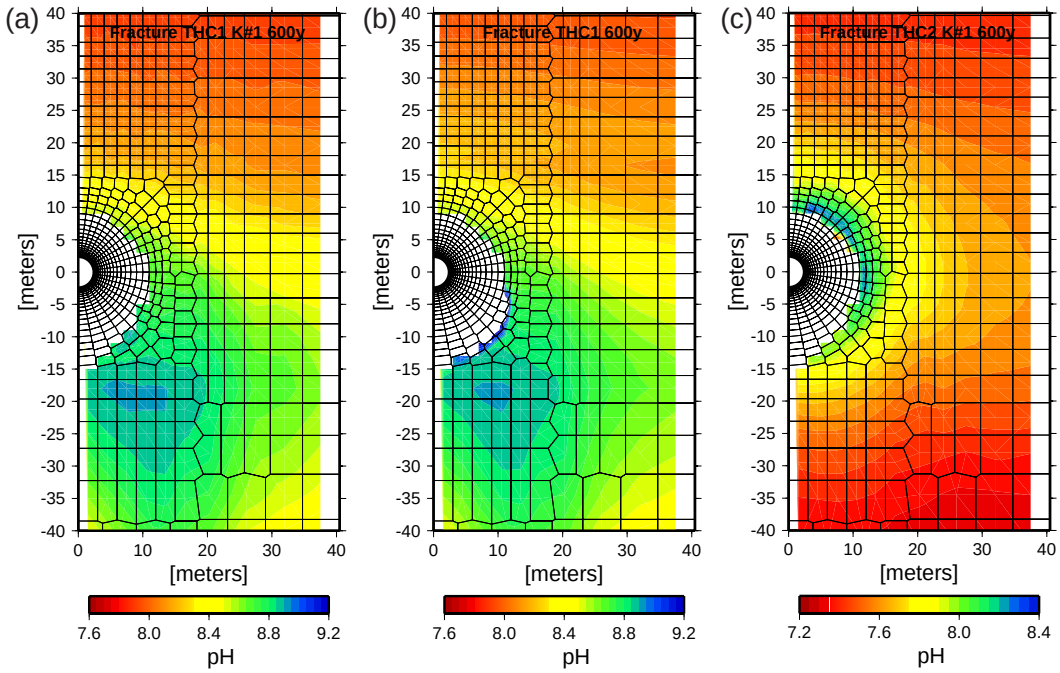

DTN: LB0011DSTTHCR1.002 [161282]

Figure 6.6-9. Fracture Water pH after 600 Years (white area is dry): (a) Extended Geochemical System—Permeability Realization #1; (b) Extended Geochemical System—Initially Homogeneous Tptpmn; (c) Base-Case Geochemical System—Permeability Realization #1

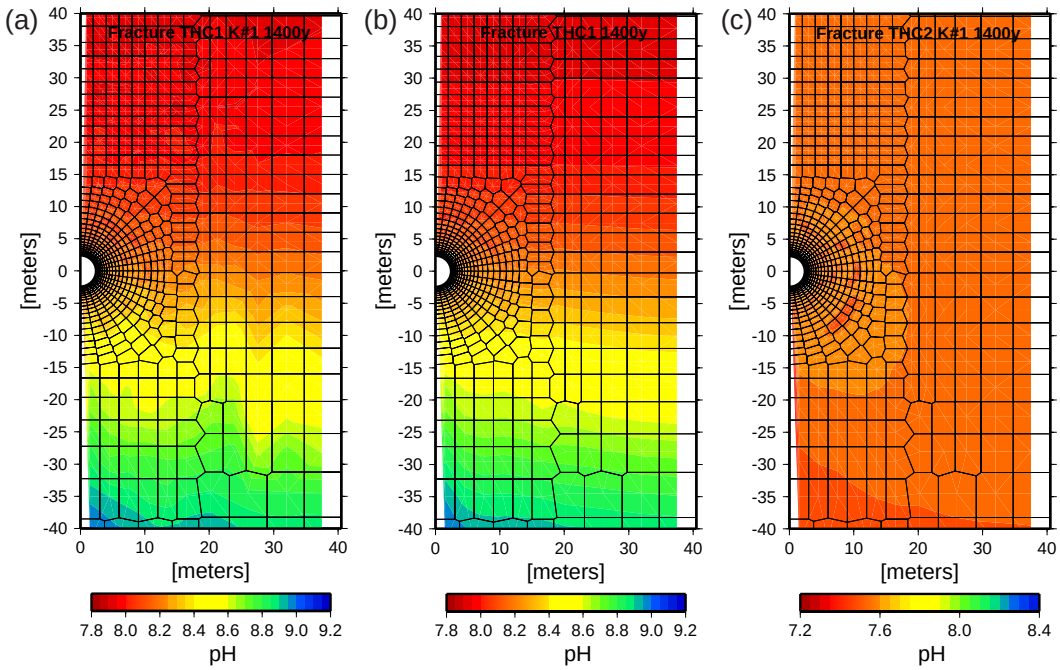

DTN: LB0011DSTTHCR1.002 [161282]

Figure 6.6-10. Fracture Water pH after 1,400 Years (white area surrounding drift is dry): (a) Extended Geochemical System—Permeability Realization #1; (b) Extended Geochemical System—Initially Homogeneous Tptpmn; (c) Base-Case Geochemical System—Permeability Realization #1

Chloride is an important indicator of salt-concentration effects, because the solubility of sodium chloride is high and chloride is essentially conservative up to the limit of halite saturation. Chloride concentrations in fracture water after 600 years (log scale) are shown in Figure 6.6-11. This figure shows a very narrow region of higher concentrations at the edge of the boiling zone surrounded by a much larger zone of dilute concentrations. An extensive, more dilute drainage zone is prominent for several tens of meters below the drift. This zone reflects the processes of strong dilution resulting from condensate formation, with limited fracture-matrix interaction, fracture drainage, and condensate shedding around the drift. The lowest concentrations are below the drift, where condensate formation in the shadow zone has experienced the least amount of mixing with the ambient percolation flux. The highest concentrations tend to be at the boiling front mostly above and to the side of the drift, where reflux and boiling of the ambient percolation flux are greatest.

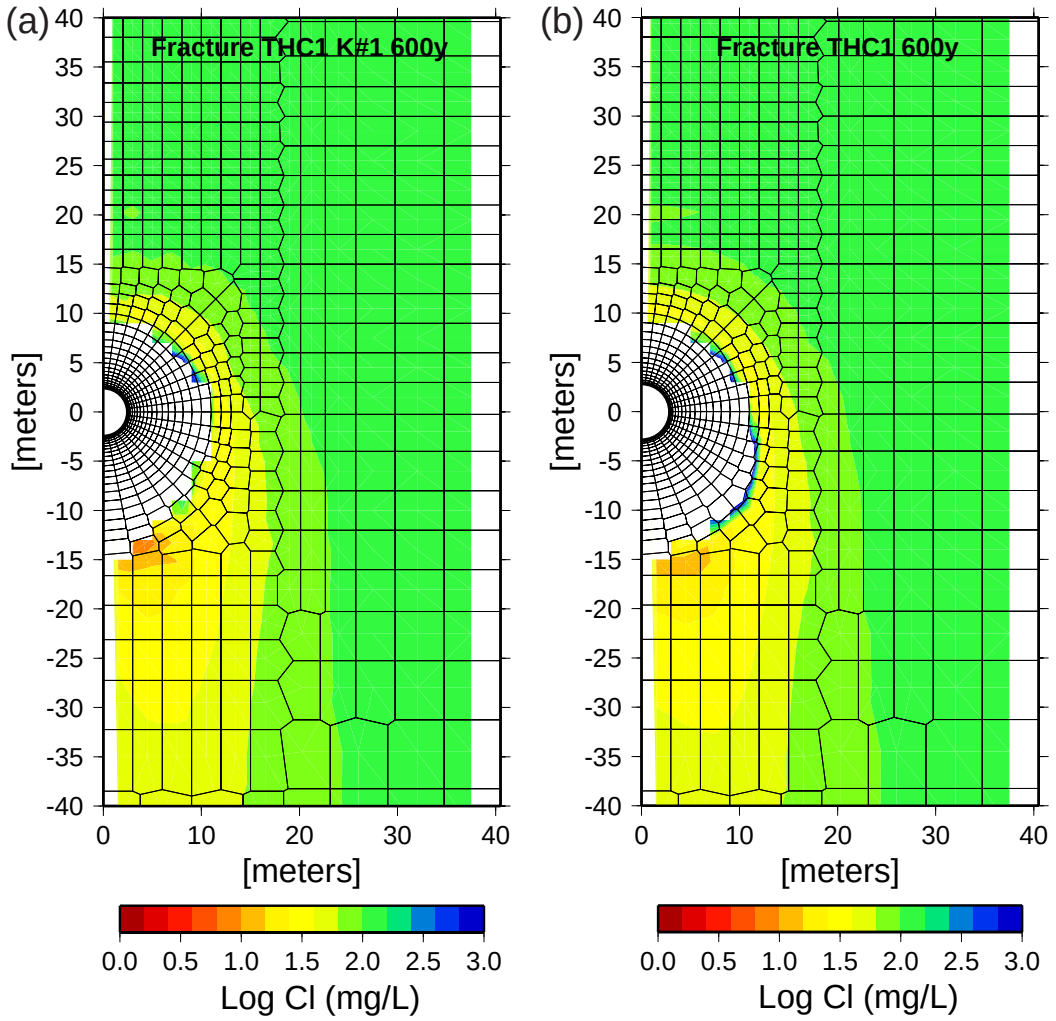

DTN: LB0011DSTTHCR1.002 [161282]

Figure 6.6-11. Chloride (Cl) Concentrations in Fracture Water after 600 Years: (a) Extended Geochemical System—Permeability Realization #1 and (b) Extended Geochemical System—Initially Homogeneous Tptpmn

Fluoride is a minor constituent in the aqueous phase, but is important from the standpoint of waste package corrosion. Fluoride (F^-) concentrations after 600 years are shown in Figure 6.6-12 and show a similar pattern as Cl^-, except at the very edge of the dryout zone, where fluorite precipitation has somewhat buffered any increases in F^- concentrations. Because there are no fluorine-bearing minerals in the initial mineral assemblage, these results may be a lower range of the fluoride concentration in the percolation flux. Alternative models in the following sections employ fluorite as an initial phase in the rock and therefore bound the upper limit of fluoride addition to refluxing waters.

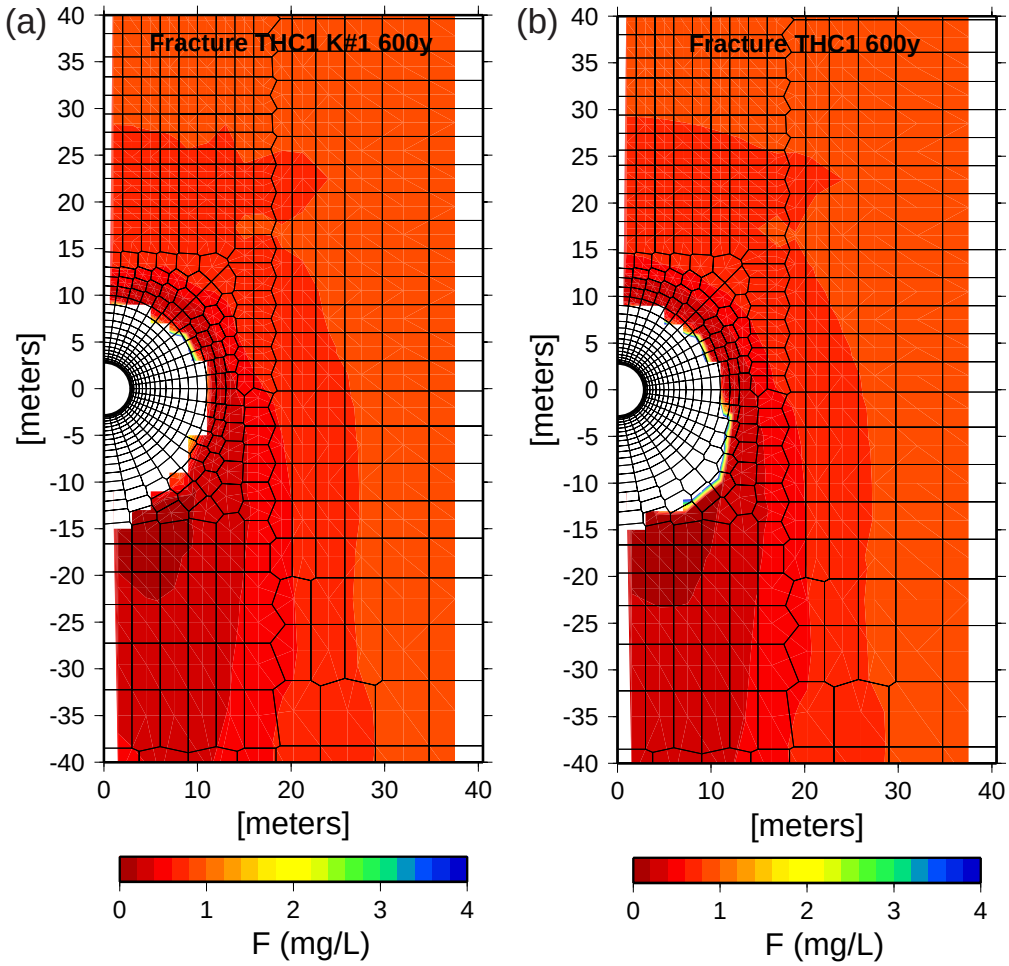

DTN: LB0011DSTTHCR1.002 [161282]

Figure 6.6-12. Fluoride (F^-) Concentrations in Fracture Water after 600 Years: (a) Extended Geochemical System—Permeability Realization #1 and (b) Extended Geochemical System—Initially Homogeneous Tptpmn

6.7 Tptpll THC MODEL REV01

The Tptpll THC Model REV01 presented in this section is similar to the model presented in Sections 6.5 and 6.6, with an almost identical drift design, identical heat load, and drift thermal properties. The main difference is that the drift is located in the Topopah Spring Tuff lower lithophysal geologic unit (the Tptpll unit, which corresponds to model layer tsw35, DTN: LB990501233129.004 [111475]). Most of the repository is planned to be located in the Tptpll unit. The stratigraphy of this model was taken at a location near the center of the repository (at approximately Nevada State Plane coordinates E170572, N233195).

This is an earlier model developed as part of REV01 investigations for comparison with the Tptpmn model, to evaluate the effect of drift location (geologic host unit and stratigraphic column) on model results. Key elements of this alternative model are the same as for the Tptpmn model described in Section 6.5, except as follows:

- The drift is located in the Tptpll unit.
- The stratigraphy represents a central location in the repository.
- The invert thickness was increased from 0.6 to 0.8 m.
- Hydrological properties were updated with the most recent data at the time this REV01 work was completed (more recent data are used for the REV02 model presented in Section 6.8).
- Rock mineralogy, volume fractions, and mineral surface areas were updated (Attachments II and IV). Also, an opal phase was added in both the base-case and extended-case geochemical system (Table 6.2-2).

The Tptpll lithostratigraphic unit differs significantly from the Tptpmn unit in the fact that it includes a significant number of lithophysal cavities. Although calibrated hydrological properties for the Tptpll are used here, lithophysae are not directly incorporated into the model, and therefore thermal-hydrological processes and associated chemical processes may be different from those in areas of high lithophysal porosity. The simulations with revised thermal properties accounting for lithophysal porosity are presented in Section 6.8.

6.7.1 Numerical Mesh (Tptpll)

Simulations were performed on a vertical 2-D mesh based on the same drift spacing and diameter as for the Tptpmn model (Section 6.5.1). Rock properties are assumed laterally homogeneous between drifts (Section 6.4.6.1), and, as in the Tptpmn model, the mesh is reduced to a 2-D half-drift model with a width of 40.5 m, corresponding to the midpoint between drifts (Figure 6.7-1). Geologic data from column “j34” of the UZ99_2_3D calibration model (DTN: LB990501233129.004 [111475]) were used to map geologic contacts into the 2-D mesh, and the mesh coordinate system was set with reference to the center of the drift (Table 6.7-1).

To limit grid orientation effects, the mesh design is mostly orthogonal, with a small radially gridded area in the immediate vicinity of the drift (Figures 6.7-1 and 6.7-2). The area extending

approximately 40 m above the drift is more finely gridded than other areas to capture THC effects potentially affecting seepage into the drift. Outside the drift, the smallest grid spacing was specified at the drift wall (20 cm), and increasing outward. A constant square cell size of 50 cm was used from approximately 5 m to 7 m above drift center, increased to a 1-meter size until 15 m above drift center, then a 2-meter size from 15 to 30 m above drift center. Unlike the Tptpmn model, all geologic layers down to the water table below the modeled drift were incorporated into the numerical mesh (Table 6.7-1). Gridblock sizes increase significantly 100 m above and below the drift to increase computing efficiency. The mesh consists of 3,202 gridblocks, including those representing matrix, fracture, and in-drift design elements.

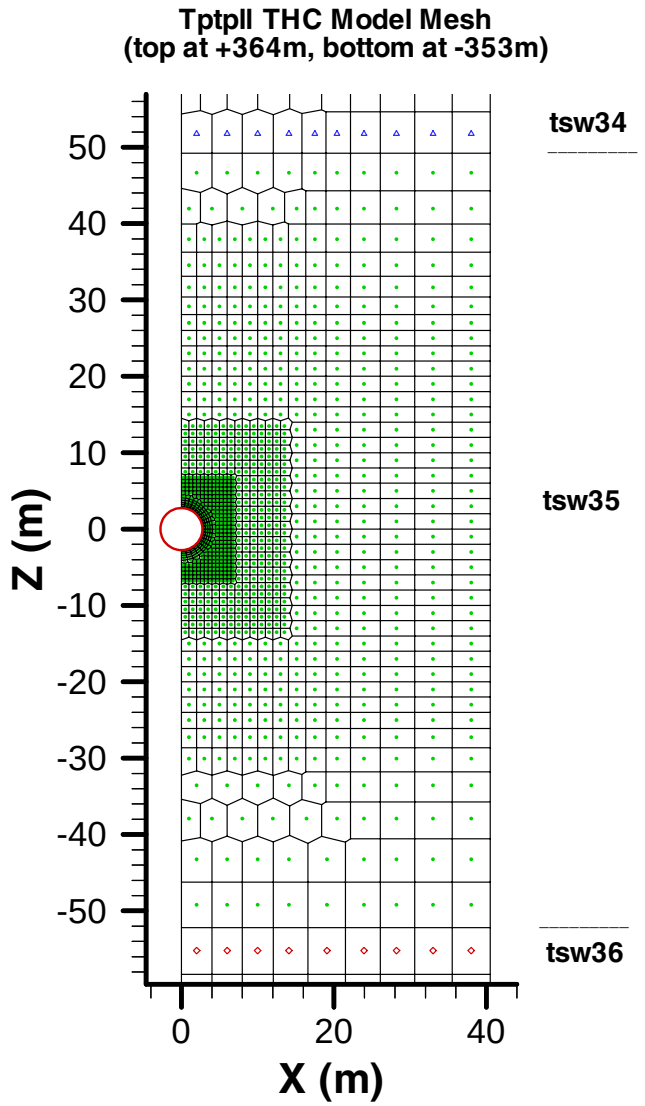

DTN: LB0011DSTTHCR1.002 [161282]

NOTE: Grid detail around (0, 0) is shown in Figure 6.7-2.

Figure 6.7-1. TptpII THC Model Mesh with Hydrogeologic Units Shown in the Vicinity of the Drift: Topopah Spring Tuff Middle Nonlithophysal (tsw34—triangles), Lower Lithophysal (tsw35—dots), and Lower Nonlithophysal (tsw36—diamonds) Units

Table 6.7-1. Vertical Mesh Dimensions and Geologic Contacts in the Tptpll THC Model

Model Layer	Top of Layer Elevation (m)	Mesh Top of Layer Z Coordinate (m)
Top	1446.6	363.8
tcw11	1446.6	363.8
tcw12	1419.2	336.4
tcw13	1342.1	259.3
ptn21	1326.5	243.7
ptn22	1323.1	240.3
ptn23	1321.0	238.2
ptn24	1318.2	235.4
ptn25	1312.7	229.9
ptn26	1303.6	220.8
tsw31	1294.1	211.3
tsw32	1279.7	196.9
tsw33	1249.3	166.5
tsw34	1169.2	86.4
tsw35	1132.0	49.2
Drift center	1082.8	0.0
tsw36	1030.6	-52.2
tsw37	997.4	-85.4
tsw38	980.8	-102.0
tsw39	967.0	-115.8
ch1v	956.9	-125.9
ch2v	945.2	-137.6
ch3v	931.9	-150.9
ch4z	919.2	-163.6
ch5z	906.4	-176.4
ch6	892.4	-190.4
pp4	878.5	-204.3
pp3	865.9	-216.9
pp2	833.2	-249.5
pp1	818.2	-264.6
bf3	756.7	-326.1
Bottom	730.0	-352.8

DTNs: LB0011DSTTHCR1.002 [161282] (model),
LB990501233129.004 [111475] (geologic column)

The drift discretization was unchanged from the Tptpmn model. However, gridblock designations were changed to account for a thicker invert (0.8 m) reflecting a more recent drift design (BSC 2003 [162444]). As in the Tptpmn THC Model, the invert was divided into an "upper invert" and a "lower invert" (Figure 6.7-2) for assignment of different thermal conductivities in these zones (Section 4.1.7). The preclosure and postclosure configurations implemented in this model are otherwise similar to those implemented for the Tptpmn Model (Sections 4.1.7 and 6.5.1).

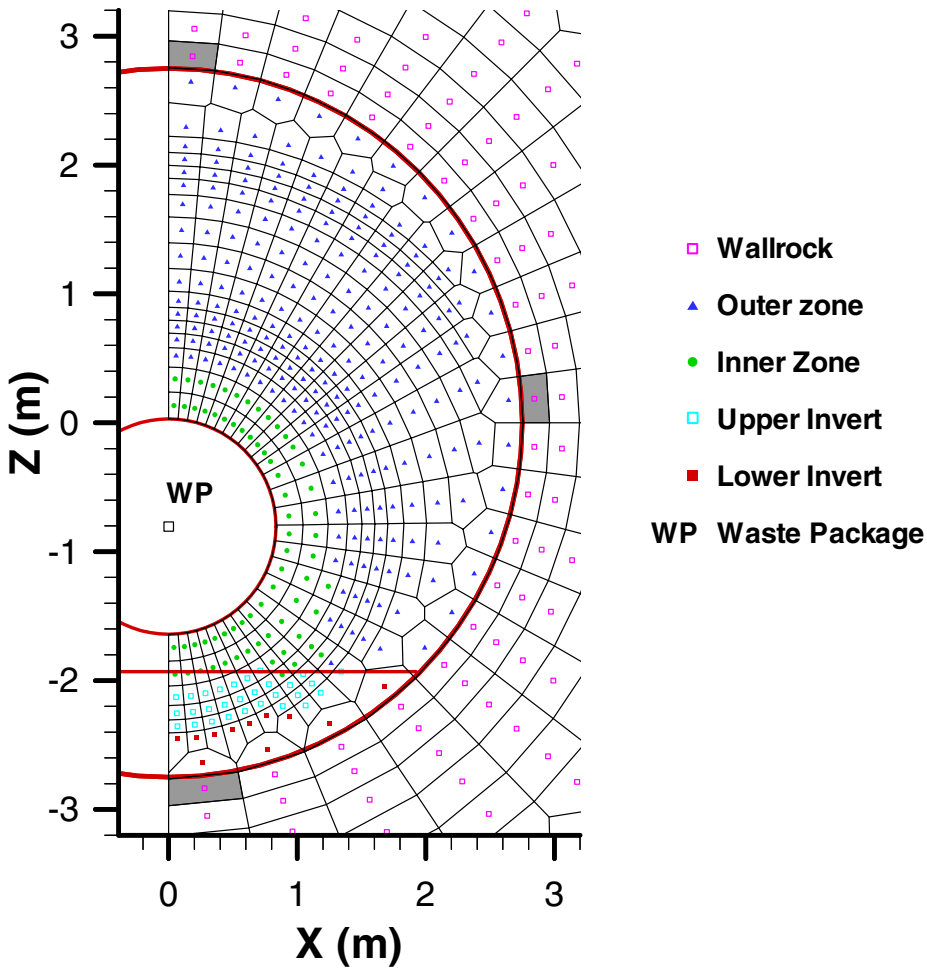

DTN: LB0011DSTTHCR1.002 [161282]

NOTE: Shaded gridblocks are those with top, side, base designations in other figures.

Figure 6.7-2. Discretization of the Repository Drift in the Tptpll THC Model

6.7.2 Boundary Conditions

The boundary conditions were set according to those appropriate for the column location near the repository center (DTN: LB990701233129.002 [125604]) (Table 6.7-2). The pressure and temperatures are constant at the top and bottom boundaries. The initial CO_2 partial pressure in the drift was set to the ambient CO_2 partial pressure in the adjacent wallrock, instead of near-atmospheric (a difference having essentially no effect on model results) as done in the Tptpmn THC Model. As for the Tptpmn THC Model, only the mean infiltration regime was implemented (Table 6.5-3).

6.7.3 Input Data and Modeling Procedure

The Tptpll THC Model was run using TOUGHREACT V2.3 (LBNL 2001 [153101]) and similar input data as discussed in Section 6.5.3 for the Tptpmn THC Model. Exceptions are revised rock properties (Section 4.1.1), revised mineralogy and mineral surface areas (Section 4.1.2,

Attachments II and IV), and an opal phase added to the base-case and extended-case geochemical systems (Table 6.2-2). Calcite was also considered as an equilibrium mineral, with the same precipitation gap as discussed in Section 6.5.3. The time-stepping scheme was also identical to the scheme used for the Tptpmn THC Model.

Rock properties included fracture permeability, porosity, and capillary properties for the Tptpll, (Table 6.4-1) calibrated in part using data from field tests conducted in the Tptpll unit. However, these data are not as recent as data used for the model revision presented in Section 6.8. The REV01 Tptpll properties, compared to Tptpmn properties, reflect a higher fracture porosity, permeability, and capillarity (Table 6.4-1). The revised Tptpll properties in the REV02 model, however, do not reflect possible increased storage owing to the presence of lithophysae, because these effects were still being investigated at the time of this earlier model revision.

Table 6.7-2. Tptpll THC Model REV01 Boundary Conditions

Boundary	Boundary Condition	Reference
Top	T = 16.13°C	Table 4.1-1
	S_g = 0.99	Table 4.1-1
	P = 84725 Pa	Table 4.1-1
	Time-varying infiltration rate (mean infiltration regime only)	Table 6.5-3
	Constant composition of infiltration and PCO_2	Table 6.2-1
Bottom	T = 32.62°C	Table 4.1-1
	S_L = 0.99999	Table 4.1-1
	P = 92000 Pa	Table 4.1-1
	Constant water composition and PCO_2	Table 6.2-1
Sides	No flux for water, gas, heat, and chemical species	Not Applicable
Drift Wall	No flux for water, gas and chemical species (except for CO_2 diffusive flux); conduction only for heat (zero permeability in drift gridblocks)	Not Applicable
Waste Package	Initial full heat load of 1.45 kW/m decreasing with time (due to radioactive decay), and reduced by 70% during the first 50 years (due to heat removal by ventilation)	Attachment VII and Table 6.4-2

NOTES: T = Temperature
S_g = Gas saturation
S_L = Liquid saturation
P = Pressure

6.7.4 Model Runs

Five simulations were performed and are summarized in Table 6.7-3.

Table 6.7-3. Tptpll THC Model REV01 Runs

Infiltration-Property Set (Table 6.5-3)	Geochemical System (Section 6.2.2.2)	Simulation Type	Run ID (Used in DTN: LB0011DSTTHCR1.002 [161282]; also see Attachment X)
Mean Infiltration	None	TH	th6_16_25_g4
Mean Infiltration	Base Case	THC	thc6_16_25_2g4
	Base Case	THC - Ambient	thc6_16_25 _2g4_amb
	Extended Case	THC	thc6_16_25_g4
	Extended Case	THC - Ambient	thc6_16_25_g4_amb

6.7.5 Simulation Results

The model results are presented below in Figures 6.7-3 through 6.7-24. In common with the Tptpmn THC Model, the focus is given to areas in the vicinity of the drift. Profiles of various predicted THC parameters through time are examined at three locations around the modeled drift: crown (model gridblocks F 121 and M 121, side (gridblocks F 44 and M 44) and base (gridblocks F 128 and M 128) (Figure 6.7-2). The locations correspond to the same locations, relative to the drift center, as those in the Tptpmn THC Model (Section 6.5). The output results were tabulated and submitted to the technical database under DTN: LB0011DSTTHCR1.001 [154759] and are discussed further below.

6.7.5.1 Thermohydrology Simulation Results (Tptpll versus Tptpmn)

The calculated trends of TH parameters in the Tptpll unit (Figures 6.7-3 to 6.7-9) are similar to those modeled in the Tptpmn unit. Nevertheless, several differences in the actual values of these parameters are noteworthy. Peak temperatures (shortly after ending ventilation) are higher by approximately 20°C in the Tptpll (Figures 6.7-3 and 6.7-5). Both dry and wet thermal conductivities of the Tptpll are lower than in the Tptpmn (in this case, by 23% and 13%, respectively). The maximum size of the dryout zone, despite the higher temperatures, decreases slightly (approximately 12 m below, 9 m to the side, and 8 m above drift center) (Figure 6.7-4) compared to the dryout extent in the Tptpmn (Figure 6.5-4), because of the higher fracture capillarity in the Tptpll. The time at which maximum dryout is calculated to occur remains near 600 years for the Tptpmn model simulations. (This is also the time at which the model infiltration rate increases from 6 to 16 mm/yr.)

At the base of the drift, fracture saturations in the Tptpll (Figure 6.7-6) are larger than in the Tptpmn and remain non-zero for a large part of the preclosure period (compared to zero values in the Tptpmn model). This results from the thicker invert combined with the higher fracture capillarity in this model. In fractures at locations not shadowed by the drift, and in the matrix, predicted liquid saturations are smaller than in the Tptpmn (Figures 6.7-6 and 6.7-7). In fractures

at the drift crown, these saturations are approximately 60% smaller because of the larger fracture and matrix permeabilities in the Tptpll. Calculated air mass fractions before and after dryout are also lower (higher water vapor content) than in the Tptpmn (Figure 6.7-8), because of the higher temperatures (and thus greater evaporation) in the Tptpll (Figure 6.7-5).

The steady-state (pre- and post-thermal load) vertical liquid flux at the drift crown in the Tptpll is close to half that in the Tptpmn (Figure 6.7-9). This is because fracture and matrix permeabilities in the Tptpll are larger (by approximately one order of magnitude) than in the Tptpmn, allowing for more lateral flow around the drift than if the permeabilities were lower. The drift crown remains well below full saturation, and therefore the drift acts as a capillary barrier. For both the Tptpll and Tptpmn cases, the flux peak at rewetting (Figure 6.7-9) may not be fully resolved. More output points over smaller time intervals may be required for a better definition. However, the peak values shown are quite small and correspond to small liquid saturations (Figure 6.7-6) that would be even smaller for simulation times closer to the precise onset of rewetting at the drift crown.

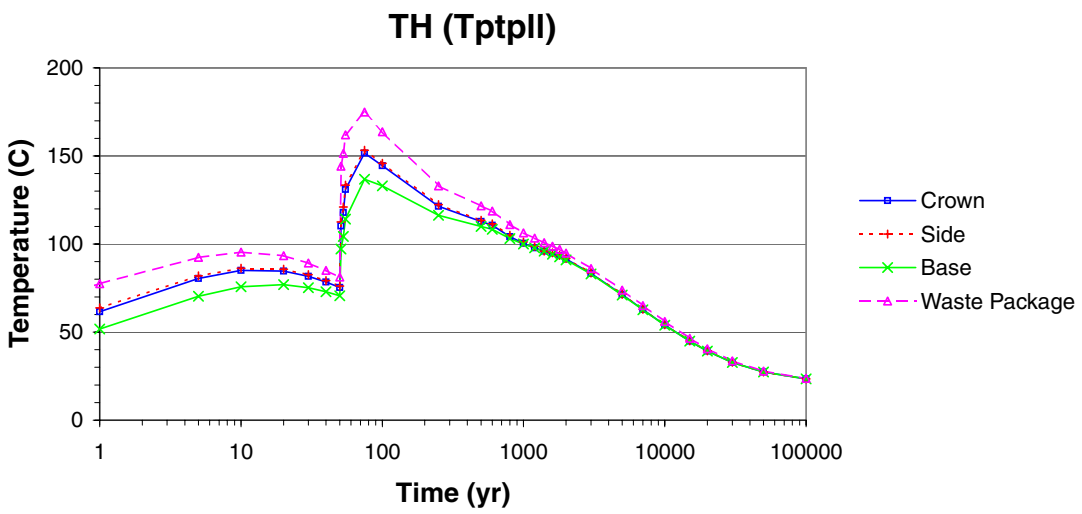

DTN: LB0011DSTTHCR1.001 [154759]

Figure 6.7-3. TH Simulation (Tptpll): Time Profiles of Modeled Temperatures in Fractures (Similar in Matrix) at Three Drift-Wall Locations and in the Waste Package

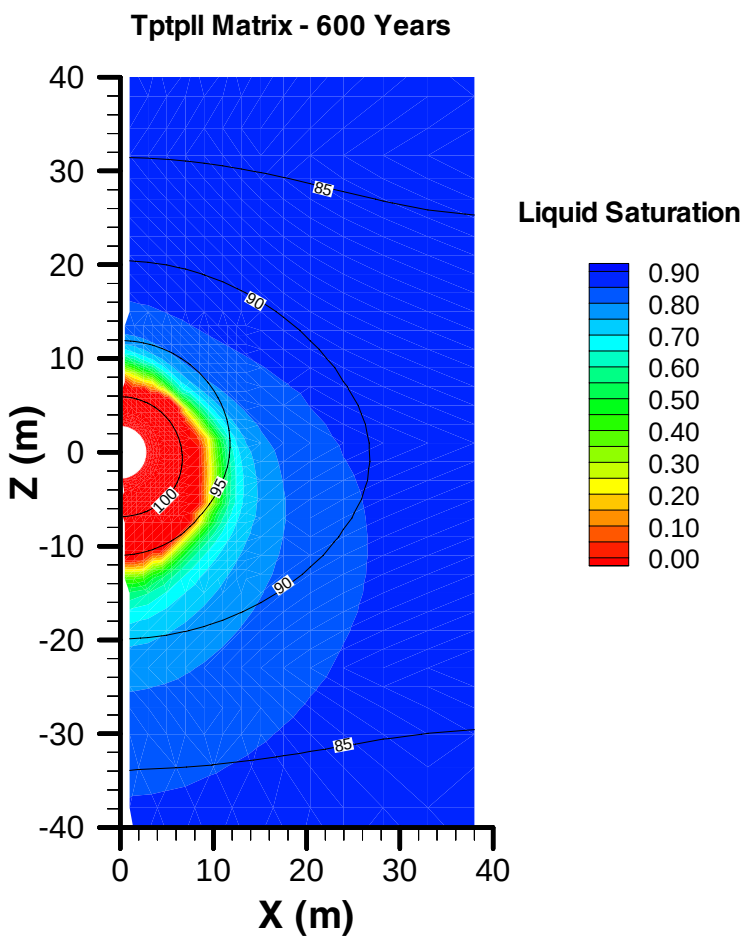

DTN: LB0011DSTTHCR1.002 [161282]

Figure 6.7-4. TH Simulation (Tptpll): Contour Plot of Modeled Temperatures (°C) and Liquid Saturations in the Matrix at 600 Years (Near Maximum Dryout-Mean Infiltration)

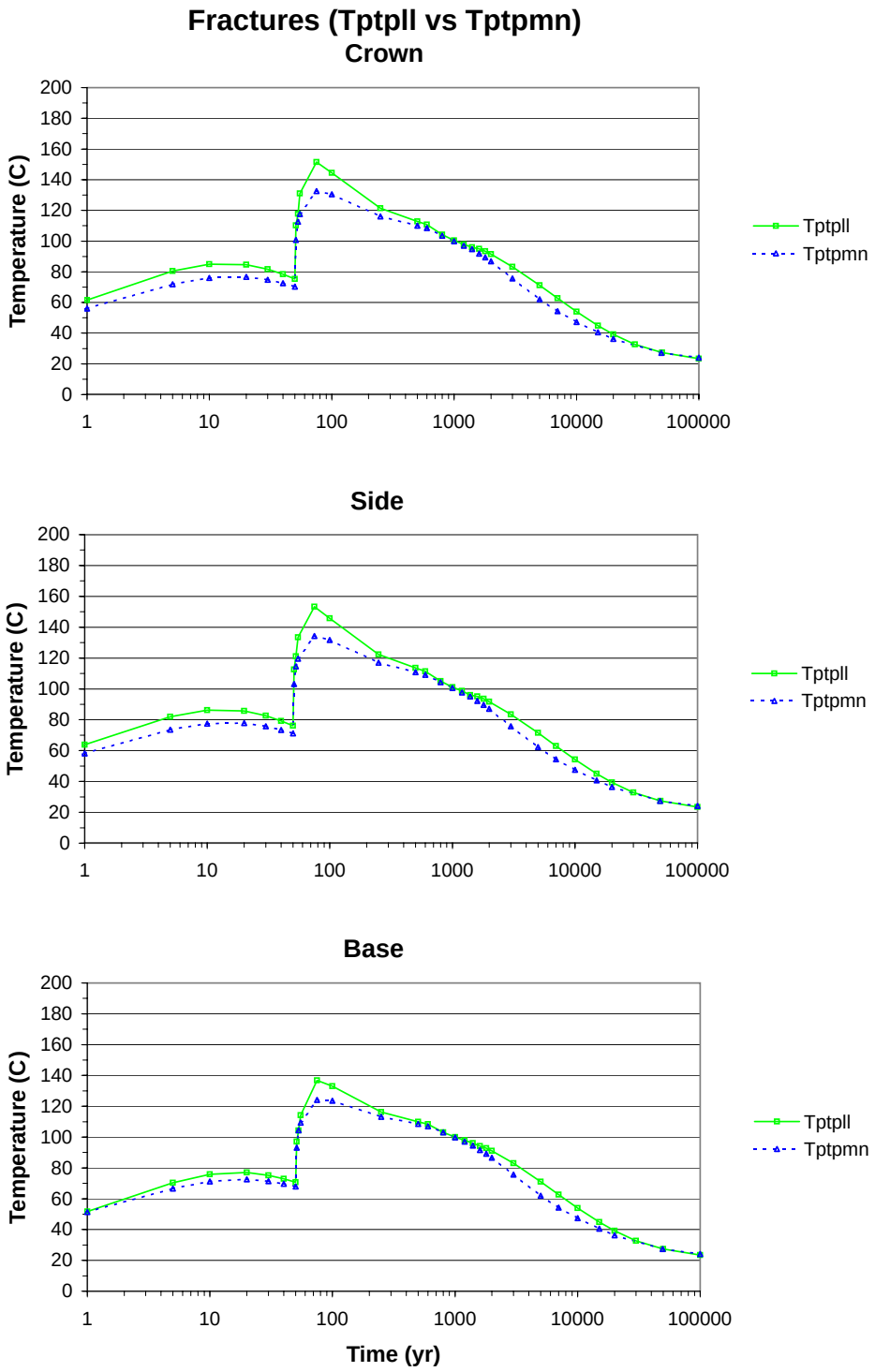

DTN: LB0011DSTTHCR1.001 [154759]

Figure 6.7-5. TH Simulation (Tptpll vs. Tptpmn): Time Profiles of Modeled Temperatures in Fractures at Three Drift-Wall Locations

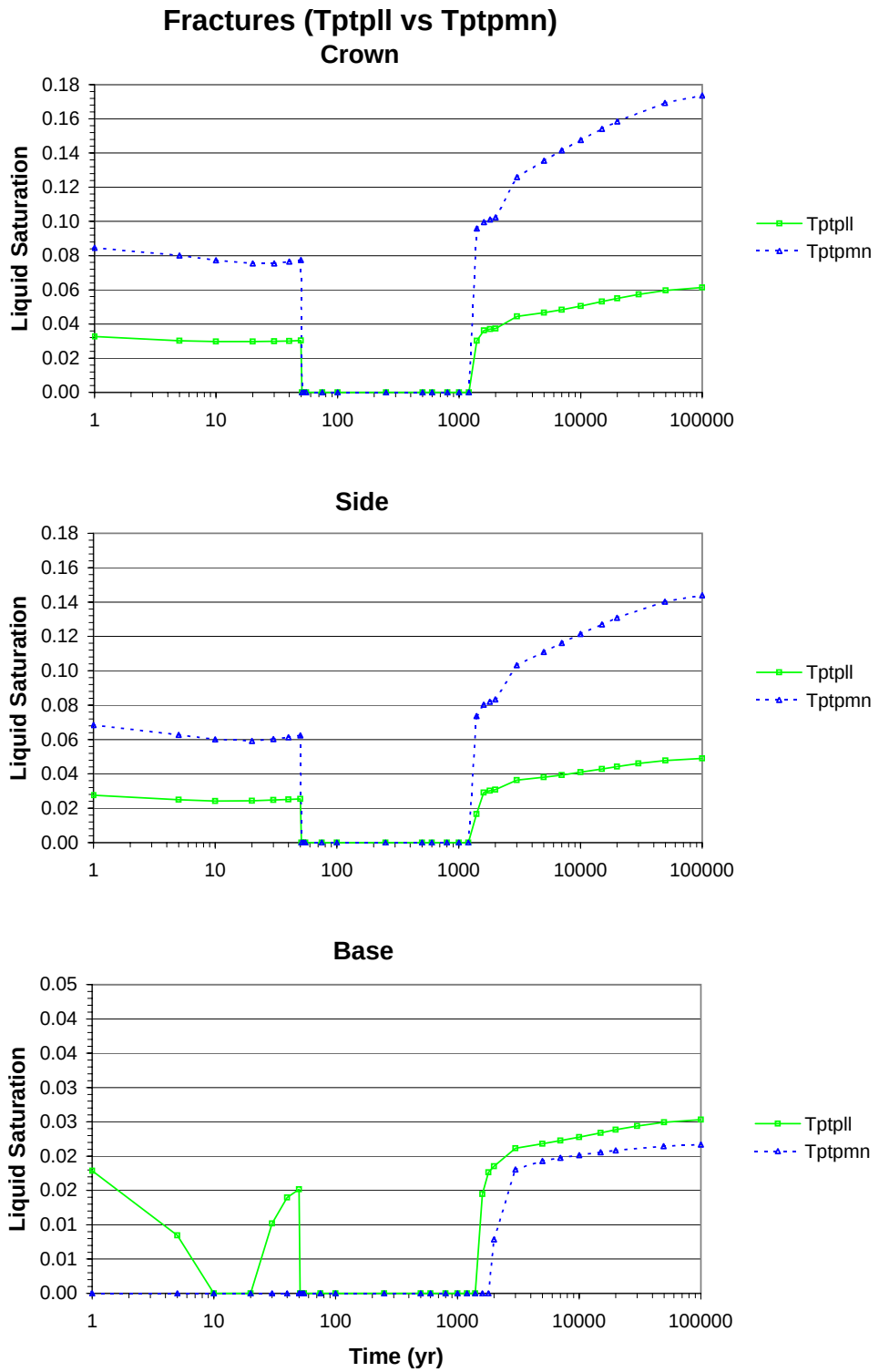

DTN: LB0011DSTTHCR1.001 [154759]

Figure 6.7-6. TH Simulation (Tptpll vs. Tptpmn): Time Profiles of Modeled Liquid Saturations in Fractures at Three Drift-Wall Locations

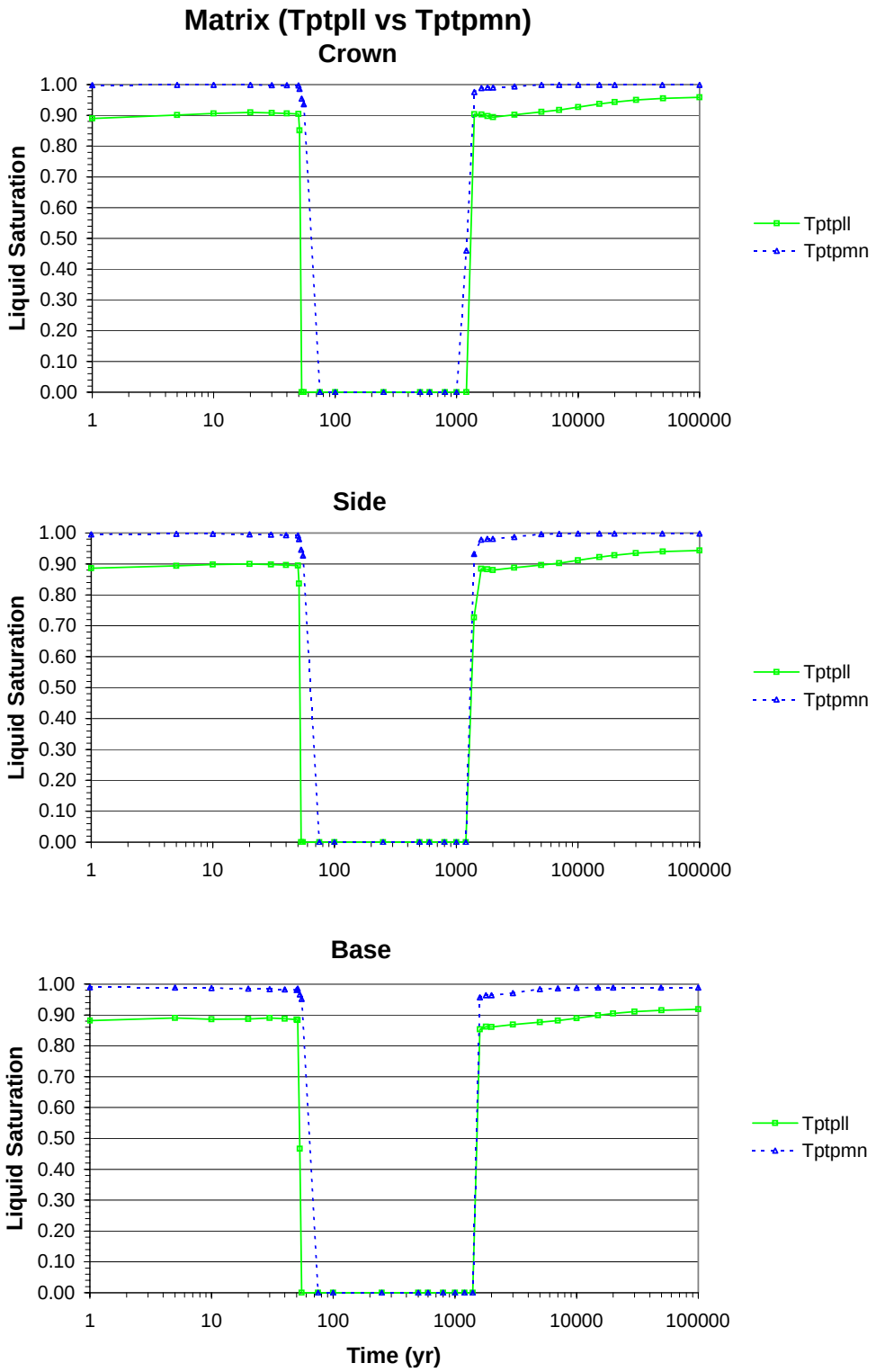

DTN: LB0011DSTTHCR1.001 [154759]

Figure 6.7-7. TH Simulation (Tptpll vs. Tptpmn): Time Profiles of Modeled Liquid Saturations in Matrix at Three Drift-Wall Locations

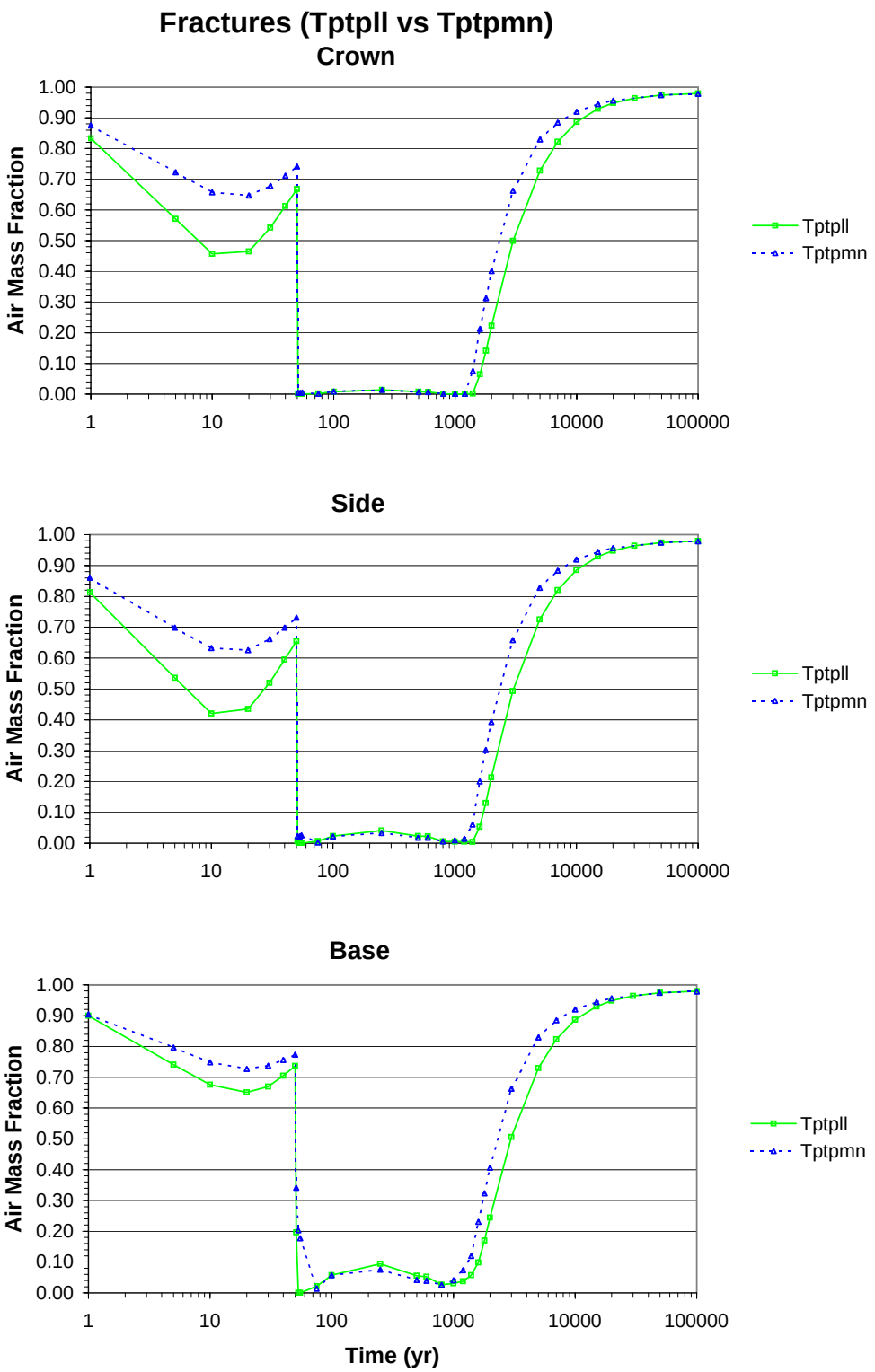

DTN: LB0011DSTTHCR1.001 [154759]

Figure 6.7-8. TH Simulation (Tptpll vs. Tptpmn): Time Profiles of Modeled Air Mass Fractions in the Gas Phase in Fractures at Three Drift-Wall Locations

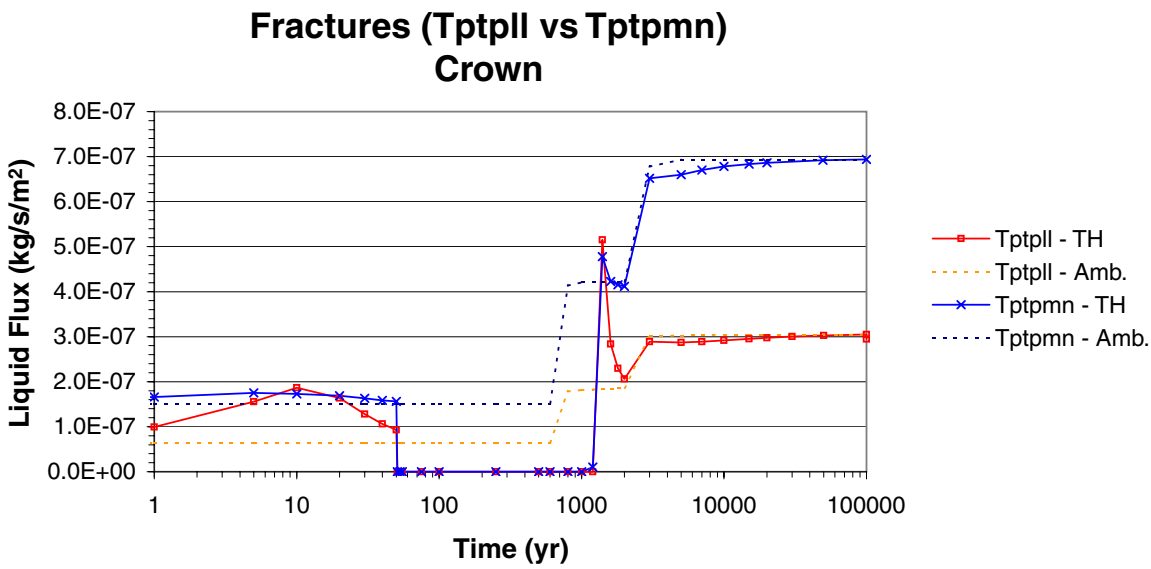

DTN: LB0011DSTTHCR1.001 [154759]

Figure 6.7-9. TH Simulation (Tptpll vs. Tptpmn): Time Profiles of Modeled Water Flux at the Drift Crown

6.7.5.2 THC Simulation Results (Tptpll REV01)

Time profiles of predicted CO_2 and various aqueous species concentrations in fractures are shown in Figures 6.7-10 through 6.7-17. As for the Tptpmn model, results of ambient and heat-load calculations for both the base-case and extended-case geochemical systems are shown on these figures. Ambient trends are fairly steady, with some fluctuations resulting mostly from changes in infiltration rates, and indicate that the ambient geochemical system for this Tptpll model is also fairly well constrained. Consequently, the minor differences in input mineralogic data and mineral surface areas between the Tptpmn model and this Tptpll model have only a small effect on predicted ambient water compositions, at least within the 100,000-year time period investigated. The same can be said for the effect of differences in hydrological properties between both units.

Under thermal loading, modeled concentration trends in fractures for the chemical species in the Tptpll model are similar to those modeled in the Tptpmn. Discussions of model results in addition to those provided below can be found in Section 6.5.5.2.

The base of the drift does not dry out during the entire time span of the preclosure period shown on the time profiles (in contrast to the Tptpmn model results). Evaporation at the base of the drift, combined with the "shadow" effect of the drift, generally results in increased concentrations at this location in both the Tptpmn and Tptpll models. However, because of the higher fracture capillarity in the Tptpll model, evaporative concentration below the drift occurs to a larger degree than in the Tptpmn model. Also, noteworthy differences exist in pH and CO_2, total carbonate (as HCO_3^-), and calcium concentrations at the side of the drift when modeled with the extended system (Figures 6.7-10 through 6.7-13). These concentrations do not return to ambient values after rewetting because of significant calcite precipitation at this location.

Before and after dryout, the greater evaporation caused by higher temperatures results in somewhat higher predicted concentrations of most aqueous species, compared to the Tptpmn model. Note that peak concentrations shown at the time of rewetting in both models (for example, sodium and chloride in Figures 6.7-14 and 6.7-16) reflect mostly the small values of the first, non-zero, liquid-saturation output by the model at a preselected time value. These "first output" saturations differ between simulations, and therefore differences (between simulations) in "first output" concentrations must be evaluated with respect to these saturations. In any case, elevated concentrations are predicted only for small liquid saturations that are not subject to significant fluid movement.

Predicted fluoride concentrations in the Tptpll model under ambient and thermal loading conditions (Figure 6.7-17) are higher than in the Tptpmn model (Figure 6.5-15) because of fluorite (CaF_2) dissolution. This mineral is included as one of the mineral constituents of the Tptpll (and of other units to a lesser extent), while it was not included as a primary mineral in the Tptpmn model. Ambient fluoride concentrations tend toward equilibrium with fluorite (5 to 6 mg/L for the modeled ambient geochemical conditions) because of the fast reaction rate of this mineral. With the extended-case geochemical system, under ambient and thermal loading conditions, modeled calcium concentrations (Figure 6.7-13) are generally smaller than predicted with the base-case system. Therefore, more fluorite is dissolved and higher fluoride concentrations are predicted with the extended-case system. This is most noticeable during the cooling period when, as noted earlier, calcium concentrations drop below ambient values (because of calcite precipitation) and fluoride concentrations remain above ambient concentrations.

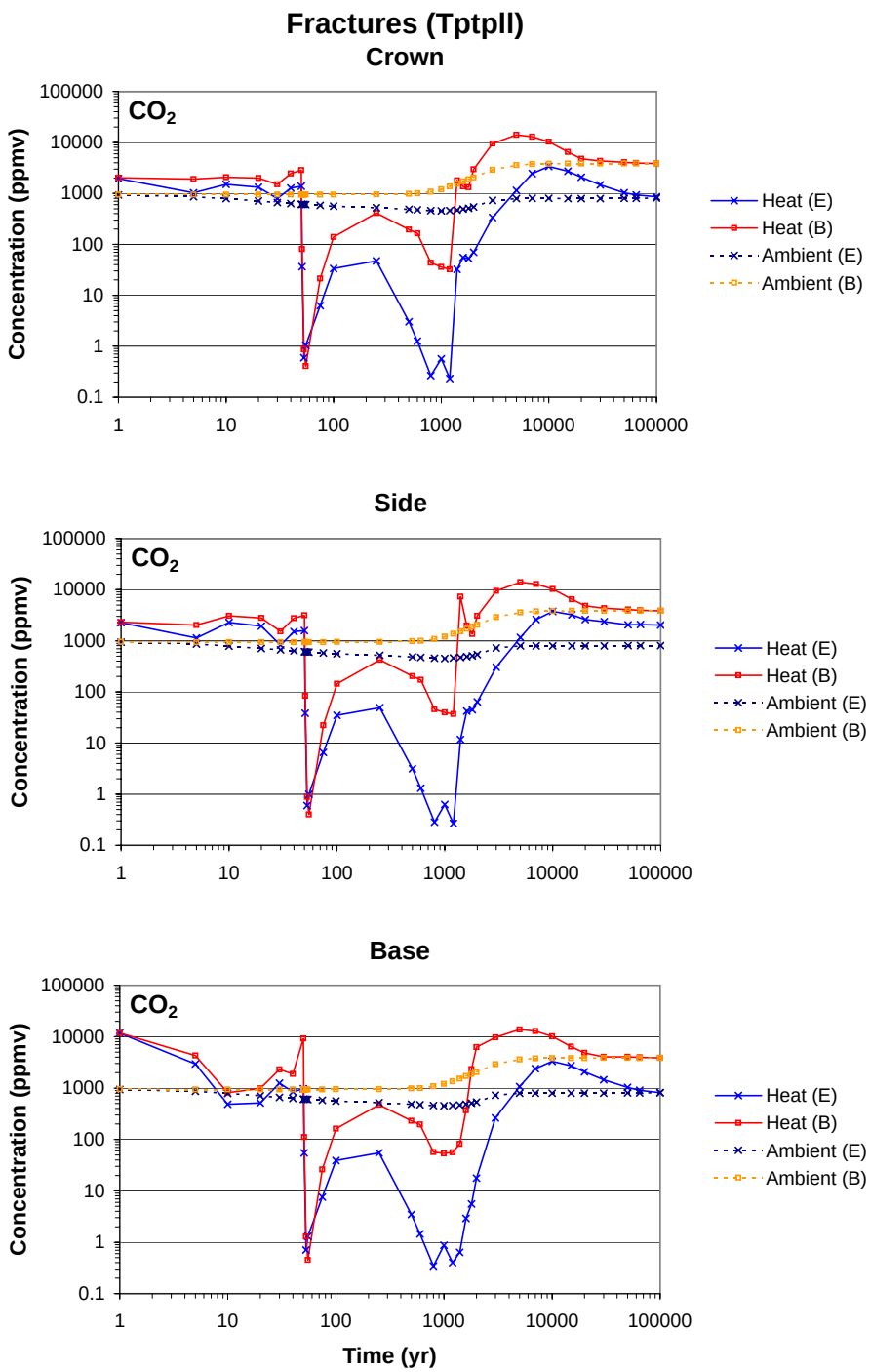

DTN: LB0011DSTTHCR1.001 [154759]

Figure 6.7-10. THC Simulation (Tptpll): Time Profiles of Modeled CO_2 Concentrations in the Gas Phase in Fractures at Three Drift-wall Locations under Heating (Heat) and Non-Heating (Ambient) Conditions for the Extended (E) and Base-Case (B) Geochemical Systems

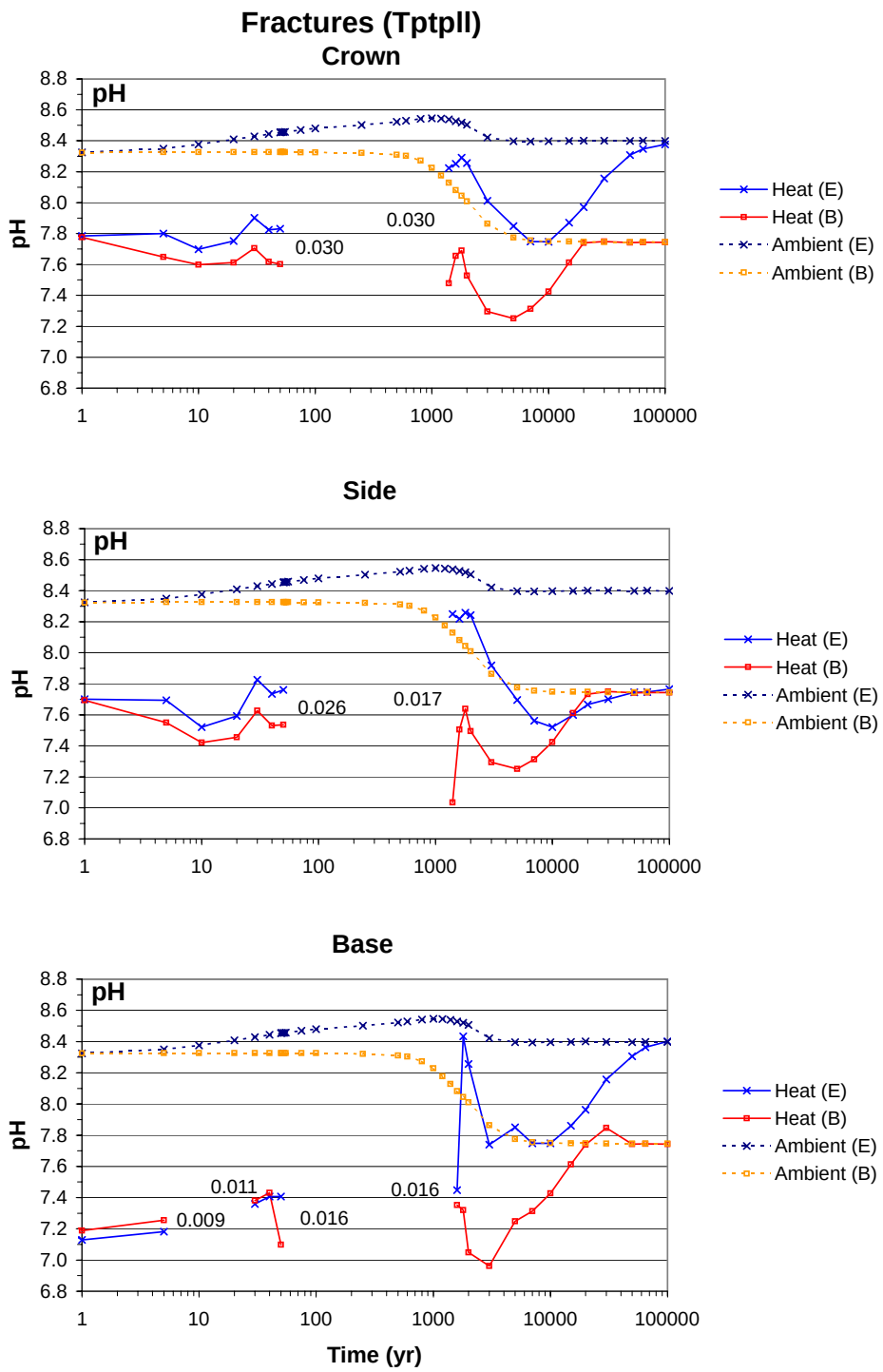

DTN: LB0011DSTTHCR1.001 [154759]

NOTE: The dryout period is left blank. Numbers by each curve indicate the last output liquid saturation before dryout and the first output liquid saturation during rewetting.

Figure 6.7-11. THC Simulation (Tptpll): Time Profiles of the Modeled pH of Fracture Water at Three Drift-Wall Locations under Heating (Heat) and Non-Heating (Ambient) Conditions for the Extended-Case (E) and Base-Case (B) Geochemical Systems

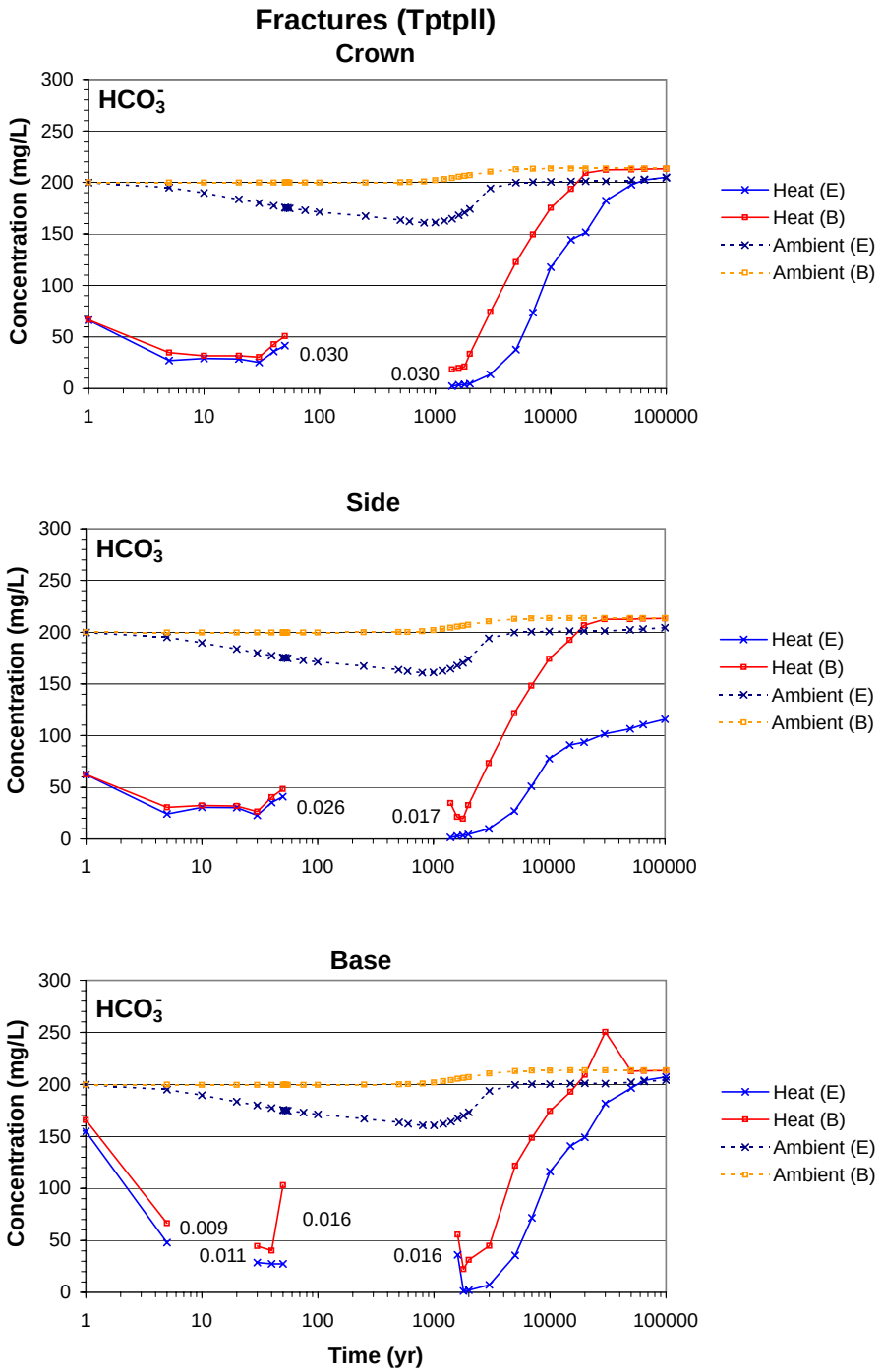

DTN: LB0011DSTTHCR1.001 [154759]

NOTE: The dryout period is left blank. Numbers by each curve indicate the last output liquid saturation before dryout and the first output liquid saturation during rewetting.

Figure 6.7-12. THC Simulation (Tptpll): Time Profiles of Modeled Total Aqueous Carbonate Concentrations (as HCO_3^-) in Fracture Water at Three Drift-Wall Locations under Heating (Heat) and Non-Heating (Ambient) Conditions for the Extended (E) and Base-Case (B) Geochemical Systems

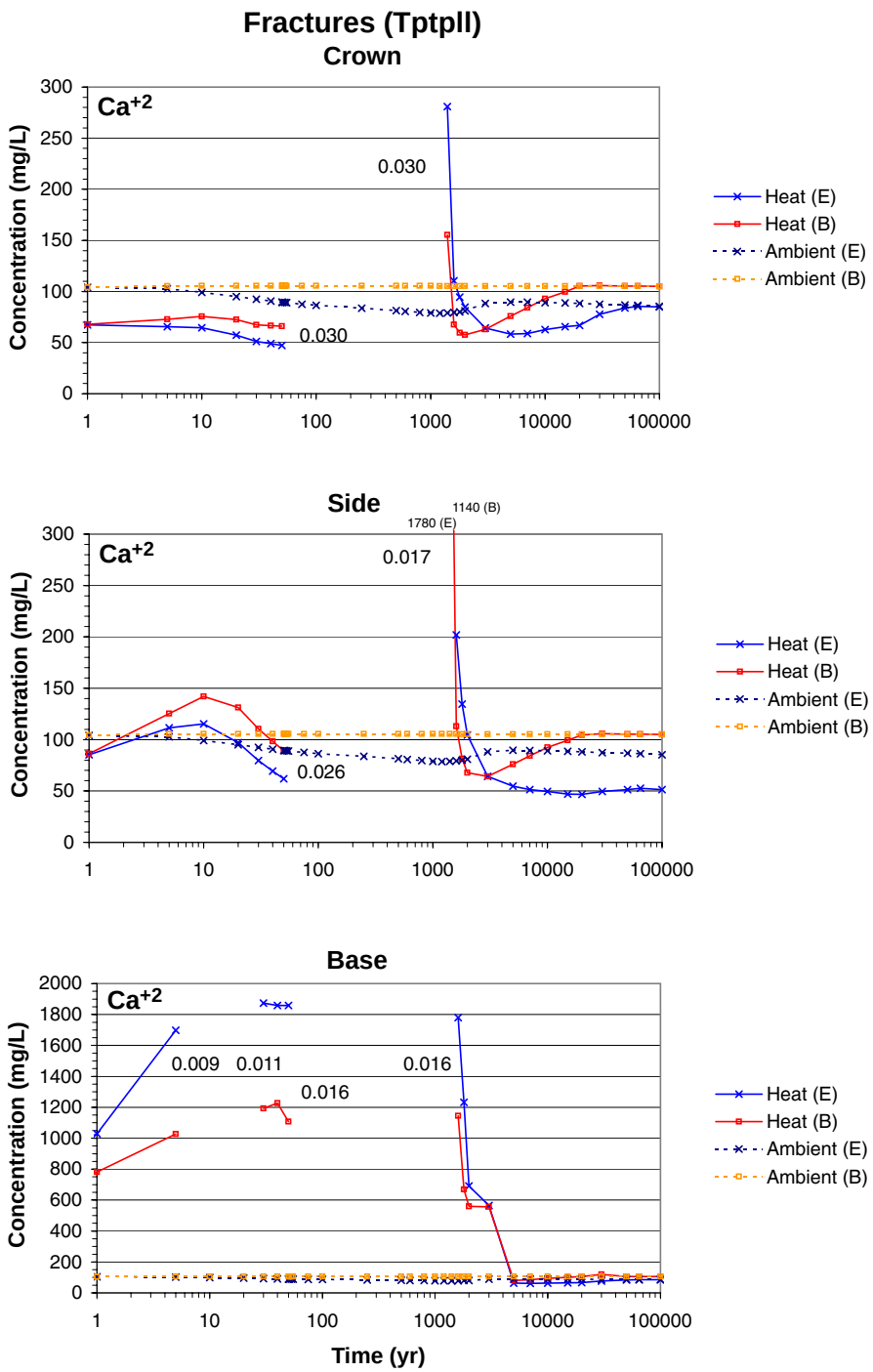

DTN: LB0011DSTTHCR1.001 [154759]

NOTE: The dryout period is left blank. Numbers by each curve indicate the last output liquid saturation before dryout and the first output liquid saturation during rewetting.

Figure 6.7-13. THC Simulation (Tptpll): Time Profiles of Modeled Total Aqueous Calcium Concentrations in Fracture Water at Three Drift-Wall Locations under Heating (Heat) and Non-Heating (Ambient) Conditions for the Extended (E) and Base-Case (B) Geochemical Systems

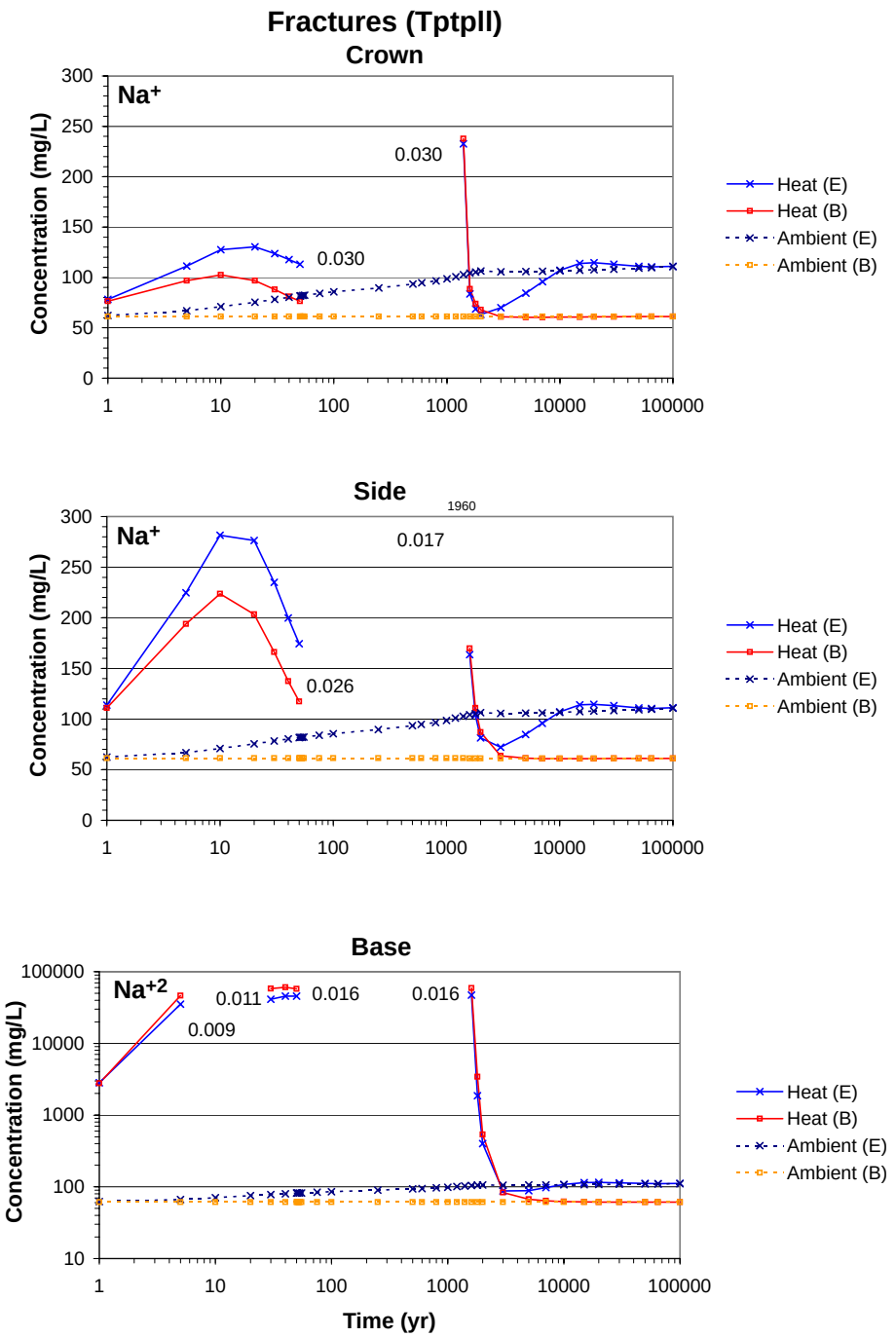

DTN: LB0011DSTTHCR1.001 [154759]

NOTE: The dryout period is left blank. Numbers by each curve indicate the last output liquid saturation before dryout and the first output liquid saturation during rewetting.

Figure 6.7-14. THC Simulation (Tptpll): Time Profiles of Modeled Total Aqueous Sodium Concentrations in Fracture Water at Three Drift-Wall Locations under Heating (Heat) and Non-Heating (Ambient) Conditions for the Extended (E) and Base-Case (B) Geochemical Systems

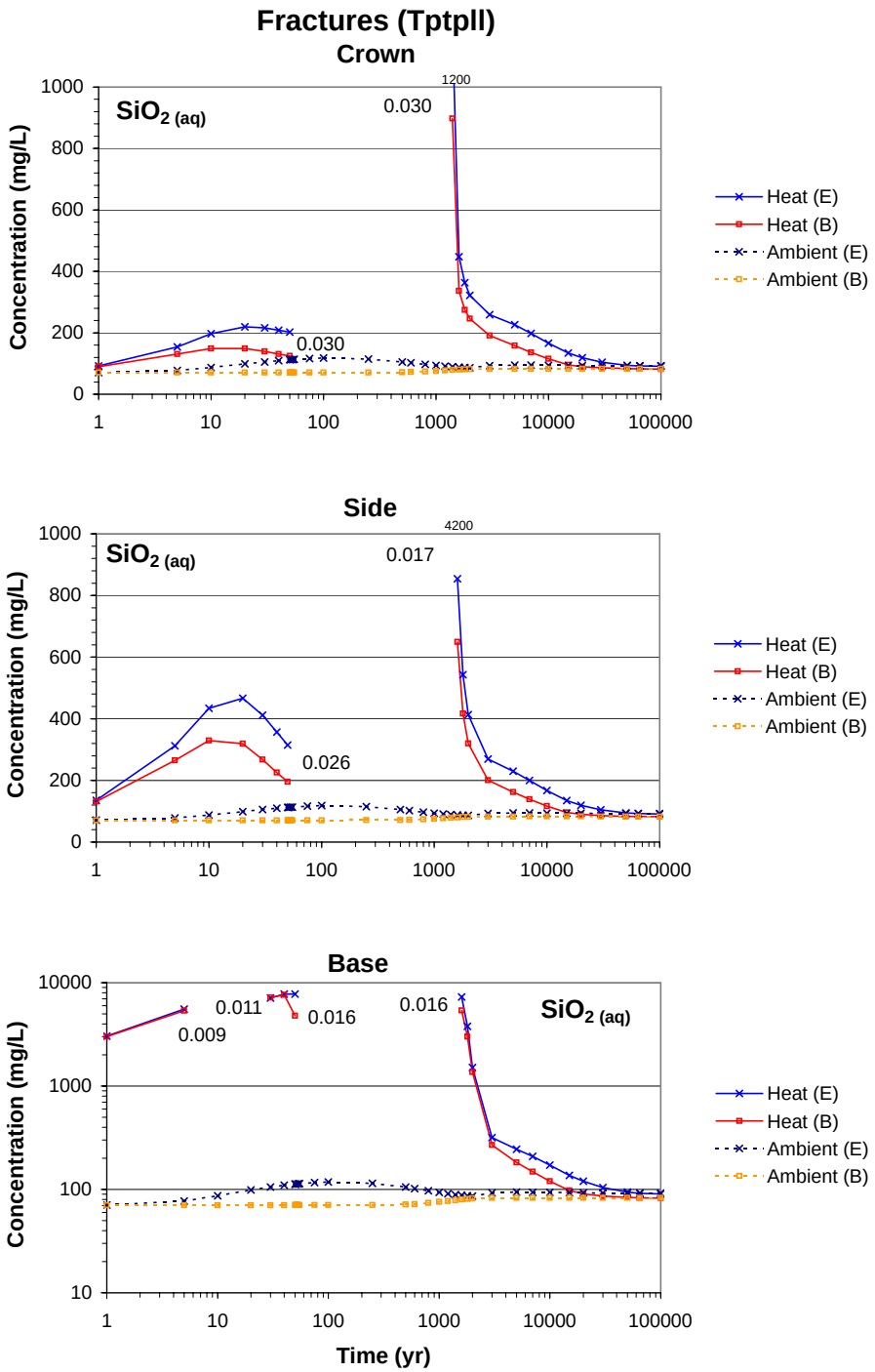

DTN: LB0011DSTTHCR1.001 [154759]

NOTE: The dryout period is left blank. Numbers by each curve indicate the last output liquid saturation before dryout and the first output liquid saturation during rewetting.

Figure 6.7-15. THC Simulation (Tptpll): Time Profiles of Modeled Total Aqueous Silica Concentrations in Fracture Water at Three Drift-Wall Locations under Heating (Heat) and Non-Heating (Ambient) Conditions for the Extended (E) and Base-Case (B) Geochemical Systems

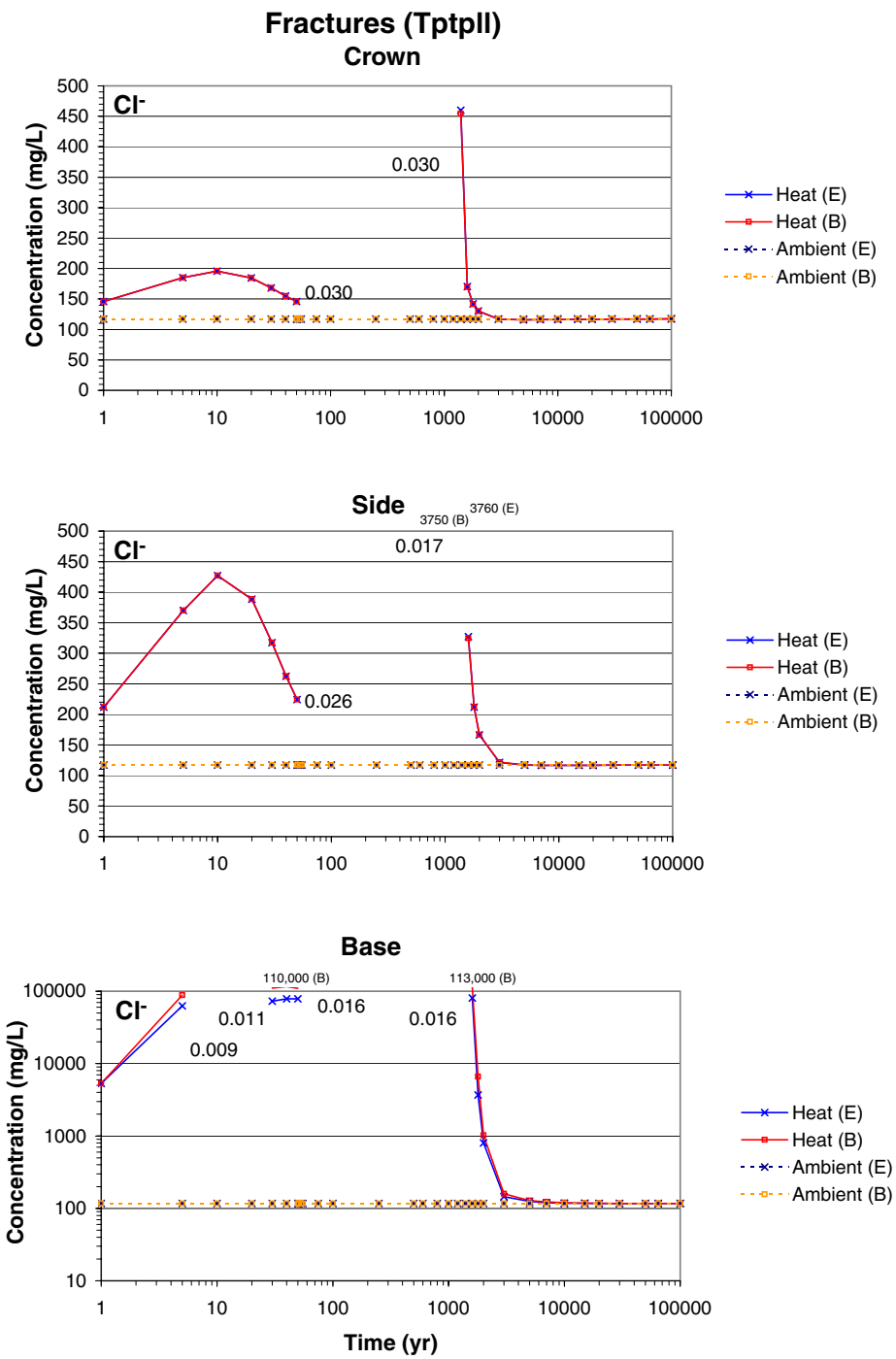

DTN: LB0011DSTTHCR1.001 [154759]

NOTE: The dryout period is left blank. Numbers by each curve indicate the last output liquid saturation before dryout and the first output liquid saturation during rewetting.

Figure 6.7-16. THC Simulation (Tptpll): Time Profiles of Modeled Total Aqueous Chloride Concentrations in Fracture Water at Three Drift-Wall Locations under Heating (Heat) and Non-Heating (Ambient) Conditions for the Extended (E) and Base-Case (B) Geochemical Systems

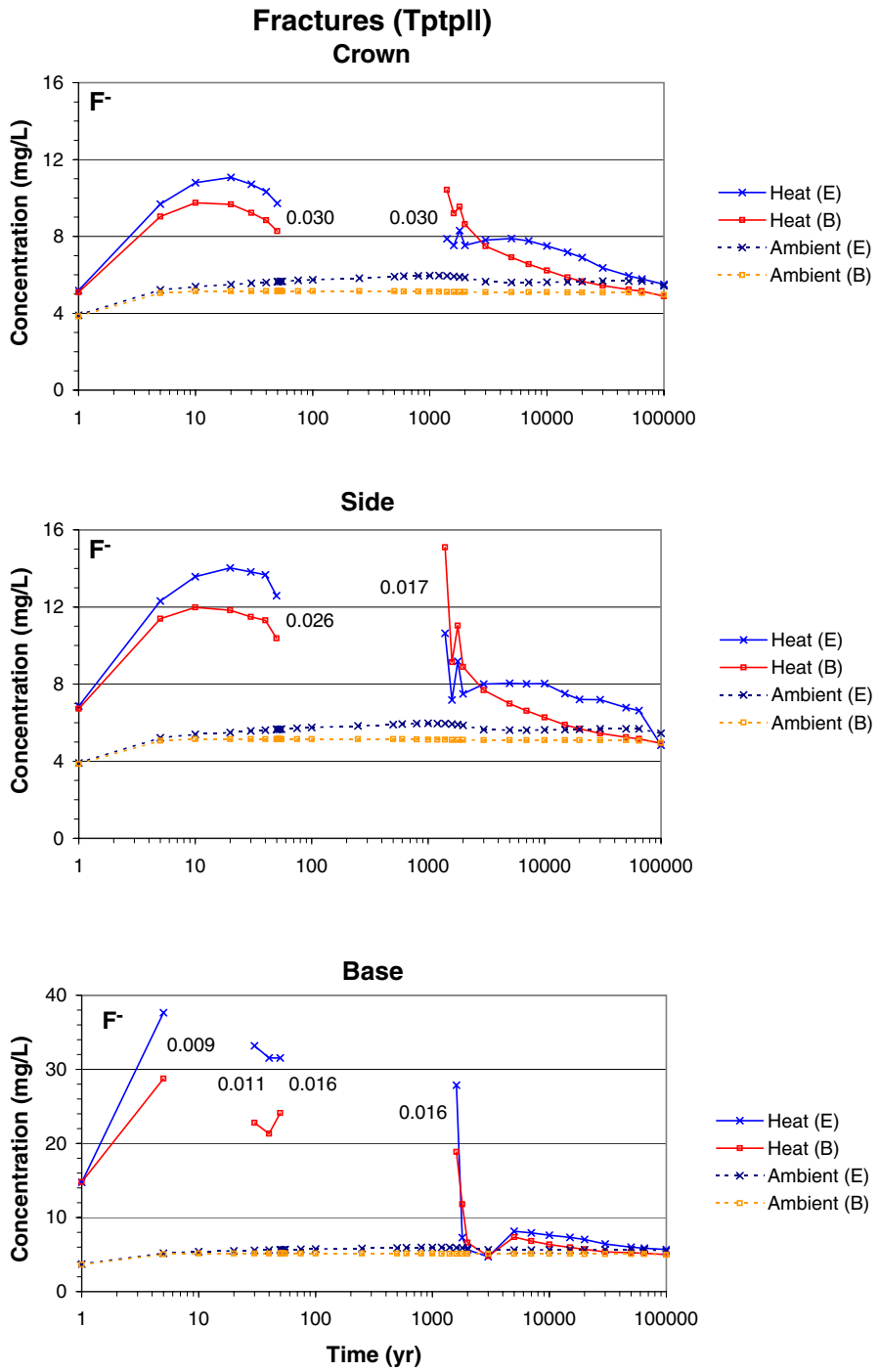

DTN: LB0011DSTTHCR1.001 [154759]

NOTE: The dryout period is left blank. Numbers by each curve indicate the last output liquid saturation before dryout and the first output liquid saturation during rewetting.

Figure 6.7-17. THC Simulation (Tptpll): Time Profiles of Modeled Total Fluoride Concentrations in Fracture Water at Three Drift-Wall Locations under Heating (Heat) and Non-Heating (Ambient) Conditions for the Extended (E) and Base-Case (B) Geochemical Systems

The pattern in fracture porosity changes around the drift is similar to that predicted in the Tptpmn model, with a reduction concentrated in a zone approximately 9 m above drift center, coinciding with the maximum extent of the dryout zone (Figures 6.7-18 through 6.7-22). Note that irregular patterns in these figures result, in part, from numerical effects. In light of the fact that the natural system is heterogeneous (e.g., see Section 6.6.2), these numerical effects are not important. They result from very small disturbances in calculated mineral precipitation amounts and become visible because of the cumulative effect over long simulated periods of time.

A larger fracture porosity reduction (near 1%) occurs at the base of the drift than predicted with the Tptpmn model. This decrease results from higher evaporative concentration (from higher temperature) than in the Tptpmn. As in the Tptpmn simulations, amorphous silica accounts for most of the porosity decrease between approximately 600 and 2,000 years (mostly near or below 0.3%), followed by calcite precipitation at later stages of cooling accounting for the remaining bulk of the porosity decrease (up to 1% after 100,000 years) (Figure 6.7-20). Late calcite precipitation is caused by the warming of percolating waters as they flow back towards the vicinity of the drift which has not completely cooled. As in the Tptpmn model, the porosity decrease predicted with the base-case and extended-case geochemical systems is similar, with generally more late calcite precipitation predicted using the extended-case system.

Clays, and primarily illite (Figure 6.7-21), precipitate in very small quantities. As in the Tptpmn model, stellerite (a calcium zeolite) is predicted to dissolve in the fractures of most gridblocks (Figures 6.7-22a and b). Relatively minor and short-lived stellerite precipitation does occur below the drift in fractures and matrix during the initial cooling stage (Figure 6.7-22a). Precipitation of other zeolites is negligible in the vicinity of the drift.

The method for coupling fracture permeability to fracture porosity is the same here as implemented in the Tptpmn simulations (Sections 6.5 and 6.6). Some flux reduction at the drift crown, mostly after 20,000 years, is predicted using the extended geochemical system (Figure 6.7-24), because more calcite precipitates at this location than with the base-case system. However, the mineral precipitation pattern around the drift is irregular, an artifact in part caused by numerical effects, and therefore calculated flux variations may be exaggerated. Mineral precipitation is predicted to decrease the fracture permeability around the drift sufficiently to have a small effect on liquid saturations (Figure 6.7-23), but not enough to affect the general thermal hydrology around the drift. A similar conclusion was reached for the Tptpmn model using both homogeneous (Section 6.5) and heterogeneous (Section 6.6) fracture permeability distributions. However, in both these models, as mentioned earlier, the precipitation of minerals upon influx of water in gridblocks that remain dry was not taken into account. More recent simulations presented in Section 6.8 account for this effect, and consider a smaller initial fracture porosity. These simulations show a significantly greater decrease in porosity above the drift, leading to a noticeable diversion of water percolating around the drift.

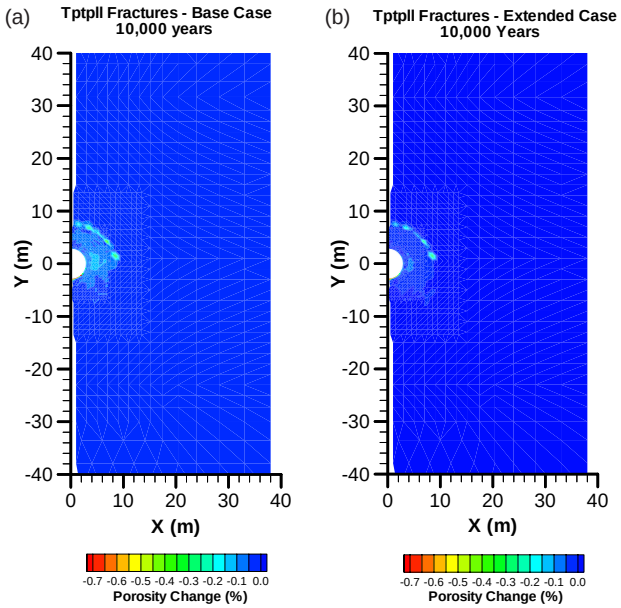

DTN: LB0011DSTTHCR1.002 [161282]

NOTE: Decrease in porosity is due to the precipitation of primarily amorphous silica between 600 and 2,000 years.

Figure 6.7-18. THC Simulation (Tptpll): Contour Plot of Modeled Fracture Porosity Change at 10,000 Years for (a) Base-Case Geochemical System and (b) Extended-Case System

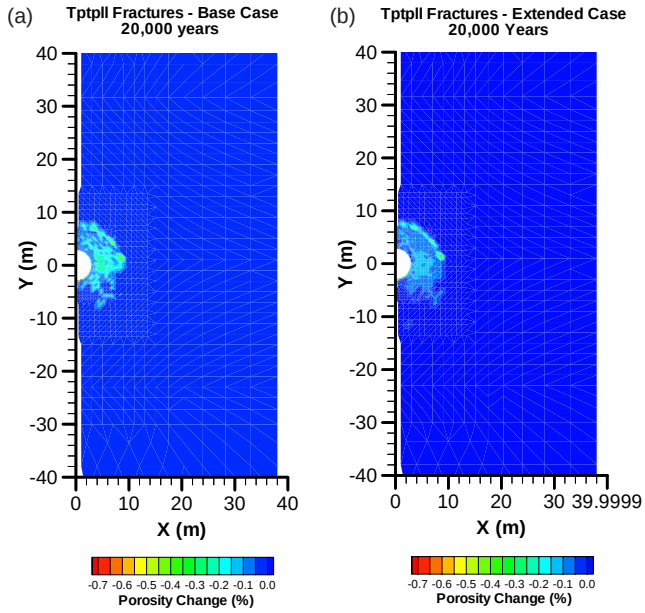

DTN: LB0011DSTTHCR1.002 [161282]

NOTE: Decrease in porosity is due primarily to deposition of calcite in addition to earlier precipitated amorphous silica.

Figure 6.7-19. THC Simulation (Tptpll): Contour Plot of Modeled Fracture Porosity Change at 20,000 Years for (a) Base-Case Geochemical System and (b) Extended-Case System

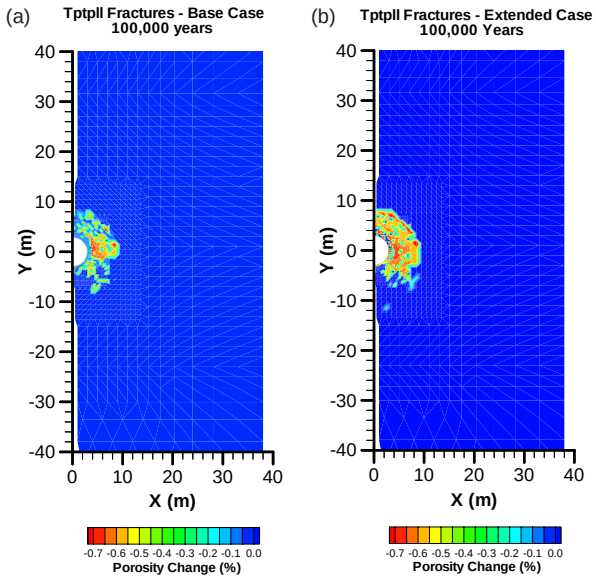

DTN: LB0011DSTTHCR1.002 [161282]

NOTE: Decrease in porosity is due primarily to late deposition of calcite in addition to earlier precipitated amorphous silica.

Figure 6.7-20. THC Simulation (Tptpll): Contour Plot of Modeled Fracture Porosity Change at 100,000 Years for (a) Base-Case Geochemical System and (b) Extended-Case System

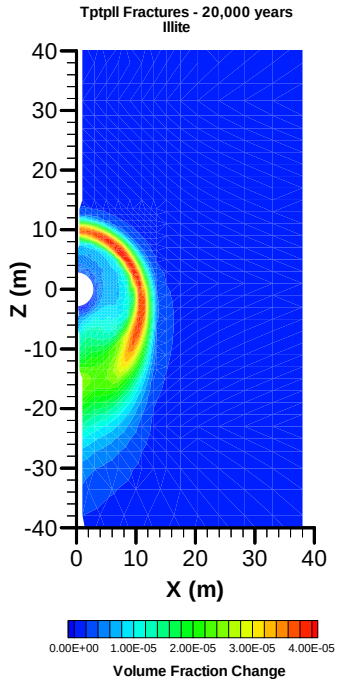

DTN: LB0011DSTTHCR1.002 [161282]

NOTE: Pattern and amounts do not vary significantly after the time of maximum dryout around 600 years.

Figure 6.7-21. THC Simulation (Tptpll): Contour Plot of Modeled Volume Fraction Change Due to Illite Precipitation in Fractures at 20,000 Years

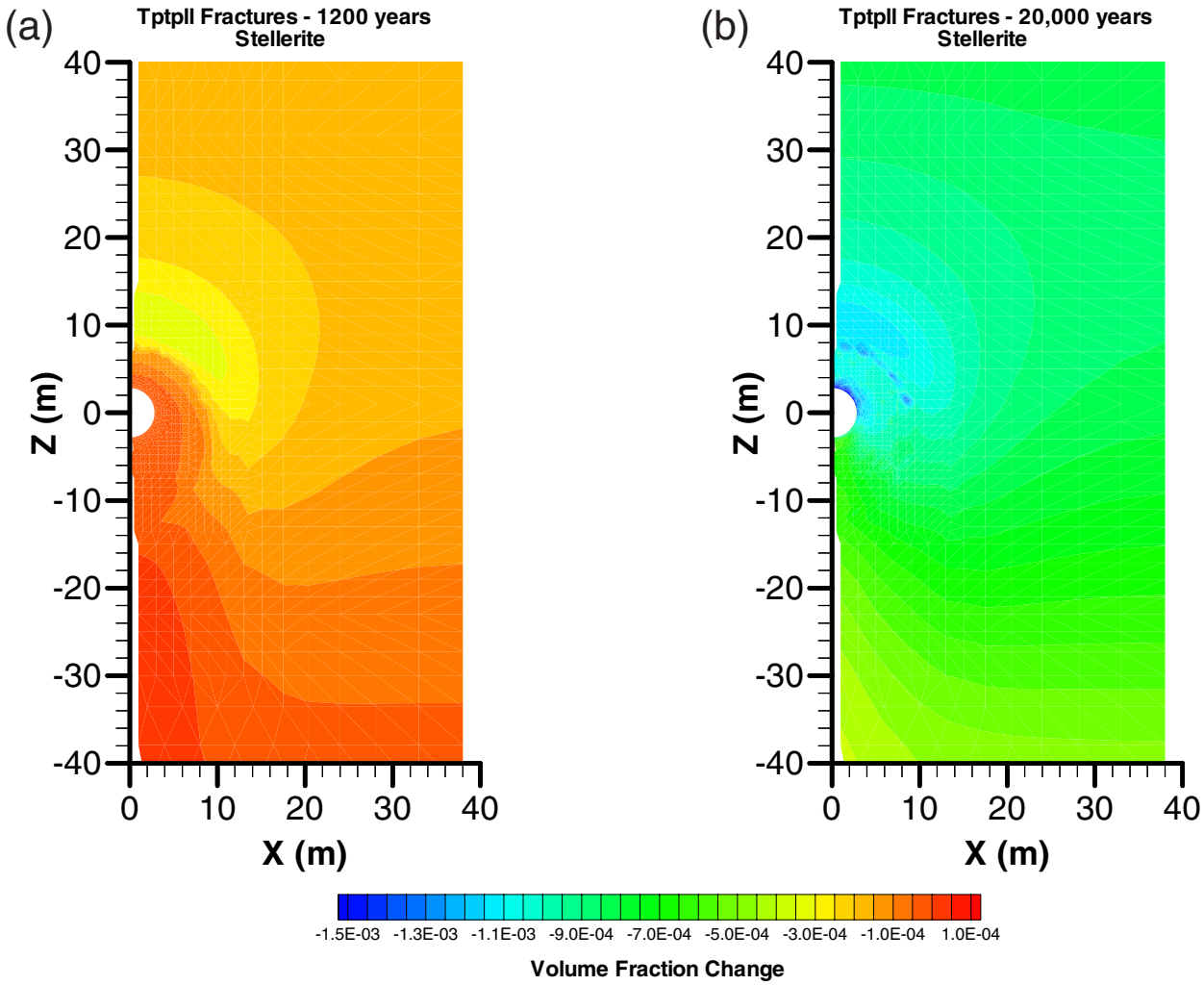

DTN: LB0011DSTTHCR1.002 [161282]

NOTE: Precipitation of other zeolites is negligible.

Figure 6.7-22. THC Simulation (Tptpll): Contour Plot of Modeled Volume Fraction Change Due to Stellerite (Ca-Zeolite) Precipitation in Fractures at (a) 1,200 Years (Some Precipitation below the Drift) and (b) at 20,000 Years (Dissolution)

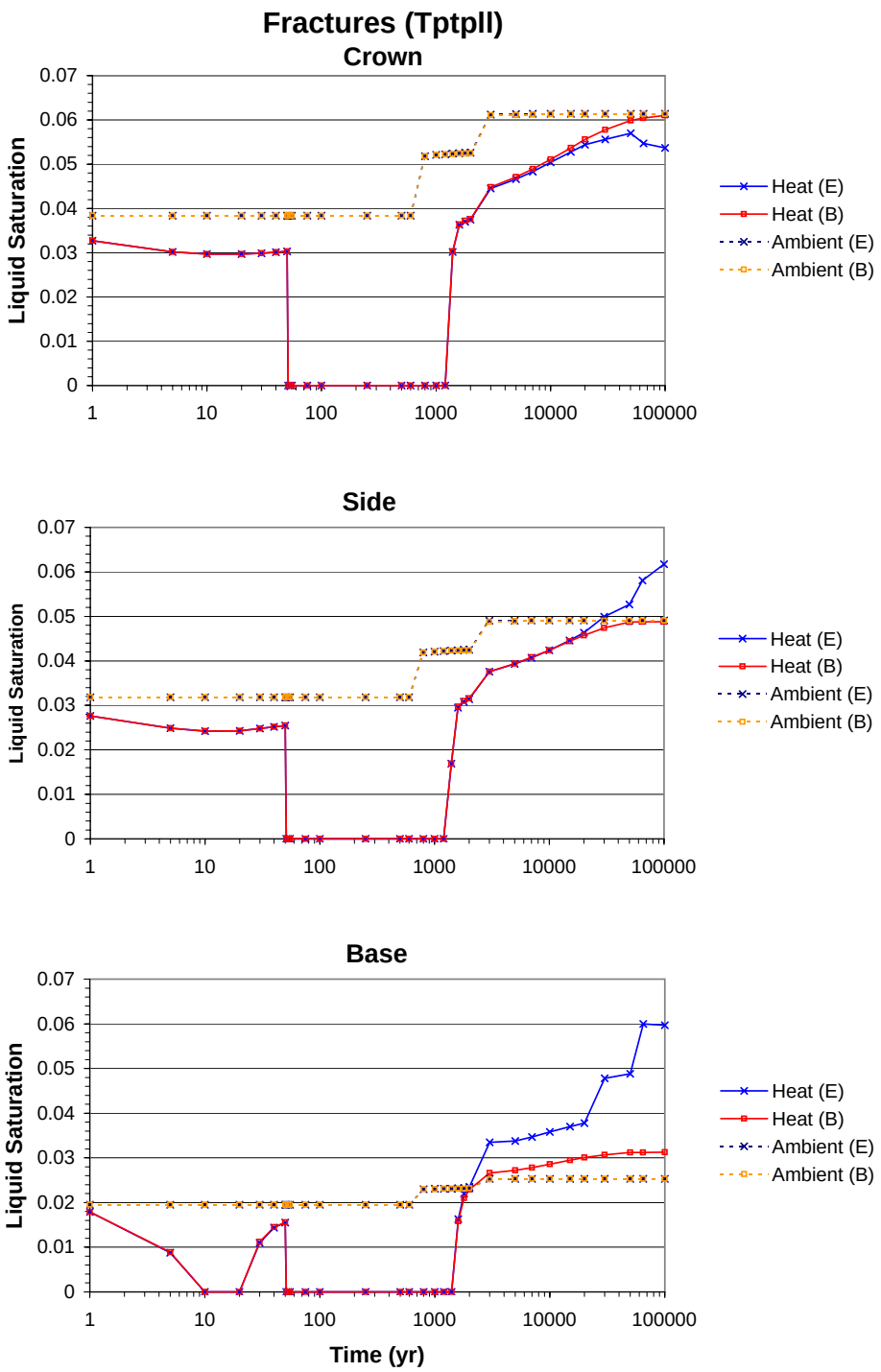

DTN: LB0011DSTTHCR1.001 [154759]

Figure 6.7-23. TH and THC Simulations (Tptpll): Comparison of Modeled Liquid Saturations in Fractures at Three Drift-Wall Locations under Heating (Heat) and Non-Heating (Ambient) Conditions for the Extended-Case (E) and Base-Case (B) Geochemical Systems

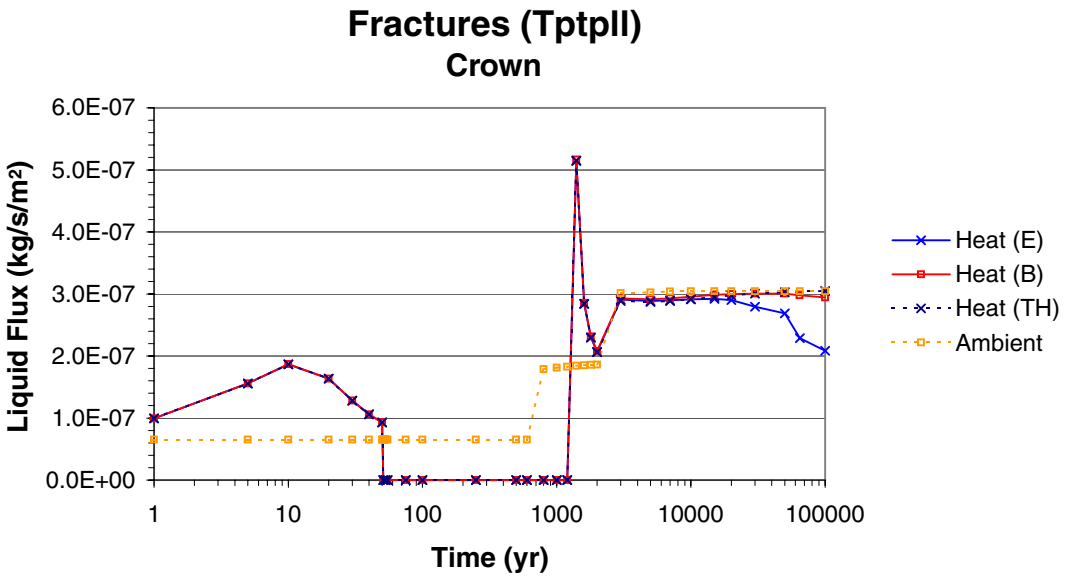

DTN: LB0011DSTTHCR1.001 [154759]

NOTE: Flux variations after 20,000 years may be exaggerated (see text).

Figure 6.7-24. TH and THC Simulations (Tptpll): Comparison of Modeled Liquid Flux at the Drift Crown in Fractures under Heating (Heat) and Non-Heating (Ambient) Conditions for the Extended-Case (E) and Base-Case (B) Geochemical Systems, and without Chemical Reactions (TH)

6.8 Tptpll THC MODEL REV02

The Tptpll THC Model REV02 presented in this section is an update of the REV01 model presented in Section 6.7. This model uses the same stratigraphic column and numerical grid (including drift design) as the REV01 model, but with updated rock thermal and hydrological properties. In-drift thermal properties remain unchanged since the REV01 model. Key elements of this model include:

- Initial heat load of (1.45 kW/m) (Attachment VIII)
- 50-year preclosure period with 86.3% ventilation efficiency
- Drift in the Tptpll unit
- Model stratigraphy at a location near the center of the repository (at approximately Nevada State Plane coordinates E170572, N233195)
- Use of an extended-case geochemical system (Section 6.2.2.2)
- Drift wall open to fluid and gas advective and diffusive fluxes
- Vapor pressure lowering due to capillary pressure (Section 6.4.6)
- Updated rock thermal and hydrological properties (Section 4.1.2)
- Updated thermodynamic data (Attachment VI and Section 4.1.4)
- Updated kinetic data (Section 4.1.5 and Table 4.1-4)
- Use of most recent TOUGHREACT V3.0 (LBNL 2002 [161256]). This version takes into account the precipitation of solids in dry gridblocks where water influx occurs and therefore models more precisely the mineral deposition at the boiling front.

In addition, this revised model was used to conduct a broader range of evaluations than done previously with the Tptpll THC Model REV01, including simulations using:

- Different input thermodynamic data (ambient conditions)
- Five different input water compositions (Section 6.2.2.1 and Table 6.2-1)
- Fixed and variable infiltration rates
- Different water-vapor-pressure models (with and without vapor-pressure lowering)
- Two values of CO_2 gas molecular diameter (resulting in a six-fold difference in the diffusion coefficient).

6.8.1 Numerical Mesh (Tptpll)

Simulations of thermal loading were performed on a vertical 2-D mesh identical to the mesh described in Section 6.7.1 (Figure 6.7-1), and representing the same stratigraphic column (Table 6.7-1). The drift discretization was not changed from REV01 (Figure 6.7-2), with the same preclosure and postclosure configurations as implemented previously (Section 4.1.7 and 6.7.1).

Simulations of ambient conditions (no thermal load) were run with a one-dimensional (vertical column) grid having the same stratigraphy and vertical discretization as the Tptpll 2-D mesh. This 1-D model does not have a drift opening and uses uniform vertical gridding through the area cutting across the drift on Figure 6.7-2. This approach is different than for REV01 ambient simulations (Section 6.7), which were carried out on the same 2-D mesh (including a drift opening) as used for simulating thermal loading. The use of 1-D columns here was adopted to speed up the computational effort. Because of the no-flow boundary conditions existing on each side of the model mesh, the horizontal geologic contacts, and the laterally continuous rock properties, 2-D simulations under ambient conditions are essentially the same as 1-D simulations (vertical flow only). Close to the drift, however, flow is diverted around the drift opening because of the capillary barrier created by this opening. Therefore, the only differences between 1-D and 2-D ambient simulations result from the effect of the drift opening.

6.8.2 Boundary Conditions

Boundary conditions were set as in the Tptpll THC Model REV01 (Section 6.7.2), except for the higher preclosure ventilation efficiency and another important difference: the drift wall was specified open to advective gas and liquid fluxes (Section 4.1.7) (Table 6.8-1). Also, three cases of infiltration were considered, as shown below in Table 6.8-2.

One-dimensional simulations of ambient conditions were run with the same boundary conditions as the 2-D runs, except that these simulations did not include a drift opening. A constant infiltration rate of 6 mm/yr was used in 1-D simulations to evaluate the model sensitivity to thermodynamic data (Section 6.8.5.1). The Mean Infiltration case in Table 6.8-2 (step-wise infiltration increase) was used for all other ambient simulations (Section 6.8.5.2).

Table 6.8-1. Tptpll THC Model REV02 Boundary Conditions

Boundary	Boundary Condition	Reference
Top	T = 16.13°C	Table 4.1-1
	S_g = 0.99	Table 4.1-1
	P = 84725 Pa	Table 4.1-1
	Time-varying infiltration rate (mean infiltration regime only)	Table 6.5-3
	Constant composition of infiltration and PCO_2	Table 6.2-1
Bottom	T = 32.62°C	Table 4.1-1
	S_L = 0.99999	Table 4.1-1
	P = 92000 Pa	Table 4.1-1
	Constant water composition and PCO_2	Table 6.2-1
Sides	No flux for water, gas, heat, and chemical species	Not Applicable
Drift Wall	Open to gas and liquid fluxes (advective and diffusive); conduction only for heat.	Not Applicable
Waste Package	Initial full heat load of 1.45 kW/m decreasing with time (due to radioactive decay), and reduced by 86.3% during the first 50 years (due to heat removal by ventilation)	Attachment VIII and Table 4.1-2

NOTES: T = Temperature
S_g = Gas saturation
S_L = Liquid saturation
P = Pressure

Table 6.8-2. Tptpll THC Model Infiltration Rates

Case	Infiltration Rate (mm/y)	Time Period (years)	Reference DTN
Mean Infiltration (increasing stepwise)	6	0 to 600 (present day)	Table 4.1-1
	16	600 to 2000 (monsoon)	
	25	2000 to 100,000 (glacial transition)	
Mean low (fixed)	6	0 to 100,000	NA (sensitivity only)
Mean high (fixed)	25	0 to 100,000	NA (sensitivity only)

NOTE: All simulations were carried out with the Present Day Mean calibrated rock properties set. Also see Table 6.8-4.

6.8.3 Input Data and Modeling Procedure

The Tptpll THC Model REV02 was run using TOUGHREACT V3.0 (LBNL 2002 [161256]). Simulations were carried out in the same manner as done for REV01 (Sections 6.5.3 and 6.7.3). Many input data were revised, compared to the Tptpll THC Model REV01 (Section 6.7.3). The revised data include: rock properties (Section 4.1.1, Table 6.4-1), modeled geochemical system (Table 6.2-2: the addition of nitrate and sepiolite), thermodynamic data (Attachment VI), and kinetic data (Table 4.1-4). In addition, five water compositions were considered (Table 6.2-1), as discussed in Section 6.2.2.1 and summarized below in Table 6.8-3.

Table 6.8-3. Selected Input Waters (Section 6.2.2.1) for the Tptpll THC Model REV02

Name of Alternative	Sample or Water Name	Location	Lithostratigraphic Unit
W0 (also used in REV01)	HD-PERM[1]	ESF Alcove 5	Tptpmn
W5	CS-1000/7.3-7.7/UC	ECRB Cross Drift	base of Tptpul
W4	CS-2000/16.5-21.1/UC	ECRB Cross Drift	Tptpll
W6	SD-9/990.4-991.7	Borehole SD-9	Tptpll
W7	CS-500/12.0-16.7/UC	ECRB Cross Drift	Tptpul

NOTE: [1] Average of two samples as discussed in Section 6.2.2.1.
See Table 6.2-1 for compositions.

The noteworthy revisions to the Tptpll rock properties since REV01 include a two-fold decrease in fracture porosity and permeability, a one-order-of-magnitude decrease in matrix permeability, and some decrease in the capillarity of fractures (by 20%) and rock matrix (by 40%). The revised rock thermal properties account for the presence of lithophysae in the Tptpll (and other lithophysal units), although they do not differ significantly from the earlier data (Table 6.4-1).

The diffusion coefficient of CO_2 in gas was increased in this model compared to the REV01 model. This change was unintentional and resulted from inserting a default molecular diameter (1×10^{-10} m) into the thermodynamic database during automatic conversion of this database. The value used in previous models (2.5×10^{-10} m) was specific for CO_2 (Section 4.1.6). This change in molecular diameter, through the use of Equation 4.2-1, causes approximately a six-fold increase in the CO_2 diffusion coefficient. This change, however, is within the range of uncertainty affecting the calculation of gas diffusivity in the model. It was used as an opportunity to evaluate the model sensitivity to CO_2 diffusivity. In order to do so, an additional simulation was run using the original CO_2 molecular diameter value (2.5×10^{-10} m), with results compared in Section 6.8.5.3.

Simulations of ambient conditions (i.e., without thermal loading, under natural geothermal gradient, and without drift opening) were run using the same input data as described above. However, to evaluate the model's sensitivity to thermodynamic data (Section 6.8.5.1), three different sets of thermodynamic data were used, as described further in Section 6.4.8.2: "Set 1," the current database, and alternative data sets "Set 2" and "Set 3."

The maximum time step length allowed for transport was reduced significantly, compared to REV01 simulations, to minimize the effect of numerical errors. Maximum time steps of 15 days, 1 month, 2 months, 1 year and 5 years were used for the time periods spanning 0–50, 50–600, 600–2,400, 2,400–20,000, and 20,000–100,000 years, respectively. To change infiltration rates and the maximum time step length, each run was stopped and then restarted at 50, 600, 2,000, 2,400, and 20,000 years after changing these input data. These differences apart, the same modeling procedure was applied as previously (Sections 6.5.3 and 6.7.3).

6.8.4 Model Runs

Sixteen simulations were performed, as summarized in Table 6.8-4.

Table 6.8-4. Tptpll THC Model REV02 Runs Using the Mean Infiltration Rock-Property Set for All Simulations

Input Water (Table 6.8-3)	Thermo. Data Set (Section 6.4.8.2)	Infiltration Case (Table 6.8-2)	Equation of State (EOS) Module[a]	Simulation Type	Run ID (used in Output-DTNs: LB0307DSTTHCR2.001; LB0307DSTTHCR2.002; LB0302DSCPTHCS.001; LB0302DSCPTHCS.002; also see Attachment X)
None	None	Mean Infiltration	EOS4	TH (2-D)	th6_1.45kw
W0	Set 1	Mean Infiltration	EOS4	THC (2-D)	thc6_w0
W0	Set 1	Mean Infiltration	EOS3	THC (2-D)	thc6_w0e3
W0	Set 1	Mean Infiltration	EOS3 (isothermal)	THC (1-D, ambient)	thc6_w0amb1
W0	Set 1	Mean Low (fixed)	EOS4	THC (2-D)	thc6_w0a
W0	Set 1	Mean High (fixed)	EOS4	THC (2-D)	thc25_w0
W0	Set 1[b]	Mean Infiltration	EOS4	THC (2-D)	thc6_w0b
W4	Set 1	Mean Infiltration	EOS4	THC (2-D)	thc6-w4
W4	Set 1	Mean Infiltration	EOS3 (isothermal)	THC (1-D, ambient)	thc6_w4amb1
W5	Set 1	Mean Infiltration	EOS4	THC (2-D)	thc6_w5
W5	Set 1	Mean Infiltration	EOS3 (isothermal)	THC (1-D, ambient)	thc6_w5amb1
W6	Set 1	Mean Infiltration	EOS4	THC (2-D)	thc6_w6
W6	Set 1	Mean Infiltration	EOS3 (isothermal)	THC (1-D, ambient)	thc6_w6amb1
W7	Set 1	Mean Infiltration	EOS4	THC (2-D)	thc6_w7
W0	Set 1	Mean Low (fixed)	EOS3 (isothermal)	THC (1-D, ambient)	thc6_w0amb
W0	Set 2	Mean Low (fixed)	EOS3 (isothermal)	THC (1-D, ambient)	thc6_w0_q
W0	Set 3	Mean Low (fixed)	EOS3 (isothermal)	THC (1-D, ambient)	thc6_w6_w0_q1

NOTE: [a] TOUGHREACT V3.0 (LBNL 2002 [161256]) flow modules: EOS3 neglects vapor pressure lowering due to capillary pressure; EOS4 takes this effect into account.
[b] A CO_2 molecular diameter of 2.5×10^{-10} m (Section 4.1.6) is used for this run instead of the value of 1×10^{-10} m input in other simulations listed here (see Section 6.8.3).

6.8.5 Simulation Results (Tptpll THC Model REV02)

The model results are presented below in several subsections. First, THC simulations of ambient conditions (non-heating) using different input thermodynamic data sets are discussed (Section 6.8.5.1). These simulations serve as the basis for justifying the use of revised thermodynamic data selected for this study. Results of simulations of thermal loading (TH and THC) are then presented in two parts. Predicted water chemistry trends around the drift are presented first (Section 6.8.5.2), then the effect of water-gas-rock reaction on fracture permeability and flow patterns around the drift is assessed (Section 6.8.5.3). The results are presented in a way that allows comparison with earlier models (Section 6.5 and 6.7) and also allows an assessment of model sensitivity to input water compositions, infiltration rates, water-vapor pressure models, and CO_2 effective diffusivity. All model results were submitted to the technical database under DTNs as listed in Attachment X.

6.8.5.1 Simulations of Ambient Conditions (Thermodynamic Data Sensitivity)

Results of simulations of ambient conditions are presented below to illustrate the model sensitivity to thermodynamic data, and to justify the selection of the thermodynamic data used in this study (Attachment VI and Section 4.1.4). These simulations were run with three thermodynamic data sets discussed in Section 6.4.8.2: Set 1 representing the data adopted for this study, and Set 2 and Set 3 representing alternatives (mostly data from the YMP database data0.com.R2) that were considered but not chosen for reasons given below. These simulations were run with the HD-PERM input water composition (Table 6.2-1). For consistency between all runs, the total aluminum concentration of the initial water in runs using all data sets was recomputed for equilibrium with the illite phase from these alternative thermodynamic data sets.

Predicted ambient water composition trends with the three sets of thermodynamic data are shown in Figure 6.8-1 through 6.8-3. Set 2 leads to the least stable predicted compositions, including unrealistic pH fluctuations to near 10, very large depletion of calcium and magnesium, and an increase in sodium concentrations to around 500 mg/L after 100,000 years. On the other hand, the simulation with Set 1 predicts the most stable trends. Using Set 3 (i.e., by incorporating revised zeolite thermodynamic data into Set 2), trend stability improves considerably, but the magnitude of concentration changes over the 100,000-year simulated time period is still quite large for most species. With all three thermodynamic data sets, an unrealistic magnesium depletion in water is predicted to occur, primarily on account of sepiolite precipitation. However, the least predicted magnesium depletion occurs when using Set 1. Note also that simulations using Set 2 and Set 3 predict the total dissolution of calcite initially present in the model (with precipitation of zeolites and clays having calcium). Using Set 1, calcite dissolution is not predicted. For these reasons, Set 1 was deemed a better alternative than either Set 2 or Set 3, because it yields long-term water compositions more consistent with observed data than the other two sets. For these reasons, Set 1 was adopted for the rest of this study. It should be recalled here that most of these thermodynamic data are from the YMP database data0.com.R2, with changes from this database documented under DTN: LB0307THMBDRTM.001 [164434] (and summarized in Section 4.1.4 for major changes).

These simulations illustrate that for any fixed water composition close to equilibrium with a mineral assemblage, a small change in thermodynamic data can reverse the calculated degree of

saturation (i.e., from supersaturation to undersaturation and vice versa) of minerals in that water, and thus reverse the calculated direction of reactions between these phases. In such instances, different water-composition trends can be predicted regardless of the magnitude of reaction rates assumed in the model. In such cases, the reliability of model results can be more affected by thermodynamic data than by kinetic data.

Free energies for minerals such as clays and zeolites may never be known accurately enough such that adjustments within the (sometimes already small) uncertainty in these values will always be necessary for long-term ambient simulations. Whether these adjustment provide values that are better, or not, than the data0.ymp.R2 data depends on the data themselves and their intended use. For clay minerals, because the adjustments were made to better match measured water compositions at YM, these adjustments may in part compensate for other effects not directly modeled such as more complex solid solutions or ion exchange processes. Therefore, these values may not be “better” than those in the data0.ymp.R2 database, but are better suited for long-term reactive transport simulations at Yucca Mountain. For stellerite, the dominant zeolitic mineral in repository units, it would appear that the data used here (Fridriksson et al. 2001 [160460]) may be superior to the R2 data.

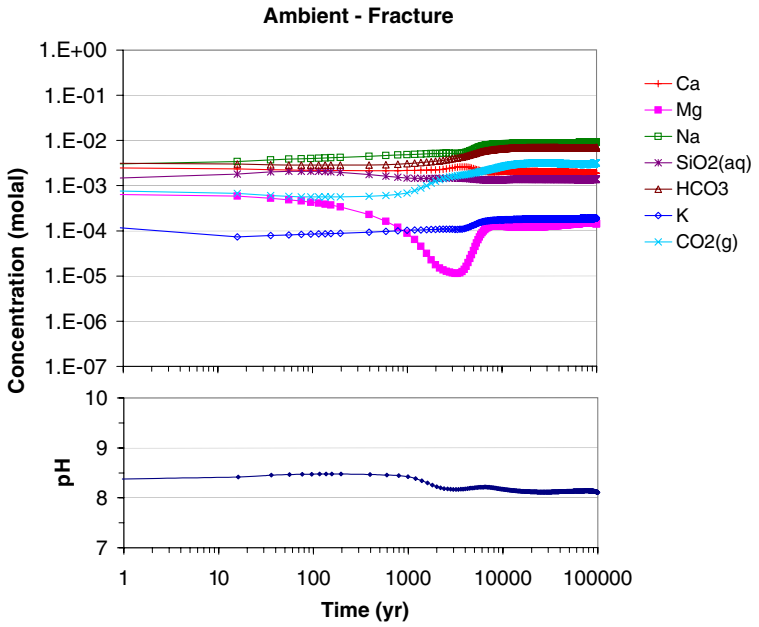

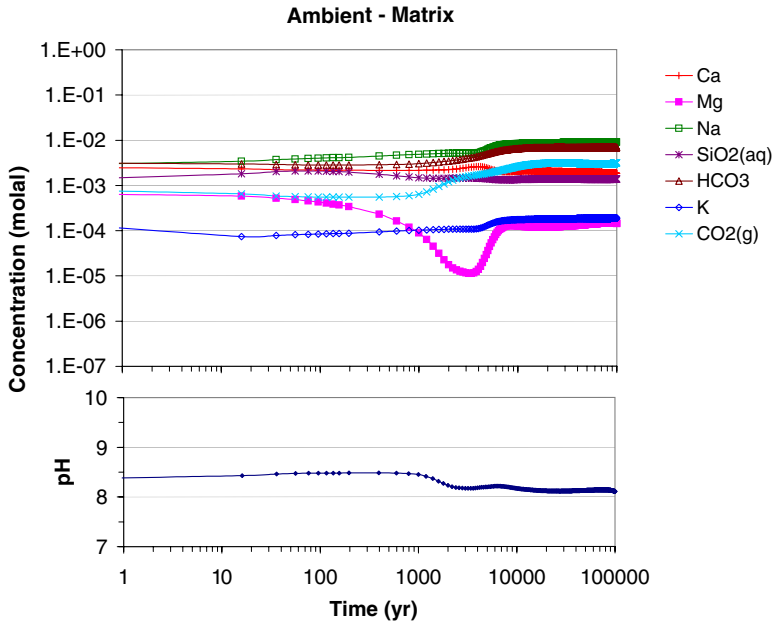

Output-DTN: LB0307DSTTHCR2.001

NOTE: Infiltration is constant at 6 mm/yr.

Figure 6.8-1. Predicted Water Compositions without Thermal Loading (in the Tptpll Lithostratigraphic Unit at the Repository Location) Using the Thermodynamic Data Adopted for This Study (Data Set 1—Attachment VI)

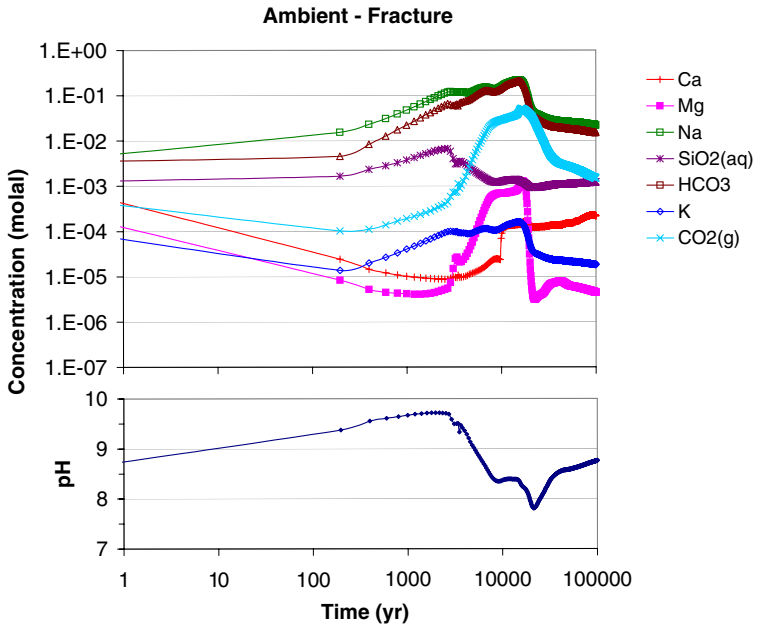

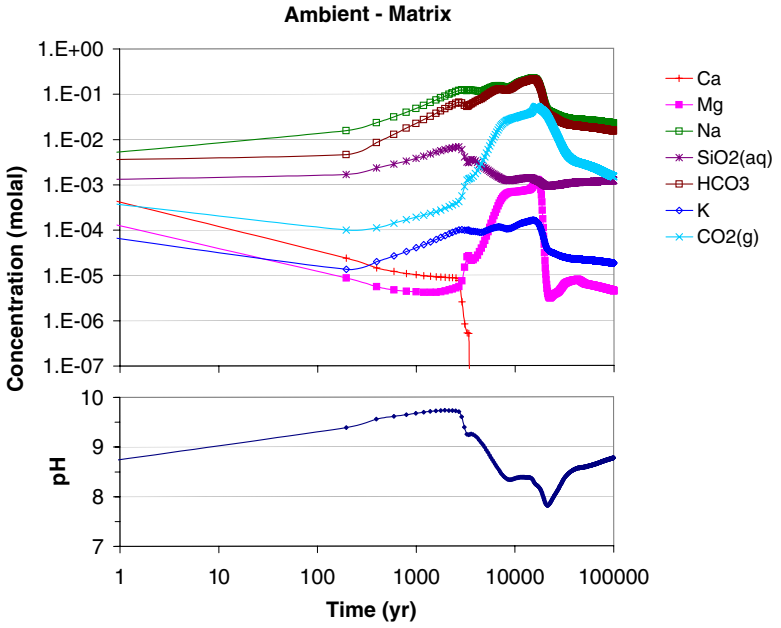

Output-DTN: LB0307DSTTHCR2.001

NOTE: Infiltration is constant at 6 mm/yr.

Figure 6.8-2. Predicted Water Compositions without Thermal Loading (in the Tptpll Lithostratigraphic Unit at the Repository Location) Using Thermodynamic Data from Data Set 2 (Section 6.4.8.2)

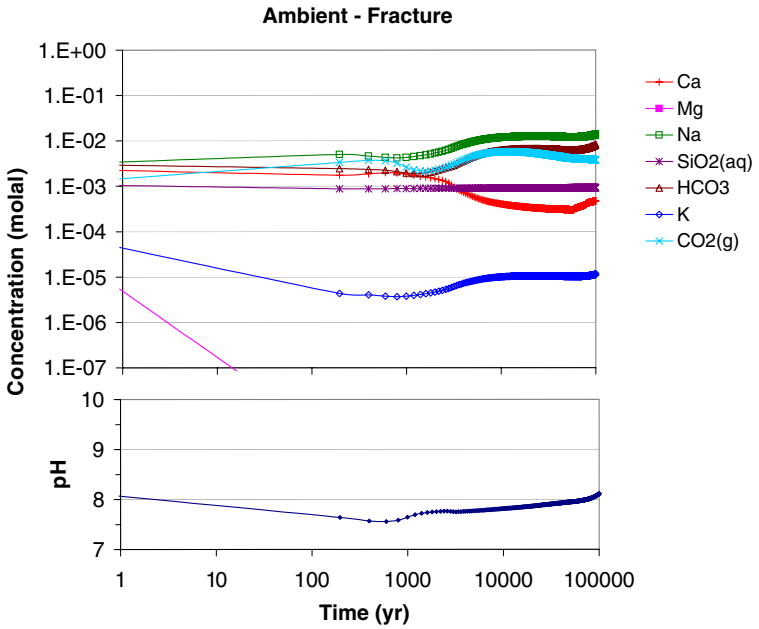

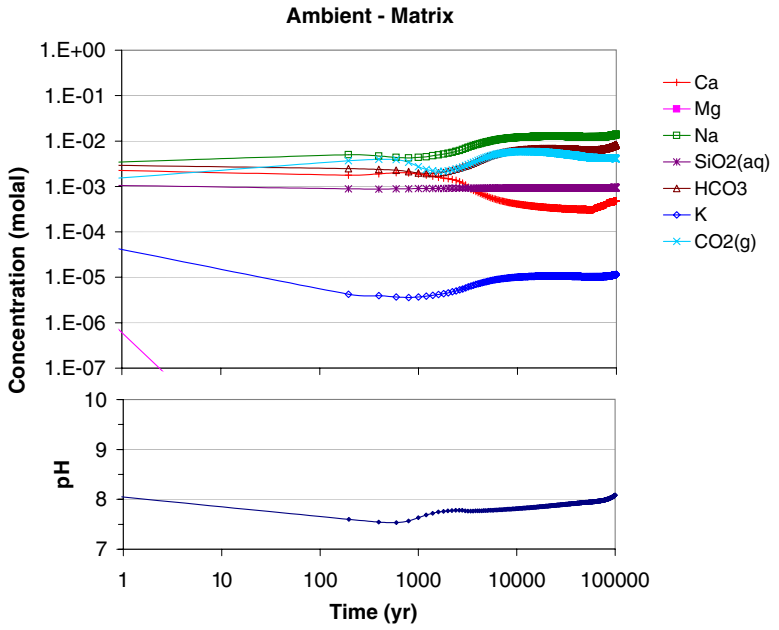

Output-DTN: LB0307DSTTHCR2.001

NOTE: Infiltration is constant at 6 mm/yr.

Figure 6.8-3. Predicted Water Compositions without Thermal Loading (in the Tptpll Lithostratigraphic Unit at the Repository Location) Using Thermodynamic Data from Data Set 3 (Section 6.4.8.2)

6.8.5.2 TH Results (No Chemical Reactions)

The results of TH simulations are shown in Figures 6.8-4 through 6.8-10. This set of figures parallels Figures 6.7-3 through 6.7-9 to facilitate comparison with the results of earlier simulations. It should be recalled that REV01 simulations were run with the EOS3 option of TOUGHREACT V3.0 [161256] (no vapor-pressure lowering caused by capillary pressure), whereas most REV02 simulations were carried out with the EOS4 option of TOUGHREACT V3.0 [161256] (taking this effect into account).

Modeled peak temperatures are approximately 10 degrees lower than in the REV01 model (Figures 6.8-4 and 6.8-5), mostly as a result of updated rock properties, but also because of the vapor-pressure-lowering effect, which was not considered in previous model revisions (see also temperature profiles from THC simulations discussed later). Preclosure temperatures around the drift are up to 30 degrees lower than in REV01 simulations (Figure 6.8-5), primarily because the heat removal rate (86.3%) is larger than what was used previously (70%). The main impact of vapor-pressure lowering is the smaller extent of dryout around the drift in the rock matrix than in fractures, even though temperatures are essentially the same in both media (Figure 6.8-6; also compare with Figure 6.7-4). Consequently, the rock matrix at the drift wall is predicted to rewet earlier (at around 200 to 300 years) than in previous models (1,200 to 1,400 years) (Figure 6.8-8). In fractures, however, the time of rewetting around the drift wall is similar for both model revisions (Figure 6.8-7). Predicted postclosure air mass fractions around the drift also did not change significantly from REV01 (Figure 6.8-9). The predicted vertical water percolation flux at the drift crown is somewhat higher during postclosure than calculated in REV01 (Figure 6.8-10; note that peaks of flux in this figure may not be fully resolved because such peaks are narrow relative to the time intervals specified for data output from the simulations). The predicted ambient water flux in the revised model (Figure 6.8-10) is for a 1-D column without a drift opening. It is larger than the flux calculated for ambient conditions in the REV01 model because it does not take into account the diverting effect of a drift opening (i.e., the diversion of percolating water around the drift capillary barrier). At most times (except around 50 and 1,200 years), the ambient water flux without a drift opening is also larger than the predicted flux above the drift under thermal loading conditions (Figure 6.8-10). Calculated temperatures, liquid saturations, and fluxes shown here are consistent with results of TH simulations presented in BSC (2003 [161530], Section 6.2.3). The vertical flux is further discussed in Section 6.8.5.4.

Note that in all models presented in this report, the drying of the rock caused by drift ventilation (i.e., the physical removal of moisture from wallrock by ventilation) is not considered. This drying could reduce the amount of water available for mobilization by boiling during postclosure. However, sensitivity studies in BSC (2001 [155950], Section 5.3.2.4.4) indicate that inclusion of preclosure dryout due to ventilation has little effect on TH conditions around the drift during the postclosure period, compared to a model that does not account for the influence of preclosure dryout. Therefore, inclusion of preclosure dryout is not expected to have a large effect on thermal seepage. The effect of evaporative concentration on pore water compositions would be more pronounced during preclosure than predicted here. However, the small effect of preclosure dryout on postclosure TH conditions is not expected to significantly affect water compositions during postclosure.

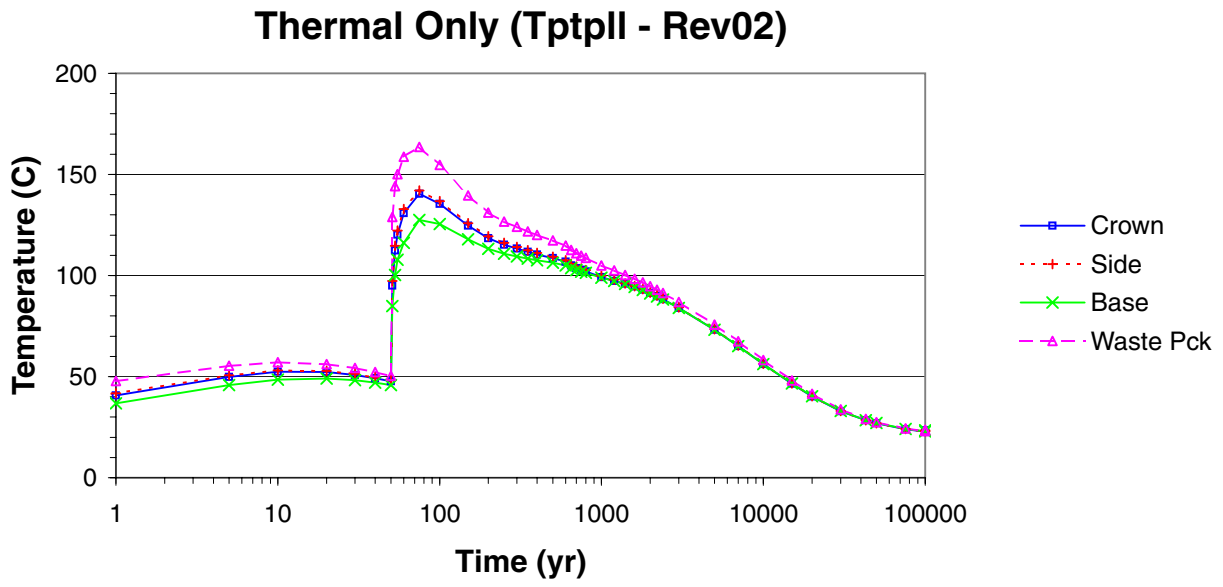

Output-DTN: LB0307DSTTHCR2.002

Figure 6.8-4. TH Simulation (Tptpll, REV02): Time Profiles of Modeled Temperatures in Fractures (Similar in Matrix) at Three Drift-Wall Locations and in the Waste Package

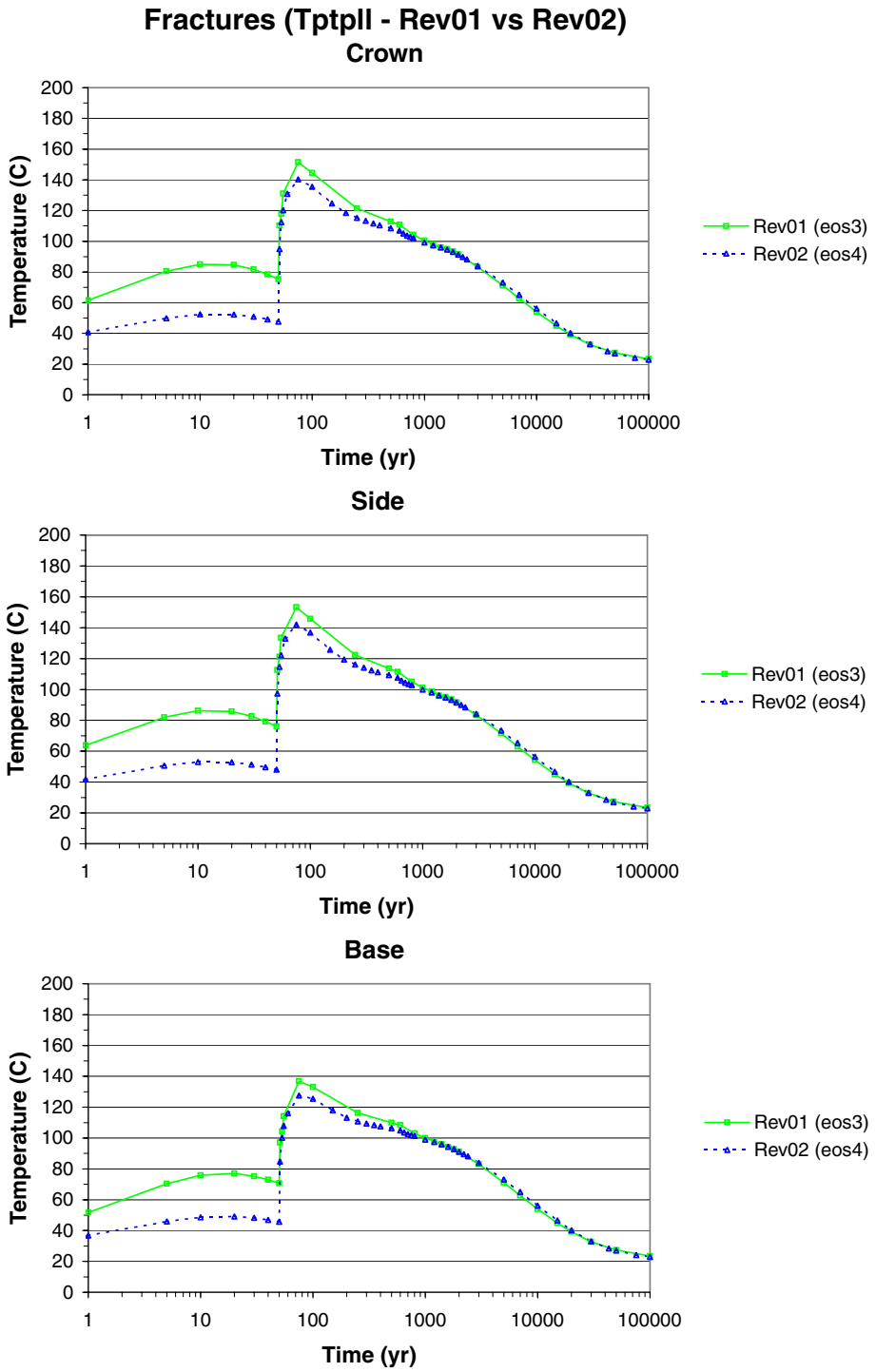

Output-DTN (REV02): LB0307DSTTHCR2.002
DTN (REV01): LB0011DSTTHCR1.001 [154759]

Figure 6.8-5. TH Simulation (Tptpll, REV01 vs. REV02): Time Profiles of Modeled Temperatures in Fractures at Three Drift-Wall Locations

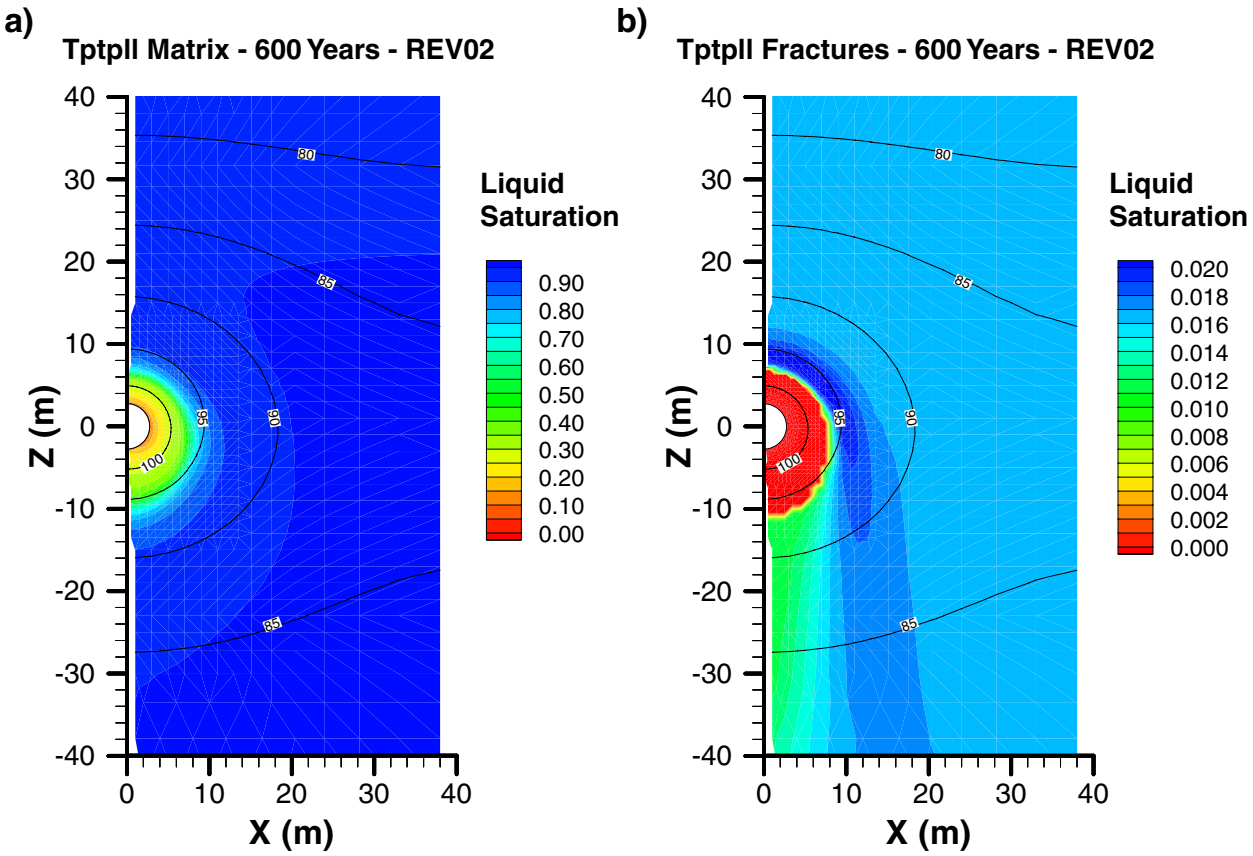

Output-DTN: LB0307DSTTHCR2.001

NOTE: Rewetting of the matrix at the drift wall has already occurred (See Figure 6.8-8).

Figure 6.8-6. TH Simulation (Tptpll, REV02): Contour Plot of Modeled Temperatures (°C) and Liquid Saturations in the Matrix and Fractures at 600 Years (Near the Time of Maximum Dryout in Fractures)

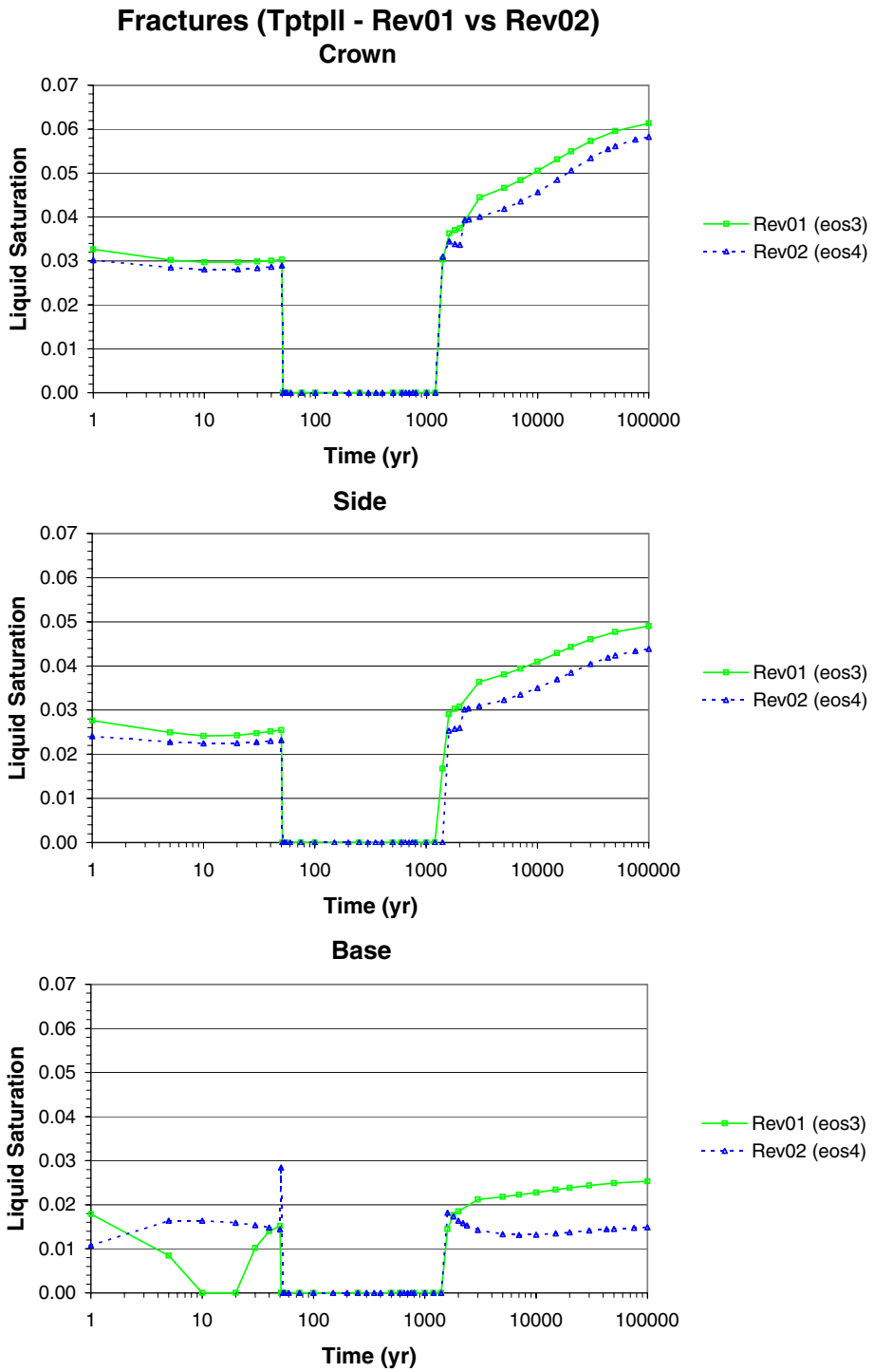

Output-DTN (REV02): LB0307DSTTHCR2.002
DTN (REV01): LB0011DSTTHCR1.001 [154759]

Figure 6.8-7. TH Simulation (Tptpll, REV01 vs. REV02): Time Profiles of Modeled Liquid Saturations in Fractures at Three Drift-Wall Locations

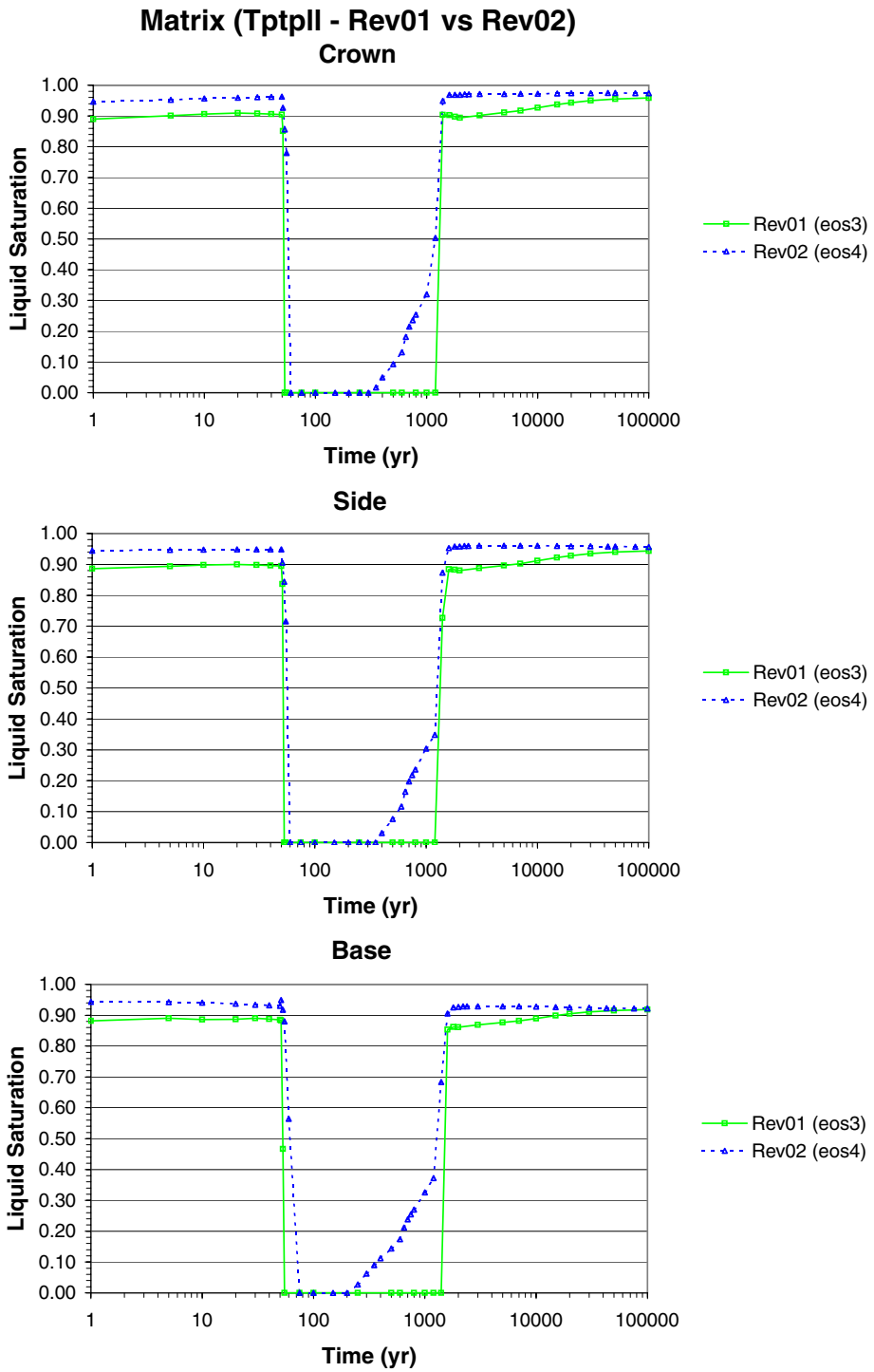

Output-DTN (REV02): LB0307DSTTHCR2.002
DTN (REV01): LB0011DSTTHCR1.001 [154759]

Figure 6.8-8. TH Simulation (Tptpll, REV01 vs. REV02): Time Profiles of Modeled Liquid Saturations in Matrix at Three Drift-Wall Locations

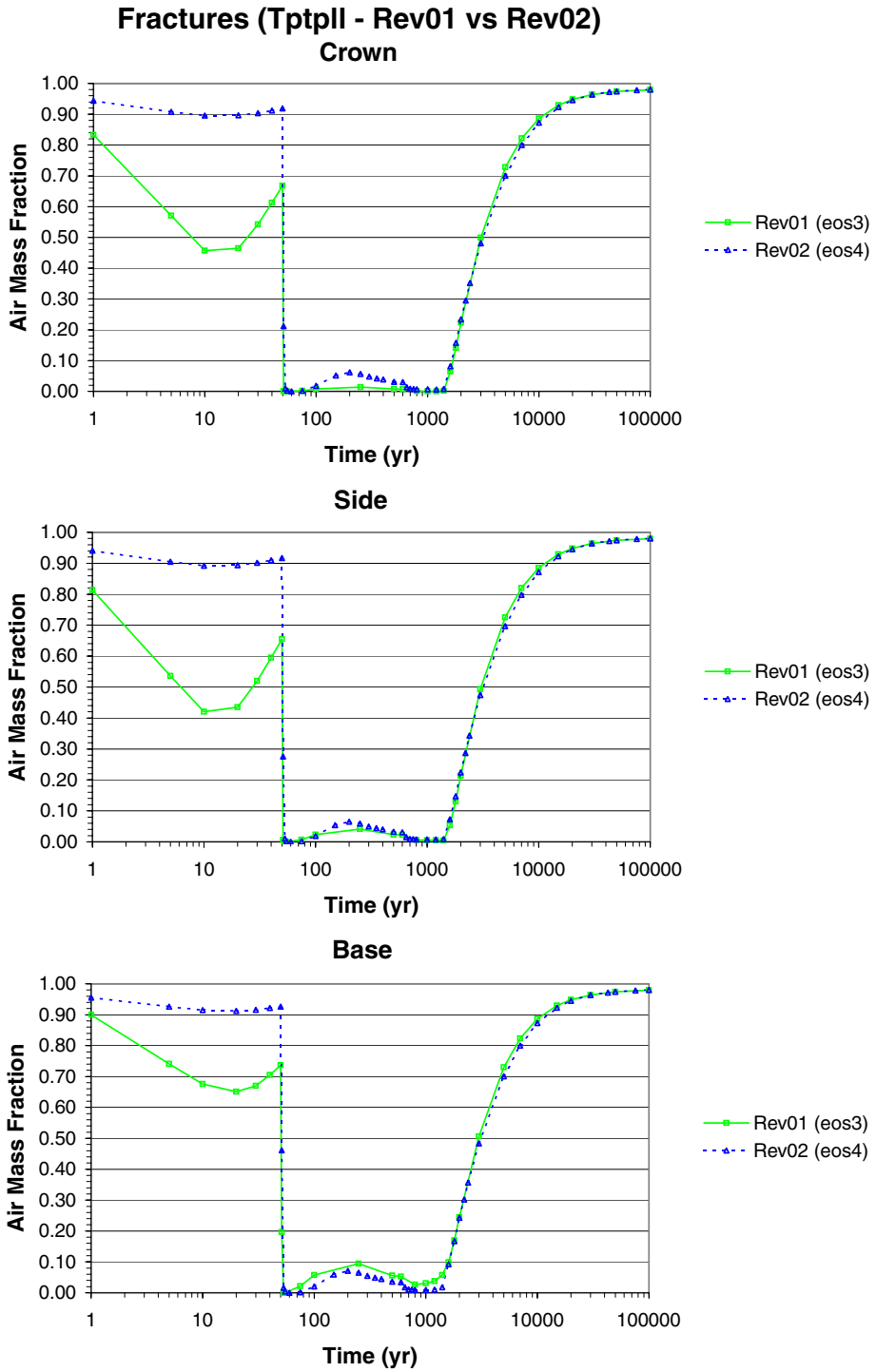

Output-DTN (REV02): LB0307DSTTHCR2.002
DTN (REV01): LB0011DSTTHCR1.001 [154759]

Figure 6.8-9. TH Simulation (Tptpll, REV01 vs. REV02): Time Profiles of Modeled Air Mass Fractions in the Gas Phase in Fractures at Three Drift-Wall Locations

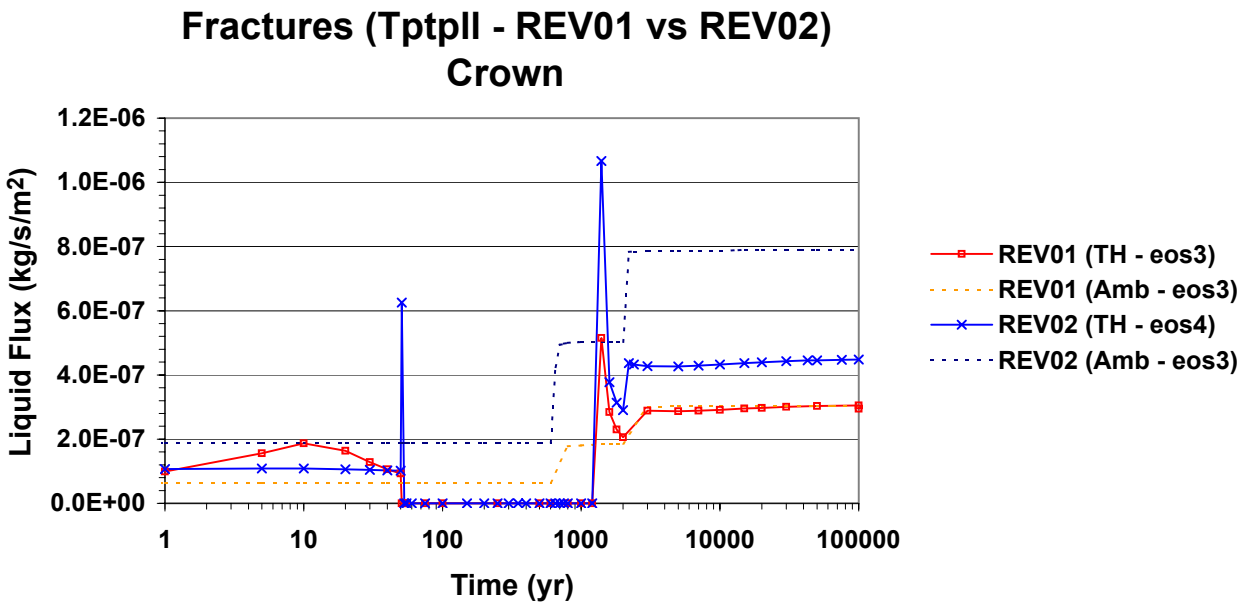

Output-DTN (REV02): LB0307DSTTHCR2.002
DTN (REV01): LB0011DSTTHCR1.001 [154759]

NOTE: Note that REV01 ambient simulations include the drift opening, whereas REV02 ambient simulations do not (See text).

Figure 6.8-10. TH Simulation (Tptpll, REV01 vs. REV02): Time Profiles of Modeled Water Flux at the Drift Crown

6.8.5.3 Water Chemistry Trends

6.8.5.3.1 Drift Wall (REV01 versus REV02)

Time profiles similar to those predicted for the REV01 model are discussed below for the same previously selected drift locations: crown (model gridblocks "F 121" and "M 121", side (gridblocks "F 44" and "M 44") and base (gridblocks "F 128" and "M 128") (Figure 6.7-2). As in previous models, these were calculated using the HD-PERM water (W0) as input water composition. The results shown are for an extended-case geochemical system and for cases with and without water vapor pressure lowering caused by capillary pressure (runs referred to as "eos4" and "eos3, respectively). Because these simulations were run with a six-fold increase in the CO_2 diffusion coefficient compared to earlier models (Section 6.8.3), model results are also presented for another eos4 THC simulation considering the same CO_2 diffusion coefficient as earlier runs.

Predicted time profiles of temperature, CO_2 gas concentrations, and aqueous species total concentrations (fracture medium) are shown in Figures 6.8-11 through 6.8-20. They are directly comparable to profiles presented in Section 6.7 for the REV01 model. Predicted trends in fracture gas and water chemistry through time remain generally the same as in REV01. The processes driving these trends are discussed in Sections 6.5.5 and 6.7.5 and are not repeated here.

Postclosure temperature profiles from THC simulations (Figure 6.8-11) are similar for model runs with and without vapor-pressure lowering, but with slightly higher peak temperatures

predicted with the latter. These profiles also indicate that the principal cause for the difference in peak temperatures between the REV01 and REV02 model is not the selected water vapor pressure models, but the change in rock properties from REV01 to REV02.

With respect to predicted water and gas chemistry trends at the drift wall, the most noticeable difference between this model revision and REV01 is the trend of calculated CO_2 concentrations (Figure 6.8-12). Although generally similar, the rise in CO_2 concentrations above ambient values occurs much earlier in the current model (starting at around 600 years instead of 2,000 years in REV01). This earlier rise, as well as subsequently higher predicted CO_2 concentrations, is observed in simulations both with and without vapor pressure lowering (Figure 6.8-12). These effects are attributed mostly to the effect of opening the drift wall to gas advection (the drift was closed to such fluxes in earlier model revisions). The simulation with a lower CO_2 diffusion coefficient consistent with the value used in REV01 also predicts that the CO_2 concentrations will start rising earlier and rising to higher values than in previous models (Figure 6.8-12). The increase in the CO_2 diffusion coefficient (six fold here) causes somewhat higher predicted CO_2 concentrations in the gas phase, although the effect is most noticeable during early stages of the dryout period (Figure 6.8-12). In all cases, the predicted CO_2 concentrations at the drift wall remain below 10,000 ppmv for the entire simulated time period. As noted in earlier models, CO_2 concentrations drop quickly at the onset of dryout, shortly after 50 years, because of displacement by steam. Fluctuations during the dryout period (Figure 6.8-12) appear to result from the competing effect of CO_2 displacement by steam (from the drift outwards), and increased diffusion of CO_2 towards the drift resulting from rising temperatures after all water boils out.

The predicted pH values in fracture water (Figure 6.8-13) are consistent with modeled trends of CO_2 concentrations. Compared to earlier simulations, the lower temperatures during preclosure (due to higher heat removal efficiency) yield lower CO_2 partial pressures and thus higher pH values (generally by less than a half unit). After closure, the higher predicted CO_2 concentrations yield lower pH values (mostly by less than a half unit). The choice of the water-vapor pressure model and the difference in the CO_2 diffusion coefficient have only a small effect on predicted pH values (differences mostly within less than 0.2 pH units; Figure 6.8-13). The predicted pH range of water in fractures at the drift wall for all cases is neutral to slightly alkaline (pH 7 to 8.6) and remains essentially below predicted ambient values (8.2–8.6) for the entire simulated time period. The total carbonate concentrations (shown as HCO_3^- on Figure 6.8-14) are depressed, relative to ambient values, because of the exsolution of CO_2 gas driven by elevated temperatures.

The predicted time profiles for other constituents (Figures 6.8-15 through 6.8-20) do not show much sensitivity to the choice of water-vapor pressure model or the CO_2 diffusion coefficient. In most cases, elevated concentrations are predicted at the time the drift rewets, followed by a steep fall towards ambient values (e.g. Figure 6.8-18). As noted earlier, these temporarily elevated concentrations are caused by the rewetting of areas where evaporative concentration took place during dryout. The precipitation of salts upon complete dryout is accounted for in this model (it was not in previous model revisions), and the dissolution of these salts upon rewetting causes higher concentration peaks of dissolved constituents than predicted previously. Nevertheless, these relatively elevated concentrations are predicted only at small liquid saturations at which no significant fluid flow could occur. The improved treatment of mineral precipitation at the boiling

front also results in the prediction of lower, more realistic aqueous silica concentrations than in earlier models (Figure 6.8-17).

Nitrate is included in the present simulations in contrast to REV01 simulations where it was omitted. Prior to REV02 of this report, other investigators have estimated concentration trends of this anion on the basis of predicted chloride concentration and the NO_3/Cl ratio in the initial water (Figure 6.8-20). Although nitrate is treated as a conservative species, its mass inventory is accounted for upon complete dryout by forming sodium nitrate, using all the available nitrate in solution (without equilibrium calculations; see Section 6.4.5). Upon rewetting, it dissolves faster than chlorides because of its greater solubility, causing a temporary increase in the NO_3/Cl ratio of rewetting waters. However, this effect is barely noticeable (Figure 6.8-21).

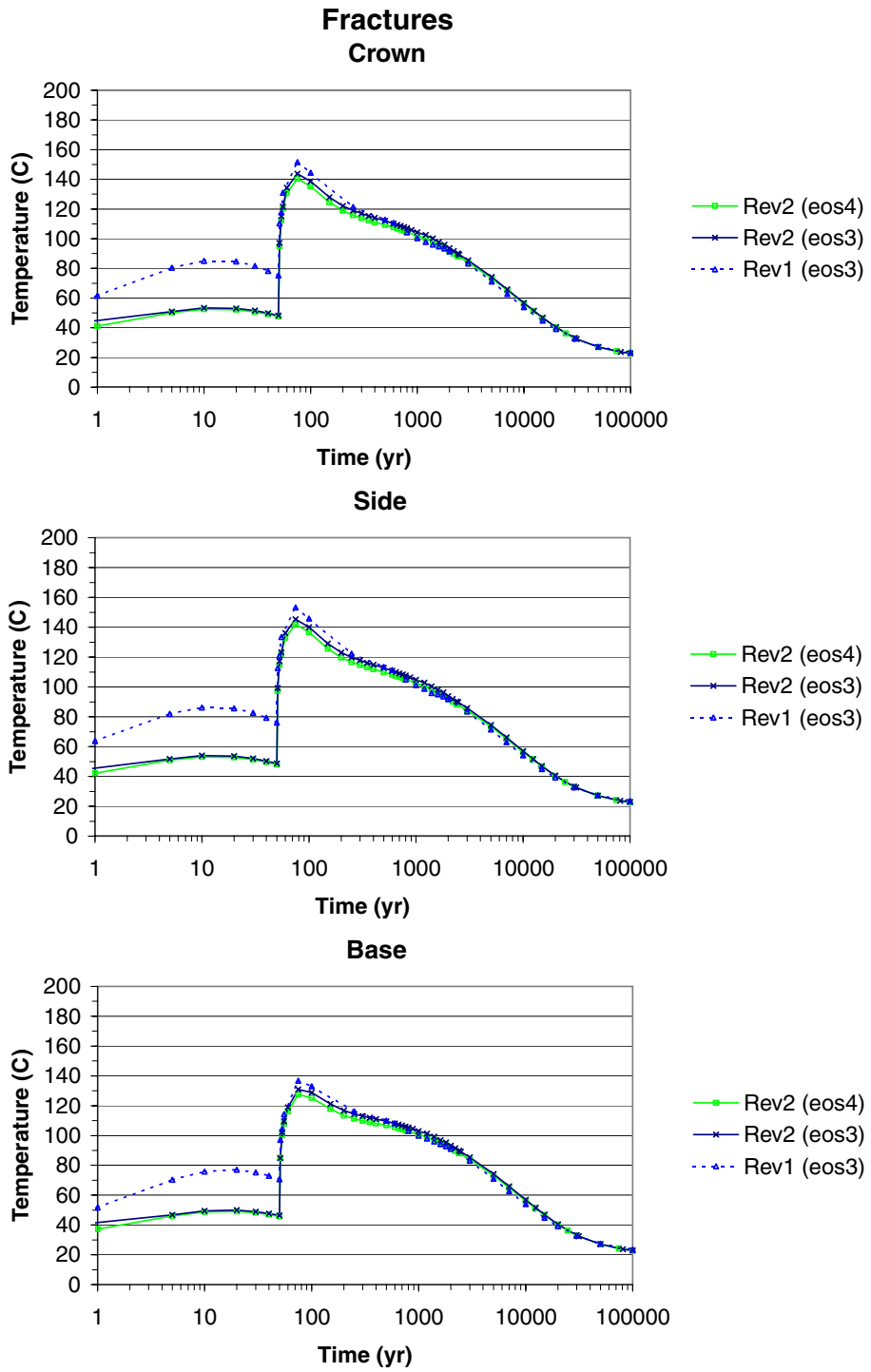

Output-DTNs (REV02): LB0302DSCPTHCS.002, LB0307DSTTHCR2.002
DTN (REV01): LB0011DSTTHCR1.001 [154759]

Figure 6.8-11. THC Simulation (Tptpll, REV01 vs. REV02): Time Profiles of Modeled Temperatures at Three Drift-Wall Locations With and Without Water-Vapor-Pressure Lowering (eos4 and eos3, respectively)

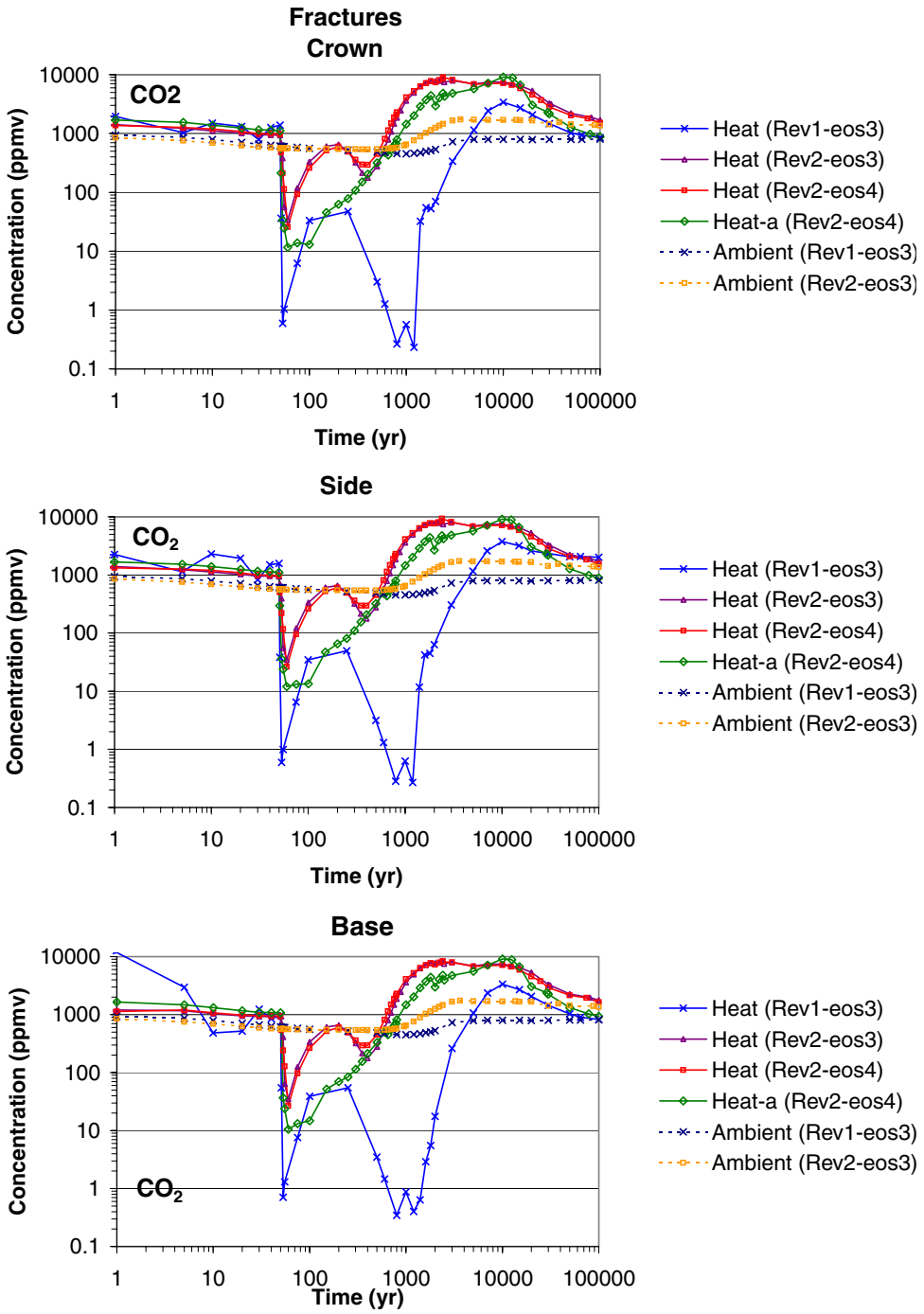

Output-DTNs (REV02): LB0302DSCPTHCS.002, LB0307DSTTHCR2.002
DTN (REV01): LB0011DSTTHCR1.001 [154759]

NOTE: REV01 Simulations and the REV02 Simulation Labeled "Heat-a" were run with the CO_2 diffusion coefficient six times smaller than other simulations (see text).

Figure 6.8-12. THC Simulation (Tptpll, REV01 vs. REV02): Time Profiles of Modeled CO_2 Concentrations in the Gas Phase in Fractures at Three Drift-wall Locations under Heating (Heat) and Non-Heating (Ambient) Conditions, Including (eos4) and Excluding (eos3) Water-Vapor-Pressure Lowering

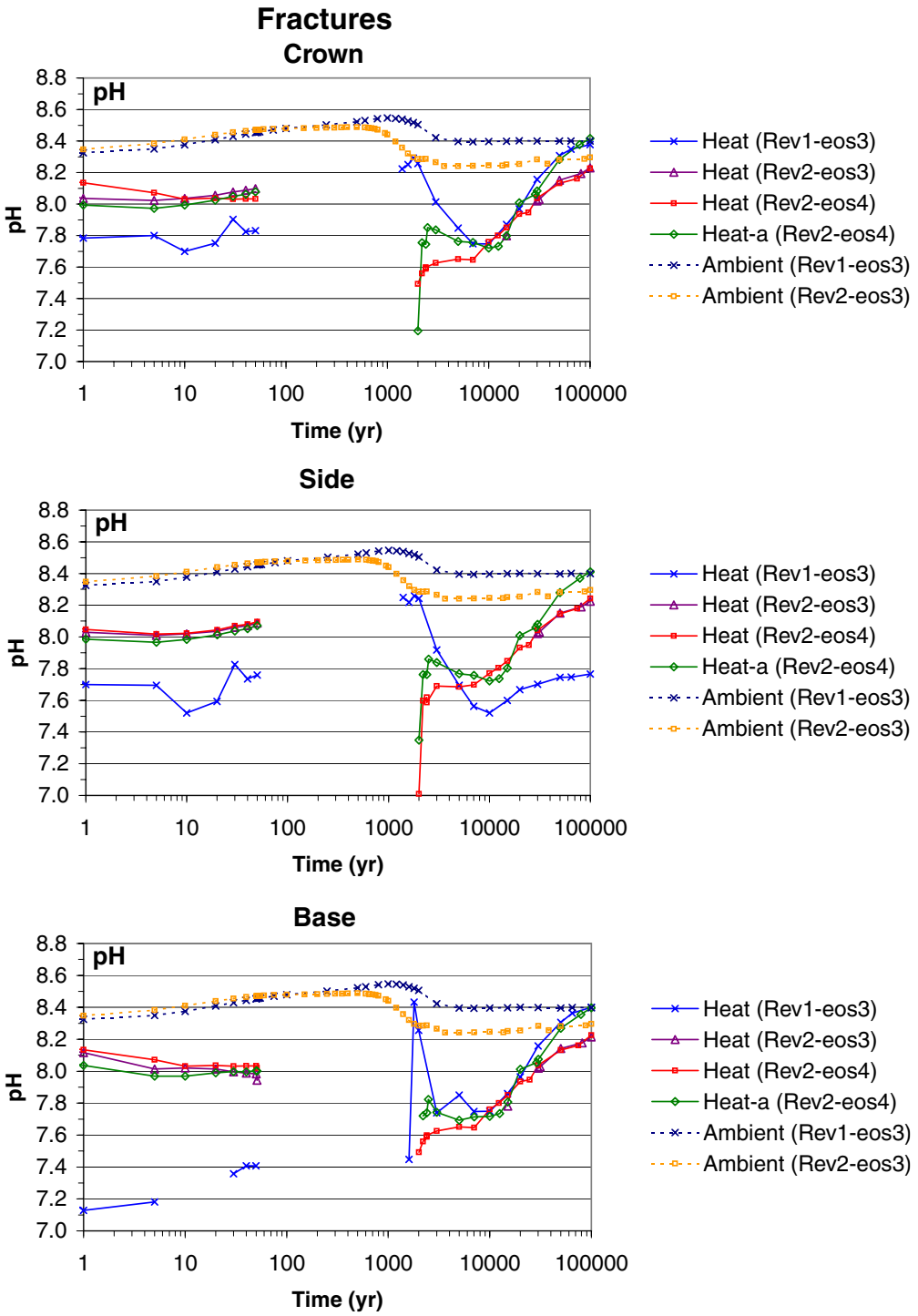

Output-DTNs (REV02): LB0302DSCPTHCS.002, LB0307DSTTHCR2.002
DTN (REV01): LB0011DSTTHCR1.001 [154759]

NOTE: REV01 Simulations and the REV02 Simulation Labeled "Heat-a" were run with the CO_2 diffusion coefficient six times smaller than other simulations (see text).

Figure 6.8-13. THC Simulation (Tptpll, REV01 vs. REV02): Time Profiles of the Modeled pH of Fracture Water at Three Drift-Wall Locations under Heating (Heat) and Non-Heating (Ambient) Conditions, Including (eos4) and Excluding (eos3) Water-Vapor-Pressure Lowering

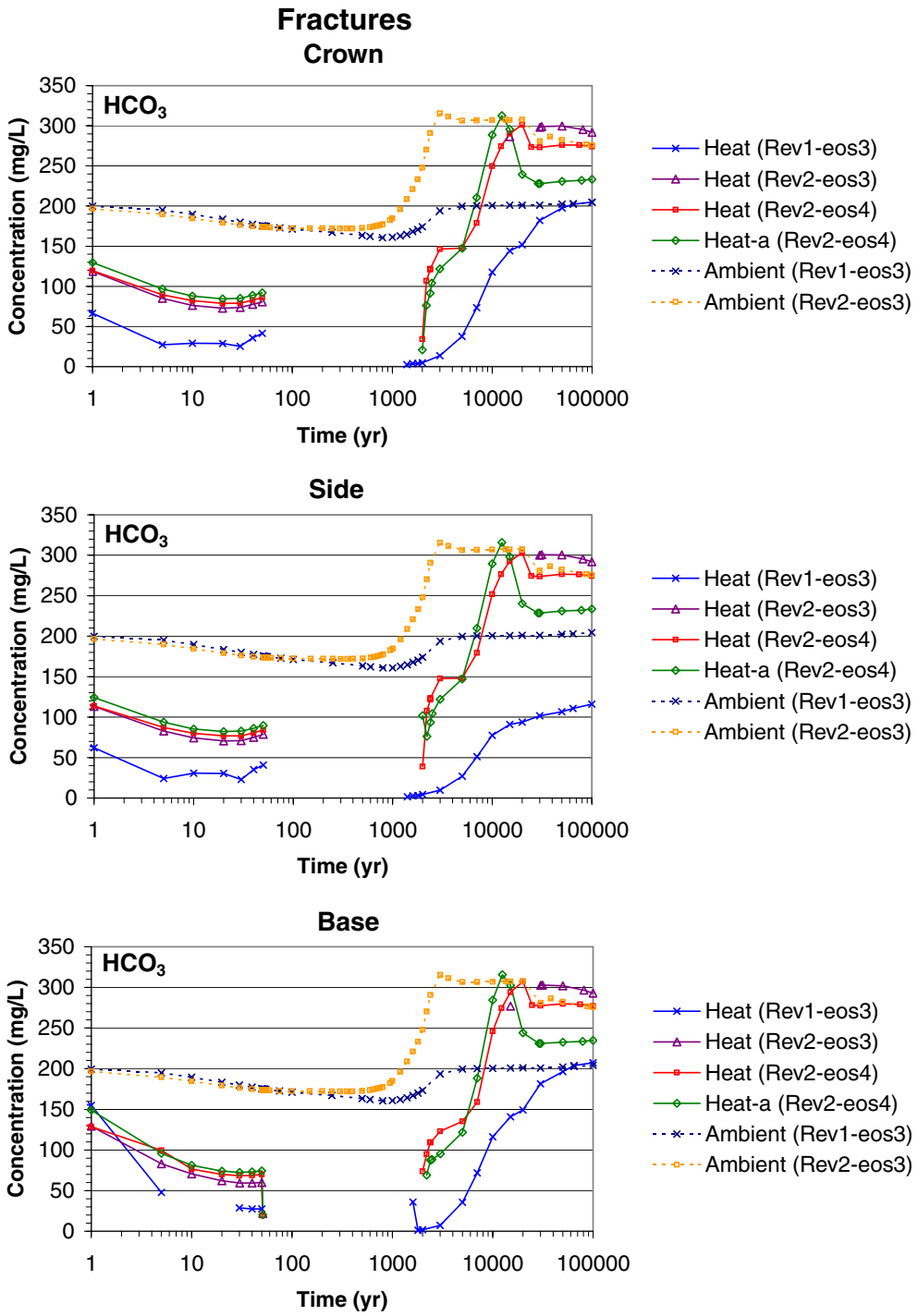

Output-DTNs (REV02): LB0302DSCPTHCS.002, LB0307DSTTHCR2.002
DTN (REV01): LB0011DSTTHCR1.001 [154759]

NOTE: REV01 Simulations and the REV02 Simulation Labeled "Heat-a" were run with the CO_2 diffusion coefficient six times smaller than other simulations (see text).

Figure 6.8-14. THC Simulation (Tptpll, REV01 vs. REV02): Time Profiles of Modeled Total Aqueous Carbonate Concentrations (as HCO_3^-) in Fracture Water at Three Drift-Wall Locations, under Heating (Heat) and Non-Heating (Ambient) Conditions, Including (eos4) and Excluding (eos3) Water-Vapor-Pressure Lowering

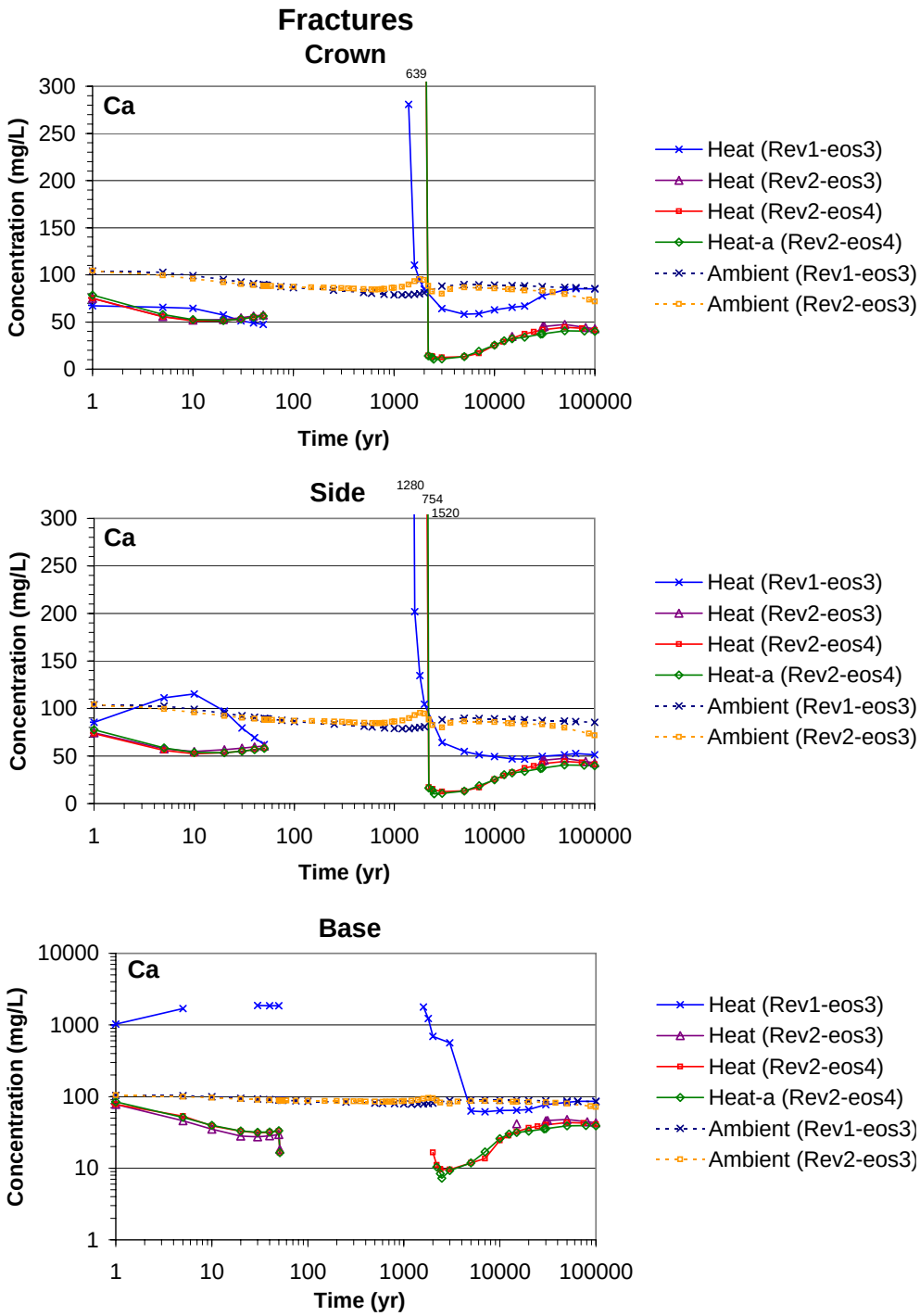

Output-DTNs (REV02): LB0302DSCPTHCS.002, LB0307DSTTHCR2.002
DTN (REV01): LB0011DSTTHCR1.001 [154759]

NOTE: REV01 Simulations and the REV02 Simulation Labeled "Heat-a" were run with the CO_2 diffusion coefficient six times smaller than other simulations (see text).

Figure 6.8-15. THC Simulation (Tptpll, REV01 vs. REV02): Time Profiles of Modeled Total Aqueous Calcium Concentrations in Fracture Water at Three Drift-Wall Locations, under Heating (Heat) and Non-Heating (Ambient) Conditions, Including (eos4) and Excluding (eos3) Water-Vapor-Pressure Lowering

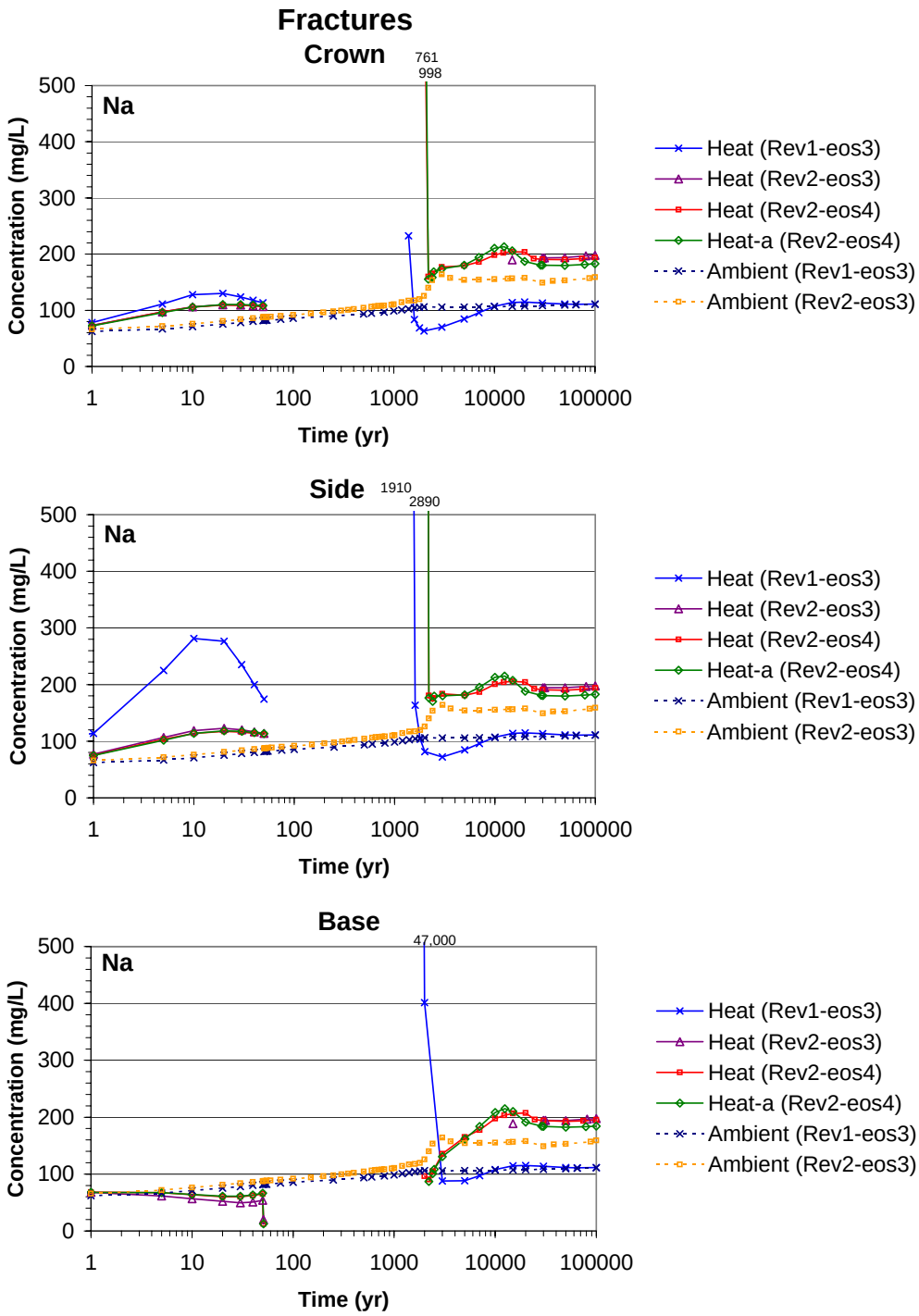

Output-DTNs (REV02): LB0302DSCPTHCS.002, LB0307DSTTHCR2.002
DTN (REV01): LB0011DSTTHCR1.001 [154759]

NOTE: REV01 Simulations and the REV02 Simulation Labeled "Heat-a" were run with the CO_2 diffusion coefficient six times smaller than other simulations (see text).

Figure 6.8-16. THC Simulation (Tptpll, REV01 vs. REV02): Time Profiles of Modeled Total Aqueous Sodium Concentrations in Fracture Water at Three Drift-Wall Locations, under Heating (Heat) and Non-Heating (Ambient) Conditions, Including (eos4) and Excluding (eos3) Water-Vapor-Pressure Lowering

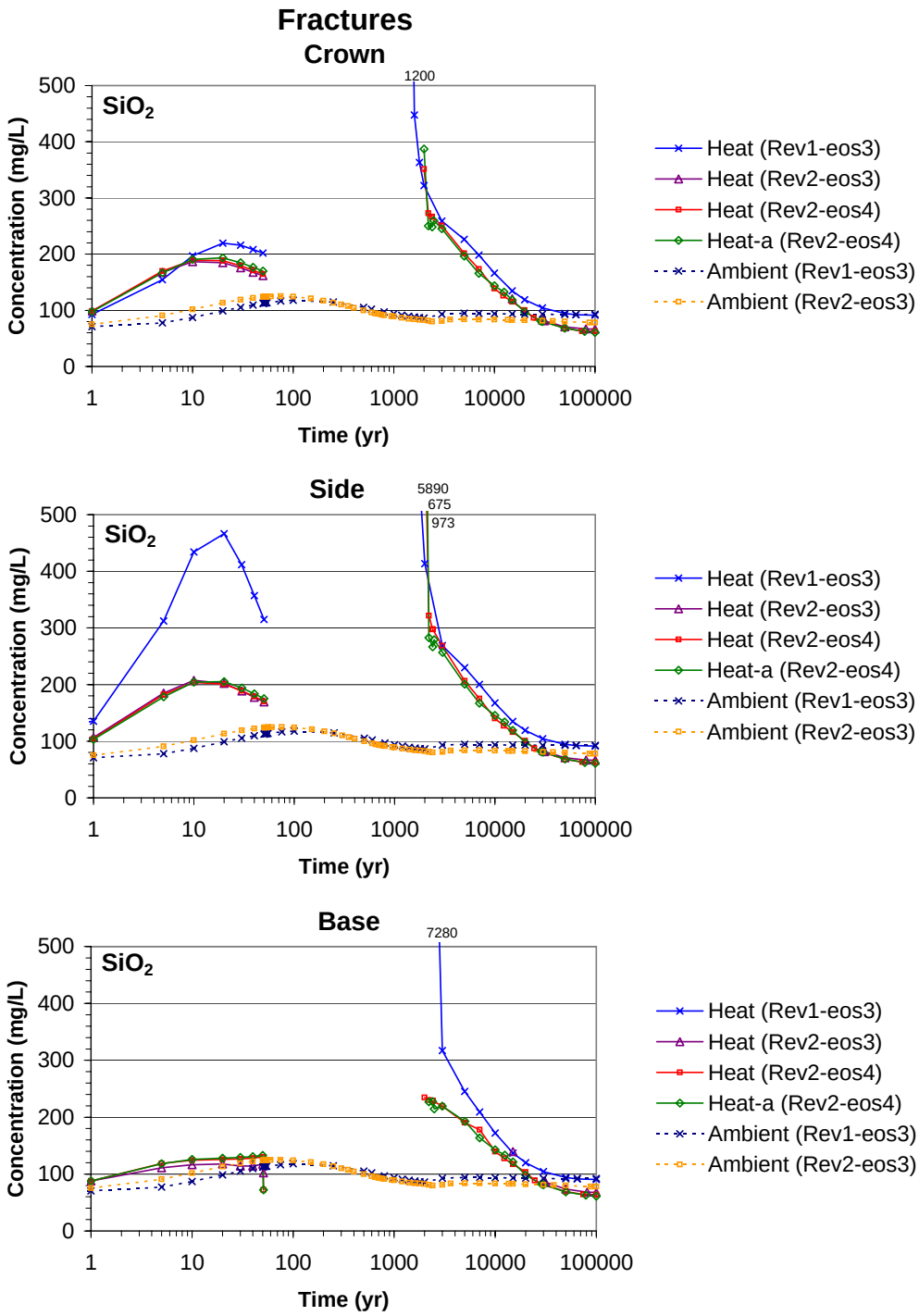

Output-DTNs (REV02): LB0302DSCPTHCS.002, LB0307DSTTHCR2.002
DTN (REV01): LB0011DSTTHCR1.001 [154759]

NOTE: REV01 Simulations and the REV02 Simulation Labeled "Heat-a" were run with the CO_2 diffusion coefficient six times smaller than other simulations (see text).

Figure 6.8-17. THC Simulation (Tptpll, REV01 vs. REV02): Time Profiles of Modeled Total Aqueous Silica Concentrations in Fracture Water at Three Drift-Wall Locations, under Heating (Heat) and Non-Heating (Ambient) Conditions, Including (eos4) and Excluding (eos3) Water-Vapor-Pressure Lowering

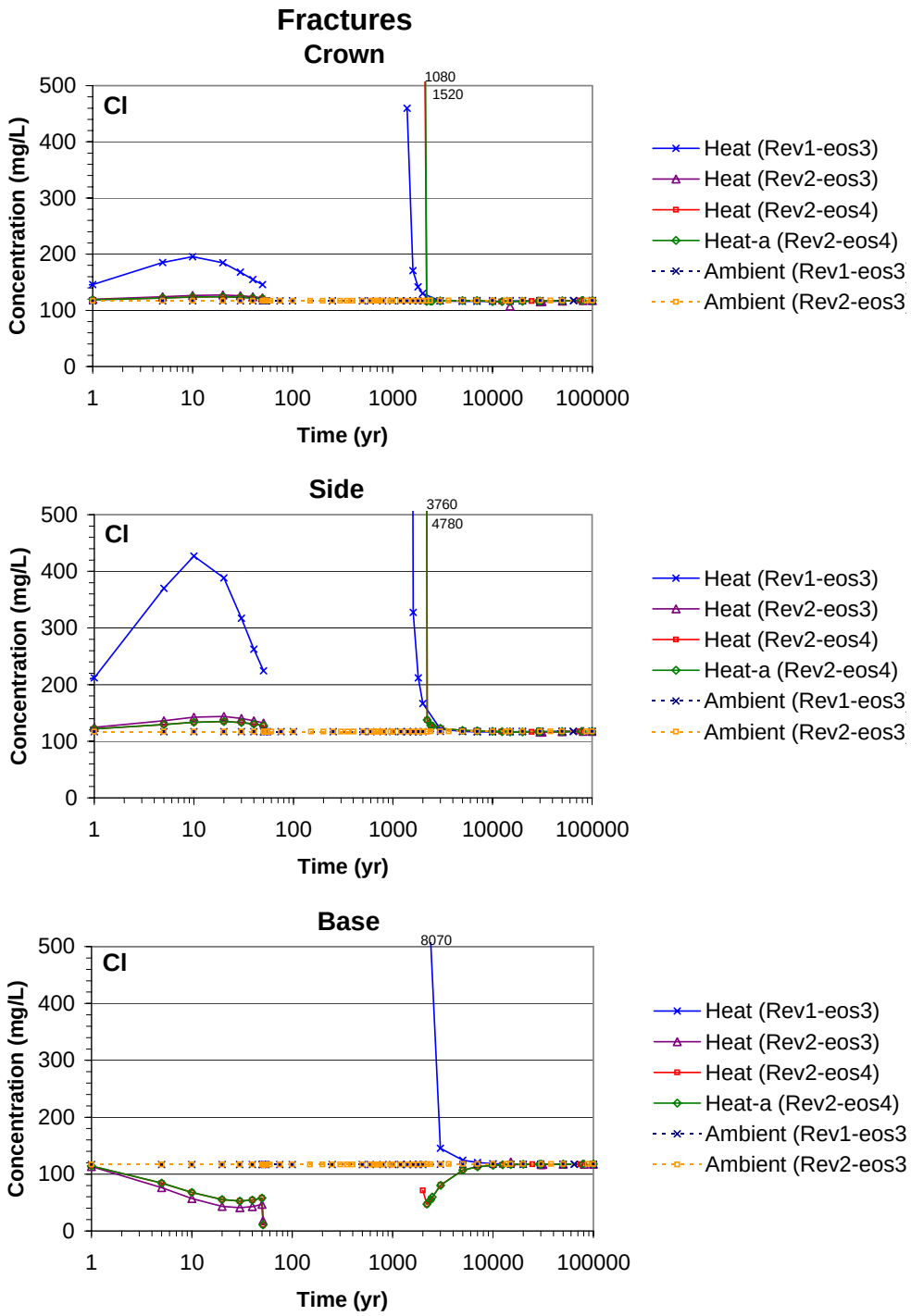

Output-DTNs (REV02): LB0302DSCPTHCS.002, LB0307DSTTHCR2.002
DTN (REV01): LB0011DSTTHCR1.001 [154759]

NOTE: REV01 Simulations and the REV02 Simulation Labeled "Heat-a" were run with the CO_2 diffusion coefficient six times smaller than other simulations (see text).

Figure 6.8-18. THC Simulation (Tptpll, REV01 vs. REV02): Time Profiles of Modeled Total Aqueous Chloride Concentrations in Fracture Water at Three Drift-Wall Locations, under Heating (Heat) and Non-Heating (Ambient) Conditions, Including (eos4) and Excluding (eos3) Water-Vapor-Pressure Lowering

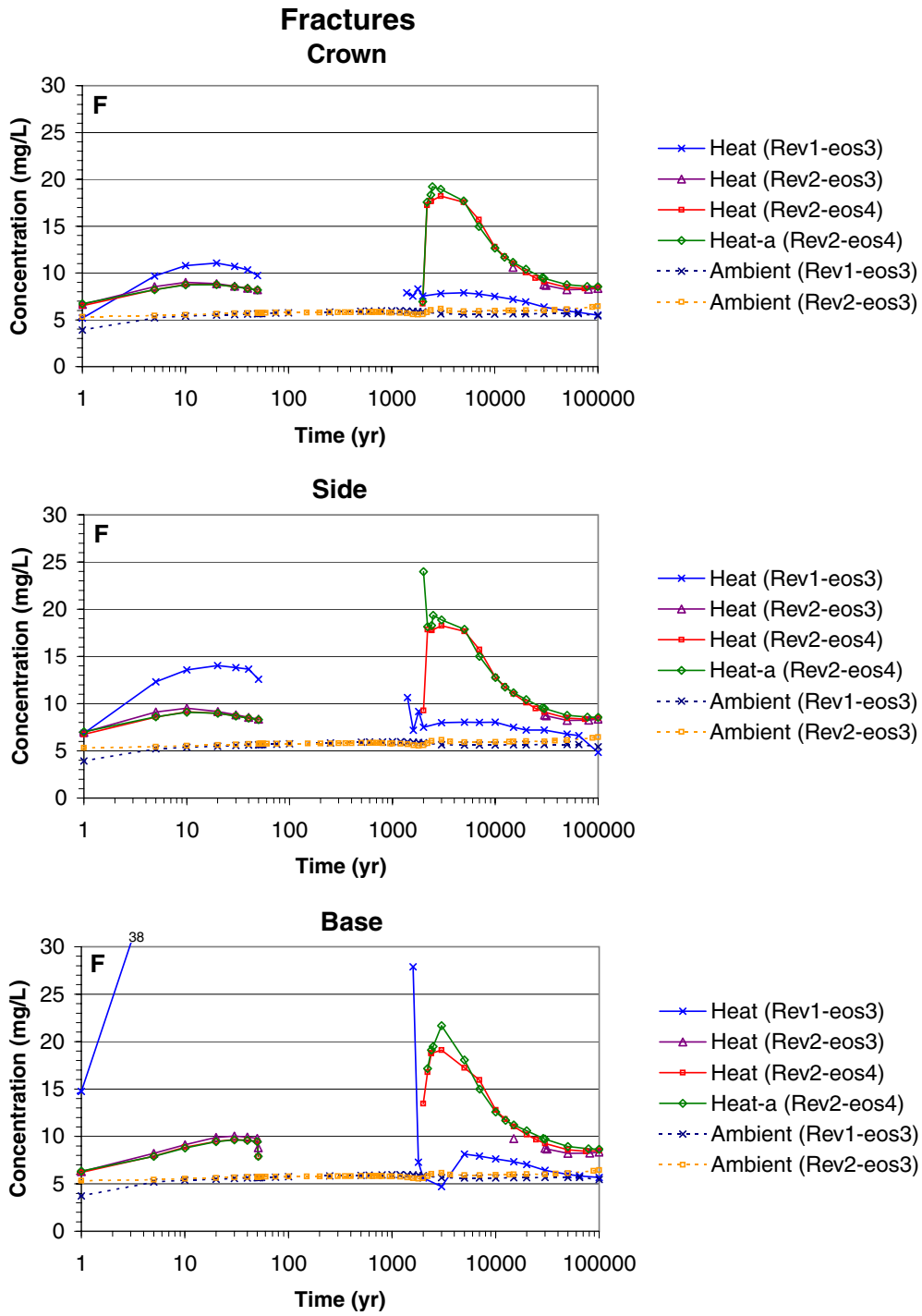

Output-DTNs (REV02): LB0302DSCPTHCS.002, LB0307DSTTHCR2.002
DTN (REV01): LB0011DSTTHCR1.001 [154759]

NOTE: REV01 Simulations and the REV02 Simulation Labeled "Heat-a" were run with the CO_2 diffusion coefficient six times smaller than other simulations (see text).

Figure 6.8-19. THC Simulation (Tptpll, REV01 vs. REV02): Time Profiles of Modeled Total Fluoride Concentrations in Fracture Water at Three Drift-Wall Locations, under Heating (Heat) and Non-Heating (Ambient) Conditions, Including (eos4) and Excluding (eos3) Water-Vapor-Pressure Lowering

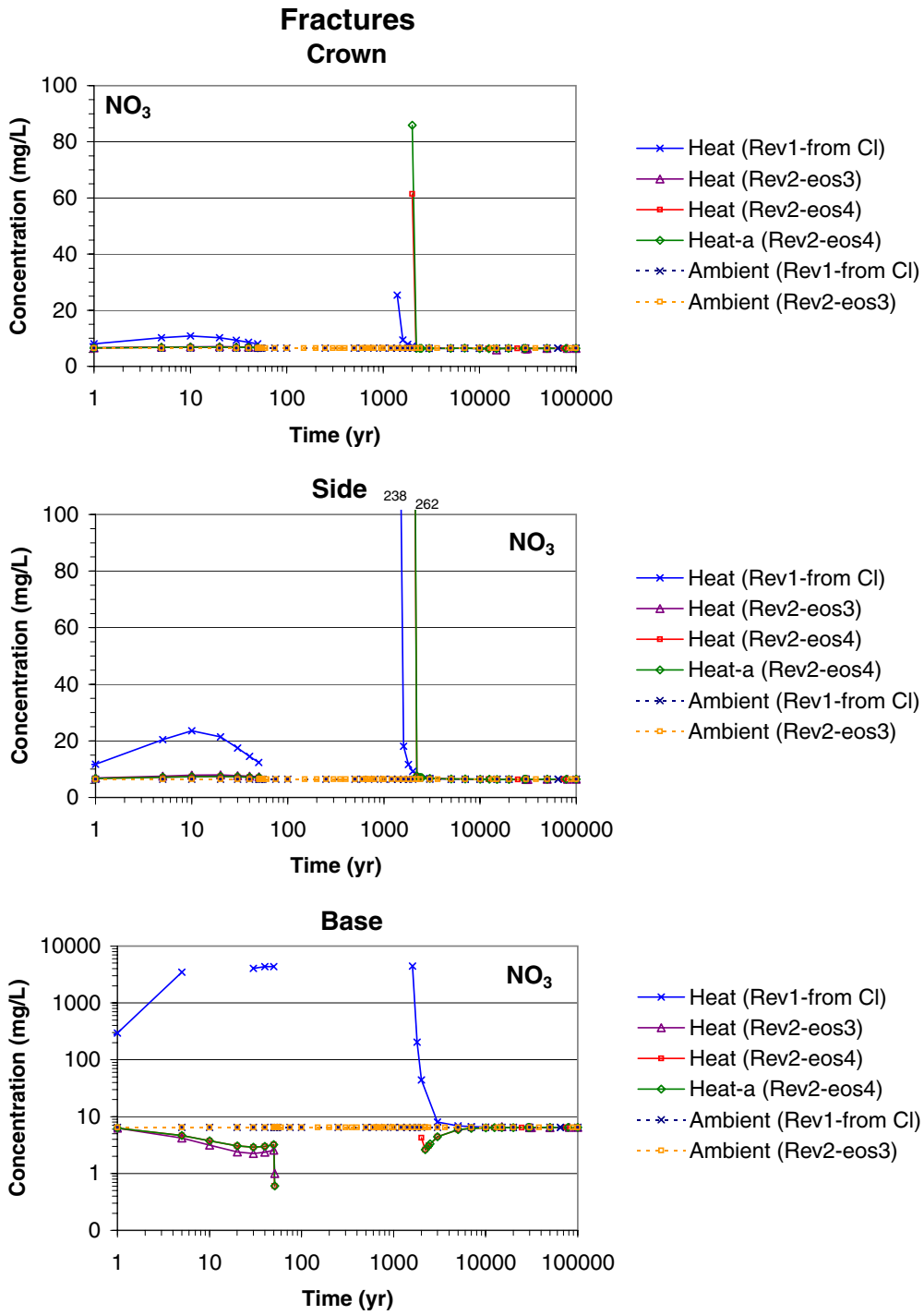

Output-DTNs (REV02): LB0302DSCPTHCS.002, LB0307DSTTHCR2.002
DTN (REV01): LB0011DSTTHCR1.001 [154759]

NOTE: REV01 Simulations and the REV02 Simulation Labeled "Heat-a" were run with the CO_2 diffusion coefficient six times smaller than other simulations (see text).

Figure 6.8-20. THC Simulation (Tptpll, REV01 vs. REV02): Time Profiles of Modeled Total Nitrate Concentrations in Fracture Water at Three Drift-Wall Locations, under Heating (Heat) and Non-Heating (Ambient) Conditions, Including (eos4) and Excluding (eos3) Water-Vapor-Pressure Lowering

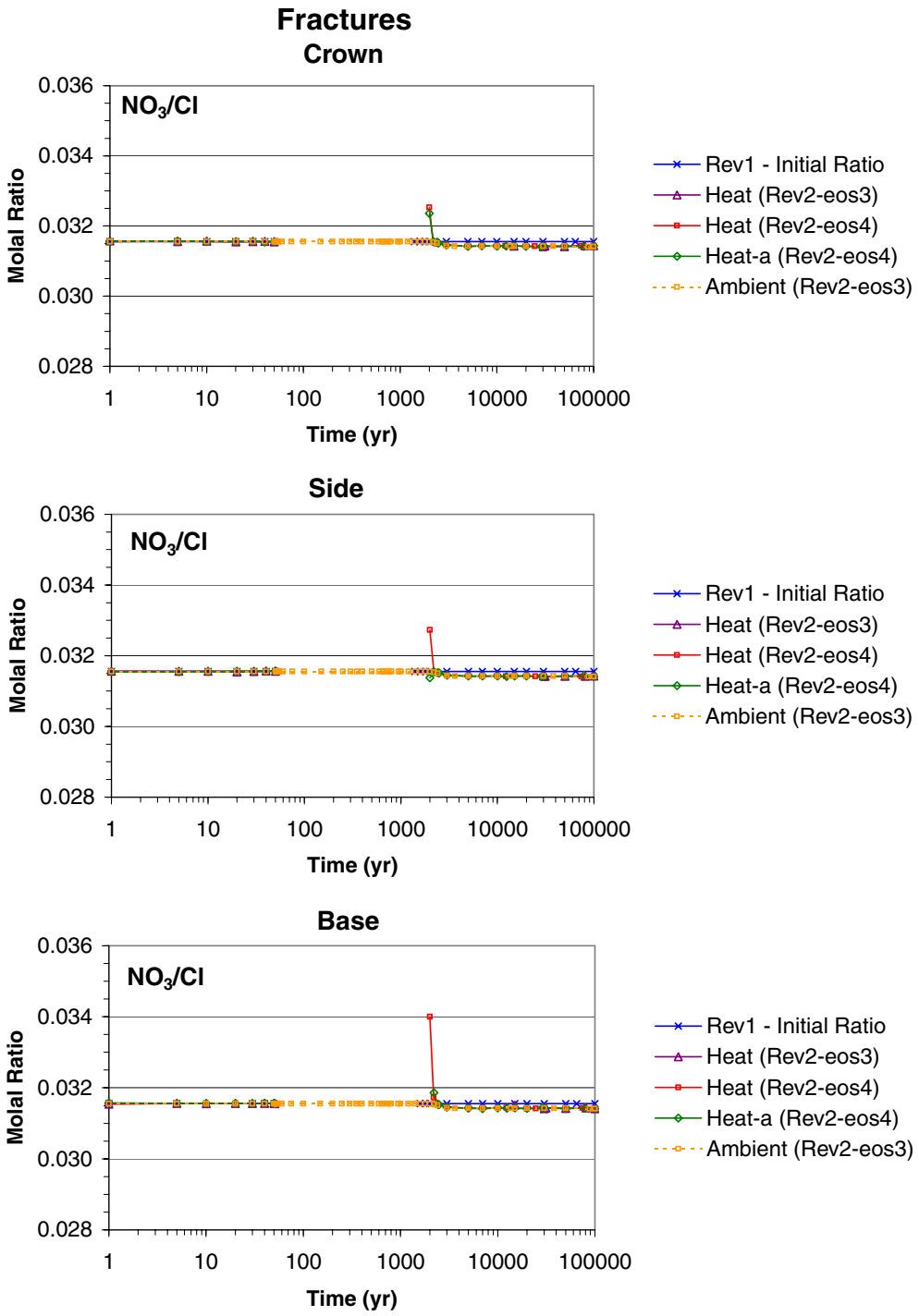

Output-DTNs (REV01): LB0302DSCPTHCS.002, LB0307DSTTHCR2.002
DTN (REV01): LB0011DSTTHCR1.001 [154759]

NOTE: REV01 Simulations and the REV02 Simulation Labeled "Heat-a" were run with the CO_2 diffusion coefficient six times smaller than other simulations (see text).

Figure 6.8-21. THC Simulation (Tptpll, REV01 vs. REV02): Time Profiles of Modeled Total Nitrate to Chloride Ratio at Three Drift-Wall Locations, under Heating (Heat) and Non-Heating (Ambient) Conditions, Including (eos4) and Excluding (eos3) Water-Vapor-Pressure Lowering

6.8.5.3.2 "High"-Liquid Saturation Zone Above Drift Crown (Tptpll REV02)

As reported in previous sections of this report, predicted concentration profiles at fixed model gridblocks at the crown, side, and base of the drift provide only limited information on the chemistry of waters that could seep into drifts. Such profiles do not fully capture the spatial variability of model results around the drift and, more importantly, cannot show water compositions as long as the selected model gridblocks remain dry. To complement results shown in previous sections and to better capture spatial variability, as well as predicted water compositions during the dryout period, concentration time-profiles were also generated for dynamic zones following the expanding, then receding, boiling and condensation fronts around the drift. Most of the model results extracted in this way (using CUTCHEM V1.0 (LBNL 2002 [161127])) will be presented in the upcoming revision of *Abstraction of Drift-Scale Coupled Processes* (CRWMS M&O 2000 [123916]). Here, some of these results are presented for gridblocks with highest liquid saturation above the drift in fractures. More specifically, data were extracted for model gridblocks located within a 45-degree arc from the drift crown down, and for the first six of such gridblocks having the highest liquid saturation in fractures, within 25 m from drift centerline.

Various time profiles are shown below for data extracted in this manner (thus, data for six gridblocks are plotted per point in time for each run). To assess the model sensitivity to initial water compositions and other alternative conceptualizations, time profiles were generated for simulations considering:

- The five different input initial water compositions described in Section 6.2.2.1: W0, the composition used so far (HD-PERM), and alternative compositions W4 through W7

- Three different infiltration scenarios (using the HD-PERM input water composition): stepwise increase from 6 to 25 mm/yr, fixed 6 mm/yr, and fixed 25 mm/yr (Table 6.8-2)

- The two different water vapor-pressure models implemented in TOUGHREACT V3.0 (LBNL 2002 [161256] modules EOS4 and EOS3 (using the HD-PERM input water composition): with and without vapor-pressure lowering due to capillary pressure.

Therefore, time profiles generated in this way capture a spread of concentrations related to (1) the natural variability of input water compositions, (2) alternative model conceptualizations, and (3) for each model run at any given time, the spatial variability of model results for gridblocks of highest liquid saturation above the drift crown. In addition to this spread, fluctuations of computed concentrations with time arising from THC effects (as discussed below) are also captured.

The distance from drift center, temperature, and liquid saturation in model gridblocks having the highest liquid saturation (above the drift) picked up by the extraction procedure (using CUTCHEM V1.0 (LBNL 2002 [161127]) are shown in Figures 6.8-22, 6.8-23, and 6.8-24, respectively (these figures exclude a few points extracted at times around 50 years and located approximately 24 m away from the drift center). These data provide a context for the chemistry profiles discussed below. For simulated times up to 50 years, all data are from zones directly above, and adjacent to, the drift crown (i.e., at a distance approximately 2.8 m from drift center)

(Figure 6.8.22). From the onset of boiling at approximately 50 years, high-liquid-saturation gridblocks are all from the condensation (reflux) zone above the drift. Later, after the collapse of the boiling front, gridblocks with the highest liquid saturation are located either directly adjacent to the drift crown (e.g., some of the W0 data on Figure 6.8-22) or further away, adjacent to zones of reduced permeability formed by prior mineral deposition at the boiling front. These zones are discussed in Section 6.8.5.4.

After the onset of boiling, starting at approximately 50 years, the temperature in the most highly liquid-saturated gridblocks remains nearly constant (near 96°C, the boiling point for the modeled elevation), as would be expected in the zone of condensation and reflux (Figure 6.8-23). For most runs, the boiling temperature in these gridblocks is maintained until around 1,000 years. The boiling front is predicted to collapse a few hundred years earlier for the case with the higher constant infiltration rate of 25 mm/yr (Figure 6.8-23). This period of time, during which temperatures are maintained at the boiling point of water, is hereafter referred to as the "boiling period." Temperature profiles predicted with the various runs are quite similar, except for the shorter boiling period at higher infiltration. The greatest predicted temperature difference between simulations (around 5°C) is also caused by differences in infiltration rate.

For a given run, and at a given time, predicted liquid saturations in the first six gridblocks with highest liquid saturation (above the drift) are fairly uniform (Figure 6.8-24), because these data represent areas of highest liquid saturation in a laterally homogenous model. Consequently, corresponding concentration time-profiles (Figures 6.8-25 through 6.8-38), for each run at any given time, also show less spatial variability than would evaporated waters from gridblocks with much smaller and variable liquid saturations (such as at the boiling front). Therefore, examining the variability of predicted water compositions in zones of highest liquid saturation provides a better means of evaluating the model sensitivity to various input data or model conceptualizations than would examination of predicted water compositions directly at the boiling front. This is the main reason for focusing on zones of highest liquid saturation. However, when evaluating the compositional variability of waters that could seep into a drift during the boiling period (by somehow penetrating the dryout zone), the predicted water composition at the boiling front should also be considered. This variability will be assessed in the upcoming revision of *Abstraction of Drift-Scale Coupled Processes* (CRWMS M&O 2000 [123916]).

Predicted profiles of concentration versus time for CO_2 gas and aqueous species of interest are shown in Figures 6.8-25 through 6.8-38. Three observations are particularly significant:

(1) In general, these figures indicate that the different input water compositions (i.e., natural variability) produce a larger relative spread in predicted water and gas compositions than the range of infiltration rates considered or the selected water-vapor pressure module;

(2) At any one point, the relative spread of predicted concentrations for the various modeled alternatives (at those gridblocks with highest liquid saturation above the drift crown) generally does not exceed an order of magnitude and is often much less (see Section 6.9-2; details will also be provided in upcoming revision of *Abstraction of Drift-Scale Coupled Processes* (CRWMS M&O 2000 [123916]));

(3) Finally, for all simulations shown, the predicted general concentration trends are quite similar.

The modeled CO_2 concentrations in zones of condensation and reflux (Figure 6.8-25) are initially higher than at drift wall locations shown previously, because heat mobilizes CO_2 outwards from the drift wall (see also Section 7.1). However, CO_2 concentrations eventually also decrease in the reflux/condensation zone because of continued depletion of aqueous carbonate (Figure 6.8-27) from CO_2 exsolution and calcite precipitation (see below). The subsequent trend of rising CO_2 concentration (from approximately 600 to 2,000 years) (Figure 6.8-25) was also noted earlier for locations at the drift wall (Figure 6.8-12). Note that during this time period, when the CO_2 concentrations are rising (from approximately 600 to 2000 years), the spread of these concentrations is sharply reduced compared to the spread during other simulated time intervals (Figure 6.8-25a). This appears to be caused by the arrival of percolating water with a significantly higher dissolved CO_2 content than the locally decarbonated water. This temporarily higher dissolved CO_2 content in percolation water results from prior mobilization of CO_2 gas from matrix water into fractures, further up the stratigraphic column. The case with a decrease in CO_2 diffusion coefficient (Figure 6.8-25b) shows a similar rise but occurring at a somewhat delayed time, due to the decreased diffusive mobility. The decreasing pH values from approximately 600 to 2000 years (Figure 6.8-26) is also consistent with the arrival of more carbonated water from prior CO_2 gas mobilization. After approximately 2000 years, the spread in concentrations increases again as these concentrations become less driven by the mobilization of CO_2 and more by water-rock interactions that are more sensitive to the composition of infiltration water (even though all waters are set with the same CO_2 partial pressure at the top model boundary). Also, the increase in infiltration rate at 2000 years exacerbates this effect. The profiles of total aqueous carbonate concentrations (Figure 6.8-27) are consistent with this trend, showing a significant decrease in relative spread when concentrations increase after approximately 600 years until about 2000 years, then spreading wider again after that time.

After the rise in CO_2 concentrations, the simulation using a constant 6 mm/yr infiltration rate predicts an earlier decrease in these concentrations than other simulations (all using 25 mm/yr in this time period) (Figure 6.8-25b). In the 25 mm/yr cases, CO_2 concentrations diminish at later times because more CO_2 was mobilized (exsolved from incoming water) prior to the collapse of the boiling front. Note that in the 6 mm/yr case, CO_2 concentrations rise again somewhat after 15,000 years because of a second small pulse of slightly more carbonated water percolating downwards (related to the various degrees of water-rock interaction in the different stratigraphic units further above the drift).

The predicted range of pH values covered by all simulations (Figure 6.8-26) is from approximately 7.2 to 8.4. This range is fairly small and is similar to the range predicted previously for locations directly adjacent to the drift wall. After long periods of time (> 10,000 years), predicted pH values for runs using the different input water compositions tend to converge towards similar ambient values (in the 8.2–8.4 range after 100,000 years). Values of pH rise towards these ambient values after a decrease (from approximately 600 to 2,000 years) caused by the percolation of more carbonated and thus slightly more acidic waters as discussed above. For some of the waters considered, these long-term ambient values are slightly higher than initial values (in the ~8–8.3 range, see Table 6.2-1) because the long-term alteration of rock-forming minerals (e.g., Equations. 6.5-1 and 6.5-2) tends to drive the pH up.

The concentration profiles of conservative species such as chloride (Figure 6.8-28) (and also nitrate in simulations presented here; Figure 6.8-29) are useful in evaluating the degree of dilution and evaporative concentration in the areas for which predicted water compositions are shown. Dilution from condensation initially occurs (within a factor of around 10) after the onset of boiling. However, later in the boiling period, evaporative concentration takes over (also within a factor of around 10, compared to initial values). Comparing the chloride concentration profiles (Figure 6.8-28) with profiles showing the distance from drift center at which these concentrations occur (Figure 6.8-22) helps in distinguishing the following successive stages in the evolution of water composition in the condensation zone:

1. A dilution stage occurs when the dryout zone is expanding, roughly from 50 to around 100-150 years. It is caused by steam originating from water boiling in the rock matrix then migrating and condensing into fractures (Section 6.2.1.1).

2. An evaporative concentration stage takes place while the high liquid saturation zone remains essentially stationary. The water in fractures is concentrated by boiling the percolating water, with no or little additional influx of condensation water derived from boiling matrix water. This stage lasts approximately from 150 years to 600 years for most waters, but is shorter by several hundred years under the higher infiltration rate (Figure 6.8-28).

3. A "back-to-ambient" stage starts while boiling is still occurring, after approximately 600 years (and earlier at higher infiltration rates), then continuing after the collapse of the boiling front. During this stage, the dilution by percolating waters overcomes the effect of evaporative concentration and brings concentrations back to their ambient values.

The effects of these three distinct stages are visible on the predicted concentration trends of most constituents. In the case of chloride, looking at the results of all simulations, concentrations drop to as low as around 1 ppm (with Water W6) during the dilution stage and rise to as high as approximately 1,500 ppm (with Water W0) during the evaporative concentration stage (Figure 6.8-28).

The trends of most other aqueous species can be evaluated in terms of the degree of dilution, concentration, and mineral reaction taking place. By dividing aqueous species concentrations by chloride concentrations, the relative degree of mineral dissolution or precipitation can be evaluated. However, the variations of these ratios do not necessarily indicate that reactions are taking place in the gridblocks where the ratios are evaluated. Reactions in the rock matrix could also affect these ratios in fracture water if significant diffusion were to occur between fractures and matrix. Reactions above areas being investigated could also affect these ratios. In the present simulations, in zones of highest liquid saturation above the drift crown, predicted increases in Ca/Cl in fractures during the dilution stage (after the onset of boiling and steam condensation) (Figure 6.8-31) result from calcite dissolution in fractures. This dissolution is enhanced by the somewhat lower pH of condensation waters caused by CO_2 dissolution (see also Section 7.1). After this time, when evaporative concentration takes over, Ca/Cl ratios decrease through precipitation of calcite and, to a lesser extent, of stellerite. The trends of Ca/Cl ratios in logarithmic form (Figure 6.8-31) are similar and somewhat parallel for all simulations,

suggesting that the degree of reaction involving calcium minerals is similar in all cases considered.

The Na/Cl ratios in fracture water also increase initially during the dilution stage (Figure 6.8-33), but much less than Ca/Cl ratios. The increase in this case results from albite dissolution (accompanied by stellerite precipitation, e.g., Equations 6.5-1 and 6.5-2), which occurs at a much slower rate than calcite dissolution. After the dilution stage, the Na/Cl ratios decrease significantly, even though albite is still dissolving in fractures. The Na/Cl decrease in this case appears to result from sodium diffusion into the rock matrix where albite precipitation is taking place (not shown here). This trend is eventually reversed by the continued alteration of albite to stellerite in fractures, which becomes even more pronounced as the evaporative stage ends. Like the Ca/Cl ratios, the similar and somewhat parallel trends of Na/Cl ratios (in logarithmic form) would suggest that all waters react to a similar degree with sodium phases.

As discussed in Section 6.2.2.1, the ratio of calcium to total aqueous carbonate concentration (expressed here as Ca/HCO_3) gives some indication of the likelihood for a water to evolve towards a potentially deleterious calcium chloride brine upon continued evaporation. These brines are more likely to form in initial waters with a Ca/HCO_3 molal ratio greater than 0.5 (or, in equivalents, a ratio greater than 1). These values are exceeded during the evaporative concentration stage for all considered initial water compositions (Figure 6.8-34). However, Waters W0 and W7 display Ca/HCO_3 ratios significantly higher than the other waters. Water W4 shows the lowest ratios.

Ratios of nitrate to chloride (Figure 6.8-35) remain essentially constant. This is expected because redox processes are not considered in these simulations, and solid nitrate and chloride phases are formed only upon complete dryout (Section 6.4.5). The redissolution of nitrate and chloride salts formed during dryout has a short-lived, hardly noticeable effect in zones with the highest liquid saturations.

The predicted magnesium concentrations (Figure 6.8-36) reflect the effects of the dilutive and evaporative concentration stages discussed earlier, but remain significantly depressed below ambient values after the boiling period. The magnesium depletion is caused by the precipitation of sepiolite early in the simulations. This depletion is also observed in the simulations of ambient conditions (Section 6.8.5.1) and is not consistent with observed water compositions at Yucca Mountain. One reason may be that sepiolite is either too stable or that it does not belong in the set of selected potential secondary minerals. REV01 simulations (ambient and thermal pulse) without sepiolite in the geochemical system did not predict such magnesium depletion. Another reason for underestimating magnesium concentrations could be the lack of primary magnesium-bearing minerals in simulations (e.g., biotite). These minerals, however, occur in small amounts in the repository host units. Younger calcite at Yucca Mountain has been reported to contain up to around 1% (by weight) magnesium (Wilson et al. 2000 [154279]). Therefore, taking this into account in simulations would also have an effect on predicted magnesium concentrations. This would contribute more magnesium in solution during calcite dissolution, but could also result in magnesium depletion upon calcite precipitation (under both thermal loading and ambient conditions).

Predicted dissolved silica concentration profiles (Figure 6.8-37) show the same effects of dilution and evaporative concentration as most other species. Profiles of SiO_2/Cl ratios (not shown here) have the same general shape as the Ca/Cl profiles (Figure 6.8-31) and indicate significant silica dissolution during the dilution stage, as would be expected. Later, continued reflux and boiling lead to an increase in concentrations. Predicted concentrations eventually reached values greater than the solubility of amorphous silica (around 350 ppm at 95°C). This is because at this point, the calculated precipitation rate of amorphous silica, although quite fast, cannot keep up with the boiling rate. In the natural system, these elevated concentrations (up to around 1,200 ppm) may not be reached.

Predicted fluoride concentrations (Figure 6.8-38) follow a trend similar to the trend of silica and other aqueous species. The host rock is modeled with a small, ubiquitous amount of primary fluorite. As noted earlier, because the reaction rate of fluorite is fast, waters generally reach saturation with respect to this mineral. During the boiling and refluxing stage, concentrations up to around 40 ppm are predicted, which are much larger than the concentration (~ 1.4 ppm) calculated by equilibrating fluorite with the solution, using the maximum calcium concentrations (around 0.02 molal, see Figure 6.8-30) predicted during that time period. In this case also, the precipitation rate of fluorite cannot keep up with the boiling rate. Eventually, concentrations come back to values dictated by equilibrium of ambient waters with fluorite (typically in the 4–8 ppm range).

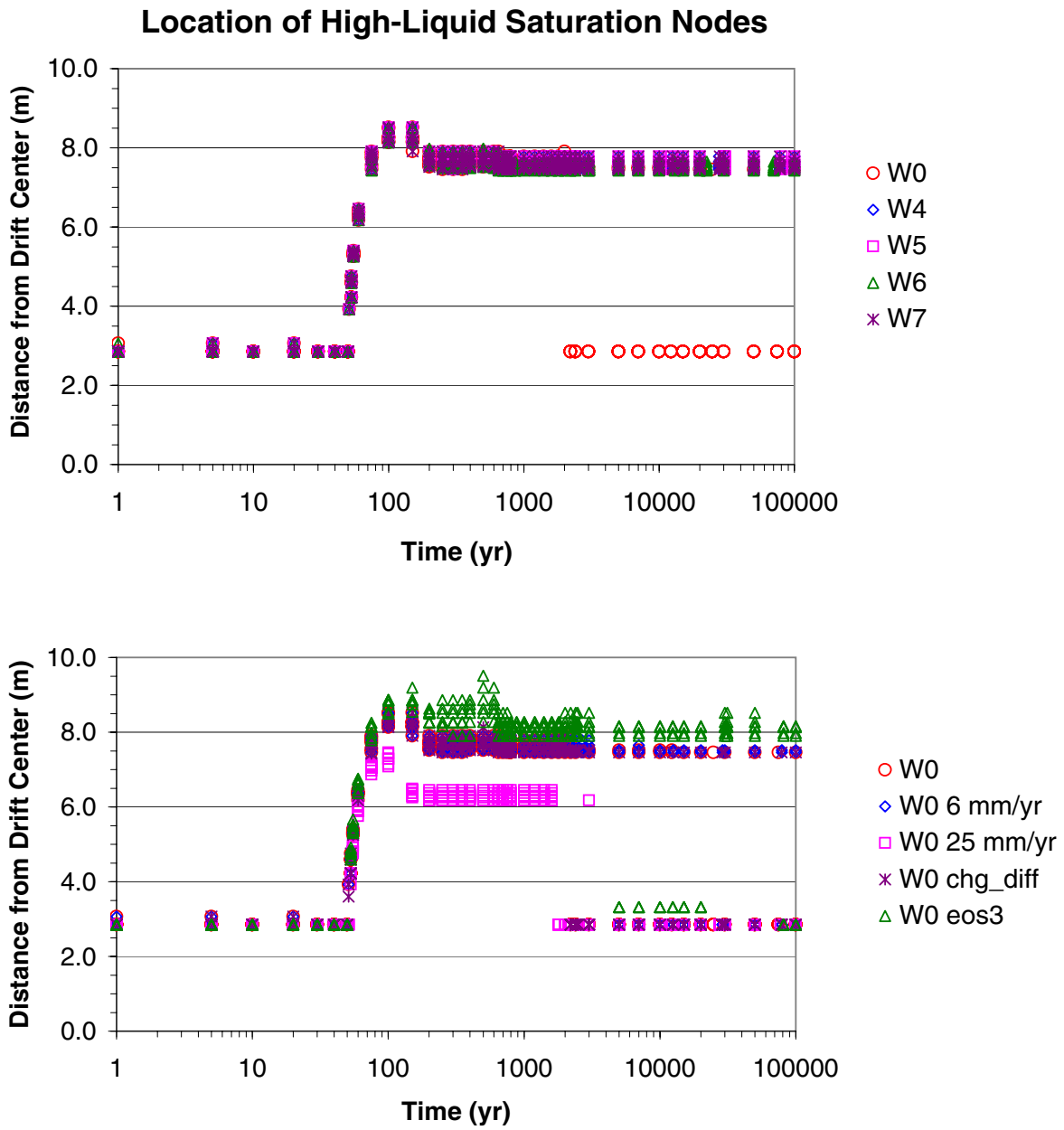

Output-DTNs: LB0302DSCPTHCS.002, LB0307DSTTHCR2.002

NOTE: Gridblocks are those with highest liquid saturation in fractures within a 25 m radius from drift center and a 45° arc from the drift crown. Data are shown for simulations using different initial water compositions (W0 – W7). Except as noted below, all simulations were run using a stepwise-increasing infiltration rate (6, 16, and 25 mm/y) and with vapor pressure lowering. Alternatives using Water W0 include simulations without vapor pressure lowering (W0 - eos3), and with fixed 25 and 6 mm/y infiltration rates (W0 - 6 mm/y and W0 - 25 mm/y, respectively).

Figure 6.8-22. THC Simulations (Tptpll Model REV02): Location of Model Gridblocks for Data Shown on Figures 6.8-23–6.8-38, for Each Time When Model Output Is Produced

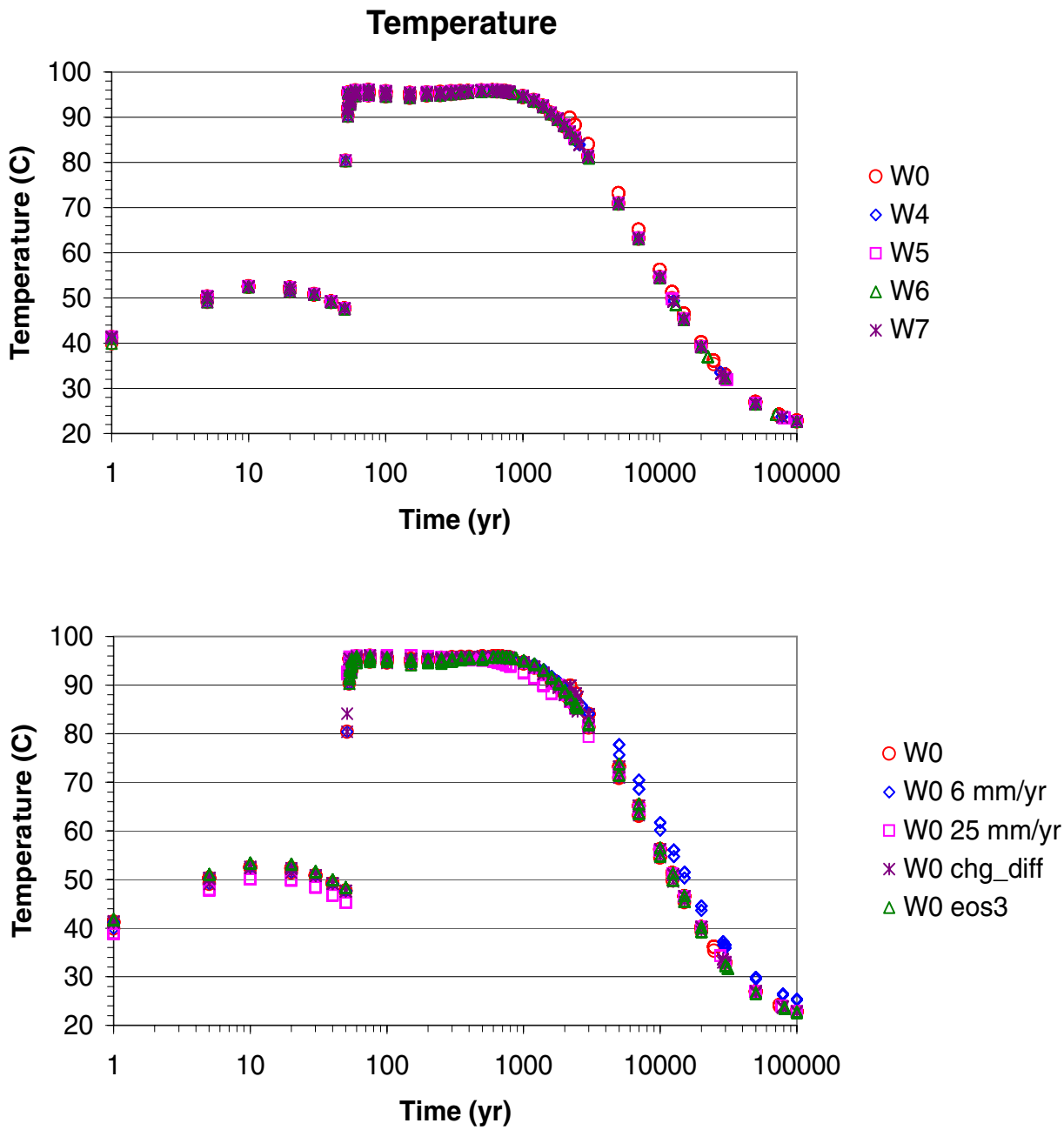

Output-DTNs: LB0302DSCPTHCS.002, LB0307DSTTHCR2.002

NOTE: Gridblocks are those with highest liquid saturation in fractures within a 25 m radius from drift center and a 45° arc from the drift crown. Data are shown for simulations using different initial water compositions (W0 – W7). Except as noted below, all simulations were run using a stepwise-increasing infiltration rate (6, 16, and 25 mm/y) and with vapor pressure lowering. Alternatives using Water W0 include simulations without vapor pressure lowering (W0 - eos3), and with fixed 25 and 6 mm/y infiltration rates (W0 - 6 mm/y and W0 - 25 mm/y, respectively).

Figure 6.8-23. THC Simulations (Tptpll Model REV02): Time Profiles of Modeled Temperatures in Fracture Water, in Areas of Highest Liquid Saturation above the Drift Crown

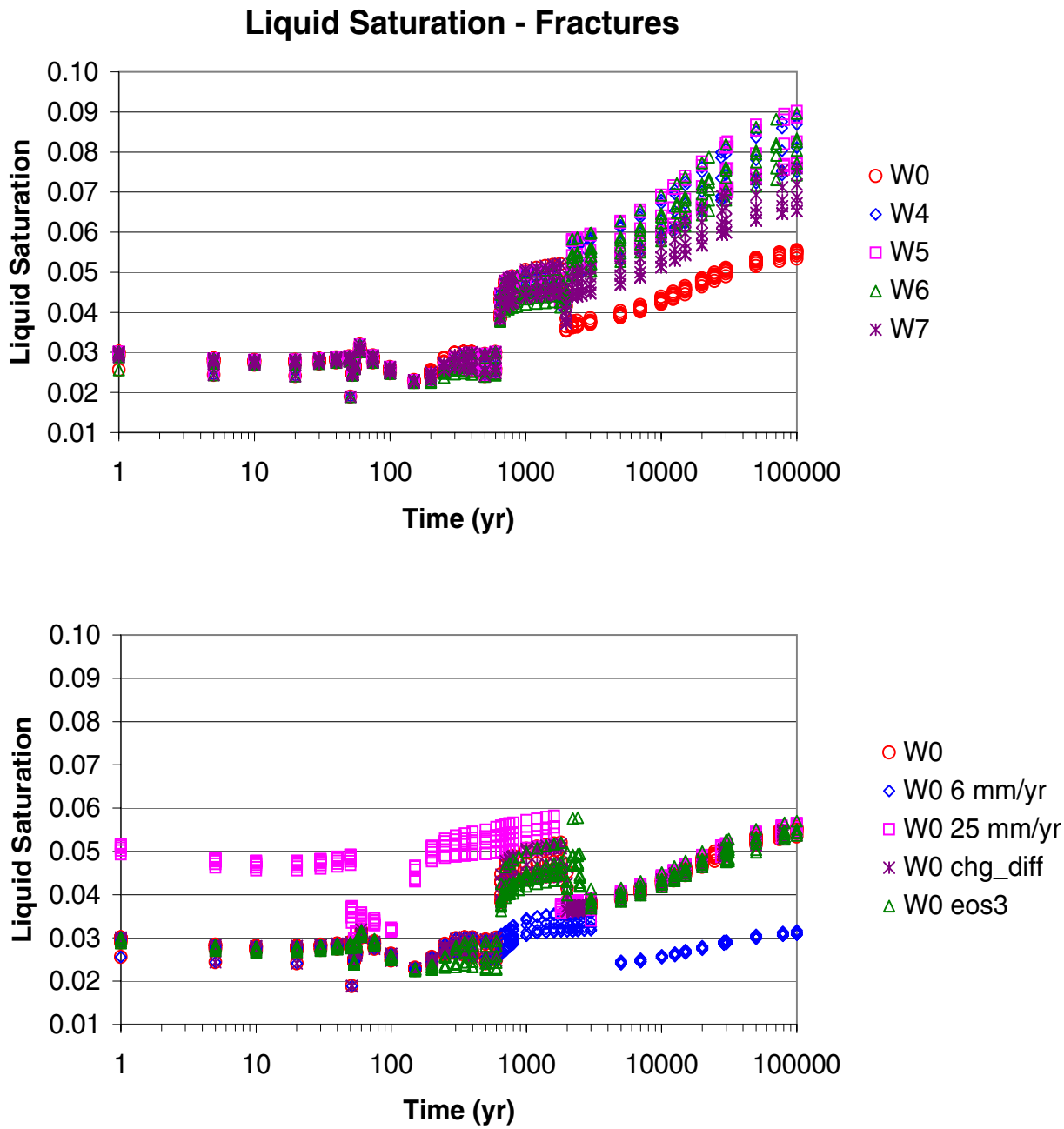

Output-DTNs: LB0302DSCPTHCS.002, LB0307DSTTHCR2.002

NOTE: Gridblocks are those with highest liquid saturation in fractures within a 25 m radius from drift center and a 45° arc from the drift crown. Data are shown for simulations using different initial water compositions (W0 – W7). Except as noted below, all simulations were run using a stepwise-increasing infiltration rate (6, 16, and 25 mm/y) and with vapor pressure lowering. Alternatives using Water W0 include simulations without vapor pressure lowering (W0 - eos3), and with fixed 25 and 6 mm/y infiltration rates (W0 - 6 mm/y and W0 - 25 mm/y, respectively).

Figure 6.8-24. THC Simulations (Tptpll Model REV02): Time Profiles of Modeled Liquid Saturations in Fracture Water, in Areas of Highest Liquid Saturation above the Drift Crown

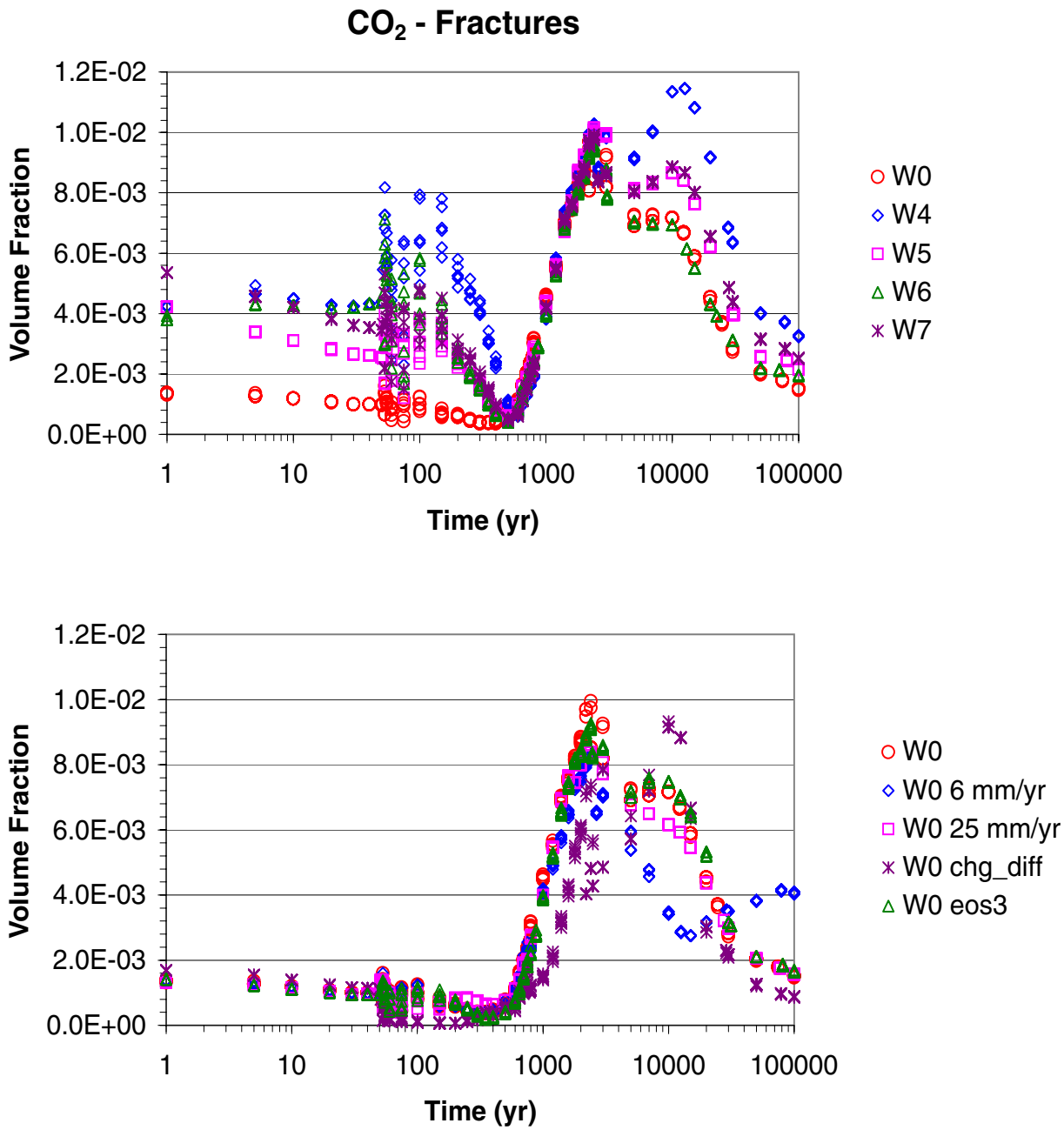

Output-DTNs: LB0302DSCPTHCS.002, LB0307DSTTHCR2.002

NOTE: Gridblocks are those with highest liquid saturation in fractures within a 25 m radius from drift center and a 45° arc from the drift crown. Data are shown for simulations using different initial water compositions (W0 – W7). Except as noted below, all simulations were run using a stepwise-increasing infiltration rate (6, 16, and 25 mm/y) and with vapor pressure lowering. Alternatives using Water W0 include simulations without vapor pressure lowering (W0 - eos3), and with fixed 25 and 6 mm/y infiltration rates (W0 - 6 mm/y and W0 - 25 mm/y, respectively).

Figure 6.8-25. THC Simulations (Tptpll Model REV02): Time Profiles of Modeled CO_2 Gas Concentrations in Fracture Water, in Areas of Highest Liquid Saturation above the Drift Crown

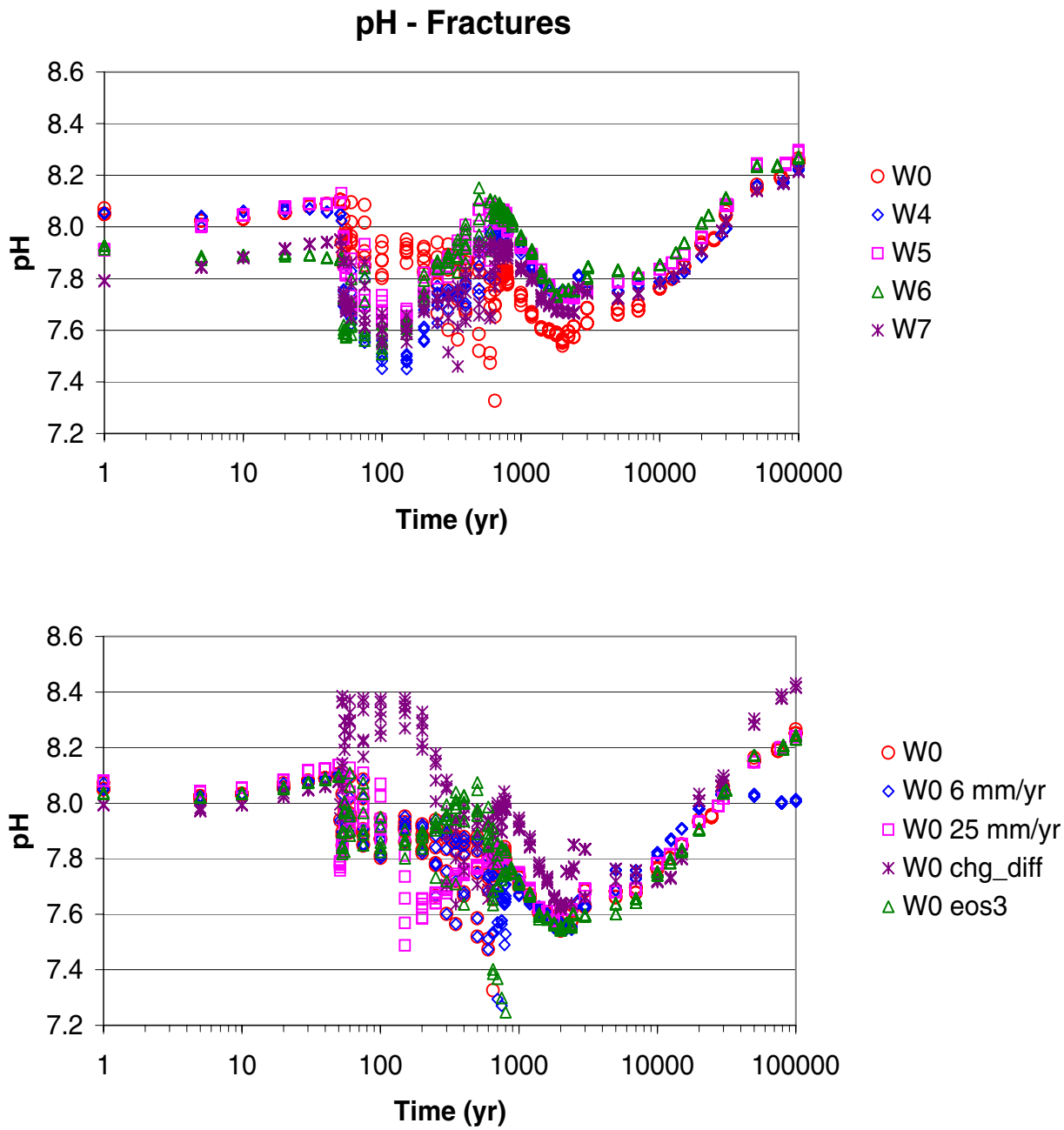

Output-DTNs: LB0302DSCPTHCS.002, LB0307DSTTHCR2.002

NOTE: Gridblocks are those with highest liquid saturation in fractures within a 25 m radius from drift center and a 45° arc from the drift crown. Data are shown for simulations using different initial water compositions (W0 – W7). Except as noted below, all simulations were run using a stepwise-increasing infiltration rate (6, 16, and 25 mm/y) and with vapor pressure lowering. Alternatives using Water W0 include simulations without vapor pressure lowering (W0 - eos3), and with fixed 25 and 6 mm/y infiltration rates (W0 - 6 mm/y and W0 - 25 mm/y, respectively).

Figure 6.8-26. THC Simulations (Tptpll Model REV02): Time Profiles of Modeled pH in Fracture Water, in Areas of Highest Liquid Saturation above the Drift Crown

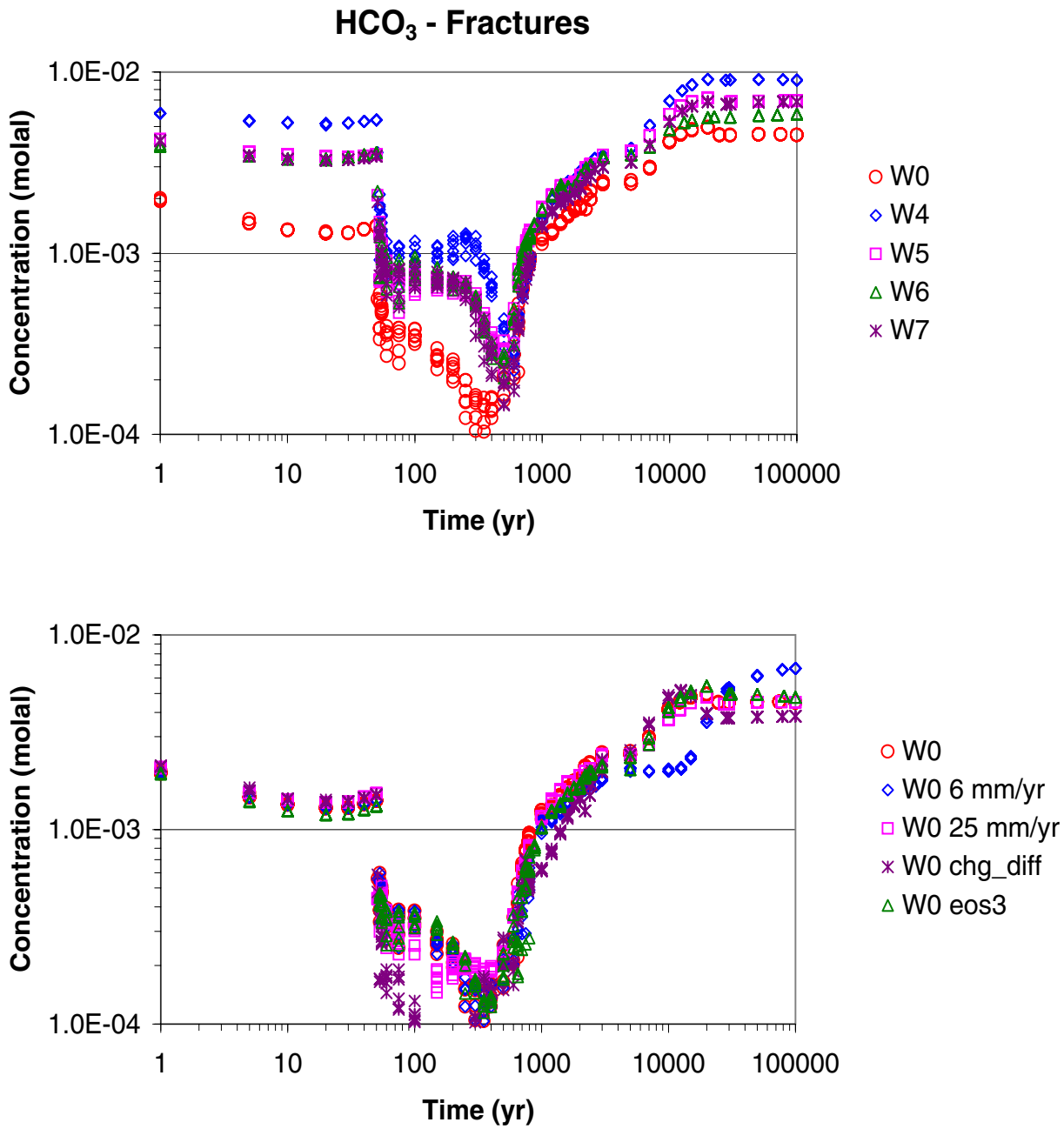

Output-DTNs: LB0302DSCPTHCS.002, LB0307DSTTHCR2.002

NOTE: Gridblocks are those with highest liquid saturation in fractures within a 25 m radius from drift center and a 45° arc from the drift crown. Data are shown for simulations using different initial water compositions (W0 – W7). Except as noted below, all simulations were run using a stepwise-increasing infiltration rate (6, 16, and 25 mm/y) and with vapor pressure lowering. Alternatives using Water W0 include simulations without vapor pressure lowering (W0 - eos3), and with fixed 25 and 6 mm/y infiltration rates (W0 - 6 mm/y and W0 - 25 mm/y, respectively).

Figure 6.8-27. THC Simulations (Tptpll Model REV02): Time Profiles of Modeled Total Aqueous Carbonate Concentrations (as HCO_3) in Fracture Water, in Areas of Highest Liquid Saturation above the Drift Crown

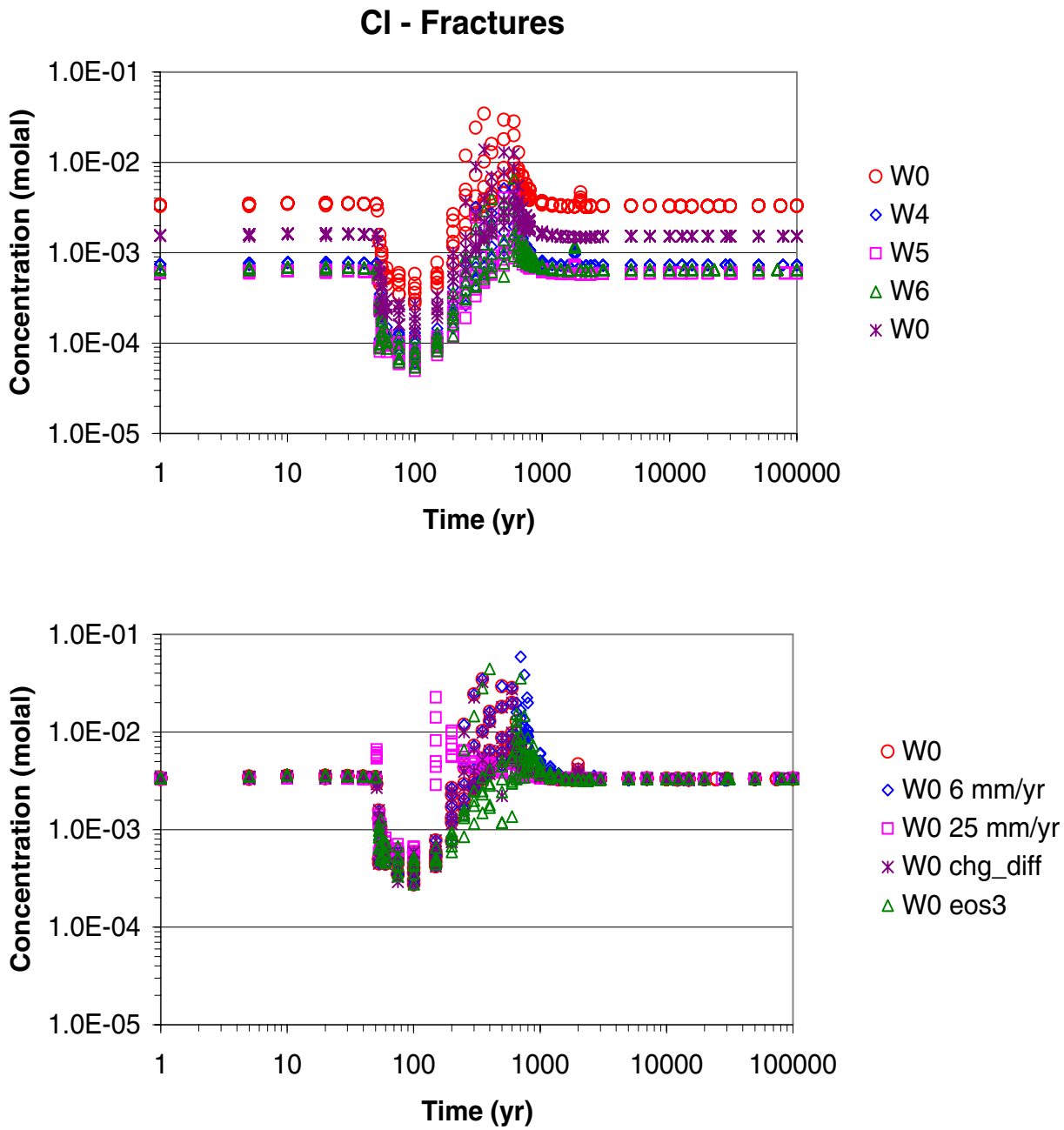

Output-DTNs: LB0302DSCPTHCS.002, LB0307DSTTHCR2.002

NOTE: Gridblocks are those with highest liquid saturation in fractures within a 25 m radius from drift center and a 45° arc from the drift crown. Data are shown for simulations using different initial water compositions (W0 – W7). Except as noted below, all simulations were run using a stepwise-increasing infiltration rate (6, 16, and 25 mm/y) and with vapor pressure lowering. Alternatives using Water W0 include simulations without vapor pressure lowering (W0 - eos3), and with fixed 25 and 6 mm/y infiltration rates (W0 - 6 mm/y and W0 - 25 mm/y, respectively).

Figure 6.8-28. THC Simulations (Tptpll Model REV02): Time Profiles of Modeled Total Aqueous Chloride Concentrations in Fracture Water, in Areas of Highest Liquid Saturation above the Drift Crown

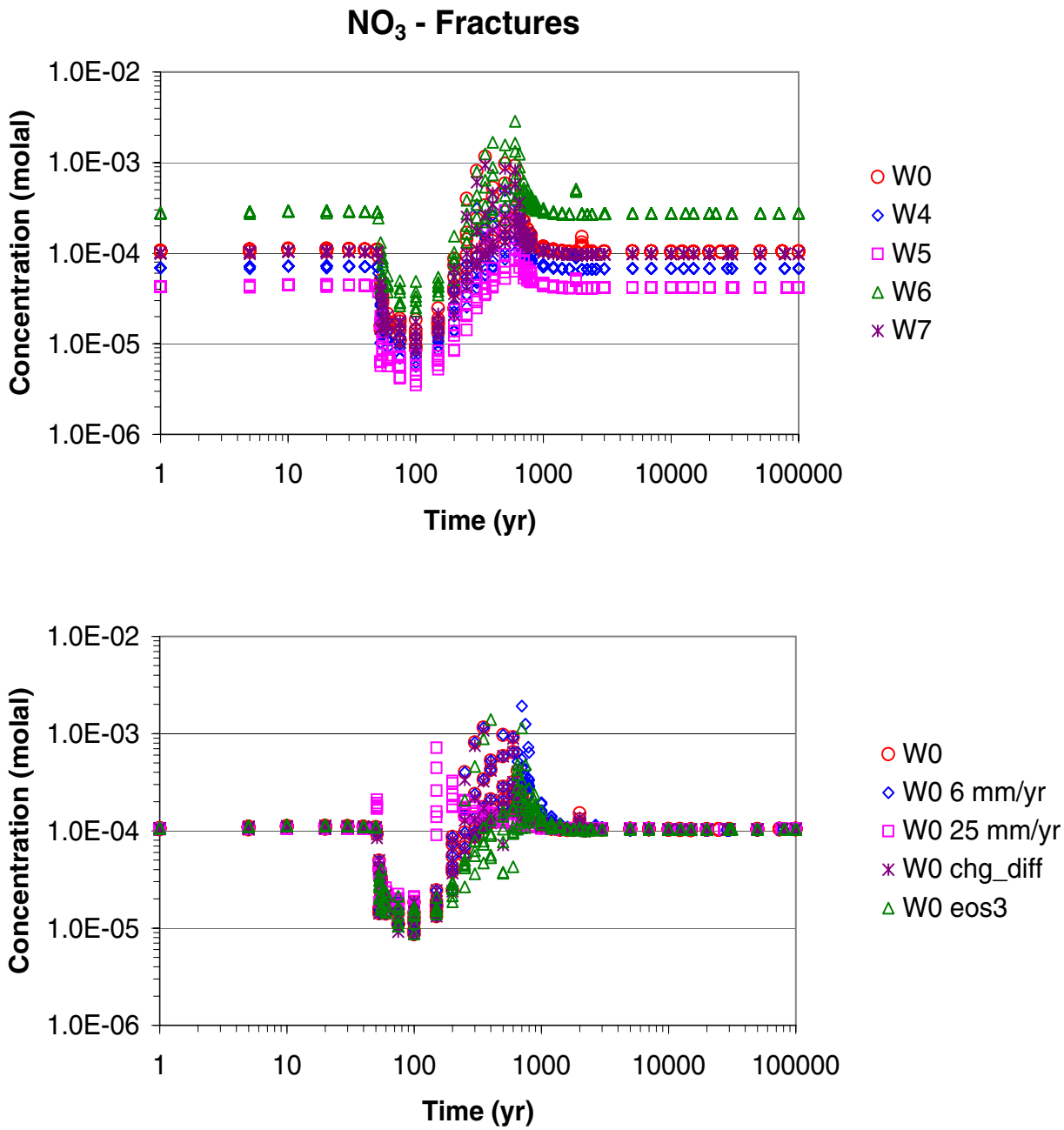

Output-DTNs: LB0302DSCPTHCS.002, LB0307DSTTHCR2.002

NOTE: Gridblocks are those with highest liquid saturation in fractures within a 25 m radius from drift center and a 45° arc from the drift crown. Data are shown for simulations using different initial water compositions (W0 – W7). Except as noted below, all simulations were run using a stepwise-increasing infiltration rate (6, 16, and 25 mm/y) and with vapor pressure lowering. Alternatives using Water W0 include simulations without vapor pressure lowering (W0 - eos3), and with fixed 25 and 6 mm/y infiltration rates (W0 - 6 mm/y and W0 - 25 mm/y, respectively).

Figure 6.8-29. THC Simulations (Tptpll Model REV02): Time Profiles of Modeled Total Aqueous Nitrate Concentrations in Fracture Water, in Areas of Highest Liquid Saturation above the Drift Crown

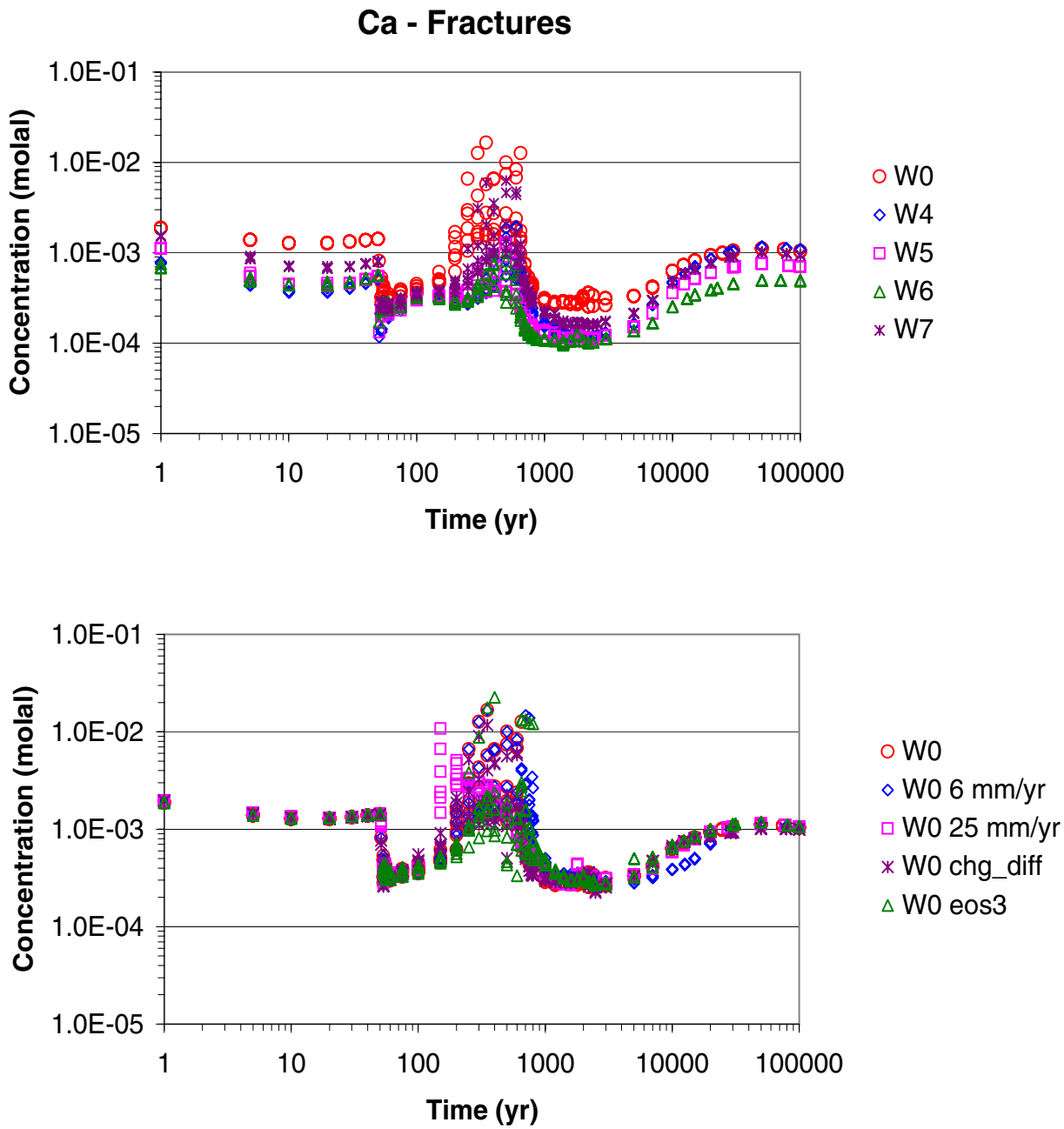

Output-DTNs: LB0302DSCPTHCS.002, LB0307DSTTHCR2.002

NOTE: Gridblocks are those with highest liquid saturation in fractures within a 25 m radius from drift center and a 45° arc from the drift crown. Data are shown for simulations using different initial water compositions (W0 – W7). Except as noted below, all simulations were run using a stepwise-increasing infiltration rate (6, 16, and 25 mm/y) and with vapor pressure lowering. Alternatives using Water W0 include simulations without vapor pressure lowering (W0 - eos3), and with fixed 25 and 6 mm/y infiltration rates (W0 - 6 mm/y and W0 - 25 mm/y, respectively).

Figure 6.8-30. THC Simulations (Tptpll Model REV02): Time Profiles of Modeled Total Aqueous Calcium Concentrations in Fracture Water, in Areas of Highest Liquid Saturation above the Drift Crown

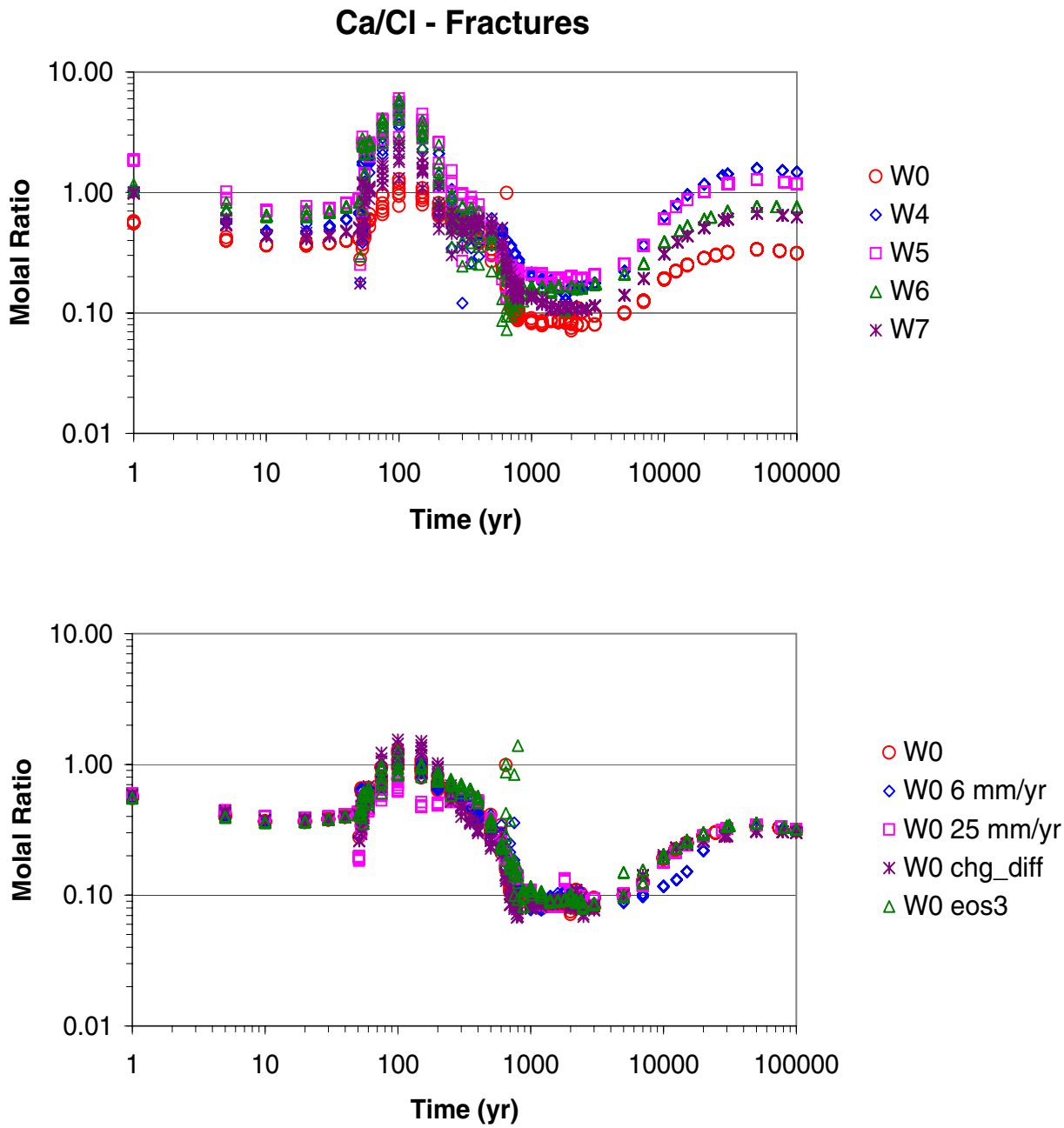

Output-DTNs: LB0302DSCPTHCS.002, LB0307DSTTHCR2.002

NOTE: Gridblocks are those with highest liquid saturation in fractures within a 25 m radius from drift center and a 45° arc from the drift crown. Data are shown for simulations using different initial water compositions (W0 – W7). Except as noted below, all simulations were run using a stepwise-increasing infiltration rate (6, 16, and 25 mm/y) and with vapor pressure lowering. Alternatives using Water W0 include simulations without vapor pressure lowering (W0 - eos3), and with fixed 25 and 6 mm/y infiltration rates (W0 - 6 mm/y and W0 - 25 mm/y, respectively).

Figure 6.8-31. THC Simulations (Tptpll Model REV02): Time Profiles of Modeled Total Aqueous Calcium to Chloride Ratios in Fracture Water, in Areas of Highest Liquid Saturation above the Drift Crown

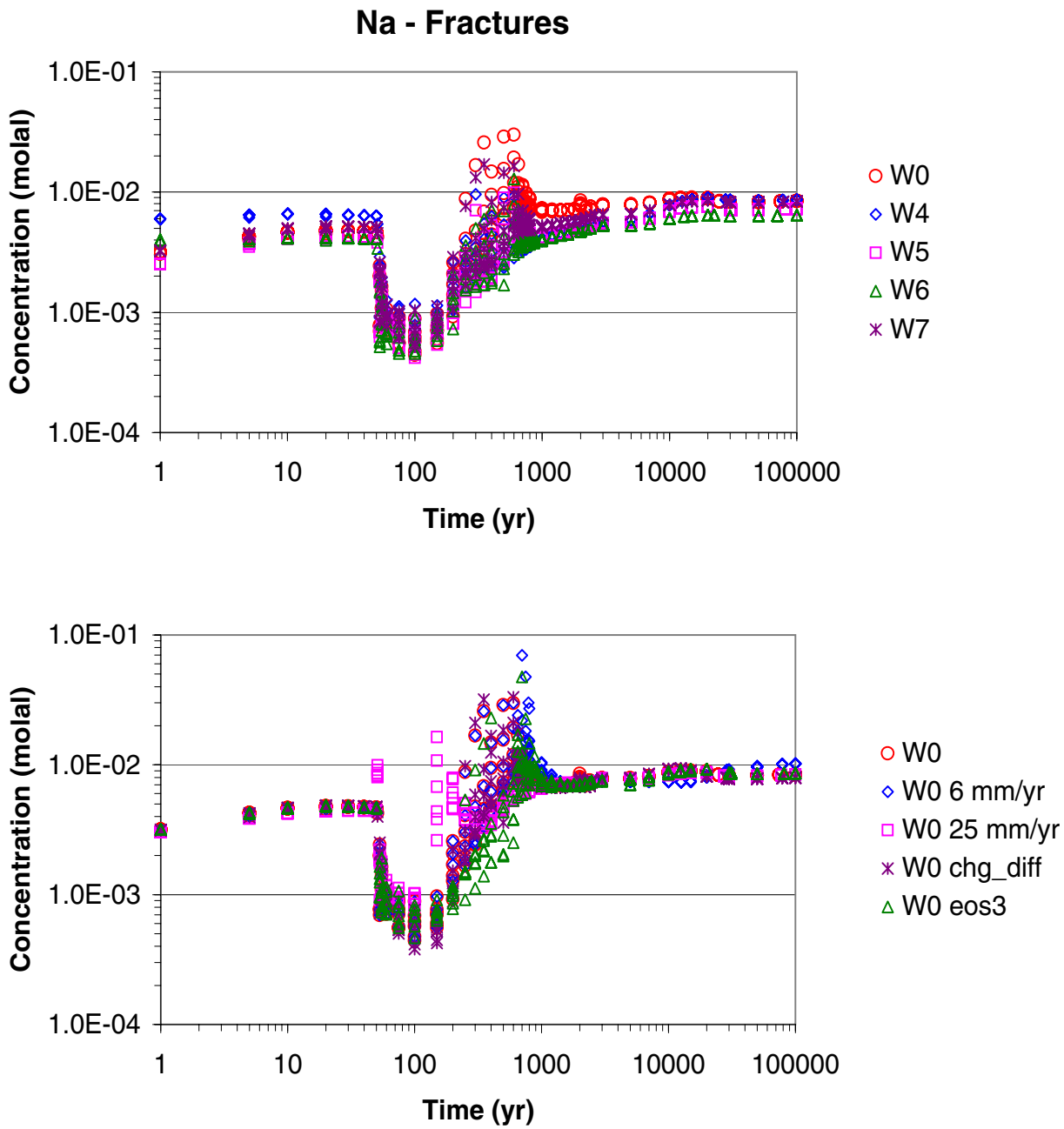

Output-DTNs: LB0302DSCPTHCS.002, LB0307DSTTHCR2.002

NOTE: Gridblocks are those with highest liquid saturation in fractures within a 25 m radius from drift center and a 45° arc from the drift crown. Data are shown for simulations using different initial water compositions (W0 – W7). Except as noted below, all simulations were run using a stepwise-increasing infiltration rate (6, 16, and 25 mm/y) and with vapor pressure lowering. Alternatives using Water W0 include simulations without vapor pressure lowering (W0 - eos3), and with fixed 25 and 6 mm/y infiltration rates (W0 - 6 mm/y and W0 - 25 mm/y, respectively).

Figure 6.8-32. THC Simulations (Tptpll Model REV02): Time Profiles of Modeled Total Aqueous Sodium Concentrations in Fracture Water, in Areas of Highest Liquid Saturation above the Drift Crown

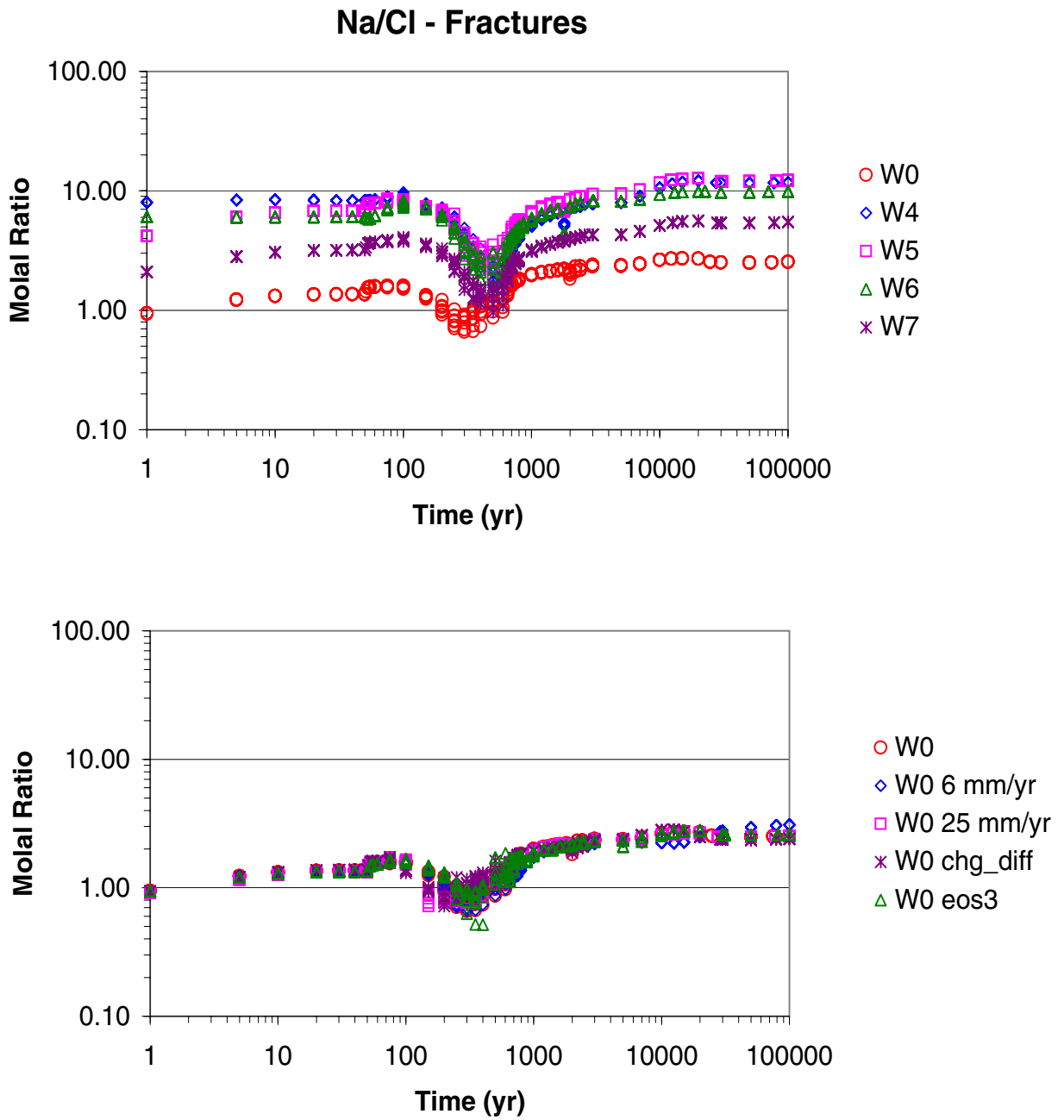

Output-DTNs: LB0302DSCPTHCS.002, LB0307DSTTHCR2.002

NOTE: Gridblocks are those with highest liquid saturation in fractures within a 25 m radius from drift center and a 45° arc from the drift crown. Data are shown for simulations using different initial water compositions (W0 – W7). Except as noted below, all simulations were run using a stepwise-increasing infiltration rate (6, 16, and 25 mm/y) and with vapor pressure lowering. Alternatives using Water W0 include simulations without vapor pressure lowering (W0 - eos3), and with fixed 25 and 6 mm/y infiltration rates (W0 - 6 mm/y and W0 - 25 mm/y, respectively).

Figure 6.8-33. THC Simulations (Tptpll Model REV02): Time Profiles of Modeled Total Aqueous Sodium to Chloride Ratios in Fracture Water, in Areas of Highest Liquid Saturation above the Drift Crown

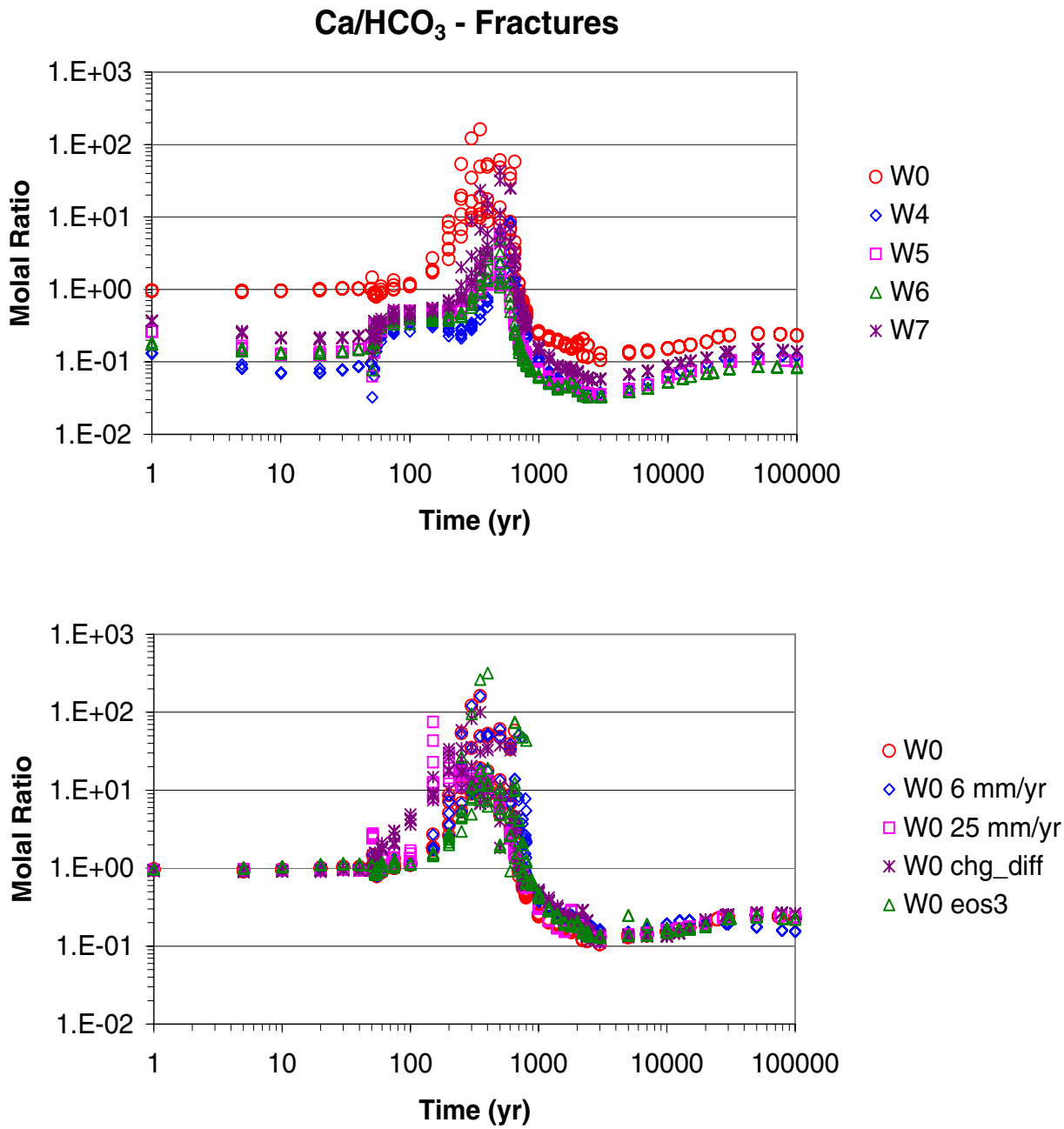

Output-DTNs: LB0302DSCPTHCS.002, LB0307DSTTHCR2.002

NOTE: Gridblocks are those with highest liquid saturation in fractures within a 25 m radius from drift center and a 45° arc from the drift crown. Data are shown for simulations using different initial water compositions (W0 – W7). Except as noted below, all simulations were run using a stepwise-increasing infiltration rate (6, 16, and 25 mm/y) and with vapor pressure lowering. Alternatives using Water W0 include simulations without vapor pressure lowering (W0 - eos3), and with fixed 25 and 6 mm/y infiltration rates (W0 - 6 mm/y and W0 - 25 mm/y, respectively).

Figure 6.8-34. THC Simulations (Tptpll Model REV02): Time Profiles of Modeled Total Aqueous Calcium to Carbonate Ratios in Fracture Water, in Areas of Highest Liquid Saturation above the Drift Crown

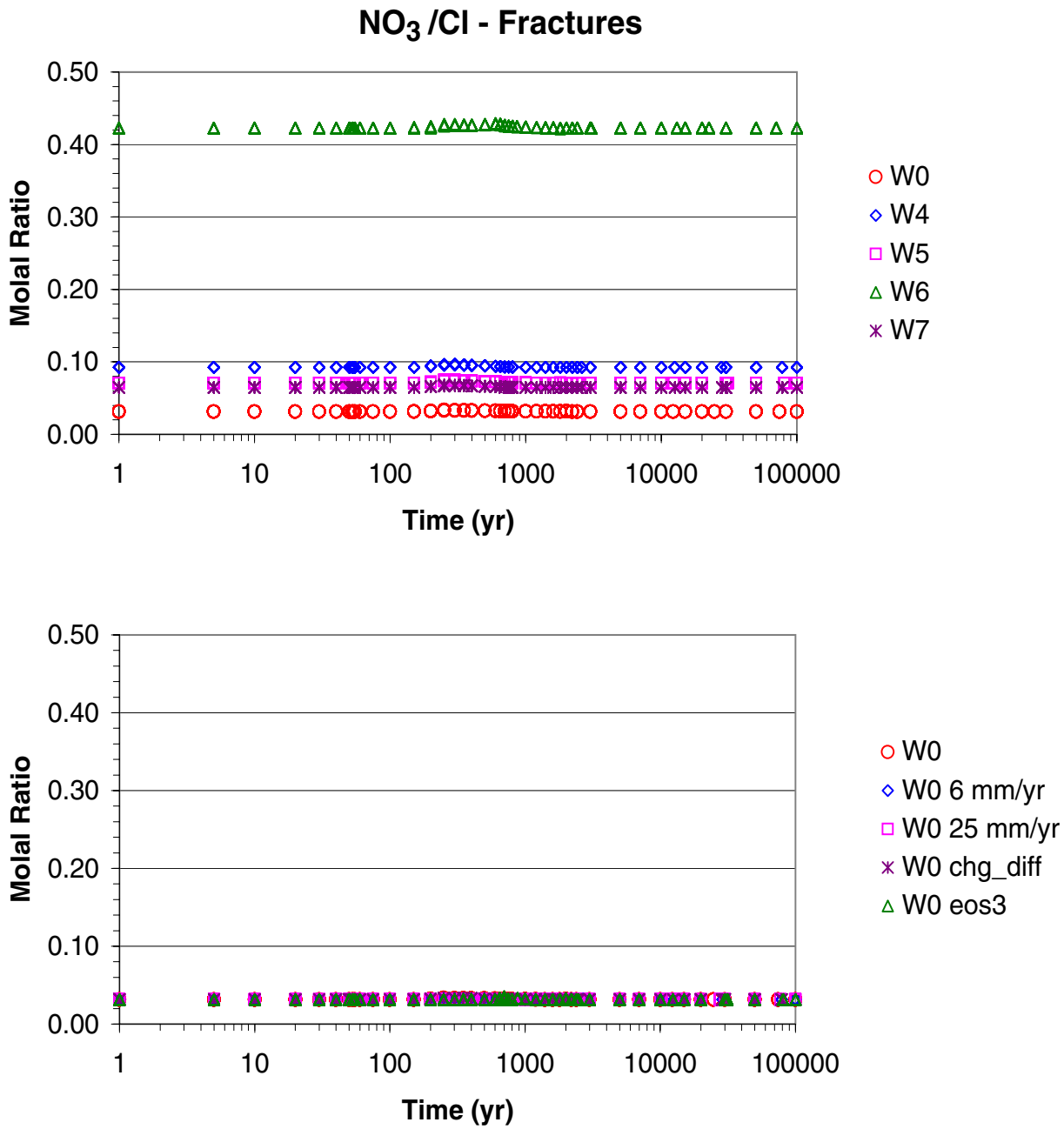

Output-DTNs: LB0302DSCPTHCS.002, LB0307DSTTHCR2.002

NOTE: Gridblocks are those with highest liquid saturation in fractures within a 25 m radius from drift center and a 45° arc from the drift crown. Data are shown for simulations using different initial water compositions (W0 – W7). Except as noted below, all simulations were run using a stepwise-increasing infiltration rate (6, 16, and 25 mm/y) and with vapor pressure lowering. Alternatives using Water W0 include simulations without vapor pressure lowering (W0 - eos3), and with fixed 25 and 6 mm/y infiltration rates (W0 - 6 mm/y and W0 - 25 mm/y, respectively).

Figure 6.8-35. THC Simulations (Tptpll Model REV02): Time Profiles of Modeled Total Aqueous Nitrate to Chloride Ratios in Fracture Water, in Areas of Highest Liquid Saturation above the Drift Crown

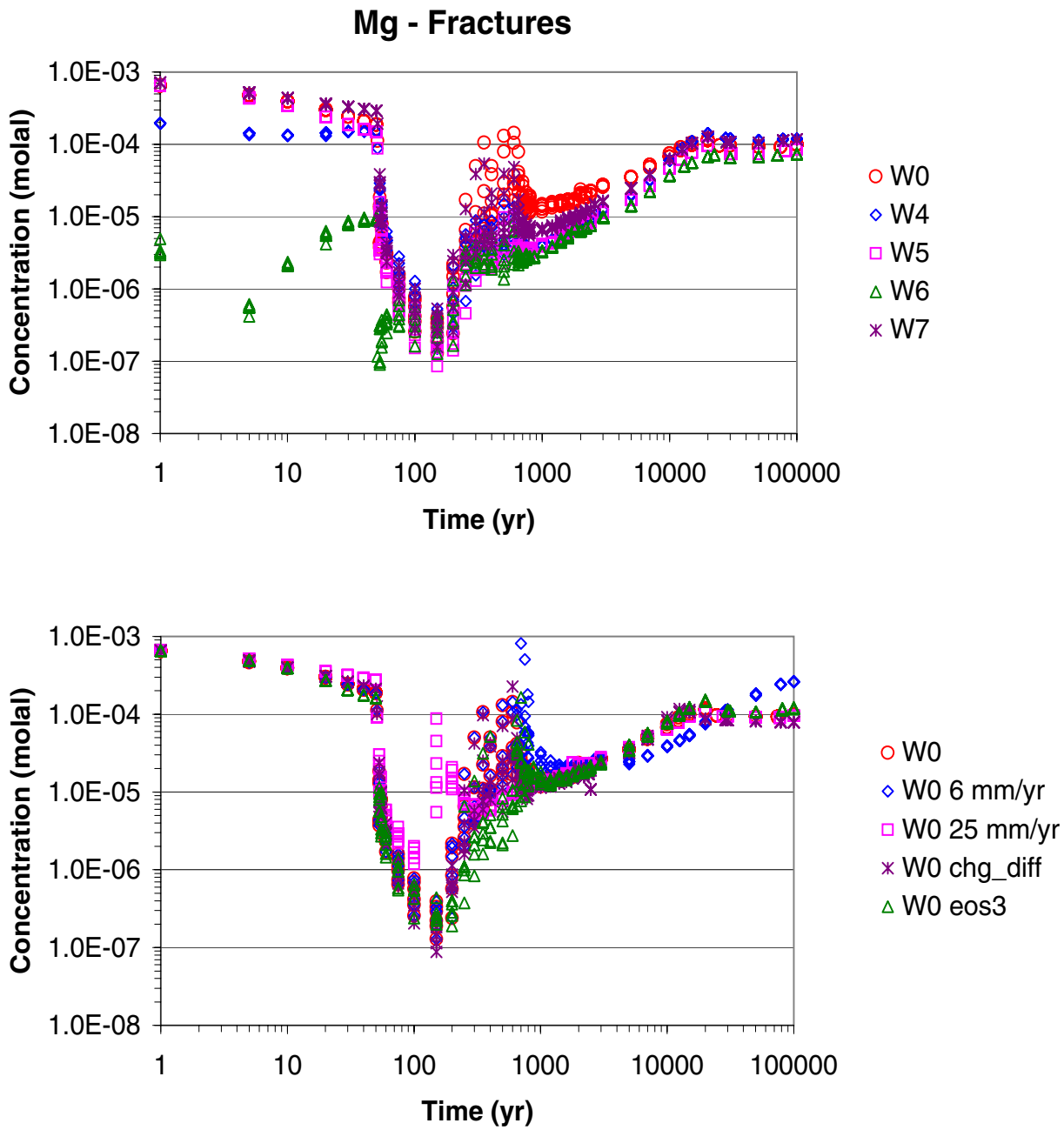

Output-DTNs: LB0302DSCPTHCS.002, LB0307DSTTHCR2.002

NOTE: Gridblocks are those with highest liquid saturation in fractures within a 25 m radius from drift center and a 45° arc from the drift crown. Data are shown for simulations using different initial water compositions (W0 – W7). Except as noted below, all simulations were run using a stepwise-increasing infiltration rate (6, 16, and 25 mm/y) and with vapor pressure lowering. Alternatives using Water W0 include simulations without vapor pressure lowering (W0 - eos3), and with fixed 25 and 6 mm/y infiltration rates (W0 - 6 mm/y and W0 - 25 mm/y, respectively).

Figure 6.8-36. THC Simulations (Tptpll Model REV02): Time Profiles of Modeled Total Aqueous Magnesium Concentrations in Fracture Water, in Areas of Highest Liquid Saturation above the Drift Crown

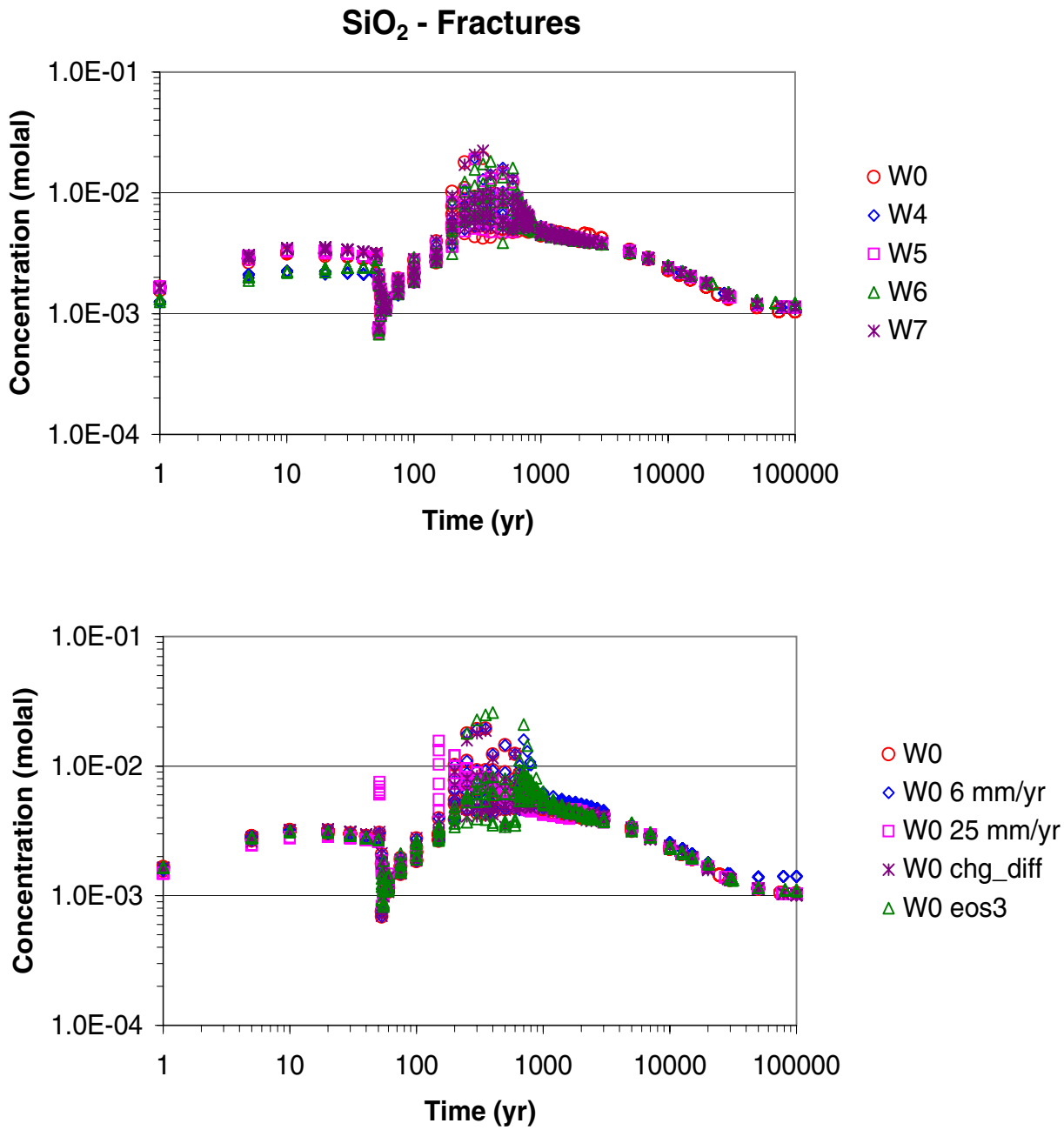

Output-DTNs: LB0302DSCPTHCS.002, LB0307DSTTHCR2.002

NOTE: Gridblocks are those with highest liquid saturation in fractures within a 25 m radius from drift center and a 45° arc from the drift crown. Data are shown for simulations using different initial water compositions (W0 – W7). Except as noted below, all simulations were run using a stepwise-increasing infiltration rate (6, 16, and 25 mm/y) and with vapor pressure lowering. Alternatives using Water W0 include simulations without vapor pressure lowering (W0 - eos3), and with fixed 25 and 6 mm/y infiltration rates (W0 - 6 mm/y and W0 - 25 mm/y, respectively).

Figure 6.8-37. THC Simulations (Tptpll Model REV02): Time Profiles of Modeled Total Aqueous Silica Concentrations in Fracture Water, in Areas of Highest Liquid Saturation above the Drift Crown

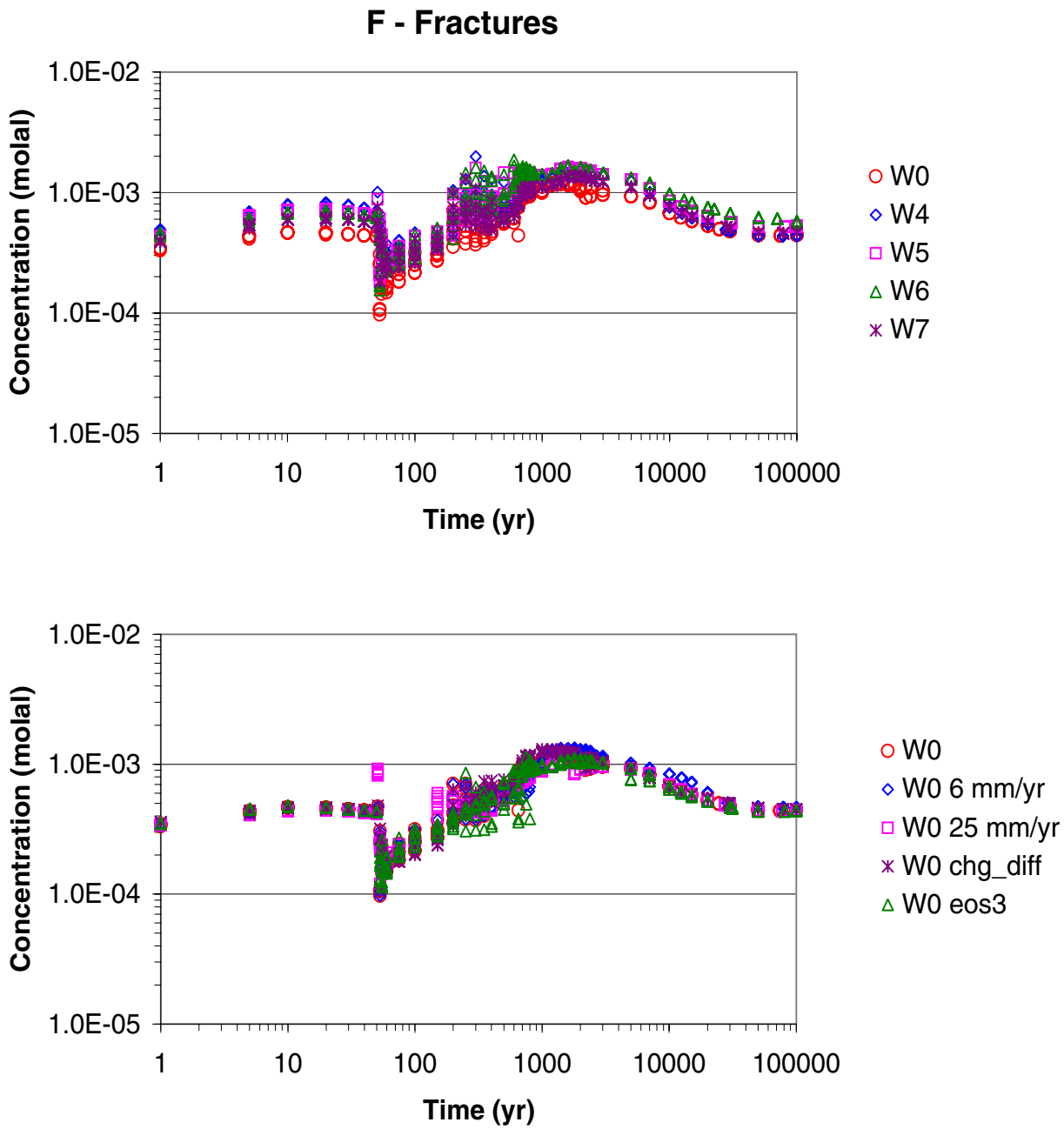

Output-DTNs: LB0302DSCPTHCS.002, LB0307DSTTHCR2.002

NOTE: Gridblocks are those with highest liquid saturation in fractures within a 25 m radius from drift center and a 45° arc from the drift crown. Data are shown for simulations using different initial water compositions (W0 – W7). Except as noted below, all simulations were run using a stepwise-increasing infiltration rate (6, 16, and 25 mm/y) and with vapor pressure lowering. Alternatives using Water W0 include simulations without vapor pressure lowering (W0 - eos3), and with fixed 25 and 6 mm/y infiltration rates (W0 - 6 mm/y and W0 - 25 mm/y, respectively).

Figure 6.8-38. THC Simulations (Tptpll Model REV02): Time Profiles of Modeled Total Aqueous Fluoride Concentrations in Fracture Water, in Areas of Highest Liquid Saturation above the Drift Crown

6.8.5.4 Mineral Alteration and Porosity/Permeability Changes (Tptpll REV02)

The predicted effect of water-rock-gas interactions on flow patterns around the drift is much more noticeable in this model revision than in REV01. This is because simulations (using TOUGHREACT V3.0 (LBNL 2002 [161256])) make use of a better treatment of mineral precipitation at the boiling front than previously. In addition, the REV02 fracture porosity is approximately half the value used in REV01 simulations.

To provide a baseline for evaluating the effect of mineral precipitation and dissolution on flow, results of a TH simulation are evaluated first. A contour plot of predicted liquid saturations for the simulation (Figure 6.8-39) shows that at 2,400 years, well after the end of the boiling phase, the predicted liquid saturations in the vicinity of the drift reflect the capillary barrier effect of the drift. Ambient water percolation is deflected around the drift (even at much higher infiltration rates than considered here). As a result, liquid saturations in fractures are somewhat increased above the drift crown, relative to ambient values, and significantly decreased below the drift ("shadow" zone).

In contrast, a similar contour map of liquid saturations predicted with Water W0 using a THC simulation (Figure 6.8-40a) shows that after the same simulated time period, a zone of higher liquid saturation has formed 7–8 meters above the drift, reflecting partial deflection of flow at this location. This kind of "umbrella" effect results from a thin region of significantly lower permeability (Figure 6.8-40b) created by prior mineral deposition at the boiling front. In this case, the permeability has decreased by a factor of about 10 in this area. As a result, the shadow zone extends somewhat deeper below the drift, and liquid saturations at the drift crown are somewhat reduced, compared to the TH prediction. Similar figures for results using Water W5 as input initial composition show a more pronounced "umbrella" effect (Figures 6.8-41a), with the permeability decreasing by two to three orders of magnitude (Figure 6.8-41b) in the thin region of mineral precipitation. The results using the other waters are very similar. Consequently, the shadow zone below the drift is extended significantly. The time of fracture rewetting around the drift is delayed, and the vertical flux at the drift crown is reduced by up to a factor of 10 compared to the ambient flux without drift opening (Figure 6.8-42a).

Other THC simulations using Water W0 and the two fixed infiltration rates (6 and 25 mm/y), as well as the simulation neglecting water-vapor-pressure lowering, also predict to various degrees an umbrella effect above the drift (Figure 6.8-42b). The effect is most noticeable with the simulation without vapor-pressure lowering, which predicts that the rewetting of fractures at the drift crown is delayed until approximately 20,000 years and around 12,000 years in the matrix. However, in this case, this stronger effect could be unrealistic because some amount of water-vapor-pressure lowering is expected to occur in the natural system. By retaining more water in the matrix, fracture rewetting would be facilitated, because less imbibition of fracture water would occur into the matrix. It should also be noted that the revised rock properties used in this model, with a significant decrease in matrix permeability but also a decrease in capillary suction compared to REV01 properties (Table 6.4-1), make it more difficult for the rock to rewet after dryout.

The vertical flux predicted at the drift crown at 2,000 years (Figure 6.8-42a or b), without considering THC processes, can be compared with the vertical flux value shown in BSC (2003

[161530], Figure 6.2.3.1-3) for the same time period. Both values are consistent (2.9×10^{-7} kg m^{-2} s^{-1}, which yields approximately 9.5 mm/yr using the water density at the corresponding temperature [960 kg m^{-3}]). The flux peak on Figure 6.8-42 (a or b) at 1400 years (1.07×10^{-6} kg m^{-2} s^{-1}) corresponds to approximately 35 mm/year, consistent with values predicted a few meters above the drift at 1000 years in BSC (2003 [161530], Figure 6.2.3.1-3). As already mentioned in Sections 6.7.5.1 and 6.8.5.2, these peaks may not be fully resolved. However, these are much smaller than the percolation rate required for seepage to occur (250 mm/yr in BSC 2003 [161530], Section 6.2.3.2.3). When THC processes are taken into account, as discussed earlier, percolation rates at the drift crown are even smaller because percolating water is partly diverted by the zone of lower permeability created by mineral precipitation above the drift. However, the model considers a homogeneous fracture permeability and therefore cannot capture potential flow focussing through this zone of lower permeability. Because this zone is very thin and located several meters above the drift crown (Figure 6.8-41b), the focussing of flow locally through this zone is not anticipated to increase vertical fluxes at the drift crown much beyond what is predicted without considering THC processes.

In all simulations, the permeability decrease results primarily from the precipitation of amorphous silica and, to a lesser extent, calcite (Figures 6.8-43 through 6.8-46). The fracture porosity is predicted to decrease by approximately 4–7%, depending on the simulation. The maximum porosity decrease is predicted to occur in a thin zone during refluxing at the edge of the dryout zone, before the collapse of this zone around the drift. During that time, salt and gypsum precipitation account for up to around 15% of the volume of precipitated minerals (Figure 6.8-45). Gypsum precipitation is noticeable only with Waters W0 and W7, as expected, because these waters initially contain a higher proportion of calcium. Both salts and gypsum quickly redissolve when the fractures rewet. By 2,400 years, with all simulations except that without vapor-pressure lowering, fractures have rewetted, and the amount of precipitated solids (Figure 6.8-46) is predicted to remain essentially unchanged for the remainder of the entire simulated time period. For a long period of time in the simulation without vapor-pressure lowering, any water entering fractures immediately evaporates. This causes further salt deposition until well after 2,400 years, most notably directly above the drift crown (Figure 6.8-43), even though temperatures are well below boiling by this time. Increasing the infiltration rate from a fixed rate of 6 to 25 mm/year does not significantly alter the amount of precipitated solids, but shifts the mineral deposition zone towards the drift by approximately 1 m (Figure 6.8-44).

Other minerals besides amorphous silica, calcite, gypsum, and salts form or dissolve in small amounts. Some albite dissolution accompanied by stellerite precipitation is predicted to occur in fractures (typically 0.1% of the porosity or less). Illite and stellerite are predicted to be the most significant minerals precipitating in the rock matrix, with maximum amounts around 1% of the matrix porosity.

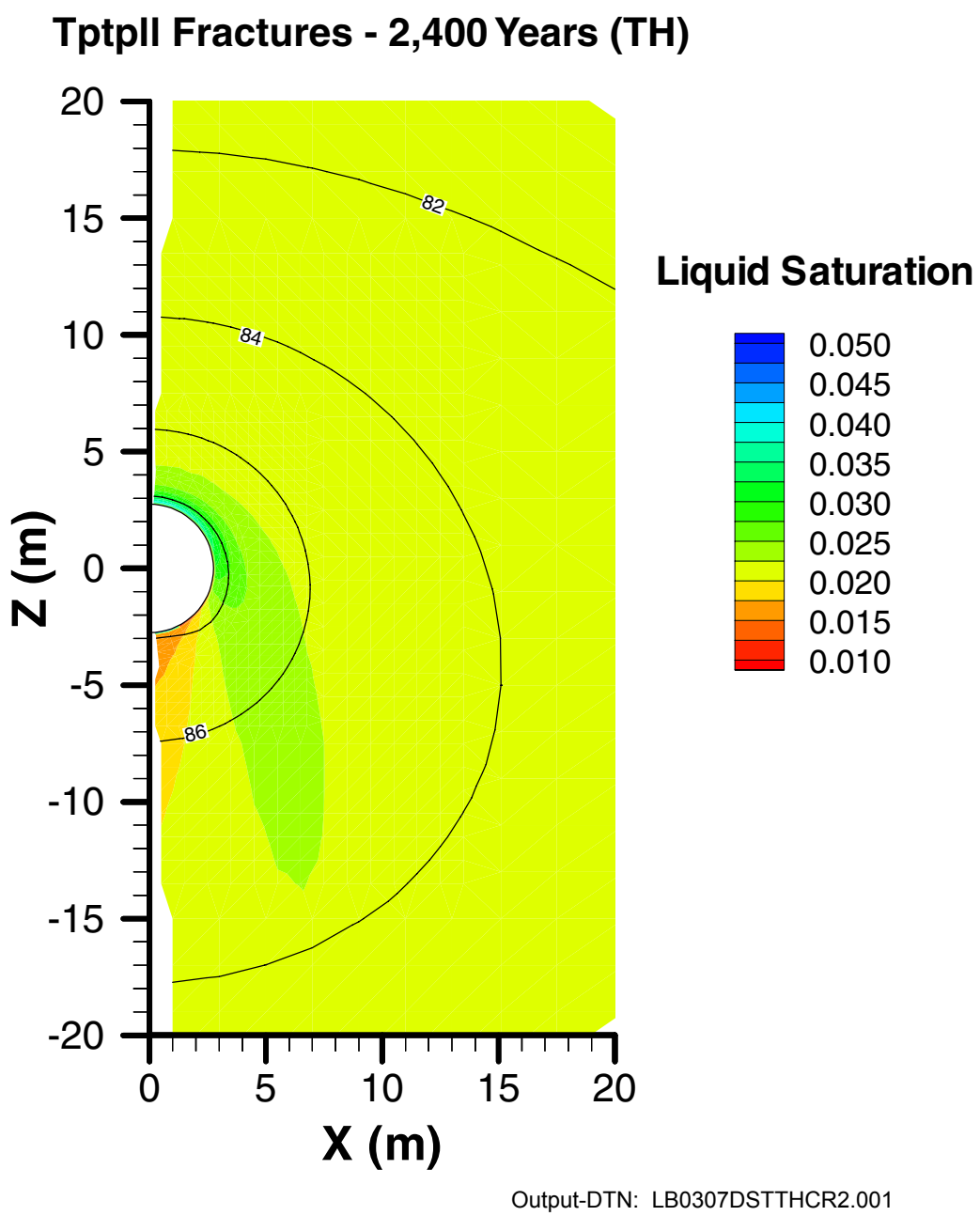

Figure 6.8-39. TH Simulation (Tptpll): Contour Plot of Modeled Liquid Saturation and Temperature Contours (°C) in Fractures at 2,400 Years (No Chemical Reactions)

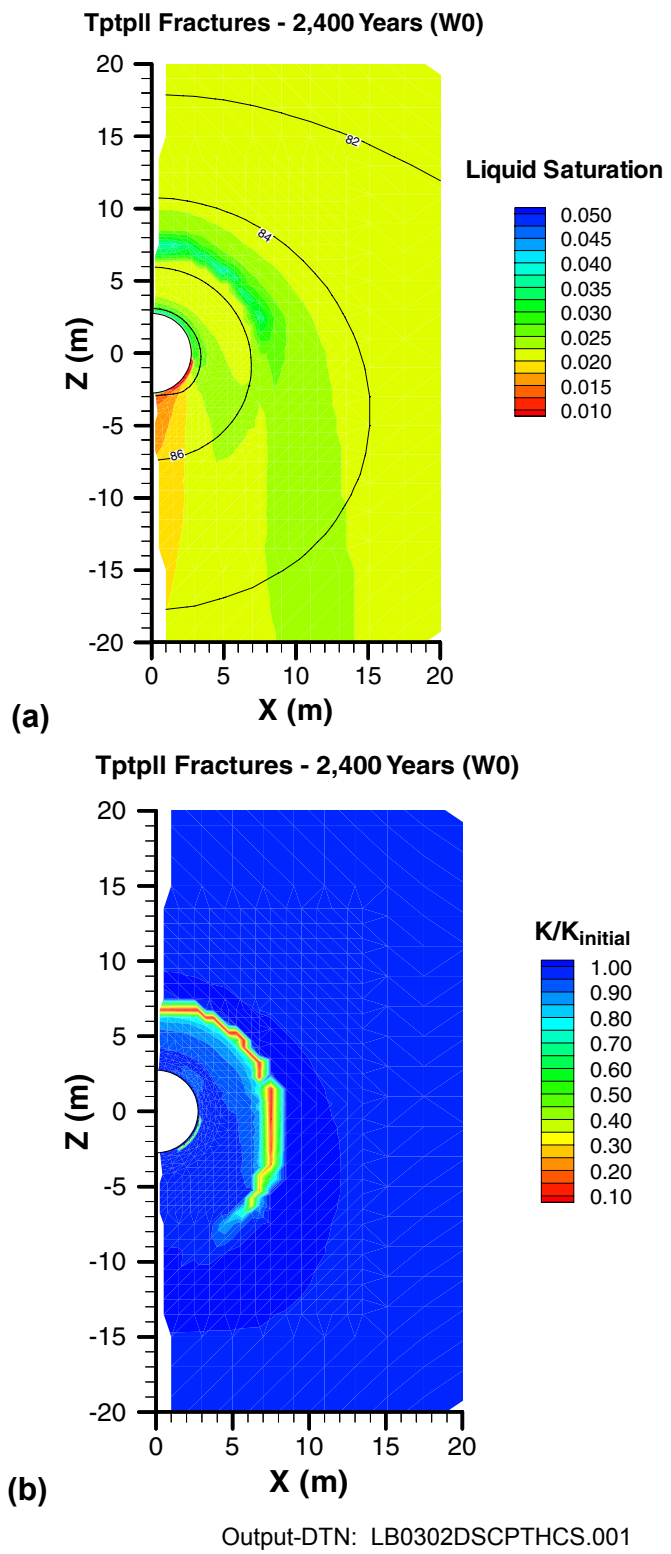

Output-DTN: LB0302DSCPTHCS.001

Figure 6.8-40. THC Simulation (Tptpll—Water W0): Contour Plot of Modeled (a) Liquid Saturation and Temperature Contours (°C) and (b) Permeability Change in Fractures at 2,400 Years

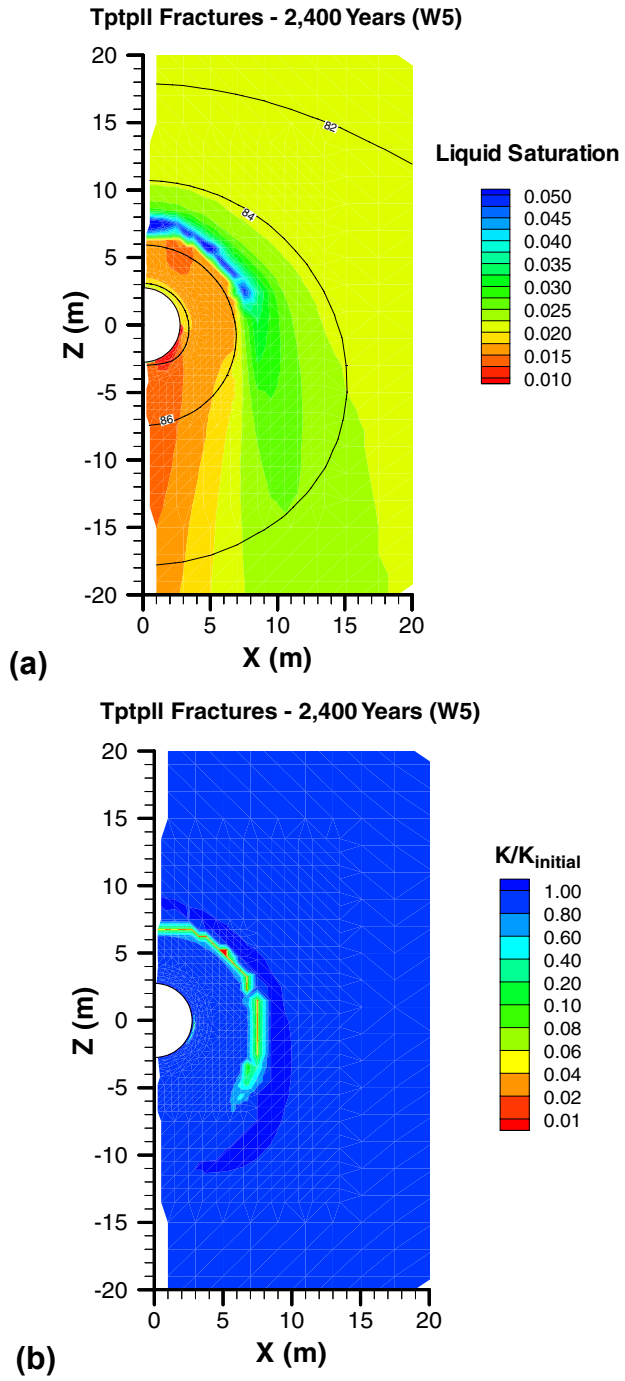

Output-DTN: LB0302DSCPTHCS.001

Figure 6.8-41. THC Simulation (Tptpll—Water W5): Contour Plot of Modeled (a) Liquid Saturation and Temperature Contours (°C) and (b) Permeability Change in Fractures at 2,400 Years

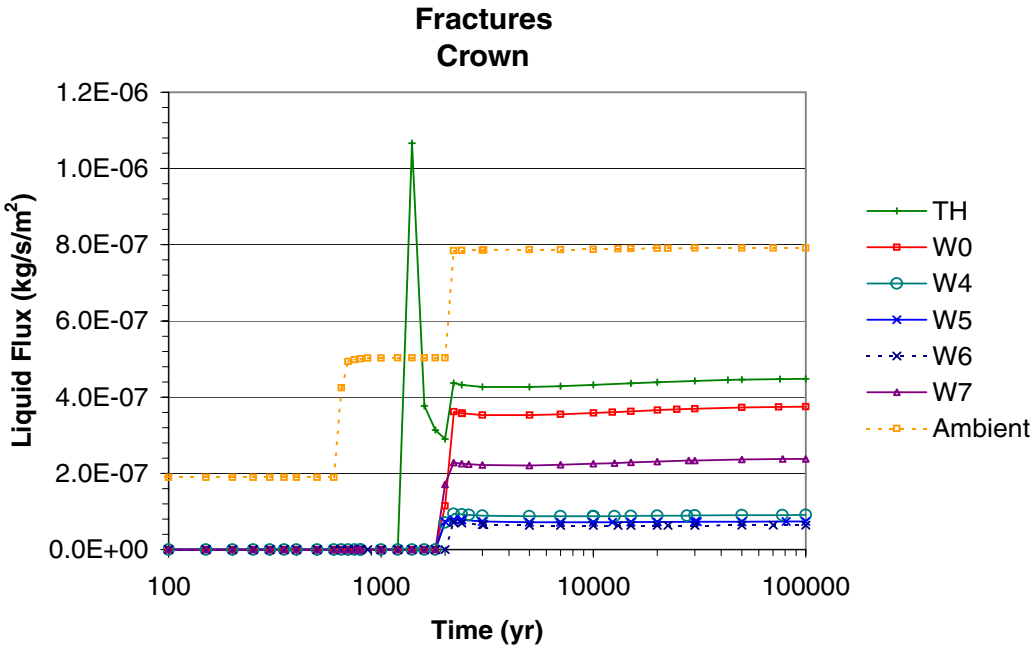

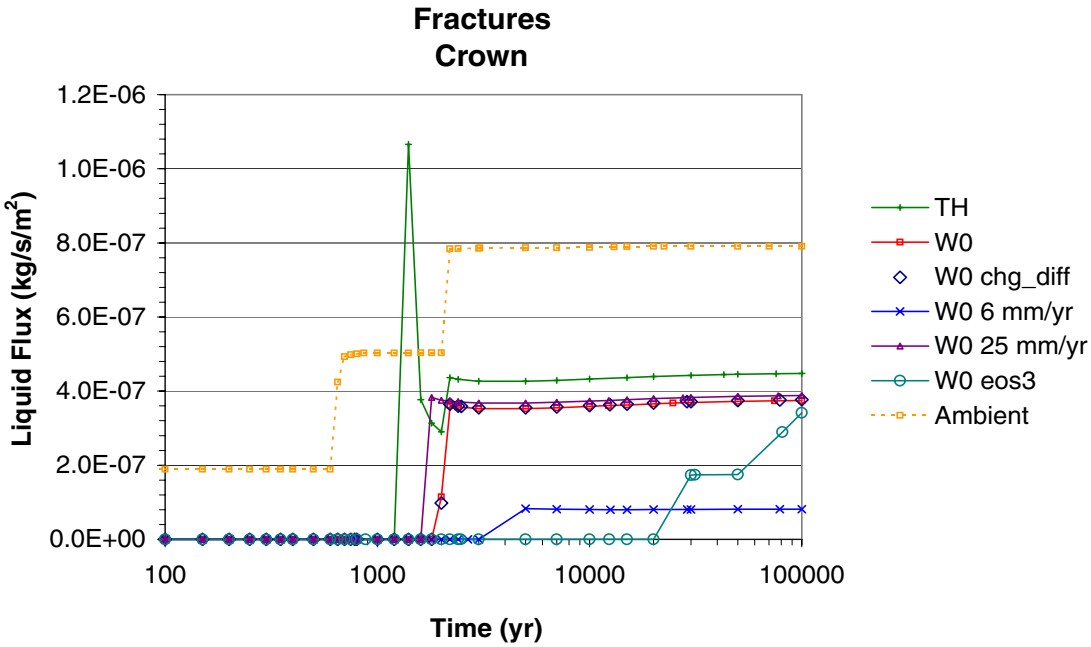

Output-DTNs: LB0302DSCPTHCS.002, LB0307DSTTHCR2.002

NOTE: Except as noted below, simulations consider vapor-pressure lowering and a stepwise-increasing infiltration rate (Table 6.8-2). Results are shown for various thermal loading simulations including: no chemical reactions (TH), five different input water compositions (W0, W4–W7), no vapor pressure lowering (W0—eos3), and two fixed infiltration rates (W0—6 mm/y and W0—25 mm/y). Predicted fluxes are also shown for ambient conditions (Ambient), without thermal load or a drift opening.

Figure 6.8-42. TH and THC Simulations (Tptpll): Comparison of Modeled Liquid Flux at the Drift Crown in Fractures at 2,400 Years

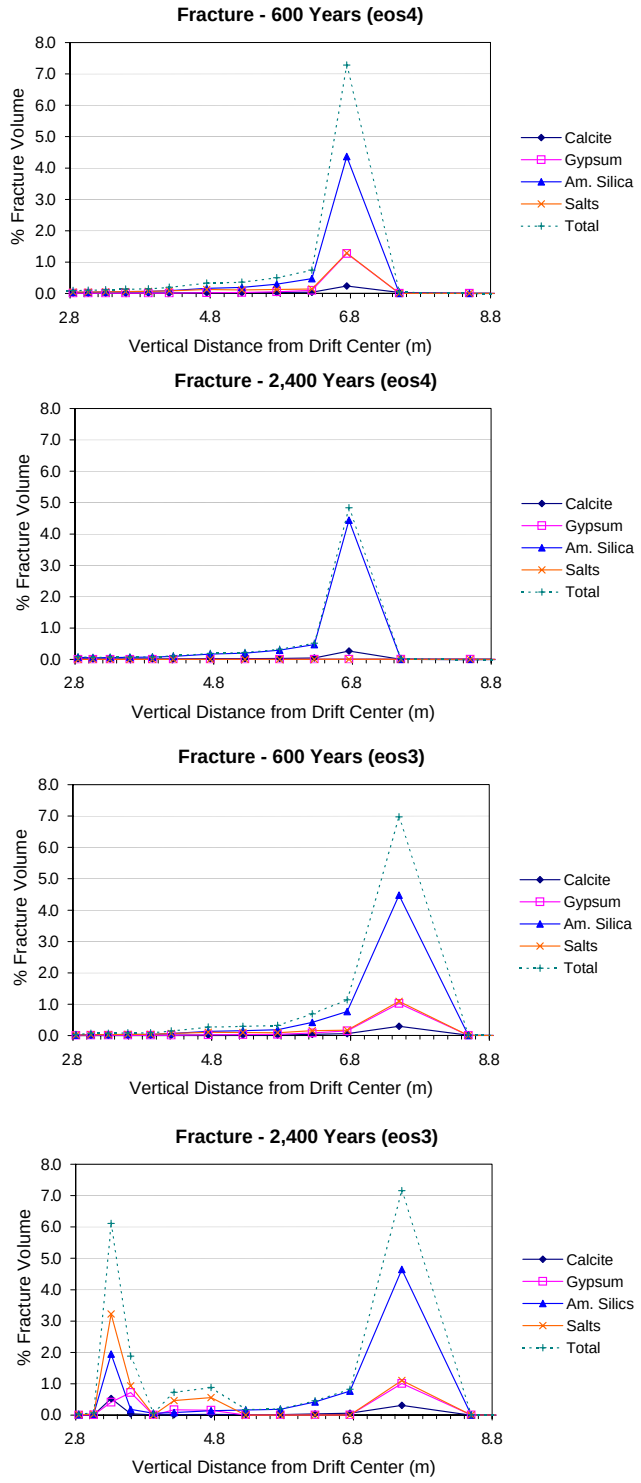

Output-DTNs: LB0302DSCPTHCS.001, LB0307DSTTHCR2.001

NOTE: Profiles are shown for simulated times of 600 and 2,400 years, for simulations using Water W0 with vapor-pressure lowering (eos4) and without this effect (eos3). Infiltration rates are increasing from 6, to 16, to 25 mm/year in a stepwise manner (Table 6.8-2).

Figure 6.8-43. THC Simulations (Tptpll): Vertical Profile of Predicted Mineral Abundances above the Drift Crown

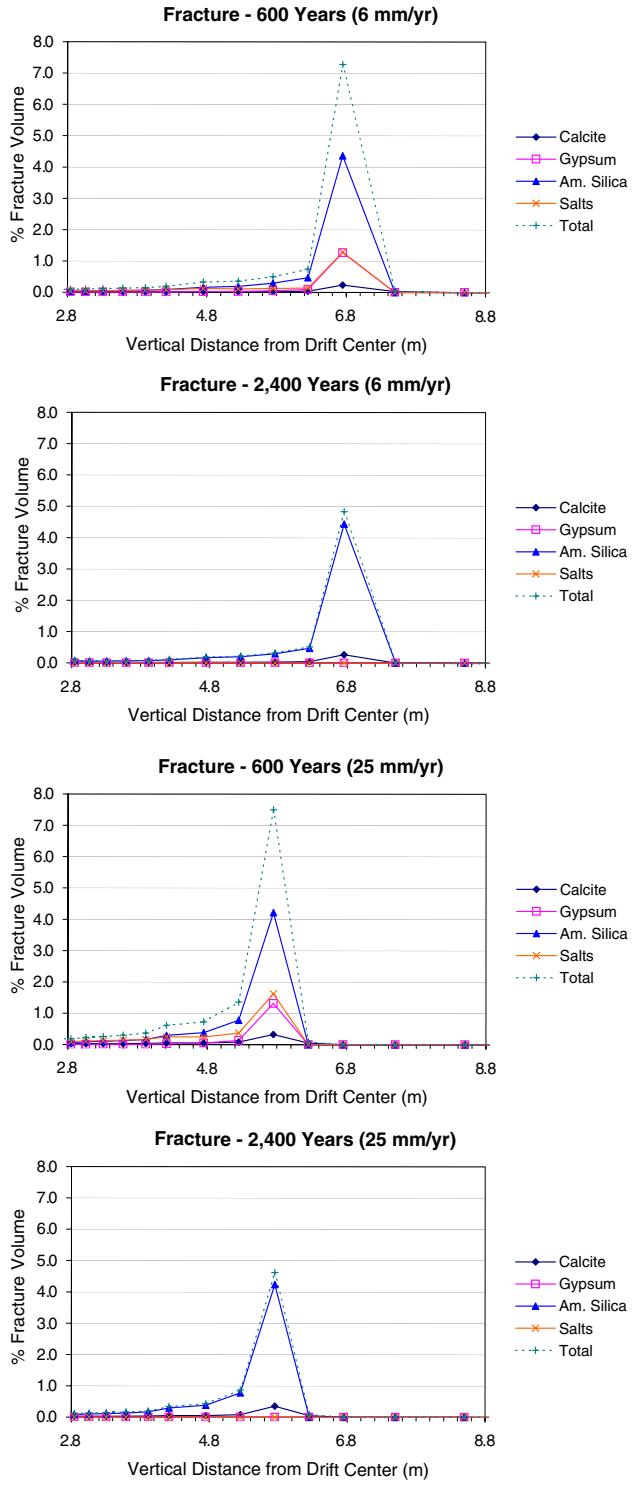

Output-DTNs: LB0302DSCPTHCS.001, LB0307DSTTHCR2.001

NOTE: Profiles are shown for simulated times of 600 and 2,400 years, for simulations using Water W0 with vapor-pressure lowering, and two different fixed infiltration rates (6 and 25 mm/year).

Figure 6.8-44. THC Simulations (Tptpll): Vertical Profile of Predicted Mineral Abundances above the Drift Crown

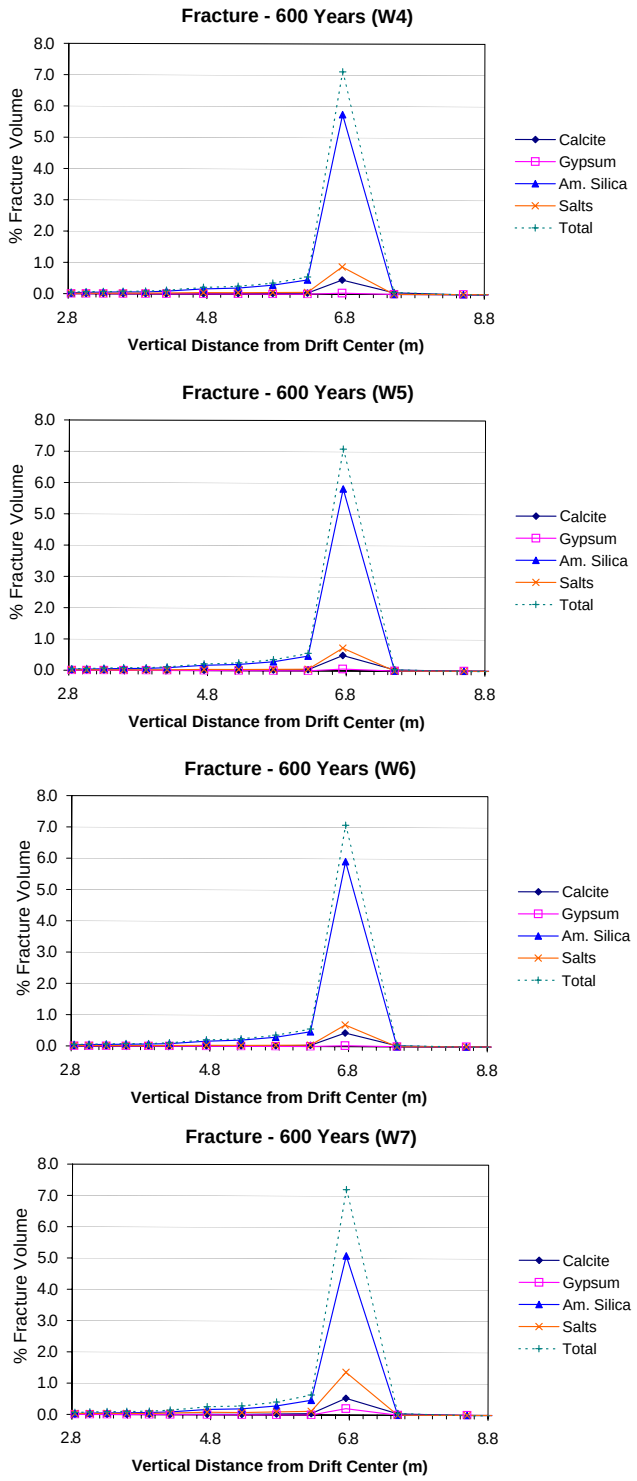

Output-DTNs: LB0302DSCPTHCS.001, LB0307DSTTHCR2.001

NOTE: Profiles are shown for a simulated time of 600 years, for simulations using vapor-pressure lowering and four different input water compositions (W4–W7).

Figure 6.8-45. THC Simulations (Tptpll): Vertical Profile of Predicted Mineral Abundances above the Drift Crown

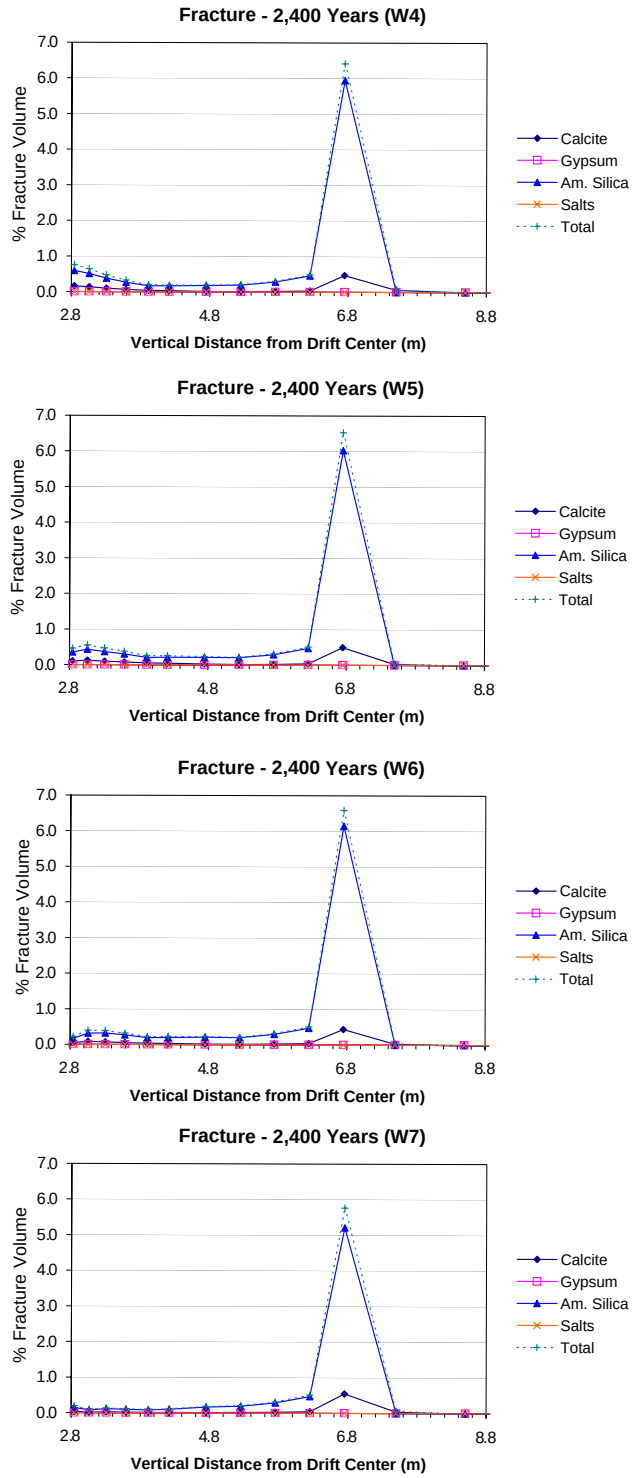

Output-DTNs: LB0302DSCPTHCS.001, LB0307DSTTHCR2.001

NOTE: Profiles are shown for a simulated time of 2,400 years, for simulations using vapor-pressure lowering and four different input water compositions (W4–W7). These profiles remain essentially unchanged for the rest of the simulated time period (100,000 years).

Figure 6.8-46. THC Simulations (Tptpll): Vertical Profile of Predicted Mineral Abundances above the Drift Crown

6.9 MODEL UNCERTAINTY

6.9.1 Potential Sources of Uncertainty

The simulations of THC processes include coupling between heat, water, and vapor flow, aqueous and gaseous species transport, kinetic and equilibrium mineral-water reactions, and feedback of mineral precipitation/dissolution on porosity, permeability, and capillary pressure (hydrological properties) for a dual-permeability (fracture-matrix) system. As such, the THC Seepage Model takes into account the effects of mineral dissolution and precipitation, the effects of carbon dioxide exsolution and transport in the region surrounding emplacement drifts, and the resulting changes to porosity, permeability, seepage, and chemical composition of percolating waters. The large number of input parameters, the numerical methods implemented in simulating these complex coupled processes, and the simplification and approximations pertaining to the physical setup of the model, all contribute to uncertainties in the predictions from these models. Uncertainties in model input data that could affect calculated water and gas compositions include:

- Thermodynamic data (equilibrium constants for mineral-water reactions and aqueous species dissociation)
- Kinetic data (rate constants, reactive surface areas, and activation energies)
- Initial compositions of pore water and pore gas
- Initial composition of infiltrating water and gas
- Infiltration rates
- Transport parameters (diffusion coefficients of aqueous species and gases, tortuosity)
- Initial rock mineralogy (model location and stratigraphy)
- Number of geochemical constituents included the simulations
- Number and types of potential secondary mineral phases
- Rock thermal, physical, and hydrological properties (including input data for both water-saturated and unsaturated rock)

Process model uncertainties may also affect the calculated water and gas compositions. These include:

- Formulation of models to simulate fluid flow in dual permeability media (e.g., fracture-matrix interactions; relative permeability and saturation-capillary pressure models)
- Activity coefficient models
- Kinetic mineral precipitation and dissolution models

- Inclusion or exclusion of certain specific thermal, hydrological, or chemical processes (e.g., active fracture model, vapor pressure lowering, mineral solid solutions, redox reactions)

Uncertainties in the setup of the model could also affect the results of the THC Seepage Model. These include:

- Physical model representation (stratigraphic/geologic extrapolations)
- Representation of the fracture and matrix continua in the model mesh
- Model discretization (in space and time)
- Boundary conditions (e.g., drift open versus closed to fluid flow)

Of these uncertainties, those directly affecting chemical processes would be most likely to have the most effect on predicted water and gas compositions. Such uncertainties, their treatment in the model, and their effect on model results are summarized in Table 6.9-1.

Note that temperature is also a critical parameter affecting modeling results, although it cannot be considered an uncertainty by itself (temperature can generally be predicted to within a few degrees; it is therefore not included in Table 6.9-1). Temperature directly affects equilibrium constants and reaction rates, the degree of water evaporation and boiling, and the amount of carbon dioxide volatilization from pore water, with direct implications for computed water and gas chemistries. Uncertainties affecting predicted temperatures could significantly affect computed aqueous and gas species concentrations. However, important changes in design heat load are likely to affect model results more than uncertainties associated with input parameters used to calculate temperatures (e.g., rock thermal conductivity and heat capacity). In this report, only the heat load from the current repository design was considered. This heat load leads to temperatures in the vicinity of emplacement drifts that exceed the boiling point of water for several hundred years if ventilation is not maintained after the 50-year preclosure period. The increased water-rock-gas interactions resulting from higher temperatures are expected to affect water chemistry and flow to a greater extent than if a lower heat load were considered. However, some of the effects of elevated temperatures, such as dryout and reduced permeabilities caused by mineral precipitation, could have positive aspects with respect to repository performance.

6.9.2 Evaluation of Model Result Uncertainty

The number of simulations that were performed to evaluate the uncertainty in model results was limited because the simulation of coupled THC processes is computation-intensive (typically 5–10 days CPU-time for one simulation). Nevertheless, the model sensitivity to key input parameters was evaluated (Sections 6.5–6.8). Furthermore, confidence in model results was obtained by comparing model results against data from the DST and laboratory experiments (Section 7), and improving the model conceptualization and mathematical formulation (Section 6.2–6.4) as necessary as to yield a reasonably good agreement between calculated and measured data (i.e., validation during development, as per AP-SIII.10Q, 5.4.1b, providing additional confidence).

In this study, the spread in predicted concentrations of aqueous species and CO_2 gas (i.e. Figures 6.8-12–6.8-21 and 6.8-25–6.8-38) is related to:

- The natural variability of input water compositions (Sections 6.2.2.1)
- The various investigated model conceptualizations (vapor-pressure model, drift location, stratigraphic columns, open versus closed drift wall) (Table 6-1)
- Ranges of input parameters other than water composition (in this case infiltration rates and CO_2 diffusion coefficients) (Section 6.8.5.3).

The relative spread caused by the variability of input water compositions (computed as standard deviation) is shown as a function of time in Table 6.9-2. This spread is up to around one order of magnitude and in many cases much less. As shown by comparing Figures 6.8-25a–6.8-38a with Figures 6.8-25b–6.8-38b, this spread is in most cases larger than the spread introduced by the various model conceptualizations and ranges of other input data considered in the model. Further evaluations of the spread in model result, as it directly ties to uncertainty, will be presented in the upcoming revision of *Abstraction of Drift-Scale Coupled Processes* (CRWMS M&O 2000 [123916]).

Uncertainties in kinetic and thermodynamic data could affect the standard deviations shown in Table 6.9-2, although the results of model validation against the DST and other laboratory experiments (Section 7), as well as the results of simulations of ambient conditions (Section 6.8.5.1), suggest these data are constrained to the extent that the model results are generally consistent with measured data. The model validation results (Section 7) also provide confidence that some of the other uncertainties listed in Table 6.9-1 do not significantly affect the spread in model results. This could be because model validation results are either not very sensitive to these uncertainties (at least over the period of time covered by the validation simulations) or that the effects of some of these uncertainties cancel out. Long-term effects of some of these uncertainties (e.g., ion exchange reactions, precipitation/nucleation kinetics) on model results may need further investigation, although it can be argued that the effect of these uncertainties on model results are already mostly captured by the variability in pore-water compositions input into the model.

Table 6.9-1. Summary of Uncertainties Affecting Chemical Processes in the THC Seepage Model

Category	Issue	Treatment	Consequences
Conceptual uncertainties	Geochemical system considered (minerals, gases, and aqueous species)	Treated by including major rock-forming minerals, major aqueous species, and major gases of interest (CO_2, air, water vapor) in the system, and also minor minerals such as clays. Effects of secondary mineral phase precipitation is most uncertain at higher temperatures and may require further evaluation. Uncertainty is limited under ambient conditions if ambient water concentrations can be reproduced. Trace minerals and aqueous species are not considered (not within the current scope for the THC Seepage Model). However, results of model validation (Section 7) against the Drift Scale Test and other experiments suggest the geochemical system, as modeled, is constrained enough to reproduce the experimental data within validation criteria. Also, the range of incoming waters considered in the model capture, at least in some part, the range of uncertainties related to the geochemical system.	Precipitation of secondary phases not currently included in simulations could affect the predicted composition of waters around the drift at high temperature. Reactions involving trace minerals (e.g., other clay minerals or Mg, Fe, Mn minerals) could affect pH which, in turn, could affect the precipitation/dissolution of other mineral phases and indirectly affect the concentrations of major species. The type of mineral precipitating could also affect the calculated porosity change (i.e., effect of different molar volume), although this effect would be minimal because the bulk of the precipitation consists of amorphous silica. Uncertainties affecting the precipitation of secondary phases would increase at near dryout conditions, however, such conditions (i.e., small liquid saturations) are not conducive to seepage.
	Drift wall conceptualization : closed vs. open to advective fluid flow; also, hydrological effect of ventilation is neglected.	Both cases of open and closed drift wall were addressed. Infiltration rates (even at high rates indicative of future wet climates) are below seepage thresholds, so there is little effect of closing the drift wall on water percolation fluxes around the drift. Evaporative concentration effects (due to ventilation) are indirectly taken into account by “downstream” in-drift evaporation models.	Boundary conditions of pressure and relative humidity in the drift could affect evaporative concentration effects at the drift wall, mostly during the preclosure ventilation period. In-drift interactions are not considered (this was not a goal of the THC Seepage Model).
	Precipitation/nucleation kinetics	Not treated This affects minerals such as silica and calcite, which have fast reaction rates. The reaction of calcite at equilibrium with a supersaturation gap (as done here) may approximate nucleation processes. Silica precipitation is modeled with a very fast reaction rate.	In areas where rapid boiling occurs, predicted silica concentrations are overestimated and silica precipitation is underestimated. However, the water saturation in these areas is very small and therefore the actual amounts of silica are minute.
	Water chemistry is not computed below a set water saturation limit (10^{-5}) or above a set ionic strength limit (4) (Activity coefficient model limitations)	In REV02 models, salt precipitation in the last remaining water when boiling or evaporating is taken into account using a simple model (Section 6.4.5). These salts are then available for dissolution upon rewetting, providing a conceptually correct (although simplified) representation of actual processes accompanying dryout and rewetting. In REV01 models, the composition of the last aqueous phase for which geochemical speciation is computed (prior to dryout) is saved. Water with this composition is assumed to mix instantly with percolating water during rewetting.	In REV02 models, the type and sequence of salts assumed to precipitate upon dryout affects computed water compositions at the very early stages of rewetting only. In REV01 models, assuming instant dissolution may overpredict dissolved salt concentrations when rewetting occurs.

Table 6.9-1. Summary of Uncertainties Affecting Chemical Processes in the THC Seepage Model (continued)

Category	Issue	Treatment	Consequences
Conceptual uncertainties (cont.)	Vapor pressure lowering due to capillary pressure	Treated by running simulations with and without vapor pressure lowering.	No large effect on computed gas and water chemistries. However, a large effect on the predicted time of rewetting of fractures and matrix at the drift wall was observed. Neglecting vapor pressure lowering could increase the effect of evaporative concentration around the drift, resulting in higher water salinities, although this was not noticeable.
	Oxidation-reduction processes are neglected	Not treated (considers only oxidized conditions) Oxidizing conditions prevail in the unsaturated zone at Yucca Mountain such that the redox species considered in the THC Seepage Model (iron and sulfate) occur only in their oxidized state.	Limited anticipated effect because of the prevailing oxidized conditions. Likely no effect for iron and sulfate in the current models. Redox reactions involving microbial processes and species not presently modeled (nitrates, phosphates) could have a limited effect on pH.
	Mineral solid-solutions	Ideal solid-solution treatment for clays; no treatment for other minerals. Taken indirectly into account through adjustments of thermodynamic data necessary to reproduce ambient water compositions. Compositions of primary solid solution phases, when known, are directly taken into account by the relative amounts of individual end-members input into the model. Individual mineral phases with fixed solid-solution compositions (determined by analysis) are included in the simulations (e.g. zeolites).	Limited anticipated effect because solid solutions are partially treated as described in the adjacent table column. In the current THC Seepage Model, this would primarily affect the composition of precipitating alkali feldspars (thus affecting predicted Na and K concentrations). However, these minerals form nearly pure secondary phases in nature (i.e., as modeled). Zeolites in the repository host units (mostly stellerite) are not abundant and not particularly variable in composition.
	Ion-exchange and surface complexation	Not treated Dominant primary rock minerals in the repository host units are not strong ion exchangers (for major ions). THC seepage simulations do not include trace elements that could be strongly affected by surface complexation.	Limited effect for the current application range of the THC Seepage Model. However, a limited shift in the predicted concentrations of Na, K, Ca, and Mg could still affect significantly the composition of end-brines upon complete evaporation.
	Capillary pressure effect on chemical potentials of reacting species	Not treated It is taken indirectly into account through adjustments of thermodynamic data such that ambient water compositions can be reproduced.	Could potentially shift predicted concentrations of some species.
Data uncertainties	Infiltration water and initial pore-water composition	Five alternate water analyses are used in REV02 simulations, covering fairly well the compositional variability of pore waters in repository host units. Uncertainty can be assessed by comparing predictions of ambient water compositions with measured ambient pore-water compositions and pore-gas CO_2 concentrations.	Input water compositions affect predicted water compositions around the drift, and likely more so through infiltration/transport than through reaction.

Table 6.9-1. Summary of Uncertainties Affecting Chemical Processes in the THC Seepage Model (continued)

Category	Issue	Treatment	Consequences
Data uncertainties (cont.)	Carbon dioxide partial pressures	Composition of infiltrating water input into the model essentially dictates the boundary CO_2 pressure; therefore the uncertainty in infiltrating water composition overcomes this uncertainty. However, here, various infiltrating waters were assumed to equilibrate at the same boundary CO_2 pressure (around 3200 ppmv).	A large effect is not expected within the possible range of observed natural concentrations, because the range of thermally induced CO_2 partial pressures is much larger than (and thus overwhelms) background concentrations.
	Thermodynamic and kinetic data	Treated partly through sensitivity studies on long-term behavior of ambient system chemistry, assuming a fixed infiltration rate and different thermodynamic data for clays and zeolites (the model is very sensitive to the thermodynamic data for these minerals). When possible within the uncertainty of the original data, treated by revising the data to reproduce observed water compositions and mineralogical data. Other uncertainties treated through model validation (Drift Scale Test and laboratory experiments).	Currently one of the main uncertainties affecting predicted water compositions around the drift. However, it can be constrained by adjustments and model validation against observed data, such that ambient simulations predict concentrations consistent with observed values.
	Host rock mineralogy	Treated by considering alternative drift locations (Tptpmn versus Tptpll host rock unit). Bulk chemical composition of the repository host units do not differ significantly.	No significant effect on the predicted compositions of major aqueous species. Small amounts of fast reacting minerals containing elements present in minor quantities in pore water (e.g., fluorite) can have a large effect on the predicted concentrations of these minor species (e.g., F^-)
	Infiltration rates	Alternative infiltration rate scenarios are used.	Between 6 and 25 mm/y, there is a small effect on predicted concentrations at the drift wall. The effect would be greater under lower rates of infiltration (when reaction effects start to dominate transport), but such conditions would be less likely to cause in-drift seepage. At high-infiltration rates, most conducive to in-drift seepage, water compositions are more function of transport than of reaction with host rock minerals, such that the uncertainty regarding the composition of the infiltration water, rather than the rate of mineral dissolution/ precipitation, becomes more important.

Table 6.9-1. Summary of Uncertainties Affecting Chemical Processes in the THC Seepage Model (continued)

Category	Issue	Treatment	Consequences
Parameter uncertainties	Heterogeneity	Heterogeneous fracture permeability treated in REV01. Heterogeneity in matrix properties not treated. Local heterogeneity in mineralogy not treated; however, the bulk composition of host rocks is fairly uniform. Heterogeneity in initial water geochemistry not treated directly; treated indirectly through testing with alternate water compositions.	Possible local changes in predicted water compositions around the drift. However, the bulk composition of waters around the drift is not expected to be significantly affected, because the rock chemical composition and mineralogy in the repository units is fairly homogeneous.
	Transport parameters (effective diffusivity)	The CO_2 diffusion coefficient was changed by a factor of 6 between REV01 and REV02 analyses (and a factor of 30 since pre-REV01 simulations). Sensitivity to diffusion coefficient for aqueous species was not investigated. However, tortuosity was changed from 0.2 to 0.7 between earlier report revisions (REV00 and REV01) without noticeable effect.	CO_2 diffusion coefficient mainly affects in-drift predicted CO_2 concentrations during dryout. At other times, predicted CO_2 concentrations are mainly dictated by water compositions.

Table 6.9-2. Standard Deviations[1] in Water and Gas Compositions Predicted Using Five Different Input Water Compositions (W0, W4, W5, W6, and W7)

Time (yr)	pH	Ca	Mg	Na	Cl	SiO_2(aq)	HCO_3	SO_4
0	0.11	0.11	0.52	0.18	0.29	0.08	0.14	0.37
1	0.10	0.17	0.90	0.13	0.29	0.05	0.16	0.37
53	0.14	0.15	0.82	0.25	0.37	0.20	0.22	0.44
100	0.13	0.04	0.23	0.11	0.31	0.06	0.16	0.39
200	0.09	0.23	0.38	0.16	0.40	0.14	0.23	0.46
300	0.10	0.40	0.35	0.26	0.46	0.19	0.30	0.51
400	0.11	0.35	0.38	0.24	0.40	0.16	0.22	0.44
500	0.15	0.41	0.49	0.29	0.44	0.17	0.13	0.51
600	0.17	0.42	0.47	0.26	0.40	0.16	0.13	0.45
700	0.10	0.24	0.34	0.15	0.31	0.06	0.10	0.38
801	0.10	0.20	0.28	0.12	0.30	0.04	0.07	0.37
1,000	0.09	0.16	0.23	0.10	0.29	0.02	0.06	0.37
1,200	0.09	0.15	0.22	0.09	0.29	0.02	0.08	0.37
2,000	0.08	0.18	0.19	0.08	0.32	0.01	0.07	0.38
2,200	0.06	0.18	0.17	0.06	0.29	0.02	0.08	0.37
2,400	0.06	0.18	0.17	0.06	0.29	0.02	0.07	0.37
5,000	0.05	0.14	0.14	0.06	0.29	0.01	0.07	0.37
10,000	0.03	0.14	0.10	0.06	0.29	0.01	0.08	0.37
20,000	0.04	0.14	0.11	0.06	0.29	0.01	0.09	0.37
100,000	0.03	0.13	0.08	0.05	0.29	0.02	0.10	0.37
Time (yr)	**K**	**F**	**NO_3**	**CO_2 (gas)**	**Ca/HCO_3**	**NO_3/Cl**	**Na/Cl**	**Ca/Cl**
0	0.06	0.30	0.27	0.23	0.19	0.38	0.36	0.24
1	0.12	0.06	0.27	0.21	0.30	0.38	0.34	0.17
53	0.24	0.25	0.35	0.32	0.33	0.38	0.27	0.31
100	0.11	0.08	0.30	0.29	0.19	0.38	0.29	0.27
200	0.16	0.12	0.33	0.32	0.45	0.38	0.32	0.21
300	0.27	0.18	0.42	0.34	0.68	0.37	0.28	0.19
400	0.24	0.13	0.40	0.25	0.53	0.37	0.19	0.12
500	0.29	0.12	0.39	0.13	0.51	0.37	0.17	0.11
600	0.27	0.13	0.41	0.08	0.54	0.38	0.16	0.17
700	0.16	0.08	0.29	0.07	0.33	0.38	0.17	0.16
801	0.12	0.07	0.28	0.07	0.27	0.38	0.18	0.14
1,000	0.10	0.05	0.27	0.03	0.22	0.38	0.20	0.15
1,200	0.09	0.04	0.27	0.01	0.23	0.38	0.21	0.15
2,000	0.08	0.07	0.28	0.01	0.25	0.38	0.23	0.15
2,200	0.07	0.07	0.27	0.03	0.26	0.38	0.23	0.12
2,400	0.07	0.07	0.27	0.02	0.25	0.38	0.23	0.12
5,000	0.07	0.06	0.27	0.04	0.21	0.38	0.23	0.15
10,000	0.06	0.05	0.27	0.08	0.17	0.38	0.25	0.20
20,000	0.06	0.06	0.27	0.12	0.15	0.38	0.26	0.22
100,000	0.05	0.05	0.27	0.11	0.15	0.38	0.26	0.24

Output-DTN: LB0307DSTTHCR2.002

NOTE: [1] Standard deviations are computed using data depicted in Figures 6-25a through 6-28a (zones of highest liquid saturation above the drift) and represent:

- For pH, standard deviation of pH values in (±) pH units
- For other data, standard deviation of logarithmic values: i.e., (±) change in log10 values of concentrations and concentration ratios around the mean of log10 values (thus, a value of 0.5 corresponds to a total spread of one order of magnitude)

7. VALIDATION

This section describes models and data used to validate the Drift Scale thermal-hydrological-chemical (THC) process model and input for the Drift Scale THC Seepage Model. The primary means of validation of the Drift Scale THC Seepage Model is the Drift Scale Test (DST) THC Model and the data collected from the DST. The DST THC Model and validation of model simulation results to measurements are presented in Section 7.1. The validation of the THC models by comparison to chemical data on water and gas samples is subject to a variety of uncertainties. These uncertainties are discussed in detail throughout Section 7, but can be summarized as follows. First, TH processes can lead to differences in the chemistry of water and gases by a few orders of magnitude (e.g., see Section 7.1.10.2) over very small increments in temperature as a result of boiling and mineral-water reactions. In contrast, temperature exhibits much less variation in space, because it is governed mainly by conduction in the rock matrix. Second, strong differences in aqueous species concentrations that develop in pore water in fractures and the adjacent matrix can be maintained owing to the slow rates of diffusion of aqueous species (e.g., see Section 7.1.11.3). Third, changes that the samples undergo during their extraction from the rock (e.g., cooling, degassing, condensation) have the potential for shifting the aqueous species compositions by a few orders of magnitude.

Reaction-transport experiments and associated modeling used to validate specific aspects of the Drift Scale THC models are presented in Sections 7.2 and 7.3. Sources of data used for model validation are shown in Table 7-1.

Table 7-1. Sources of Data Used for Model Validation or Corroboration

DTNs	Description
Plug Flow Reactor Data	
LB0011THCDISSX.001 [153380]	Experimental Data
Fracture Seal Experiment	
LB0101THCPRCPX.001 [154577]	Experimental data
Mineralogical Data (DST)	
LA0201SL831225.001 [158426]	Sidewall core sample mineralogical analyses
Analytical Water and Gas Chemistry Data	
LB0102CO2DST98.001 [159306]	CO_2 gas analyses (1st, 2nd, 3rd and 7th Qtr.)
LB990630123142.003 [111476]	4th, 5th, and 6th Qtr. DST CO_2 data
LB000121123142.003 [146451]	DST CO_2 data (Aug. '99 – Nov. '99)
LB0011CO2DST08.001 [153460]	DST CO_2 data (Nov. '99 – Aug. 2000)
CRWMS M&O 2001 [153814]	DST CO_2 data (July '98)
LB0208ISODSTHP.001 [161638]	DST CO_2 and isotopic data (combined)
MO0005PORWATER.000 [150930]	Analyses of pore waters from Alcove 5 core samples in the ESF (HD-PERM-2 and HD-PERM-3 samples)
LL990702804244.100 [144922]	Aqueous chemistry of water sampled from the DST (6/4/98 to 3/30/99)
LL001100931031.008 [153288]	Aqueous chemistry of water sampled from the DST (collected 10/27/99 to 1/25/00)

Table 7-1. Sources of Data Used for Model Validation or Corroboration (continued)

DTNs	Description
MO0207AL5WATER.001 [159300]	DST Field measurements
SN0203F3903102.001 [159133]	DST Field measurements
LL020405123142.019 [159307]	DST Aqueous chemistry
LL020302223142.015 [159134]	DST Aqueous chemistry
LL001200231031.009 [153616]	Aqueous chemistry of water sampled from the DST (8/9/99 and 8/10/99)
MO0101SEPFDDST.000 [153711]	Field pH of water sampled from DST on 5/23/00 and 6/29/00

7.1 THE DRIFT SCALE TEST THC MODEL

The DST is the second underground thermal test to be carried out in the Exploratory Studies Facility (ESF) at Yucca Mountain, Nevada. The purpose of the test is to evaluate the coupled thermal, hydrological, chemical, and mechanical processes that take place in unsaturated fractured tuff over a range of temperatures (approximately 25°C to 200°C). Details regarding the DST layout, borehole orientations, operation of the test, and measurements performed (as well as their uncertainties) are discussed in Section 6.3 of the *Thermal Testing Measurements Report* (BSC 2002 [160771]) and in *Drift Scale Test As-Built Report* (CRWMS M&O 1998 [111115]). Information on these aspects of the DST is not repeated in this report unless directly related to the geochemical data collected and used for model validation.

In brief, the DST consists of an approximately 50 m long drift that is 5 m in diameter. Nine electrical floor canister heaters were placed in this drift (the Heated Drift) to simulate nuclear-waste-bearing containers. Electrical heaters were also placed in a series of horizontal boreholes (wing heaters) drilled perpendicular outward from the central axis of the Heated Drift. These heaters were emplaced to simulate the effect of adjacent emplacement drifts. The DST heaters were activated on December 3, 1997, with a planned period of 4 years of heating, followed by 4 years of cooling. After just over 4 years, the heaters were switched off on January 14, 2002, and since that time the test area has been slowly cooling.

This section describes the DST THC Model, discusses simulations of THC processes during the DST, and presents comparisons to geochemical measurements performed on gas, water, and mineral samples collected from the DST. The DST THC Model is a forward numerical model used to gain insight into THC processes taking place during heating of the unsaturated devitrified tuffs. The DST THC Model provides the main validation test for the extension of the Drift-Scale THC conceptual model to the Drift Scale THC Seepage Model. The Drift-Scale THC conceptual models are described in Sections 6.1 to 6.4. The DST THC Model is compared with, but not calibrated to geochemical data collected from the DST. The calibrated drift-scale hydrological properties and thermal properties used as inputs are based on Yucca Mountain site data and not data specific to the DST. Some modifications were made to the thermodynamic data to capture aspects of the ambient-system pore-water chemistry (discussed in Section 4.1.4). The rationale for using hydrological and thermal properties that are not specific to the DST is discussed in Section 7.1.1. Model adjustments specific to the DST are made only to the connectivity of the

Heated Drift to the Access Drift, in order to capture (approximately) the heat losses through the bulkhead separating these tunnels.

Processes and data collected primarily during the heating phase of the DST are discussed in this Model Report. Simulation results from the DST THC Model REV01 were compared to the first 32 months of measured gas and water chemistry data. REV02 simulations build on the sensitivity studies and analyses performed for REV01, and therefore most REV01 sensitivity simulations were not repeated for REV02. REV02 simulation results are compared to data from the full four-year heating phase (for data that are available) as a part of the model validation.

The DST is not yet complete; it is expected that additional test data, when available, could provide further support to model validation. Specifically, model validation activities are expected to extend beyond the documented completion date for this Model Report, for several reasons. First, this Model Report predominantly treats data collected during the heating phase of the DST, and it is important to extend model validation to include data from the cooling phase with associated modeling. Second, analyses of new cores drilled through the boiling zone are underway, and other boreholes designed specifically for chemical analyses have not been completed. These will provide a much more complete validation for mineral deposition in fractures and compositions and quantities of water imbibed into the rock matrix. Third, there are additional stable and radiogenic isotopic data that have not yet been fully incorporated into the conceptual/numerical models describing THC processes. Such models and data will provide alternative validation methods for assessing the model's ability to represent TH and THC processes in the DST. Although new information and data from the DST will strengthen the model validation, this section will provide numerous comparisons of mineral, water, and gas chemistry that document that the validation criteria have been met.

7.1.1 Modeling Approach

The objectives of this work were to make predictions of the coupled thermal, hydrological, and chemical processes, followed by model refinement and comparison to measured data. The DST THC Model is not calibrated to geochemical measurements from the DST. Comparisons to measured geochemical data are the main method used in this Model Report for model validation. However, a better understanding of coupled processes is more important than matching all measured data, so that the models can be applied to long-term predictions of near-field THC processes. Furthermore, the simulations performed with the DST THC Model did not use site-specific (from the DST test block) thermal or hydrological properties. Therefore, the model provides a good test of whether site-wide hydrological and thermal properties can adequately capture processes that may take place at a specific location.

The modeling approach involves the creation of a numerical grid, as well as the selection and/or development of thermal, hydrological, mineralogical, aqueous, and gaseous species geochemical input data. It also involves the selection of appropriate thermal and hydrological models, as well as chemical, thermodynamic, and kinetic data and models. The approach and input data are described as follows in Sections 7.1.2 to 7.1.5.

7.1.2 Drift Scale Test 2-D Numerical Grid

The two-dimensional dual-permeability numerical grid for the DST represents a vertical cross section through the Heated Drift at a distance approximately 30 m from the bulkhead, separating the Heated Drift from the Access Drift (Figure 7.1-1a).

The REV01 mesh consists of 4,485 gridblocks, including fracture and matrix (DTN: LB0101DSTTHGRD.001 [153687]) (Figure 7.1-1b). The top boundary is approximately 99 m above the drift center, with the bottom boundary at approximately 157 m below the center. Connections between the interior of the Heated Drift and the Heater Test Alcove included gridblocks designed to act as a bulkhead and as insulating material. Within the drift, heat is applied directly to the drift wall instead of explicitly representing the electric heaters and calculating the heat transfer across the air mass inside the drift. The DST includes a plane of linear wing heaters on each side of the drift that are given small gridblocks in the model. Small gridblocks are also employed adjacent to the wing heaters and drift wall to capture the strong gradients in temperature and liquid saturation in these regions (Figure 7.1-1c). Radial mesh blocks in the drift interior were removed from the original mesh and replaced near the drift base by Cartesian gridblocks to represent the concrete invert (Figure 7.1-1c).

Minor modifications to the REV01 mesh were made for REV02 simulations. Gridblocks representing the insulation/bulkhead were removed, and the Heated Drift gridblock was connected directly to the Heater Test Alcove gridblock. The connection area and distance were adjusted so that heat loss from the drift resulted in roughly similar crown temperatures to the maximum observed values. This was done to simulate heat and mass losses through the bulkhead, instead of reducing power by a set factor, as was done in the REV01 simulations. In the approximate location of the observation drift, the gridblock volumes were increased to a large value to represent connection to the atmosphere (Figure 7.1-1b). Gridblocks that were removed previously (to represent a no-flux boundary for the observation drift) were added and connected to adjacent gridblocks. The distances from the drift center gridblock and the connecting elements were modified to represent the true distance, so that heat could be applied to the drift center and not to the elements at the drift walls (method used in REV01).

7.1.3 Heater Power

The DST THC Model employs a 9-month initial period at ambient temperature, corresponding approximately to the time that was required to set up the test. The wing heaters are split into inner and outer zones, with more power applied to the outer zone to approximate the presence of an adjacent parallel drift. In REV01, heat was applied at the drift wall into small gridblocks. In REV02, heat was applied solely to the drift-center gridblock, which is connected to all surrounding gridblocks. The positions of gridblocks representing heaters are shown in Figure 7.1-1c.

The REV01 heating schedule employed in the simulations is based on calibrated heater power measurements from DTN: MO0007SEPDSTPC.001 [153707]. The REV01 simulations were started with a 10% lower baseline power output to account for approximate differences between a 2-D model and heat losses in a 3-D experiment. Three 5% reductions in power during the year 2000 were implemented in the simulations, based on the estimated power reductions (DTN:

MO0012SEPDSTPC.002 [153708]). These simulations included 9 months at ambient temperature followed by 3 years of heating.

The REV02 heating schedule was based on step-wise averages of the 10-day incremented power data (DTN: MO0208RESTRDST.002 [161129]). The sources for this 10-day incremented power data are given in Table 7.1-1. The step-wise power distribution reflects the power output more closely than the simple averages used in REV01. Intentional power reductions were directly accounted from the power data, and more accurate time information gathered from the DTNs listed in Table 7.1-1.

Table 7.1-1. Input DTNs Used for Estimating Times/Dates of Power Reductions and Outages for REV02 Simulations

Power Data Sources	Dates
MO0208RESTRDST.002 [161129]	Heating Phase (10-day increments)
MO9807DSTSET01.000 [113644]	11/7/97 – 5/3/98
MO9810DSTSET02.000 [113662]	6/1/98 – 8/31/98
MO9906DSTSET03.000 [113673]	9/1/98 – 5/31/99
MO0001SEPDSTPC.000 [153836]	6/1/99 – 10/31/99
MO0007SEPDSTPC.001 [153707]	11/1/99 – 5/31/00
MO0012SEPDSTPC.002 [153708]	6/1/00 – 11/30/00
MO0107SEPDSTPC.003 [158321]	12/1/00 – 5/31/01
MO0202SEPDSTTV.001 [158320]	6/1/01 – 1/14/02

The DTNs in Table 7.1-1 were also used to estimate the length of the longer (approximately greater than 1/2 day) temporary power outages. Table 7.1-2 gives the step-wise averaged power data implemented in the REV02 DST THC Model simulations. Each time in Table 7.1-2 represents the initiation of a specific period of heating or power loss that continues until the succeeding time. The simulations were run for the full period of heating plus a 4-year period of cooling (shown by hypothetical end time at the base of Table 7.1-2).

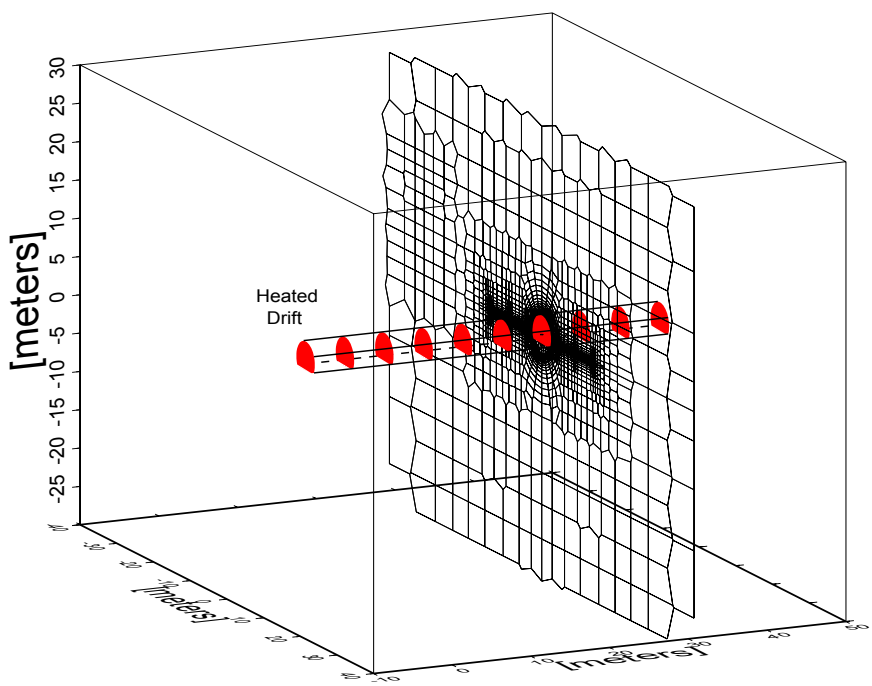

Output-DTN: LB0307DSTTHCR2.001

Figure 7.1-1a. Three-Dimensional Schematic Diagram of the DST Showing Perspective View of Numerical Mesh for DST THC Model Simulations (Mesh Extends In All Directions from Area Shown)

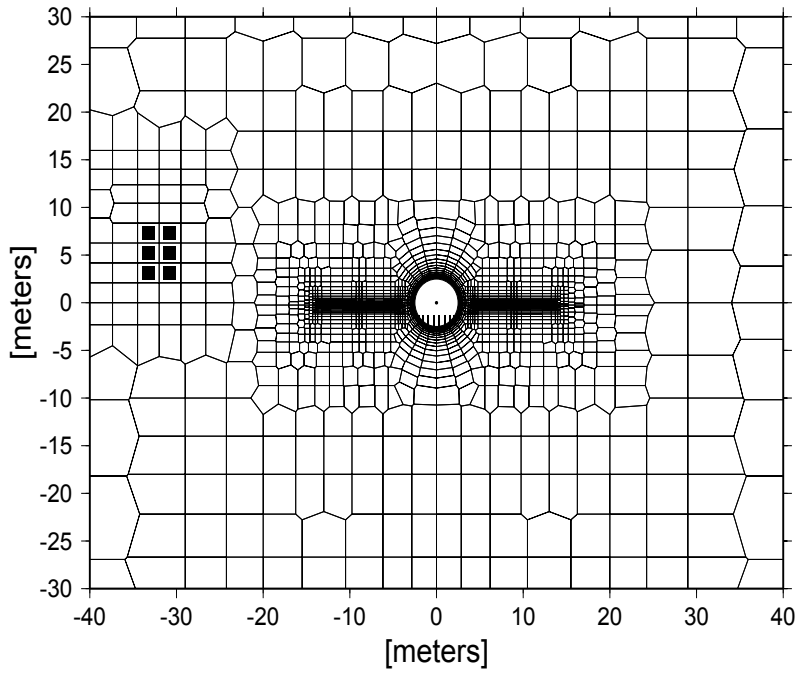

Output-DTN: LB0307DSTTHCR2.001

NOTE: The Observation Drift is shown as black squares. Mesh extends outside the area shown (see text). The Heated Drift is a circular region at the center.

Figure 7.1-1b. Numerical Mesh for DST THC Model Simulations

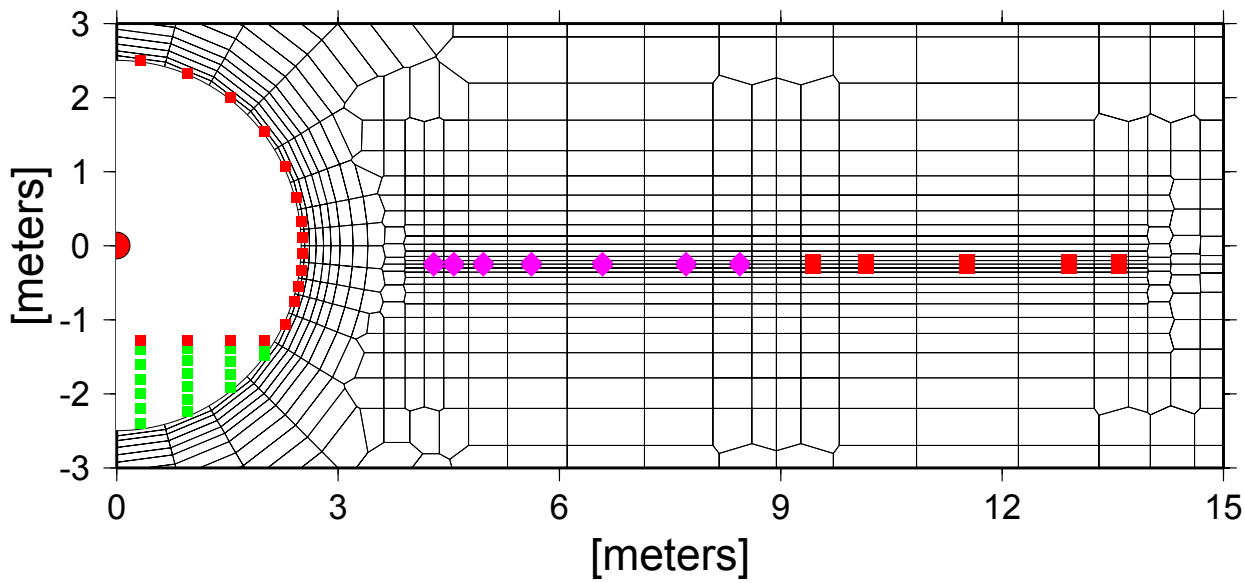

Output-DTN: LB0307DSTTHCR2.001

NOTE: Inner (violet diamonds closer to drift) and outer wing heater (red squares) indicate gridblock coordinates. Heat was applied to gridblocks marked along inside of drift for REV01, and at drift center for REV02. Green squares indicate gridblock locations for the concrete invert.

Figure 7.1-1c. Enlarged View of the Numerical Grid Showing the Locations of Gridblocks Representing the Heated Drift, Wing Heaters, and Concrete Invert

Table 7.1-2. Step-Wise Averaged Power Data for REV02 Simulations

Date	Time (s)	Time (days)	Canister Power (watts)	WH (inner) Power (watts)	WH (outer) Power (watts)	Comments
3/5/97	0.00000E+00	0.00	0.0000	0.0000	0.0000	pre-test
12/3/97	2.35872E+07	273.00	1091.3740	1232.4007	1626.7690	heaters turned on
3/15/98	3.24000E+07	375.00	1091.3740	0.0000	0.0000	outage - right rib
3/16/98	3.25080E+07	376.25	1091.3740	1232.4007	1626.7690	
4/12/98	3.48192E+07	403.00	1077.9972	1198.5773	1582.1220	
8/10/98	4.51872E+07	523.00	1119.6842	1201.8035	1586.3807	
1/27/99	5.98752E+07	693.00	0.0000	0.0000	0.0000	power outage
1/27/99	5.99400E+07	693.75	1123.5789	1204.4465	1589.8693	
2/16/99	6.16032E+07	713.00	1102.5965	1189.0805	1569.5862	
5/27/99	7.02432E+07	813.00	0.0000	0.0000	0.0000	power outage
5/27/99	7.03080E+07	813.75	1102.5965	1189.0805	1569.5862	
5/29/99	7.04160E+07	815.00	0.0000	0.0000	0.0000	power outage
5/30/99	7.04808E+07	815.75	1087.8653	1155.5245	1525.2923	
6/18/99	7.21440E+07	835.00	0.0000	0.0000	0.0000	power outage
6/19/99	7.22088E+07	835.75	1087.8653	1155.5245	1525.2923	
7/9/99	7.39584E+07	856.00	0.0000	0.0000	0.0000	power outage
7/15/99	7.44768E+07	862.00	1087.8653	1155.5245	1525.2923	
8/27/99	7.81920E+07	905.00	0.0000	0.0000	0.0000	power outage
8/29/99	7.83216E+07	906.50	1087.8653	1155.5245	1525.2923	
11/22/99	8.57088E+07	992.00	1087.8653	0.0000	0.0000	outage - right rib
11/24/99	8.58816E+07	994.00	1087.8653	1155.5245	1525.2923	
2/11/00	9.27072E+07	1073.00	0.0000	0.0000	0.0000	power outage
2/11/00	9.27720E+07	1073.75	1078.8421	1184.6642	1563.7568	
3/2/00	9.44352E+07	1093.00	1029.1930	1115.3660	1472.2831	power reduction
3/12/00	9.52992E+07	1103.00	0.0000	0.0000	0.0000	power loss
3/13/00	9.54072E+07	1104.25	1029.1930	1115.3660	1472.2831	
5/2/00	9.97056E+07	1154.00	964.5263	1040.2813	1373.1713	power reduction
8/15/00	1.08778E+08	1259.00	917.3463	978.7397	1291.9364	power reduction
1/20/01	1.22429E+08	1417.00	0.0000	0.0000	0.0000	power outage
1/21/01	1.22515E+08	1418.00	917.3463	978.7397	1291.9364	
5/1/01	1.31155E+08	1518.00	875.5711	925.4672	1221.6168	power reduction
7/1/01	1.36426E+08	1579.00	0.0000	0.0000	0.0000	power outage
7/1/01	1.36490E+08	1579.75	875.5711	925.4672	1221.6168	
8/22/01	1.40918E+08	1631.00	826.8171	875.8317	1156.0979	power reduction
1/14/02	1.53446E+08	1776.00	0.0000	0.0000	0.0000	heaters turned off
1/14/06	2.79677E+08	3237.00	0.0000	0.0000	0.0000	cooling period end

NOTE: Input DTNs for REV02 power data are listed in Table 7.1-1. Each time represents the initiation of a particular period of heating (or power loss) that continues until the next time in the table. Data are for a 2-D vertical slice.

7.1.4 Hydrological and Geochemical Input Data

Sources of hydrological and geochemical input data are listed in Table 4.1-1 (REV02) and 6.4-2 (REV01). Other details regarding the use or modifications to these data are given in Sections 7.1.5 and 7.1.6.

Thermodynamic data are described in Section 4.1.4 and presented in Attachments V (REV01) and VI (REV02). Kinetic data are given in Table 6.4-3 (REV01) and Table 4.1-4 (REV02). Initial mineral volume fractions for REV01 simulations are given in Attachment I. REV02 mineral volume fractions were modified slightly to reflect the mineralogical assemblage used in the Tptpll THC Seepage Model REV02, i.e., the addition of fluorite and opal to the initial assemblage. In REV02, the mineral names were also modified to be consistent with the name conventions used in the REV02 thermodynamic database. Mineral reactive surface areas are given in Attachment III, again with slight modification to reflect additional minerals in REV02.

7.1.5 Initial and Boundary Conditions: Hydrological and Thermal

Hydrological and thermal initial and boundary conditions were derived from the UZ Flow Model. Input data to these models (hydrological and thermal properties) are qualified and have been taken from the TDMS, and the UZ Flow Model has been calibrated to these data. Models and data for the ambient geochemistry of the UZ at Yucca Mountain (i.e. Cl, Sr, calcite) support the infiltration rates used as boundary conditions for the UZ Flow and Transport Model (Sonnenthal and Bodvarsson 1999 [117127], p. 107; Liu et al. 2003 [162470]; Xu et al. 2003 [162124]). This confidence in the initial and boundary conditions in turn provides confidence in the DST THC model. The methods used to set the initial and boundary conditions are described immediately below.

For REV01 simulations, the steady-state liquid saturations, temperatures, and pressures were obtained using the calibrated drift-scale hydrological parameter set for the present climate (mean infiltration) with a local infiltration rate of 1.05 mm/yr (DTN: LB991091233129.001 [125868]). The REV01 hydrological properties are listed in Table 6.4-1.

Steady-state liquid saturations, temperatures, and pressures were obtained for REV02 simulations using the updated drift-scale thermal-hydrological property set (DTN: LB0208UZDSCPMI.002 [161243]). The REV02 hydrological properties are listed in Table 6.4-1. Modifications were made to the fracture medium void fraction (usually set to 0.99 or 1.0) to be consistent with the revised REV02 fracture porosities (DTN: LB0210THRMLPRP.001 [160799]). This modification has approximately the same effect as changing the relative volumes of the fracture and matrix gridblocks (the usual procedure for implementing fracture porosity).

The top and bottom boundaries were set to constant temperature, pressure, and liquid saturation, based on steady-state values obtained from simulations of a 1-D column extending from the land surface to the water table. The top boundary of the 2-D model extends 150 m above and below the drift center, but does not reach either the land surface or the water table. Under these conditions, the percolation flux at the top boundary is approximately 0.5 mm/yr. The bottom boundary condition is open to gas and to liquid flow. The side boundaries of the domain are located 81.5 m away from the drift center on each side (outside of the test influence area) and are

no-flux for mass and heat. The air pressure and temperature in the observation drift are set to constant values, and therefore do not reflect temporal fluctuations in barometric pressure or tunnel air temperatures. The Heated Drift wall is open to advection and conduction of heat and mass (e.g., air, water vapor, and CO_2).

7.1.6 Initial and Boundary Conditions: Geochemical

Initial and boundary geochemical conditions were set using qualified data, based on pore water and mineralogical analyses and taken from the TDMS. Because these data are qualified, this confidence in the initial and boundary conditions in turn provides confidence in the DST THC model. The methods used to set the initial and boundary conditions are described immediately below.

Initial geochemical data used in the simulations are given in Attachments I–VI (sources in Tables 4.1-1 and 6.4-2). All aqueous and gaseous species concentrations in the rock were initially set to a uniform value (Section 6.2.2.1). The Heater Alcove and Observation Drift CO_2 concentrations were fixed to approximately that of the atmosphere. The Heated Drift CO_2 concentration was initially set to the same value as that in the Observation Drift, but was allowed to exchange CO_2 with the Heater Test Alcove and with the surrounding rock. REV01 simulations were run using the extended-case and base-case geochemical systems described in Section 6.2.2.2 and in Table 6.2-2. REV02 simulations were performed with the updated REV02 extended-case geochemical system (Table 6.2-2).

Both the top and bottom boundary conditions are open to gas and aqueous species transport. The top and bottom boundaries were also set so that no mineral reactions take place (and therefore no changes in aqueous species concentrations occur as a result of mineral-water reactions). Their volumes were set to extremely large values, so that they act essentially as constant concentration boundaries. The side boundaries are no-flux for gas and aqueous-species transport.

7.1.7 Model Validation Methods, Criteria, and Limitations

In the following sections, data and predictions are reviewed to demonstrate that the criteria specified in the TWP have been met for the DST THC Model. Because the THC Seepage Model uses the same conceptualization and mathematical treatment of THC coupled processes as the DST THC Model, including the same thermodynamic and kinetic data, DST model validation effectively validates the THC Seepage Model. Additional validation of the THC model is presented in Sections 7.2 and 7.3, where results of laboratory plug-flow and fracture boiling experiments are compared to simulations. It is important to recognize that although the DST THC Model validates the methodology and inputs used in the THC Seepage Models, the time-scales of interest are different by several orders of magnitudes and thus the relative importance of various reaction-transport processes can lead to different long-term behavior.

The models were validated—that is, needed confidence in the models was gained—by the following methods listed in AP-SIII.10Q, Section 5.4.1 (c). These are: Method 1, Corroboration with Experimental Data; and Method 3, Corroboration with Refereed Journal Literature (AP-SIII.10Q, 5.4.1(d)). These validation methods provide the most confidence in the conceptual and numerical models and their outputs.

While this model report has been independently reviewed under LBNL procedure, YMP-LBNL-QIP-6.1, *Document Review* as planned in the TWP (BSC 2002 [160819], Section 2.8 and Attachment I, Section I-3-4-1), this review is not considered to be one of the methods of validation for this model report.

7.1.7.1 Validation Method 1—Corroboration with Experimental Data

Data from the DST used for comparison consist of analyses of water and gas samples from borehole intervals between packers and observations of mineral precipitation in boreholes. Intervals were selected for comparison based upon the availability of a long, continuous sample record and the absence of confounding factors, such as the sampling interval being too long to compare with a particular gridblock or pair of gridblocks, or boreholes being near either end of the DST and affected by three-dimensional transport (see below). The locations of the hydrology boreholes, sampling intervals, and temperature sensors are shown in Figure 7.1-2.

Differences between the DST THC Model predictions and the DST measurements are important to this validation. There are several reasons (listed below) why observations may disagree with predictions, and yet be consistent with validation of the DST THC Model. Individual data points may not agree closely with model predictions, but model validation requirements can be met. It is important that these considerations are kept in mind when reviewing the model comparisons to measured data.

1. The DST THC model is a continuum model, using average hydrological, thermal, and mineralogical properties for individual hydrostratigraphic units at Yucca Mountain, rather than specifically for the DST.

2. The continuum model does not simulate individual fractures, which may intersect boreholes near sampling points, their aperture and frequency resulting in different flow rates and temperatures, thus affecting the chemistry of the gas and water samples in that interval.

3. All samples were taken from long borehole intervals (approximately 8-10 m long), which cross regions of large gradients in gas species concentrations (up to a few orders of magnitude) and exhibit temperature variations of tens of degrees. Furthermore, the samples are only known to have been derived from the borehole itself and may not have the same composition as the gas and liquid flowing in fractures. In addition, waters collected from boreholes have resided in the boreholes for different lengths of time, interacting with the surface of the borehole, interchanging components with the matrix, affected by gas flow and condensation in the borehole, and interacting with engineered materials. In contrast, the model results represent compositions in fractures or matrix at an instant in time.

4. The model represents a two-dimensional slice taken approximately at mid-length of the DST; it does not simulate transport in the third dimension. A 3-D model at the minimum resolution required for a reactive-transport simulation would have in excess of 100,000 gridblocks, which would be computationally infeasible (several months or more of computation time). Because the initial permeabilities and geochemical

properties are unknown at every point inside the rock, a 3-D model would not be expected to significantly improve matches to geochemical data, because the model would still rely on average properties. Although a 3-D model would reduce some of the uncertainty because of slight improvements in capturing the distribution of heat, fluid, and chemical species transport, it would not yield any significant improvement in the conceptual understanding or validation of the model approach and input data.

5. The model does not consider all deviations from planned operation. These deviations include the exact time periods of power losses, variations or uncertainty in heat losses through the bulkhead, changes in pressure owing to forced ventilation, the effect of the many boreholes on the behavior of the system, and barometric pressure changes. Because of this, and reasons 1, 2, and 4 above, the changes occurring at a particular time in the model may be shifted from that occurring in the DST by several months or more, depending on the time when the temperatures are similar or the point at which water completely evaporates.

6. Gas and water samples are affected by condensation of water vapor as the sample cools in the collection tubes from the borehole interval to the sample containers. This results in a variety of changes to the gas and water compositions. CO_2 concentrations in the gas can increase dramatically as the water vapor is preferentially removed from the gas. Many aqueous species concentrations will become lower as the sample is diluted by pure water condensed in the tubes and mixed with the water being sampled. The pH of the water may drop as the pure condensate formed under an elevated partial pressures of CO_2 is mixed with the water from the borehole.

Given these considerations, and the model requirements in mind, the criterion for model validation is that any two of these three criteria be satisfied for a majority of the samples collected (but not all samples if conditions as given above are expected to be important):

- Observed concentrations of gas and aqueous species match predicted concentrations within an order of magnitude (e.g., one pH unit). This range is reasonable because chemical potential is proportional to the logarithm of concentration.

- The simulated trend of CO_2 over time in the sampling interval is clearly followed. “Clearly followed” is understood to mean that model and observations show the same initial trend of increase or decrease, and any observed reversal is predicted. Simulated CO_2 concentrations will be within one order of magnitude of measured data

- Observations of mineral precipitation shall agree qualitatively with predictions of locations where mineral precipitation is most likely to occur.

7.1.7.2 Validation Method 3—Corroboration with Refereed Journals or Literature

This validation has been corroborated by publication in a refereed technical journal as allowed by AP-SIII.10Q, Section 5.4.1(d) (Xu et al. 2001 [161864]).

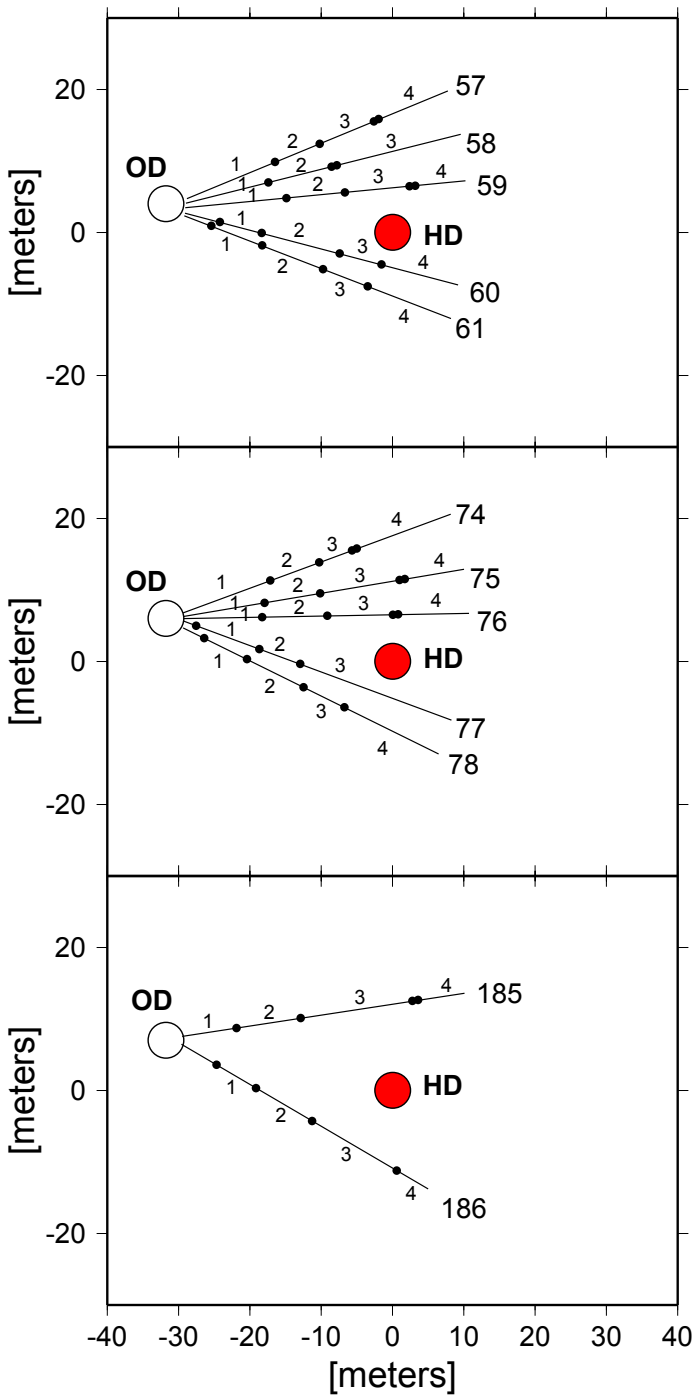

(coordinates from DTN: MO0002ABBLSLDS.000 [147304])

NOTE: Borehole intervals are designated as 1, 2, 3, and 4 moving away from the Observation Drift (open circle designated "OD"). Temperature sensors (not labeled) are shown as the small closed circles, and are designated similarly to the intervals (i.e., sensor 60-4 is the 4th sensor from the Observation Drift).
OD = Observation Drift; HD = Heated Drift.

Figure 7.1-2. Locations of Hydrology Boreholes, Sampling Intervals (numbered) and Temperature Sensors

7.1.8 THC Simulations

In the following sections, simulations performed for REV01 and REV02 of this Model Report are described. Several sensitivity runs were performed for REV01 that show the effects of changing various geochemical model parameters. In REV02, other sensitivity simulations were performed to complement those done in REV01. In some cases where the results are similar to those presented for REV01, only REV02 simulation results are shown, with discussion on any differences observed. The specific updates and simulations are listed in the following subsections.

7.1.8.1 REV01 Simulations

Six THC simulations of the DST were performed to investigate various aspects of the DST THC model thermodynamic and kinetic data and conceptual models for mineral reactions. All REV01 simulations were performed using TOUGHREACT V2.3 (LBNL 2001 [153101]). All were run for 9 months of ambient open-drift conditions, followed by 3 years of heating. The maximum time step was one day, using the sequential noniterative approach. Coupling of permeability to fracture aperture changes was employed; however, the changes to flow are very minor over the short time of the DST. Based on differences in the geochemical system and treatment of important mineral reaction rates, the simulations are designated in the figures as follows:

1. Base-case CC Kin: Base case, including fluorite (Table 6.2-2). Calcite (CC) is treated as a kinetic mineral with the published value of the kinetic-rate constant.

2. Extended CC Kin: Extended case (Table 6.2-2, includes aluminosilicates and iron oxides). Calcite is treated as a kinetic mineral with the published value of the kinetic rate constant.

3. Base-case CC Eq: Base case, including fluorite. Calcite is treated as an equilibrium mineral.

4. Extended CC Eq: Extended case. Calcite is treated as an equilibrium mineral.

5. Extended An Full: Extended case. The full reactive surface area is used for anorthite (1000 times larger than in (2) and (4) above). Calcite is treated as a kinetic mineral with the published value of the kinetic rate constant.

6. Base-case No CC: Base case, including fluorite. Calcite was removed from this simulation to address observations of lower pH waters that may have condensed in or near the walls of boreholes where water was collected without interacting with calcite.

All input and output data files for the REV01 simulations are given in Attachment X.

7.1.8.2 REV02 Updates and Simulations

Several updates were made for the simulations in REV02 of this Model Report. They include:

1. Revisions to the numerical mesh to account for heat input at the drift center and heat and mass transfer across the Heated Drift and Observation Drift walls (see Section 7.1.2).

2. Revision of input heater power (see Section 7.1.3).

3. Use of REV02 calibrated thermal-hydrological properties (see Table 6.4-1).

4. Use of REV02 thermodynamic data (see Attachment VI).

5. Use of REV02 kinetic data (see Section 4.1.5 and Table 4.1-4).

6. Added nitrate to aqueous species (see HD-PERM water, Table 6.2-1).

7. Added fluorite and opal to the primary mineral assemblage and sepiolite as a potential precipitating phase (see Section 6.2.2.2 and Table 6.2-2).

8. Added various salt minerals as potential precipitating phases (or as phases formed during flow into dry blocks; see Section 6.4.5).

9. Use of an improved method for mineral precipitation at the boiling front that was implemented in TOUGHREACT V3.0 (LBNL 2002 [161256]).

Three additional THC simulations and two TH simulations were performed for REV02 of this Model Report using TOUGHREACT V3.0 (LBNL 2002 [161256]).

1. Extended Case (REV02), EOS3, higher CO_2 diffusion coefficient (value used in most REV02 THC Seepage Model simulations) [simulation dstrev2_thc7].

2. Extended Case (REV02), EOS4, REV01 CO_2 diffusion coefficient [simulation dstrev2_thc8].

3. Extended Case (REV02), EOS3, REV01 CO_2 diffusion coefficient [simulation dstrev2_thc9].

4. EOS3 TH simulation [simulation dstrev2_th12].

5. EOS4 TH simulation [simulation dstrev2_th13].

The REV02 extended-case geochemical system was used for all THC simulations performed for REV02 because the THC Seepage Model considered only this geochemical system. Results from the “high” diffusion coefficient Simulation “1” are not shown because validation is based on the parameter values within the range expected. All input and output data files for the REV02 DST THC simulations are given in Attachment X.

7.1.9 Simulation Results: Thermal and Hydrological Evolution

The main driving force for changes in the hydrological and chemical behavior of the system is the strong thermal load applied to the system. The resulting changes in temperature, liquid

saturation, and gas-phase composition lead to changes in the chemistry of water and gas, as well as mineral dissolution and precipitation. A more complete discussion of thermal-hydrological processes is presented in BSC (2003 [161530]). Key aspects of the thermal-hydrological behavior of the DST that drive the chemical evolution of the system are discussed briefly in this section.

The simulation results for the TH evolution of the DST, as well as all other simulation results shown in this section, are based on Simulation "2" above, performed using the EOS4 module in TOUGHREACT V3.0 (LBNL 2002 [161256]). TH (and chemical) results were nearly identical to those not using the vapor-pressure-lowering (EOS3) in Simulation "3," and the latter are therefore not shown. Outputs from all simulations are, however, included in the data submittal to the TDMS. The relatively minor difference in the results is largely related to the implementation of revised capillary pressure curves in the REV02 hydrological parameter set. The REV02 property set has a maximum capillary pressure of 10^8 Pa, which results in a relatively small change in the saturation-temperature history in the rock as it is heated. Low matrix permeabilities in the REV02 parameter set lead to higher matrix pore pressure, thus delaying boiling more substantially than the capillary-pressure-lowering effect. In addition, coupled effects of mineral precipitation/dissolution on flow did not significantly affect the TH evolution of the DST.

The modeled temperatures in the drift reflect the heat input at the drift center (at the approximate location of the electrical canister heater) and subsequent heat transfer to the drift wall (Figure 7.1-3). Differences in temperature between the drift center and the drift wall (Figure 7.1-3) near the top (drift crown) are approximately 20°C, similar to the differences observed between electrical canister temperatures and drift-crown temperature measurements (e.g., DTN: MO0007SEPDSTPC.001 [153707]). Sharp temperature drops are the result of power losses, heater failures, and/or intentional power reductions.

Drift-wall temperatures predicted by the two-dimensional model eventually exceed the maximum measured values by about 20°C. However, predicted temperatures in the rock are typically closer to measured values (Figure 7.1-4). There are several reasons for the elevated temperature in the drift. First, the 2-D cross section can only approximate the exchange of heat through the rock along the axis of the DST. Second, heat lost through the bulkhead by a combination of advection and diffusion is uncertain and can only be approximated using porous flow equations in a basically one-dimensional manner and with a 2-D model. Therefore, this model is most applicable to areas near the center of the test—away from both the bulkhead and the opposite end of the Heated Drift.

Other factors that control the temperature response of the drift wall include thermal properties (conductivity, heat capacity) of the rock and the representation of heat transfer processes in the drift (approximate treatment of thermal radiation and convection). The rate of temperature increase at the drift wall could only be approximated because the model employs a temperature-independent rock heat capacity, does not consider thermal radiation, and does not include a rigorous model for gas convection in the drift. However, the comparison of temperatures measured in the rock, compared to the modeled temperatures, provides the true test of the validity of the model for heat transfer to the rock. Confidence in the approximations employed is gained through the closeness of the modeled temperatures to those measured in the rock (Figure 7.1-4).

The modeled distributions of fracture and matrix liquid saturation (with temperature contours overlain) are shown in Figures 7.1-5a–d. The plots correspond to one and four years from the initiation of the heating phase. The extent of the dryout zone increases over the heating period and is larger in the fractures than the matrix. A wider spatial interval between the 90°C and 100°C isotherms indicates the presence of an isothermal boiling/condensation (heat pipe) zone, which is especially well developed above the wing heaters. An extensive drainage zone extending several tens of meters in the fractures below the heaters contrasts with a very narrow high-saturation zone above the heaters, where water is continuously diverted around the heated zone. The narrow band of increased fracture saturation above the heaters is characterized by temperatures of about 90–95°C. Typically, water was collected from hydrology boreholes when this heat-pipe zone intersected the borehole intervals (BSC 2003 [161530]).

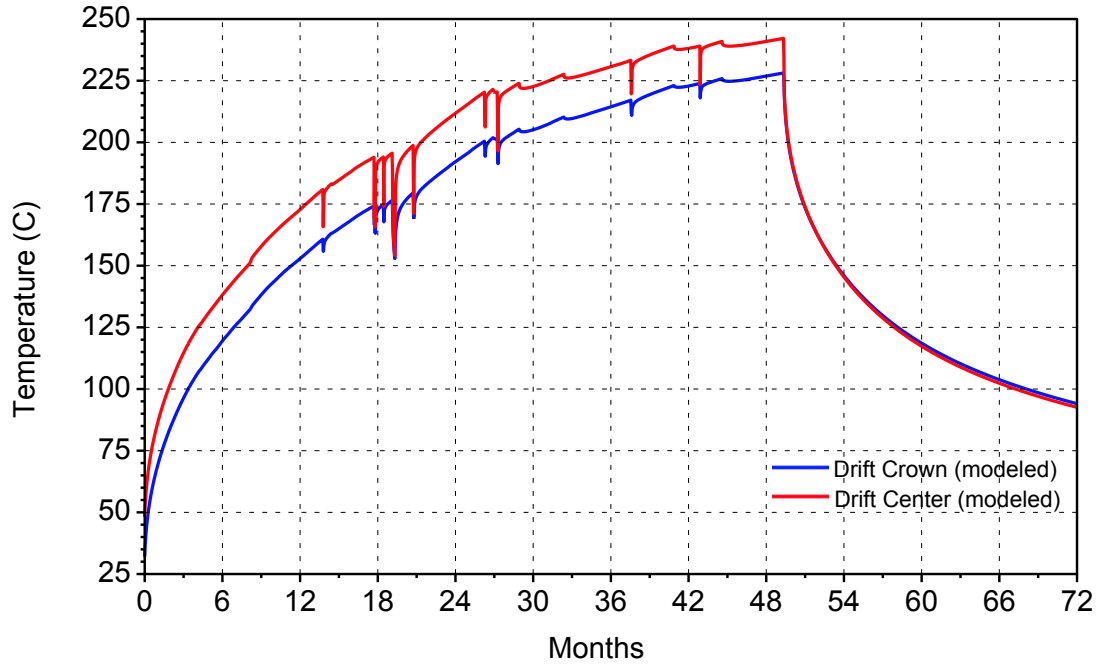

Output-DTN: LB0307DSTTHCR2.001

Figure 7.1-3. Drift Center and Drift Crown Modeled Temperatures over the First Six Years of the DST

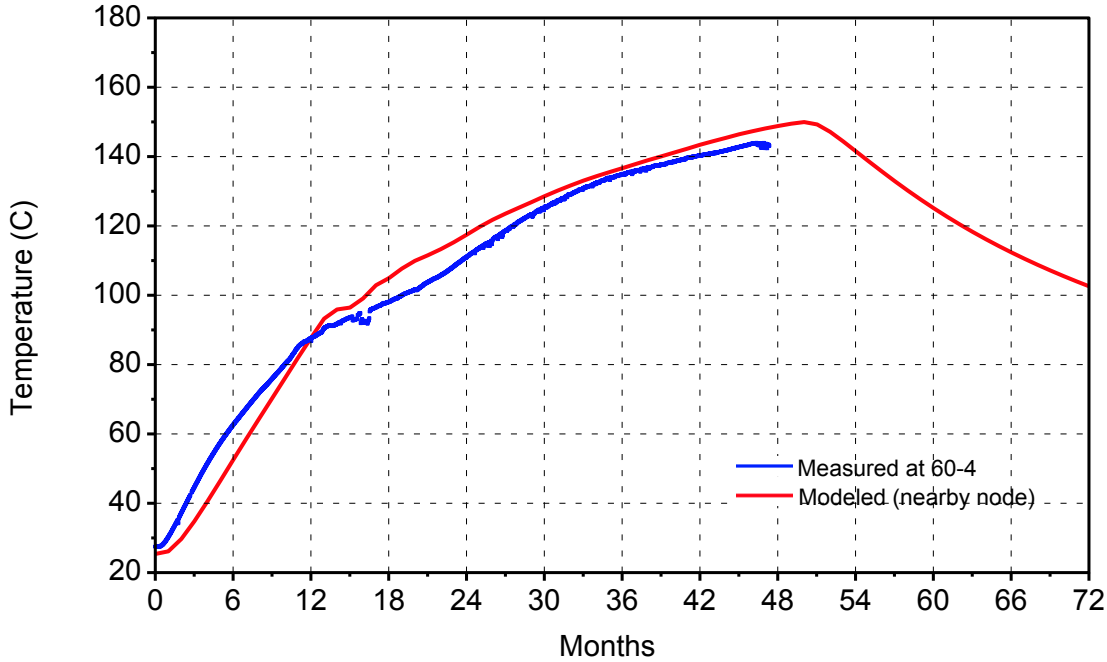

Output-DTN: LB0307DSTTHCR2.001 (modeled)
Table 7.1-1 (DTNs for measured temperatures)

NOTE: Modeled Temperatures are for a Nearby Grid Node. Location of temperature sensor is on Figure 7.1-2.

Figure 7.1-4. Comparison of Modeled and Measured Temperatures over Time for the Sensor Located at Hydrology Borehole Packer 60-4

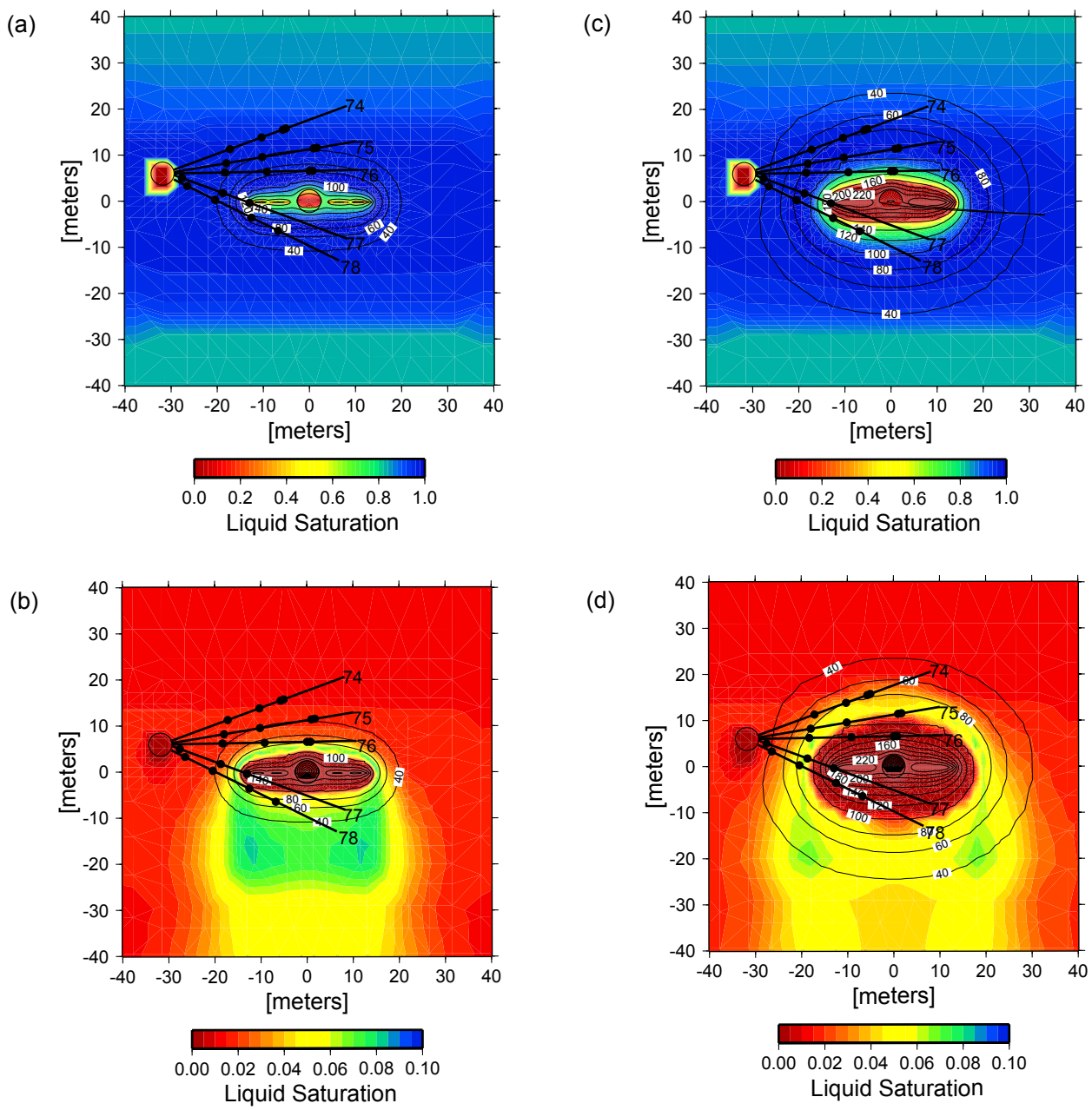

Output-DTN: LB0307DSTTHCR2.001

Figure 7.1-5. Liquid Saturation (Colors) and Temperature (Contour Lines) in the DST (Base Case) at One Year (Matrix – a, Fracture – b) and at Four Years (Matrix – c, Fracture – d)

7.1.10 Gas-Phase CO_2 Evolution: Measured Compositions and Simulation Results

The evolution of CO_2 concentrations in the gas phase is discussed in this section. Simulation results are compared to concentrations measured in gas samples taken from boreholes during the entire heating phase of the DST. The concentration of CO_2 in the gas phase is a function of temperature, pressure, aqueous-phase chemistry, mineral-water reactions, and advective and diffusive transport. From a model validation standpoint, the strong effect of CO_2 partial pressure on water pH and the final brine composition formed upon evaporation make the analysis of CO_2 distributions in the DST important. Numerous measurements of CO_2 concentrations in gas collected from the DST have been made as a function of space and time, and therefore, a more complete comparison of the model results to CO_2 data can be made than to the relatively fewer number of water-chemistry measurements. CO_2 concentrations in gases collected from the DST also provide a qualitative measure of the influence of atmospheric gas on the system, because of the relatively low and constant value in the atmosphere (≈ 400 ppmv). Isotopic compositions of CO_2 (discussed in Section 7.1.14) yield insight into the sources of CO_2.

7.1.10.1 Gas Sampling and CO_2 Measurements

Gas sampling, analytical methods, and compositional data are discussed in Section 6.3.4.2 of BSC (2002 [160771]). Gas samples were taken from several meter-long borehole intervals that spanned a wide range of temperatures as a result of their orientation relative to the heaters. As part of the sampling procedure, the gas samples had much of their water vapor removed before analyses were performed, and therefore measured CO_2 concentrations are for the noncondensible gas fraction. The noncondensible gas fraction is very high (>95%) at the ambient temperature of about 25°C, but may drop to extremely low values (< 1%) under boiling conditions. Hence, reported CO_2 concentrations at temperatures close to boiling are much higher than if the measurements were made on a "complete" gas composition (air + CO_2 + H_2O). This effect must be considered when comparing model results to measured values.

An example of the distributions of measured CO_2 concentrations (DTNs listed in Table 7-1) after one year and after 15 months of heating is shown in Figure 7.1-6. Comparison of the 15-month to the one-year data shows that in nearly all of the boreholes, the CO_2 concentrations are higher at 15 months, owing to heating of pore water and exsolution of CO_2 into the gas phase. Areas that have maintained CO_2 concentrations close to the ambient value in the "rock' of around 1,000 ppmv (log ppmv = -3) can be seen near the observation drift. However, very close to the Observation Drift, some of the values are lower, suggesting that mixing with atmospheric gas may have taken place.

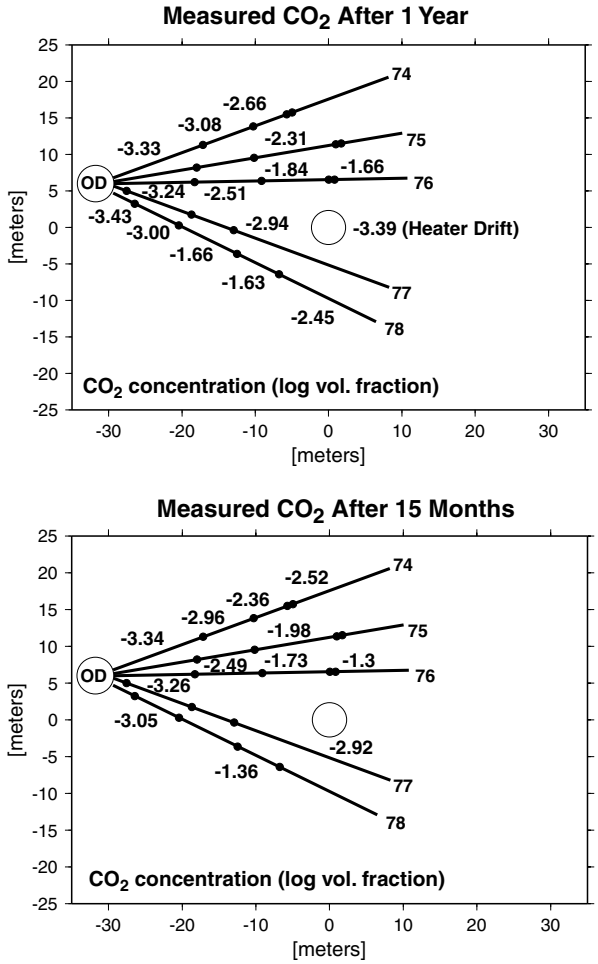

DTN: LB990630123142.003 [111476]

NOTE: Concentrations refer to intervals between pairs of points.

Figure 7.1-6. Measured Concentrations of CO_2 (Log Volume Fraction) in Gas Phase around the DST at 1 Year and at 15 Months

7.1.10.2 Modeled Spatial Distribution of CO_2

Model results are presented for the REV02 extended system (described in Table 6.2-2). Modeled distributions of CO_2 concentrations (log ppmv) in fractures are shown at yearly intervals during the heating phase (Figure 7.1-7) and during the cooling phase (Figure 7.1-8). Over the heating phase of 4 years, a region of highly elevated CO_2 concentrations, centered approximately at the 60°C isotherm, is seen to move gradually outward from the heaters. Outside this region, CO_2 concentrations gradually decrease to the ambient value in equilibrium with pore water (approximately 1,000 ppmv). Maximum CO_2 concentrations of around 50,000 ppmv are located above and below the wing heaters and the Heated Drift. Towards the heaters, CO_2 concentrations drop off more sharply with increasing temperature, decreasing to values below 10 ppmv. This sharp decline takes place as a result of the CO_2 degassed during heating of the pore water, its transport outward, and the displacement of air and CO_2 by steam generated during boiling.

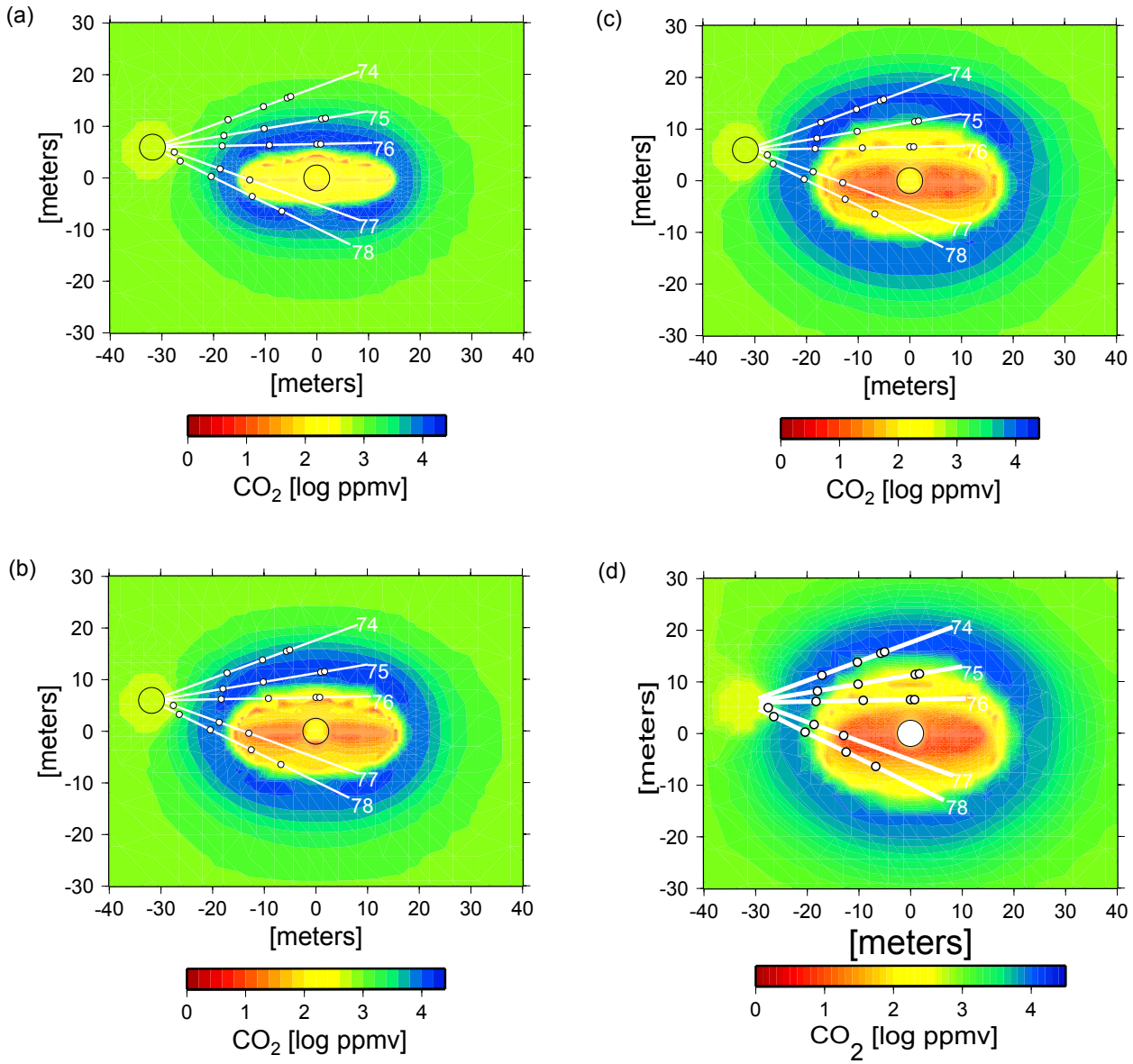

Output-DTN: LB0307DSTTHCR2.001

Figure 7.1-7. Modeled Gas Phase CO_2 Concentrations (Log ppmv) in Fractures during the Heating Phase of the DST at 1, 2, 3, and 4 years

The zone of maximum CO_2 concentrations also transects the hydrology borehole intervals as it migrates outwards, with some intervals registering a two order-of-magnitude variation between them.

The effect of the atmospheric CO_2 concentration of the gas in the Observation Drift on its surroundings is evident up to about 10 m from the drift wall. However, effects on the fracture gas composition are relatively minor beyond about 5 m from the drift wall. Carbon dioxide concentrations in the Heated Drift stay close to the atmospheric value, owing to transport (advection and diffusion) between the Heater Test Alcove (set to atmospheric CO_2) and the Heated Drift.

The modeled cooling phase of the DST (Figure 7.1-8) is characterized by a gradual re-equilibration of CO_2 concentrations throughout the DST area, via cooling, gas-phase diffusion, and flow of gas and water. Exchange of atmospheric gas among the Heated Drift, the Heater Test Alcove, and the rock around the Heated Drift is clearly evident.

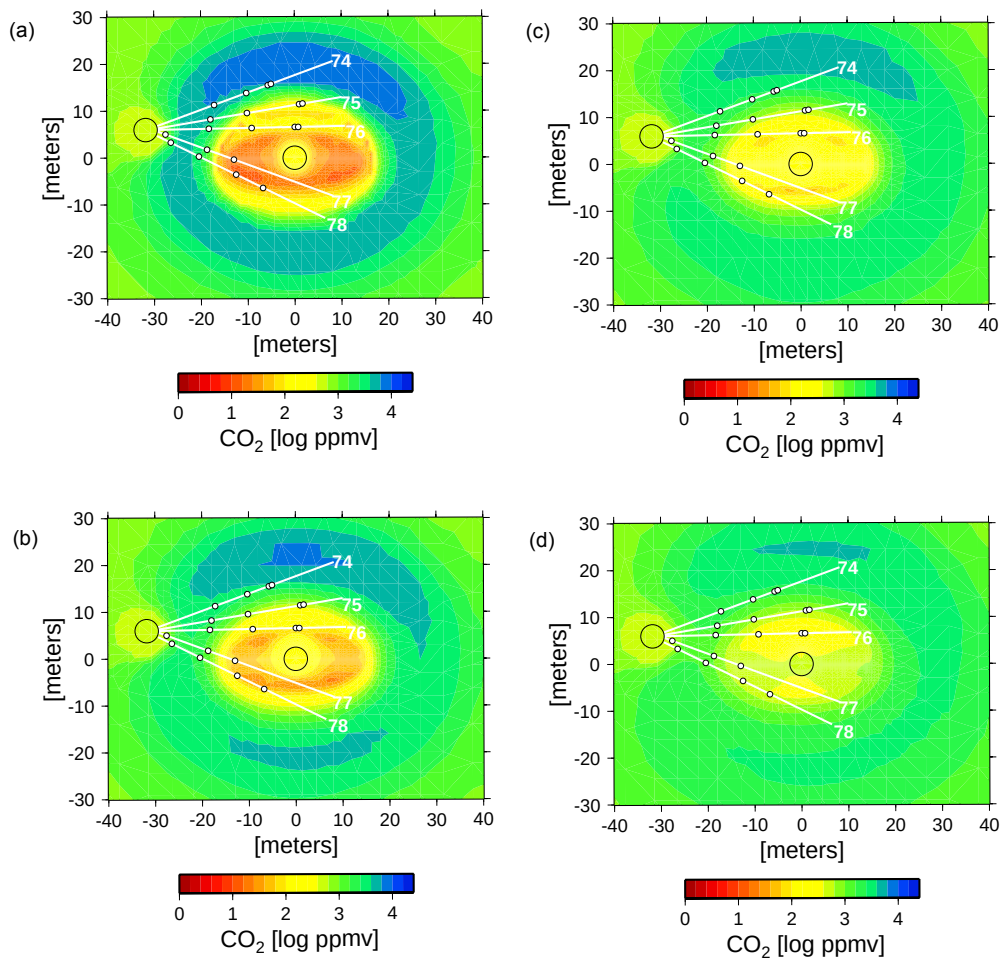

Output-DTN: LB0307DSTTHCR2.001

Figure 7.1-8. Modeled Gas Phase CO_2 Concentrations (Log ppmv) in Fractures during the Cooling Phase of the DST at 5, 6, 7, and 8 years

7.1.10.3 Modeled and Measured CO_2 Concentrations Over Time

Validation of the DST THC Model for the prediction of the temporal evolution of CO_2 concentrations was performed by comparison of measured values from intervals repeatedly sampled from February 1998 through January 2002 (DTNs listed in Table 7-1) to model results. The locations of the gridblock central coordinates relative to the gas collected in borehole intervals from which the gas samples were taken are illustrated in Figure 7.1-9. Because the measured concentrations come from borehole intervals that are several meters long, and not from a specific location, model data are chosen from the gridblock closest to the center of the interval. If a gridblock is not centered on the borehole, a gridblock closest to the center is chosen on the outer (cooler) side of the borehole. Gridblocks on the cooler side should compare more closely to the measured data because the 2-D model, having no heat loss in the rock perpendicular to the drift, produces temperatures that are somewhat higher than the measured temperatures after approximately the first year of heating. However, measured temperatures may be higher prior to that time (refer back to the temperature comparison in Figure 7.1-4).

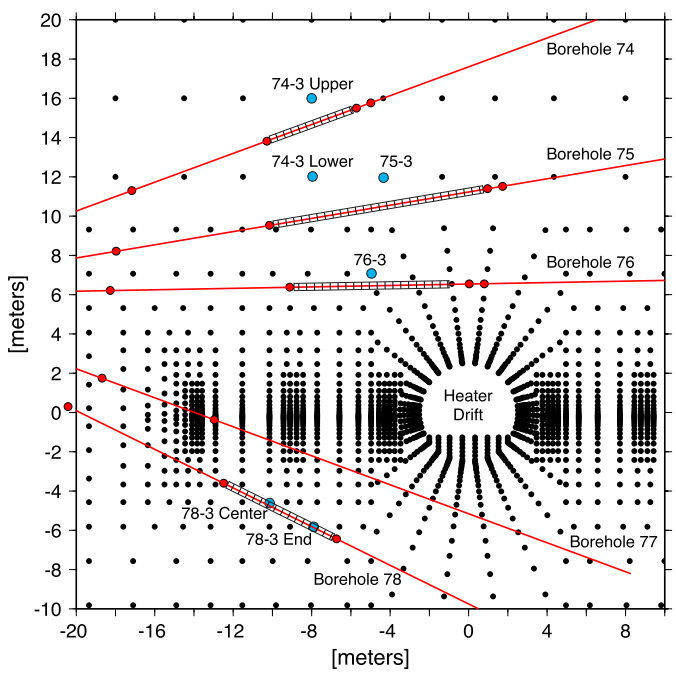

DTN: LB991200DSTTHC.002 [142162]

NOTE: Borehole intervals from which gas samples were taken are shown in the hachured regions.

Figure 7.1-9. Close-Up of DST Grid, Showing Nodes Used to Extract Model Data for Comparison to Concentrations Measured in Gas Samples

The results obtained using the REV01 parameters for the base-case and extended-case systems are shown in Figure 7.1-10. The measured concentrations have not been corrected for the loss of water owing to condensation of steam in these plots. These corrections were applied to the more complete data set shown later in this section and compared to REV02 model results. Measured CO_2 concentrations in borehole 74 interval 3 (hereafter, referred to as "borehole-interval 74-3" or just 74-3) shown in Figure 7.1-10a (the uppermost, lowest-temperature interval) are well-

bracketed by the two geochemical systems. The base-case simulations yield the highest concentrations of CO_2, owing to differences in water chemistry (e.g., generally lower pH) and their effect on the equilibrium partial pressure of CO_2. The measured concentrations show a sharp increase at 24 months. This is partly a result of the relatively low value around 21 months, which apparently was affected by an earlier temporary power loss (see Table 7.1-2 for dates of power losses). After 24 months, the measured concentrations declined moderately, whereas the modeled concentrations continued to rise, albeit more slowly. This decrease in measured CO_2 concentrations may reflect the power reductions that were implemented during 2000. The trend in modeled CO_2 concentrations for 75-3 is similar to the measured trend, with a sharp reduction in concentration after 24 months (Figure 7.1-10b). The upper interval closest to the heaters is 76-3, in which the measured data (Figure 7.1-10c) shows a large decline after 21 months, which has predicted to occur earlier than actually observed. This difference may between prediction and observation result from the gridblock being closer to the interval in 76-3 than in 74-3 and 75-3, and therefore slightly hotter at a given time. In borehole interval 78-3 (Figure 7.1-10d), the simulated trends in CO_2 concentrations in the early and late time periods are similar to the measured values, but the maximum measured values are higher. Because of the steep angle of the borehole relative to the temperature isotherms, mixing of higher and lower concentrations likely took place in this interval.

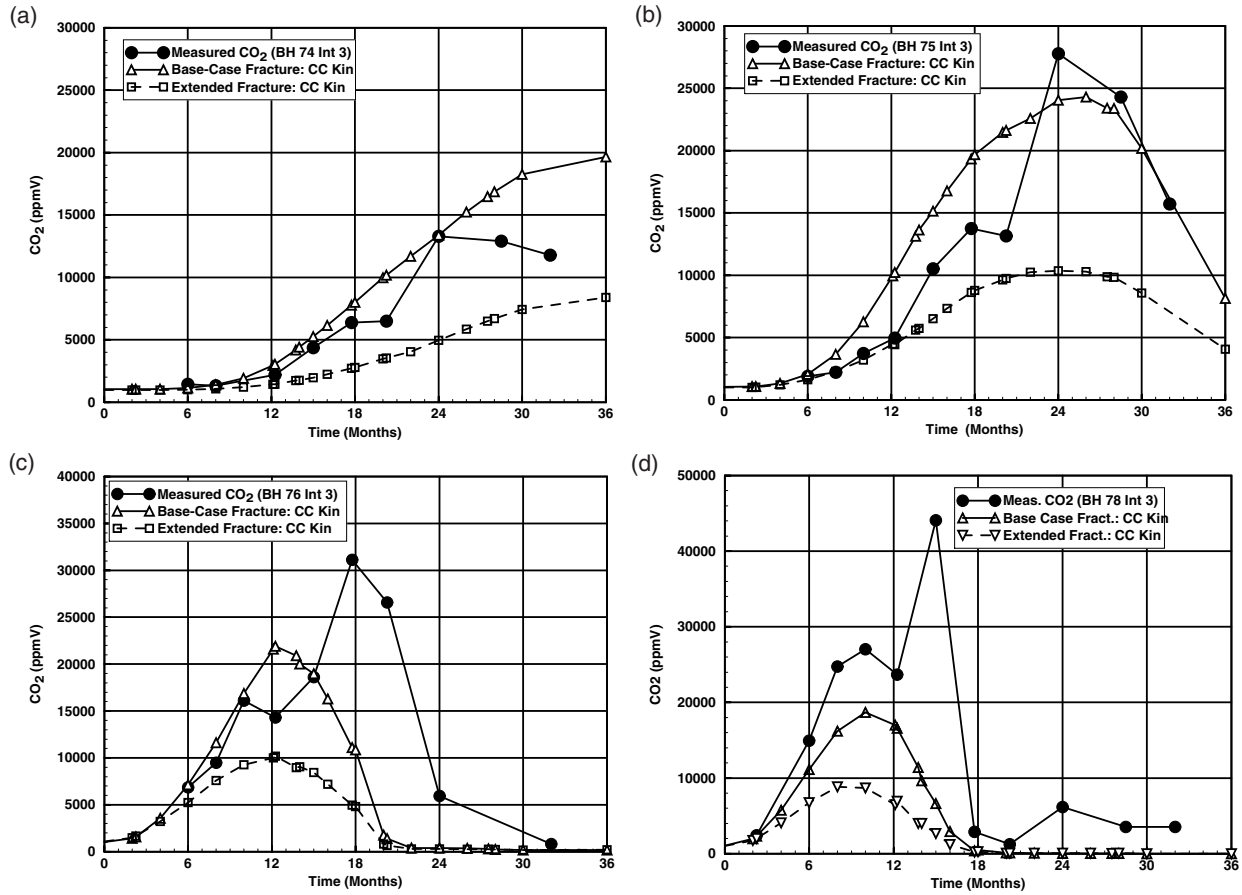

DTNs: LB0011DSTTHCR1.002 [161282] (simulated), LB0102CO2DST98.001 [159306] (measured), LB990630123142.003 [111476] (measured), LB000121123142.003 [146451] (measured), LB0011CO2DST08.001 [153460] (measured), CRWMS M&O 2001 [153814] (measured)

Figure 7.1-10. Comparison of Modeled CO_2 Concentrations (Base Case CC Kin and Extended Case CC Kin) in Fractures to Measured Concentrations in Boreholes: (a) Borehole Interval 74-3 at Node Above Interval; (b) Borehole Interval 75-3; (c) Borehole Interval 76-3; (d) Borehole Interval 78-3 at Node Near End of Interval

The strong increase in measured CO_2 concentrations in 76-3 and 78-3 to values significantly higher than the predicted concentrations, after an apparent earlier maximum, occurs at different times in the two intervals. This difference cannot be explained simply by a change in the heater power output. The measured CO_2 concentrations in gas samples collected at close to boiling temperatures are significantly affected by the amount of water vapor in the gas phase. The samples are "dried" by condensing much of the water out at a low temperature (~ 4°C), and therefore, the measured concentrations reflect the CO_2 in the air after water has been condensed out. The model results include the water-vapor component and which may be very different from the measured value, once the air-mass fraction drops to a low value and the CO_2/air ratio increases through the condensation of the water vapor. Therefore, modeled and measured compositions become less directly comparable at higher temperatures. The second peak in the measured concentrations in 76-3 and 78-3 may therefore be explained by the rapid decline in the air mass fraction during boiling.

Differences in the calculated CO_2 concentrations in the extended geochemical system (compared to the base case) are a result of dissolution and precipitation of various aluminosilicate minerals, such as stellerite, heulandite, anorthite, and smectite. Feldspar dissolves to form zeolites, thus increasing the pH through hydrolysis reactions. This, in turn, decreases the CO_2 partial pressures through aqueous species reactions involving carbonate species (CO_2 is more soluble at elevated pH). Another controlling factor is the flux of aqueous species through percolation and of CO_2 through gas-phase diffusion, relative to the rates of mineral reactions. The percolation flux has little effect over a few years, so that for comparison of the model results, the relative rates of reaction remain as the main reason for the difference between base-case and extended-case CO_2 concentrations.

Some shifts in the ambient system CO_2 concentrations over a relatively short time (away from the areas of thermal effects) indicate that either the relative mineral-water reaction rates are somehow dissimilar to the real system, or that calculated starting water bicarbonate concentration (via charge balance) was off, or the measured pH was altered through the sample collection procedure. Because the starting water was supersaturated in calcite, the latter scenario is a distinct possibility. In addition, the uncertainties in thermodynamic data for the aluminosilicates (e.g., zeolites and clays), the unknown reaction rates for many of the minerals, and the use of endmember minerals rather than solid solutions must play a role in the evaluation of the results. However, increases in CO_2 concentrations as a result of pore water degassing far exceed the changes due to ambient system disequilibrium.

The base-case geochemical system appears to compare more closely than the extended system for CO_2 concentrations. However, the increasing water-vapor fraction in the gas phase over time means that actual CO_2 concentrations in the vapor phase are increasingly depressed in comparison with measured values. This fact may be used to infer that the extended system CO_2 values could be closer to the actual values, if the measured concentrations were corrected for the vapor that was removed during sample collection. Yet, evidence that the base-case geochemical system may actually yield CO_2 concentrations closer to the measured values comes from the better match to pH values measured in waters collected from boreholes.

Figure 7.1-11 shows measured CO_2 concentrations that have been corrected for the effect of water-vapor condensation during sample collection. More details regarding the effect and the process involved in the correction procedure are given following the discussion of REV02 results in this section. Additional measured and modeled data are presented up to the end of the heating phase of the DST (including a few measurements performed about 1 month into the cooling phase). Simulated CO_2 concentrations obtained for the REV02 extended case are similar to those for REV01 (Figure 7.1-11). In the hottest interval (76-3) the concentrations remained low from 2 years after heating was initiated until after the cooling phase had begun. Except for one sample that may have been predominantly water vapor, similar but delayed behavior took place in 75-3. Modeled compositions shown for 74-3 are given as an average of the values from the “upper” and “lower” gridblocks shown in Figure 7.1-9. Maximum CO_2 concentrations in the model simulations are closer to the REV01 base-case concentrations and the measured concentrations, even though the REV02 model input also included aluminosilicates. This result suggests that the REV02 geochemical input data (thermodynamic and kinetic data) are improved overall. Also, because the thermal and hydrological properties have changed, as well as the heat input function, factors leading to the improved result cannot be directly pinpointed.

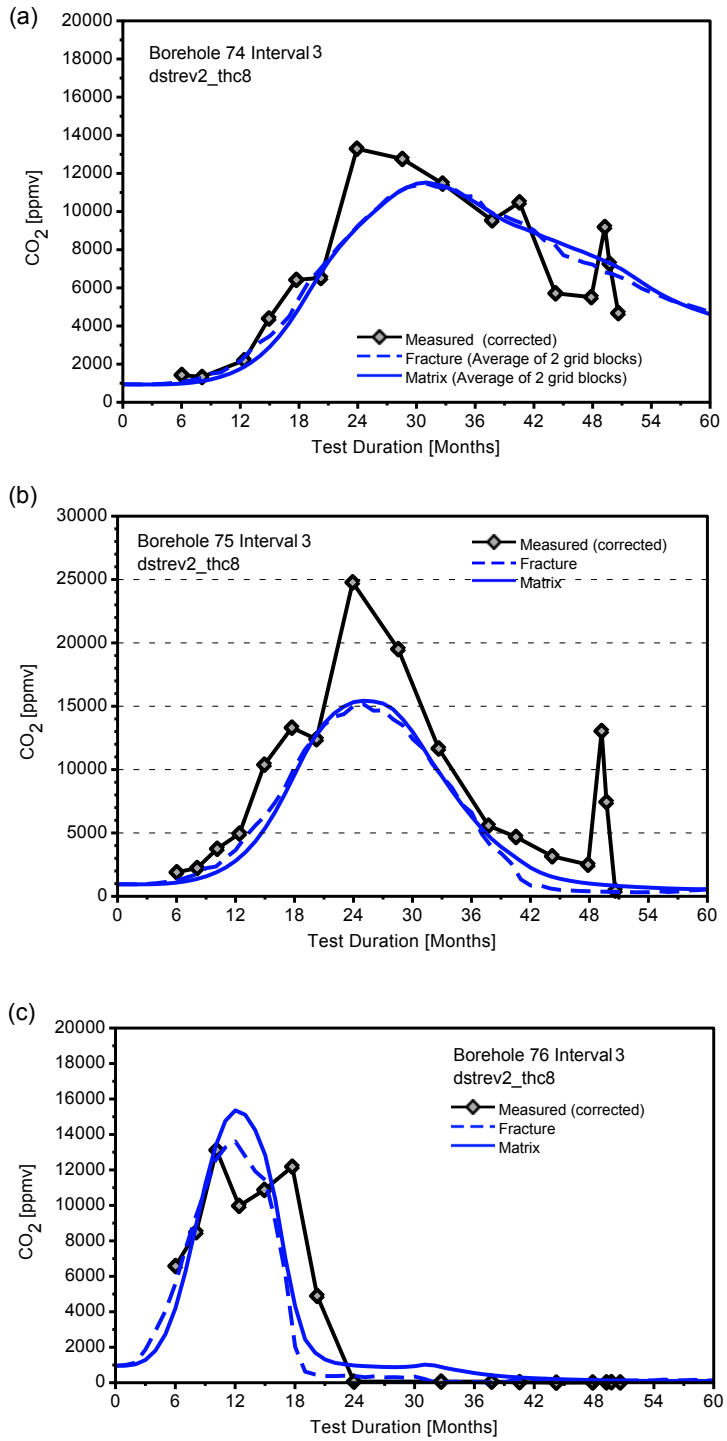

DTNs: LB0208ISODSTHP.001 [161638] (measured CO_2 uncorrected), LB0307DSTTHCR2.001 (modeled)

Figure 7.1-11. Comparison of REV02 Modeled CO_2 Concentrations (extended case) in Fractures to Measured (Corrected) Concentrations in Boreholes: (a) Borehole Interval 74-3 (Average of Bounding Gridblocks); (b) Borehole Interval 75-3; (c) Borehole Interval 76-3

To assess the effect of water extraction from the gas during collection, CO_2 concentrations were corrected for the approximate amount of water removed during chilling of the gas sample from the temperature of the sampling interval to 25°C. The method assumes that the gas is vapor-saturated, removes the appropriate amount of water vapor to the amount at saturation at 25°C, and adds some of the CO_2 into solution (the condensate) as HCO_3^-, based on the equilibrium partitioning of CO_2 into H_2O. The actual temperature of the chiller was 4°C; however, the efficiency of the unit was such that not all water was taken out when the gas was at boiling temperatures (BSC 2003 [161530]). Therefore, for consistency, the chill temperature was set to 25°C for all samples. Because the difference in water-vapor content between 25°C and 4°C is small, this approximation is valid. For samples with temperatures below approximately 60°C, the correction is very small; however, at temperatures near boiling, the correction may be close to an order of magnitude. The corrections are documented in Wang (2003 [161665], SN-LBNL-SCI-112-V2, pp. 60–63).

The effect of the correction on the measured CO_2 concentrations is a gradual (but increasing) reduction up to the boiling temperature, where the sharp "second" spike in the uncorrected data largely disappears. It is clear that the correction to the measured concentrations substantially improves the comparison to the modeled data at higher temperatures. Figure 7.1-12 shows an example of the effect of the correction on the CO_2 concentrations for borehole interval 75-3.

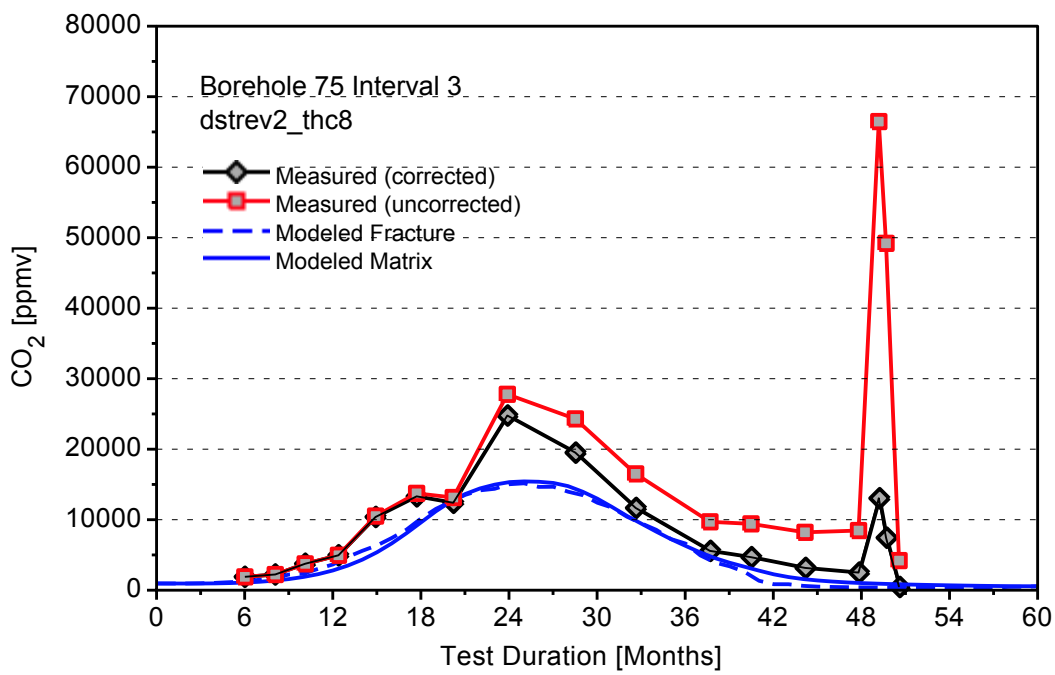

DTNs: LB0208ISODSTHP.001 [161638] (measured CO_2 uncorrected), LB0307DSTTHCR2.001 (modeled)

Figure 7.1-12. Comparison of Measured and Corrected Concentrations for Borehole Interval 75-3 and the REV02 Model Simulation Results

Trends in modeled CO_2 concentrations are clearly followed for all borehole intervals evaluated. Deviations in concentrations for certain samples can be attributed to the factors discussed in Section 7.1.7. The comparison of simulated and measured (corrected) CO_2 concentrations are

generally within a factor of 2, and in most cases within an order of magnitude, except for very low concentration samples where the values are strongly affected by condensation of water vapor and for the various reasons discussed in Section 7.1.7. Therefore, the validation criteria (1 and 2) discussed in Section 7.1.7 have been met.

7.1.11 Aqueous Species Evolution

7.1.11.1 Chemistry of Waters Sampled during the Drift Scale Test

Water samples were collected from several hydrology boreholes during the heating phase of the DST. Collection dates, volumes, and field measurements (e.g., pH) for all water samples are presented in Table 6.3.4.1-1 of BSC (2002 [160771]). Cation and anion analyses of the water samples are given in Table 6.3.4.1-2 (DTN: LL020709923142.023 [161677]) of the same report. The latter table lists all samples that were analyzed, regardless of their origin. In particular, many samples were collected from borehole intervals above boiling temperatures and were clearly derived from water vapor that condensed in the tubing leading out of the interval. In most cases such samples are clearly recognizable from the water samples pumped directly out of boreholes (and in contact with rock), based on (1) their significantly lower pH (most below pH 5) relative to "true" water samples (nearly all above pH 6), (2) their extremely low anion and cation content (total dissolved solids around 10 ppm or less), and (3) very low total Si concentrations (most much less than 10 mg/L) compared to water samples having total Si concentrations mostly greater than 40 mg/L.

Specific exceptions to these criteria are those samples collected from intervals at high temperatures (> 140°C) that have relatively low pH values (< pH 4), elevated F^- concentrations (> 10 mg/L) and relatively high total Si values, but contain few other measurable constituents. Experimental studies confirmed the hypothesis that the breakdown of fluoroelastomer packer materials at elevated temperatures was responsible for the unusual water compositions that formed as high-temperature vapor condensed in tubing and was collected as water (BSC 2002 [160771]). In addition, some waters may have been affected by the degradation of neoprene packers in sub-boiling zones, such as the high Cl water collected from Borehole 59, interval 4 (Williams 2003 [163765]). Also note that samples of water from boreholes may be affected in subtle ways by the above processes.

In this report, chemical analyses of water samples that have compositions indicating that they were wholly or mostly derived from water that had resided in a borehole (rather than formed during condensation of water vapor in the collection tube) are given in Table 7.1-3. The intervals where these waters were collected are shown as the blue shaded zones in Figure 7.1-13. The water samples collected during the test were obtained from zones that were hotter than the temperatures given for the samples, because the samples cooled substantially as they were pumped out of the rock through the sample collection tubing, and into the sample containers. Also listed in Table 7.1-3 are the compositions of pore waters that had been ultracentrifuged out of the rock matrix from a dry-drilled borehole near the DST ("HD-PERM" designations).

Table 7.1-3. Measured Concentrations in Tptpmn Pore Water from Alcove 5 and Chemistry of Water Samples from Hydrology Boreholes

SMF No. (SPC0...)	1002488	1002586	1002525	05279699	05279689	0527915[8]	0527977[8]	0527916[8]	0541804[8]	0541804[6,8]	05043968	0529637-#1[8]	0529637-#2[8]
Collection Date	Pre-Htng.	Pre-Htng.	Pre-Htng.	06/04/98	06/04/98	08/12/98	06/04/98	8/12/98	11/12/98	11/12/98	01/26/99	03/30/99	03/30/99
Collection Time												9:50 AM	9:55 AM
Sample ID	PERM-1[4]	PERM-2[4]	PERM-3[4]	BH 60-2	BH 60-2	BH 60-2	BH 60-3	BH 60-3	BH 60-3	BH 60-3	BH 60-3	BH 60-3	BH 60-3
Field pH [2]	7.79	8.32	8.31	7.5	na	6.9	7.7	6.8	6.92	6.92	7.4	8.0	na
Metals / Cations													
Na (mg/L)	60.5	61.0	61.5	20.0	na	20.4	24.0	17.2	10.1	20.3	19.1	11.2	11.0
Si (mg/L)	37	31	35	56	na	51.8	41	43.5	60.0	53.8	65.0	62.8	59.8
Ca (mg/L)	98.17	106.17	96.67	20	na	19.9	25	18.7	15.3	13.9	5.93	2.06	2.27
K (mg/L)	6.0	7.0	9.0	6.0	na	5.4	4.5	4.5	8.7	7.8	4.1	2.4	2.4
Mg (mg/L)	25.65	16.55	17.35	2.9	na	1.21	5.7	4.0	3.35	3.00	1.17	0.27	0.26
Al (mg/L)	< 0.06	< 0.06	< 0.06	0.12	na	< 0.06	0.017 [5]	0.003 [5]	0.033 [5]	0.033 [5]	< 0.06	0.36, 0.27 [5]	0.36, 0.27 [5]
B (mg/L)	3.05	2.75	2.75	1.2	na	1.84	0.92	1.14	1.58	1.41	1.75	2.10	2.11
S (mg/L)	42.25	38.6	38.65	5.5	na	4.5	9.2	5.2	11.6	10.5	6.4	1.83	1.82
Fe (mg/L)	< 0.02	< 0.02	< 0.02	0.04	na	0.02	< 0.02	0.12	0.02	< 0.02	< 0.02	< 0.02	< 0.02
Li (mg/L)	0.1	0.45	0.05	0.07	na	0.03	0.07	0.040	0.040	0.040	0.02	0.02	< 0.01
Sr (mg/L)	1.4	1	1.05	0.18	na	0.11	0.34	2.21	0.22	0.20	0.09	0.02	0.02
Anions													
HCO_3 (mg/L)[3]				na	na	na	na	na	na	na	41	25.0	na
F (mg/L)	0.36	0.96	0.76	na	1.00	0.71	0.82	0.43	0.49	0.50	1.27	1.02	0.97
Cl (mg/L)	122.73	109.93	123.13	na	10	6.14	16	5.52	19.5	19.6	10.3	4.15	3.92
Br (mg/L)	0.6	0.76	1.2	na	0.84	0.05	0.73	0.21	0.6	0.51	0.15	< 0.04	< 0.04
SO_4 (mg/L)	124.18	111.38	119.78	na	17	4.88	30	8.81	30.6	30.8	13.5	3.83	3.75
PO_4 (mg/L)	< 0.07	< 0.07	< 0.07	na	< 0.07	0.25	< 0.07	0.16	< 0.2	< 0.2	< 0.05	< 0.05	< 0.05
NO_2 (mg/L)	< 0.04	< 0.04	< 0.04	na	< 0.01	< 0.04	< 0.01	< 0.04	< .10	< .10	< .03	< 0.03	< 0.03
NO_3 (mg/L)	21.72	2.52	10.40	na	3.00	0.46	3.6	0.60	3.38	3.17	2.56	0.92	0.84

Table 7.1-3. Measured Concentrations in Tptpmn Pore Water from Alcove 5 and Chemistry of Water Samples from Hydrology Boreholes (continued)

SMF No. (SPC0...)	0551159[8]	0551160[8]	0557029[8]	0557032	0557033[8]	0557080	0557081	0557083	0557022	0550671	0550673	0550681	0550682
Collection Date	08/09/99	08/09/99	10/27/99	10/27/99	10/27/99	11/30/99	11/30/99	11/30/99	01/25/00	01/25/00	01/25/00	05/23/00	05/23/00
Collection Time													
Sample ID	BH 59-2(AC)	BH 59-2(BC)	BH 59-2	BH 59-2	BH 59-2	BH 59-2	BH 59-2	BH 59-2	BH 59-2	BH 59-2	BH 59-2	BH 59-2	BH 59-2
Field pH [2]	na	na	na	5.93	6.08	6.86	7.24	na	7.07	6.68	na	6.96	6.96
Metals / Cations													
Na (mg/L)	30	24	na	9.2	9.2	6.6	7.7	na	8.1	6.6	na	17	18
Si (mg/L)	78	81	na	44.5	44.9	38.0	39.9	na	42.8	41.7	na	59.4	59.2
Ca (mg/L)	47	39	na	7.53	7.47	4.33	5.63	na	7.54	2.89	na	4.7	4.4
K (mg/L)	8	6	na	3.4	3.6	2.6	3.0	na	3.6	2.8	na	4.3	4.4
Mg (mg/L)	13	11	na	1.81	1.72	1.02	1.38	na	1.78	0.72	na	1.1	1.1
Al (mg/L)	< 0.2	< 0.2	na	0.033 [7]	0.033 [7]	0.030	0.030	na	< 0.05	0.043	na	< 0.053	< 0.053
B (mg/L)	0.8	0.6	na	0.27	0.21	0.14	0.17	na	0.29	0.21	na	na	na
S (mg/L)	22	17	na	2.52	2.50	0.76	1.33	na	6.44	0.65	na	na	na
Fe (mg/L)	0.41	0.32	na	0.20	0.19	0.09	0.14	na	0.07	< 0.02	na	< 0.038	< 0.038
Li (mg/L)	< 4	< 4	na	0.16	0.01	0.01	0.01	na	< 0.01	< 0.01	na	0.021	0.022
Sr (mg/L)	0.54	0.45	na	0.11	0.08	0.06	0.08	na	0.091	0.036	na	< 0.013	< 0.013
Anions													
HCO_3 (mg/L)[3]	na	na	23.5	na	23.5	na	na	22.3	na	na	22.8	31.4	31.4
F (mg/L)	0.725	0.575	0.27	na	0.27	na	na	0.35	na	na	0.73	0.58	0.55
Cl (mg/L)	88.3	71.0	9.5	na	9.1	na	na	5.0	na	na	3.8	10.15	10.6
Br (mg/L)	0.515	0.46	0.61	na	0.58	na	na	< 0.03	na	na	< 0.1	< 0.1	0.38
SO_4 (mg/L)	64.2	53.5	6.2	na	6.3	na	na	2.8	na	na	1.8	2.9	3.18
PO_4 (mg/L)	< 0.02	< 0.02	< 0.02	na	< 0.02	na	na	< 0.02	na	na	0.62	< 0.2	< 0.2
NO_2 (mg/L)	< 0.007	< 0.007	< 0.007	na	< 0.007	na	na	< 0.007	na	na	< 0.05	< 0.06	< 0.06
NO_3 (mg/L)	3.79	2.83	1.32	na	1.40	na	na	< 0.02	na	na	0.77	0.56	0.54

Table 7.1-3. Measured Concentrations in Tptpmn Pore Water from Alcove 5 and Chemistry of Water Samples from Hydrology Boreholes (continued)

SMF No. (SPC0...)	0550684	0550693	0550694	0550691	0550689	0550690	0530398	0557036[8]	0557038[8]	0552575	0557043	0541803[8]	0541803[6,8]
Collection Date	05/23/00	06/29/00	06/29/00	06/29/00	06/29/00	06/29/00	01/23/01	10/27/99	10/27/99	11/30/99	11/30/99	11/12/98	11/12/98
Collection Time													
Sample ID	BH 59-2	BH 59-2	BH 59-2	BH 59-2	BH 59-2	BH 59-2	BH 59-2	BH 59-3	BH 59-3	BH 59-3	BH 59-3	BH 59-4	BH 59-4
Field pH [2]	6.95	6.99-7.08	6.99-7.08	7.00	na	na	na	na	6.64	7.47	na	6.63	6.63
Metals / Cations													
Na (mg/L)	17	16	15	< 4.8	na	na	29	na	19.3	15.6	na	22.6	135
Si (mg/L)	59.3	62.7	57.5	36.3	na	na	84.5	na	84.2	92.5	na	33.5	44.2
Ca (mg/L)	4.5	4.3	3.8	2.0	na	na	7.8	na	13.2	2.86	na	476	450
K (mg/L)	4.4	4.7	4.2	2.5	na	na	5.8	na	5.6	3.9	na	29.5	37.8
Mg (mg/L)	1.1	1.1	1.0	0.54	na	na	1.8	na	1.49	0.29	na	64.1	83.9
Al (mg/L)	< 0.053	< 0.053	< 0.053	< 0.11	na	na	< 0.053	na	0.040	0.071	na	0.01 [5]	< 0.06
B (mg/L)	na	na	na	na	na	na	na	na	0.86	1.06	na	4.47	4.13
S (mg/L)	na	na	na	na	na	na	na	na	14.48	3.25	na	50.7	64.8
Fe (mg/L)	< 0.038	< 0.038	< 0.038	< 0.076	na	na	< 0.038	na	< 0.02	< 0.02	na	< 0.02	< 0.02
Li (mg/L)	0.021	0.019	0.018	0.010	na	na	0.033	na	0.02	0.02	na	0.21	0.20
Sr (mg/L)	< 0.013	< 0.013	< 0.013	< 0.026	na	na	< 0.013	na	0.13	0.03	na	4.02	3.71
Anions													
HCO_3 (mg/L)[3]	31.4	na	na	na	29.4	29.4	na	12.4	12.4	na	20.7	na	na
F (mg/L)	0.49	na	na	na	0.18	0.15	0.78	0.64	0.73	na	1.3	0.8	4.3
Cl (mg/L)	10.15	na	na	na	0.90	0.32	25.20	12.9	12.9	na	8.8	1,130	1,250
Br (mg/L)	< 0.1	na	na	na	0.62	0.48	< 0.1	0.89	0.51	na	< 0.03	1.13	< 0.07
SO_4 (mg/L)	3.1	na	na	na	0.5	0.42	9.5	40.7	40.3	na	8.2	226	213
PO_4 (mg/L)	< 0.2	na	na	na	< 0.2	< 0.2	< 0.2	< 0.04	< 0.04	na	< 0.02	< 5	< 0.2
NO_2 (mg/L)	< 0.06	na	na	na	< 0.06	< 0.06	< 0.06	< 0.01	< 0.01	na	< 0.007	< 3	< 10
NO_3 (mg/L)	0.71	na	na	na	0.65	0.48	0.99	3.06	3.05	na	2.4	3.12	7.81

Table 7.1-3. Measured Concentrations in Tptpmn Pore Water from Alcove 5 and Chemistry of Water Samples from Hydrology Boreholes (continued)

SMF No. (SPC0...)	0504397[8]	0551169[8]	0559464	0559458	0559456	1016082	0557040[8]	0552578	0552579	0550697	0541805[8]	0541805[6,8]	0527961[8]
Collection Date	01/26/99	08/10/99	04/17/01	04/17/01	04/17/01	01/07/02	10/27/99	11/30/99	11/30/99	05/23/00	11/12/98	11/12/98	01/26/99
Collection Time													
Sample ID	BH 59-4	BH 61-3	BH 76-2	BH 76-2	BH 76-2	BH 76-2	BH 76-3	BH 76-3	BH 76-3	BH 76-3	BH 186-3	BH 186-3	BH 186-3
Field pH [2]	na	na	7.68	8.22	8.29	7.8	6.14-6.46	6.94	na	6.92-6.96	6.83	6.83	7.2
Metals / Cations													
Na (mg/L)	219	19	9	9	9	na	64.5	28.2	na	29	105	17.0	25.9
Si (mg/L)	12.0	67	42.6	44.1	45.6	na	133.4	92.8	na	96.0	16.0	27.2	49.3
Ca (mg/L)	429	14	1.3	1.1	1.3	na	59.5	22.3	na	7.1	11.5	20.2	2.92
K (mg/L)	29.7	5	1.6	1.6	1.9	na	13.4	7.4	na	6.5	3.5	3.9	5.9
Mg (mg/L)	164	3.2	0.27	0.22	0.23	na	13.8	4.71	na	1.4	5.1	5.68	6.32
Al (mg/L)	0.086 [5]	< 0.2	0.42	0.43	0.45	na	0.010	0.031	na	< 0.053	< 0.003 [5]	< 0.003 [5]	< 0.06
B (mg/L)	6.68	1.5	na	na	na	na	2.38	0.81	na	na	0.51	0.58	0.84
S (mg/L)	109	3.1	na	na	na	na	34.55	9.46	na	na	8.47	9.42	7.9
Fe (mg/L)	< 0.02	1.2	0.40	0.40	0.39	na	< 0.02	0.10	na	< 0.038	0.02	< 0.02	0.09
Li (mg/L)	0.33	< 4	0.0098	0.010	0.0076	na	0.13	0.04	na	0.045	0.05	0.05	0.05
Sr (mg/L)	5.84	0.14	< 0.013	< 0.013	< 0.013	na	0.78	0.26	na	< 0.013	0.30	0.34	0.37
Anions													
HCO_3 (mg/L)[3]	na	na	na	na	na	< 5	na	na	82.3	na	na	na	116
F (mg/L)	0.51	0.835	na	0.38	0.47	0.4	1.11	na	1.3	0.76	0.56	0.62	1.20
Cl (mg/L)	1,160	24.1	na	1.9	1.71	2.75	81.9	na	19	14.5	18.7	18.6	23.3
Br (mg/L)	1.51	0.35	na	< 0.1	< 0.1	< 0.2	0.97	na	< 0.03	< 0.1	0.67	0.60	0.32
SO_4 (mg/L)	240	9.13	na	0.89	0.85	1.02	94.6	na	26.0	4.98	26.3	26.2	21
PO_4 (mg/L)	< 0.5	< 0.02	na	< 0.2	< 0.2	< 0.3	< 0.02	na	< 0.02	< 0.2	< 0.2	< 0.2	< 0.1
NO_2 (mg/L)	< .3	< 0.007	na	< 0.06	< 0.06	< 0.2	< 0.007	na	< 0.007	< 0.06	< .1	< .1	< 0.05
NO_3 (mg/L)	11.6	0.825	na	< 0.09	< 0.09	< 0.2	6.42	na	2.5	1.47	7.47	7.27	6.73

NOTES: [1] na = not available; < = not detected (less than "practical reporting limit"); Field chemistry of samples for high fluoride study (11/8/01 to 12/5/01) are reported in Table 6.3.4.5-1 of BSC (2002 [160771]).

[2] See entry in Table 6.3.4.1-1 of BSC (2002 [160771]) for temperature of pH measurements.

[3] HCO_3^- - field measurement.

[4] Pore water samples (baseline): sample ultracentrifuged from borehole core.

[5] Low detection limit analysis - sample filtered to 0.10 mm and acidified.

[6] Sample filtered in the field and laboratory (LLNL) prior to analyses.

[7] Sample ID SPC0057028 submitted for low detection for Al analysis.

[8] Analytical results are corroborating data (as defined in Section 3.6 of AP-SIII.3Q) and non-qualified.

See Table 7-1 for Source DTNs.

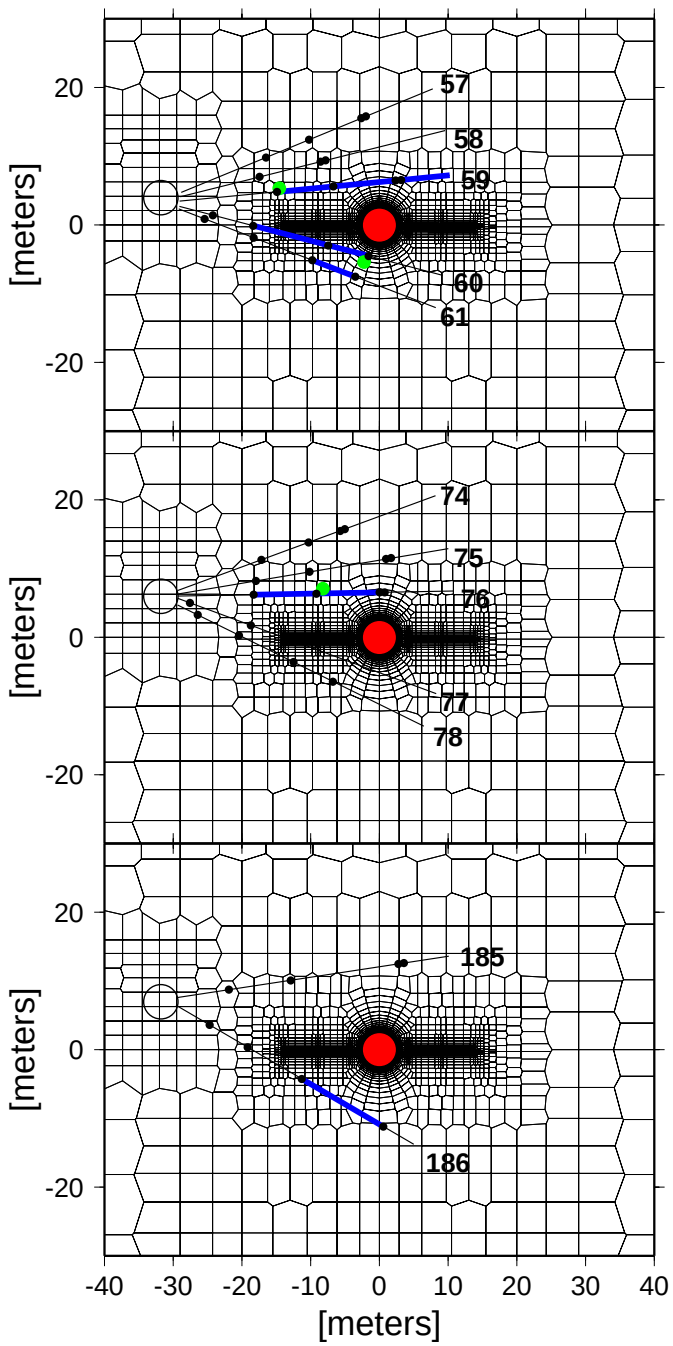

DTNs: LB0307DSTTHCR2.001 (mesh—Output-DTN), MO0002ABBLSLDS.000 [147304] (sensors and boreholes)

Source: BSC (2002 [160771]) - water collection locations.

NOTE: Only those waters having the distinct criteria discussed in this section were considered to have been liquid in the borehole. Locations where comparisons were made to measured compositions are shown as green circles. The Heater Drift is shown in red.

Figure 7.1-13 Zones Where Water Was Collected from Hydrology Boreholes Superimposed (Thick Shading in Blue) on the Model Grid

Some of the processes that could explain the water chemistry of samples collected in the hydrology boreholes include mixing of pure condensate water with fracture pore waters, equilibration of condensate waters with matrix pore waters via molecular diffusion, reaction of condensate waters with fracture-lining minerals, and mineral precipitation. Waters that were collected from the hydrology boreholes at elevated temperatures are generally more dilute (lower Cl^- and SO_4^{2-}) and lower in pH than the initial pore water. Aqueous silica concentrations are similar to or much higher than in the pore water, indicating that these waters are not simple mixtures of pore water and pure condensate water. Some clear trends in water chemistry of the condensate waters over time are increases in pH and SiO_2 (aq) concentration and a drop in Ca^{2+}. The higher silica concentration in the waters collected at later times in several boreholes (and at higher temperatures), relative to chloride and the initial pore-water silica concentration, is consistent with dissolution of a silicate phase, rather than with increased concentration via boiling. Concentrations of K^+, Mg^{2+}, and Na^+ are also higher than what would be expected by dilution of original pore water (as evidenced by the low chloride concentrations). Therefore, the silicate phases that dissolved must have been some combination of silica polymorphs (i.e., opal, cristobalite, tridymite, and quartz) and feldspar, clays, or zeolites, rather than just a pure silica phase. Many of the waters show a drop in Ca^{2+} over time, consistent with calcite precipitation as the water was heated further and underwent CO_2 degassing.

These water samples are considered to be representative of fracture waters produced by THC processes in the region around the DST. However, the borehole intervals from which the waters were collected are approximately 8-10 m in length and at times have temperatures several tens of degrees different at each end (also see Section 7.1.7). Therefore, vapor flow from the hot end to the cool end of an interval, accompanied by condensation and reaction with the rock lining the borehole, could account for some of the water found in the boreholes. Because the borehole surface mineralogy is not identical to the fracture surface mineralogy, the water chemistry in the borehole may have some differences to the chemistry of water in the fractures. Yet, because the rock surface in the borehole was freshly drilled, it may be more reactive with respect to silicate mineral reactions, hence potentially producing higher concentrations of species making up the silicate mineral phases. The fresh mineral surfaces in the borehole could therefore result in dissolution rates greater than that in the fractures even though the surface area of the smooth borehole is likely to be less than that of the irregular fracture surface.

Further discussion of water chemistry in the DST and comparisons to model results is given in the following section (Section 7.1.11.2). In REV01, model results were compared to water collected from borehole intervals 59-2 (above the heaters) and 60-3 (below the heaters). In REV02, model results are compared to a more complete data set from these intervals and also to borehole interval 76-3, which is above the heaters in an array closer to the area where the maximum drift crown temperature was reached (30 m from the bulkhead). Waters were collected from other borehole intervals, but on only one or two occasions. Compositional trends from so few samples cannot be discerned, nor is validation of the model by comparison to these samples very useful. However, they do provide additional information on the range of potential water compositions.

7.1.11.2 Evolution in the pH of Waters from the DST

In this section, model simulations of the evolution of pH in space and time are shown, followed by comparisons of pH measurements of waters collected from boreholes and model results at specific locations. The pH of waters in the rock is a function of the coupled thermal, chemical and transport processes taking place in the fractures and matrix as the system undergoes heating. The water chemistry can also be affected near rock interfaces, such as at the drift wall. Here, exchange of atmospheric air with gas in the rock takes place via advective transport and diffusion, or by simple degassing of water owing to barometric pressure changes.

The modeled spatial distribution of pH (using the REV02 input data) in fracture water at various times during the heating phase is shown in Figure 7.1-14. The times correspond approximately to the dates when water was sampled from hydrology borehole intervals, which are also highlighted. Based on the compositions of ambient pore water ultracentrifuged from the rock in the DST block, the pH of waters in the region of the DST likely started out between approximately 7.8 and 8.3 (Table 7.1-3). The initial pH of the water used in the DST THC Model simulation is approximately 8.3. The most obvious effect of heating is a reduction in pH to about 7.2 in the condensate region, corresponding approximately to the increases in CO_2 concentrations shown in Figure 7.1-11. As for the CO_2 concentrations, the low pH zone increases in size and moves outward with time. Close to the dryout zone, the pH of the water increases, owing to boiling, degassing, and outward transport of the CO_2. Another important factor affecting the pH is the reaction rates of certain minerals, such as feldspars, that upon dissolution consume H^+, resulting in a rise in pH. Clearly, the significantly higher pH values of waters sampled from the boreholes, compared to the very dilute low pH waters formed from vapor condensing in the sample collection tubes, attests to the strong effect of mineral-water reactions on the pH.

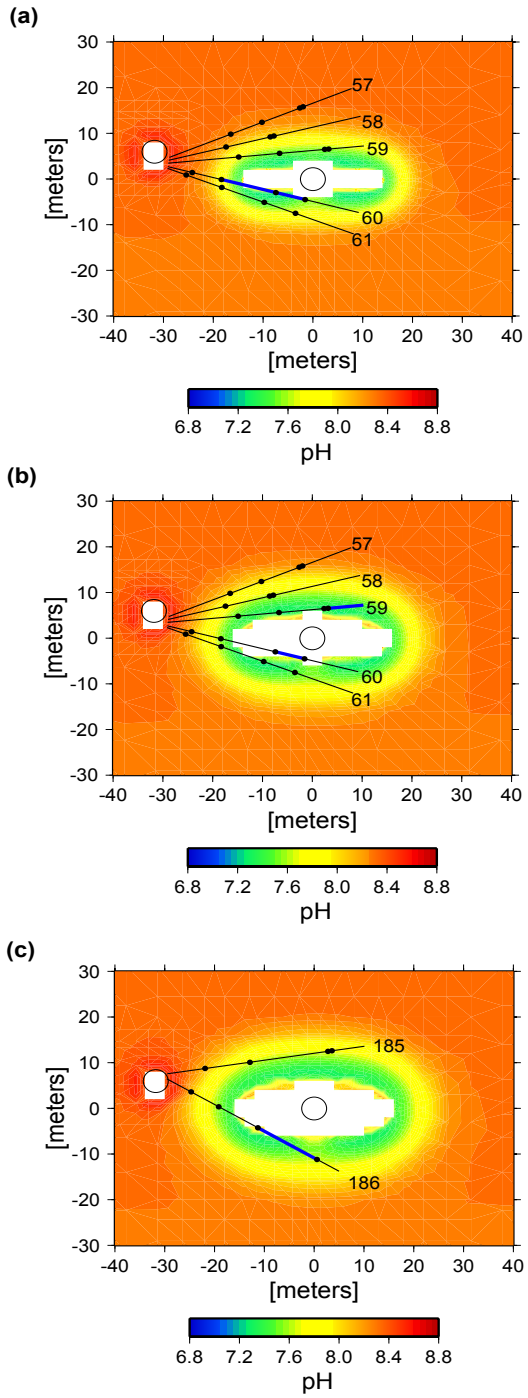

Output-DTN: LB0307DSTTHCR2.001 (modeled)

Source: BSC (2002 [160771], Table 6.3.4.1-1)-water collection locations.

NOTE: The intervals where water was sampled are more thickly shaded (in blue). Areas of zero liquid saturation are blanked out in white.

Figure 7.1-14. Modeled Distribution of pH in Fractures at Various Times When Water Was Sampled from Hydrology Borehole Intervals (REV02 Simulation): (a) 6 Months, (b) 11 Months, and (c) 14 Months

Figures 7.1-15a and b show the evolution of pH in the sampled waters compared to the modeled base-case and extended systems (REV01 simulations). Modeled pH values are given for the temperature in the rock, whereas field measurements of pH are reported for the temperature at the time of the measurement. The temperatures at which the pH was measured were typically much lower than that in the rock where the sample originated (BSC 2002 [160771], p. 6.3-42). This could result in greater differences between modeled and measured pH values, but the effect is uncertain because several competing processes could be taking place as the water is sampled. These processes include (1) degassing of CO_2 from the water leading to an increase in pH, (2) condensation of water vapor under higher partial pressures of CO_2 and mixing with the water leading to a decrease in pH, and (3) equilibration of water in equilibrium with a lower partial pressure of CO_2 than the atmosphere with air in the Observation Drift, leading to an increase in pH. Certainly, some vapor condensation is likely to have affected some samples more than others, as evidenced by the many water samples that formed solely from condensation in the sampling tubes.

The early trend to lower pH is related to the addition of condensate to this area and to increases in CO_2 in the gas phase (caused by boiling closer to the heaters and diffusive and advective gas transport outwards). Later increases in pH are related to boiling of the water in this area, leading to a reduction in CO_2 concentrations as the temperature reaches boiling and the zone finally dries out. The model results for interval 60-3, showing complete dryout at approximately 18 months, are consistent with the observation that water was absent from this interval shortly after the last sample was collected, after 16 months of heating. In spite of these uncertainties (and those discussed in Section 7.1.7), both geochemical systems capture the trend in pH of fracture waters in this region. However, the base-case system captures the drop in pH more closely than the extended system. The system without calcite also shows a reasonable match to the measured pH values compared to the other simulations.

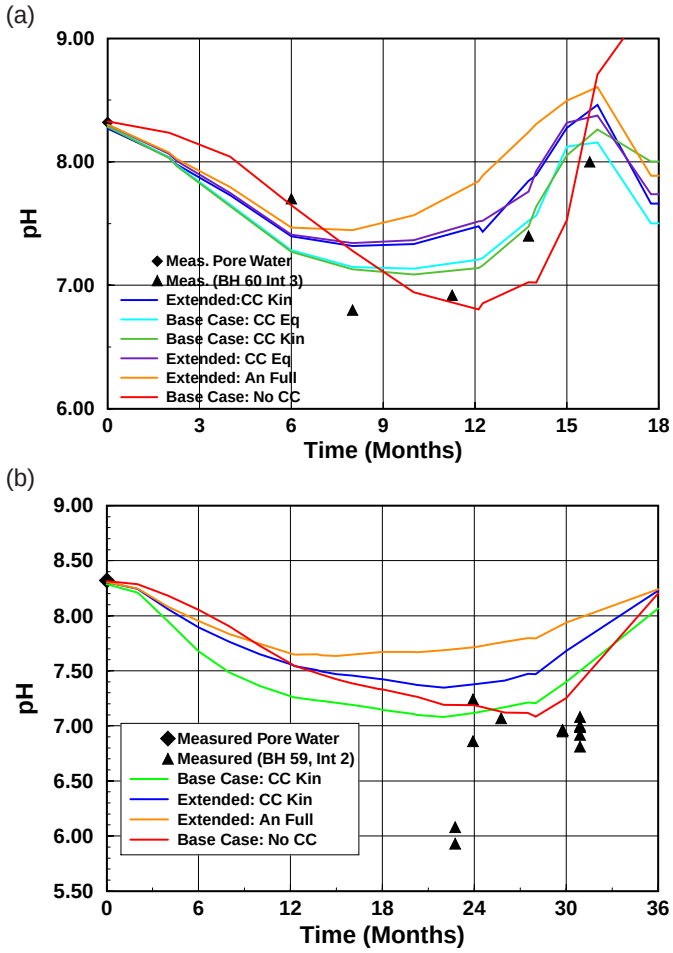

DTNs: LB0011DSTTHCR1.002 [161282] (simulated)
LL020709923142.023 [161677] (measured)

NOTE: The ambient pore-water pH is approximately 8.3. "CC" refers to calcite.

Figure 7.1-15. Changes in pH in Water Samples Collected from Borehole Intervals (a) 60-3 and (b) 59-2 Compared to REV01 Modeled Fracture Water pH at Nearby Model Grid Nodes

Results for the REV02 model system are shown for borehole intervals 60-3, 59-2, and 76-3 in Figure 7.1-16. The modeled trends in pH are similar to those in the REV01 extended case and to the measured pH values. However, the minimum pH is not as low as that measured, nor as low as the base-case pH. Yet the differences between the measured and modeled pH values are generally less than one pH unit, within a fairly narrow range of approximately pH 6 and pH 8. In 59-2 and especially in 76-3, the drop in pH is considerably earlier than in the measured pH values. Part of this discrepancy is related to the higher modeled temperatures after one year (compared to those measured) resulting in an earlier arrival of the condensation "pulse" from the advancement of the boiling zone. Higher pH values may also result from the larger reaction rates for aluminosilicates at higher temperatures. In addition, local permeability heterogeneity could result in earlier or later changes because of the flow of gas and or water preferentially through large fractures. Except for a few samples with lower pH values, the minimum pH values in the model results are within one pH unit of the minimum values measured. Given all of the uncertainties in the collection of water samples, and in the comparison of the model results to measured values (see Section 7.1.7 and previous discussion in this section), the requirements for model validation (one pH unit and trends where observable) have been met.

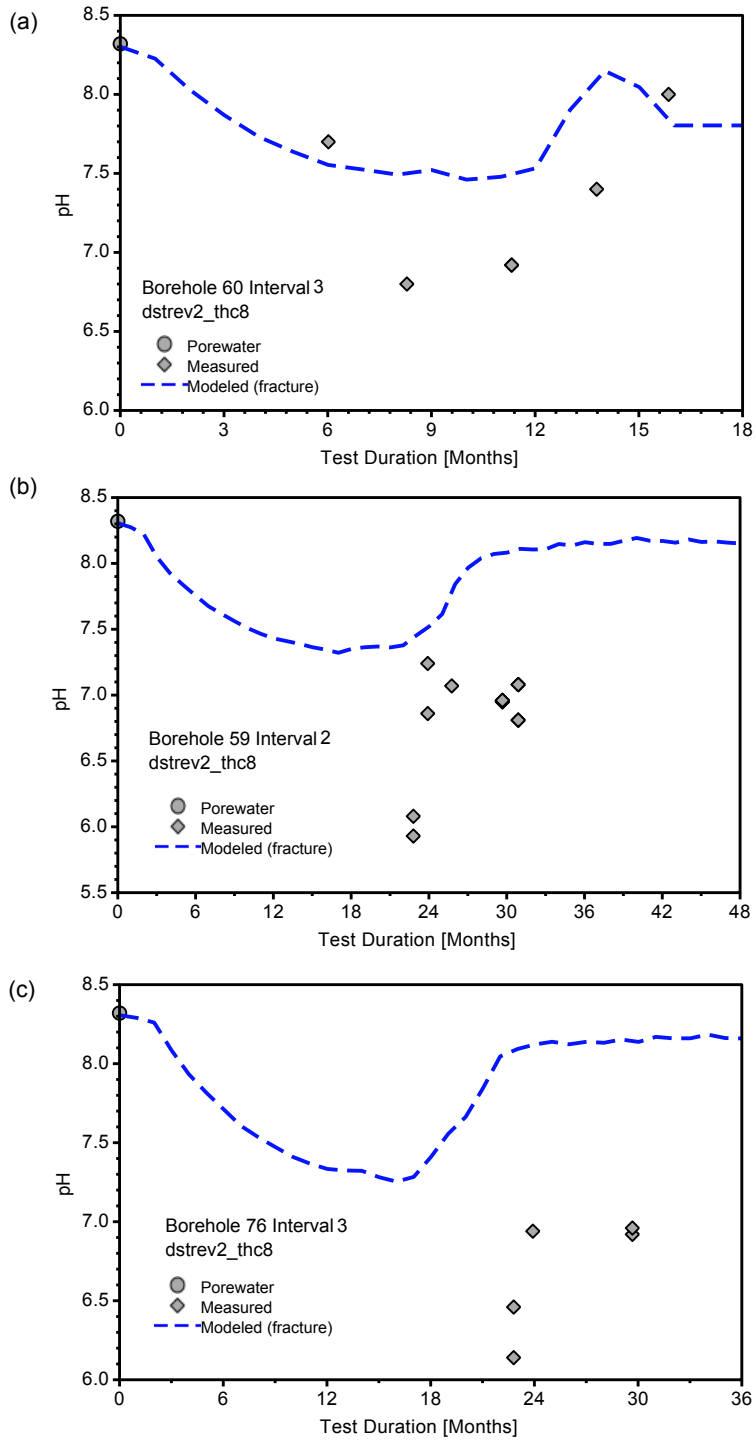

DTNs: LL020709923142.023 [161677] (measured),
LB0307DSTTHCR2.001 (modeled)

NOTE: The ambient pore-water pH is approximately 8.3.

Figure 7.1-16. Comparison of Measured pH in Water Samples Collected from Borehole Intervals (a) 60-3, (b) 59-2, and (c) 76-3 to REV02 Modeled Fracture Water pH at Representative Model GridBlocks

7.1.11.3 Evolution of Anion and Cation Concentrations

The effects of dilution through condensation of pure water vapor, increases in concentration caused by boiling, and fracture-matrix interaction can be assessed by examining the variation in conservative species such as chloride (Cl^-) and sulfate (SO_4^{2-}). These species are conservative because chloride and sulfate-bearing minerals, such as halite and gypsum (or anhydrite), are not present in the rock initially and precipitate under more saline conditions, expected only at the final drying stages of the dilute waters observed in the rock at Yucca Mountain. In this section, results are compared from the REV01 and REV02 model systems to measured concentrations. For conservative anions, the primary differences seen in concentrations between the two revisions should be a result of the different hydrological properties, because the initial water compositions are the same. Primarily, the lower matrix permeability (about one order of magnitude less) in the REV02 hydrological property set resulted in a smaller rate of gas flow out of the matrix into fractures and thus lower fracture saturations.

The modeled spatial variations in Cl^- concentrations in fracture and matrix are plotted in Figure 7.1-17 (REV02 simulation), at times of 1 year and 4 years during the heating phase. The main effect is a marked decrease in Cl^- concentrations within fractures in the condensation and drainage zones. In the matrix, there is significant dilution in the condensation zones, and significant increases in concentration near the edge of the dryout zone. Differences in the hydrological properties used in REV01 did not fundamentally change the spatial pattern of conservative anion concentrations, and therefore REV01 results are not shown as contour plots. However, differences between REV01 and REV02 concentrations are evident in the plots of concentrations over time at particular borehole interval locations, shown below.

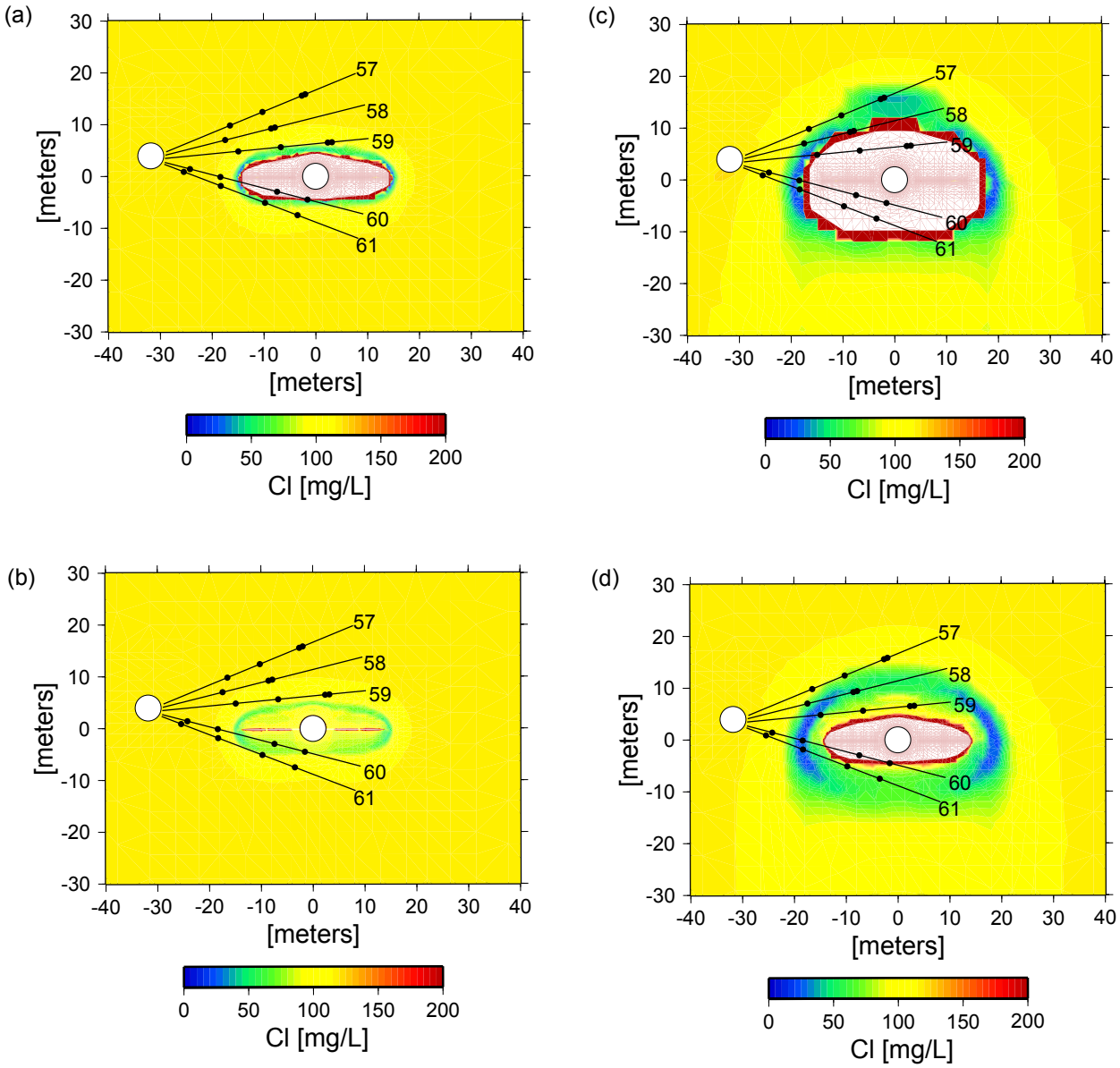

Output-DTN: LB0307DSTTHCR2.001

NOTE: Areas of zero liquid saturation are blanked out in white.

Figure 7.1-17. Modeled Distribution of Cl^- in Fractures and Matrix at One and Four Years during the Heating Phase of the DST (REV02 Simulation): (a) Fracture—1 year, (b) Matrix—1 Year, (c) Fracture—4 years, and (d) Matrix—4 years

REV01 modeled variations in Cl^- are shown in Figure 7.1-18a,b and for SO_4^{2-} in Figure 7.1.19a,b. The model results capture the overall extent of dilution, or fracture-matrix interaction in the system (compared to the initial matrix pore water), for both chloride and sulfate. The largest discrepancy in interval 60-3 is at the earliest time, when the first waters collected are more dilute than the modeled fracture waters. However, compared to the modeled concentrations of Cl^- and SO_4^{2-} in matrix water, the fracture waters are more dilute and quite similar to the samples collected from the boreholes. It is expected that waters found in boreholes should be similar to fracture water and not to matrix water, because the matrix permeability is too low to allow significant water movement. In borehole interval 59-2, the earliest collected samples are more closely matched than the later collected samples, although the overall trend is still captured reasonably well. The sharp increase in modeled concentrations at later times is a result of boiling and evaporative concentration. Ionic strengths eventually reach values greater than those for which accurate aqueous species activities are calculated (maximum ionic strengths of approximately 2 to 6). However, under such conditions, modeled water saturations are generally well below the level (< 1%) where significant amounts of water are present and would be collected.

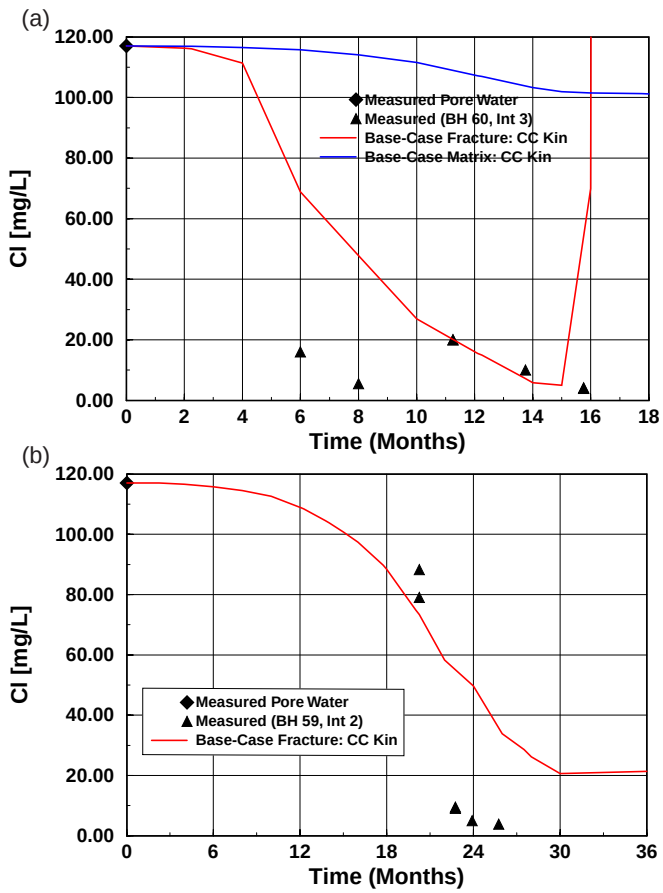

DTNs: LB0011DSTTHCR1.002 [161282] (simulated),
LL020709923142.023 [161677] (measured)

Figure 7.1-18. Changes in Cl^- (mg/L) in Water Samples Collected from Borehole Intervals (a) 60-3 and (b) 59-2, Compared to REV01 Modeled Fracture Water Cl^-

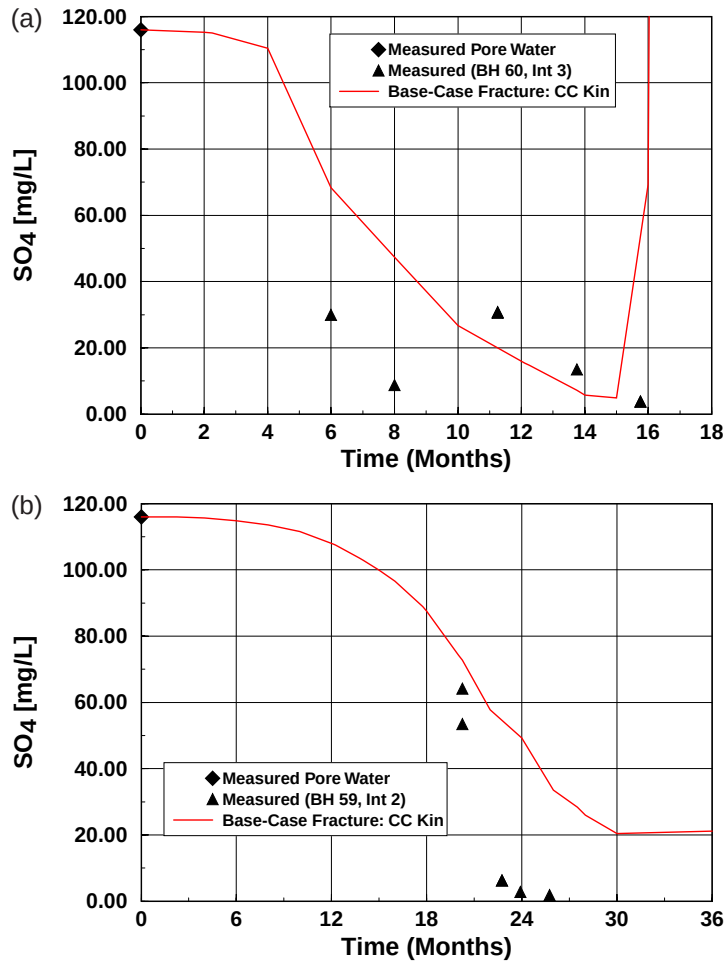

DTNs: LB0011DSTTHCR1.002 [161282] (simulated),
LL020709923142.023 [161677] (measured)

Figure 7.1-19. SO_4^{2-} Concentrations (mg/L) in Water Samples Collected from Borehole Intervals (a) 60-3 and (b) 59-2, Compared to REV01 Modeled Fracture Water SO_4^{2-}

In comparison, Cl^- and SO_4^{2-} concentrations from the REV02 simulation (Figures 7.1-20 and 7.1-21) do not match the pattern of measured concentrations as well as the REV01 results, nor do they reach the low values observed. This can be attributed to the different hydrological properties, which in REV02 led to large pressure buildups in the matrix and less vapor transport out of the matrix. The reduction in vapor transport out of the matrix led to lower liquid saturations in the fractures and a weaker dilution effect on the ambient fracture pore water. Despite these differences, the trends are to more dilute compositions compared to the pore water, and many measured concentrations are within an order of magnitude of the modeled values. Therefore, the DST THC Model meets the model validation requirements for chloride and sulfate concentrations.

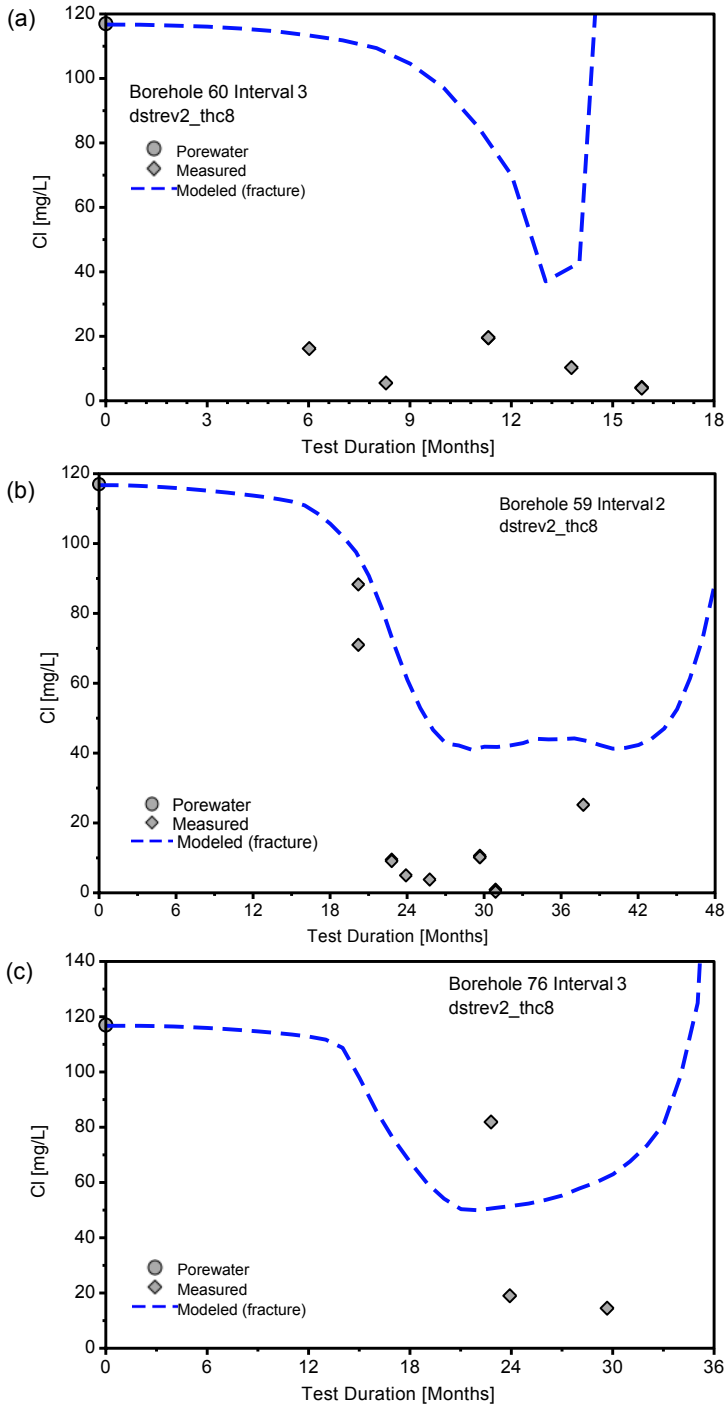

DTNs: LL020709923142.023 [161677] (measured),
LB0307DSTTHCR2.001 (modeled)

Figure 7.1-20. Cl^- Concentrations (mg/L) in Water Samples Collected from Borehole Intervals (a) 60-3, (b) 59-2, and (c) 76-3 Compared to REV02 Modeled Fracture Water Cl^-

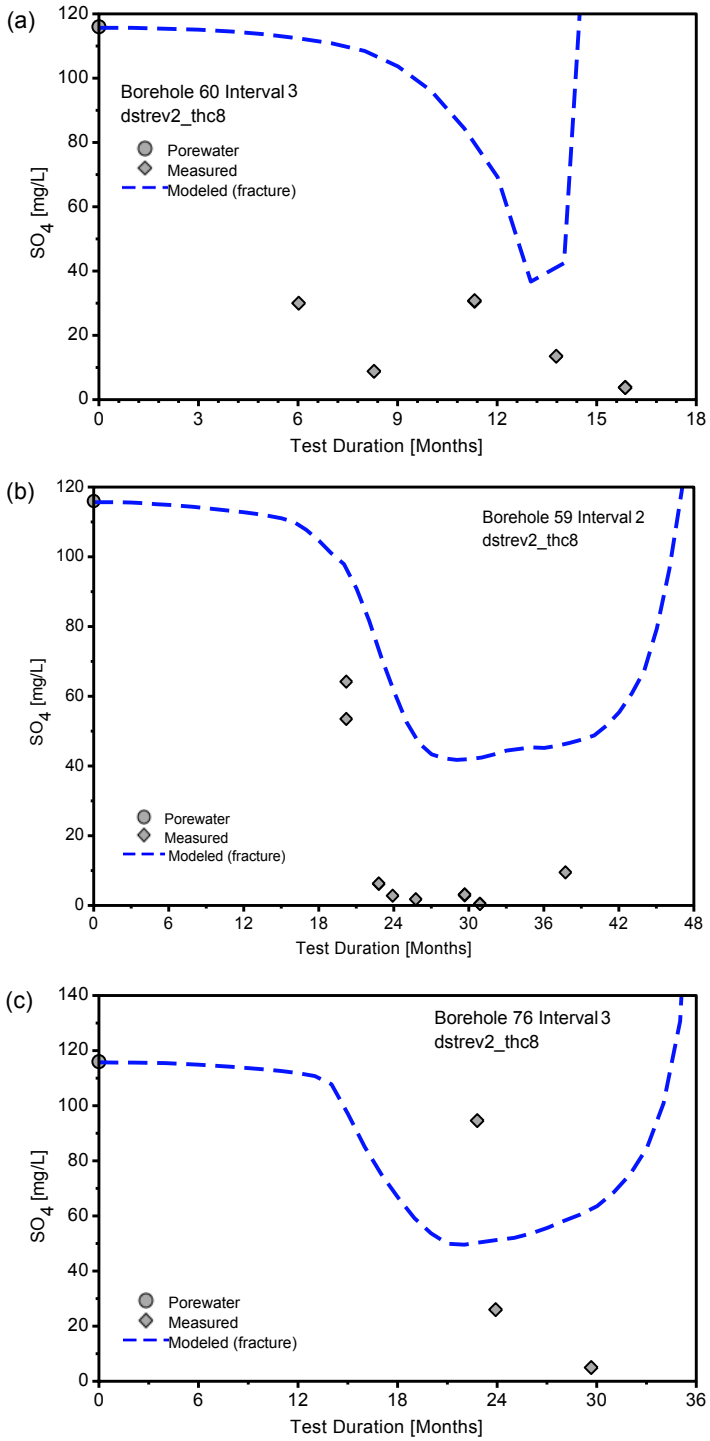

DTNs: LL020709923142.023 [161677] (measured),
LB0307DSTTHCR2.001 (modeled)

Figure 7.1-21. SO_4^{2-} Concentrations (mg/L) in Water Samples Collected from Borehole Intervals (a) 60-3, (b) 59-2, and (c) 76-3 Compared to REV02 Modeled Fracture Water SO_4^{2-}

Measured sodium concentrations (Na^+; Figures 7.1-22a,b) are also much lower than in the initial pore water and are close to the REV01 modeled concentrations. However, the extent of dilution in interval 60-3 is by only a factor of about three to six times, whereas for Cl^- it was from about six to about 20. This difference indicates some contribution of water-rock interaction to the Na^+ concentrations, which is shown in the REV01 extended-case model results as a shift to higher Na^+ concentrations from the base-case results. The origin of the sodium in the DST waters could be alkali feldspar and/or reaction or exchange with clays. In the model simulations, the main source of Na^+ is from alkali feldspar dissolution. As in the Cl^- and SO_4^{2-} variations over time, the sharp rise to higher concentrations at later times is a result of rapid dryout.

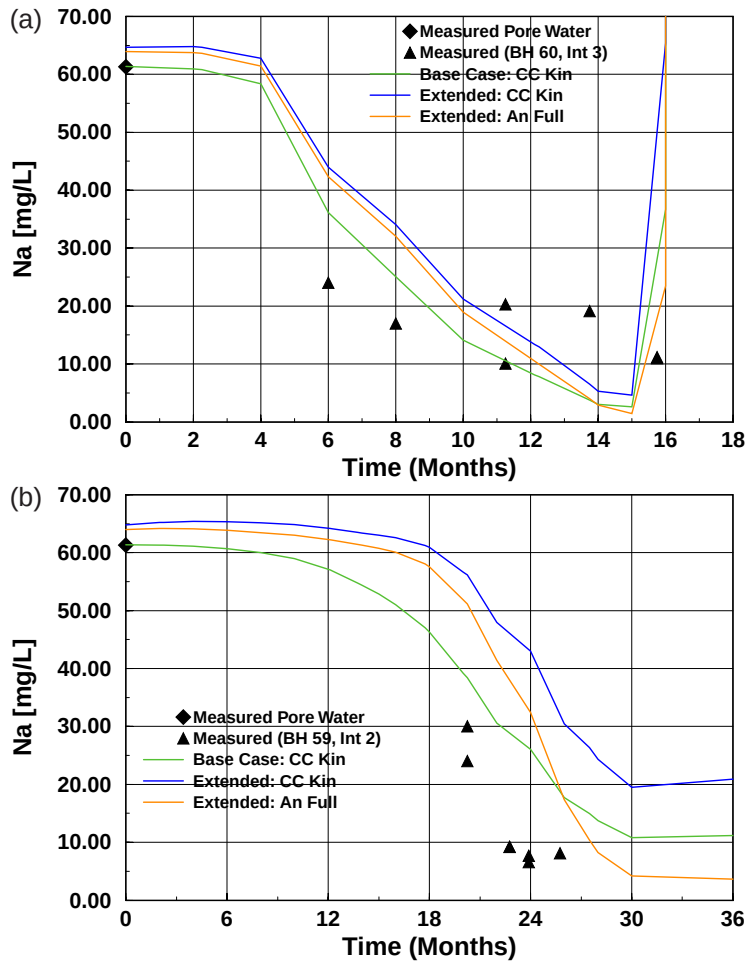

DTNs: LB0011DSTTHCR1.002 [161282] (simulated),
LL020709923142.023 [161677] (measured)

Figure 7.1-22. Na^+ Concentrations (mg/L) in Water Samples Collected from Borehole Intervals (a) 60-3 and (b) 59-2, Compared to REV01 Modeled Na^+ Concentrations in Fractures

Na^+ concentrations in the REV02 simulation (Figure 7.1-23) are elevated with respect to the REV01 results and the modeled concentrations in the 60-3 and 59-2 boreholes, but are closer to the measured values in borehole interval 76-3. The shape of the modeled Na^+ curve shows an increase with temperature, prior to the main condensation pulse, which was absent in the REV01 simulated Na^+ concentrations. This increase clearly results from the higher reactivity of albite, which also leads to increases in pH and a reduction in the partial pressure of CO_2. In the actual rock, it is likely that albite had undergone preferential weathering over several million years of infiltration and is coated by later-formed clays, silica polymorphs, and Ca-rich zeolites. Although the comparisons are not as good as those for REV01, most samples are within the model validation criteria.

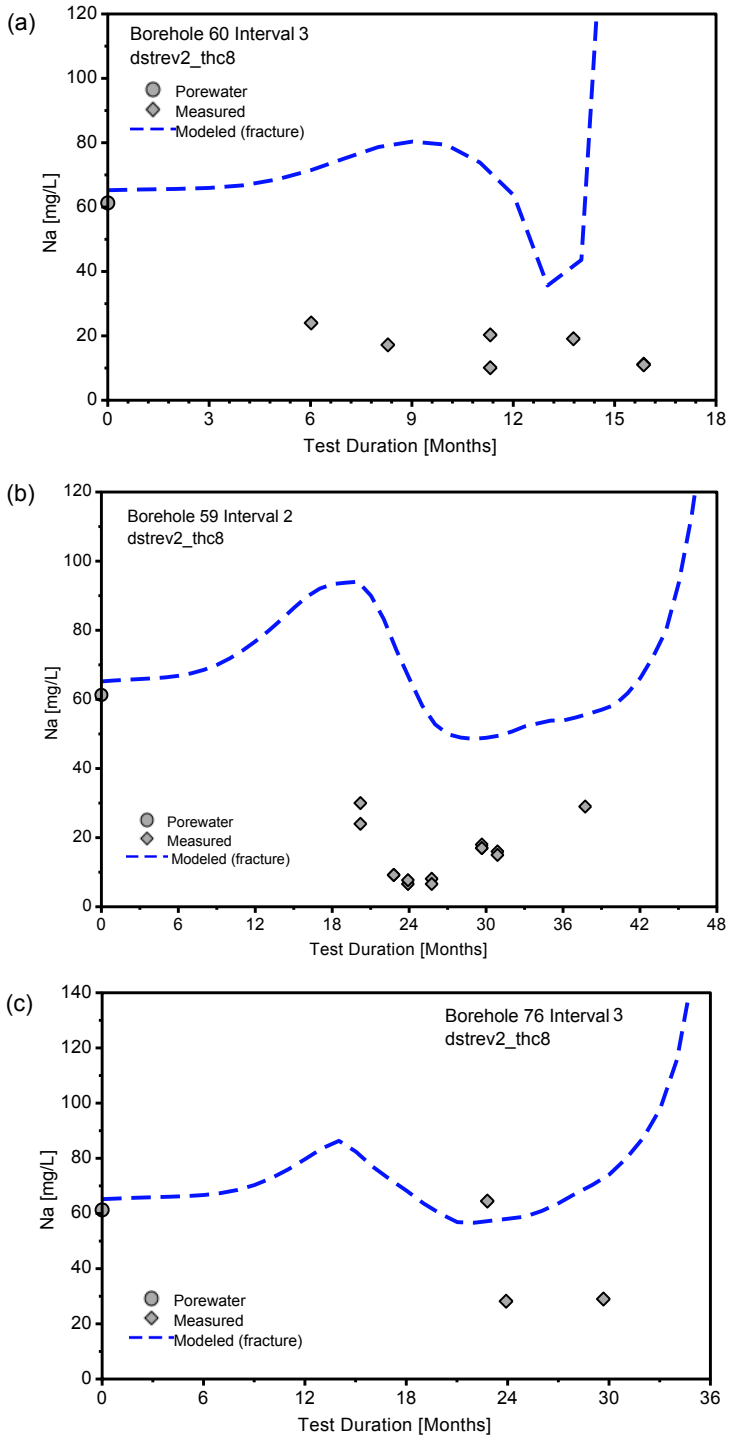

DTNs: LL020709923142.023 [161677] (measured),
LB0307DSTTHCR2.001 (modeled)

Figure 7.1-23. Na^+ Concentrations (mg/L) in Water Samples Collected from Borehole Intervals (a) 60-3, (b) 59-2, and (c) 76-3 REV02 Modeled Na^+ Concentrations in Fractures

Calcium is more sensitive to water-rock interaction than some other species because of the fast reaction rate of calcite, its lower solubility with increasing temperature, and the common occurrence of calcite in fractures. Other potential sources of Ca^{2+} in the rock include Ca-rich zeolites, such as stellerite that are abundant in fractures. Waters collected from intervals 60-3 and 59-2 show a significant drop from the pore-water concentration (about 100 mg/L) to below 10 mg/L, with a consistent decrease over time in 60-3 (Figure 7.1-24a). The continued drop in Ca^{2+} in 60-3 and the very low concentrations in 59-2 (Figure 7.1-24b) may be caused by calcite precipitation, because of its decreased solubility with increasing temperature. The model results in Figures 7.1-24a and b also show a similar, but smaller, reduction in calcium concentration.

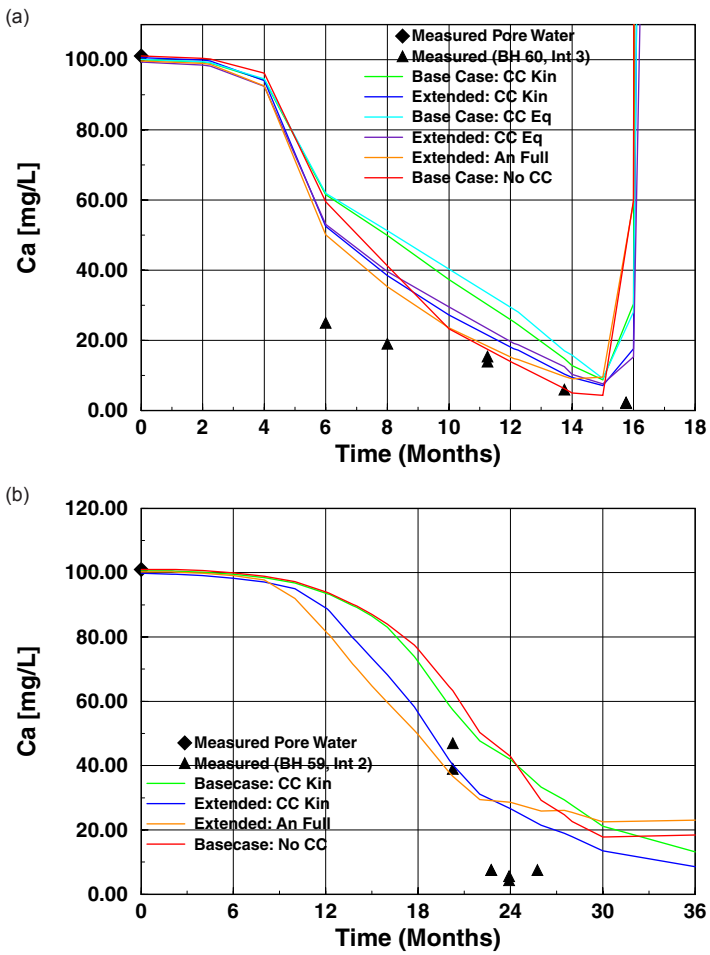

DTNs: LB0011DSTTHCR1.002 [161282] (simulated),
LL020709923142.023 [161677] (measured)

Figure 7.1-24. Ca^{2+} Concentrations (mg/L) in Water Samples Collected from Borehole Intervals (a) 60-3 and (b) 59-2 Compared to REV01 Modeled Ca^{2+} in Fracture Water

Ca^{2+} concentrations in the REV02 simulation (Figure 25a,b,c) are slightly elevated with respect to the REV01 results and the modeled concentrations in the 60-3 and 59-2 boreholes, but are close to the measured values in all the boreholes. The shape of the REV02-modeled Ca^{2+} curve in 60-3 does not exhibit as early an initial dilution-induced drop in concentration; instead, the reduction occurs later, when the strong condensation pulse is encountered and increasing temperature results in calcite precipitation. Similar to the REV01 results, the Ca^{2+} concentration

increases as boiling proceeds and the remaining water is evaporated. The model results capture the trend in the Ca^{2+} concentrations and are, in most cases, within one order of magnitude of the measured values. Therefore, the validation criteria for Ca^{2+} in the DST THC Model have been met.

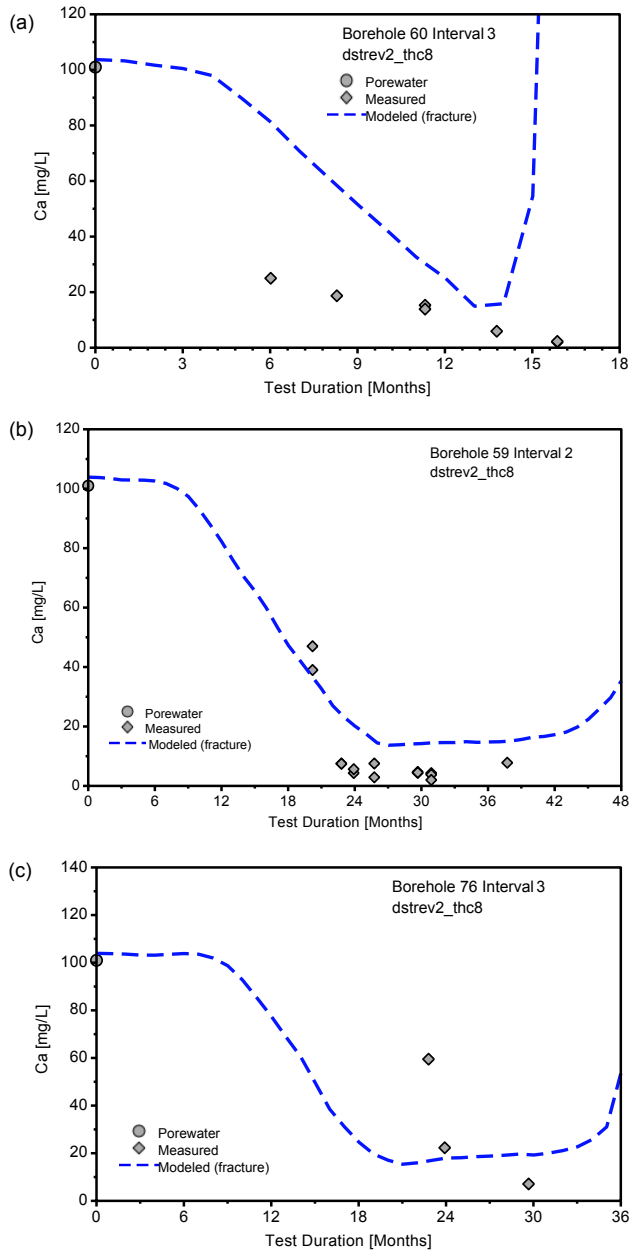

DTNs: LL020709923142.023 [161677] (measured),
LB0307DSTTHCR2.001 (modeled)

Figure 7.1-25. Ca^{2+} Concentrations (mg/L) in Water Samples Collected from Borehole Intervals (a) 60-3, (b) 59-2, and (c) 76-3 Compared to REV02 Modeled Ca^{2+} in Fracture Water

Measured silica concentrations (Figures 7.1-26a,b and 7.1-27a,b,c) show an increase to significantly higher concentrations in the borehole waters compared to the initial pore-water concentration. REV01 model concentrations in borehole interval 60-3 (Figure 7.1-26a) decrease to lower values, although the extent of dilution is moderated by water-rock reaction. In borehole interval 59-2, the extended-case results compare well with concentrations in those waters collected later (Figure 7.1-26b), although the earliest samples also had much higher concentrations. For comparison, modeled matrix silica concentrations for these same locations are similar to the measured values and trends, especially in interval 60-3. Because the concentrations of conservative species, such as chloride and sulfate, are close to the measured values, the possibility of greater fracture-matrix interaction is unlikely. Modeled Na^+ and K^+ concentrations also do not deviate substantially from measured values, suggesting that the additional silica is not likely to have been derived from increased dissolution of feldspars. Thus, the higher measured silica concentrations are likely to be a result of a higher effective reaction rate for a silica phase in the fractures (possibly opal-CT) or reaction of "fresh" mineral surfaces (i.e., cristobalite or quartz) in the borehole walls.

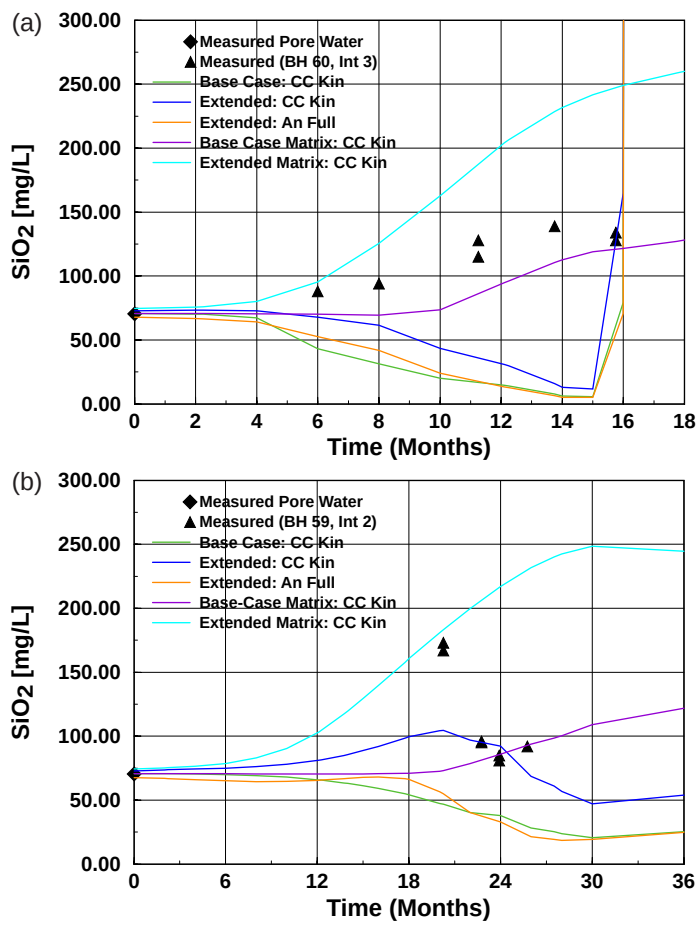

DTNs: LB0011DSTTHCR1.002 [161282] (simulated),
LL020709923142.023 [161677] (measured)

Figure 7.1-26. $SiO_{2(aq)}$ Concentrations (mg/L) in Water Samples Collected from Borehole Intervals (a) 60-3 and (b) 59-2 Compared to REV01 Modeled Fracture Water $SiO_{2(aq)}$ Concentrations

In the REV02 simulations, the initial mineral assemblage was modified to include opal, reflecting its observed association with calcite in fracture coatings. The addition of this phase, along with the increased concentrations of species as a result of a weaker dilution effect and modifications to the thermodynamic data, resulted in much higher modeled aqueous-silica concentrations in the REV02 simulations (Figure 7.1-27a,b,c). The REV02 modeled silica concentrations in fracture waters capture the strong increases observed in the measured compositions, especially those seen in the borehole intervals overlying the heaters (59-2 and 76-3). In 76-3, the first water sample collected had a silica concentration of over 280 mg/L, compared to about 180 mg/L in the model simulation. The two waters collected later had silica concentration around 200 mg/L, which was closer to the REV02 model results. Except for two samples in 60-3, for which the model predicts an earlier rise in concentration, simulated SiO_2 values are within an order of magnitude of the observed ones, and therefore the model results meet the validation requirements.

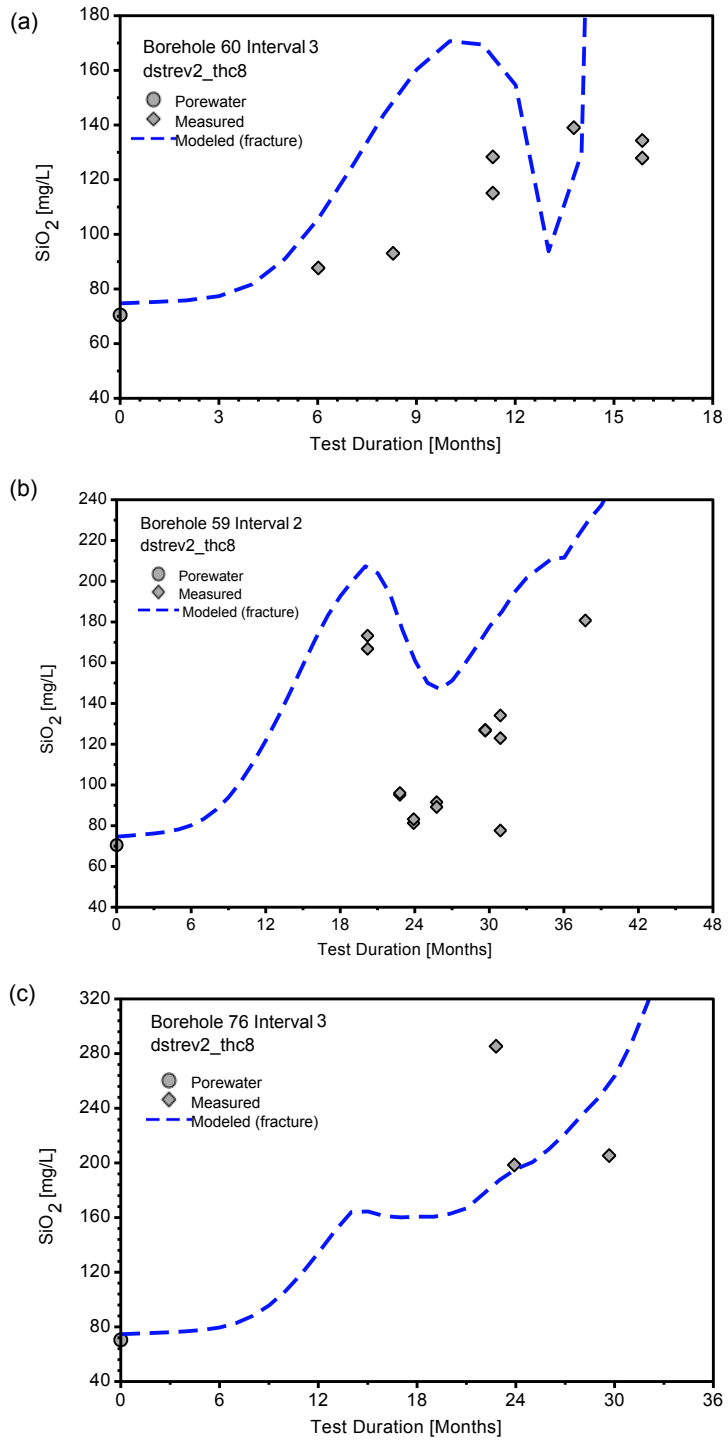

DTNs: LL020709923142.023 [161677] (measured),
LB0307DSTTHCR2.001 (modeled)

Figure 7.1-27. $SiO_{2(aq)}$ Concentrations (mg/L) in Water Samples Collected from Borehole Intervals (a) 60-3, (b) 59-2, and (c) 76-3 Compared to REV02 Modeled Fracture Water $SiO_{2(aq)}$ Concentrations

REV01 modeled and measured potassium (K^+) concentrations are shown in Figures 7.1-28a and b for borehole intervals 59-2 and 60-3. REV01-modeled concentrations, although initially lower, quickly rise during heating and are similar to the measured values. A deviation occurs in K^+ at the initial time, because of some disequilibrium in the initial pore water with the model mineral assemblage. Measured concentrations in waters collected from the boreholes are significantly higher than would be expected from simple dilution of ambient fracture or matrix pore water, indicating that reactions with K-feldspar have likely taken place.

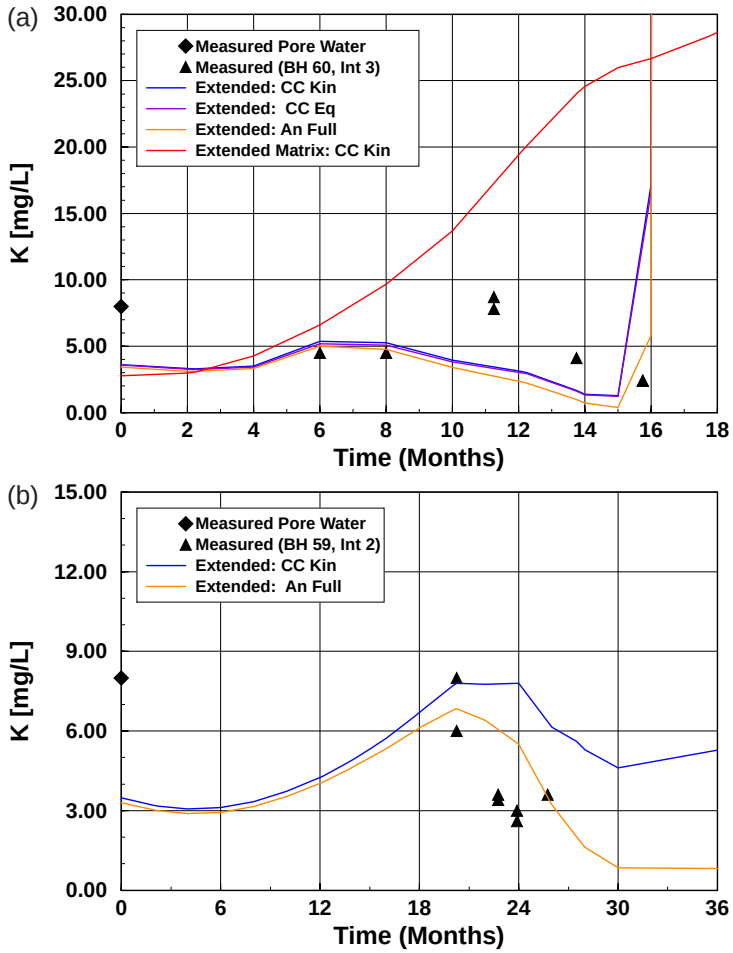

DTNs: LB0011DSTTHCR1.002 [161282] (simulated),
LL020709923142.023 [161677] (measured)

Figure 7.1-28. K^+ Concentrations (mg/L) in Water Samples Collected from Borehole Intervals (a) 60-3 and (b) 59-2 Compared to REV01 Modeled Fracture Water K^+ Concentrations

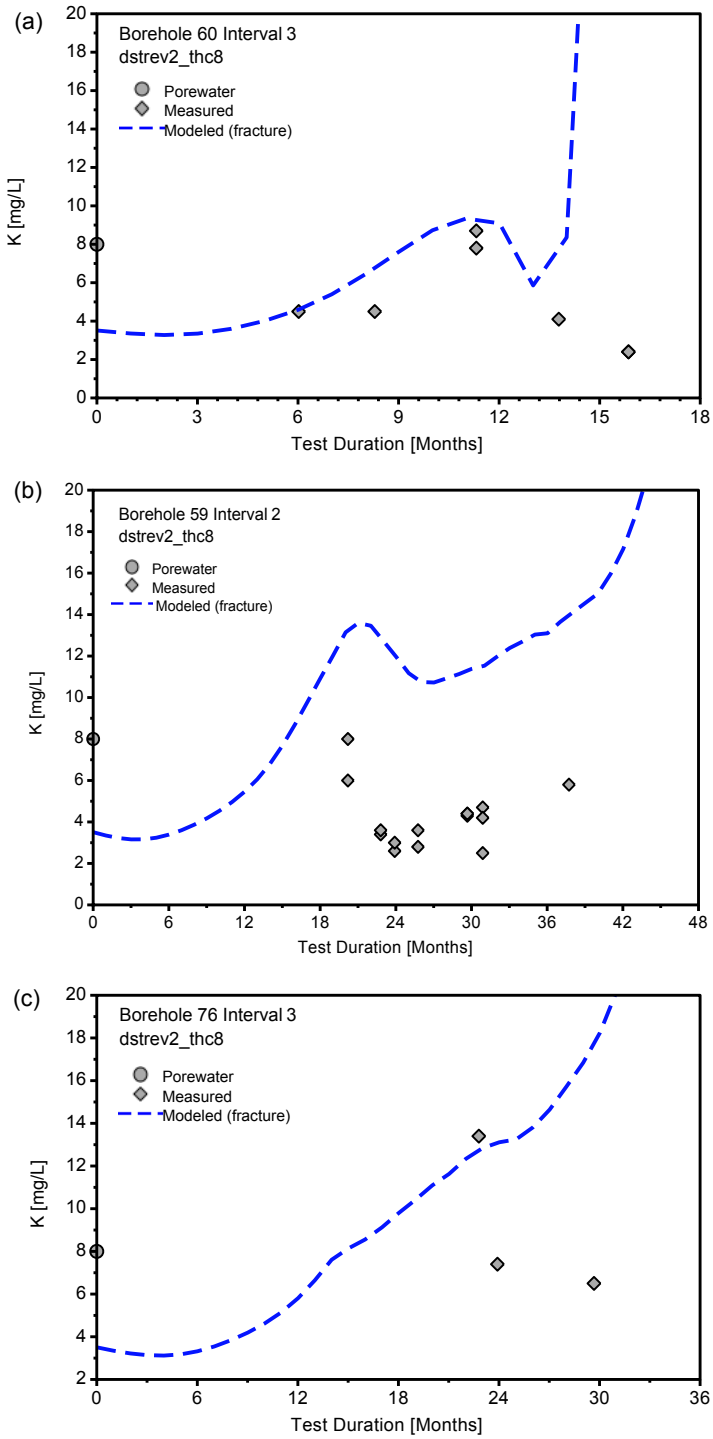

DTNs: LL020709923142.023 [161677] (measured),
LB0307DSTTHCR2.001 (modeled)

Figure 7.1-29. K^+ Concentrations (mg/L) in Water Samples Collected from Borehole Intervals (a) 60-3, (b) 59-2, and (c) 76-3 Compared to REV02 Modeled Fracture Water K^+ Concentrations

REV02-modeled concentrations of K^+, like those of Na^+, increase to values somewhat higher than the measured concentrations. However, trends between modeled and measured data are similar, suggesting that a reduction in the K-feldspar reactivity and an increase in the dilution effect would result in a closer match to the measured concentrations. The modifications to hydrological and thermodynamic (and/or kinetic) data required for such reduction in reactivity would be consistent with the shifts needed for both the conservative species, such as Cl^- and SO_4^{2-}, as well as for Na^+. The lower matrix permeability used in REV02 induces slower transfer of pore water to enter into the fractures, and results in lower dilution of the conservative species. The inclusion of calcite and feldspar phases also increase the concentrations of silica, Na and K in the fractures.

The fact that Na^+ and K^+ show similar trends over time is consistent with their predominance in either an alkali feldspar solid-solution phase, such as sanidine, and/or as closely intergrown exsolved phases from a precursor solid-solution alkali feldspar mineral. All model results meet the validation requirements (trend to higher concentrations than in the initial pore water and within an order-of magnitude).

Fewer bicarbonate (HCO_3^-) concentrations were measured in the borehole waters because of difficulties making the measurements in the field. Available measurements are plotted in Figures 7.1-30a and b compared to the REV01 model results. Measured bicarbonate concentrations are much lower than the initial pore-water concentration, a pattern that is captured well by the model. This trend results from the combined effects of dilution and loss of dissolved CO_2 to the vapor phase at higher temperatures. Given the limited quantity of measured data, it is not possible to distinguish which geochemical system (base case or extended case) better predicts the bicarbonate concentration.

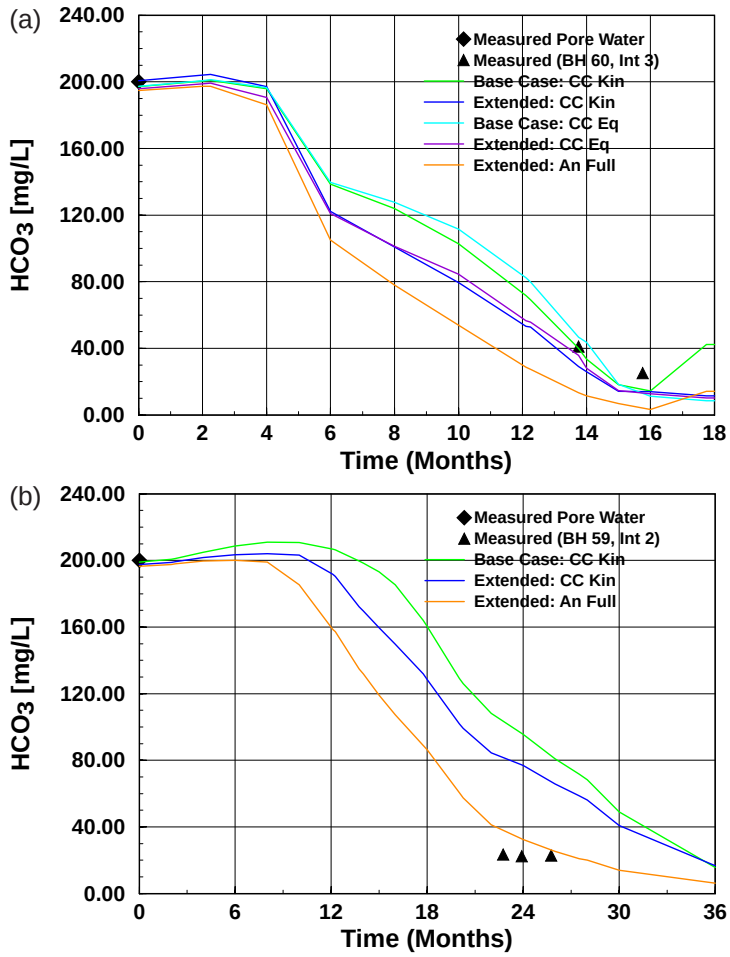

DTNs: LB0011DSTTHCR1.002 [161282] (simulated),
LL020709923142.023 [161677] (measured)

Figure 7.1-30. HCO_3^- Concentrations (mg/L) in Water Samples Collected from Borehole Intervals (a) 60-3 and (b) 59-2 Compared to REV01 Modeled Fracture Water HCO_3^- Concentrations

A few additional HCO_3^- concentrations were measured in borehole interval 59-2 and in interval 76-3 since the last revision of this document. These are plotted in Figure 7.1-31, along with REV02-modeled concentrations. REV02 HCO_3^- concentrations compare well to the measured concentrations. Another important aspect to the validation of the DST THC Model is that the REV01 model results are similar to the concentrations measured in 59-2 after the modeling was documented in the previous (REV01) model report. This prediction of the later measurements also supports the validation of the DST THC Model. Therefore, REV01 and REV02 model results for HCO_3^- meet the model validation criteria.

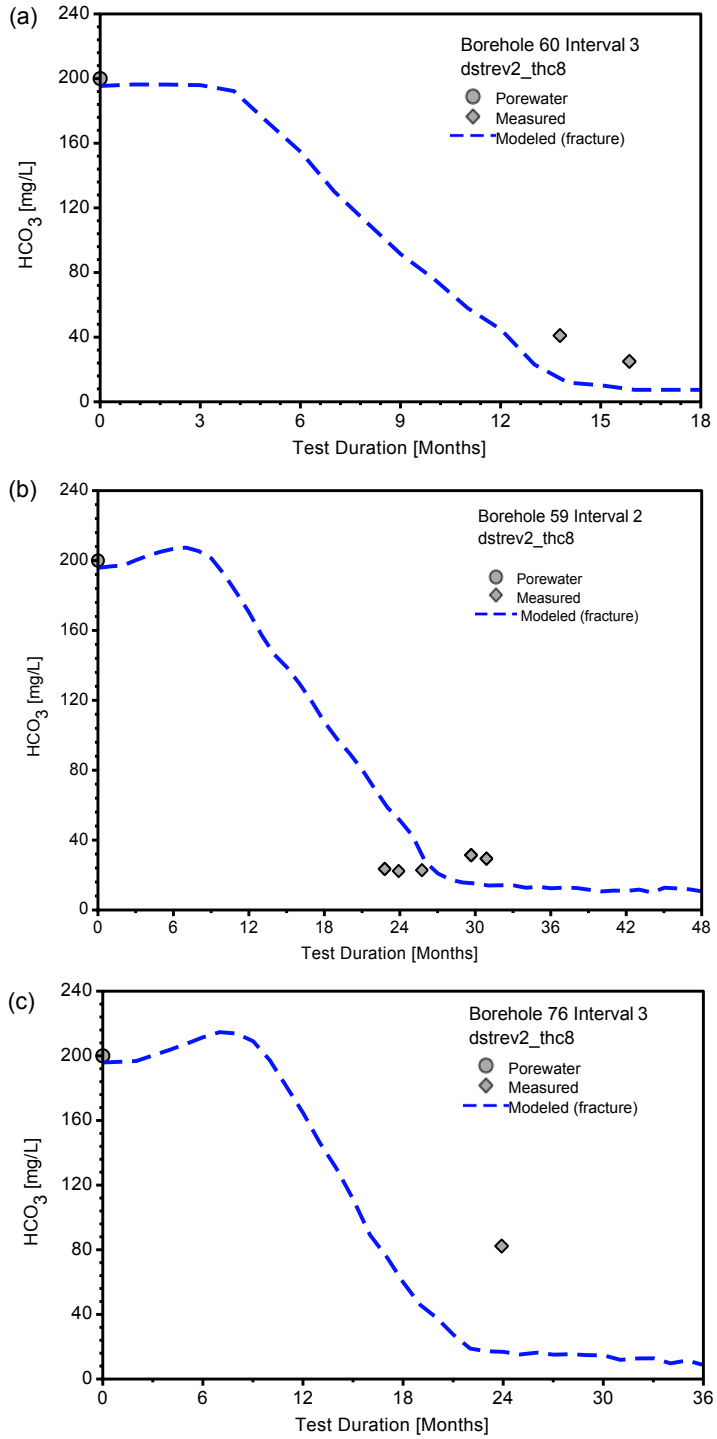

DTNs: LL020709923142.023 [161677] (measured),
LB0307DSTTHCR2.001 (modeled)

Figure 7.1-31. HCO_3^- Concentrations (mg/L) in Water Samples Collected from Borehole Intervals (a) 60-3, (b) 59-2, and (c) 76-3 Compared to REV02 Modeled Fracture Water HCO_3^- Concentrations

Modeled concentrations of some additional aqueous species (Mg^{2+}, NO_3^-, and F^-) in the REV02 simulation are compared to measured compositions from 59-2, 60-3, and 76-3 in Figures 7.1-32 through 7.1-34.

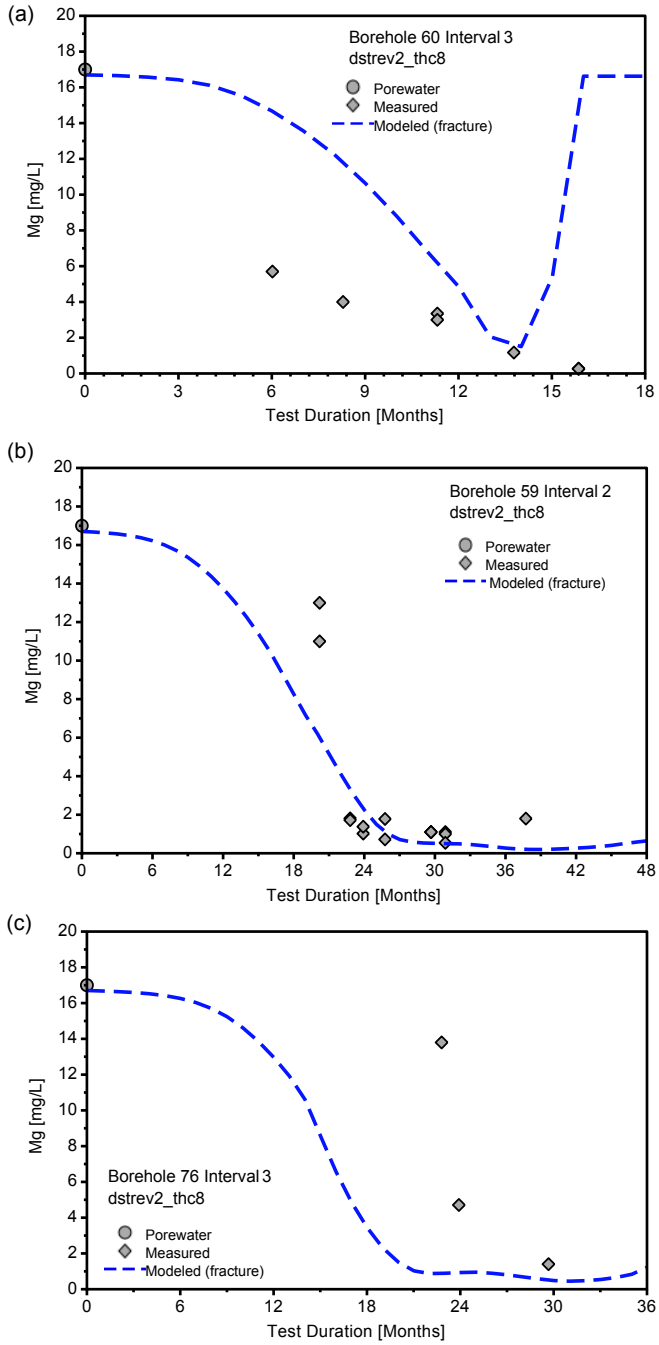

DTNs: LL020709923142.023 [161677] (measured),
LB0307DSTTHCR2.001 (modeled)

Figure 7.1-32. Mg^{2+} Concentrations (mg/L) in Water Samples Collected from Borehole Intervals (a) 60-3, (b) 59-2, and (c) 76-3 Compared to REV02 Modeled Fracture Water Mg^{2+} Concentrations

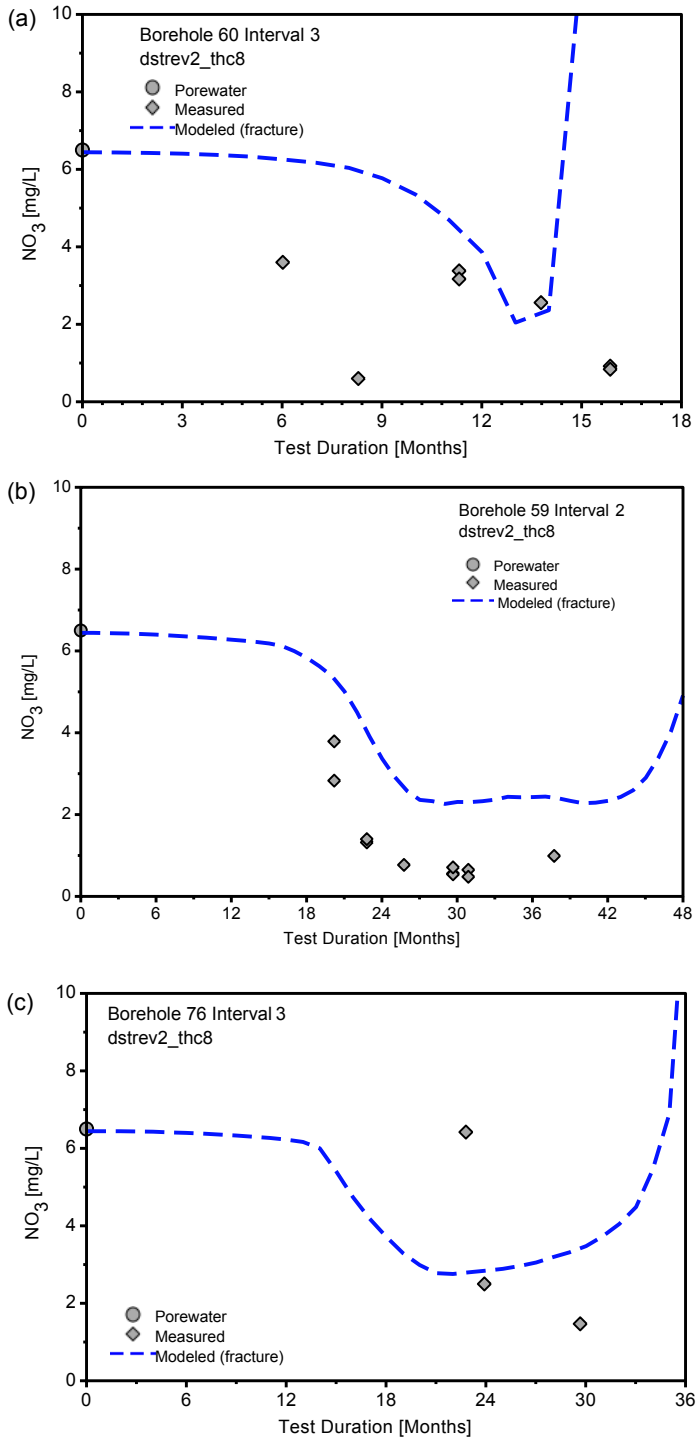

DTNs: LL020709923142.023 [161677] (measured),
LB0307DSTTHCR2.001 (modeled)

Figure 7.1-33. NO_3^- Concentrations (mg/L) in Water Samples Collected from Borehole Intervals (a) 60-3, (b) 59-2, and (c) 76-3 Compared to REV02 Modeled Fracture Water NO_3^- Concentrations

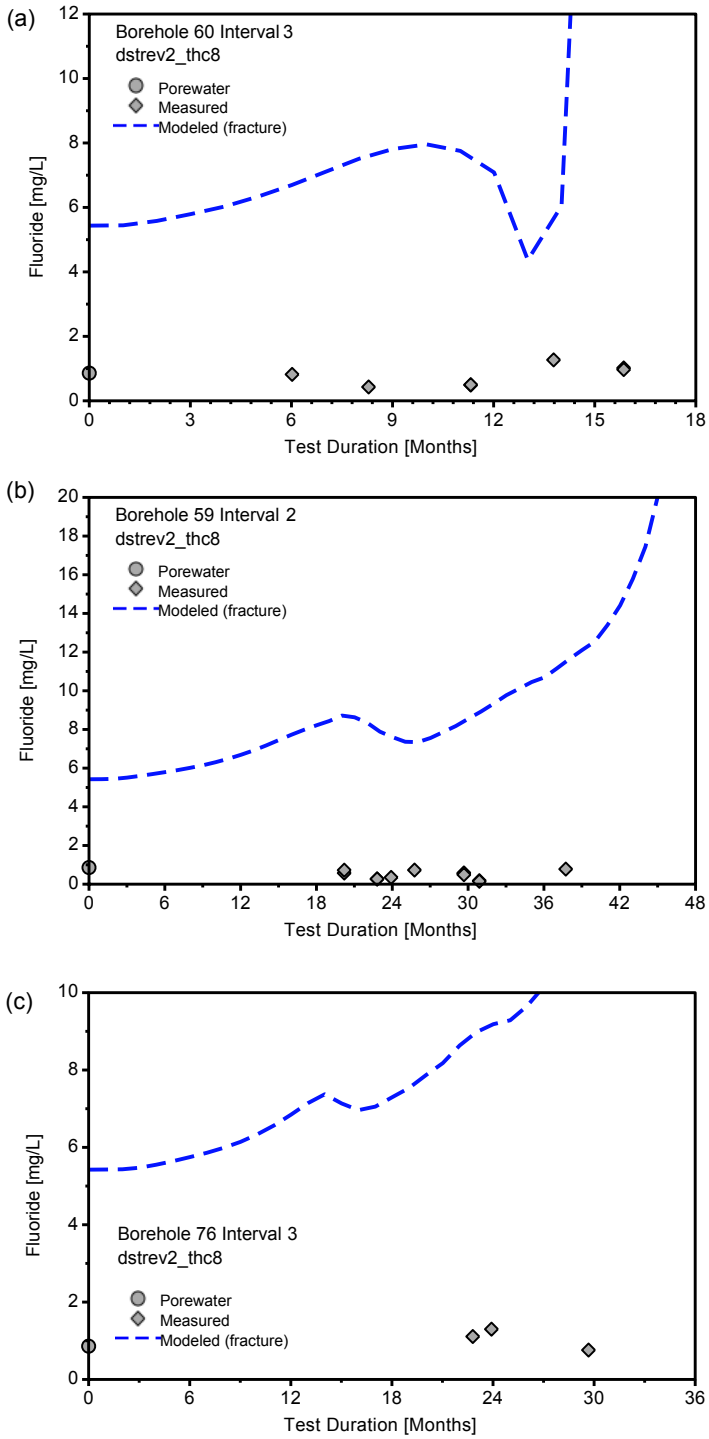

DTNs: LL020709923142.023 [161677] (measured),
LB0307DSTTHCR2.001 (modeled)

Figure 7.1-34. F^- Concentrations (mg/L) in Water Samples Collected from Borehole Intervals (a) 60-3, (b) 59-2, and (c) 76-3 Compared to REV02 Modeled Fracture Water F^- Concentrations

Measured Mg^{2+} concentrations (from Figure 7.1-32) show initial concentrations closer to the pore-water value of about 17 mg/L, and then a considerable drop in all the borehole intervals. Modeled Mg^{2+} concentrations show a similar pattern and are close to the measured concentrations. The sharp drop in the modeled concentrations is related to a combination of dilution from condensate and the precipitation of sepiolite (a Mg-rich sheet silicate). It is not clear whether precipitation of an Mg-rich phase takes place in the boiling zone in the rock, because the extent of dilution of Mg^{2+} is roughly similar to that observed for the conservative species, such as Cl^-. Some Mg^{2+} is likely incorporated into calcite that is precipitated as the condensate water above the heaters drains down and boils, although this may have a minimal effect on Mg^{2+} concentrations. The thermodynamic model for calcite does not include Mg^{2+}, and therefore, another Mg-bearing phase (i.e., sepiolite) take up some of the Mg^{2+}. Most samples fall within an order of magnitude of the model results, thus meeting the validation requirements.

Nitrate (NO_3^-) was added to the list of modeled species for the REV02 simulation, owing to its importance for the evolution of final salt compositions in potential seepage waters. Nitrate is highly soluble, and there are no nitrate minerals initially present in the tuff. The pore water has somewhat more variable nitrate concentrations compared to Cl^- and SO_4^{2-}. The greater variability in pore-water concentrations may be a result of biologically mediated nitrogen reduction, possibly after sample collection. Measured and modeled nitrate concentrations are shown in Figure 7.1-33. Concentrations measured in waters collected from the hydrology boreholes are almost all lower than those from the pore water, showing a similar pattern as Cl^- and SO_4^{2-}. This finding suggests that over the time scale of the experiment, nitrate acts as a conservative species and may not have been affected significantly by biological activity in the rock. REV02 modeled concentrations capture the measured pattern of nitrate concentrations quite well, although the dilution effect is not as strong; this effect is similar to that seen for most other weakly reactive or nonreactive species. Model validation requirements for NO_3^- were met, both in terms of the trend and range of values (except for a few samples).

Fluorite was added to the initial mineral assemblage for the REV02 simulations. Fluorite is observed sporadically in the Yucca Mountain tuffs, and fluoride concentrations should reflect the presence of this mineral. However, fluoride concentrations in the pore water measured around the DST (see Table 7.1-3) are less than 1 mg/L, much lower than the equilibrium solubility of fluorite (around 4-5 mg/L at ambient temperatures). In addition, almost all waters from the hydrology boreholes have measured fluoride concentrations of around 1 mg/L or less, with only one sample at about 4 mg/L. The measured values are shown in Figure 7.1-34 for borehole intervals 59-2, 60-3, and 76-3, compared to the REV02 model results. The modeled fluoride concentrations quickly rise from the initial concentration of less than 1 mg/L to several mg/L, eventually attaining much higher values as increasing temperatures result in much higher fluorite solubility. The increase is also related to the fast dissolution rate of fluorite. Thus, simulations using the REV01 mineral assemblage, without fluorite as a initial mineral phase, capture the change in fluoride concentrations more closely around the DST than the REV02 simulation results. Even though the REV02 model results do not capture the trend in the fluoride concentrations, many of these samples meet the validation requirement for an order-of-magnitude deviation. They also bound the upper limit for the repository units and exemplify the sensitivity of the model to the initial starting conditions.

7.1.12 Mineralogical Changes

As the last few sections have documented, marked changes have taken place in the water and gas chemistry in the DST, owing to thermal-hydrological processes as well as mineral-water-gas reactions. The total amount of minerals precipitated or dissolved, though, may be exceedingly small, even though the effect on the water composition is quite strong. The strong effect on the water composition is related to the water/rock ratio, which is very low in the unsaturated low-porosity fractured tuff. The system is also characterized by an exceedingly low percolation flux of only a few millimeters per year or less, and therefore the ambient water has a long residence time. This section documents the predicted changes in mineralogy over the heating phase of the DST and compares the results to a few measurements made from *in situ* sidewall core samples obtained from above-boiling zones. First, REV01 results are discussed, for which no measurements were available, although they act as a prediction because they were performed prior to the measurements. Following the discussion of the REV01 results, REV02 simulated changes in mineral abundances are compared to the sidewall core samples.

Although calcite is not a major phase in the tuffs at Yucca Mountain, its rapid reaction rate, pH sensitivity, strong effect on pH, and presence almost entirely in fracture coatings make it an important mineral phase. REV01 predicted changes in calcite volume percent in fractures after three years of heating are shown in Figure 7.1-35. The simulated changes in calcite abundances show a well-defined region of precipitation in the fractures above and to the margins of the Heated Drift and wing heaters. Strong dissolution is evident below the wing heaters, especially in the drainage zones. Precipitation in the matrix is driven mainly by increasing temperature and pH, whereas in the fractures there is continuous boiling of condensate waters as they drain back to the heat source from the overlying condensation zone. These waters pick up Ca^{2+} through interaction with calcite and from mixing of ambient fracture pore water. The continuous process of condensate formation and drainage leads to a well-defined zone of calcite precipitation in the fractures above the heaters. The results are also consistent with the decrease in Ca^{2+} seen in the condensate waters over time (Table 7.1-3, see also Section 7.1.11.2).

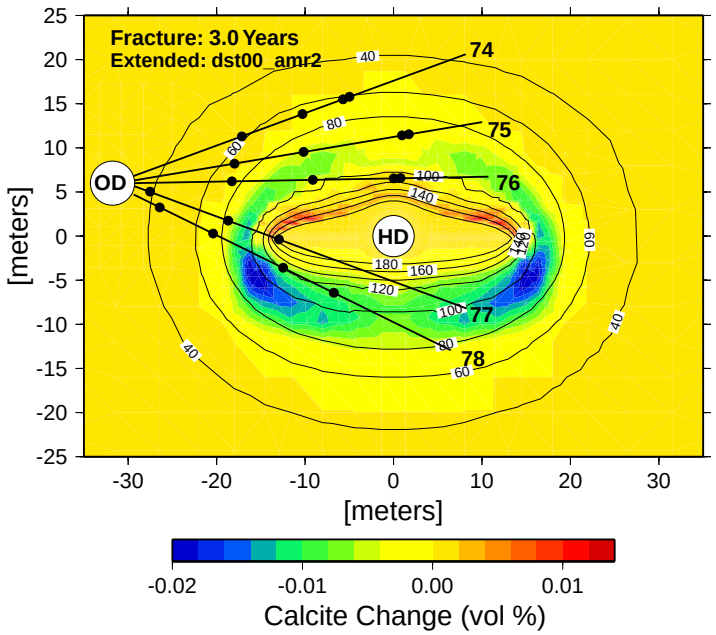

DTN: LB0011DSTTHCR1.002 [161282]

NOTE: Modeled temperature contours are overlain, as well as boreholes and approximate locations of temperature sensors.

Figure 7.1-35. Modeled (REV01) Volume Percent Change in Calcite in Fractures after 3 Years of Heating

Areas of modeled amorphous silica precipitation are shown in Figure 7.1-36 for the extended system (cc kin). Silica concentrations are closest to measured values (Figure 7.1-26) in the extended system, and therefore amounts of amorphous silica precipitated should be closer to those in the rock than the amounts produced by the base-case system model simulations. Like calcite, amorphous silica precipitation is concentrated in the reflux zones above the heaters. However, because silica phases have increased solubility at higher temperatures, the zone of amorphous silica precipitation is confined to regions where the temperatures are at or above boiling and evaporation was the primary mechanism for mineral precipitation. Although the volumetric percentage of amorphous silica that has precipitated is small, the greatest amount of precipitation occurs at the outer edge of the wing heaters (where flow is focused into boiling regions).

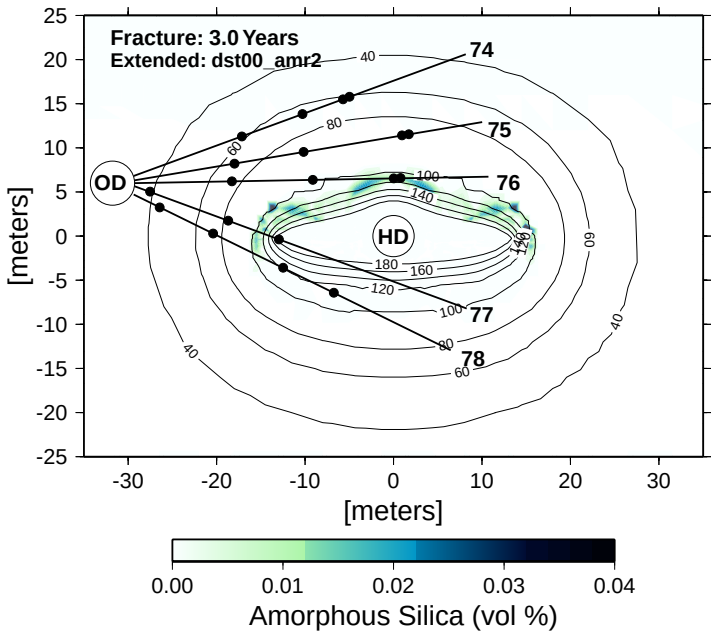

DTN: LB0011DSTTHCR1.002 [161282]

NOTE: Modeled temperature contours are overlain, as well as boreholes and approximate locations of temperature sensors.

Figure 7.1-36. Modeled (REV01) Volume Percent Amorphous Silica in Fractures after 3 Years of Heating

Since the last revision of this Model Report, a series of small core samples was analyzed for evidence of mineral alteration during the heating phase of the DST. The first set of samples was obtained in November 2000 by sidewall coring of fractures in "chemistry" boreholes 53 and 54, which were originally designed for water sampling. However, the SEAMIST pad system employed in those boreholes failed to provide uncontaminated water samples owing to the engineering materials in the boreholes and the unknown compositions of the pads. The collection and analyses of the rock samples are documented in BSC (2002 [160771], Section 6.3.4.3). Chemical analyses, identification, and description of mineral alteration products for a few of the samples are given in DTN: LA0201SL831225.001 [158426]. Because only a small portion of the core has been analyzed and only a few results are available, the comparisons to model results are limited. The data submitted represent observations and analyses from two locations taken about 1 m apart in an above-boiling region above the heaters.

Calcite, amorphous silica, and a calcium sulfate phase (tentatively identified as gypsum) are the only phases in these samples identified so far as products of the processes taking place during the DST (DTN: LA0201SL831225.001 [158426]). Amorphous silica was common in both samples, whereas calcite and gypsum were only described from the sample further into the above-boiling zone (the other sample was from the outer edge). Although anhydrite is thermodynamically more stable than gypsum under the conditions of the DST, gypsum was observed in analyses of borehole surfaces from the Single Heater Test (DTN: LA0009SL831151.001 [153485]). On the basis of this identification, the calcium sulfate phase observed in the DST sidewall core samples was considered to be gypsum (BSC 2002 [160771], Section 6.3.4.3).

From these descriptions, amorphous silica was the dominant phase precipitated during boiling, with much lesser amounts of calcite and gypsum. Amorphous silica appears as glassy coatings covering larger areas of the surface, commonly in the form of thin curled sheets and fine tubules. Calcite typically is found as scattered, small late-stage mounds, with gypsum as very late-formed scattered crystals on top of other phases. The actual percentage of mineral precipitates in the fracture system could not be determined from this type of localized analysis. Some of the silica coatings were approximately 10–20 µm thick, with discrete gypsum crystals up to 80 µm long. Given a uniform 10 µm thick layer of mineral precipitates on one side of all fractures, with a hypothetical range in fracture aperture of 100 to 1,000 µm, the proportion of fracture volume filled would range from 1 to 10%. Because many of the coatings are much less than 10 µm thick and do not cover all areas of every fracture, the volume filled is likely to be less than 1%.

Figures 7.1-37 through 7.1-39 show the REV02 modeled distributions of calcite, amorphous silica, and gypsum in the DST at the time the samples were collected. This time (35 months) is nearly the same as the three-year REV01 results presented above, so the comparison of the different model results can also be made. The location of borehole 54 is plotted, as well as the sites where the mineral was observed in a sidewall core sample. The modeled distributions of other, much more minor phases are not shown, because it is not possible yet to validate their abundances.

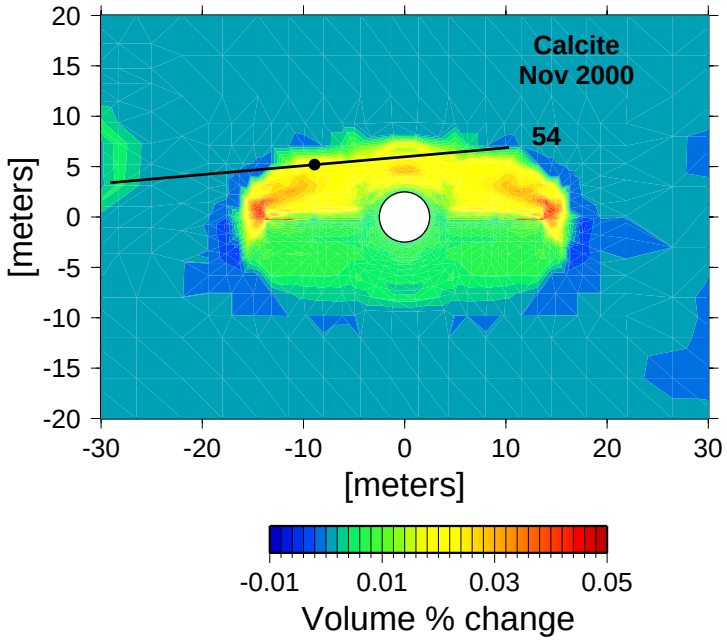

DTNs: LB0307DSTTHCR2.001 (modeled), LA0201SL831225.001 [158426] (measured)

NOTE: Chemistry borehole 54 is shown, with location of observed calcite (filled circle) formed during DST.

Figure 7.1-37. Modeled Volume Percent Change in Calcite in Fractures as of November 2000 (35 Months of Heating)

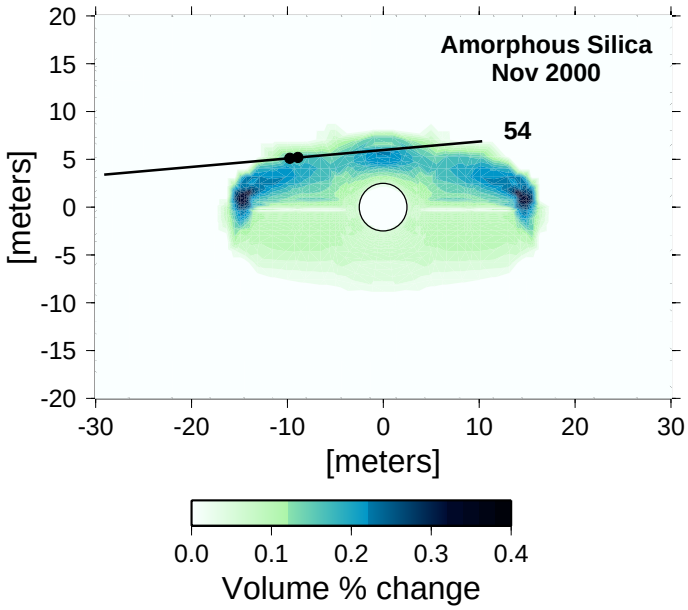

DTNs: LB0307DSTTHCR2.001 (modeled), LA0201SL831225.001 [158426] (measured)

NOTE: Chemistry borehole 54 is shown, with location of observed amorphous silica (filled circle) formed during DST.

Figure 7.1-38. Modeled Volume Percent Amorphous Silica in Fractures as of November 2000 (35 Months of Heating)

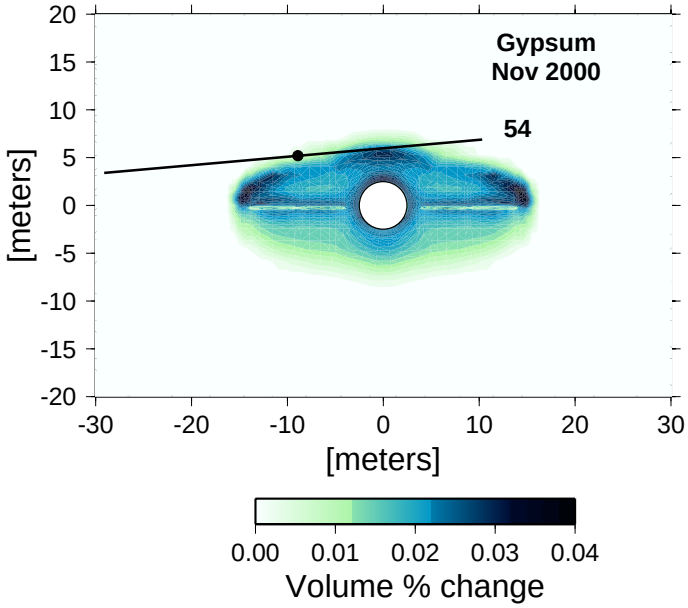

DTNs: LB0307DSTTHCR2.001 (modeled), LA0201SL831225.001 [158426] (measured)

NOTE: Chemistry borehole 54 is shown, with location of observed gypsum (filled circle) formed during DST.

Figure 7.1-39. Modeled Volume Percent Gypsum in Fractures as of November 2000 (35 Months of Heating)

The modeled distribution of calcite in the REV02 simulation (Figure 7.1-37) is similar to the REV01 results (Figure 7.1-35), but calcite abundances in the precipitation zone above the heaters are higher. This increase in calcite precipitation is primarily a result of an improved mass-conservation formulation for mineral precipitation at the boiling front that was implemented in TOUGHREACT V3.0 (LBNL 2002 [161256]). Another less important factor is the somewhat lower fracture porosity in the REV02 hydrological property set. Although calcite dissolution appears to be minor, it is similar to that presented in the REV01 simulation. It is, however, volumetrically less than precipitation in the REV02 simulation. The location of modeled calcite precipitation matches the location of observed calcite in the sidewall core sample.

Like calcite, the modeled distribution of amorphous silica in the REV02 simulation (Figure 7.1-37) is similar to the REV01 results (Figure 7.1-35), but the abundances in the precipitation zone above the heaters are higher. This increase in amorphous silica precipitation is mainly a combined effect of the much higher aqueous silica concentrations in the REV02 simulated water compositions, which are much closer to measured values, (see Figure 7.1-27) and the improved mass conservation formulation in TOUGHREACT V3.0 (LBNL 2002 [161256]). The net result is an increase of about a factor of ten in the maximum volume change in amorphous silica. The maximum amount of amorphous silica precipitated is about 0.4% after 3 years and less than about 1% for the entire duration of the DST. There is also an excellent correspondence in the region of modeled amorphous silica precipitation and the observed amorphous silica in the sidewall core samples from borehole 54. Although the observations of mineral coatings on a few samples cannot be used to judge the total amount of mineral precipitated, the small volumes precipitated in the model are consistent with the generally thin coatings observed.

Precipitation of gypsum is localized to the zones where modeled sulfate concentrations become very high as a result of boiling (Figure 7.1-39). The observed location of gypsum in the sidewall core sample is consistent with the model results, which show this sample to be just within the edge of the modeled zone of precipitation. Further sampling through the center of the boiling zone should help delineate the pattern of mineral precipitation for all the phases.

The observation of significantly greater amorphous silica precipitation compared to calcite and gypsum, with the latter phases occurring in roughly equivalent amounts, is also consistent with the REV02 model results. Although the maximum amount of amorphous silica precipitated is about an order of magnitude greater than calcite, there are not enough samples to determine the spatial distribution of these phases and whether areas exist where the relative proportions differ. One additional borehole has been drilled through the boiling zone, and two others planned, to examine the distribution of mineral alteration and the effects on matrix pore-water composition. These boreholes will allow for a systematic examination of fracture mineral alteration away from the localized TH effects induced by open boreholes. Given that the three observed mineral phases are in the locations predicted by the model simulations, the validation criteria have been met.

7.1.13 Porosity and Permeability Changes

The predicted maximum change in fracture porosity in the REV01 simulations was about 0.1%. Although the simulations were carried out with a feedback between mineral

dissolution/precipitation and porosity, permeability, and capillary pressure changes, the effect on the latter parameters and on fluid flow was negligible. The greatest change took the form of a few-meters-wide zone of decreased porosity a few meters above the Heated Drift and wing heaters.

The predicted amorphous silica abundances are about an order of magnitude greater in the REV02 simulations than in the REV01 simulations (Section 7.1.12). Consequently, fracture porosity changes are expected to be about one order of magnitude higher. Figure 7.1-40 shows the change in fracture porosity after 4 years of heating in the DST. The areas above the Heated Drift and near the edges of the wing heaters show the greatest reduction in fracture porosity, reaching somewhat less than -0.8%. This is nearly a factor of ten greater than in the REV01 simulations. Areas of slight fracture porosity increases in the model results can be found in the outer condensation zones, yet they are not evident in the contour plot.

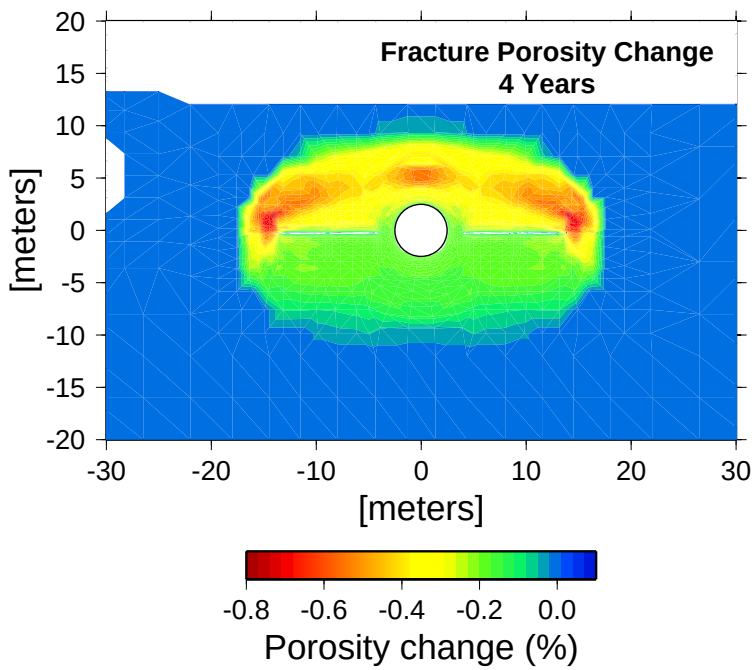

Output-DTN: LB0307DSTTHCR2.001

NOTE: Negative values indicate a net porosity reduction resulting from mineral precipitation, and positive values indicate a net porosity increase resulting from mineral dissolution.

Figure 7.1-40. Change in Fracture Porosity after Four Years of Heating

As discussed in the preceding section, several factors are responsible for the modeled increased mineral volume changes in fractures. The increase in aqueous silica concentrations from the addition of opal as a starting mineral phase, changes in the thermodynamic data, a reduction of the initial fracture porosity to 0.0085 from 0.01, and the improved-mass balance formulation at the boiling front in TOUGHREACT V3.0 (LBNL 2002 [161256]) are all contributing factors.

Changes in matrix porosity after four years of heating are shown in Figure 7.1-41. Reductions in matrix porosity are limited solely to the dryout zone where mineral precipitation accompanied boiling of the *in situ* pore water. Increases in matrix porosity are actually greater than the

reductions and are evident throughout the condensation zones, where imbibition of dilute water must have led to mineral dissolution. Areas of strong fracture drainage around the outer edges of the heated zone apparently led to the highest level of matrix imbibition and mineral dissolution in the matrix. The porosity increase in the matrix is, however, approximately two orders of magnitude less than the porosity decrease in the fractures.

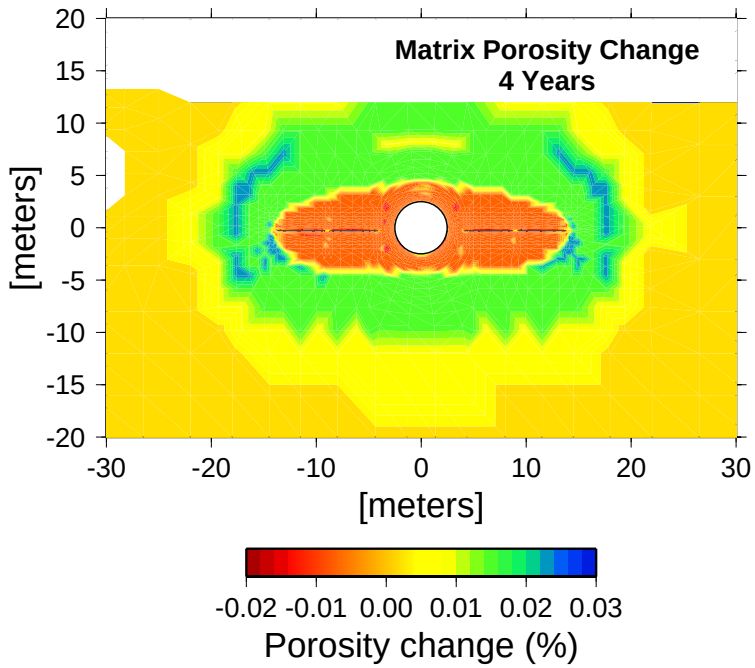

Output-DTN: LB0307DSTTHCR2.001

NOTE: Negative values indicate a net porosity reduction resulting from mineral precipitation, and positive values indicate a net porosity increase resulting from mineral dissolution.

Figure 7.1-41. Change in Matrix Porosity after Four Years of Heating

Fracture permeability changes resulting from mineral precipitation and dissolution are tied to changes in porosity and more directly to fracture aperture changes. Changes in fracture porosity of less than 1% of the original value would have a correspondingly small effect on fracture permeability. These results are consistent with the observations of minimal changes in air permeability during the DST, which have been attributed predominantly to water saturation changes (mostly in the condensation zones, where mineral precipitation is negligible) (BSC 2002 [160771], p. 6.3-15).

7.1.14 Isotopic Compositions of Gases and Water: Model Corroboration Using ^{14}C in CO_2

Gas-phase CO_2 concentrations and stable isotopic ratios ($\delta^{13}C$, $\delta^{18}O$, δD, and ^{14}C) were measured from gases pumped from hydrology boreholes (BSC 2002 [160771], Table 6.3.4.2-1). For the gas-phase compositions, direct comparisons of model results have been made only to CO_2 concentrations. Isotopic ratios of carbon ($\delta^{13}C$), oxygen ($\delta^{18}O$), and hydrogen (δD) are sensitive to fractionation effects between the liquid and gas phases as well as to diffusive fractionation, owing to the differing masses of the isotopes. Thus, they are useful in interrogating

thermal-hydrological transport processes. These fractionation effects are pronounced at lower temperatures, such that the relatively minor extent of water-rock interaction is strongly masked. Thus, they are less useful for directly investigating mineral alteration during the DST.

Relative to the stable carbon isotopes (^{12}C and ^{13}C), carbon-14 (^{14}C) abundances are minimally affected by fractionation because their activities vary over a large range, owing to the geologically short time for the radioactive decay of this species ($t_{1/2} \approx 5{,}000$ years). The virtual lack of ^{14}C in carbonate minerals at Yucca Mountain (because these materials are predominantly tens of thousands to millions of years old) allows for a sensitive indicator of the dissolution of calcite. Fortuitously, ^{14}C activities in the gas phase in the rock, at approximately the level of the Tptpmn unit, are close to 0.5 (fraction modern carbon) for several measurements done in different areas (BSC 2002 [160247], Table 20 (p. I-39), Figure 44 (p. II-46)). The convention "fraction modern carbon" refers to the activity of ^{14}C prior to atmospheric testing of nuclear weapons. Thus, the present-day activity of atmospheric ^{14}C is somewhat greater than one, because of the addition of ^{14}C through weapons testing. In the subsurface at Yucca Mountain, therefore, any addition of atmospheric CO_2 to the rock gas will drive its ^{14}C activity from about 0.5 towards 1.0, whereas dissolution of calcite will drive the activity to close to zero.

Measured ^{14}C activities in CO_2 from several hydrology borehole intervals (BH74-3, BH75-3, BH76-3, and BH78-3) are shown in Figure 7.1-42 over much of the heating phase of the DST. Unfortunately, an initial, unperturbed gas sample was not analyzed; however, the earliest samples collected had ratios around 0.4. All of the zones show a significant drop-off over time to values below 0.2 and several to around 0.1 or less. By projecting the trajectories of these early slopes back to time zero, the zones appear to converge to an initial activity close to 0.5. Note that all of the samples analyzed from rock gas (over 40 measurements) had activities below 0.5. Two measurements of gas from the Heated Drift (taken after about 12 and 44 months) were also analyzed and show nearly identical values of about 0.98, which is almost entirely atmospheric in composition. Thus, it is clear that the gas in the Heated Drift is exchanging freely with the atmosphere, even though the pore water in the rock is generating abundant CO_2 with low ^{14}C activities.

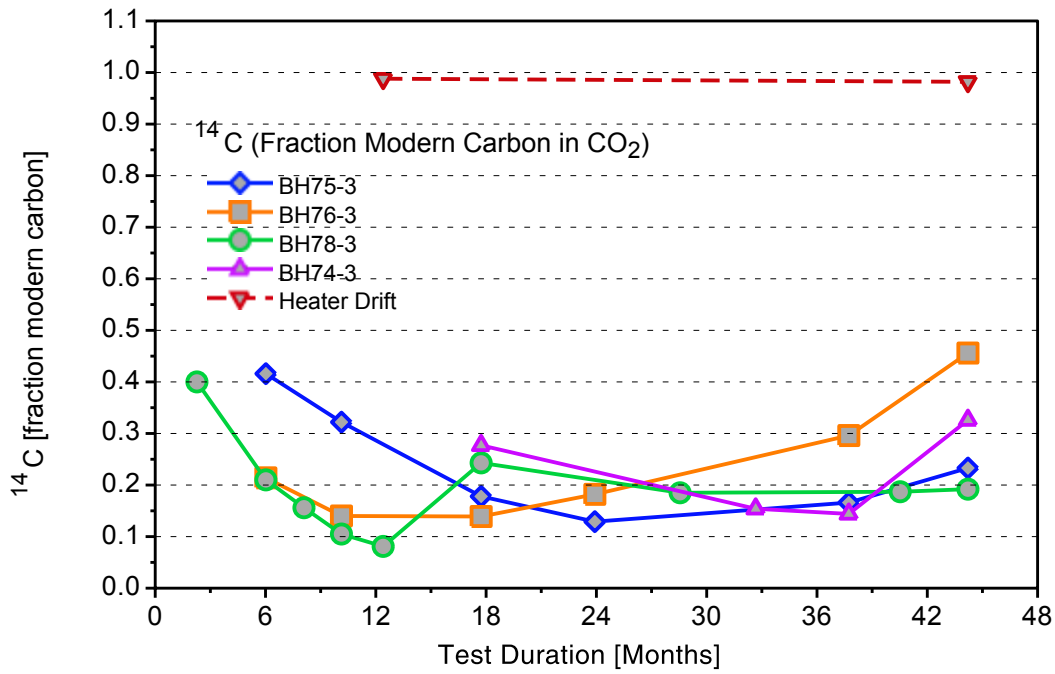

Source: BSC 2002 [160771], Table 6.3.4.2-1.

NOTE: Two samples collected from the Heater Drift were also analyzed.

Figure 7.1-42. Measured Activities of ^{14}C (Expressed as a Fraction of Modern Carbon) in CO_2 from Gas Collected in Several Hydrology Boreholes over Most of the Heating Phase of the DST

It can be concluded from these data that little atmospheric CO_2 has affected the CO_2 in the rock gas. Although atmospheric gas has undoubtedly been introduced into the system through gas-permeability testing and drilling, the relatively low CO_2 concentration in atmospheric air (≈ 400 ppmv) compared to the ambient rock gas (≈ 1,000 ppmv) and to the large concentrations generated during heating (> 10,000 ppmv) make atmospheric contamination of CO_2 more difficult.

The strong drop-off of ^{14}C in the gas over time is caused primarily by the dissolution of calcite having little or no ^{14}C. The pore water could also be heterogeneous with respect to ^{14}C, the interiors of the matrix blocks having "older" water than the exterior. The latter explanation, though, is implausible, owing to the rapid diffusivity of CO_2 in the gas phase in the unsaturated matrix and the rapid equilibration of CO_2 with bicarbonate in the aqueous phase. Furthermore, this possibility is not supported by the gradual return in all of the measured borehole intervals to higher ^{14}C activities. Finally, ^{14}C activities as low as 0.08 have not been observed in the gas phase in the UZ at Yucca Mountain and would imply isolated water with ages of close to 15,000 years.

Another aspect to the trend in ^{14}C activities can be found by examining their relation to the CO_2 in the gas phase. The abundance of ^{14}C in the gas is governed by the equilibrium between HCO_3^- in the water and CO_2 in the gas phase. Under closed conditions, the gas should be in equilibrium with the water. This is assumed in modeling the CO_2 concentrations in the DST, where there is excellent correspondence between modeled and measured values. The overall trend in ^{14}C activities seen in Figure 7.1-42 is inversely related to the changes in CO_2 concentrations

observed in these intervals. The timing of the peak in CO_2 concentration and the low in ^{14}C activity is also very close (see Figure 7.1-11). A comparison of measured CO_2 (corrected for water-vapor removal) and ^{14}C is shown for three borehole intervals in Figure 7.1-43. It is apparent that at the highest CO_2 concentrations reached in each zone, the ^{14}C activities are also among the lowest.

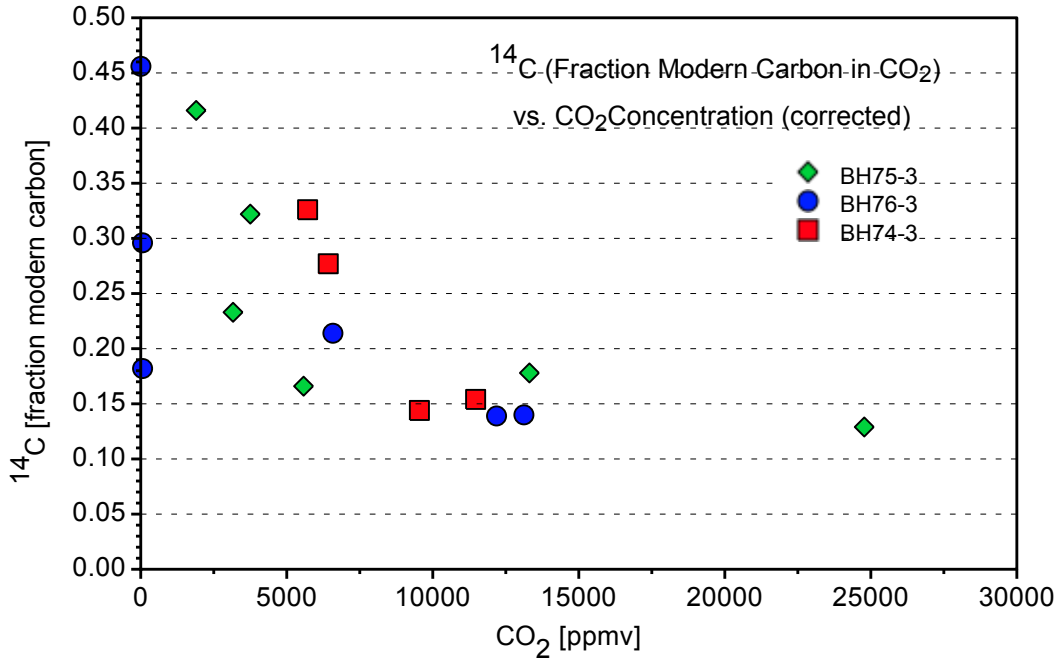

Source: BSC 2002 [160771], Table 6.3.4.2-1.

Figure 7.1-43. Measured Activities of ^{14}C (Expressed as a Fraction of Modern Carbon) Compared to Measured CO_2 (Corrected for Water Vapor Removal) from Gas Collected in Some Hydrology Boreholes over Most of the Heating Phase of the DST

The peak in CO_2 concentrations observed in the model results, and in the measured values, takes place at temperatures of close to 60°C, well below boiling and prior to the dilution of the gas phase by significant quantities of water vapor. This temperature region is characterized by some vapor condensation (Figure 7.1-5), a lowering of pH (Figure 7.1-14), and calcite dissolution (Figures 7.1-35 and 7.1-37) in the model simulations. Therefore, the trend to low ^{14}C activities in the areas where calcite is predicted to dissolve is consistent with the model results and with the aqueous- and gas-phase chemical data that have been used to validate the model.

7.2 SIMULATION OF PLUG-FLOW REACTOR EXPERIMENT

A tuff dissolution experiment was used to test geochemical models that were developed for the DST THC and the Tptpmn and Tptpll THC seepage models. The tuff dissolution experiment was performed under isothermal elevated temperature conditions with well-constrained initial water and rock compositions. Measured water compositions of samples obtained during the duration of the experiment also allowed the evaluation of kinetically controlled reactions with time. A number of simulations were run to evaluate the sensitivity of the geochemical models to the mineral surface area, rock composition, mineral thermodynamic data, and changes to the TOUGHREACT code.

A plug-flow reactor experiment was performed as part of a study investigating mineral dissolution and precipitation (Figure 7.2-1). Topopah Spring tuff (Tptpmn) obtained from overcores from borehole ESF-TMA-TC-H-1 was crushed, sieved, and washed. Material was combined from the 75–150 μm (89%) and 150–212 μm (11%) fractions (DTN: LB0011THCDISSX.001 [153380]). Scanning electron microscope images of the tuff (Fig. 7.2-2) indicate that the actual grain sizes are smaller than the nominal sieve-size fractions, with values ranging from 30 to 180 μm (DTN: LB0011THCDISSX.001 [153380]). The crushed tuff was added to a 29.8 cm long by 7.5 cm diameter polypropylene tube. The filled tube had a measured porosity of 37.5%.

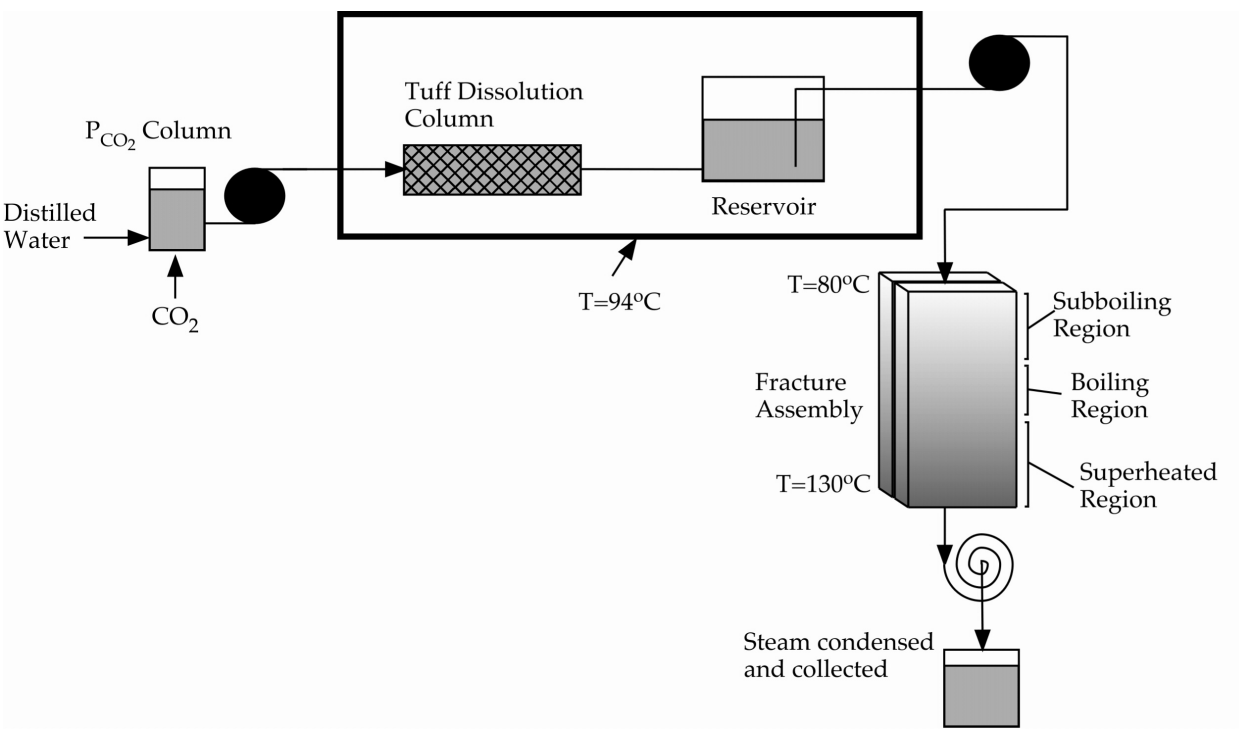

DTN: LB0101THCPRCPX.001 [154577]

Figure 7.2-1. Schematic Diagram of the Tuff Plug-Flow and Fracture Sealing Experiments

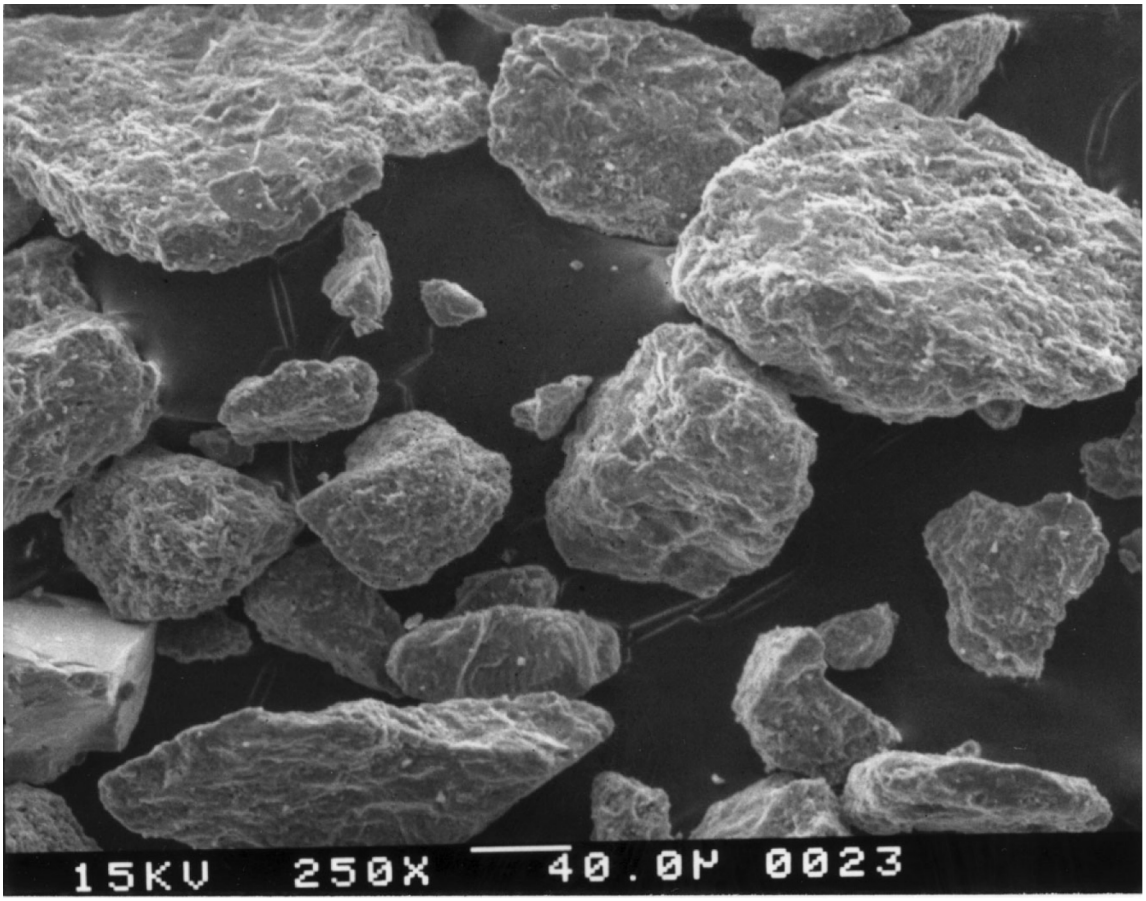

DTN: LB0011THCDISSX.001 [153380]

NOTE: The grains have a fairly wide range in diameter (30–180 μm), with irregular shapes and rough surfaces, contributing to a larger surface area per unit weight value.

Figure 7.2-2. SEM Image of Topopah Spring Tuff Grains Used for Plug-Flow Experiment

The inlet fluid consisted of deionized water initially equilibrated using a CO_2/N_2 gas mixture with 50,200 ppm CO_2 at 17°C. The resulting water had a measured pH of 4.58 (DTN: LB0011THCDISSX.001 [153380]). This water was heated to 94°C and then introduced into the tuff column (also at 94°C) at a rate of 25 mL/h. Water exiting the tuff column was collected in a reservoir and sampled periodically for chemical analysis over the length of the experiment (63.8 days). A fraction of the water exiting the tuff column was directly used in an experiment evaluating the effects of boiling on mineral dissolution and precipitation and fluid flow in a fracture. The sampled waters for the plug-flow reactor experiment were allowed to cool and equilibrate with the atmosphere at room temperature. These sampling conditions resulted in changes to the pH and bicarbonate values, because of the loss of CO_2 gas.

A series of isothermal 1-D TOUGHREACT V2.2 (LBNL 1999 [153219]) and V2.3 (LBNL 2001 [153101]) simulations were performed to model this dissolution, using a 149-element mesh, with dimensions and interface areas identical to those of the plug-flow experiment, plus one additional boundary element to obtain the appropriate outlet conditions (Dobson 2001 [160252], p. 9). The goals of these simulations were to validate the geochemical model developed for the THC

models presented in this Model Report and test the sensitivity of the simulations to changes in input parameters, such as reactive surface area and mineralogy.

Initial mineralogy used for plug-flow simulations was obtained from the Tptpmn (tsw34) matrix composition reported in Attachment I (tswm4) (DTN: LB991200DSTTHC.003 [161276]). K-smectite was not considered in simulations run using TOUGHREACT V2.3 (LBNL 2001 [153101]), consistent with the revised "extended" mineralogical system used for the Tptpll THC simulations in Section 6.5.5.2 (Table 6.2-2). The corresponding volume fraction of K-smectite was either added to illite or disregarded, as noted for each sensitivity run. An initial fluid composition was calculated (Table 7.2-1) using SOLVEQ/CHILLER V1.0 (LBNL 1999 [153217]) and the measured pH and CO_2 concentration (Dobson 2001 [160252], pp. 18–22, 45–51). Trace amounts of other dissolved constituents were used in the simulation to reduce computational problems caused by zero values. The column was assumed to be liquid-saturated, with no separate gas phase present.

Table 7.2-1. Initial Water Composition for Tuff Plug-Flow Simulations

Species	Concentration (moles/liter)	Concentration (mg/liter)
Na^+	1.000E-10	2.299E-06
K^+	1.000E-10	3.910E-06
Ca^{2+}	1.000E-10	4.008E-06
Mg^{2+}	1.000E-10	2.431E-06
HCO_3^-	1.943E-03	1.186E+02
$SiO_{2(aq)}$	1.000E-10	6.008E-06
Cl^-	1.000E-10	3.545E-06
SO_4^{2-}	1.000E-10	9.606E-06
F^-	1.000E-10	1.900E-06
AlO_2^-	1.000E-10	5.898E-06
$HFeO_{2(aq)}$	1.000E-10	8.885E-06
pH (20°C)	4.58	

DTN: LB0011THCDISSM.001 [153381]

NOTE: Bicarbonate (HCO_3^-) concentrations represent the sum of all carbonate species present.

A total column flow-through time of 19.75 hours was determined using the calculated pore volume of 493.7 cm^3 and the flow rate of 25 mL/h. This time corresponds to a flow-through time of 477 seconds per element block (Dobson 2001 [160252], pp. 10–11). The maximum time step (360 seconds) for each of the simulations was chosen to be smaller than this value. The temperature of the simulation was fixed at 94°C.

Two simulations were performed using TOUGHREACT V2.2 (LBNL 1999 [153219]), and three additional simulations were made with TOUGHREACT V2.3 (LBNL 2001 [153101]) (Table 7.2-2). Two different grain-size models were used for the TOUGHREACT V2.2 (LBNL 1999 [153219]) simulations to evaluate the sensitivity of surface-area values on kinetic mineral reactions (Dobson 2001 [160252], pp. 17–18). Because no BET (Brunauer-Emmett-Teller)

measurement data were available, simple geometric models were constructed to derive surface area to volume values for the minerals. The first simulation employed mineral surface areas calculated using spherical grains with a diameter of 60 μm, with clay minerals represented by rectangular plates having dimensions of 60 × 60 × 1.2 μm. The second simulation used spherical grains with diameters of 120 μm and clay minerals with dimensions 120 × 120 × 2.4 μm. The results of these simulations are depicted in Figures 7.2-3 (a–f).

Table 7.2-2. Summary Table of Tuff Dissolution Simulations

Run #	TOUGHREACT version	Thermodynamic database	Grain size surface area model	Thermodynamic representation of potassium feldspar	Thermodynamic representation of K-smectite
1	V2.2 [153219]	thermokapps2.05.dat *	60 μm dia.	microcline	K-smectite
2	V2.2 [153219]	thermokapps2.05.dat *	120 μm dia.	microcline	K-smectite
3	V2.3 [153101]	thermok2.07.dat †	60 μm dia.	microcline	not used
4	V2.3 [153101]	thermok2.07.dat †	60 μm dia.	K-feldspar	not used
5	V2.3 [153101]	thermok2.07.dat †	60 μm dia.	K-feldspar	illite

NOTE: * DTN: LB0101DSTTHCR1.005 [161676]
† DTN: LB0101DSTTHCR1.006 [161280]

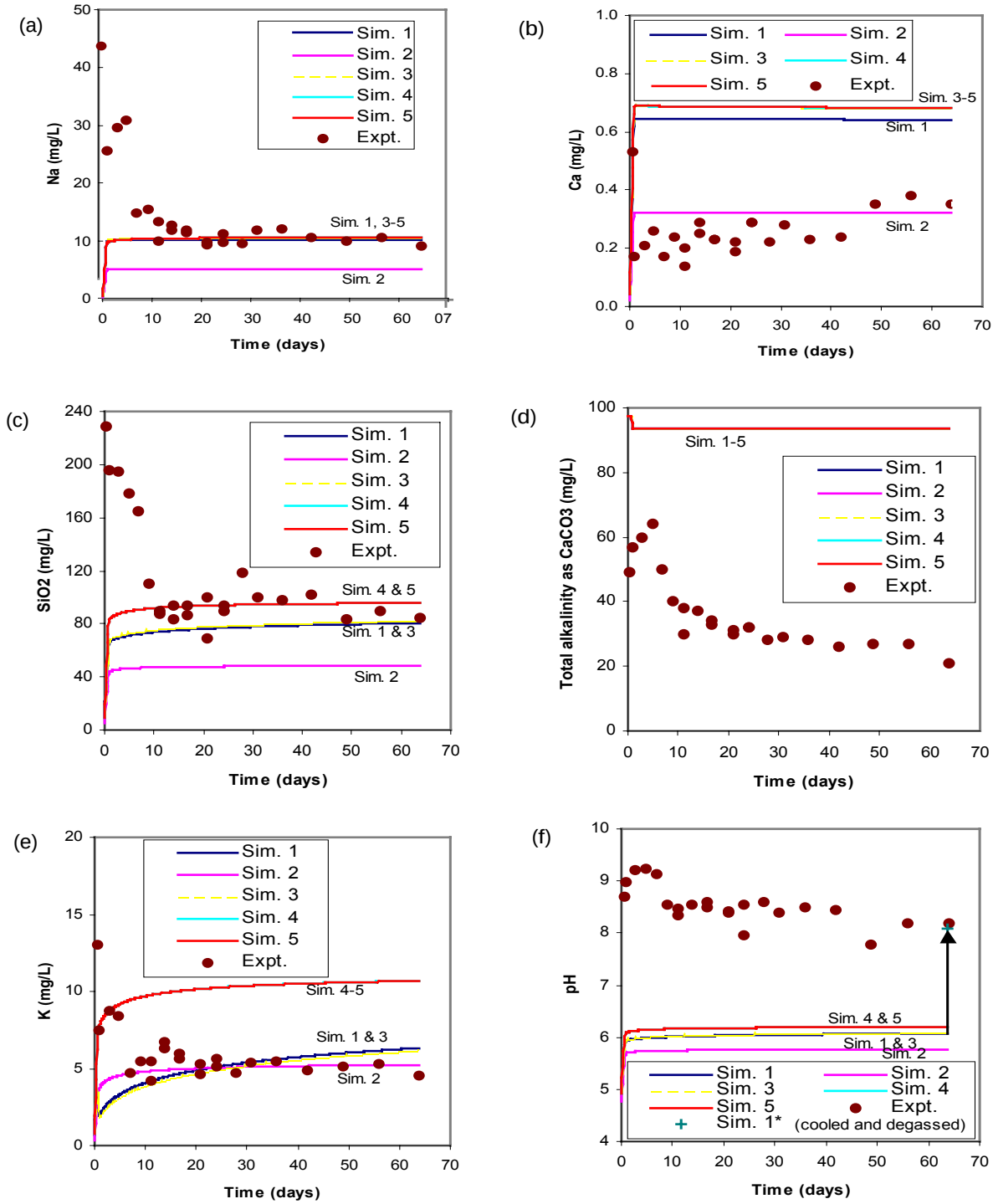

Output-DTN: LB0301PLUGFLOW.001
DTN: LB0011THCDISSX.001 [153380] (measured data)

NOTE: Plots show variations with time for Na^+ (a), Ca^{2+} (b), $SiO_{2(aq)}$ (c), total alkalinity as $CaCO_3$ (d), K^+ (e), and pH (f).

Figure 7.2-3. Comparison of Measured and Simulated Results of Tuff Dissolution Plug-Flow Experiment

7.2.1 Validation Criteria

The criteria for model validation are specified in the *Technical Work Plan for: Performance Assessment Unsaturated Zone* (BSC 2002 [160819], Attachment I, Section I-3-4-1). The model validation criterion applicable to this work is that the modeled concentrations for the major (>1 mg/L) dissolved species in the effluent should be within one order of magnitude of the measured average steady-state concentrations. This range is reasonable because chemical potential is proportional to the logarithm of activity. Discussion of uncertainty associated with coupled process (THC) modeling is presented in Section 6.9.

7.2.2 Results of Simulations and Comparison to Measured Data

The measured concentrations of all dissolved components initially increased rapidly, and then declined until about 11 days, after which relatively steady concentrations were achieved (Figure 7.2-3). The high initial measured concentrations may have resulted from the dissolution of fine tuff particles not removed in the washing process, which resulted in a much higher available reactive surface area at the start of the experiment, or from the initial mineral surfaces being more reactive because of crushing and surface roughness, none of which is accounted for in the simulations.

A comparison of the simulated compositions of the major dissolved species with the average steady-state fluid composition from the tuff dissolution experiment is presented in Table 7.2-3. All of the simulation results fall within the low- and high-bound validation criteria values. Although all of the simulations met these criteria, some of the simulations exhibited closer matches with the measured results of the plug-flow experiments (Figure 7.2-3; Dobson 2001 [160252], pp. 30–34). Large (up to 100%) differences were observed between the two grain-size models for Na^+, $SiO_{2(aq)}$, and Ca^{2+} concentrations. These variations result from the two-fold difference in calculated initial surface areas that affect the kinetic mineral reactions controlling the concentrations of these species in solution. There is a close match between the measured and calculated concentrations of Na^+ and $SiO_{2(aq)}$ for the 60 μm grain-size (larger surface area/unit volume) simulation. As a result, the surface areas corresponding to this grain-size model were used for subsequent TOUGHREACT V2.3 (LBNL 2001 [153101]) simulations of the plug-flow experiment.

Table 7.2-3. Validation of Tuff Dissolution Simulations

	Run	Na^+ (mg/L)	K^+ (mg/L)	Ca^{2+} (mg/L)	$SiO_{2(aq)}$ (mg/L)	alkalinity (mg/L $CaCO_3$)
Steady-state experimental value (average composition of 17 samples, collected between day 11 and 64)		11.1	5.3	0.26	91.8	30.2
Low bound of validation criteria		1.1	0.53	0.026	9.2	3.0
High bound of validation criteria		111	53.2	2.6	918	302
Simulation values (final compositions)	1	10.4	6.3	0.64	80.6	93.6
	2	5.3	5.2	0.32	48.4	93.6
	3	10.8	6.2	0.68	82.4	93.6
	4	10.7	10.7	0.68	95.7	93.6
	5	10.7	10.7	0.68	95.7	93.6

Source: Experimental data from LB0011THCDISSX.001 [153380]. Simulation results from Output-DTN: LB0301PLUGFLOW.001.

None of the simulation results directly fits the measured values of pH and total alkalinity. The discrepancy in pH can be attributed to the exposure of the plug-flow effluent to air and the subsequent cooling and degassing of the outflow solution before analysis. The outflow pH values match the simulated results closely after they have been corrected for these processes (using SOLVEQ/CHILLER V1.0 (LBNL 1999 [153217])) (Dobson 2001 [160252], pp. 35–38). Although the model alkalinity values are lower than the measured values, they are within the order-of-magnitude validation range as specified in Section 7.2.1.

A second set of simulations was conducted using TOUGHREACT V2.3 (LBNL 2001 [153101]) (Dobson 2001 [160252], pp. 39–44, 60). Version 2.3 of the code has various improvements related to parameters used for calculating water-rock interaction. This version also utilized a thermodynamic database (thermok2.07.dat; Attachment V) that differs in several respects from the database (thermokapps2.05.dat; BSC 2002 [158375], Attachment V) used in the TOUGHREACT V2.2 (LBNL 1999 [153219]) simulations. Other changes included modified activity coefficients, the removal of K-smectite as a mineral phase, and the incorporation of a smectite solid-solution model. Several changes were made for the TOUGHREACT V2.3 (LBNL 2001 [153101]) simulations. For all runs, smectite end members were considered as a solid solution. Different initial surface areas for minerals not initially present were used for the V2.3 (LBNL 2001 [153101]) runs as a sensitivity study on this parameter (Dobson 2001 [160252], pp. 16, 39). For two of the runs, thermodynamic data for microcline were substituted by K-spar for the potassium feldspar. The simulations also evaluated the removal of the K-smectite component from the new thermodynamic database. One simulation added the K-smectite mineral fraction to the illite component. In the other two simulations, the K-smectite fraction was simply removed from the initial composition. The 60 μm grain size model was used for all of the TOUGHREACT V2.3 (LBNL 2001 [153101]) simulations.

Several important observations can be obtained from the TOUGHREACT V2.3 (LBNL 2001 [153101]) simulations. First, TOUGHREACT V2.3 (LBNL 2001 [153101]) and its thermodynamic database produced results similar to those generated using V2.2 (LBNL 1999 [153219]). Most of the concentration profiles have steady-state compositions slightly higher than the corresponding values obtained from the TOUGHREACT V2.2 (LBNL 1999 [153219]) runs. These higher compositions result from the incorporation of the change in water density to the mineral surface area calculations in V2.3. Some of the fluid concentration profiles are more abrupt with the new simulations, perhaps because of changes in the initial precipitation rate of new secondary phases.

The model does not appear to be sensitive to small changes in illite content. This insensitivity suggests that this phase is not being dissolved during the experiment and thus does not contribute to the outflow fluid composition. However, major differences were observed for potassium when a small adjustment was made to the thermodynamic data for potassium feldspar. It is, therefore, critical to select the proper thermodynamic data for the key mineral phases that buffer the main chemical constituents in the fluid.

A number of important observations and conclusions can be derived from the tuff dissolution experiment and simulations:

- A good match was obtained between the water compositions for the observed and simulated plug-flow reactions, meeting the model validation criterion specified in Section 7.2.1.

- The simulations are sensitive to a number of parameters, including the initial mineral assemblage, the thermodynamic database used, and (most importantly) the mineral surface area.

- Minor differences in model results obtained using two versions (TOUGHREACT V2.2 (LBNL 1999 [153219]) and V2.3 (LBNL 2001 [153101])) of the TOUGHREACT code result primarily from the temperature-pressure-corrected density values of water used in the mineral surface area calculations incorporated in V2.3 (LBNL 2001 [153101]).

- Differences between the modeled and measured values in pH result from cooling and degassing of the experimental samples after exiting the tuff dissolution column. This illustrates the potential for fluid-chemistry changes during collection in samples obtained from the DST experiment (Section 7.1).

This model validation work satisfies the goals set forth in the TWP (BSC 2002 [160819], Attachment I, Section I-3-4-1), and thus no further validation work associated with the plug-flow experiment is planned.

7.3 SIMULATION OF FRACTURE SEALING EXPERIMENT

The fracture sealing experiment was designed to emulate and evaluate the effects of condensate reflux through a fracture network and into a boiling environment (Figure 7.2-1). Two saw-cut blocks of welded rhyolite ash-flow tuff, measuring 31.7 cm tall, 16.2 cm wide, and 3.2 cm thick,

were separated by 17.7 μm gold shims to create a vertical planar fracture (DTN: LB0101THCPRCPX.001 [154577]). The blocks (SPC 00540498), obtained from the Tptpmn at Alcove 6 in the ESF at Yucca Mountain, contained a small fracture, but do not have any visible lithophysal cavities (DTN: LB0101THCPRCPX.001 [154577]). The mineralogy of the tuff samples was assumed to be similar to the samples used for the tuff dissolution experiment.

The outer surfaces of the blocks were sealed with Dow Corning 1199 silicone, and the vertical sides of the fracture were sealed with an aluminum sheet coated with silicone. Polypropylene endcaps were secured to the assembly with stainless steel bands, with ports at the top and bottom to allow for the introduction of fluid at the top and collection of vapor at the base.

Heating was accomplished through the use of electrical resistance heaters mounted directly on the sides of the blocks. A vertical temperature gradient was established within the block assembly, with a temperature of 80°C at the top and 130°C at the bottom. Temperatures were monitored throughout the experiment with a series of thermocouples located at 2.7, 7.1, 11.5, 15.9, 20.3, 24.7, and 29.1 cm from the base of the blocks, and 0.6 cm from the fracture surface along the centerline of the block (DTN: LB0101THCPRCPX.001 [154577]).

The dimensions of the fracture and the temperature gradient were selected based on relations derived from Phillips (1994 [154459]; 1996 [152005]), Darcy's law, and the cubic law. A hydraulic aperture of 31 μm (DTN: LB0101THCPRCPX.001 [154577]) was calculated using the initial measured air permeability of the fracture and the relation for smooth laminar flow in a channel (permeability = aperture^2/12). The difference between this value and the gold shim thickness (17.7 μm) was attributed to surface roughness and a slight waviness in the ground-flat rock surfaces.

After steady-state chemical conditions were attained in the plug-flow reactor, a portion of the water generated from the reactor was flowed at a rate of 10.8 mL/hr into the top of the fracture (DTN: LB0101THCPRCPX.001 [154577]). After 5 days, the fracture began to seal, as evidenced by a declining outflow rate, leaks in the inlet side of the fracture, and the need for increased pressure to maintain a constant inlet flow rate. After several unsuccessful attempts to plug leaks and the near-zero rate of effluent (condensed vapor) collection, it was concluded that the aperture was effectively sealed.

After cooling, the fracture was opened and examined to determine the location and nature of secondary mineral formation. The precipitate (identified as mainly amorphous silica from SEM x-ray analyses and visual and petrographic examination) was deposited almost exclusively at temperatures exceeding 100°C (Figure 7.3-1). The morphology of the precipitate differed as a function of temperature, as described in Table 7.3-1. Bridging structures of amorphous silica that formed during the experiment in both the saw-cut fracture and a natural fracture (Figure 7.3-2) appear to obstruct fluid flow within the fracture system. Similar precipitate morphologies for secondary opal-A deposited on fracture and borehole surfaces were noted at the Single Heater Test site (CRWMS M&O 1999 [129261], Sections 6.4.3.1 and 6.4.5).

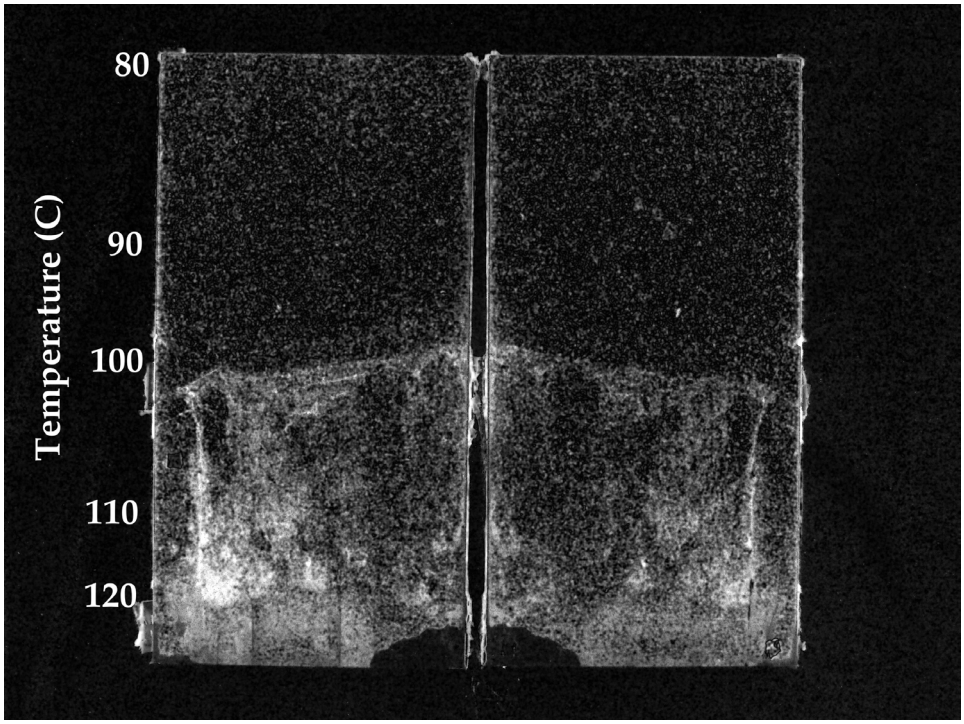

DTN: LB0101THCPRCPX.001 [154577]

NOTE: Enhanced image shows fracture temperature profile and fluorescing precipitate (light shades) under ultraviolet illumination on both fracture faces. Vertical dimension is 0.317 m.

Figure 7.3-1. Opened Fracture Faces at Conclusion of Fracture Sealing Experiment

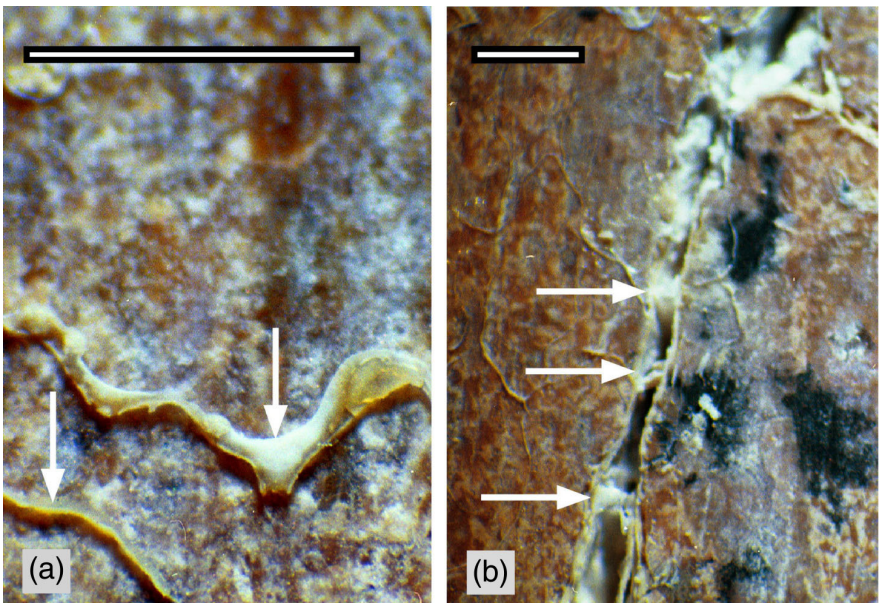

DTN: LB0101THCPRCPX.001 [154577]

NOTE: Scale bars are 0.5 mm.

Figure 7.3-2. Bridging Structures (Identified with Arrows) (a) Extending Outward from Flat Fracture Face; (b) Spanning Aperture in Cross-Cutting Natural Fracture

Table 7.3-1. Characteristics of Fracture Precipitate

Temperature range	Textural characteristics
Sub-boiling	Sparse, fine-grained precipitate
~ 100°C	Solid, well-formed bridging structures Some light wall coating
~ 110°C	Vitreous, wall-coating precipitate with bridging structures
~ 120°C	Very porous, veiny, honeycomb-like bridging structures

Source: Kneafsey et al. 2001 [154460].

Fracture sealing occurred after 5 days, with only a relatively small fraction (1.2–4.7%) of the total fracture porosity filled with solid precipitate (consisting primarily of amorphous silica). These estimates are based on dividing the total volume of dissolved solids (precipitated)—carried by (1) the volume of effluent collected and (2) the volume of water injected into the top of the fracture—by the initial fracture volume (Wang 2003 [161665], SN-LBNL-SCI-190-V2, p. 73). The difference between input and output fluid volumes results from (1) leakage occurring during the later stages of the experiment and (2) filling of matrix porosity within the tuff blocks.

TOUGHREACT V2.4 (LBNL 2001 [160880]) simulations were performed to model fracture sealing, using a mesh configuration with dimensions (in one dimension) identical to those of the tuff fracture experiment. The objectives of these simulations were to validate the geochemical model developed for the THC models presented in this Model Report and test the sensitivity of the simulations to using kinetic versus equilibrium thermodynamic controls for the precipitation and dissolution of amorphous silica (thermodynamic data taken from Attachment V (DTN: LB0101DSTTHCR1.006 [161280]); kinetic data are summarized in Table 6.4-3). Assuming symmetry, only one half of the system was modeled. The mesh design contains two columns of rock blocks and one column of fracture blocks, with each column consisting of 317 elements having a fixed height of 1 mm. The cells of the outermost rock block have fixed temperatures to approximate the experimental temperature gradient (80–130°C). The simulations had a maximum time step of 0.333 s. Fluid with a composition (Table 7.3-2) based on the average composition of the plug-flow reactor effluent (DTN: LB0011THCDISSX.001 [153380]) was injected into the uppermost fracture element. The lowermost fracture element was assigned a very large ($>10^{50}$ m^3) volume to act as a constant pressure and temperature boundary. The initial rock mineralogy was considered to be the same as that used in the plug-flow experiment (the Tptpmn (tsw34) matrix composition reported in Attachment I (DTN: LB991200DSTTHC.003 [161276]). The initial fracture permeability was set to that obtained in the experiment (8.03×10^{-11} m^2: DTN: LB0101THCPRCPX.001 [154577]), whereas the flow rate and fracture width were reduced in half (5.4 mL/h and 15.5 μm, respectively) to account for the assumption of symmetry. To simplify the simulation, the rock matrix blocks were assigned a zero permeability value to force the injected water to flow though and interact only with the fracture elements. Thus, the matrix elements served only as a heat transport mechanism. Different simulations were run for a period of 5.8 days (500,000 s) with amorphous silica controlled by either equilibrium or kinetic conditions. The cubic law was used to specify the relation between porosity and permeability. The results of these simulations are depicted in Figures 7.3-3 (a) and (b).

Table 7.3-2. Initial Water Composition for Fracture Sealing Simulations

Species	Concentration (moles/liter)	Concentration (mg/liter)
Na^+	4.75E-04	10.92
K^+	1.38E-04	5.40
Ca^{2+}	5.64E-06	0.23
Mg^{2+}	1.00E-10	0.00000243
HCO_3^-	3.17E-04	19.34
SiO_2	1.53E-03	92.22
AlO_2^-	1.00E-10	0.00000590
$HFeO_2$	1.00E-10	0.00000889
pH	8.32	

Source: Average of Frac Pump samples from DTN: LB0011THCDISSX.001 [153380].

NOTE: Nominal concentrations (1.00E-10 mol/L) were assigned to species that were below detection in the experimental study. HCO_3^- was estimated assuming a 1:1 molar correspondence with calcite alkalinity. This value should have been 2:1 (2 moles of bicarbonate per mole of calcite) to maintain milliequivalence (see text for discussion).

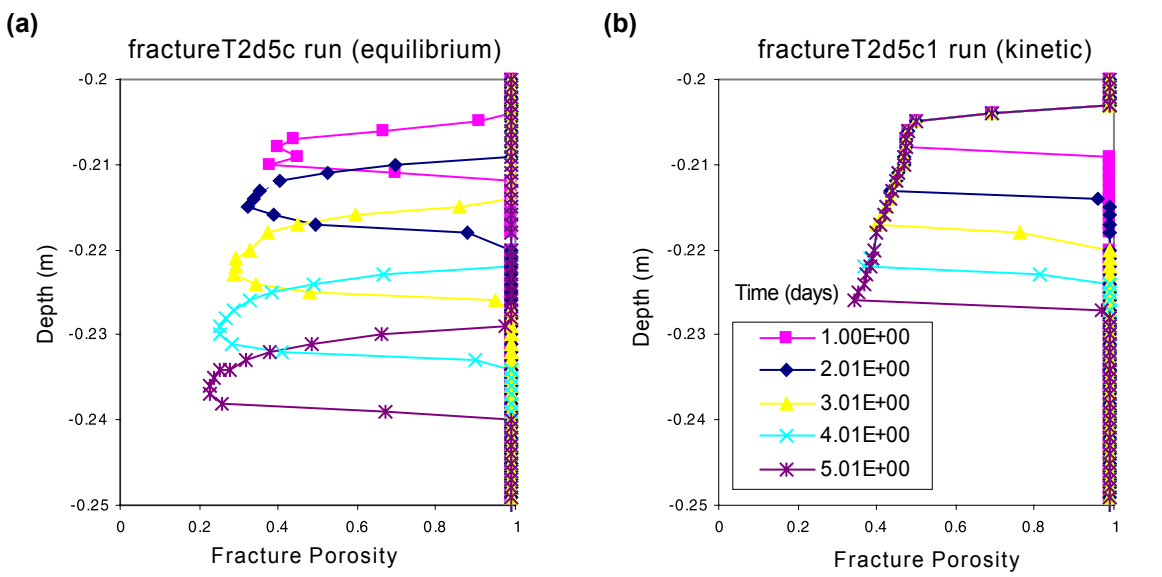

Output-DTN: LB0301FRACSEAL.002

NOTE: Area plotted represents lower portion of two-phase zone (see Figure 7.3-4).

Figure 7.3-3. Porosity vs. Depth over Time for Simulated (a) Equilibrium and (b) Kinetic Control of Amorphous Silica in Fracture Sealing Experiment

7.3.1 Validation Criteria

The criteria for model validation are specified in the *Technical Work Plan for: Performance Assessment Unsaturated Zone* (BSC 2002 [160819], Attachment I, Section I-3-4-1). The model validation criteria applicable for the fracture sealing experiment are that the distribution of precipitated minerals should be qualitatively similar to experimental observations, and that the major solid constituents should be the same. These criteria were deemed reasonable because they capture the two main observed results of the experiments: the location of the precipitate, and its mineralogy. Discussion of uncertainty associated with coupled process (THC) modeling is presented in Section 6.9.

7.3.2 Results of Simulations and Comparison to Measured Data

The simulation results indicated the formation of a nearly isothermal two-phase region (Figure 7.3-4), with an overlying water column below and a vapor zone below. The precipitation of amorphous silica at the base of the two-phase zone accounted for all of the porosity and permeability reduction in the fracture system. A gradual pressure buildup, caused by the reduction of the fracture aperture, occurred at the top of the fracture system, resulting in a downward shift in the base of the boiling zone (and region of silica precipitation) over time. The experimental system experienced a similar phenomena, as reduced permeability led to the need for higher inlet pressure to sustain a constant injection rate, resulting in fluid leaking out along the sides and top of the fracture system.

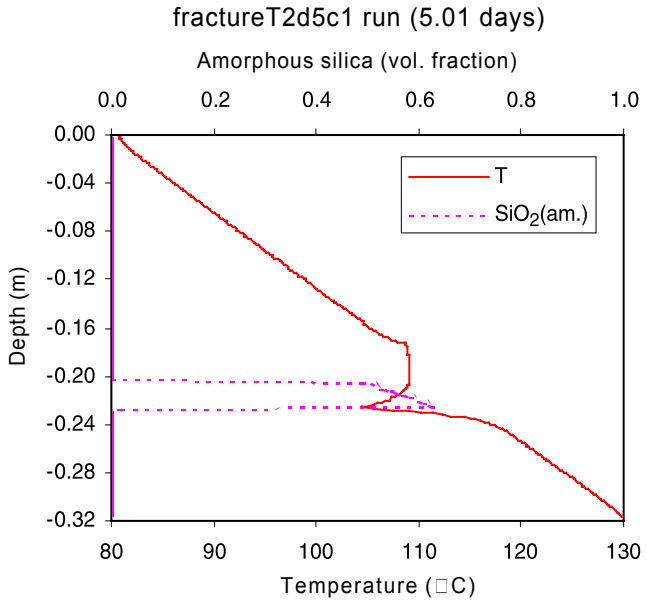

Output-DTN: LB0301FRACSEAL.002

NOTE: Simulation has amorphous silica controlled by kinetic precipitation and dissolution.

Figure 7.3-4. Simulated Temperature Profile and Volume Fraction of Amorphous Silica vs. Depth at 5.01 Days

The thickness and location of the silica precipitation zone were different in the kinetic and equilibrium simulations (Figures 7.3-3 (a and b)). The simulations conducted using equilibrium precipitation and dissolution for amorphous silica showed the effects of both precipitation and dissolution, as the trailing (upper) edge of the silica front underwent dissolution with time. In the kinetic simulations, almost no dissolution of precipitated amorphous silica occurred, resulting in a thicker band of silica that occluded less of the fracture aperture. The maximum porosity and permeability reduction (for a given fracture element) was greater for the equilibrium simulation, with a 79% porosity reduction and a permeability reduction of over 99% over the 5.8-day simulation. The kinetic simulation had maximum porosity and permeability reductions of 66% and 96%, respectively.

Significant permeability reductions occurred within 5 days after initiation of fluid flow for both the experiment and the simulations. The presence of silica precipitate throughout the boiling zone in the experimental fracture system suggests that the kinetic simulation (which retains early-formed precipitate) is a more appropriate match to the experimental results. Some of the differences between the experiment and the simulations may result from variability in the two-dimensional fracture surface in the experiment.

Both of the simulations met the validation criteria relating to the distribution and type of secondary mineral precipitation. Amorphous silica was the dominant secondary mineral phase in both the experiment and simulations. The simulated amorphous silica precipitation was restricted to the lower portion of the two-phase zone, at temperatures of around 105–109°C (Figures 7.3-3 (a and b) and 7.3-4), consistent with the observed pattern of mineralization along the fracture surface in the experiment (Figure 7.3-1). At 5 days, the total fracture-porosity-reduction values resulting from silica precipitation in the equilibrium and kinetic simulations were 2.2 and 3.9 percent, respectively, comparable to the calculated values of 0.9–3.6% total-fracture-porosity reduction resulting from silica mineralization during the experiment (Wang 2003 [161665], SN-LBNL-SCI-190-V2, p. 73). Even though the fracture permeability at the conclusion of the experiment was not measured, the observed near-cessation of fluid flow through the fracture after 5 days indicates a significant reduction in fracture permeability. The minimum simulated permeability values at 5 days of 9.65×10^{-13} m^2 and 3.39×10^{-12} m^2 for the equilibrium and kinetic experiments, respectively, represent permeability reductions of 99% and 96%.

This model validation work satisfies the goals set forth in the TWP (BSC 2002 [160819], Attachment I, Section I-3-4-1), and thus no further validation work associated with the fracture sealing experiment is planned.

8. CONCLUSIONS

This Model Report documents the THC Seepage Model (Sections 4 and 6), the Drift Scale Test (DST) THC Model (Sections 4, 6, and 7.1), and experimental studies to validate various aspects of the models (Sections 7.2 and 7.3). The models describe coupled THC processes at the drift scale to assess (1) the chemistry of water and gas potentially entering drifts and (2) changes in permeability and flow around drifts. The THC Seepage Model was used primarily to predict the composition of waters and gases around and potentially seeping into waste emplacement drifts and the effect of water-rock interaction on flow. Key findings of this model are summarized in Figure 8-1. The DST THC Model was used primarily to validate the THC Seepage Model.

The underlying conceptual and mathematical models (Sections 6.1–6.4) provide the basis for modeling the thermal and hydrological effects of the relevant mineral-water-gas reactions and transport processes in the host rock for 100,000 years. Results are presented to evaluate the sensitivity of the models to different input parameters and conceptualizations. Validation of the models (Section 7) is accomplished through comparison of simulation results to data collected from the DST and to laboratory experiments that explore various specific aspects of the models. Validation of the models was also accomplished through publication in a refereed journal (Xu et al. 2001 [161864]). Model results have been submitted to the Technical Data Management System (TDMS) as output under DTNs listed in Section 9.4 and Attachment X of this Model Report. Applicable acceptance criteria from the YMRP addressed by this report are discussed in Section 4.2 with pointers referring to sections of this report where these criteria are addressed. The barrier capability of the natural system, including host rocks and the capillary barrier effects of drift openings, are considered throughout this report (e.g., Sections 6.8.2 and 6.8.5.2). Potential barrier effects from mineral precipitation during the normal period are also considered (Section 6.8.5.4).

8.1 MODELED COUPLED PROCESSES AND UNCERTAINTY

Simulations of THC processes include coupling among heat, water, and vapor flow, aqueous and gaseous species transport, kinetic and equilibrium mineral-water reactions, and feedback of mineral precipitation/dissolution on porosity, permeability, and capillary pressure for a dual-permeability (fracture-matrix) system. Treatment of CO_2 included gas-water equilibration, gas species diffusion, and advection. Data were incorporated from the calibrated thermal-hydrological property sets, the three-dimensional mineralogical model, the UZ Flow and Transport Model, thermal test geochemical data (fracture and matrix mineralogy, aqueous geochemistry, and gas chemistry), thermodynamic data (minerals, gases, and aqueous species), kinetic data for mineral-water reactions, and transport (diffusion coefficient) data (Section 4.1). The models include a wide range of major and minor aqueous species and minerals (primary and potential secondary phases). The following primary aqueous species are considered: H^+, Ca^{2+}, Mg^{2+}, Na^+, K^+, $SiO_{2(aq)}$, AlO_2^-, $HFeO_{2(aq)}$, SO_4^{2-}, HCO_3^-, Cl^-, NO_3^-, and F^-. Minerals include several silica phases (α-cristobalite, quartz, tridymite, amorphous silica, and opal-CT), calcite, feldspars, smectites, illite, kaolinite, sepiolite, zeolites, fluorite, hematite, goethite, gypsum, and volcanic (rhyolitic) glass. In addition to the calibration of the hydrological properties, some thermodynamic and kinetic data were revised (within their ranges of uncertainty) to yield modeled pore water compositions (under ambient temperatures and infiltration rates) close to the original measured values over long simulation times.

Many uncertainties exist in modeling coupled THC processes (see Section 6.9), because of the large amount of input data needed and the complexity of natural systems as described above and in Sections 4, 6, and 7. Therefore, a quantitative measure of model uncertainty based on the uncertainties of the data themselves is difficult. Model validation provides a better test of whether the system can be described sufficiently well for the intended purposes of the model. Validation was accomplished through analyses of the DST, plug-flow reactor experiments, and fracture sealing experiments performed under temperatures, pressures, and chemical compositions corresponding to the range expected for the repository thermal loading conditions and drift design. As summarized further in this section, results of DST THC simulations captured the important changes in pH, aqueous species concentrations, gas-phase CO_2 concentrations, and mineral deposition at specific locations over time. This provides sufficient validation of the model's capability to predict trends of spatial and temporal variations in water and gas chemistry around emplacement drifts. However, the duration of the heating phase of the DST (approximately 4 years) is short compared to the time over which the repository drifts would be above-boiling (at least one thousand years). Therefore, the DST THC Model and data from the DST cannot be used to directly validate all aspects of THC Seepage Model predictions of water chemistry, gas compositions, and permeability over very long times.

Several simulations were performed to further characterize the effects of natural variability and uncertainty on the THC Seepage Model predictions. These sensitivity analyses address the follow major issues:

1. Different repository host-rock geologic units (Tptpmn and Tptpll)
2. Alternative geochemical systems (base case and extended case, additional minerals and chemical components)
3. Alternative thermodynamic data sets (different equilibrium constants for key minerals)
4. Different treatments of mineral-water reactions (different kinetic rate constants and reactive surface areas; equilibrium vs. kinetic reactions)
5. Spatial heterogeneity in fracture permeability
6. Different infiltration rates and effects of climate change
7. Alternative water vapor pressure models
8. Alternative initial water compositions
9. Different effective CO_2 diffusivities
10. Alternative drift-wall conceptualizations (open vs. closed to liquid flow).

These THC Seepage Model simulations covered a wide range of the most important uncertainties from the standpoint of model validation, bounding analyses, conservatism, their impact on model results, and their propagation to other models. Based on the natural variability in input water composition and the resulting spread in simulation results, the uncertainties in predicted concentrations of aqueous species and of CO_2 gas are estimated to be up to about one order of magnitude (Section 6.9.2), with implications for downstream use examined below in Section 8.4.

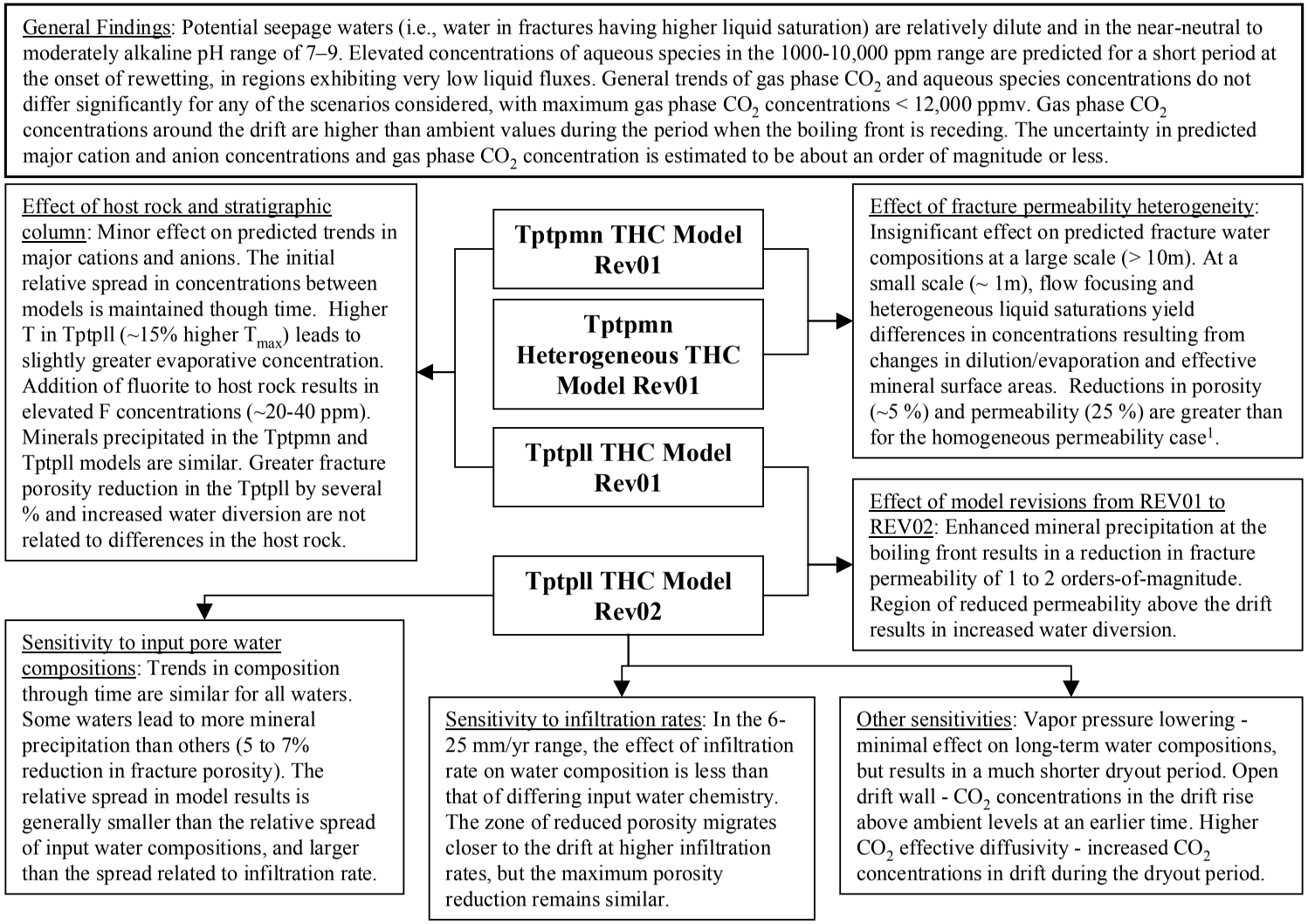

[1] The heterogeneous case was run using REV01 hydrological properties and with TOUGHREACT V2.3 [153101]. The use of REV02 properties and TOUGHREACT V3.0 [161256] resulted in greater reductions in porosity and permeability for the homogeneous permeability case, which would also be expected for the heterogeneous case.

Figure 8-1. Key Findings of the THC Seepage Model

8.2 THC SEEPAGE MODEL RESULTS

The THC Seepage Model was designed to represent waste package heating over time, changes in heat load caused by ventilation, the effective heat transfer within the drift, and THC processes in the unsaturated zone around waste emplacement drifts. Simulations considered an initial heat load of 1.45 kW/m, including a preclosure period of 50 years using two alternative ventilation efficiencies (70% and 86.3%). Model results predict the chemistry of matrix and fracture water at various locations around a drift, the times of rewetting around the drifts, and the net fluxes of water and gas near and across the drift wall for a period of 100,000 years.

The scope of this Model Report includes essentially one design heat load, resulting in temperatures near emplacement drifts that exceed the boiling point of water for several hundred years after repository closure. Temperature is a critical parameter because it strongly affects the extent of water-rock-gas interaction taking place around proposed emplacement drifts. In the cases considered here, increased water-rock-gas interaction resulting from higher temperatures is expected to affect water chemistry and flow to a greater extent than if a lower heat load were considered. The predicted extent of the dryout zone and the time of rewetting vary with the different infiltration rates and water-vapor pressure models considered. Depending on the modeled scenario, the maximum extent of the dryout zone in fractures was predicted to be between 6 and 10 m above drift center, and the predicted time of fracture rewetting at the drift crown varied between 1,200 and 2,000 years in most cases. In one case using REV02 rock properties and neglecting the effect of vapor-pressure lowering caused by capillary suction, rewetting was predicted to occur much later (i.e., between 12,000 and 20,000 years).

Similar trends in water and gas compositions were predicted for modeled cases with heat loading in the Tptpmn and in the Tptpll geologic units. At any point in time, the relative spread in predicted water compositions spatially above the drift, including alternative model conceptualizations and five different input water compositions, was generally one order of magnitude or less (Section 6.9.2). Thus, in a qualitative sense, this spread is small. However, in a quantitative sense, this same spread would be significant for parameters for which small variations in concentrations could have a large impact on the calculated end-brine compositions upon near-complete evaporation of seepage waters. For example, only slight variations in the predicted relative amounts of calcium and bicarbonate could yield different end-brine compositions, and thus lead to different scenarios regarding waste package corrosion. Recognizing this possibility, simulations employed a range of input water compositions likely to yield predicted percolation waters evolving towards a representative range of possible end-brine types (Section 6.2.2.1). Model uncertainties unrelated to input water compositions could still affect predicted percolation water compositions in a way that would also affect conclusions regarding end-brine compositions.

In general, when modeling a geochemical system without aluminum silicate minerals and glass, the predicted pH values were somewhat lower and CO_2 concentrations higher than in simulations including these phases. Clearly, the effect of mineral-water reactions on the geochemistry of waters and gases is strongly influenced by the presence of clays and zeolite minerals and very sensitive to the choice of thermodynamic properties for these minerals. Sodium concentrations under ambient conditions were predicted to increase by a factor of approximately four in 100,000 years (from the dissolution of mostly albite and glass), which could be somewhat greater than

would be expected in the natural system. In this respect, simulations including aluminosilicate minerals could provide an upper limit on effects of water-rock-gas interactions around waste emplacement drifts. In all of the modeled conceptualizations, including five representative input water compositions, relatively dilute and near-neutral to moderately alkaline water compositions were predicted in fractures around drifts, with pH values in the 7–9 range and gas-phase CO_2 concentrations remaining below 12,000 ppmv. General trends of CO_2 gas and aqueous species concentrations around the drifts did not differ significantly for any of the cases. The simulations also exhibited an increase in the CO_2 gas concentrations around the drifts during rewetting, relative to ambient values. Elevated concentrations of aqueous species relative to background values were predicted to occur temporarily at the time of rewetting in fractures, though at very low liquid saturations.

The predicted magnitude of fracture porosity change caused by water-rock interaction around waste emplacement drifts depends strongly on the initial fracture porosity (with the largest relative change for the smallest porosity), and results in large part from mineral precipitation directly at the boiling front due to evaporative concentration. Simulations carried out for REV02 of this Model Report (Section 6.8) considered a more accurate treatment of mineral precipitation at the boiling front than in REV01. For this reason, and because fracture porosity was reduced by a factor of two in the Tptpll unit compared to that used in previous Model Report revisions, a significant fracture porosity change (up to nearly 8%) was predicted compared to the results of REV01 simulations (around 1% or less fracture porosity change). As a result, the REV02 simulations predicted a significant effect of water-gas-rock interactions on flow patterns around the drift, whereas simulations from the previous revision (REV01) of this Model Report did not. REV02 simulations exhibit a thin zone of predominantly amorphous silica deposition several meters above the drift wall that reduces the percolation flux at the drift wall. This zone has a fracture permeability that is one to two orders of magnitude lower than in the surrounding rock fractures, deflecting some of the percolating water around the drift and significantly extending the shadow zone below the drift. Because the silica solubility decreases with declining temperature, the amorphous silica precipitated in fractures does not dissolve significantly into percolating water over 100,000 years.

REV01 simulations incorporated several permeability realizations for the Tptpmn unit THC Seepage Model. Steady-state (ambient temperature), TH, and THC simulations were performed using three heterogeneous fracture permeability realizations with a 4-order-of-magnitude range in permeability. All were run using the mean infiltration climate change scenario for the Tptpmn unit. The heterogeneity in fracture permeability can have varied effects on thermohydrology, including flow focusing and irregularities in the isotherms and liquid saturations. Areas of highest initial liquid saturation, also having lower permeability and generally residing above the drift, tend to show the greatest reduction in fracture permeability as a result of mineral precipitation. The effect of this localized permeability reduction tends to cause some additional flow focusing. The permeability changes (up to 25%) are considerably less than the initial range in permeability. These REV01 simulations used higher fracture porosities than those for REV02 and did not incorporate the more accurate treatment of mineral precipitation at the boiling front implemented in TOUGHREACT V3.0 (LBNL 2002 [161256]). Therefore, the REV01 simulations produced a smaller effect of mineral precipitation on fracture sealing than if REV02 properties and processes were implemented. Spatial differences in water chemistry were not affected significantly by permeability heterogeneities, and because of the strong control of the

mineral assemblage on water chemistry (and not the mineral proportions) this would also be expected to be the case if REV02 properties were used.

8.3 DST THC MODEL RESULTS (VALIDATION)

Validation of the overall approach and data embodied in the Drift Scale THC conceptual model described in this Model Report was accomplished via a comparison of measured gas compositions, water chemistry, and analyses of mineral deposition in the Drift Scale Test (DST) to DST THC Model simulation results. The DST THC Model was not expected to exactly match measurements from the DST, and the validation work combined both sensitivity studies as well as straight comparisons to measured data.

Comparisons between observed and modeled aqueous pH and CO_2 concentrations in the gas phase indicate that a limited set of aqueous species, minerals (calcite, silica phases, fluorite, and gypsum), and gases (H_2O, air, and CO_2) (base case), could describe the general evolution of DST waters with respect to pH, CO_2, and conservative anions. A more complete geochemical system (extended case), including a wide range of aluminosilicates (such as feldspars, clays and zeolites), yielded modeled aqueous silica concentrations closer to those observed, plus information on additional species (i.e., Mg^{2+}, Al^{3+}, and Fe^{3+}). However, predicted pH values for the extended system are slightly higher than those observed, and gas-phase CO_2 concentrations are slightly lower than the measured values.

In particular, simulation results compared to measured gas-phase CO_2 concentrations and the chemistry of waters collected from hydrology boreholes indicate that the model captures the general trend in concentrations in the borehole intervals where comparisons were made. Predicted locations and relative abundances of secondary minerals were consistent with *in situ* sidewall core samples retrieved from zones that had undergone boiling. The main phase was amorphous silica followed by significantly lesser amounts of calcite and gypsum. REV01 TH properties resulted in a better match for the conservative species and fluoride, because of the greater rate of condensate dilution compared to that produced using the REV02 properties. However, REV02 modeled aqueous silica concentrations were more consistent with the measured values, owing to the revised geochemical system (in particular, the addition of opal to the initial mineral assemblage). Analyses of ^{14}C concentrations in CO_2 also corroborated the model results, because of their sensitivity to calcite dissolution and drift air contamination.

The evidence based on numerous field and laboratory measurements, demonstrates that model validation criteria were met for CO_2 concentrations in gas, for several aqueous species concentrations, and for mineral precipitation in fractures. Although some disagreements between modeled and measured values exist, they could generally be attributed to sampling difficulties or the addition of a phase (such as fluorite) in the REV02 mineral assemblage that clearly made the agreement worse than for REV01. These differences, though, highlight the sensitivity of the model to various input parameters. Some heterogeneities in the measured data could not be matched by the model results, as would be expected in the comparison of an idealized model system. Although the model did not include heterogeneity in hydrological properties, and is only a 2-D representation of a 3-D system the agreement to much of the measured data gives confidence in the approach and use of “average” properties.

Confidence in various aspects of the model approach and input data used in the THC Seepage Model is also based on a comparison of modeled and measured water compositions from a laboratory plug-flow dissolution experiment using volcanic tuff from the Tptpmn unit at Yucca Mountain. The model simulations captured the magnitude and change in aqueous species concentrations measured during this experiment at elevated temperatures, and thus the validation criteria were met. A fracture sealing laboratory experiment was also simulated, with the location and amounts of amorphous silica precipitated closely comparable to that observed, also meeting the validation criteria.

The THC responses of the Yucca Mountain Drift Scale Test were independently analyzed by the participants of the DECOVALEX III project, an international research project to develop coupled models and their validation against experiments. The outcome of the analyses by the DECOVALEX participants, generally corroborative of the contents of this Model Report, are to be presented in the GeoProc2003 conference to be held in Stockholm, Sweden, and will be published in a special issue of the *International Journal of Rock Mechanics*.

8.4 UNCERTAINTIES AND RESTRICTIONS FOR DOWNSTREAM USE

Section 1.3 states the general model limitations. Potential uncertainties affecting model results were discussed in a qualitative manner in Section 6.9-1, and addressed more quantitatively in Section 6.9-2. Various alternative conceptualizations and ranges of input data were considered (summarized in Section 8.1; see also Table 6-1). In addition, confidence in the model results was obtained by comparing model results to experimental data from the DST (Section 7.1 and summarized in Section 8.3) and other laboratory experiments (Sections 7.2 and 7.3). Much of the spread in the output compositions from the THC Seepage Model simulations is caused by the natural variability of input water compositions. This spread is up to about one order of magnitude and in many cases lower (for pH, within less than a pH unit; Section 6.9-2). As mentioned in Section 8.2, this margin of uncertainty could be problematic for aqueous species for which small differences in concentrations (by much less than one order of magnitude) could upon evaporation have a large impact on calculated end-brine compositions (e.g., calcium and bicarbonate) because of small changes in their concentration ratios. On the other hand, the input data and model conceptualizations considered in this study all yield similar trends in modeled aqueous species and gas-phase CO_2 concentrations over time. Therefore, it is essential for each downstream user to carefully evaluate the results presented here in light of the level of certainty required.

INTENTIONALLY LEFT BLANK

9. INPUTS AND REFERENCES

The following is a list of the references cited in this document. Column 1 represents the unique six digit numerical identifier (the Document Input Reference System [DIRS] number), which is placed in the text following the reference callout (e.g., BSC 2002 [160819]). The purpose of these numbers is to assist the reader in locating a specific reference. Within the reference list, multiple sources by the same author (e.g., BSC 2002) are sorted alphabetically by title.

9.1 DOCUMENTS CITED

153329 Arnórsson, S. and Stefánsson, A. 1999. "Assessment of Feldspar Solubility Constants in Water in the Range 0° to 350°C at Vapor Saturation Pressures." *American Journal of Science*, *299*, (3), 173-209. New Haven, Connecticut: Yale University, Kline Geology Laboratory. TIC: 249258.

101379 Bear, J. 1988. *Dynamics of Fluids in Porous Media*. New York, New York: Dover Publications. TIC: 217568.

155950 BSC (Bechtel SAIC Company) 2001. *FY 01 Supplemental Science and Performance Analyses, Volume 1: Scientific Bases and Analyses*. TDR-MGR-MD-000007 REV 00 ICN 01. Las Vegas, Nevada: Bechtel SAIC Company. ACC: MOL.20010801.0404; MOL.20010712.0062; MOL.20010815.0001.

156065 BSC (Bechtel SAIC Company) 2001. *In-Drift Precipitates/Salts Analysis*. ANL-EBS-MD-000045 REV 00 ICN 03. Las Vegas, Nevada: Bechtel SAIC Company. ACC: MOL.20011212.0252.

164414 BSC (Bechtel SAIC Company) 2001. *Software Baseline Request for LBNL-2000-242, TOUGHREACT V. 2.3*. 10396-2.3-00. Las Vegas, Nevada: Bechtel SAIC Company. ACC: MOL.20020123.0010.

160247 BSC (Bechtel SAIC Company) 2002. *Analysis of Geochemical Data for the Unsaturated Zone*. ANL-NBS-HS-000017 REV 00 ICN 02. Las Vegas, Nevada: Bechtel SAIC Company. ACC: MOL.20020314.0051.

158375 BSC (Bechtel SAIC Company) 2002. *Drift-Scale Coupled Processes (DST and THC Seepage) Models*. MDL-NBS-HS-000001 REV 01 ICN 02. Las Vegas, Nevada: Bechtel SAIC Company. ACC: MOL.20020312.0156.

159124 BSC (Bechtel SAIC Company) 2002. *Geologic Framework Model (GFM2000)*. MDL-NBS-GS-000002 REV 01. Las Vegas, Nevada: Bechtel SAIC Company. ACC: MOL.20020530.0078.

159906 BSC (Bechtel SAIC Company) 2002. *Invert Effective Thermal Conductivity Calculation*. 000-00C-WIS0-00100-000-00A. Las Vegas, Nevada: Bechtel SAIC Company. ACC: MOL.20020828.0178.

159527 BSC (Bechtel SAIC Company) 2002. *Repository Design, Repository/PA IED Subsurface Facilities Plan Sht. 1 of 5, Sht. 2 of 5, Sht. 3 of 5, Sht. 4 of 5, and Sht. 5 of 5*. DWG-MGR-MD-000003 REV A. Las Vegas, Nevada: Bechtel SAIC Company. ACC: MOL.20020601.0194.

160819 BSC (Bechtel SAIC Company) 2002. *Technical Work Plan for: Performance Assessment Unsaturated Zone*. TWP-NBS-HS-000003 REV 02. Las Vegas, Nevada: Bechtel SAIC Company. ACC: MOL.20030102.0108.

160771 BSC (Bechtel SAIC Company) 2002. *Thermal Testing Measurements Report*. ANL-NBS-HS-000041 REV 00. Las Vegas, Nevada: Bechtel SAIC Company. ACC: MOL.20021004.0314.

160146 BSC (Bechtel SAIC Company) 2002. *Total System Performance Assessment-License Application Methods and Approach*. TDR-WIS-PA-000006 REV 00. Las Vegas, Nevada: Bechtel SAIC Company. ACC: MOL.20020923.0175.

164454 BSC (Bechtel SAIC Company) 2002. *Users Manual (UM) for TOUGHREACT V3.0*. 10396-UM-3.0-00. Las Vegas, Nevada: Bechtel SAIC Company. ACC: MOL.20030411.0090.

161760 BSC (Bechtel SAIC Company) 2002. *Ventilation Model Repor*t. ANL-EBS-MD-000030 REV 02. Las Vegas, Nevada: Bechtel SAIC Company. ACC: MOL.20030102.0140.

160975 BSC (Bechtel SAIC Company) 2002. *Ventilation Model*. ANL-EBS-MD-000030 REV 01 ICN 01. Las Vegas, Nevada: Bechtel SAIC Company. ACC: MOL.20021106.0055.

160109 BSC (Bechtel SAIC Company) 2003. *Development of Numerical Grids for UZ Flow and Transport Modeling*. ANL-NBS-HS-000015 REV 01. Las Vegas, Nevada: Bechtel SAIC Company. ACC: DOC.20030404.0005.

161530 BSC (Bechtel SAIC Company) 2003. *Drift-Scale Coupled Processes (DST and TH Seepage) Models*. MDL-NBS-HS-000015 REV 00. Las Vegas, Nevada: Bechtel SAIC Company. URN-1087

161519 BSC (Bechtel SAIC Company) 2003. *Interlocking Drip Shield*. 000-MW0-TED0-00101-000-00A, -00102-000-00A, and -00103-000-00A. 3 Sheets. Las Vegas, Nevada: Bechtel SAIC Company. ACC: ENG.20030205.0001; ENG.20030205.0002; ENG.20030205.0003.

164053 BSC (Bechtel SAIC Company) 2003. *Repository Design Project, RDP/PA IED Typical Waste Package Components Assembly 1 of 9*. 800-IED-WIS0-00201-000-00A. Las Vegas, Nevada: Bechtel SAIC Company. ACC: ENG.20030702.0001.

164052 BSC (Bechtel SAIC Company) 2003. *Repository Design Project, Repository/PA IED Emplacement Drift Committed Materials 1 of 2*. 800-IED-WIS0-00301-000-00A. Las Vegas, Nevada: Bechtel SAIC Company. ACC: ENG.20030627.0003.

162444 BSC (Bechtel SAIC Company) 2003. *Repository Design Project, Repository/PA IED Emplacement Drift Committed Materials*. 800-IED-EBS0-00301-000-00A. Las Vegas, Nevada: Bechtel SAIC Company. ACC: ENG.20030311.0022.

164069 BSC (Bechtel SAIC Company) 2003. *Repository Design Project, Repository/PA IED Emplacement Drift Configuration 1 of 2*. 800-IED-EBS0-00201-000-00A. Las Vegas, Nevada: Bechtel SAIC Company. ACC: ENG.20030630.0002.

161727 BSC (Bechtel SAIC Company) 2003. *Repository Design, Repository/PA IED Subsurface Facilities*. 800-IED-EBS0-00402-000-00B. Las Vegas, Nevada: Bechtel SAIC Company. ACC: MOL.20030109.0146.

161731 BSC (Bechtel SAIC Company) 2003. *Repository Design, Repository/PA IED Subsurface Facilities*. 800-IED-EBS0-00403-000-00B. Las Vegas, Nevada: Bechtel SAIC Company. ACC: MOL.20030109.0147.

100617 Buscheck, T.A. and Nitao, J.J. 1993. "Repository-Heat-Driven Hydrothermal Flow at Yucca Mountain, Part I: Modeling and Analysis." *Nuclear Technology, 104*, (3), 418-448. La Grange Park, Illinois: American Nuclear Society. TIC: 224039.

161770 Canori, G.F. and Leitner, M.M. 2003. *Project Requirements Document*. TER-MGR-MD-000001 REV 01. Las Vegas, Nevada: Bechtel SAIC Company. ACC: DOC.20030404.0003.

105210 Carlos, B.A.; Chipera, S.J.; Bish, D.L.; and Craven, S.J. 1993. "Fracture-Lining Manganese Oxide Minerals in Silicic Tuff, Yucca Mountain, Nevada, U.S.A." *Chemical Geology, 107*, 47-69. Amsterdam, The Netherlands: Elsevier. TIC: 208629.

124275 Carroll, S.; Mroczek, E.; Alai, M.; and Ebert, M. 1998. "Amorphous Silica Precipitation (60 to 120°C): Comparison of Laboratory and Field Rates." *Geochimica et Cosmochimica Acta, 62*, (8), 1379-1396. New York, New York: Elsevier. TIC: 243029.

111115 CRWMS M&O (Civilian Radioactive Waste Management System Management and Operating Contractor) 1998. *Drift Scale Test As-Built Report*. BAB000000-01717-5700-00003 REV 01. Las Vegas, Nevada: CRWMS M&O. ACC: MOL.19990107.0223.

129261 CRWMS M&O 1999. *Single Heater Test Final Report*. BAB000000-01717-5700-00005 REV 00 ICN 1. Las Vegas, Nevada: CRWMS M&O. ACC: MOL.20000103.0634.

123916 CRWMS M&O 2000. *Abstraction of Drift-Scale Coupled Processes*. ANL-NBS-HS-000029 REV 00. Las Vegas, Nevada: CRWMS M&O. ACC: MOL.20000525.0371.

151951 CRWMS M&O 2000. *Engineered Barrier System: Physical and Chemical Environment Model*. ANL-EBS-MD-000033 REV 01. Las Vegas, Nevada: CRWMS M&O. ACC: MOL.20001228.0081.

144454 CRWMS M&O 2000. *Mountain-Scale Coupled Processes (TH) Models*. MDL-NBS-HS-000007 REV 00. Las Vegas, Nevada: CRWMS M&O. ACC: MOL.19990721.0528.

149137 CRWMS M&O 2000. *Repository Subsurface Design Information to Support TSPA-SR*. Input Transmittal PA-SSR-99218.Tc. Las Vegas, Nevada: CRWMS M&O. ACC: MOL.20000424.0690.

151014 CRWMS M&O 2000. *Tabulated In-Drift Geometric and Thermal Properties Used in Drift-Scale Models for TSPA-SR*. CAL-EBS-HS-000002 REV 00. Las Vegas, Nevada: CRWMS M&O. ACC: MOL.20000718.0219.

120903 CRWMS M&O 2000. *Ventilation Model*. ANL-EBS-MD-000030 REV 00. Las Vegas, Nevada: CRWMS M&O. ACC: MOL.20000107.0330.

153814 CRWMS M&O 2001. *Updated CO2 Analysis of Gas Samples Collected from the Drift Scale Test*. Input Transmittal 00423.T. Las Vegas, Nevada: CRWMS M&O. ACC: MOL.20010202.0170.

100439 de Marsily, G. 1986. *Quantitative Hydrogeology: Groundwater Hydrology for Engineers*. San Diego, California: Academic Press. TIC: 208450.

160252 Dobson, P. 2001. Evaluation of Local Altered Hydraulic Characteristics and the Effects of Near Field Thermal and Chemical Alterations (YMP-LBNL-DSM-ELS-PD-1). Scientific Notebook SN-LBNL-SCI-190-V1. ACC: MOL.20010521.0134.

135997 Doughty, C. 1999. "Investigation of Conceptual and Numerical Approaches for Evaluating Moisture, Gas, Chemical, and Heat Transport in Fractured Unsaturated Rock." *Journal of Contaminant Hydrology, 38*, (1-3), 69-106. New York, New York: Elsevier. TIC: 244160.

140067 Drever, J.I. 1997. *The Geochemistry of Natural Waters, Surface and Groundwater Environments*. 3rd Edition. Upper Saddle River, New Jersey: Prentice Hall. TIC: 246732.

117799 Ehrlich, R.; Etris, E.L.; Brumfield, D.; Yuan, L.P.; and Crabtree, S.J. 1991. "Petrography and Reservoir Physics III: Physical Models for Permeability and Formation Factor." *AAPG Bulletin, 75*, (10), 1579-1592. Tulsa, Oklahoma: American Association of Petroleum Geologists. TIC: 246294.

154365 Freeze, G.A.; Brodsky, N.S.; and Swift, P.N. 2001. *The Development of Information Catalogued in REV00 of the YMP FEP Database*. TDR-WIS-MD-000003 REV 00 ICN 01. Las Vegas, Nevada: Bechtel SAIC Company. ACC: MOL.20010301.0237.

160460 Fridriksson, T.; Neuhoff, P.S.; Arnórsson, S.; and Bird, D.K. 2001. "Geological Constraints on the Thermodynamic Properties of the Stilbite—Stellerite Solid Solution in Low-Grade Metabasalts." *Geochimica et Cosmochimica Acta, 65*, (21), 3993-4008. [New York, New York]: Elsevier. TIC: 253460.

144877 Garrels, R.M. and Christ, C.L. 1990. *Solutions, Minerals, and Equilibria*. Boston, Massachusetts: Jones and Barlett Pulishers. TIC: 223483.

160465 Gunnarsson, I. and Arnórsson, S. 2000. "Amorphous Silica Solubility and the Thermodynamic Properties of H{subscript 4}SiOº{subscript 4} in the Range of 0º to 350ºC at P{subscript sat}." *Geochimica et Cosmochimica Acta, 64*, (13), 2295-2307. [New York, New York]: Elsevier. TIC: 250506.

160900 Haukwa, C. 2001. Unsaturated Zone Modeling & Synthesis-Intermediate UZ Modeling (YMP-LBNL-GSB-1.6.4). Scientific Notebook SN-LBNL-SCI-085-V2. ACC: MOL.20020204.0074.

106024 Helgeson, H.C.; Kirkham, D.H.; and Flowers, G.C. 1981. "Theoretical Prediction of the Thermodynamic Behavior of Aqueous Electrolytes at High Pressures and Temperatures: IV. Calculation of Activity Coefficients, Osmotic Coefficients, and Apparent Molal and Standard and Relative Partial Molal Properties to 600ºC and 5 kb." *American Journal of Science, 281*, (10), 1249-1516. New Haven, Connecticut: Yale University, Kline Geology Laboratory. TIC: 238264.

145636 Kneafsey, T.J. and Pruess, K. 1998. "Laboratory Experiments on Heat-Driven Two-Phase Flows in Natural and Artificial Rock Fractures." *Water Resources Research, 34*, (12), 3349-3367. Washington, D.C.: American Geophysical Union. TIC: 247468.

154460 Kneafsey, T.J.; Apps, J.A.; and Sonnenthal, E.L. 2001. "Tuff Dissolution and Precipitation in a Boiling, Unsaturated Fracture." *"Back to the Future - Managing the Back End of the Nuclear Fuel Cycle to Create a More Secure Energy Future," Proceedings of the 9th International High-Level Radioactive Waste Management Conference (IHLRWM), Las Vegas, Nevada, April 29-May 3, 2001*. La Grange Park, Illinois: American Nuclear Society. TIC: 247873.

128132 Kulik, D.A. and Aja, S.U. 1997. "The Hydrothermal Stability of Illite: Implications of Empirical Correlations and Gibbs Energy Minimization." *Proceedings of the Fifth International Symposium on Hydrothermal Reactions, Gatlinburg, Tennessee, July 20-24, 1997*. Palmer, D.A. and Wesolowski, D.J., eds. Pages 288-292. Oak Ridge, Tennessee: Oak Ridge National Laboratory. TIC: 247217.

100051 Langmuir, D. 1997. *Aqueous Environmental Geochemistry*. Upper Saddle River, New Jersey: Prentice Hall. TIC: 237107.

117091 Lasaga, A.C. 1998. *Kinetic Theory in the Earth Sciences*. Princeton, New Jersey: Princeton University Press. TIC: 246279.

126599 Levy, S.S.; Fabryka-Martin, J.T.; Dixon, P.R.; Liu, B.; Turin, H.J.; and Wolfsberg, A.V. 1997. "Chlorine-36 Investigations of Groundwater Infiltration in the Exploratory Studies Facility at Yucca Mountain, Nevada." *Scientific Basis for Nuclear Waste Management XX, Symposium held December 2-6, 1996, Boston, Massachusetts*. Gray, W.J. and Triay, I.R., eds. *465*, 901-908. Pittsburgh, Pennsylvania: Materials Research Society. TIC: 238884.

123032 Lide, D.R., ed. 1993. *CRC Handbook of Chemistry and Physics*. 74th Edition. Boca Raton, Florida: CRC Press. TIC: 209252.

162470 Liu, H-H.; Haukwa, C.B.; Ahlers, C.F.; Bodvarsson, G.S.; Flint, A.L.; and Guertal, W.B. 2003. "Modeling Flow and Transport in Unsaturated Fractured Rock: An Evaluation of the Continuum Approach." *Journal of Contaminant Hydrology, 62-63*, 173-188. New York, New York: Elsevier. TIC: 254205.

105729 Liu, H.H.; Doughty, C.; and Bodvarsson, G.S. 1998. "An Active Fracture Model for Unsaturated Flow and Transport in Fractured Rocks." *Water Resources Research, 34*, (10), 2633-2646. Washington, D.C.: American Geophysical Union. TIC: 243012.

161130 Mercury, L. and Tardy, Y. 2001. "Negative Pressure of Stretched Liquid Water. Geochemistry of Soil Capillaries." *Geochimica et Cosmochimica Acta, 65,* (20), 3391-3408. [New York, New York]: Elsevier. TIC: 253758.

163274 NRC (U.S. Nuclear Regulatory Commission) 2003. *Yucca Mountain Review Plan, Final Report*. NUREG-1804, Rev. 2. Washington, D.C.: U.S. Nuclear Regulatory Commission, Office of Nuclear Material Safety and Safeguards. TIC: 254568.

154459 Phillips, O.M. 1994. "Liquid Infiltration Through the Boiling-Point Isotherm in a Desiccating Fractured Rock Matrix." *High Level Radioactive Waste Management, Proceedings of the Fifth Annual International Conference, Las Vegas, Nevada, May 22-26, 1994. 4*, 2189-2196. La Grange Park, Illinois: American Nuclear Society. TIC: 210984.

152005 Phillips, O.M. 1996. "Infiltration of a Liquid Finger Down a Fracture into Superheated Rock." *Water Resources Research, 32*, (6), 1665-1670. [Washington, D.C.]: American Geophysical Union. TIC: 239025.

101699 Pokrovskii, V.A. and Helgeson, H.C. 1995. "Thermodynamic Properties of Aqueous Species and the Solubilities of Minerals at High Pressures and Temperatures: The System Al2O3-H2O-NaCl." *American Journal of Science, 295*, 1255-1342. New Haven, Connecticut: Yale University, Kline Geology Laboratory. TIC: 236803.

144794 Pruess, K. 1997. "On Vaporizing Water Flow in Hot Sub-Vertical Rock Fractures." *Transport in Porous Media, 28*, (3), 335-372. Boston, Massachusetts: Kluwer Academic Publishers. TIC: 238922.

144801 Pruess, K.; Tsang, Y.W.; and Wang, J.S.Y. 1984. *Numerical Studies of Fluid and Heat Flow Near High-Level Nuclear Waste Packages Emplaced in Partially Saturated Fractured Tuff*. LBL-18552. Berkeley, California: Lawrence Berkeley Laboratory. TIC: 211033.

100818 Pruess, K.; Wang, J.S.Y.; and Tsang, Y.W. 1990. "On Thermohydrologic Conditions Near High-Level Nuclear Wastes Emplaced in Partially Saturated Fractured Tuff, 1. Simulation Studies with Explicit Consideration of Fracture Effects." *Water Resources Research, 26*, (6), 1235-1248. [Washington, D.C.]: American Geophysical Union. TIC: 221923.

117901 Reed, M.H. 1982. "Calculation of Multicomponent Chemical Equilibria and Reaction Processes in Systems Involving Minerals, Gases and an Aqueous Phase." *Geochimica et Cosmochimica Acta, 46*, (4), 513-528. New York, New York: Pergamon Press. TIC: 224159.

101709 Rimstidt, J.D. 1997. "Quartz Solubility at Low Temperatures." *Geochimica et Cosmochimica Acta, 61*, (13), 2553-2558. New York, New York: Pergamon Press. TIC: 239020.

101708 Rimstidt, J.D. and Barnes, H.L. 1980. "The Kinetics of Silica–Water Reactions." *Geochimica et Cosmochimica Acta, 44*, 1683-1699. [New York, New York]: Pergamon Press. TIC: 219975.

107109 Robie, R.A.; Hemingway, B.S.; and Fisher, J.R. 1979. *Thermodynamic Properties of Minerals and Related Substances at 298.15 K and 1 Bar (10{superscript 5} Pascals) Pressure and at Higher Temperatures*. U.S. Geological Survey Bulletin 1452. Washington, D.C.: U.S. Government Printing Office. TIC: 230505.

154862 Rosenberg, N.D.; Gdowski, G.E.; and Knauss, K.G. 2001. "Evaporative Chemical Evolution of Natural Waters at Yucca Mountain, Nevada." *Applied Geochemistry, 16*, ([9-10]), 1231-1240. [New York, New York]: Pergamon. TIC: 249879.

128146 Slider, H.C. 1976. *Practical Petroleum Reservoir Engineering Methods, An Energy Conservation Science*. Tulsa, Oklahoma: Petroleum Publishing Company. TIC: 247798.

117127 Sonnenthal, E.L. and Bodvarsson, G.S. 1999. "Constraints on the Hydrology of the Unsaturated Zone at Yucca Mountain, NV from Three-Dimensional Models of Chloride and Strontium Geochemistry." *Journal of Contaminant Hydrology, 38*, (1-3), 107-156. New York, New York: Elsevier. TIC: 244160.

160898 Spycher, N. 2001. Drift Scale Modeling (YMP-LBNL-DSM-NS-1). Scientific Notebook SN-LBNL-SCI-141-V1. ACC: MOL.20011017.0003.

101480 Steefel, C.I. and Lasaga, A.C. 1994. "A Coupled Model for Transport of Multiple Chemical Species and Kinetic Precipitation/Dissolution Reactions with Application to Reactive Flow in Single Phase Hydrothermal Systems." *American Journal of Science, 294*, (5), 529-592. New Haven, Connecticut: Yale University, Kline Geology Laboratory. TIC: 235372.

144878 Steefel, C.I. and Lichtner, P.C. 1998. "Multicomponent Reactive Transport in Discrete Fractures: I. Controls on Reaction Front Geometry." *Journal of Hydrology, 209*, 186-199. New York, New York: Elsevier. TIC: 247524.

153578 Stefánsson, A. and Arnórsson, S. 2000. "Feldspar Saturation State in Natural Waters." *Geochimica et Cosmochimica Acta, 64*, (15), 2567-2584. New York, New York: Elsevier. TIC: 249336.

137577 Tsang, Y.W. and Birkholzer, J.T. 1999. "Predictions and Observations of the Thermal-Hydrological Conditions in the Single Heater Test." *Journal of Contaminant Hydrology, 38*, (1-3), 385-425. New York, New York: Elsevier. TIC: 244160.

157427 Vaniman, D.T.; Chipera, S.J.; Bish, D.L.; Carey, J.W.; and Levy, S.S. 2001. "Quantification of Unsaturated-Zone Alteration and Cation Exchange in Zeolitized Tuffs at Yucca Mountain, Nevada, USA." *Geochimica et Cosmochimica Acta, 65*, (20), 3409-3433. [New York, New York]: Elsevier. TIC: 251574.

161665 Wang, J.S. 2003. "Scientific Notebooks Referenced in Model Report N0120/U0110, Drift-Scale Coupled Processes (DST and THC Seepage) Models MDL-NBS-HS-000001 REV 02." Interoffice correspondence from J.S. Wang (BSC) to File, June 6, 2003, with attachments. ACC: MOL.20030611.0079.

163765 Williams, N.H. 2003. "Contract No. DE-AC28-01RW1210 – Transmittal of White Paper, Effects of Neoprene on Water in the Drift Scale Test." Letter from N.H. Williams (BSC) to J.D. Ziegler (DOE/ORD), February 4, 2003, 0129035843, with enclosure. ACC: MOL.20030206.0211.

154279 Wilson, N.S.F.; Cline, J.S.; and Lundberg, S.A.W. 2000. "Paragenesis and Chemical Composition of Secondary Mineralization at Yucca Mountain, Nevada." *Abstracts with Programs - Geological Society of America, 32*, (7), A-260. Boulder, Colorado: Geological Society of America. TIC: 249113.

117170 Xu, T. and Pruess, K. 1998. *Coupled Modeling of Non-Isothermal Multi-Phase Flow, Solute Transport and Reactive Chemistry in Porous and Fractured Media: 1. Model Development and Validation*. LBNL-42050. Berkeley, California: Lawrence Berkeley National Laboratory. TIC: 243735.

156280 Xu, T. and Pruess, K. 2001. "Modeling Multiphase Non-Isothermal Fluid Flow and Reactive Geochemical Transport in Variably Saturated Fractured Rocks: 1. Methodology." *American Journal of Science, 301*, 16-33. [New Haven, Connecticut: Yale University, Kline Geology Laboratory]. TIC: 251482.

101751 Xu, T.; Pruess, K.; and Brimhall, G. 1998. *An Improved Equilibrium-Kinetics Speciation Algorithm for Redox Reactions in Variably Saturated Subsurface Flow Systems*. LBNL-41789. Berkeley, California: Lawrence Berkeley National Laboratory. TIC: 240019.

162124 Xu, T.; Sonnenthal, E.; and Bodvarsson, G. 2003. "A Reaction-Transport Model for Calcite Precipitation and Evaluation of Infiltration Fluxes in Unsaturated Fractured Rock." *Journal of Contaminant Hydrology, 64*, ([1-2]), 113-127. New York, New York: Elsevier. TIC: 254008.

161864 Xu, T.; Sonnenthal, E.; Spycher, N.; Pruess, K.; Brimhall, G.; and Apps, J. 2001. "Modeling Multiphase Non-Isothermal Fluid Flow and Reactive Geochemical Transport in Variably Saturated Fractured Rocks: 2. Applications to Supergene Copper Enrichment and Hydrothermal Flows." *American Journal of Science, 301*, (1), 34-59. New Haven, Connecticut: Yale University, Kline Geology Laboratory. TIC: 253949.

100194 Yang, I.C.; Rattray, G.W.; and Yu, P. 1996. *Interpretation of Chemical and Isotopic Data from Boreholes in the Unsaturated Zone at Yucca Mountain, Nevada*. Water-Resources Investigations Report 96-4058. Denver, Colorado: U.S. Geological Survey. ACC: MOL.19980528.0216.

Software Cited

153217 LBNL (Lawrence Berkeley National Laboratory) 08/29/1999. *Software Code: SOLVEQ/CHILLER*. V1.0. PC w/Windows OS. 10057-1.0-00.

153216 LBNL (Lawrence Berkeley National Laboratory) 09/17/1999. *Software Code: AMESH*. V1.0. DEC and SUN w/Unix OS. 10045-1.0-00.

153219 LBNL (Lawrence Berkeley National Laboratory) 09/21/1999. *Software Code: TOUGHREACT*. V2.2. DEC and SUN w/Unix OS. 10154-2.2-00.

153090 LBNL (Lawrence Berkeley National Laboratory) 09/22/2000. *Software Routine Report: assign.f*. V1.0. SUN w/Unix OS. 10315-1.0-00.

153089 LBNL (Lawrence Berkeley National Laboratory) 09/22/2000. *Software Routine Report: exclude.f*. V1.0. SUN w/Unix OS. 10316-1.0-00.

153087 LBNL (Lawrence Berkeley National Laboratory) 09/22/2000. *Software Routine Report: kswitch*. V1.0. SUN w/Unix OS. 10319-1.0-00.

153091 LBNL (Lawrence Berkeley National Laboratory) 09/22/2000. *Software Routine Report: merggrid2.f*. V1.0. SUN w/Unix OS. 10314-1.0-00.

153092 LBNL (Lawrence Berkeley National Laboratory) 09/22/2000. *Software Routine Report: mk_circ2*. V1.0. SUN w/Unix OS. 10312-1.0-00.

152883 LBNL (Lawrence Berkeley National Laboratory) 09/22/2000. *Software Routine: flipk*. V1.0. SUN w/Unix OS. 10320-1.0-00.

152902 LBNL (Lawrence Berkeley National Laboratory) 09/22/2000. *Software Routine: kreg*. V1.0. SUN w/Unix OS. 10318-1.0-00.

152901 LBNL (Lawrence Berkeley National Laboratory) 09/22/2000. *Software Routine: mk_incon*. V1.0. SUN w/Unix OS. 10350-1.0-00.

152900 LBNL (Lawrence Berkeley National Laboratory) 09/22/2000. *Software Routine: regress*. V1.0. PC w/Windows OS. 10321-1.0-00.

152899 LBNL (Lawrence Berkeley National Laboratory) 09/22/2000. *Software Routine: switch*. V1.0. PC w/Windows OS. 10322-1.0-00.

153068 LBNL (Lawrence Berkeley National Laboratory) 11/03/2000. *Software Routine Report: mk_grav2.f*. V1.0. SUN w/Unix OS. 10379-1.0-00.

153082 LBNL (Lawrence Berkeley National Laboratory) 11/03/2000. *Software Routine Report: mrgdrift.f*. V1.0. SUN w/Unix OS. 10380-1.0-00.

153083 LBNL (Lawrence Berkeley National Laboratory) 11/03/2000. *Software Routine Report: sav1d_dst2d.f*. V1.0. SUN w/Unix OS. 10381-1.0-00.

153218 LBNL (Lawrence Berkeley National Laboratory) 1999. *Software Code: SUPCRT92*. V1.0. PC w/Windows OS and MAC w/MAC OS. 10058-1.0-00.

153100 LBNL (Lawrence Berkeley National Laboratory) 2000. *Software Code: GSLIB*. V1.0SISIMV1.204. SUN w/Unix OS. 10397-1.0SISIMV1.204-00.

146496 LBNL (Lawrence Berkeley National Laboratory) 2000. *Software Code: TOUGH2*. V1.4. Sun Workstation and DEC/ALPHA. 10007-1.4-01.

153067 LBNL (Lawrence Berkeley National Laboratory) 2000. *Software Routine Report: 2kgridv1a.for*. V1.0. PC w/Windows OS. 10382-1.0-00.

153085 LBNL (Lawrence Berkeley National Laboratory) 2000. *Software Routine Report: avgperm.f*. V1.0. DEC & SUN w/UNIX OS. 10378-1.0-00.

153093 LBNL (Lawrence Berkeley National Laboratory) 2000. *Software Routine: mk_rect2*. V1.0. SUN w/Unix OS. 10313-1.0-00.

153101 LBNL (Lawrence Berkeley National Laboratory) 2001. *Software Code: TOUGHREACT*. V2.3. SUN and DEC w/Unix OS. 10396-2.3-00.

160880 LBNL (Lawrence Berkeley National Laboratory) 2001. *Software Code: TOUGHREACT*. V2.4. SunOS 5.5.1, Dec Alpha TRU64 Unix & OS1 V4.0. 10396-2.4-00.

161127 LBNL (Lawrence Berkeley National Laboratory) 2002. *Software Code: CUTCHEM*. V1.0. DEC ALPHA/OSF1 V5.1, PC /WINDOWS 2000/NT 4.0/98. 10898-1.0-00.

161263 LBNL (Lawrence Berkeley National Laboratory) 2002. *Software Code: DBCONV*. V1.0. PC/Windows 98/NT; DEC-Alpha/OSF1 V5.1; SunOS 5.5.1. 10893-1.0-00.

161258 LBNL (Lawrence Berkeley National Laboratory) 2002. *Software Code: KREG*. V1.1. SUN UltraSparc with Unix SunOS 5.5.1, WINDOWS 2000/NT/98, Dec Alpha with OSF1 V5.1. 10318-1.1-00.

161259 LBNL (Lawrence Berkeley National Laboratory) 2002. *Software Code: KSWITCH*. V1.1. PC with WINDOWS 2000/NT/98, Dec Alpha with OSF1 V5.1, SUN OS 5.5.1. 10319-1.1-00.

161262 LBNL (Lawrence Berkeley National Laboratory) 2002. *Software Code: THERMOCHK*. V1.1. PC/Windows 98/NT/2000; DEC-Alpha/OSF1 V5.1; SunOS 5.5.1. 10895-1.1-00.

161256 LBNL (Lawrence Berkeley National Laboratory) 2002. *Software Code: TOUGHREACT*. V3.0. DEC-Alpha with Unix OSF1 V5.1 and OSF1 V5.0, Sun Solaris 5.5.1, Linux Redhat 7.2. 10396-3.0-00.

161491 LBNL (Lawrence Berkeley National Laboratory) 2003. *Software Code: TOUGH2*. V1.6. PC/MS-DOS under Windows 98, Sun UltraSparc OS 5.5.1, DEC-Alpha OSF1 V4.0. 10007-1.6-01.

9.2 CODES, STANDARDS, REGULATIONS, AND PROCEDURES

156605 10 CFR 63. Energy: Disposal of High-Level Radioactive Wastes in a Geologic Repository at Yucca Mountain, Nevada. Readily available.

AP-2.22Q, Rev. 0, ICN 1. *Classification Criteria and Maintenance of the Monitored Geologic Repository Q-List.* Washington, D.C.: U.S. Department of Energy, Office of Civilian Radioactive Waste Management. ACC: DOC.20030422.0009.

AP-SI.1Q, Rev. 5, ICN 1. *Software Management.* Washington, D.C.: U.S. Department of Energy, Office of Civilian Radioactive Waste Management. ACC: DOC.20030708.0001.

AP-SIII.3Q, Rev. 1, ICN 2. *Submittal and Incorporation of Data to the Technical Data Management System*. Washington, D.C.: U.S. Department of Energy, Office of Civilian Radioactive Waste Management. ACC: MOL.20020701.0177.

AP-SIII.10Q, Rev. 1, ICN 2. *Models.* Washington, D.C.: U.S. Department of Energy, Office of Civilian Radioactive Waste Management. ACC: DOC.20030627.0003.

AP-SV.1Q, Rev. 0, ICN 3. *Control of the Electronic Management of Information*. Washington, D.C.: U.S. Department of Energy, Office of Civilian Radioactive Waste Management. ACC: MOL.20020917.0133.

YMP-LBNL-QIP-6.1 Rev. 8, Mod. 1. *Document Review*. Berkeley, California: Lawrence Berkeley National Laboratory. ACC: MOL.20030724.0162.

YMP-LBNL-QIP-SV.0, Rev. 2, Mod. 1. *Management of YMP-LBNL Electronic Data*. Berkeley, California: Lawrence Berkeley National Laboratory. ACC: MOL.20020717.0319.

9.3 SOURCE DATA, LISTED BY DATA TRACKING NUMBER

160899 GS020408312272.003. Collection and Analysis of Pore Water Samples for the Period from April 2001 to February 2002. Submittal date: 04/24/2002.

153485 LA0009SL831151.001. Fracture Mineralogy of the ESF Single Heater Test Block, Alcove 5. Submittal date: 09/28/2000.

158426 LA0201SL831225.001. Chemical, Textural, and Mineralogical Characteristics of Sidewall Samples from the Drift Scale Test. Submittal date: 01/10/2002.

113495 LA9908JC831321.001. Mineralogic Model "MM3.0" Version 3.0. Submittal date: 08/16/1999.

146447 LA9912SL831151.001. Fracture Mineralogy of Drill Core ESF-HD-TEMP-2. Submittal date: 01/05/2000.

146449 LA9912SL831151.002. Percent Coverage by Fracture-Coating Minerals in Core ESF-HD-TEMP-2. Submittal date: 01/05/2000.

146451 LB000121123142.003. Isotope Data for CO2 Gas Samples Collected From the Hydrology Holes of the ESF Drift Scale Test for the Period August 9, 1999 through November 30, 1999. Submittal date: 01/21/2000.

153460 LB0011CO2DST08.001. Isotope Data for CO2 from Gas Samples Collected from Hydrology Holes in Drift-Scale Test. Submittal date: 12/09/2000.

153470 LB0011DSTFRAC1.001. Drift-Scale Properties Update: 1. Updated Drift-Scale Properties. This is Input Data for AMR U0110 (MDL-NBS-HS-000001 REV01). Submittal date: 12/06/2000.

154759 LB0011DSTTHCR1.001. Tables Showing Geochemical and Drift-Scale Seepage Model Data Which are Presented in AMR U0110/N0120, "Drift-Scale Coupled Processes (DST and THC Seepage) Models REV01". Submittal date: 12/19/2000.

161282 LB0011DSTTHCR1.002. Model Input and Output Files, Excel Spreadsheets and Resultant Figures which are Presented in AMR U0110/N0120, "Drift-Scale Coupled Processes (DST and THC Seepage) Models REV 01". Submittal date: 12/19/2000.

153381 LB0011THCDISSM.001. Comparison Modeling for TPTPMN Tuff Dissolution Experiment: 1. Input Data for AMR U0110 REV01. Submittal date: 12/07/2000.

154578 LB0011THCDISSM.002. Comparison Modeling for TPTPMN Tuff Dissolution Experiment: 2. Output Data for AMR U0110 REV01. Submittal date: 12/07/2000.

153380 LB0011THCDISSX.001. Summary of Results from TPTPMN Tuff Dissolution Experiment. Submittal date: 12/07/2000.

161277 LB0101DSTTHCR1.002. Attachment II - Mineral Initial Volume Fractions for TPTPLL THC Model for AMR N0120/U0110 REV01, "Drift-Scale Coupled Processes (Drift-Scale Test and THC Seepage) Models.". Submittal date: 01/26/2001.

161278 LB0101DSTTHCR1.003. Attachment III - Mineral Reactive Surface Areas: TPTPMN and DST THC Models for AMR N0120/U0110 REV01, "Drift-Scale Coupled Processes (Drift-Scale Test and THC Seepage) Models.". Submittal date: 01/26/2001.

161279 LB0101DSTTHCR1.004. Attachment IV - Mineral Reactive Surface Areas: TPTPLL THC Model for AMR N0120/U0110 REV01, "Drift-Scale Coupled Processes (Drift-Scale Test and THC Seepage) Models.". Submittal date: 01/26/2001.

161676 LB0101DSTTHCR1.005. Attachment V-Thermodynamic Database: TPTPMN THC Backfill and DST THC REV00 Models, for AMR N0120/U0110 REV01 "Drift-Scale Coupled Processes (Drift-Scale Test and THC Seepage) Models.". Submittal date: 01/26/2001.

161280 LB0101DSTTHCR1.006. Attachment VI - Thermodynamic Database: TPTPMN THC (No Backfill) and DST THC REV01 Models for AMR N0120/U0110 REV01, "Drift-Scale Coupled Processes (Drift-Scale Test and THC Seepage) Models.". Submittal date: 01/26/2001.

161281 LB0101DSTTHCR1.007. Attachment VIII - Waste Package Average Heat Transfer: TPTPMN/TPTPLL No-Backfill and THC Models for AMR N0120/U0110 REV01, "Drift-Scale Coupled Processes (Drift-Scale Test and THC Seepage) Models.". Submittal date: 01/26/2001.

153687 LB0101DSTTHGRD.001. 2D Finite Element Mesh Used for DST THC Model Simulations (Input to AMR N0120/U0110 REV. 01). Submittal date: 01/05/2001.

154577 LB0101THCPRCPX.001. Summary of Results from TPTPMN Tuff Precipitation Experiment. Submittal date: 02/13/2001.

159306 LB0102CO2DST98.001. Concentration Data for CO2 from Gas Samples Collected from Hydrology Holes in Drift-scale Test. Submittal date: 02/28/2001.

159525 LB0205REVUZPRP.001. Fracture Properties for UZ Model Layers Developed from Field Data. Submittal date: 05/14/2002.

159672 LB0207REVUZPRP.002. Matrix Properties for UZ Model Layers Developed from Field and Laboratory Data. Submittal date: 07/15/2002.

161638 LB0208ISODSTHP.001. Isotope Data and CO2 Analysis for the Heating Phase of the DST. Submittal date: 08/09/2002.

161243 LB0208UZDSCPMI.002. Drift-Scale Calibrated Property Sets: Mean Infiltration Data Summary. Submittal date: 08/26/2002.

160799 LB0210THRMLPRP.001. Thermal Properties of UZ Model Layers: Data Summary. Submittal date: 10/25/2002.

164433 LB0307KNTDBRTM.001. Kinetic Database for Reactive Transport Modeling. Submittal date: 07/22/2003.

164434 LB0307THMDBRTM.001. Thermodynamic Database for Reactive Transport Modeling. Submittal date: 07/22/2003.

111475 LB990501233129.004. 3-D UZ Model Calibration Grids for AMR U0000, "Development of Numerical Grids of UZ Flow and Transport Modeling". Submittal date: 09/24/1999.

105888 LB990601233124.001. Seepage Data Feed to UZ Drift-Scale Flow Model for TSPA-SR. Submittal date: 06/18/1999.

111476 LB990630123142.003. Fourth, Fifth, and Sixth Quarters TDIF Submission for the Drift Scale Test, September 1998 to May 1999. Submittal date: 06/30/1999.

125604 LB990701233129.002. 3-D Model Calibration Grid for Calculation of Flow Fields Using #3 Perched Water Conceptual Model (Non-Perched Water Model) for AMR U0050, "UZ Flow Models and Submodels". Submittal date: 03/11/2000.

110226 LB990861233129.001. Drift Scale Calibrated 1-D Property Set, FY99. Submittal date: 08/06/1999.

125868 LB991091233129.001. One-Dimensional, Mountain-Scale Calibration for AMR U0035, "Calibrated Properties Model". Submittal date: 10/22/1999.

111480 LB991091233129.006. Thermal Properties and Tortuosity Factor for the UZ Model Layers for AMR U0090, "Analysis of Hydrologic Properties Data". Submittal date: 10/15/1999.

142162 LB991200DSTTHC.002. Model Input and Output Files, Excel Spreadsheets and Resultant Figures Which are Presented in AMR N0120/U0110, "Drift-Scale Coupled Processes (Drift-Scale Test and THC Seepage) Models". Submittal date: 03/11/2000.

161276 LB991200DSTTHC.003. Mineral Initial Volume Fractions: Attachment II of AMR N0120/U0110, "Drift-Scale Coupled Processes (Drift-Scale Test and THC Seepage) Models.". Submittal date: 03/11/2000.

104055 LB997141233129.001. Calibrated Basecase Infiltration 1-D Parameter Set for the UZ Flow and Transport Model, FY99. Submittal date: 07/21/1999.

142884 LL000114004242.090. TSPA-SR Mean Calculations. Submittal date: 01/28/2000.

153288 LL001100931031.008. Aqueous Chemistry of Water Sampled from Boreholes of the Drift Scale Test (DST). Submittal date: 11/10/2000.

153616 LL001200231031.009. Aqueous Chemistry of Water Sampled from Boreholes of the Drift Scale Test (DST). Submittal date: 12/04/2000.

159134 LL020302223142.015. Aqueous Geochemistry of DST Samples Collected from HYD Boreholes. Submittal date: 03/07/2002.

159307 LL020405123142.019. Aqueous Geochemistry of Condensed Fluids Collected During Studies of Introduced Materials. Submittal date: 05/22/2002.

161677 LL020709923142.023. Aqueous Geochemistry of Borehole Waters Collected in the Heating Phase of the DST. Submittal date: 07/26/2002.

144922 LL990702804244.100. Borehole and Pore Water Data. Submittal date: 07/13/1999.

153836 MO0001SEPDSTPC.000. Drift Scale Test (DST) Temperature, Power, Current, and Voltage Data for June 1, 1999 through October 31, 1999. Submittal date: 01/12/2000.

147304 MO0002ABBLSLDS.000. As-Built Borehole Locations and Sensor Locations for the Drift Scale Test Given in Local (DST) Coordinates. Submittal date: 02/01/2000.

150930 MO0005PORWATER.000. Perm-Sample Pore Water Data. Submittal date: 05/04/2000.

153707 MO0007SEPDSTPC.001. Drift Scale Test (DST) Temperature, Power, Current, and Voltage Data for November 1, 1999 through May 31, 2000. Submittal date: 07/13/2000.

153708 MO0012SEPDSTPC.002. Drift Scale Test (DST) Temperature, Power, Current, and Voltage Data for June 1, 2000 through November 30, 2000. Submittal date: 12/19/2000.

153711 MO0101SEPFDDST.000. Field Measured Data of Water Samples from the Drift Scale Test. Submittal date: 01/03/2001.

158321 MO0107SEPDSTPC.003. Drift Scale Test (DST) Temperature, Power, Current, and Voltage Data for December 1, 2000 through May 31, 2001. Submittal date: 07/06/2001.

158320 MO0202SEPDSTTV.001. Drift Scale Test (DST) Temperature, Power, Current, and Voltage Data for June 1, 2001 through January 14, 2002. Submittal date: 02/28/2002.

158910 MO0204SPATHDYN.000. Thermodynamic Data Input Files for Geochemical Calculations. Submittal date: 04/01/2002.

159300 MO0207AL5WATER.001. Water Sampling in Alcove 5 (Results from 2/4/1997 through 4/20/1999). Submittal date: 07/11/2002.

161129 MO0208RESTRDST.002. Restructured Drift Scale Test (DST) Heating Phase Power and Temperature Data. Submittal date: 08/06/2002.

161496 MO0301SEPFEPS1.000. LA FEP List. Submittal date: 01/21/2003.

161756 MO0302SPATHDYN.000. Thermodynamic Data Input Files - Data0.YMP.R2. Submittal date: 02/05/2003.

113644 MO9807DSTSET01.000. Drift Scale Test (DST) Temperature, Power, Current, Voltage Data for November 7, 1997 through May 31, 1998. Submittal date: 07/09/1998.

113662 MO9810DSTSET02.000. Drift Scale Test (DST) Temperature, Power, Current, Voltage Data for June 1 through August 31, 1998. Submittal date: 10/09/1998.

113673 MO9906DSTSET03.000. Drift Scale Test (DST) Temperature, Power, Current, and Voltage Data for September 1, 1998 through May 31, 1999. Submittal date: 06/08/1999.

153364 SN0002T0872799.009. Effective Thermal Conductivity Parameter for the No Backfill Case Implemented in the Drift-Scale Models used in TSPA-SR. Submittal date: 02/10/2000.

159133 SN0203F3903102.001. Drift Scale Test Water Sampling (with Results from 4/17/2001 through 1/14/2002). Submittal date: 03/29/2002.

111485 SN9907T0872799.001. Heat Decay Data and Repository Footprint for Thermal-Hydrologic and Conduction-Only Models for TSPA-SR (Total System Performance Assessment-Site Recommendation). Submittal date: 07/27/1999.

9.4 OUTPUT DATA, LISTED BY DATA TRACKING NUMBER

LB0301FRACSEAL.001. Comparison Modeling for Tptpmn Tuff Fracture Sealing Experiment: Supporting Files. Submittal date: 01/27/2003.

LB0301FRACSEAL.002. Comparison Modeling for Tptpmn Tuff Fracture Sealing Experiment: Data Summary. Submittal date: 01/27/2003.

LB0301PLUGFLOW.001. Comparison Modeling for Tptpmn Tuff Dissolution Experiment: Data Summary Files. Submittal date: 01/13/2003.

LB0302DSCPTHCS.001. Drift-Scale Coupled Processes (THC Seepage) Model: Simulations. Submittal date: 02/11/2003.

LB0302DSCPTHCS.002. Drift-Scale Coupled Processes (THC Seepage) Model: Data Summary. Submittal date: 02/11/2003.

LB0307DSTTHCR2.001. Drift-Scale Coupled Processes (DST Seepage) Model: Simulations. Submittal date: 07/24/2003.

LB0307DSTTHCR2.002. Drift-Scale Coupled Processes (DST Seepage) Model: Data Summary. Submittal date: 07/24/2003.

INTENTIONALLY LEFT BLANK

ATTACHMENT I – MINERAL INITIAL VOLUME FRACTIONS: Tptpmn THC Model REV01, Tptpmn THC Heterogeneous Model REV01 and DST THC Model REV01

(DTN: LB991200DSTTHC.003 [161276])

Unit	Rock Name	Zone	K-feldspar	Albite	Anorthite	Ca-Smectite	Na-Smectite	Mg-Smectite	K-Smectite	Illite	Tridymite
Tcw3	tcwm3	1	0.0946	0.0699	0.0024	0.0407	0.0175	0.0407	0.0175	0.0129	0.0000
	tcwf3	2	0.0946	0.0699	0.0024	0.0407	0.0175	0.0407	0.0175	0.0129	0.0000
Ptn1	ptnm1	3	0.0377	0.0279	0.0009	0.0643	0.0276	0.0643	0.0276	0.0204	0.0000
	ptnf1	4	0.0377	0.0279	0.0009	0.0643	0.0276	0.0643	0.0276	0.0204	0.0000
Ptn2	ptnm2	5	0.0449	0.0332	0.0011	0.0568	0.0244	0.0568	0.0244	0.0180	0.0000
	ptnf2	6	0.0449	0.0332	0.0011	0.0568	0.0244	0.0568	0.0244	0.0180	0.0000
Ptn3	ptnm3	7	0.0156	0.0116	0.0004	0.0095	0.0041	0.0095	0.0041	0.0030	0.0000
	ptnf3	8	0.0156	0.0116	0.0004	0.0095	0.0041	0.0095	0.0041	0.0030	0.0000
Ptn4	ptnm4	9	0.0806	0.0595	0.0020	0.0209	0.0090	0.0209	0.0090	0.0066	0.0000
	ptnf4	10	0.0806	0.0595	0.0020	0.0209	0.0090	0.0209	0.0090	0.0066	0.0000
Ptn5	ptnm5	11	0.0965	0.0712	0.0024	0.0090	0.0039	0.0090	0.0039	0.0029	0.0000
	ptnf5	12	0.0965	0.0712	0.0024	0.0090	0.0039	0.0090	0.0039	0.0029	0.0000
Ptn6	ptnm6	13	0.0855	0.0631	0.0021	0.0329	0.0141	0.0329	0.0141	0.0104	0.0000
	ptnf6	14	0.0855	0.0631	0.0021	0.0329	0.0141	0.0329	0.0141	0.0104	0.0000
Tsw31	tswm1	15	0.2358	0.1741	0.0059	0.0001	0.0001	0.0001	0.0001	0.0000	0.0000
	tswf1	16	0.2358	0.1741	0.0059	0.0001	0.0001	0.0001	0.0001	0.0000	0.0000
Tsw32	tswm2	17	0.4025	0.2973	0.0100	0.0027	0.0012	0.0027	0.0012	0.0009	0.0919
	tswf2	18	0.2435	0.1798	0.0061	0.0174	0.0074	0.0174	0.0074	0.0055	0.0556
Tsw33	tswm3	19	0.3051	0.2253	0.0076	0.0131	0.0056	0.0131	0.0056	0.0042	0.1071
	tswf3	20	0.1846	0.1363	0.0046	0.0237	0.0102	0.0237	0.0102	0.0075	0.0648
Tsw34	tswm4	21	0.3096	0.2286	0.0077	0.0081	0.0035	0.0081	0.0035	0.0026	0.0489
	tswf4	22	0.1873	0.1383	0.0047	0.0207	0.0089	0.0207	0.0089	0.0066	0.0296
Tsw35	tswm5	23	0.3051	0.2253	0.0076	0.0082	0.0035	0.0082	0.0035	0.0026	0.0597
	tswf5	24	0.1846	0.1363	0.0046	0.0207	0.0089	0.0207	0.0089	0.0066	0.0361
Tsw36	tswm6	25	0.3094	0.2285	0.0077	0.0074	0.0032	0.0074	0.0032	0.0024	0.0137
	tswf6	26	0.1872	0.1382	0.0047	0.0202	0.0087	0.0202	0.0087	0.0064	0.0083
Tsw37	tswm7	27	0.3057	0.2257	0.0076	0.0079	0.0034	0.0079	0.0034	0.0025	0.0077
	tswf7	28	0.1849	0.1366	0.0046	0.0205	0.0088	0.0205	0.0088	0.0065	0.0047
Tsw38	tswm8	29	0.0878	0.0648	0.0022	0.0180	0.0077	0.0180	0.0077	0.0057	0.0054
	tswf8	30	0.0878	0.0648	0.0022	0.0180	0.0077	0.0180	0.0077	0.0057	0.0054
Ch2	ch2mz	31	0.0370	0.0273	0.0009	0.0060	0.0026	0.0060	0.0026	0.0019	0.0000
	ch2fz	32	0.0370	0.0273	0.0009	0.0060	0.0026	0.0060	0.0026	0.0019	0.0000

Unit	Rock Name	Zone	Cristobalite	Quartz	Glass	Hematite	Calcite	Stellerite	Heulandite	Mordenite	Clinoptilolite
Tcw3	tcwm3	1	0.1323	0.0037	0.4580	0.0000	0.0000	0.0000	0.0329	0.0110	0.0659
	tcwf3	2	0.1323	0.0037	0.4580	0.0000	0.0000	0.0000	0.0329	0.0110	0.0659
Ptn1	ptnm1	3	0.0000	0.0009	0.7283	0.0000	0.0000	0.0000	0.0000	0.0000	0.0000
	ptnf1	4	0.0000	0.0009	0.7283	0.0000	0.0000	0.0000	0.0000	0.0000	0.0000
Ptn2	ptnm2	5	0.0350	0.0157	0.6895	0.0002	0.0000	0.0000	0.0000	0.0000	0.0000
	ptnf2	6	0.0350	0.0157	0.6895	0.0002	0.0000	0.0000	0.0000	0.0000	0.0000
Ptn3	ptnm3	7	0.0763	0.0009	0.8652	0.0000	0.0000	0.0000	0.0000	0.0000	0.0000
	ptnf3	8	0.0763	0.0009	0.8652	0.0000	0.0000	0.0000	0.0000	0.0000	0.0000
Ptn4	ptnm4	9	0.0524	0.0139	0.7254	0.0000	0.0000	0.0000	0.0000	0.0000	0.0000
	ptnf4	10	0.0524	0.0139	0.7254	0.0000	0.0000	0.0000	0.0000	0.0000	0.0000
Ptn5	ptnm5	11	0.0214	0.0094	0.7679	0.0024	0.0000	0.0000	0.0000	0.0000	0.0000
	ptnf5	12	0.0214	0.0094	0.7679	0.0024	0.0000	0.0000	0.0000	0.0000	0.0000
Ptn6	ptnm6	13	0.0083	0.0142	0.7129	0.0024	0.0070	0.0000	0.0000	0.0000	0.0000
	ptnf6	14	0.0083	0.0142	0.7129	0.0024	0.0070	0.0000	0.0000	0.0000	0.0000
Tsw31	tswm1	15	0.0915	0.0047	0.4550	0.0050	0.0276	0.0000	0.0000	0.0000	0.0000
	tswf1	16	0.0915	0.0047	0.4550	0.0050	0.0276	0.0000	0.0000	0.0000	0.0000
Tsw32	tswm2	17	0.1516	0.0079	0.0152	0.0044	0.0095	0.0011	0.0000	0.0001	0.0000
	tswf2	18	0.0917	0.0048	0.0092	0.0027	0.0257	0.3257	0.0000	0.0001	0.0000
Tsw33	tswm3	19	0.2336	0.0760	0.0000	0.0036	0.0000	0.0000	0.0000	0.0000	0.0000
	tswf3	20	0.1413	0.0460	0.0000	0.0022	0.0200	0.3250	0.0000	0.0000	0.0000
Tsw34	tswm4	21	0.2588	0.1202	0.0000	0.0004	0.0000	0.0000	0.0000	0.0000	0.0000
	tswf4	22	0.1566	0.0727	0.0000	0.0002	0.0200	0.3250	0.0000	0.0000	0.0000
Tsw35	tswm5	23	0.1660	0.2037	0.0000	0.0017	0.0050	0.0000	0.0000	0.0000	0.0000
	tswf5	24	0.1004	0.1232	0.0000	0.0010	0.0230	0.3250	0.0000	0.0000	0.0000
Tsw36	tswm6	25	0.1509	0.2643	0.0000	0.0020	0.0000	0.0000	0.0000	0.0000	0.0000
	tswf6	26	0.0913	0.1599	0.0000	0.0012	0.0200	0.3250	0.0000	0.0000	0.0000
Tsw37	tswm7	27	0.2273	0.2004	0.0000	0.0005	0.0000	0.0000	0.0000	0.0000	0.0000
	tswf7	28	0.1375	0.1212	0.0000	0.0003	0.0200	0.3250	0.0000	0.0000	0.0000
Tsw38	tswm8	29	0.1557	0.0244	0.5629	0.0000	0.0000	0.0000	0.0119	0.0040	0.0238
	tswf8	30	0.1557	0.0244	0.5629	0.0000	0.0000	0.0000	0.0119	0.0040	0.0238
Ch2	ch2mz	31	0.1609	0.0326	0.0000	0.0000	0.0000	0.0000	0.2166	0.0722	0.4333
	ch2fz	32	0.1609	0.0326	0.0000	0.0000	0.0000	0.0000	0.2166	0.0722	0.4333

ATTACHMENT II – MINERAL INITIAL VOLUME FRACTIONS: Tptpll THC Models (REV01 and REV02) and DST THC Model REV02

(DTN: LB0101DSTTHCR1.002 [161277])

Rock	Zone	K-Feldspar	Albite	Anorthite	Ca-Smectite	Na-Smectite	Mg-Smectite	Illite	Tridymite	Cristobalite	Quartz
tcwm1	1	0.36911	0.27257	0.00917	0.00198	0.00085	0.00198	0.00148	0.10285	0.21294	0.00942
tcwf1	2	0.36911	0.27257	0.00917	0.00198	0.00085	0.00198	0.00148	0.10285	0.21294	0.00942
tcwm2	3	0.36911	0.27257	0.00917	0.00198	0.00085	0.00198	0.00148	0.10285	0.21294	0.00942
tcwf2	4	0.36911	0.27257	0.00917	0.00198	0.00085	0.00198	0.00148	0.10285	0.21294	0.00942
tcwm3	5	0.16239	0.11992	0.00403	0.04403	0.01887	0.04403	0.03284	0.00000	0.12577	0.00744
tcwf3	6	0.16239	0.11992	0.00403	0.04403	0.01887	0.04403	0.03284	0.00000	0.12577	0.00744
ptnm1	7	0.05149	0.03802	0.00128	0.02441	0.01046	0.02441	0.01821	0.00015	0.01460	0.00702
ptnf1	8	0.05149	0.03802	0.00128	0.02441	0.01046	0.02441	0.01821	0.00015	0.01460	0.00702
ptnm2	9	0.05148	0.03802	0.00128	0.02441	0.01046	0.02441	0.01821	0.00015	0.01460	0.00702
ptnf2	10	0.05148	0.03802	0.00128	0.02441	0.01046	0.02441	0.01821	0.00015	0.01460	0.00702
ptnm3	11	0.05149	0.03802	0.00128	0.02441	0.01046	0.02441	0.01821	0.00015	0.01460	0.00702
ptnf3	12	0.05149	0.03802	0.00128	0.02441	0.01046	0.02441	0.01821	0.00015	0.01460	0.00702
ptnm4	13	0.05149	0.03802	0.00128	0.02441	0.01046	0.02441	0.01821	0.00015	0.01460	0.00702
ptnf4	14	0.05149	0.03802	0.00128	0.02441	0.01046	0.02441	0.01821	0.00015	0.01460	0.00702
ptnm5	15	0.05136	0.03793	0.00128	0.02435	0.01044	0.02435	0.01817	0.00015	0.01460	0.00702
ptnf5	16	0.05136	0.03793	0.00128	0.02435	0.01044	0.02435	0.01817	0.00015	0.01460	0.00702
ptnm6	17	0.05137	0.03794	0.00128	0.02436	0.01044	0.02436	0.01817	0.00015	0.01457	0.00701
ptnf6	18	0.05137	0.03794	0.00128	0.02436	0.01044	0.02436	0.01817	0.00015	0.01457	0.00701
tswm1	19	0.10362	0.07652	0.00257	0.00213	0.00091	0.00213	0.00159	0.00112	0.01999	0.00118
tswf1	20	0.10362	0.07652	0.00257	0.00213	0.00091	0.00213	0.00159	0.00112	0.01999	0.00118
tswm2	21	0.38312	0.28291	0.00952	0.00343	0.00147	0.00343	0.00256	0.15942	0.13313	0.00473
tswf2	22	0.23179	0.17116	0.00576	0.01767	0.00757	0.01767	0.01318	0.09645	0.08054	0.00286
tswm3	23	0.36306	0.26810	0.00902	0.00777	0.00333	0.00777	0.00580	0.05630	0.23767	0.02695
tswf3	24	0.21965	0.16220	0.00546	0.02029	0.00870	0.02029	0.01514	0.03406	0.14379	0.01630
tswm4	25	0.32265	0.23826	0.00802	0.00517	0.00221	0.00517	0.00385	0.02310	0.35588	0.02526
tswf4	26	0.19520	0.14415	0.00485	0.01872	0.00802	0.01872	0.01396	0.01397	0.21530	0.01529
tswm5	27	0.34968	0.25822	0.00869	0.00686	0.00294	0.00686	0.00512	0.02321	0.18589	0.14046
tswf5	28	0.21155	0.15622	0.00526	0.01974	0.00846	0.01974	0.01473	0.01404	0.11247	0.08498
tswm6	29	0.36268	0.26782	0.00901	0.00327	0.00140	0.00327	0.00244	0.00195	0.16651	0.16845
tswf6	30	0.21942	0.16203	0.00545	0.01757	0.00753	0.01757	0.01311	0.00118	0.10074	0.10191
tswm7	31	0.36322	0.26822	0.00902	0.00328	0.00140	0.00328	0.00244	0.00195	0.16676	0.16870
tswf7	32	0.21975	0.16227	0.00546	0.01758	0.00753	0.01758	0.01311	0.00118	0.10089	0.10206
tswm8	33	0.11030	0.08145	0.00274	0.04279	0.01834	0.04279	0.03192	0.00000	0.09981	0.00790
tswf8	34	0.11030	0.08145	0.00274	0.04279	0.01834	0.04279	0.03192	0.00000	0.09981	0.00790
tswm9	35	0.06105	0.04508	0.00152	0.02739	0.01174	0.02739	0.02044	0.00000	0.06216	0.01481
tswf9	36	0.06105	0.04508	0.00152	0.02739	0.01174	0.02739	0.02044	0.00000	0.06216	0.01481
ch1mv	37	0.07829	0.05781	0.00195	0.00747	0.00320	0.00747	0.00557	0.00586	0.06920	0.03831
ch1fv	38	0.07829	0.05781	0.00195	0.00747	0.00320	0.00747	0.00557	0.00586	0.06920	0.03831

Rock	Zone	Glass	Hematite	Calcite	Stellerite	Heulandite	Mordenite	Clinoptilolite	Kaolinite	Am. Silica	Opal	Fluorite
tcwm1	1	0.00139	0.00000	0.00358	0.00000	0.00083	0.00028	0.00167	0.00000	0.00000	0.00990	0.00000
tcwf1	2	0.00139	0.00000	0.00358	0.00000	0.00083	0.00028	0.00167	0.00000	0.00000	0.00990	0.00000
tcwm2	3	0.00139	0.00000	0.00358	0.00000	0.00083	0.00028	0.00167	0.00000	0.00000	0.00990	0.00000
tcwf2	4	0.00139	0.00000	0.00358	0.00000	0.00083	0.00028	0.00167	0.00000	0.00000	0.00990	0.00000
tcwm3	5	0.43046	0.00000	0.00032	0.00000	0.00000	0.00000	0.00000	0.00000	0.00000	0.00990	0.00000
tcwf3	6	0.43046	0.00000	0.00032	0.00000	0.00000	0.00000	0.00000	0.00000	0.00000	0.00990	0.00000
ptnm1	7	0.78888	0.00000	0.01086	0.00000	0.00008	0.00003	0.00017	0.00000	0.00000	0.00990	0.00000
ptnf1	8	0.78888	0.00000	0.01086	0.00000	0.00008	0.00003	0.00017	0.00000	0.00000	0.00990	0.00000
ptnm2	9	0.78876	0.00015	0.01086	0.00000	0.00008	0.00003	0.00017	0.00000	0.00000	0.00990	0.00000
ptnf2	10	0.78876	0.00015	0.01086	0.00000	0.00008	0.00003	0.00017	0.00000	0.00000	0.00990	0.00000
ptnm3	11	0.78888	0.00000	0.01086	0.00000	0.00008	0.00003	0.00017	0.00000	0.00000	0.00990	0.00000
ptnf3	12	0.78888	0.00000	0.01086	0.00000	0.00008	0.00003	0.00017	0.00000	0.00000	0.00990	0.00000
ptnm4	13	0.78888	0.00000	0.01086	0.00000	0.00008	0.00003	0.00017	0.00000	0.00000	0.00990	0.00000
ptnf4	14	0.78888	0.00000	0.01086	0.00000	0.00008	0.00003	0.00017	0.00000	0.00000	0.00990	0.00000
ptnm5	15	0.78694	0.00239	0.01083	0.00000	0.00008	0.00003	0.00017	0.00000	0.00000	0.00990	0.00000
ptnf5	16	0.78694	0.00239	0.01083	0.00000	0.00008	0.00003	0.00017	0.00000	0.00000	0.00990	0.00000
ptnm6	17	0.78707	0.00228	0.01084	0.00000	0.00008	0.00003	0.00017	0.00000	0.00000	0.00990	0.00000
ptnf6	18	0.78707	0.00228	0.01084	0.00000	0.00008	0.00003	0.00017	0.00000	0.00000	0.00990	0.00000
tswm1	19	0.75630	0.00485	0.01693	0.00000	0.00005	0.00002	0.00009	0.00000	0.00000	0.00990	0.00010
tswf1	20	0.75630	0.00485	0.01693	0.00000	0.00005	0.00002	0.00009	0.00000	0.00000	0.00990	0.00010
tswm2	21	0.00070	0.00439	0.00110	0.00010	0.00000	0.00001	0.00000	0.00000	0.00000	0.00990	0.00010
tswf2	22	0.00042	0.00265	0.02046	0.32181	0.00000	0.00001	0.00000	0.00000	0.00000	0.00990	0.00010
tswm3	23	0.00000	0.00353	0.00067	0.00000	0.00001	0.00000	0.00003	0.00000	0.00000	0.00990	0.00010
tswf3	24	0.00000	0.00214	0.02020	0.32175	0.00001	0.00000	0.00002	0.00000	0.00000	0.00990	0.00010
tswm4	25	0.00000	0.00036	0.00007	0.00000	0.00000	0.00000	0.00000	0.00000	0.00000	0.00990	0.00010
tswf4	26	0.00000	0.00022	0.01984	0.32175	0.00000	0.00000	0.00000	0.00000	0.00000	0.00990	0.00010
tswm5	27	0.00000	0.00162	0.00038	0.00000	0.00002	0.00001	0.00005	0.00000	0.00000	0.00990	0.00010
tswf5	28	0.00000	0.00098	0.02003	0.32175	0.00001	0.00000	0.00003	0.00000	0.00000	0.00990	0.00010
tswm6	29	0.00000	0.00194	0.00007	0.00000	0.00035	0.00012	0.00071	0.00000	0.00000	0.00990	0.00010
tswf6	30	0.00000	0.00118	0.01984	0.32175	0.00021	0.00007	0.00043	0.00000	0.00000	0.00990	0.00010
tswm7	31	0.00000	0.00049	0.00007	0.00000	0.00035	0.00012	0.00071	0.00000	0.00000	0.00990	0.00010
tswf7	32	0.00000	0.00029	0.01984	0.32175	0.00021	0.00007	0.00043	0.00000	0.00000	0.00990	0.00010
tswm8	33	0.49522	0.00000	0.00039	0.00000	0.01691	0.00564	0.03381	0.00000	0.00000	0.00990	0.00010
tswf8	34	0.49522	0.00000	0.00039	0.00000	0.01691	0.00564	0.03381	0.00000	0.00000	0.00990	0.00010
tswm9	35	0.69427	0.00000	0.00005	0.00000	0.00723	0.00241	0.01446	0.00000	0.00000	0.00990	0.00010
tswf9	36	0.69427	0.00000	0.00005	0.00000	0.00723	0.00241	0.01446	0.00000	0.00000	0.00990	0.00010
ch1mv	37	0.50592	0.00000	0.00024	0.00000	0.06265	0.02088	0.12529	0.00000	0.00000	0.00990	0.00000
ch1fv	38	0.50592	0.00000	0.00024	0.00000	0.06265	0.02088	0.12529	0.00000	0.00000	0.00990	0.00000

Rock	Zone	K-Feldspar	Albite	Anorthite	Ca-Smectite	Na-Smectite	Mg-Smectite	Illite	Tridymite	Cristobalite	Quartz
ch2mv	39	0.09836	0.07263	0.00244	0.00691	0.00296	0.00691	0.00515	0.00079	0.05704	0.04824
ch2fv	40	0.09836	0.07263	0.00244	0.00691	0.00296	0.00691	0.00515	0.00079	0.05704	0.04824
ch3mv	41	0.04708	0.03477	0.00117	0.00216	0.00093	0.00216	0.00161	0.00001	0.04663	0.02747
ch3fv	42	0.04708	0.03477	0.00117	0.00216	0.00093	0.00216	0.00161	0.00001	0.04663	0.02747
ch4mz	43	0.04820	0.03559	0.00120	0.00058	0.00025	0.00058	0.00043	0.00000	0.03726	0.02878
ch4fz	44	0.04820	0.03559	0.00120	0.00058	0.00025	0.00058	0.00043	0.00000	0.03726	0.02878
ch5mz	45	0.04551	0.03361	0.00113	0.00046	0.00020	0.00046	0.00035	0.00000	0.02171	0.02707
ch5fz	46	0.04551	0.03361	0.00113	0.00046	0.00020	0.00046	0.00035	0.00000	0.02171	0.02707
ch6mv	47	0.09931	0.07334	0.00247	0.00620	0.00266	0.00620	0.00463	0.00000	0.05861	0.09735
ch6fv	48	0.09931	0.07334	0.00247	0.00620	0.00266	0.00620	0.00463	0.00000	0.05861	0.09735
pp4m	49	0.08283	0.06116	0.00206	0.00829	0.00355	0.00829	0.00619	0.00003	0.06691	0.01512
pp4f	50	0.08283	0.06116	0.00206	0.00829	0.00355	0.00829	0.00619	0.00003	0.06691	0.01512
pp3m	51	0.36843	0.27207	0.00915	0.00332	0.00142	0.00332	0.00248	0.00590	0.07075	0.24829
pp3f	52	0.36843	0.27207	0.00915	0.00332	0.00142	0.00332	0.00248	0.00590	0.07075	0.24829
pp2m	53	0.36843	0.27207	0.00915	0.00332	0.00142	0.00332	0.00248	0.00590	0.07075	0.24829
pp2f	54	0.36843	0.27207	0.00915	0.00332	0.00142	0.00332	0.00248	0.00590	0.07075	0.24829
pp1m	55	0.09931	0.07334	0.00247	0.00620	0.00266	0.00620	0.00463	0.00000	0.05861	0.09735
pp1f	56	0.09931	0.07334	0.00247	0.00620	0.00266	0.00620	0.00463	0.00000	0.05861	0.09735
bf3m4	57	0.36843	0.27207	0.00915	0.00332	0.00142	0.00332	0.00248	0.00590	0.07075	0.24829
bf3f4	58	0.36843	0.27207	0.00915	0.00332	0.00142	0.00332	0.00248	0.00590	0.07075	0.24829

Rock	Zone	Glass	Hematite	Calcite	Stellerite	Heulandite	Mordenite	Clinoptilolite	Kaolinite	Am. Silica	Opal	Fluorite
ch2mv	39	0.60921	0.00000	0.00000	0.00000	0.02384	0.00795	0.04768	0.00000	0.00000	0.00990	0.00000
ch2fv	40	0.60921	0.00000	0.00000	0.00000	0.02384	0.00795	0.04768	0.00000	0.00000	0.00990	0.00000
ch3mv	41	0.73775	0.00000	0.00000	0.00000	0.02651	0.00884	0.05302	0.00000	0.00000	0.00990	0.00000
ch3fv	42	0.73775	0.00000	0.00000	0.00000	0.02651	0.00884	0.05302	0.00000	0.00000	0.00990	0.00000
ch4mz	43	0.73310	0.00000	0.00003	0.00000	0.03123	0.01041	0.06246	0.00000	0.00000	0.00990	0.00000
ch4fz	44	0.73310	0.00000	0.00003	0.00000	0.03123	0.01041	0.06246	0.00000	0.00000	0.00990	0.00000
ch5mz	45	0.77556	0.00000	0.00004	0.00000	0.02520	0.00840	0.05040	0.00000	0.00000	0.00990	0.00000
ch5fz	46	0.77556	0.00000	0.00004	0.00000	0.02520	0.00840	0.05040	0.00000	0.00000	0.00990	0.00000
ch6mv	47	0.32953	0.00000	0.00150	0.00000	0.09249	0.03083	0.18497	0.00000	0.00000	0.00990	0.00000
ch6fv	48	0.32953	0.00000	0.00150	0.00000	0.09249	0.03083	0.18497	0.00000	0.00000	0.00990	0.00000
pp4m	49	0.49175	0.00000	0.00163	0.00000	0.07269	0.02423	0.14538	0.00000	0.00000	0.00990	0.00000
pp4f	50	0.49175	0.00000	0.00163	0.00000	0.07269	0.02423	0.14538	0.00000	0.00000	0.00990	0.00000
pp3m	51	0.00003	0.00474	0.00000	0.00000	0.00005	0.00002	0.00010	0.00000	0.00000	0.00990	0.00000
pp3f	52	0.00003	0.00474	0.00000	0.00000	0.00005	0.00002	0.00010	0.00000	0.00000	0.00990	0.00000
pp2m	53	0.00003	0.00474	0.00000	0.00000	0.00005	0.00002	0.00010	0.00000	0.00000	0.00990	0.00000
pp2f	54	0.00003	0.00474	0.00000	0.00000	0.00005	0.00002	0.00010	0.00000	0.00000	0.00990	0.00000
pp1m	55	0.32953	0.00000	0.00150	0.00000	0.09249	0.03083	0.18497	0.00000	0.00000	0.00990	0.00000
pp1f	56	0.32953	0.00000	0.00150	0.00000	0.09249	0.03083	0.18497	0.00000	0.00000	0.00990	0.00000
bf3m4	57	0.00003	0.00474	0.00000	0.00000	0.00005	0.00002	0.00010	0.00000	0.00000	0.00990	0.00000
bf3f4	58	0.00003	0.00474	0.00000	0.00000	0.00005	0.00002	0.00010	0.00000	0.00000	0.00990	0.00000

ATTACHMENT III – MINERAL REACTIVE SURFACE AREAS: Tptpmn THC Model REV01, Tptpmn THC Heterogeneous Model REV01 and DST THC Model REV01

(DTN: LB0101DSTTHCR1.003 [161278])

Unit	Rock Name	Zone	K-Feldspar	Albite	Anorthite	Ca-Smectite	Na-Smectite	Mg-Smectite	K-Smectite	Illite	Tridymite
Tcw3	tcwm3	1	98.0	98.0	98.0	1516.3	1516.3	1516.3	1516.3	1516.3	98.0
	tcwf3	2	394.8	394.8	394.8	394.8	394.8	394.8	394.8	394.8	394.8
Ptn1	ptnm1	3	7.6	7.6	7.6	2253.3	2253.3	2253.3	2253.3	2253.3	7.6
	ptnf1	4	142.8	142.8	142.8	142.8	142.8	142.8	142.8	142.8	142.8
Ptn2	ptnm2	5	8.6	8.6	8.6	2484.8	2484.8	2484.8	2484.8	2484.8	8.6
	ptnf2	6	184.6	184.6	184.6	184.6	184.6	184.6	184.6	184.6	184.6
Ptn3	ptnm3	7	7.1	7.1	7.1	1721.5	1721.5	1721.5	1721.5	1721.5	7.1
	ptnf3	8	1099.6	1099.6	1099.6	1099.6	1099.6	1099.6	1099.6	1099.6	1099.6
Ptn4	ptnm4	9	9.3	9.3	9.3	2356.2	2356.2	2356.2	2356.2	2356.2	9.3
	ptnf4	10	44.5	44.5	44.5	44.5	44.5	44.5	44.5	44.5	44.5
Ptn5	ptnm5	11	11.0	11.0	11.0	2666.7	2666.7	2666.7	2666.7	2666.7	11.0
	ptnf5	12	276.2	276.2	276.2	276.2	276.2	276.2	276.2	276.2	276.2
Ptn6	ptnm6	13	10.0	10.0	10.0	2666.7	2666.7	2666.7	2666.7	2666.7	10.0
	ptnf6	14	1553.3	1553.3	1553.3	1553.3	1553.3	1553.3	1553.3	1553.3	1553.3
Tsw31	tswm1	15	57.0	57.0	57.0	694.3	694.3	694.3	694.3	694.3	57.0
	tswf1	16	1102.4	1102.4	1102.4	1102.4	1102.4	1102.4	1102.4	1102.4	1102.4
Tsw32	tswm2	17	109.2	109.2	109.2	1317.4	1317.4	1317.4	1317.4	1317.4	109.2
	tswf2	18	530.8	530.8	530.8	530.8	530.8	530.8	530.8	530.8	530.8
Tsw33	tswm3	19	105.6	105.6	105.6	1303.3	1303.3	1303.3	1303.3	1303.3	105.6
	tswf3	20	1056.7	1056.7	1056.7	1056.7	1056.7	1056.7	1056.7	1056.7	1056.7
Tsw34	tswm4	21	89.8	89.8	89.8	1086.6	1086.6	1086.6	1086.6	1086.6	89.8
	tswf4	22	2126.9	2126.9	2126.9	2126.9	2126.9	2126.9	2126.9	2126.9	2126.9
Tsw35	tswm5	23	98.2	98.2	98.2	1195.3	1195.3	1195.3	1195.3	1195.3	98.2
	tswf5	24	1382.3	1382.3	1382.3	1382.3	1382.3	1382.3	1382.3	1382.3	1382.3
Tsw36	tswm6	25	90.8	90.8	90.8	1098.1	1098.1	1098.1	1098.1	1098.1	90.8
	tswf6	26	1289.1	1289.1	1289.1	1289.1	1289.1	1289.1	1289.1	1289.1	1289.1
Tsw37	tswm7	27	82.4	82.4	82.4	996.5	996.5	996.5	996.5	996.5	82.4
	tswf7	28	1289.1	1289.1	1289.1	1289.1	1289.1	1289.1	1289.1	1289.1	1289.1
Tsw38	tswm8	29	40.4	40.4	40.4	526.7	526.7	526.7	526.7	526.7	40.4
	tswf8	30	1746.2	1746.2	1746.2	1746.2	1746.2	1746.2	1746.2	1746.2	1746.2
Ch2	ch2mz	31	44.5	44.5	44.5	2024.7	2024.7	2024.7	2024.7	2024.7	44.5
	ch2fz	32	1570.8	1570.8	1570.8	1570.8	1570.8	1570.8	1570.8	1570.8	1570.8

DTN

Unit	Rock Name	Zone	Cristobalite	Quartz	Glass	Hematite	Calcite	Stellerite	Heulandite	Mordenite	Clinoptilolite
Tcw3	tcwm3	1	98.0	98.0	98.0	128.7	128.7	128.7	128.7	128.7	128.7
	tcwf3	2	394.8	394.8	394.8	394.8	394.8	394.8	394.8	394.8	394.8
Ptn1	ptnm1	3	7.6	7.6	7.6	9.6	9.6	9.6	9.6	9.6	9.6
	ptnf1	4	142.8	142.8	142.8	142.8	142.8	142.8	142.8	142.8	142.8
Ptn2	ptnm2	5	8.6	8.6	8.6	10.5	10.5	10.5	10.5	10.5	10.5
	ptnf2	6	184.6	184.6	184.6	184.6	184.6	184.6	184.6	184.6	184.6
Ptn3	ptnm3	7	7.1	7.1	7.1	7.3	7.3	7.3	7.3	7.3	7.3
	ptnf3	8	1099.6	1099.6	1099.6	1099.6	1099.6	1099.6	1099.6	1099.6	1099.6
Ptn4	ptnm4	9	9.3	9.3	9.3	10.0	10.0	10.0	10.0	10.0	10.0
	ptnf4	10	44.5	44.5	44.5	44.5	44.5	44.5	44.5	44.5	44.5
Ptn5	ptnm5	11	11.0	11.0	11.0	11.3	11.3	11.3	11.3	11.3	11.3
	ptnf5	12	276.2	276.2	276.2	276.2	276.2	276.2	276.2	276.2	276.2
Ptn6	ptnm6	13	10.0	10.0	10.0	11.3	11.3	11.3	11.3	11.3	11.3
	ptnf6	14	1553.3	1553.3	1553.3	1553.3	1553.3	1553.3	1553.3	1553.3	1553.3
Tsw31	tswm1	15	57.0	57.0	57.0	59.0	59.0	59.0	59.0	59.0	59.0
	tswf1	16	1102.4	1102.4	1102.4	1102.4	1102.4	1102.4	1102.4	1102.4	1102.4
Tsw32	tswm2	17	109.2	109.2	109.2	111.9	111.9	111.9	111.9	111.9	111.9
	tswf2	18	530.8	530.8	530.8	530.8	530.8	530.8	530.8	530.8	530.8
Tsw33	tswm3	19	105.6	105.6	105.6	110.7	110.7	110.7	110.7	110.7	110.7
	tswf3	20	1056.7	1056.7	1056.7	1056.7	1056.7	1056.7	1056.7	1056.7	1056.7
Tsw34	tswm4	21	89.8	89.8	89.8	92.3	92.3	92.3	92.3	92.3	92.3
	tswf4	22	2126.9	2126.9	2126.9	2126.9	2126.9	2126.9	2126.9	2126.9	2126.9
Tsw35	tswm5	23	98.2	98.2	98.2	101.5	101.5	101.5	101.5	101.5	101.5
	tswf5	24	1382.3	1382.3	1382.3	1382.3	1382.3	1382.3	1382.3	1382.3	1382.3
Tsw36	tswm6	25	90.8	90.8	90.8	93.2	93.2	93.2	93.2	93.2	93.2
	tswf6	26	1289.1	1289.1	1289.1	1289.1	1289.1	1289.1	1289.1	1289.1	1289.1
Tsw37	tswm7	27	82.4	82.4	82.4	84.6	84.6	84.6	84.6	84.6	84.6
	tswf7	28	1289.1	1289.1	1289.1	1289.1	1289.1	1289.1	1289.1	1289.1	1289.1
Tsw38	tswm8	29	40.4	40.4	40.4	44.7	44.7	44.7	44.7	44.7	44.7
	tswf8	30	1746.2	1746.2	1746.2	1746.2	1746.2	1746.2	1746.2	1746.2	1746.2
Ch2	ch2mz	31	44.5	44.5	44.5	171.9	171.9	171.9	171.9	171.9	171.9
	ch2fz	32	1570.8	1570.8	1570.8	1570.8	1570.8	1570.8	1570.8	1570.8	1570.8

ATTACHMENT IV – MINERAL REACTIVE SURFACE AREAS: Tptpll THC Models (REV01 and REV02) and DST THC Model REV02

(DTN: LB0101DSTTHCR1.004 [161279])

Rock	Zone	K-Feldspar	Albite	Anorthite	Ca-Smectite	Na-Smectite	Mg-Smectite	Illite	Tridymite	Cristobalite	Quartz
tcwm1	1	110.5	110.5	110.5	1516.3	1516.3	1516.3	1516.3	110.5	110.5	110.5
tcwf1	2	394.8	394.8	394.8	394.8	394.8	394.8	394.8	394.8	394.8	394.8
tcwm2	3	110.5	110.5	110.5	1516.3	1516.3	1516.3	1516.3	110.5	110.5	110.5
tcwf2	4	394.8	394.8	394.8	394.8	394.8	394.8	394.8	394.8	394.8	394.8
tcwm3	5	110.5	110.5	110.5	1516.3	1516.3	1516.3	1516.3	110.5	110.5	110.5
tcwf3	6	394.8	394.8	394.8	394.8	394.8	394.8	394.8	394.8	394.8	394.8
ptnm1	7	8.7	8.7	8.7	2253.3	2253.3	2253.3	2253.3	8.7	8.7	8.7
ptnf1	8	142.8	142.8	142.8	142.8	142.8	142.8	142.8	142.8	142.8	142.8
ptnm2	9	9.6	9.6	9.6	2484.8	2484.8	2484.8	2484.8	9.6	9.6	9.6
ptnf2	10	184.6	184.6	184.6	184.6	184.6	184.6	184.6	184.6	184.6	184.6
ptnm3	11	6.7	6.7	6.7	1721.5	1721.5	1721.5	1721.5	6.7	6.7	6.7
ptnf3	12	1099.6	1099.6	1099.6	1099.6	1099.6	1099.6	1099.6	1099.6	1099.6	1099.6
ptnm4	13	9.1	9.1	9.1	2356.2	2356.2	2356.2	2356.2	9.1	9.1	9.1
ptnf4	14	44.5	44.5	44.5	44.5	44.5	44.5	44.5	44.5	44.5	44.5
ptnm5	15	10.3	10.3	10.3	2666.7	2666.7	2666.7	2666.7	10.3	10.3	10.3
ptnf5	16	276.2	276.2	276.2	276.2	276.2	276.2	276.2	276.2	276.2	276.2
ptnm6	17	10.3	10.3	10.3	2666.7	2666.7	2666.7	2666.7	10.3	10.3	10.3
ptnf6	18	1553.3	1553.3	1553.3	1553.3	1553.3	1553.3	1553.3	1553.3	1553.3	1553.3
tswm1	19	57.2	57.2	57.2	694.3	694.3	694.3	694.3	57.2	57.2	57.2
tswf1	20	1102.4	1102.4	1102.4	1102.4	1102.4	1102.4	1102.4	1102.4	1102.4	1102.4
tswm2	21	110.0	110.0	110.0	1317.4	1317.4	1317.4	1317.4	110.0	110.0	110.0
tswf2	22	530.8	530.8	530.8	530.8	530.8	530.8	530.8	530.8	530.8	530.8
tswm3	23	107.4	107.4	107.4	1303.3	1303.3	1303.3	1303.3	107.4	107.4	107.4
tswf3	24	1056.7	1056.7	1056.7	1056.7	1056.7	1056.7	1056.7	1056.7	1056.7	1056.7
tswm4	25	90.7	90.7	90.7	1086.6	1086.6	1086.6	1086.6	90.7	90.7	90.7
tswf4	26	2126.9	2126.9	2126.9	2126.9	2126.9	2126.9	2126.9	2126.9	2126.9	2126.9
tswm5	27	99.0	99.0	99.0	1195.3	1195.3	1195.3	1195.3	99.0	99.0	99.0
tswf5	28	844.7	844.7	844.7	844.7	844.7	844.7	844.7	844.7	844.7	844.7
tswm6	29	92.0	92.0	92.0	1098.1	1098.1	1098.1	1098.1	92.0	92.0	92.0
tswf6	30	1289.1	1289.1	1289.1	1289.1	1289.1	1289.1	1289.1	1289.1	1289.1	1289.1
tswm7	31	83.6	83.6	83.6	996.5	996.5	996.5	996.5	83.6	83.6	83.6
tswf7	32	1289.1	1289.1	1289.1	1289.1	1289.1	1289.1	1289.1	1289.1	1289.1	1289.1
tswm8	33	36.0	36.0	36.0	526.7	526.7	526.7	526.7	36.0	36.0	36.0
tswf8	34	1746.2	1746.2	1746.2	1746.2	1746.2	1746.2	1746.2	1746.2	1746.2	1746.2
tswm9	35	36.0	36.0	36.0	526.7	526.7	526.7	526.7	36.0	36.0	36.0
tswf9	36	1007.4	1007.4	1007.4	1007.4	1007.4	1007.4	1007.4	1007.4	1007.4	1007.4
ch1mv	37	152.6	152.6	152.6	2024.7	2024.7	2024.7	2024.7	152.6	152.6	152.6
ch1fv	38	683.0	683.0	683.0	683.0	683.0	683.0	683.0	683.0	683.0	683.0

Rock	Zone	Glass	Hematite	Calcite	Stellerite	Heulandite	Mordenite	Clinoptilolite	Kaolinite	Am. Silica	Opal	Fluorite
tcwm1	1	110.5	128.7	128.7	128.7	128.7	128.7	128.7	1516.3	1516.3	1516.3	128.7
tcwf1	2	394.8	394.8	394.8	394.8	394.8	394.8	394.8	394.8	394.8	394.8	394.8
tcwm2	3	110.5	128.7	128.7	128.7	128.7	128.7	128.7	1516.3	1516.3	1516.3	128.7
tcwf2	4	394.8	394.8	394.8	394.8	394.8	394.8	394.8	394.8	394.8	394.8	394.8
tcwm3	5	110.5	128.7	128.7	128.7	128.7	128.7	128.7	1516.3	1516.3	1516.3	128.7
tcwf3	6	394.8	394.8	394.8	394.8	394.8	394.8	394.8	394.8	394.8	394.8	394.8
ptnm1	7	8.7	9.6	9.6	9.6	9.6	9.6	9.6	2253.3	2253.3	2253.3	9.6
ptnf1	8	142.8	142.8	142.8	142.8	142.8	142.8	142.8	142.8	142.8	142.8	142.8
ptnm2	9	9.6	10.5	10.5	10.5	10.5	10.5	10.5	2484.8	2484.8	2484.8	10.5
ptnf2	10	184.6	184.6	184.6	184.6	184.6	184.6	184.6	184.6	184.6	184.6	184.6
ptnm3	11	6.7	7.3	7.3	7.3	7.3	7.3	7.3	1721.5	1721.5	1721.5	7.3
ptnf3	12	1099.6	1099.6	1099.6	1099.6	1099.6	1099.6	1099.6	1099.6	1099.6	1099.6	1099.6
ptnm4	13	9.1	10.0	10.0	10.0	10.0	10.0	10.0	2356.2	2356.2	2356.2	10.0
ptnf4	14	44.5	44.5	44.5	44.5	44.5	44.5	44.5	44.5	44.5	44.5	44.5
ptnm5	15	10.3	11.3	11.3	11.3	11.3	11.3	11.3	2666.7	2666.7	2666.7	11.3
ptnf5	16	276.2	276.2	276.2	276.2	276.2	276.2	276.2	276.2	276.2	276.2	276.2
ptnm6	17	10.3	11.3	11.3	11.3	11.3	11.3	11.3	2666.7	2666.7	2666.7	11.3
ptnf6	18	1553.3	1553.3	1553.3	1553.3	1553.3	1553.3	1553.3	1553.3	1553.3	1553.3	1553.3
tswm1	19	57.2	59.0	59.0	59.0	59.0	59.0	59.0	694.3	694.3	694.3	59.0
tswf1	20	1102.4	1102.4	1102.4	1102.4	1102.4	1102.4	1102.4	1102.4	1102.4	1102.4	1102.4
tswm2	21	110.0	111.9	111.9	111.9	111.9	111.9	111.9	1317.4	1317.4	1317.4	111.9
tswf2	22	530.8	530.8	530.8	530.8	530.8	530.8	530.8	530.8	530.8	530.8	530.8
tswm3	23	107.4	110.7	110.7	110.7	110.7	110.7	110.7	1303.3	1303.3	1303.3	110.7
tswf3	24	1056.7	1056.7	1056.7	1056.7	1056.7	1056.7	1056.7	1056.7	1056.7	1056.7	1056.7
tswm4	25	90.7	92.3	92.3	92.3	92.3	92.3	92.3	1086.6	1086.6	1086.6	92.3
tswf4	26	2126.9	2126.9	2126.9	2126.9	2126.9	2126.9	2126.9	2126.9	2126.9	2126.9	2126.9
tswm5	27	99.0	101.5	101.5	101.5	101.5	101.5	101.5	1195.3	1195.3	1195.3	101.5
tswf5	28	844.7	844.7	844.7	844.7	844.7	844.7	844.7	844.7	844.7	844.7	844.7
tswm6	29	92.0	93.2	93.2	93.2	93.2	93.2	93.2	1098.1	1098.1	1098.1	93.2
tswf6	30	1289.1	1289.1	1289.1	1289.1	1289.1	1289.1	1289.1	1289.1	1289.1	1289.1	1289.1
tswm7	31	83.6	84.6	84.6	84.6	84.6	84.6	84.6	996.5	996.5	996.5	84.6
tswf7	32	1289.1	1289.1	1289.1	1289.1	1289.1	1289.1	1289.1	1289.1	1289.1	1289.1	1289.1
tswm8	33	36.0	44.7	44.7	44.7	44.7	44.7	44.7	526.7	526.7	526.7	44.7
tswf8	34	1746.2	1746.2	1746.2	1746.2	1746.2	1746.2	1746.2	1746.2	1746.2	1746.2	1746.2
tswm9	35	36.0	44.7	44.7	44.7	44.7	44.7	44.7	526.7	526.7	526.7	44.7
tswf9	36	1007.4	1007.4	1007.4	1007.4	1007.4	1007.4	1007.4	1007.4	1007.4	1007.4	1007.4
ch1mv	37	152.6	171.9	171.9	171.9	171.9	171.9	171.9	2024.7	2024.7	2024.7	171.9
ch1fv	38	683.0	683.0	683.0	683.0	683.0	683.0	683.0	683.0	683.0	683.0	683.0

Rock	Zone	K-Feldspar	Albite	Anorthite	Ca-Smectite	Na-Smectite	Mg-Smectite	Illite	Tridymite	Cristobalite	Quartz
ch2mv	39	152.6	152.6	152.6	2024.7	2024.7	2024.7	2024.7	152.6	152.6	152.6
ch2fv	40	758.9	758.9	758.9	758.9	758.9	758.9	758.9	758.9	758.9	758.9
ch3mv	41	152.6	152.6	152.6	2024.7	2024.7	2024.7	2024.7	152.6	152.6	152.6
ch3fv	42	758.9	758.9	758.9	758.9	758.9	758.9	758.9	758.9	758.9	758.9
ch4mz	43	152.6	152.6	152.6	2024.7	2024.7	2024.7	2024.7	152.6	152.6	152.6
ch4fz	44	1570.8	1570.8	1570.8	1570.8	1570.8	1570.8	1570.8	1570.8	1570.8	1570.8
ch5mz	45	152.6	152.6	152.6	2024.7	2024.7	2024.7	2024.7	152.6	152.6	152.6
ch5fz	46	1570.8	1570.8	1570.8	1570.8	1570.8	1570.8	1570.8	1570.8	1570.8	1570.8
ch6mv	47	152.6	152.6	152.6	2024.7	2024.7	2024.7	2024.7	152.6	152.6	152.6
ch6fv	48	1016.4	1016.4	1016.4	1016.4	1016.4	1016.4	1016.4	1016.4	1016.4	1016.4
pp4m	49	152.6	152.6	152.6	2024.7	2024.7	2024.7	2024.7	152.6	152.6	152.6
pp4f	50	1570.8	1570.8	1570.8	1570.8	1570.8	1570.8	1570.8	1570.8	1570.8	1570.8
pp3m	51	152.6	152.6	152.6	2024.7	2024.7	2024.7	2024.7	152.6	152.6	152.6
pp3f	52	871.1	871.1	871.1	871.1	871.1	871.1	871.1	871.1	871.1	871.1
pp2m	53	152.6	152.6	152.6	2024.7	2024.7	2024.7	2024.7	152.6	152.6	152.6
pp2f	54	871.1	871.1	871.1	871.1	871.1	871.1	871.1	871.1	871.1	871.1
pp1m	55	152.6	152.6	152.6	2024.7	2024.7	2024.7	2024.7	152.6	152.6	152.6
pp1f	56	1570.8	1570.8	1570.8	1570.8	1570.8	1570.8	1570.8	1570.8	1570.8	1570.8
bf3m4	57	152.6	152.6	152.6	2024.7	2024.7	2024.7	2024.7	152.6	152.6	152.6
bf3f4	58	2228.3	2228.3	2228.3	2228.3	2228.3	2228.3	2228.3	2228.3	2228.3	2228.3

Rock	Zone	Glass	Hematite	Calcite	Stellerite	Heulandite	Mordenite	Clinoptilolite	Kaolinite	Am. Silica	Opal	Fluorite
ch2mv	39	152.6	171.9	171.9	171.9	171.9	171.9	171.9	2024.7	2024.7	2024.7	171.9
ch2fv	40	758.9	758.9	758.9	758.9	758.9	758.9	758.9	758.9	758.9	758.9	758.9
ch3mv	41	152.6	171.9	171.9	171.9	171.9	171.9	171.9	2024.7	2024.7	2024.7	171.9
ch3fv	42	758.9	758.9	758.9	758.9	758.9	758.9	758.9	758.9	758.9	758.9	758.9
ch4mz	43	152.6	171.9	171.9	171.9	171.9	171.9	171.9	2024.7	2024.7	2024.7	171.9
ch4fz	44	1570.8	1570.8	1570.8	1570.8	1570.8	1570.8	1570.8	1570.8	1570.8	1570.8	1570.8
ch5mz	45	152.6	171.9	171.9	171.9	171.9	171.9	171.9	2024.7	2024.7	2024.7	171.9
ch5fz	46	1570.8	1570.8	1570.8	1570.8	1570.8	1570.8	1570.8	1570.8	1570.8	1570.8	1570.8
ch6mv	47	152.6	171.9	171.9	171.9	171.9	171.9	171.9	2024.7	2024.7	2024.7	171.9
ch6fv	48	1016.4	1016.4	1016.4	1016.4	1016.4	1016.4	1016.4	1016.4	1016.4	1016.4	1016.4
pp4m	49	152.6	171.9	171.9	171.9	171.9	171.9	171.9	2024.7	2024.7	2024.7	171.9
pp4f	50	1570.8	1570.8	1570.8	1570.8	1570.8	1570.8	1570.8	1570.8	1570.8	1570.8	1570.8
pp3m	51	152.6	171.9	171.9	171.9	171.9	171.9	171.9	2024.7	2024.7	2024.7	171.9
pp3f	52	871.1	871.1	871.1	871.1	871.1	871.1	871.1	871.1	871.1	871.1	871.1
pp2m	53	152.6	171.9	171.9	171.9	171.9	171.9	171.9	2024.7	2024.7	2024.7	171.9
pp2f	54	871.1	871.1	871.1	871.1	871.1	871.1	871.1	871.1	871.1	871.1	871.1
pp1m	55	152.6	171.9	171.9	171.9	171.9	171.9	171.9	2024.7	2024.7	2024.7	171.9
pp1f	56	1570.8	1570.8	1570.8	1570.8	1570.8	1570.8	1570.8	1570.8	1570.8	1570.8	1570.8
bf3m4	57	152.6	171.9	171.9	171.9	171.9	171.9	171.9	2024.7	2024.7	2024.7	171.9
bf3f4	58	2228.3	2228.3	2228.3	2228.3	2228.3	2228.3	2228.3	2228.3	2228.3	2228.3	2228.3

ATTACHMENT V – THERMODYNAMIC DATABASE: REV01 THC Models

(DTN: LB0101DSTTHCR1.006 [161280])

Mineral	Molecular Weight (g/mol)	Molar Volume (cm^3/mol)	Reaction Stoichiometry[1]	log (K)					
				0 (°C)	25 (°C)	60 (°C)	100 (°C)	150 (°C)	200 (°C)
albite-low	262.223	100.07	(1)alo2-, (1)na+, (3)sio2(aq)	-21.694	-20.177	-18.362	-16.684	-15.094	-13.986
anorthite	278.207	100.79	(2)alo2-, (1)ca+2, (2)sio2(aq)	-21.229	-20.484	-19.64	-18.96	-18.514	-18.485
calcite	100.087	36.934	(1)ca+2, (-1)h+, (1)hco3-	2.226	1.849	1.333	0.774	0.1	-0.584
SiO2(amor.)	60.084	29	(1)sio2(aq)	-2.871	-2.663	-2.423	-2.205	-1.99	-1.82
cristobalite-a	60.084	25.74	(1)sio2(aq)	-3.63	-3.332	-2.99	-2.678	-2.371	-2.129
fluorite	78.075	24.542	(1)ca+2, (2)f-	-10.31	-10.037	-9.907	-9.967	-10.265	-10.784
goethite	88.854	20.82	(1)hfeo2	-12.78	-11.483	-10.202	-9.208	-8.407	-7.92
glass1	56.588	23.978	(-0.0362)h2o, (0.15)alo2-, (0.0021)ca+2,(0.0654)h+, (0.0042)k+,(0.0003)mg+2, (0.0756)na+,(0.7608)sio2(aq), (0.007)hfeo2	-4.55	-4.39	-4.2	-4.01	-3.83	-3.71
glass	60.084	29	(1)sio2(aq)	-2.871	-2.663	-2.423	-2.205	-1.99	-1.82
gypsum	172.172	74.69	(2)h2o, (1)ca+2, (1)so4-2	-4.533	-4.482	-4.609	-4.903	-5.41	-6.127
hematite	159.692	30.274	(-1)h2o, (2)hfeo2	-26.439	-23.927	-21.485	-19.661	-18.293	-17.573
illite	378.963	135.08	(0.44)h2o, (2.06)alo2-, (1.12)h+,(0.5)k+, (0.22)mg+2,(3.72)sio2(aq)	-45.354	-41.926	-38.294	-34.994	-31.867	-29.606
k-spar	278.332	108.741	(1)alo2-, (1)k+, (3)sio2(aq)	-23.77	-21.82	-19.53	-17.44	-15.46	-14.06
kaolinite	258.16	99.52	(1)h2o, (2)alo2-, (2)h+,(2)sio2(aq)	-43.073	-39.895	-36.336	-33.181	-30.212	-28.082
quartz	60.084	22.688	(1)sio2(aq)	-4.079	-3.739	-3.349	-2.992	-2.642	-2.365
opal_proxy	60.084	29.000	(1)sio2(aq)	-3.501	-3.005	-2.627	-2.358	-2.118	-1.926
tridymite	60.084	26.586	(1)sio2(aq)	-3.872	-3.567	-3.193	-2.821	-2.394	-1.984
smectite-ca	365.394	132.51	(0.52)h2o, (1.77)alo2-, (0.145)ca+2,(0.96)h+, (0.26)mg+2,(3.97)sio2(aq)	-39.970	-36.970	-33.600	-30.610	-27.750	-25.670
smectite-na	366.25	132.51	(0.52)h2o, (1.77)alo2-, (0.96)h+,(0.26)mg+2, (0.29)na+,(3.97)sio2(aq)	-40.080	-36.980	-33.500	-30.380	-27.400	-25.210
smectite-mg	363.107	132.51	(0.52)h2o, (1.77)alo2-, (0.96)h+,(0.405)mg+2, (3.97)sio2(aq)	-40.030	-37.060	-33.730	-30.770	-27.940	-25.880
steller/10	281.733	133.1	(2.8)h2o, (0.79)alo2-, (0.39)ca+2,(0.01)na+, (2.81)sio2(aq)	-17.910	-16.400	-14.670	-13.100	-11.560	-10.420
heuland/10	279.347	126.64	(2.6)h2o, (0.8)alo2-, (0.33)ca+2,(0.04)k+, (0.1)na+,(2.8)sio2(aq)	-17.900	-16.350	-14.580	-12.970	-11.400	-10.230
mordeni/10	269.631	127.35	(2.2)h2o, (0.6)alo2-, (0.15)ca+2,(0.09)k+, (0.21)na+,(3)sio2(aq)	-16.150	-14.660	-12.950	-11.390	-9.840	-8.670
clinopt/10	277.66	126.41	(2.6)h2o, (0.68)alo2-, (0.28)ca+2,(0.08)k+, (0.04)na+,(2.92)sio2(aq)	-17.040	-15.500	-13.740	-12.130	-10.560	-9.350

Gaseous Species	Molecular Weight (g/mol)	Molecular Diameter (m)	Reaction Stoichiometry	0 (°C)	25 (°C)	60 (°C)	100 (°C)	150 (°C)	200 (°C)
CO2(g)	44.01	2.50E-10	(-1)h2o, (1)h+, (1)hco3-	-7.677	-7.818	-8.053	-8.36	-8.77	-9.217

NOTES: [1] Negative number in parenthesis indicate the species is on the left side of equation Minerals names or abbreviations above are those used in the database and may not exactly match names used in the text of the report. Names ending by /10 indicate the stoichiometry, molecular weight, molar volume, and log(K) values for those minerals were divided by 10 compared to original data. Glass phases, glass1 and glass, were used with the extended-case and base-case geochemical systems, respectively.
Data in this Attachment are associated with input file thermok2.07.dat.

Aqueous Species	r_{ej}	Charge	Reaction Stoichiometry[1]	log (K)					
				0 (°C)	25 (°C)	60 (°C)	100 (°C)	150 (°C)	200 (°C)
CO2(aq)	0.231	0	(-1)h2o, (1)h+, (1)hco3-	-6.58	-6.345	-6.268	-6.388	-6.724	-7.197
CO3-2	2.81	-2	(-1)h+, (1)hco3-	10.624	10.329	10.13	10.084	10.2	10.465
OH-	1.4	-1	(1)h2o, (-1)h+	14.94	13.995	13.027	12.255	11.631	11.284
Al(OH)2+	2.31	1	(1)alo2-, (2)h+	-13.66	-12.29	-10.83	-9.6	-8.53	-7.823
$HAlO_2$	0	0	(1)alo2-, (1)h+	-7.08	-6.45	-5.846	-5.409	-5.121	-5.035
Al+3	3.33	3	(-2)h2o, (1)alo2-, (4)h+	-25.8	-22.88	-19.57	-16.58	-13.68	-11.41
AlOH+2	2.8	2	(-1)h2o, (1)alo2-, (3)h+	-20.07	-17.93	-15.57	-13.52	-11.62	-10.24
CaCl+	2.31	1	(1)ca+2, (1)cl-	0.673	0.696	0.589	0.357	-0.04	-0.533
CaCl2(aq)	0	0	(1)ca+2, (2)cl-	0.452	0.644	0.629	0.381	-0.159	-0.911
CaCO3(aq)	0	0	(1)ca+2, (-1)h+, (1)hco3-	7.502	7.002	6.452	5.964	5.468	5.018
CaHCO3+	2.31	1	(1)ca+2, (1)hco3-	-1.095	-1.047	-1.159	-1.418	-1.859	-2.4
CaSO4(aq)	0	0	(1)ca+2, (1)so4-2	-2.071	-2.111	-2.265	-2.511	-2.91	-3.433
CaF+	2.31	1	(1)ca+2, (1)f-	-0.655	-0.682	-0.862	-1.17	-1.649	-2.215
CaOH+	2.31	1	(1)h2o, (-1)h+, (1)ca+2	14.085	12.833	11.416	10.142	8.904	7.931
HSiO3-	1.81	-1	(1)h2o, (-1)h+, (1)sio2(aq)	10.323	9.953	9.468	9.084	8.85	8.839
HCl(aq)	0.2	0	(1)cl-, (1)h+	0.661	0.67	0.689	0.62	0.41	0.092
KCl(aq)	0	0	(1)cl-, (1)k+	1.71	1.495	1.216	0.924	0.575	0.215
KHSO4(aq)	0	0	(1)h+, (1)k+, (1)so4-2	-0.435	-0.814	-1.479	-2.294	-3.341	-4.431
KSO4-	1.81	-1	(1)k+, (1)so4-2	-0.885	-0.88	-0.99	-1.194	-1.52	-1.919
HF(aq)	0.2	0	(1)h+, (1)f-	-2.985	-3.168	-3.474	-3.848	-4.338	-4.859
MgCl+	2.31	1	(1)cl-, (1)mg+2	0.049	0.135	0.055	-0.182	-0.607	-1.139
MgCO3(aq)	0	0	(-1)h+, (1)hco3-, (1)mg+2	7.74	7.35	6.926	6.563	6.204	5.872
MgHCO3+	2.31	1	(1)hco3-, (1)mg+2	-1.08	-1.036	-1.164	-1.436	-1.88	-2.415
MgSO4(aq)	0	0	(1)mg+2, (1)so4-2	-2.139	-2.412	-2.837	-3.347	-4.073	-4.955
MgF+	2.31	1	(1)mg+2, (1)f-	-1.387	-1.352	-1.478	-1.739	-2.168	-2.688
MgOH+	2.31	1	(1)h2o, (-1)h+, (1)mg+2	12.674	11.682	10.502	9.399	8.291	7.398
NaOH(aq)	0	0	(1)h2o, (-1)h+, (1)na+	15.645	14.795	13.8	12.885	11.971	11.221
NaCO3-	1.81	-1	(-1)h+, (1)hco3-, (1)na+	9.815	9.814	10.075	10.649	11.568	12.632
NaHCO3(aq)	0	0	(1)hco3-, (1)na+	-0.373	-0.154	0.11	0.411	0.793	1.213
NaHSiO3	0	0	(1)h2o, (-1)h+, (1)na+,(1)sio2(aq)	8.414	8.304	8.053	7.829	7.684	7.658
NaF(aq)	0	0	(1)na+, (1)f-	1.082	0.998	0.833	0.624	0.338	0.011
NaSO4-	1.81	-1	(1)na+, (1)so4-2	-0.677	-0.700	-0.842	-1.063	-1.389	-1.772
FeO2-	1.81	-1	(-1)h+, (1)hfeo2	10.231	9.602	8.839	8.111	7.38	6.821
FeO+	2.31	1	(-1)h2o, (1)h+, (1)hfeo2	-7.324	-6.368	-5.372	-4.561	-3.865	-3.393

Primary Aqueous Species:	r_{ej}	Charge	Molecular Weight (g/mol)
H2O	0	0	18.015
AlO2-	1.81	-1	58.98
Ca+2	2.87	2	40.078
Cl-	1.81	-1	35.453
H+	3.08	1	1.008
HCO3-	2.1	-1	61.017
K+	2.27	1	39.098
Mg+2	2.54	2	24.305
Na+	1.91	1	22.99
SiO2(aq)	0.08	0	60.084
SO4-2	3.15	-2	96.064
F-	1.33	-1	18.998
HFeO2	0	0	88.854

ATTACHMENT VI – THERMODYNAMIC DATABASE: REV02 THC Models

(DTN: LB0307THMDBRTM.001 [164434])

Mineral	Molecular Weight (g/mol)	Molar Volume (cm^3/mol)	Reaction Stoichiometry[1]	log (K)							
				0 (°C)	25 (°C)	60 (°C)	100 (°C)	150 (°C)	200 (°C)	250 (°C)	300 (°C)
albite-low	262.223	100.070	(1)alo2-, (1)na+, (3)sio2(aq)	-21.697	-20.179	-18.365	-16.686	-15.096	-13.987	-13.293	-12.963
anorthite	278.207	100.790	(2)alo2-, (1)ca+2, (2)sio2(aq)	-21.229	-20.484	-19.640	-18.960	-18.514	-18.485	-18.839	-19.547
calcite	100.087	36.934	(1)ca+2, (-1)h+, (1)hco3-	2.226	1.849	1.333	0.774	0.100	-0.584	-1.326	-2.215
clinopt/10	277.660	126.410	(2.6)h2o, (0.68)alo2-, (0.28)ca+2, (0.08)k+, (0.04)na+,(2.92)sio2(aq)	-20.216	-18.475	-16.703	-15.136	-13.577	-12.339	-11.395	-10.816
clpt/10-r02	277.660	126.410	(2.6)h2o, (0.68)alo2-, (0.28)ca+2, (0.08)k+, (0.04)na+,(2.92)sio2(aq)	-17.760	-16.020	-14.250	-12.680	-11.120	-9.880	-8.940	-8.360
cristoba-a	60.084	25.740	(1)sio2(aq)	-3.542	-3.192	-2.867	-2.589	-2.306	-2.071	-1.877	-1.742
fluorite	78.075	24.542	(1)ca+2, (2)f-	-10.310	-10.037	-9.907	-9.967	-10.265	-10.784	-11.555	-12.703
gypsum	172.172	74.690	(2)h2o, (1)ca+2, (1)so4-2	-4.533	-4.482	-4.609	-4.904	-5.410	-6.058	-6.874	-7.971
halite	58.442	27.015	(1)na+, (1)cl-	1.492	1.586	1.618	1.578	1.450	1.242	0.936	0.468
hematite	159.688	30.274	(-1)h2o, (2)hfeo2(aq)	-26.438	-23.927	-21.486	-19.661	-18.293	-17.573	-17.272	-17.248
heuland/10	279.347	126.640	(2.6)h2o, (0.8)alo2-, (0.33)ca+2, (0.04)k+, (0.1)na+, (2.8)sio2(aq)	-21.097	-19.348	-17.565	-15.992	-14.437	-13.217	-12.306	-11.779
heul/10-r02	279.347	126.640	(2.6)h2o, (0.8)alo2-, (0.33)ca+2, (0.04)k+, (0.1)na+, (2.8)sio2(aq)	-18.620	-16.870	-15.090	-13.510	-11.960	-10.740	-9.830	-9.300
illite	378.963	135.080	(0.44)h2o, (2.06)alo2-, (1.12)h+,(0.5)k+, (0.22)mg+2, (3.72)sio2(aq)	-45.566	-42.016	-38.333	-35.129	-32.064	-29.760	-28.120	-27.254
kaolinite	258.160	99.520	(1)h2o, (2)alo2-, (2)h+, (2)sio2(aq)	-43.234	-39.917	-36.348	-33.216	-30.252	-28.074	-26.558	-25.754
microcline-b	278.332	108.741	(1)alo2-, (1)k+, (3)sio2(aq)	-23.770	-21.820	-19.530	-17.440	-15.470	-14.080	-13.170	-12.670
morden/10	269.631	127.350	(2.2)h2o, (0.6)alo2-, (0.15)ca+2, (0.09)k+, (0.21)na+, (3)sio2(aq)	-19.244	-17.542	-15.820	-14.298	-12.776	-11.558	-10.617	-10.021
mord/10-r02	269.631	127.350	(2.2)h2o, (0.6)alo2-, (0.15)ca+2, (0.09)k+, (0.21)na+, (3)sio2(aq)	-16.950	-15.250	-13.530	-12.010	-10.480	-9.270	-8.330	-7.730
opal-proxy	60.084	29.000	(1)sio2(aq)	-3.501	-3.005	-2.627	-2.358	-2.118	-1.926	-1.765	-1.632
quartz	60.084	22.688	(1)sio2(aq)	-4.153	-3.743	-3.348	-3.006	-2.661	-2.376	-2.142	-1.976
sepiolite	323.913	142.830	(-4)h+, (5.5)h2o, (2)mg+2, (3)sio2(aq)	17.631	15.992	13.961	12.164	10.536	9.352	8.397	7.457
sio2(amor.)	60.084	29.000	(1)sio2(aq)	-2.954	-2.670	-2.422	-2.213	-1.998	-1.815	-1.663	-1.562
smect-ca-cal	365.394	132.510	(0.52)h2o, (1.77)alo2-, (0.145)ca+2, (0.96)h+, (0.26)mg+2, (3.97)sio2(aq)	-40.190	-36.970	-33.660	-30.790	-28.010	-25.900	-24.370	-23.550
smect-na-cal	366.250	132.510	(0.52)h2o, (1.77)alo2-, (0.96)h+, (0.26)mg+2, (0.29)na+, (3.97)sio2(aq)	-40.290	-36.980	-33.560	-30.560	-27.660	-25.440	-23.820	-22.900
smect-mg-cal	363.107	132.510	(0.52)h2o, (1.77)alo2-, (0.96)h+, (0.405)mg+2, (3.97)sio2(aq)	-40.240	-37.060	-33.790	-30.950	-28.200	-26.110	-24.600	-23.790

Mineral	Molecular Weight (g/mol)	Molar Volume (cm^3/mol)	Reaction Stoichiometry[1]	log (K)							
				0 (°C)	25 (°C)	60 (°C)	100 (°C)	150 (°C)	200 (°C)	250 (°C)	300 (°C)
steller/10	281.733	133.1	(2.8)h2o, (0.79)alo2-, (0.39)ca+2,(0.01)na+, (2.81)sio2(aq)	-21.144	-19.432	-17.691	-16.156	-14.636	-13.444	-12.553	-12.041
stell/10-r02	281.733	133.1	(2.8)h2o, (0.79)alo2-, (0.39)ca+2,(0.01)na+, (2.81)sio2(aq)	-18.37	-16.88	-15.4	-14.12	-12.86	-11.89	-11.2	-10.87
sylvite	74.551	37.524	(1)k+, (1)cl-	0.525	0.846	1.122	1.285	1.330	1.238	1.013	0.604
tridymite	60.084	26.586	(1)sio2(aq)	-3.946	-3.572	-3.193	-2.834	-2.413	-1.995	-1.587	-1.203
hydglassfe3	48.466	20.536	(-0.0006)h+, (0.5981)sio2(aq), (0.1180)alo2-, (0.0556)na+, (0.0594)k+, (0.016)ca+2, (0.0002)mg+2, (0.0055)hfeo2(aq), (0.0783)h2o	1.646	1.462	1.209	0.978	0.759	0.584	0.415	0.211
mgso4	120.369	45.250	(1)mg+2, (1)so4-2	6.237	4.882	3.1	1.263	-0.811	-2.748	-4.677	-6.787
nano3	84.995	50.000	(1)na+, (1)no3-	-0.811	-0.206	0.403	0.88	1.275	1.518	1.651	1.665
k2so4 (arcanite)	174.260	65.500	(2)k, (1)so4-2	-2.273	-1.801	-1.469	-1.365	-1.488	-1.826	-2.365	-3.19
na2so4 (thenardite)	142.043	53.330	(2)na+, (1)so4-2	-0.35	-0.309	-0.438	-0.705	-1.15	-1.716	-2.473	-3.548

Gaseous Species	Molecular Weight (g/mol)	Molecular Diameter (m)	Reaction Stoichiometry	0 (°C)	25 (°C)	60 (°C)	100 (°C)	150 (°C)	200 (°C)	250 (°C)	300 (°C)
co2(g)	44.01	2.50E-10	(-1)h2o, (1)h+, (1)hco3-	-7.677	-7.814	-8.053	-8.357	-8.769	-9.217	-9.720	-10.339

NOTES: [1] Negative number in parenthesis indicate the species is on the left side of equation.
Minerals names or abbreviations above are those used in the database and may not exactly match names used in the text of the report. Names ending by /10 indicate the stoichiometry, molecular weight, molar volume, and log(K) values for those minerals were divided by 10 compared to original data. Glass phases glass1 and glass were used with the extended-case and base-case geochemical systems, respectively.
Data in this Attachment are associated with input file thermok1.01.dat.

Aqueous Species	Molecular Weight (g/mol)	r_{ej}	Charge	Reaction Stoichiometry[1]	0 (°C)	25 (°C)	60 (°C)	100 (°C)	150 (°C)	200 (°C)	250 (°C)	300 (°C)
Al+3	26.982	3.33	3	(-2)h2o, (1)alo2-, (4)h+	-25.795	-22.883	-19.571	-16.582	-13.676	-11.409	-9.598	-8.167
Al(OH)2+	60.996	2.31	1	(1)alo2-, (2)h+	-13.655	-12.289	-10.825	-9.600	-8.530	-7.823	-7.396	-7.238
AlOH+2	43.989	2.8	2	(-1)h2o, (1)alo2-, (3)h+	-20.068	-17.926	-15.567	-13.519	-11.625	-10.242	-9.232	-8.547
CO2(aq)	44.010	0	0	(-1)h2o, (1)h+, (1)hco3-	-6.580	-6.345	-6.268	-6.388	-6.724	-7.197	-7.787	-8.528
CO3-2	60.009	2.81	-2	(-1)h+, (1)hco3-	10.624	10.329	10.130	10.084	10.200	10.465	10.871	11.464
CaCO3(aq)	100.087	0	0	(1)ca+2, (-1)h+, (1)hco3-	7.505	7.002	6.455	5.975	5.492	5.057	4.589	3.978
CaCl+	75.531	2.31	1	(1)ca+2, (1)cl-	0.356	0.293	0.094	-0.215	-0.682	-1.227	-1.870	-2.677
CaCl2(aq)	110.983	0	0	(1)ca+2, (2)cl-	0.456	0.644	0.634	0.400	-0.118	-0.844	-1.802	-3.116
CaF+	59.076	2.31	1	(1)ca+2, (1)f-	-0.655	-0.682	-0.862	-1.171	-1.650	-2.217	-2.888	-3.728
CaHCO3+	101.095	2.31	1	(1)ca+2, (1)hco3-	-1.094	-1.047	-1.158	-1.413	-1.848	-2.383	-3.027	-3.840
CaHSiO3+	117.170	2.31	1	(-1)h+, (1)ca+2, (1)h2o, (1)sio2(aq)	8.778	8.575	8.115	7.596	7.043	6.588	6.200	5.837
CaOH+	57.085	2.31	1	(-1)h+, (1)ca+2, (1)h2o	14.085	12.833	11.416	10.142	8.903	7.928	7.126	6.434
CaSO4(aq)	136.142	0	0	(1)ca+2, (1)so4-2	-2.071	-2.111	-2.265	-2.511	-2.910	-3.433	-4.144	-5.188
Fe+3	55.845	3.46	3	(3)h+, (1)hfeo2(aq), (-2)h2o	-14.305	-12.018	-9.602	-7.594	-5.807	-4.521	-3.530	-2.696
FeCl+2	91.298	2.8	2	(1)cl-, (3)h+, (-2)h2o, (1)hfeo2	-15.770	-13.498	-11.217	-9.449	-8.047	-7.230	-6.813	-6.721
FeF+2	74.843	2.8	2	(1)f-, (3)h+, (-2)h2o, (1)hfeo2(aq)	-20.032	-18.018	-16.038	-14.546	-13.418	-12.827	-12.608	-12.697
FeF2+	93.842	2.31	1	(2)f-, (3)h+, (-2)h2o, (1)hfeo2(aq)	-22.323	-20.368	-18.459	-17.037	-16.011	-15.569	-15.590	-16.086
FeO+	71.844	2.31	1	(1)h+, (-1)h2o, (1)hfeo2(aq)	-7.324	-6.368	-5.372	-4.561	-3.865	-3.393	-3.060	-2.807
FeO2-	87.844	1.81	-1	(-1)h+, (1)hfeo2(aq)	10.231	9.602	8.839	8.111	7.381	6.822	6.430	6.249
FeOH+2	72.852	2.8	2	(2)h+, (-1)h2o, (1)hfeo2(aq)	-11.409	-9.813	-8.174	-6.853	-5.727	-4.964	-4.415	-3.979
FeSO4+	151.909	2.31	1	(1)so4-2, (3)h+, (-2)h2o, (1)hfeo2(aq)	-15.846	-13.946	-12.089	-10.700	-9.681	-9.213	-9.179	-9.602
HAlO2	59.988	0	0	(1)alo2-, (1)h+	-7.080	-6.450	-5.846	-5.409	-5.119	-5.035	-5.120	-5.384
HF	20.006	0	0	(1)f-, (1)h+	-2.985	-3.168	-3.474	-3.848	-4.338	-4.859	-5.437	-6.135
HF2-	39.005	1.81	-1	(1)h+, (2)f-	-2.238	-2.551	-2.960	-3.385	-3.880	-4.374	-4.915	-5.578
HNO3(aq)	63.013	0	0	(1)h+, (1)no3-	1.540	1.303	0.952	0.556	0.074	-0.412	-0.936	-1.579
HSiO3-	77.092	1.81	-1	(-1)h+, (1)h2o, (1)sio2(aq)	9.811	9.585	9.241	8.960	8.802	8.833	9.035	9.433
KCl(aq)	74.551	0	0	(1)cl-, (1)k+	2.840	2.536	2.141	1.731	1.255	0.785	0.278	-0.344
KHSO4(aq)	136.170	0	0	(1)h+, (1)k+, (1)so4-2	2.039	1.495	0.595	-0.476	-1.817	-3.172	-4.601	-6.242
KOH(aq)	56.106	0	0	(-1)h+, (1)h2o, (1)k+	15.498	14.439	13.314	12.378	11.552	10.978	10.570	10.267
KSO4-	135.162	1.81	-1	(1)k+, (1)so4-2	-0.886	-0.880	-0.991	-1.195	-1.521	-1.921	-2.419	-3.090
MgCO3(aq)	84.314	0	0	(-1)h+, (1)hco3-, (1)mg+2	7.742	7.350	6.929	6.574	6.228	5.911	5.543	5.019
MgCl+	59.758	2.31	1	(1)cl-, (1)mg+2	0.097	0.135	0.041	-0.173	-0.537	-0.992	-1.550	-2.276
MgF+	43.303	2.31	1	(1)f-, (1)mg+2	-1.387	-1.352	-1.478	-1.739	-2.169	-2.691	-3.321	-4.125
MgHCO3+	85.322	2.31	1	(1)hco3-, (1)mg+2	-1.077	-1.036	-1.160	-1.423	-1.852	-2.369	-2.984	-3.758
MgHSiO3+	101.397	2.31	1	(-1)h+, (1)h2o, (1)mg+2, (1)sio2(aq)	8.454	8.325	7.943	7.501	7.036	6.666	6.358	6.072
MgOH+	41.312	2.31	1	(-1)h+, (1)h2o, (1)mg+2	12.674	11.683	10.502	9.399	8.291	7.392	6.634	5.967
MgSO4(aq)	120.369	0	0	(1)mg+2, (1)so4-2	-2.184	-2.230	-2.393	-2.641	-3.031	-3.539	-4.236	-5.271
NaCO3-	82.999	1.81	-1	(-1)h+, (1)hco3-, (1)na+	9.725	9.815	9.917	10.012	10.104	10.177	10.236	10.285
NaCl(aq)	58.442	0	0	(1)cl-, (1)na+	0.829	0.777	0.651	0.473	0.214	-0.093	-0.478	-1.013
NaF(aq)	41.988	0	0	(1)f-, (1)na+	1.082	0.998	0.833	0.623	0.338	0.010	-0.397	-0.957

Aqueous Species	Molecular Weight (g/mol)	r_{ej}	Charge	Reaction Stoichiometry[1]	0 (°C)	25 (°C)	60 (°C)	100 (°C)	150 (°C)	200 (°C)	250 (°C)	300 (°C)
NaHCO3(aq)	84.007	0	0	(1)hco3-, (1)na+	-0.398	-0.154	0.075	0.244	0.358	0.374	0.277	0.004
NaHSiO3(aq)	100.081	0	0	(-1)h+, (1)h2o, (1)na+, (1)sio2(aq)	7.603	7.754	7.780	7.795	7.873	8.014	8.190	8.365
NaOH(aq)	39.997	0	0	(-1)h+, (1)h2o, (1)na+	15.132	14.205	13.210	12.377	11.642	11.130	10.762	10.480
NaSO4-	119.053	1.81	-1	(1)na+, (1)so4-2	-0.677	-0.700	-0.842	-1.063	-1.389	-1.772	-2.242	-2.873
OH-	17.007	1.4	-1	(-1)h+, (1)h2o	14.940	13.995	13.027	12.255	11.631	11.284	11.168	11.300
SiF6-2	142.076	3	-2	(-2)h2o, (1)sio2(aq), (4)h+, (6)f-	-27.654	-26.275	-25.220	-24.654	-24.534	-24.919	-25.819	-27.436

Primary Aqueous Species	Molecular Weight (g/mol)	r_{ej}	Charge
H2O	18.015	0.00	0
AlO2-	58.980	1.81	-1
Ca+2	40.078	2.87	2
Cl-	35.453	1.81	-1
F-	18.998	1.33	-1
H+	1.008	3.08	1
HCO3-	61.017	2.10	-1
HFeO2(aq)	88.852	0.00	0
K+	39.098	2.27	1
Mg+2	24.305	2.54	2
Na+	22.990	1.91	1
NO3-	62.005	2.81	-1
SiO2(aq)	60.084	0.00	0
SO4-2	96.064	3.15	-2

ATTACHMENT VII – WASTE PACKAGE AVERAGE HEAT TRANSFER: All REV01 THC Seepage Models

(DTN: LB0101DSTTHCR1.007 [161281])

Time (years)	Total Heat (no ventilation) (W/meter)	Model Heat Load (W/meter)
0.01	1450.000	435.000
0.02	1448.649	434.595
0.03	1447.802	434.341
0.04	1446.966	434.090
0.05	1446.126	433.838
0.06	1445.292	433.587
0.07	1444.468	433.340
0.08	1443.617	433.085
0.09	1442.813	432.844
0.1	1441.979	432.594
0.15	1437.970	431.391
0.2	1434.003	430.201
0.25	1430.183	429.055
0.3	1426.428	427.928
0.35	1422.757	426.827
0.4	1419.171	425.751
0.45	1415.657	424.697
0.5	1412.230	423.669
0.55	1408.866	422.660
0.6	1405.590	421.677
0.65	1402.353	420.706
0.7	1399.207	419.762
0.75	1396.090	418.827
0.8	1393.072	417.922
0.85	1390.093	417.028
0.9	1387.169	416.151
0.95	1384.277	415.283
1.0	1381.471	414.441
1.5	1355.408	406.623
2.0	1332.834	399.850
2.5	1312.844	393.853
3.0	1294.686	388.406
3.5	1278.327	383.498
4.0	1263.118	378.935
4.5	1248.692	374.608
5.0	1235.091	370.527
5.5	1220.694	366.208
6.0	1207.008	362.102
6.5	1194.297	358.289
7.0	1182.135	354.641

Data from DTN: SN9907T0872799.001 [111485] multiplied by 1450/1540.413 (Total Heat) to reflect a design change at the time of REV01 work.

NOTE: Point at 50.001 years was interpolated between original data points at 50 and 55 years. From 0 to 50 years: Model Heat Load = Total Heat x 0.3 (70% heat removal)

Time (years)	Total Heat (no ventilation) (W/meter)	Model Heat Load (W/meter)
7.5	1169.685	350.905
8.0	1157.754	347.326
8.5	1146.156	343.847
9.0	1134.992	340.498
9.5	1123.659	337.098
10	1112.692	333.808
15	1011.525	303.458
20	925.760	277.728
25	848.670	254.601
30	781.226	234.368
35	721.996	216.599
40	668.553	200.566
45	620.521	186.156
50	578.485	173.545
50.001	578.477	578.477
55	540.350	540.350
60	506.148	506.148
65	475.148	475.148
70	448.192	448.192
75	422.908	422.908
80	400.854	400.854
85	380.461	380.461
90	362.592	362.592
95	345.744	345.744
100	331.164	331.164
150	238.417	238.417
200	196.608	196.608
250	172.037	172.037
300	155.179	155.179
350	142.089	142.089
400	131.355	131.355
450	122.099	122.099
500	114.135	114.135
550	106.970	106.970
600	100.772	100.772
650	95.156	95.156
700	89.938	89.938
750	85.321	85.321
800	80.938	80.938
850	76.894	76.894

Data from DTN: SN9907T0872799.001 [111485] multiplied by 1450/1540.413 (Total Heat) to reflect a design change at the time of REV01 work.

NOTE: Point at 50.001 years was interpolated between original data points at 50 and 55 years. From 0 to 50 years: Model Heat Load = Total Heat x 0.3 (70% heat removal)

Time (years)	Total Heat (no ventilation) (W/meter)	Model Heat Load (W/meter)
900	73.190	73.190
950	69.859	69.859
1000	66.992	66.992
1500	46.231	46.231
2000	36.450	36.450
2500	31.644	31.644
3000	28.693	28.693
3500	26.993	26.993
4000	25.815	25.815
4500	24.684	24.684
5000	23.772	23.772
5500	22.783	22.783
6000	22.211	22.211
6500	21.355	21.355
7000	20.624	20.624
7500	20.091	20.091
8000	19.347	19.347
8500	18.777	18.777
9000	18.174	18.174
9500	17.630	17.630
10000	17.079	17.079
15000	12.774	12.774
20000	10.009	10.009
25000	8.089	8.089
30000	6.615	6.615
35000	5.561	5.561
40000	4.774	4.774
45000	4.148	4.148
50000	3.641	3.641
55000	3.180	3.180
60000	2.862	2.862
65000	2.514	2.514
70000	2.282	2.282
75000	2.063	2.063
80000	1.869	1.869
85000	1.710	1.710
90000	1.593	1.593
95000	1.470	1.470
100000	1.372	1.372

Data from DTN: SN9907T0872799.001 [111485] multiplied by 1450/1540.413 (Total Heat) to reflect a design change at the time of REV01 work.

NOTE: Point at 50.001 years was interpolated between original data points at 50 and 55 years. From 0 to 50 years: Model Heat Load = Total Heat x 0.3 (70% heat removal)

INTENTIONALLY LEFT BLANK

ATTACHMENT VIII – WASTE PACKAGE AVERAGE HEAT TRANSFER: Tptpll THC Model REV02

Time (years)	Total Heat (no ventilation) (W/meter)	Model Heat Load (W/meter)
0	1450.000	198.650
1	1400.000	191.800
2	1360.000	186.320
3	1320.000	180.840
4	1290.000	176.730
5	1260.000	172.620
6	1230.000	168.510
7	1210.000	165.770
8	1180.000	161.660
9	1160.000	158.920
10	1140.000	156.180
11	1110.000	152.070
12	1090.000	149.330
13	1070.000	146.590
14	1050.000	143.850
15	1030.000	141.110
16	1010.000	138.370
17	995.000	136.315
18	978.000	133.986
19	961.000	131.657
20	946.000	129.602
21	929.000	127.273
22	912.000	124.944
23	897.000	122.889
24	882.000	120.834
25	868.000	118.916
26	854.000	116.998
27	840.000	115.080
28	826.000	113.162
29	813.000	111.381
30	801.000	109.737
31	787.000	107.819
32	775.000	106.175
33	762.000	104.394
34	751.000	102.887
35	740.000	101.380
36	728.000	99.736
37	716.000	98.092
38	706.000	96.722
39	695.000	95.215
40	685.000	93.845
41	675.000	92.475

Time (years)	Total Heat (no ventilation) (W/meter)	Model Heat Load (W/meter)
42	665.000	91.105
43	655.000	89.735
44	646.000	88.502
45	636.000	87.132
46	627.000	85.899
47	618.000	84.666
48	609.000	83.433
49	601.000	82.337
50	593.000	81.241
50.001	593.000	593.000
51	585.000	585.000
52	577.000	577.000
53	569.000	569.000
54	561.000	561.000
55	554.000	554.000
56	547.000	547.000
57	539.000	539.000
58	532.000	532.000
59	526.000	526.000
60	519.000	519.000
61	512.000	512.000
62	506.000	506.000
63	500.000	500.000
64	494.000	494.000
65	488.000	488.000
66	482.000	482.000
67	476.000	476.000
68	470.000	470.000
69	465.000	465.000
70	460.000	460.000
71	454.000	454.000
72	449.000	449.000
73	444.000	444.000
74	439.000	439.000
75	434.000	434.000
76	430.000	430.000
77	425.000	425.000
78	420.000	420.000
79	416.000	416.000
80	412.000	412.000
81	407.000	407.000
82	403.000	403.000
83	399.000	399.000
84	395.000	395.000
85	391.000	391.000
86	387.000	387.000
87	383.000	383.000

Time (years)	Total Heat (no ventilation) (W/meter)	Model Heat Load (W/meter)
88	379.000	379.000
89	376.000	376.000
90	372.000	372.000
91	369.000	369.000
92	365.000	365.000
93	362.000	362.000
94	359.000	359.000
95	355.000	355.000
96	352.000	352.000
97	349.000	349.000
98	346.000	346.000
99	343.000	343.000
100	340.000	340.000
110	315.000	315.000
120	294.000	294.000
140	259.000	259.000
150	245.000	245.000
160	235.000	235.000
170	225.000	225.000
180	216.000	216.000
190	208.000	208.000
200	201.000	201.000
250	176.000	176.000
300	159.000	159.000
350	145.000	145.000
400	134.000	134.000
450	125.000	125.000
500	117.000	117.000
550	110.000	110.000
600	103.000	103.000
650	97.300	97.300
700	92.100	92.100
750	87.200	87.200
800	82.800	82.800
850	78.800	78.800
900	75.000	75.000
950	71.600	71.600
1000	68.400	68.400
1500	47.300	47.300
2000	37.200	37.200
2500	32.100	32.100
3000	29.300	29.300
3500	27.500	27.500
4000	26.200	26.200
4500	25.200	25.200
5000	24.200	24.200
5500	23.400	23.400

Time (years)	Total Heat (no ventilation) (W/meter)	Model Heat Load (W/meter)
6000	22.600	22.600
6500	21.800	21.800
7000	21.100	21.100
7500	20.500	20.500
8000	19.800	19.800
8500	19.200	19.200
9000	18.600	18.600
9500	18.000	18.000
10000	17.500	17.500
15000	13.200	13.200
20000	10.200	10.200
25000	8.210	8.210
30000	6.760	6.760
35000	5.680	5.680
40000	4.850	4.850
45000	4.190	4.190
50000	3.680	3.680
55000	3.250	3.250
60000	2.880	2.880
65000	2.580	2.580
70000	2.330	2.330
75000	2.110	2.110
80000	1.910	1.910
85000	1.750	1.750
90000	1.640	1.640
95000	1.520	1.520
100000	1.400	1.400

Source: BSC (2002 [159527], Sheet 5 of 5) (see Section 4.1.7)

NOTE: Point at 50.001 years was interpolated between original data points at 50 and 55 years. From 0 to 50 years: Model Heat Load = Total Heat x (1-0.863) [86.3% heat removal]

ATTACHMENT IX – EFFECTIVE THERMAL CONDUCTIVITY FOR IN-DRIFT OPEN SPACES: Tptpmn and Tptpll THC Models

Pre-closure

Time (sec)	Time (year)	Factor
3.15360E+03	0.0	0.395
3.15360E+07	1.0	0.777
4.73040E+07	1.5	0.825
6.30720E+07	2	0.856
9.46080E+07	3	0.898
1.26144E+08	4	0.921
1.57680E+08	5	0.939
1.89216E+08	6	0.955
2.20752E+08	7	0.966
2.52288E+08	8	0.975
2.83824E+08	9	0.982
3.15360E+08	10	0.988
3.46896E+08	11	0.993
3.78432E+08	12	0.997
4.73040E+08	15	1
6.30720E+08	20	0.993
7.88400E+08	25	0.977
8.19936E+08	26	0.974
8.51472E+08	27	0.97
9.46080E+08	30	0.958
1.10376E+09	35	0.936
1.26144E+09	40	0.915
1.57680E+09	50	0.879

DTN: SN0002T0872799.009 [153364]

NOTE: $K_{thermal}$ is calculated as Max. $K_{thermal}$ x Factor

Maximum $K_{thermal}$ (W/m-K) = 10.568

Post-closure (No Backfill)

Time		Factor	
(sec)	**(year)**	**Inner**	**Outer**
1.57680E+09	50	0.879	0.879
1.608336E+09	51	0.844	0.829
1.639872E+09	52	0.892	0.878
1.734480E+09	55	0.951	0.944
1.892160E+09	60	0.988	0.986
2.049840E+09	65	1	1
2.207520E+09	70	0.995	0.998
2.365200E+09	75	0.985	0.99
2.396736E+09	76	0.983	0.988
2.428272E+09	77	0.981	0.986
2.522880E+09	80	0.973	0.98
2.838240E+09	90	0.954	0.963
3.153600E+09	100	0.932	0.943
3.185136E+09	101	0.929	0.941
3.311280E+09	105	0.918	0.929
3.468960E+09	110	0.905	0.917
3.784320E+09	120	0.882	0.896
4.099680E+09	130	0.872	0.886
4.415040E+09	140	0.864	0.879
5.045760E+09	160	0.852	0.869
5.676480E+09	180	0.839	0.857
6.307200E+09	200	0.83	0.849
6.937920E+09	220	0.818	0.838
7.884000E+09	250	0.798	0.818
9.460800E+09	300	0.763	0.784
1.103760E+10	350	0.736	0.758
1.261440E+10	400	0.707	0.729
1.419120E+10	450	0.689	0.711
1.576800E+10	500	0.677	0.7
1.734480E+10	550	0.672	0.694
1.892160E+10	600	0.667	0.69
2.207520E+10	700	0.656	0.68
2.522880E+10	800	0.646	0.67
2.838240E+10	900	0.637	0.661

DTN: SN0002T0872799.009 [153364]

NOTE: $K_{thermal}$ is calculated as Max. $K_{thermal}$ x Factor

Maximum $K_{thermal}$ (W/m-K) Inner=2.298,

Outer=14.407

Post-closure (No Backfill) (Cont.)

Time		Factor	
(sec)	(year)	Inner	Outer
3.153600E+10	1000	0.627	0.651
3.468960E+10	1100	0.619	0.643
3.784320E+10	1200	0.611	0.635
4.099680E+10	1300	0.602	0.626
4.415040E+10	1400	0.592	0.616
4.730400E+10	1500	0.582	0.605
5.045760E+10	1600	0.574	0.597
5.676480E+10	1800	0.559	0.583
6.307200E+10	2000	0.543	0.566
6.937920E+10	2200	0.533	0.555
7.884000E+10	2500	0.519	0.541
9.460800E+10	3000	0.503	0.523
1.103760E+11	3500	0.491	0.51
1.261440E+11	4000	0.48	0.499
1.419120E+11	4500	0.472	0.491
1.576800E+11	5000	0.465	0.484
1.892160E+11	6000	0.453	0.471
2.207520E+11	7000	0.444	0.461
2.522880E+11	8000	0.436	0.452
3.153600E+11	10000	0.422	0.438
4.730400E+11	15000	0.395	0.411
6.307200E+11	20000	0.378	0.393
9.460800E+11	30000	0.354	0.367
1.261440E+12	40000	0.341	0.354
1.576800E+12	50000	0.333	0.346
1.892160E+12	60000	0.326	0.339
2.522880E+12	80000	0.318	0.33
3.153600E+12	100000	0.314	0.325

DTN: SN0002T0872799.009 [153364]
NOTE: $K_{thermal}$ is calculated as Max. $K_{thermal}$ x Factor
Maximum $K_{thermal}$ (W/m-K) Inner=2.298, Outer=14.407

INTENTIONALLY LEFT BLANK

ATTACHMENT X – LIST OF MODEL INPUT AND OUTPUT FILES

X.1. REV01 INPUT AND OUTPUT FILES

These files were submitted with REV01 of this Model Report to the TDMS under DTN: LB0011DSTTHCR1.002 [161282].

1. Input and output files of simulations with the reactive transport model TOUGHREACT V2.3 (LBNL 2001 [153101]). For each simulation, these files were concatenated into one file using the Unix *tar* utility then compressed using the Unix *gzip* utility. Resulting concatenated/compressed files have the extension *.tar.gz*.

2. Summary Excel spreadsheets of seepage models output data at three locations adjacent to the drift wall (crown, side, and base).

3. Spreadsheets containing calculations have been included as part of several DTNs in order to document the embedded calculations and supplement the Scientific Notebooks. READ.ME files are also included which outline the use of calculations in each spreadsheet. The calculations can be observed by clicking on the spreadsheet cells or selecting the "Tools\Options\View\Formulas" option in MS Excel. In addition, the cell references in the equations show all cells used as input to the calculation executed in the spreadsheet. The formulae in the submitted spreadsheets use the standard functions of MS Excel 97.

<u>DST THC Model REV01 Input and Output File Folders (Simulations in Section 7.1.8.1)</u>

dst00_amr1 Base Case CC Kin
dst00_amr2 Extended CC Kin
dst00_amr3 Base Case CC Eq
dst00_amr4 Extended CC Eq
dst00_amr5 Extended An Full
dst00_amr6 Base Case No CC

More complete descriptions can be found in Section 7.1.8.1.

<u>Tptpmn THC Model REV01 Input and Output File Folders (Simulations in Table 6.5-4)</u>

th6_3_r (_, _a, _b, _c, _d)
th6_16_25_7 (_, _a, _b, _c, _d)
thc6_16_25_9 (_, _a, _b, _c, _d)
thc6_16_25_9_amb (_, _a, _b, _c, _d)
thc6_16_25_10 (_, _a, _b, _c, _d)
thc6_16_25_10_amb (_, _a, _b, _c, _d)

Tptpmn Heterogeneous THC Model REV01 Input and Output File Folders (Simulations in Table 6.6-1)

ds00ss_het1
ds00th_het1(_, _a, _b, _c)
ds00amb1_het1 (_, _a, _b, _c, _d)
ds00amb2_het1 (_, _a, _b, _c, _d)
ds00thc1_het1 (_, _a, _b, _c, _d)
ds00thc2_het1 (_, _a, _b, _c, _d)
ds00ss_het2
ds00th_het2 (_, _a, _b, _c)
ds00thc1_het2 (_, _a, _b, _c, _d)
ds00thc2_het2 (_, _a, _b, _c, _d)
ds00ss_het3
ds00th_het3 (_, _a, _b, _c)
ds00thc1_het3 (_, _a, _b, _c, _d)
ds00thc2_het3 (_, _a, _b, _c, _d)

Tptpll THC Model REV01 Input and Output File Folders (Simulations in Table 6.7-3)

th6_16_25_g4 (_, _a, _b, _c, _d)
thc6_16_25_2g4 (_, _a, _b, _c, _d)
thc6_16_25_2g4_amb (_, _a, _b, _c, _d)
thc6_16_25_g4 (_, _a, _b, _c, _d)
thc6_16_25_g4_amb (_, _a, _b, _c, _d)

X.2. REV02 INPUT AND OUTPUT FILES

The following types of files were submitted for REV02 of this Model Report to the TDMS under DTN: LB0307DSTTHCR2.001 and LB0302DSCPTHCS.001.

1. Input and output files of simulations with the reactive transport code TOUGHREACT V3.0 (LBNL 2002 [161256]). For each simulation, these files were concatenated into one file using the Unix *tar* utility then compressed using the Unix *gzip* utility. Resulting concatenated/compressed files have the extension *.tar.gz*.

2. Summary Excel spreadsheets of seepage models output data at three locations adjacent to the drift wall (crown, side, and base).

3. Spreadsheets containing calculations have been included as part of several DTNs in order to document the embedded calculations and supplement the Scientific Notebooks. READ.ME files are also included which outline the use of calculations in each spreadsheet. The calculations can be observed by clicking on the spreadsheet cells or selecting the “Tools\Options\View\Formulas” option in MS Excel. In addition, the cell references in the equations show all cells used as input to the calculation executed in the spreadsheet. The formulae in the submitted spreadsheets use the standard functions of MS Excel 97.

DST THC Model REV02 Input and Output File Folders (Simulations in Section 7.1.8.2)
(DTN: LB0307DSTTHCR2.001)
dstrev2_th12
dstrev2_th13
dstrev2_thc7
dstrev2_thc8
dstrev2_thc9

More complete descriptions can be found in Section 7.1.

Tptpll THC Model REV02 Input and Output File Folders (Simulations listed in Table 6.8-4)

(DTN: LB0307DSTTHCR2.001)
th6_1.45kw (_, _a, _b, _c)
thc6_w0e3 (_, _a, _b2, _b, bb, _c, _d)
thc6_w0a (_b, _c, _d)
thc6_w0b (_, _a, _b, _bb, _c, _d)
thc25_w0 (_, _a, _b, _c, _d)
thc6_w0_q
thc6_w0_q1
thc6_w0amb
thc6_w0amb1
thc6_w4amb1
thc6_w5amb1
thc6_w6amb1

(DTN: LB0302DSCPTHCS.001)
thc6_w0 (_, _a, _b, _bb, _c, _d)
thc6_w4 (_, _a, _b, _bb, _c, _d)
thc6_w5 (_, _a, _b, _bb, _c, _d)
thc6_w6 (_, _a, _b, _bb, _c, _d)
thc6_w7 (_, _a, _b, _bb, _c, _d)

X.3. CONTENTS OF *.tar.gz* FILES (NOTE: SOME FILE NAMES ARE LOWERCASE IN TOUGHREACT V3.0 (LBNL 2002 [161256]) AND UPPERCASE IN EARLIER VERSIONS)

flow.inp	Rock thermal and hydrological properties, run flags and other specifications (input)
flow.out	Thermal and hydrological results (gas/liquid saturation, T, P, air mass fraction, etc.) (output)
GENER	Infiltration rates, heat load, and effective thermal conductivity (input)
INCON	Initial thermal and hydrological conditions (T, P, liquid saturation, etc.) (input)
MESH	Input numerical mesh (input)

SAVE	Thermal and hydrological conditions (T, P, liquid saturation, etc.) to use for restarting a run (output, same format as INCON file)
TABLE	Miscellaneous output data
VERS	Miscellaneous output data
LINEQ	Miscellaneous output data
CHEMICAL.INP	Water chemistry, mineralogy, and CO_2 partial pressure data (input)
CHEMICAL.OUT	Echo of data read in CHEMICAL.INP
SOLUTE.INP	Run flags and other data relating to reactive transport (input)
SOLUTE.OUT	Echo of data read in SOLUTE.INP
thermk1.01.dat	Thermodynamic database for REV02 (input). Note: The solid KNO3 in this file is actually NaNO3.
TEC_CONC.DAT	Calculated concentrations of aqueous species (moles/liter) at each grid node (two records for each node - first record for fractures and second record for matrix) (output)
TEC_MIN.DAT	Calculated volume fraction change for minerals at each grid node (two records for each node - first record for fractures and second record for matrix) (output)
TEC_GAS.DAT	Calculated CO_2 volume fraction at each grid node (two records for each node - first record for fractures and second record for matrix) (output)
TIME.DAT	Chemical data at selected grid nodes (output)
chdump.dat	Chemical speciation of initial water (output) and nodes with convergence problems
inchem	Chemistry data at all grid nodes to use for restarting a run (input)
savechem	Chemistry data at all grid nodes to use for restarting a run (output, same format as INCHEM file)
ITER.DAT	Iteration information (output)
runlog.dat (run_log.dat)	Miscellaneous run-time information. Note: mass balances may not be printed out correctly in this file for runs that have been restarted (i.e., starting at times different than zero).
mbalance.out	Mass balance information for chemical species Note: mass balances may not be accurate for runs that have been restarted (i.e., starting at times different than zero). Also, mass balances do not reflect mass loss by transport into large boundary grid blocks.
GASOBS.DAT	optional tabular flow output for individual grid blocks

X.4. SUMMARY SPREADSHEETS OF THC SEEPAGE MODELS OUTPUT DATA (ALSO USED FOR PLOTTING TIME PROFILES AND TABULATING STANDARD DEVIATION)

The data in these files were extracted from output files FLOW.OUT, TEC_CONC.DAT, TEC_MIN.DAT, and TEC_GAS.DAT for each simulation and submitted to the TDMS under DTN: LB0011DSTTHCR1.001 [154759], LB0302DSCPTHCS.002, and LB0307DSTTHCR2.002.

<u>Tptpmn THC Model REV01 (TOUGHREACT V2.3 (LBNL 2001 [153101])):</u>
(DTN: LB0011DSTTHCR1.001 [154759])

th6_7.xls	TH, 6/16/25 mm/year infiltration

thc6_9base.xls	THC, base-case, 6/16/25 mm/year infiltration
thc6_9base_amb.xls	THC, no heat load, base-case, 6/16/25 mm/year infiltration
thc6_10ext.xls	THC, extended-case, 6/16/25 mm/year infiltration
thc6_10ext_amb.xls	THC, no heat load, extended-case, 6/16/25 mm/year infiltration

Tptpll THC Model REV01 (TOUGHREACT V2.3 (LBNL 2001 [153101])):
(DTN: LB0011DSTTHCR1.001 [154759])

th6_g4.xls	TH, 6/16/25 mm/year infiltration
thc6_2g4base.xls	THC, base-case, 6/16/25 mm/year infiltration
thc6_2g4base_amb.xls	THC, no heat load, base-case, 6/16/25 mm/year infiltration
thc6_2g4ext.xls	THC, extended-case, 6/16/25 mm/year infiltration
thc6_2g4ext_amb.xls	THC, no heat load, extended-case, 6/16/25 mm/year infiltration

Tptpll THC Model REV02 (TOUGHREACT V3.0 (LBNL 2002 [161256]))
(extended-case only, simulations details listed in Table 6.8-4)

(DTN: LB0302DSCPTHCS.002)

thc6_w0_r.xls	THC, Water W0, 6/16/25 mm/year (track wet nodes)
thc6_w0_drift_r.xls	THC, Water W0, 6/16/25 mm/year (drift wall only)
thc6_w4_r.xls	THC, Water W4, 6/16/25 mm/year (track wet nodes)
thc6_w4_drift_r.xls	THC, Water W4, 6/16/25 mm/year (drift wall only)
thc6_w5_r.xls	THC, Water W5, 6/16/25 mm/year (track wet nodes)
thc6_w5_drift_r.xls	THC, Water W5, 6/16/25 mm/year (drift wall only)
thc6_w6_r.xls	THC, Water W6, 6/16/25 mm/year (track wet nodes)
thc6_w6_drift_r.xls	THC, Water W6, 6/16/25 mm/year (drift wall only)
thc6_w7_r.xls	THC, Water W7, 6/16/25 mm/year (track wet nodes)
thc6_w7_drift_r.xls	THC, Water W7, 6/16/25 mm/year (drift wall only)

(DTN: LB0307DSTTHCR2.002)

th6_1.45kw.xls	TH, 6/16/25 mm/year
thc25_w0.xls	THC, Water W0, 25 mm/year (track wet nodes)
thc25_w0_drift.xls	THC, Water W0, 25 mm/year (drift wall only)
thc6_w0e3.xls	THC, Water W0, 6/16/25 mm/year, EOS3 (track wet nodes)
thc6_w0e3_drift.xls	THC, Water W0, 6/16/25 mm/year, EOS3 (drift wall only)
thc6_w0b.xls	THC, Water W0, 6/16/25 mm/year, D_{CO2} change (track wet nodes)
thc6_w0b_drift.xls	THC, Water W0, 6/16/25 mm/year, D_{CO2} change (drift wall only)
thc6_w0a.xls	THC, Water W0, 6 mm/year (track wet nodes)
thc6_w0a_drift.xls	THC, Water W0, 6 mm/year (drift wall only)
thc6_w0_amb1.xls	THC, Water W0, no heat load, 6/16/25 mm/year (drift wall only)
wo_4_5_6_7.xls	THC, Water W0, W4, W5, W6, and W7, 6/15/25 mm/year, track wet nodes (concentrations of data from files listed above under DTN: LB0302DSCPTHCS.002)
hisat_top-w04567.xls	Filtered data from w0-4-5-6-7.xls, used to tabulate standard deviations in Table 6.9-2.

X.5. PLUG FLOW REACTOR EXPERIMENT, REV01 (SECTION 7.3)

Input and output files for this section were submitted to the TDMS as DTN: LB0011THCDISSM.001 [153381] and DTN: LB0011THCDISSM.002 [154578], respectively. The input files (for DTN: LB0011THCDISSM.001 [153381]) consist of SOLVEQ/CHILLER V1.0 (LBNL 1999 [153217]) files used to calculate the initial water composition for the simulations, along with the input files for two TOUGHREACT V2.2 (LBNL 1999 [153219]) simulations and three TOUGHREACT V2.3 (LBNL 2001 [153101]) simulations. The output files (for DTN: LB0011THCDISSM.002 [154578]) consist of the output files for the TOUGHREACT V2.2 (LBNL 1999 [153219]) and V2.3 (LBNL 2001 [153101]) simulations, and SOLVEQ/CHILLER V1.0 (LBNL 1999 [153217]) files used to correct for degassing and cooling. The files for each of the DTNs were grouped into folders (one for each simulation, plus additional folders for the SOLVEQ/CHILLER runs), and these were compressed using the Windows *Winzip* V7.0 utility. A Word 97 document (LB0011THCDISSM.00# notes.doc) describing the information contained in each DTN file was included in the compressed master file for each DTN.

A common model mesh was used for all of the simulations. The mesh was generated using the file *plugmesh* and TOUGH2 V1.4 (LBNL 2000 [146496]), resulting in the output file *plugmesh.mes*. This file was edited and incorporated in the FLOW.INP file used in each simulation.

Each of the TOUGHREACT simulations is grouped in a distinct folder. These are as follows:

simulation1input	TOUGHREACT V2.2 (LBNL 1999 [153219]), 60 μm diameter grain size surface area model, potassium feldspar as microcline
simulation2input	TOUGHREACT V2.2 (LBNL 1999 [153219]), 120 μm diameter grain size surface area model, potassium feldspar as microcline

X.5.1 PLUG FLOW SIMULATIONS, REV02 (SECTION 7.2)

Output data were compiled and graphically represented in the file plugflow_data.xls in the new Output-DTN: LB0301PLUGFLOW.001. Alkalinity data (represented as mg/L calcite) were corrected as described in Wang 2003 ([161665], SN-LBNL-SCI-190-V2, p. 85) to account for an error in conversion from moles of bicarbonate to moles of calcium carbonate (two moles of bicarbonate per mole of carbonate are needed to achieve the proper milliequivalence). This correction results in a closer match between experimental and simulated alkalinity values. Experimental data for all collection times (not just after 11 days) are portrayed in the updated plots
(Figures 7.2-3a through 7.2-3f).

X.5.2 FRACTURE SEALING SIMULATIONS, REV 02 (SECTION 7.3)

The following types of files were submitted for REV02 of this Model Report to the TDMS under Output-DTN: LB0301FRACSEAL.001.

> Input files of simulations with the reactive transport model TOUGHREACT V2.4 (LBNL 2001 [160880]). Each simulation contains the input files CHEMICAL.INP, FLOW.INP, and SOLUTE.INP.
>
> Output files of simulations with the reactive transport model TOUGHREACT V2.4 (LBNL 2001 [160880]). Each simulation contains the output files CHEMICAL.OUT, FLOW.OUT, SOLUTE.OUT, TEC_CONC.DAT, TEC_GAS.DAT, and TEC_MIN.DAT.

Data summary files with graphs were submitted to the TDMS under Output-DTN: LB0301FRACSEAL.002. Data from the TEC_MIN.DAT output files were compiled, edited, and graphically represented in the files T2d5cmin.xls and T2d5c1min.xls.

INTENTIONALLY LEFT BLANK

ATTACHMENT XI – REV02 PARAMETERS FOR FRACTURE PERMEABILITY MODIFICATION

Rock Unit	a-parameter	b-parameter
tcw11	1.5385E-02	1.0870
tcw12	1.2696E-03	0.5236
tcw13	3.4483E-03	0.3584
ptn21	9.2000E-03	1.4925
ptn22	7.0922E-03	2.1739
ptn23	1.2000E-03	1.7544
ptn24	2.9412E-02	2.1739
ptn25	5.0459E-03	1.9231
ptn26	8.7079E-04	1.0309
tsw31	1.2953E-03	0.4608
tsw32	2.5857E-03	0.8929
tsw33	1.3063E-03	1.2346
tsw34	6.2777E-04	0.2315
tsw35	9.9174E-04	0.3165
tsw3[67]	1.0561E-03	0.2488
tsw38	8.2459E-04	0.2294
tsw39	1.4576E-03	1.0417
ch1Ze	1.4545E-03	25.0000
ch1VI	2.0333E-03	10.0000
ch[23456]VI	1.7907E-03	7.1429
ch[2345]Ze	8.6047E-04	7.1429
ch6	1.4545E-03	25.0000
pp4	8.6047E-04	7.1429
pp3	1.5902E-03	5.0000
pp2	1.5902E-03	5.0000
pp1	8.6047E-04	7.1429
bf3	1.5902E-03	5.0000
bf2	8.6047E-04	7.1429
tr3	1.5902E-03	5.0000
tr2	8.6047E-04	7.1429

NOTE: The calculation and use of the *a* and *b* parameters are presented in Section 6.4.4.2. Parameter *a* (b_g) is calculated using Equation 6.4-20. Parameter *b* is the inverse of the fracture frequency (derived from DTN: LB0205REVUZPRP.001 [159525]).

INTENTIONALLY LEFT BLANK